Author:
Smith, Samantha Lisa

Title:
The geochemistry and geomicrobiology of a salinity-stratified coastal carbonate aquifer : Yucatan Peninsula, Mexico

The Geochemistry and Geomicrobiology of a Salinity-Stratified Coastal Carbonate Aquifer: Yucatan Peninsula, Mexico

Samantha Lisa Smith

Department of Earth Sciences

A thesis submitted to the University of Bristol in accordance with the requirements of the degree of Ph.D. in the Faculty of Science

July 2004

72,726 words

Abstract

Geochemical and geomicrobiological data combined with *in situ* experiments and numerical modeling were used to assess the rates and distribution of modern carbonate diagenesis along the east coast of the Yucatan Peninsula platform (Mexico). The platform hosts a salinity-stratified aquifer where a thin meteoric lens is separated from underlying saline water by a well-defined mixing zone. An extensive network of flooded caves discharges brackish lens water to the Caribbean Sea, while seawater flows into the caves at depth.

Lens waters are enriched in calcium (Ca_{XS} = 2.19 ± 0.55 mM, n = 77) relative to the dilution of seawater. However, within the 'freshwater system', the majority (61%) of $CaCO_3$ dissolution occurs in the 10 m-thick vadose zone due to high ground air pCO_2 (~1.18%). Ca_{XS} combined with recharge estimates indicate a vadose dissolution rate of 22.9 metric tons/km^2/a (porosity generation = 8.64×10^{-4}%/a). Some (~9.5% of the total) dissolution may also occur in lens waters due to organic matter oxidation, however precipitation in the upper lens *via* degassing and mixing with the lens base is also likely.

Comparatively, dissolution potential is enhanced in the fresh-salt water mixing zone, however, geochemical modeling alone cannot explain the locus or extent of undersaturation. Model results from the mixing of brackish and saline water estimate maximum calcite undersaturation at ~75% seawater (SW), while field data shows two zones of undersaturation. These zones occur near the top (~35% SW) and bottom (~95% SW) of the mixing zone and *in situ* dissolution experiments reveal associated enhanced calcite dissolution. The maintenance of undersaturation is driven by increases in bacterial activity (evidenced by increases in inferred reproduction rates, decreases in pH and dissolved oxygen and increases in pCO_2). Most bacteria are heterotrophs, although acid-producing sulfur-oxidising bacteria (SOX) may also be important in driving undersaturation. Where bacterial activity approaches zero, calcite saturation (SI-C) approaches equilibrium. Despite the thermodynamic potential for Dorag dolomitisation within some (~50-80% SW) mixing zone waters, no significant amount of dolomite is found in the associated wall-rock and Mg^{2+} and Ca^{2+} concentrations are not significantly different from those expected from fresh-salt water mixing.

However, replacement dolomitisation may occur in the underlying saline zone where waters are depleted of magnesium (Mg_{XS} = -1.16 ± 3.31 mM) and enriched in calcium (Ca_{XS} = +1.24 ± 3.01 mM) (n = 48). This study offers a unique insight into the diagenetic processes within the zone of saline groundwaters and geochemical data reveal that there are two distinct 'sub-zones': shallow (<40 m water depth) and deep (>40 m). In the shallow saline zone, bacteria continue to maintain calcite undersaturation *via* organic matter breakdown and pCO_2 production, although the shallow saline groundwaters remain supersaturated with respect to disordered dolomite. In this zone, dolomitisation may also be associated with the (bacterial?) re-oxidation of reduced sulfur species (SO_{4XS} = +0.82 ± 0.40 mM, n = 34). In the deep saline zone, however, sulfate enrichment is due to the dissolution of anhydrite (AN) clasts within breccia deposits located ≥~110 m below the surface (evidenced by Ca_{XS}:SO_{4XS} ratios, $\delta^{34}S$-SO_4^{2-} values and SI-AN increases with depth). Concurrent Mg^{2+} depletions and positive Ca_{XS} (beyond that due to $CaSO_4$ dissolution) indicate replacement dolomitisation is also occurring. Petrographic results suggest wall-rock dolomite does not occur outside the saline zone, and may only occur at coastal sites, the dolomites are of seawater origin and that the amount of dolomite increases where there is interconnected porosity, reinforcing the importance of Mg-rich fluid circulation. Five shallow saline zone sites have chemistries resembling the deep saline zone. These 'outliers' may offer insight into deep saline zone circulation patterns, where upwelling of geothermally-heated water occurs through regions of increased cavernous porosity rock in response to outflowing lens waters at low tide. This brackish water outflow also results in a compensatory east to west inflow of seawater at depth. This circulation 'pattern' explains the previously unexplained co-variance of maximum saline groundwater inflow rates with low tide and minimum inflow rates with high tide.

Acknowledgements

First and foremost, I would like to thank my advisors, Dr. Fiona Whitaker and Prof. John Parkes (Cardiff University) for the patience, guidance and insight they have offered throughout the course of my Ph.D. In addition, this thesis has benefited from useful discussions with Prof. Peter Smart, Dr. Ed Hornibrook, Dr. Jim Hendry, Dr. Ron Stoessell, Dr. Luis Marin and Dr. Tom Illiffe.

Many thanks, also, to Patricia A. Beddows (Trish) for introducing me to the Yucatan Peninsula in the first place (who says two months can't change your life?). This thesis was carried out alongside Trish's, which investigated the hydrology of the Yucatan Peninsula.

For funding, I thank: University of Bristol Full Scholarship and Alumni Foundation Award; Canada Government Special Opportunities Grant; British Sedimentological Research Group (BSRG) Gill Harwood Award; British Cave Research Association (BCRA) Ghar Parau (x2), David Hood and Science Awards; Yucatan Deep Speleological Dive Team (November 2000); Grupo de Exploracion Ox Bel Ha (July 2001); Nigel Ashcroft and The Production House team/Discovery Channel (August 2002). In addition, this research has benefited financially from the RGS Ralph Brown Expedition and Gilchrist Awards, granted to Prof. Peter Smart.

Many thanks to the many field assistants who took part in this study: Joe Berg, Helen Brown, Dan Hodge, Edward Mallon, Lee Patch, Jon Telling, Christian Vizl.

For laboratory assistance at the University of Bristol: Katy Boon and Anna Goodwin

For help with training and laboratory analyses and/or use of facilities, I am very grateful to: Simon Bottrell (University of Leeds, Stable Isotopes), Chung Choi (ICP-AES), Barry Cragg (Geomicro), Ed Hornibrook (GC), Tony Kemp (ICP-MS), Stuart Kerns (SEM/XRD), Jenny Mills (IC, DOC), Richard Newman (UV vis), Jon Telling (Stable Isotopes), Pete Wellsbury (IC), Jim Wilson (XRD).

For help with computers and using computer programs: Tim Barrass, Simon Cobb, Stew Goff, Simon Lee, Simon Powell, Colin Walker. For lending me an imac when my PC failed to keep up: Ed Hornibrook.

For being great office and/or lab mates: Helen Bowes, Vicky Buckley, Sy Cobb, Barry Cragg, Jamie Cutting, Eddy Hill, Alex James, Anna-Liisa Kivimaki, Emma Leighton, Ian Mather, Caroline Peacock, Alex Poole, Joachim Rinna, Julia Shaw, Emma Todd, Jon Wade, Colin Walker, Lindsay Watt, Pete Wellsbury, Jim Wilson and Marianne.

For logistical support in the field (including air/nitrox/oxygen fills and cylinder + vehicle loans): Akumal Dive Shop, Hidden Worlds Dive Shop, Akumal Dive Centre, ProTec Dive Centre, Speleotech Diving, Scott Carnahan, Marike Jasper, Tom Wilcox, Steve Dramstad.

For diving with or for me during this study: Roberto Chavez Arce, Hazel Barton, Bernie Bernbach, Steve Bogaerts, Greg Brown, Jeff Clark, Jim Coke, Fred DeVos, Stefan Doerr, Jill Heinerth, Paul Heinerth, Doug Hoyt, Marike Jasper, Gabor Koos, Andreas Kucha, Christophe LeMaillot, Dan Lins, Andreas (Matt) Matthes, Sam Meacham, Adrian

Nieoczym, Bil Phillips, Brian and Kevin Renton, Danny Riordan, Jim Rozzi, Wes Skiles, Shauna Slingsby, Chris Stanton, Nicolai Toussaint, Pierre Turgeon, Christian Vizl.

For access to survey data, maps and/or for useful discussions about the caves: QRSS, Jim Coke, Dan Lins, Mike Madden, Buddy Quattlebaum, Chuck Stevens.

For field laboratory space and many interesting (work and non-work related) discussions: Charles Shaw and Kate Robinhawk of Centro Ecologico Akumal (CEA).

For believing in me when I was just a baby diver, for giving me my 'junior' wings and for their never-ending love and support, Kay and Gary (a.k.a. Ma 'n Pa) Walten.

Last, but in no way least: for their love, support and understanding, a huge 'Thank you' goes to my partner, Jon Telling, and my family.

* * *

This thesis is dedicated to two fellow divers and dear friends who are very much missed, but who are remembered with a smile:

Alex Poole
(1976-2002)

Marike Jasper
(1963-2004)

Author's Declaration

I declare that the work in this dissertation was carried out in accordance with the regulations of the University of Bristol. The work is original, except where indicated by special reference in the text. No part of this dissertation has been submitted for any other academic award.

Samantha L. Smith

July, 2004

We shall never cease from exploration
And the end of all our exploring
Will be to arrive where we started
And know the place for the first time

- T.S. Elliot (1888-1965)

Table of Contents

CHAPTER THREE:
Diagenesis in the Freshwater System

CHAPTER FOUR:
Diagenesis in the Fresh-Salt Water Mixing Zone: A Case Study from Sistema Naranjal (Mayan Blue Section)

CHAPTER FIVE:
Diagenesis in the Zone of Saline Groundwaters

CHAPTER SIX:
Summary, Conclusions and Future Work

List of Figures

List of Tables

Chapter 1

Introduction, Research Objectives and Study Area

1.1 The importance of understanding modern carbonate diagenesis

Diagenesis is the sum of processes acting on a sediment or sedimentary rock that cause physical and chemical changes subsequent to deposition, but prior to atmospheric contact due to uplift (weathering) or exposure to elevated temperatures upon burial (metamorphism) (Berner, 1980). Distinctions between diagenesis and weathering and diagenesis and metamorphism can be somewhat blurred. However, this thesis is concerned only with early diagenetic processes, occurring where temperatures are not appreciably above 25°C and where major uplift does not occur. Thus, the processes associated with metamorphism and weathering are not relevant to this study.

Diagenetic processes can alter the composition, texture, porosity and permeability of a sediment (Chillinger, 1979) and diagenesis of carbonate sediments and rocks plays a major role in their development as reservoirs and aquifers. This thesis considers carbonate rock diagenesis in the modern carbonate platform of the Yucatan Peninsula, Mexico, occurring syn- or post- deposition, but prior to burial.

Most modern and ancient carbonate sediments originally consist of meta-stable mineral phases, such as aragonite and high magnesium calcite. As a result, carbonate sediments are extremely susceptible to extensive early diagenetic modification (Bathurst, 1975). The altering fluid may be derived from meteoric water, saline water or a fresh-salt water mixture, under either vadose or phreatic conditions (Figure 1.1).

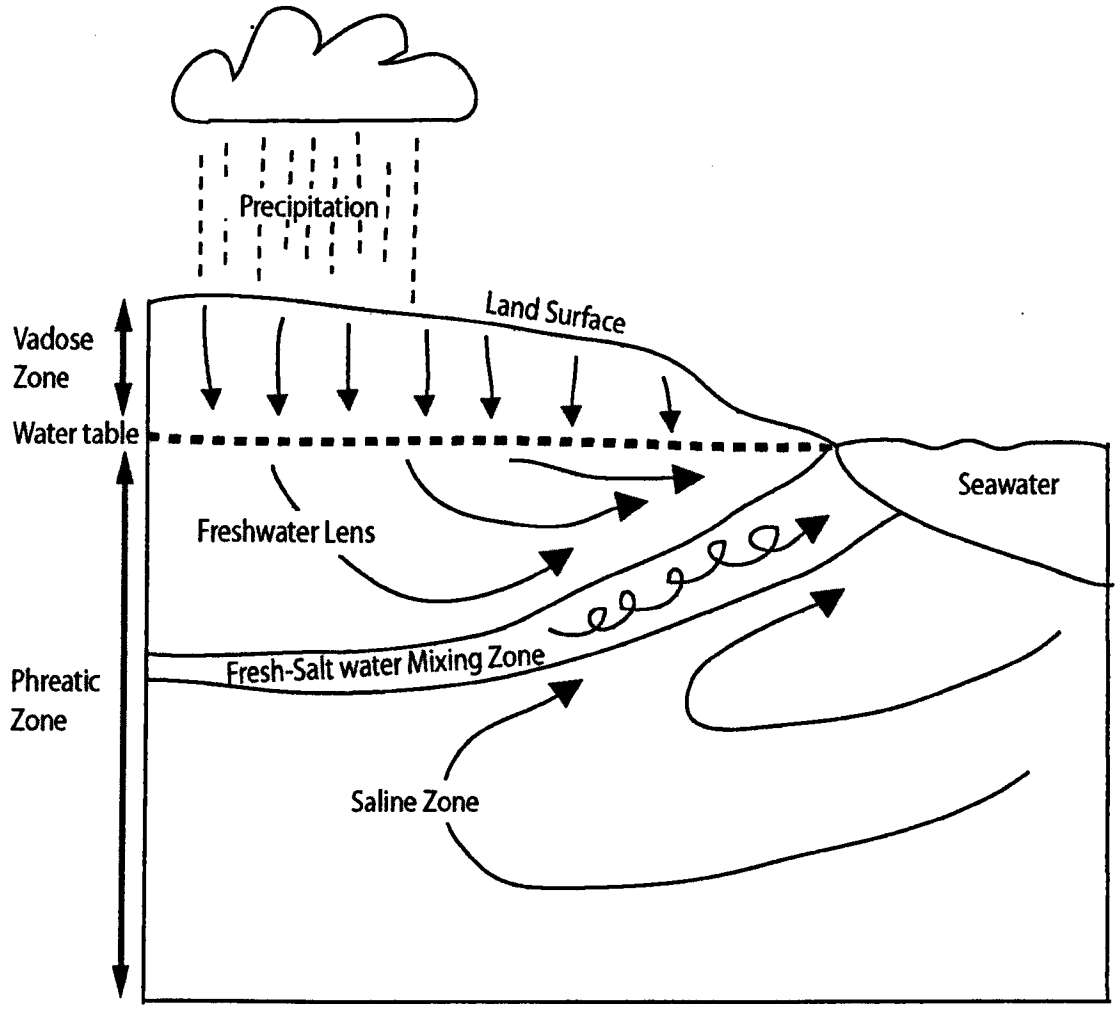

Figure 1.1 Modified 'Island Hydrology Model' showing the relative locations of the vadose and phreatic zones, freshwater lens, fresh-salt water mixing zone and saline zone.

After deposition, carbonate minerals can be modified by dissolution, reprecipitation and recrystallisation in order to achieve structural order and purity towards the mineral with the lowest Gibbs free energy (Robie et al., 1979). For example, primary meta-stable mineralogies (such as high magnesium calcite, HMC) are readily converted to low magnesium calcite (LMC) in meteoric waters or in mixtures of fresh and salt water (Longman, 1980; James and Choquette, 1984). Further diagenesis may result in the conversion of limestone to dolomite, although the process of 'dolomitisation' remains enigmatic and controversial (see, for example, Land, 1985; Hardie, 1987; Machel and Mountjoy,1986).

Microorganisms can play an important role in carbonate diagenesis, involved in both dissolution and precipitation reactions, largely due to the production and consumptionof acids and bases during their life processes (e.g. organic acids, CO_2, OH^-, HCO_3^-,NH_4^+,

H^+) (Madigan et al., 2000). For example, the production of carbonic acid during heterotrophic respiration can drive carbonate dissolution (Ford and Williams, 1989) while bacterial sulfate reduction may be important in carbonate precipitation and dolomitisation (Vasconcelos et al., 1995; Vasconcelos and McKenzie, 1997; Wright, 1999; Warthmann et al., 2000).

On a global scale, the reactions of carbonate minerals in natural waters control, in part, the chemistry of the atmosphere and oceans (Morse and MacKenzie, 1990). Carbonate rocks are also of great economic importance; they host at least 40% of the world's known hydrocarbon reserves (Ford and Williams, 1989) and it is estimated that 25% of the global population obtains their water supply from groundwaters within carbonate rocks (Ford and Williams, 1989). A better understanding of modern carbonate diagenesis can help predict the reservoir properties of ancient carbonates, and is necessary for the sound management of groundwaters, particularly in regions (such as the Yucatan Peninsula, Mexico) where fresh groundwater is the only source of potable water (Mather, 1975).

1.2 Introduction to Carbonate Geochemistry

There are four main equations used to describe carbonate equilibria and these are presented first. Of the standard atmospheric gases, CO_2 is the most soluble (e.g. 64 times more soluble than N_2; e.g. Ford and Williams, 1989) and the dissolution of atmospheric CO_2 gives:

$$CO_2(g) \leftrightarrow CO_2(aq) \qquad \text{(Equation 1.1)}$$

The hydration of CO_2 (aq), forming carbonic acid (Equation 1.2), is the main source of acidity in most natural waters (e.g. Langmuir, 1997).

$$CO_2 + H_2O \leftrightarrow H_2CO_3 \qquad (1.2)$$

Carbonic acid rapidly dissociates, providing H^+ and bicarbonate ions (Equation 1.3).

$$H_2CO_3 \leftrightarrow HCO_3^- + H^+ \qquad (1.3)$$

The bicarbonate may then dissociate (depending on the pH of the water), forming H^+ and CO_3^{2-} ions (Equation 1.4).

$$HCO_3^- \leftrightarrow H^+ + CO_3^{2-} \tag{1.4}$$

All fresh waters exposed to atmospheric CO_2 concentrations ($10^{-3.5}$ bar or ~0.03%) will contain the different species of Equations 1.1 to 1.4, regardless of whether or not carbonate rocks are present. However, within the pH range of waters within most limestone and dolomite environments (pH = 6.5 – 8.9), HCO_3^- is the predominant species and CO_3^{2-} is negligible (e.g. Figure 1.2). The relationship between pH and these species in seawater is illustrated in Figure 1.3.

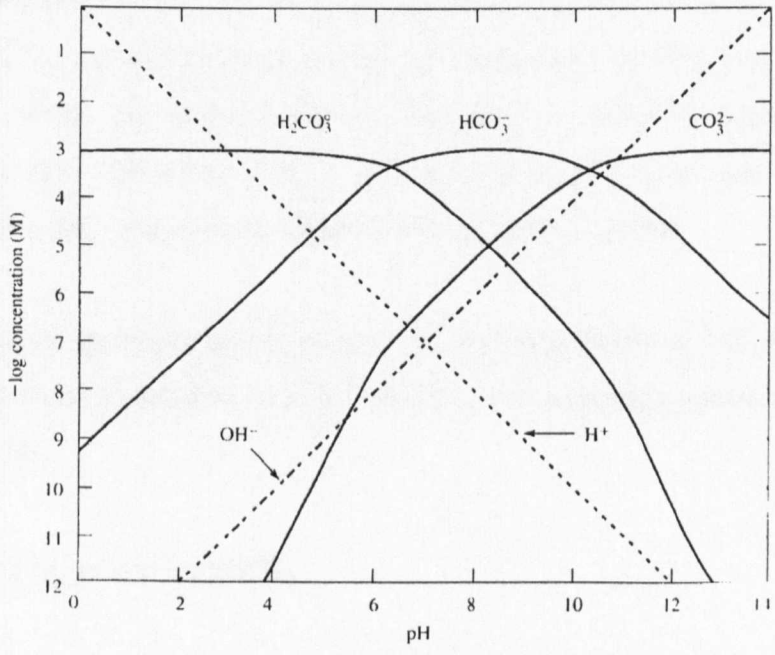

Figure 1.2 Distribution diagram for carbonate species as a function of pH, assuming the total carbonate concentration = 10^{-3} M. Concentrations of H^+ and OH^-, which are independent of the total carbonate concentration, are shown as dashed straight lines (after Langmuir, 1997).

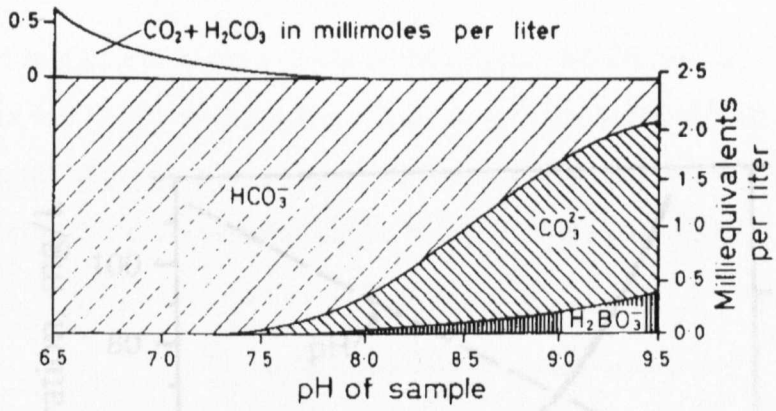

Figure 1.3 Variation in the alkalinity components of seawater with pH (after Cloud, 1962; Bathurst, 1975).

1.2.1 Factors Influencing the Solubility and Saturation State of Carbonate Minerals

i) CO_2 and pH

At Earth surface temperatures and pressures, the solubility of $CaCO_3$ in pure water in the absence of CO_2 is small (about 14.3 mg/l for calcite and 15.3 mg/l for aragonite; Bathurst, 1975). However, the addition of CO_2 to water can increase these solubilities up to hundreds of mg/l (Bathurst, 1975). As such, CO_2 is responsible for the majority of enhanced solubility of carbonate minerals (Roques 1962, 1964).

At a constant temperature, an increase in the partial pressure of CO_2 (pCO_2) will increase the concentration of carbonic acid in solution. Consequently, more calcite will dissolve (Equation 1.5).

$$CaCO_3 + H_2CO_3 \leftrightarrow Ca^{2+} + 2HCO_3^- \qquad (1.5)$$

Many processes (e.g. microbial/root respiration) occur in soils that act to increase soil CO_2 concentrations (e.g. Equation 1.6). Meteoric water percolating through such soils will (if residence time permits) equilibrate with a higher pCO_2, thus becoming more capable of limestone dissolution. Conversely, processes acting to decrease pCO_2 (such as photosynthesis, Equation 1.6 in reverse, although the reaction is not reversible in a chemical sense) cause calcite saturated waters to become supersaturated, resulting in calcite precipitation until equilibrium is reached. The effect of pCO_2 on the solubility of calcite is illustrated in Figure 1.4.

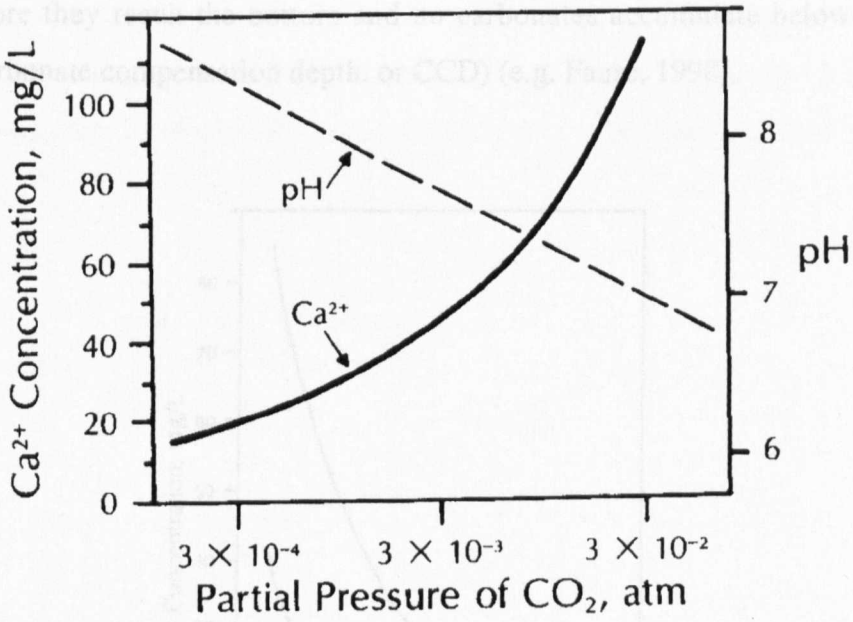

Figure 1.4 Increase in the solubility of calcite in water at 25°C with increasing partial pressure of CO_2. The solubility of calcite is expressed as the concentration of Ca^{2+} in a saturated solution, whereas the pH decreases as more CO_2 dissolves (after Faure, 1998).

$$CH_2O + O_2 \leftrightarrow CO_2 + H_2O \qquad (1.6)$$

In addition, calcite solubility increases drastically if increases in acidity are controlled outside carbonate equilibria (i.e. the solubility of calcite changes by a factor of 100 when the pH is varied by one unit; Faure, 1998).

ii) Temperature

The solubility of carbonate minerals decreases with increasing temperature, as illustrated in Figure 1.5 for calcite. Between 0 and 90°C, carbonate solubilities decrease about 6-fold for aragonite and calcite and about 14-fold for dolomite (Langmuir, 1997). This decreasing solubility with temperature is amplified by the fact that the solubility of CO_2 gas also decreases with increasing temperature (Langmuir, 1997).

iii) Ocean Depth

Also, the solubility of calcite (and aragonite) increases with increasing depth and, as a result, carbonate particles dissolve as they sink through ocean waters. Whether or not

these particles reach the bottom of the ocean depends on the rates and which they sink and dissolve and the depth of the water. If deep enough (~500 m), all carbonate particles dissolve before they reach the bottom and no carbonates accumulate below this critical depth (the carbonate compensation depth, or CCD) (e.g. Faure, 1998).

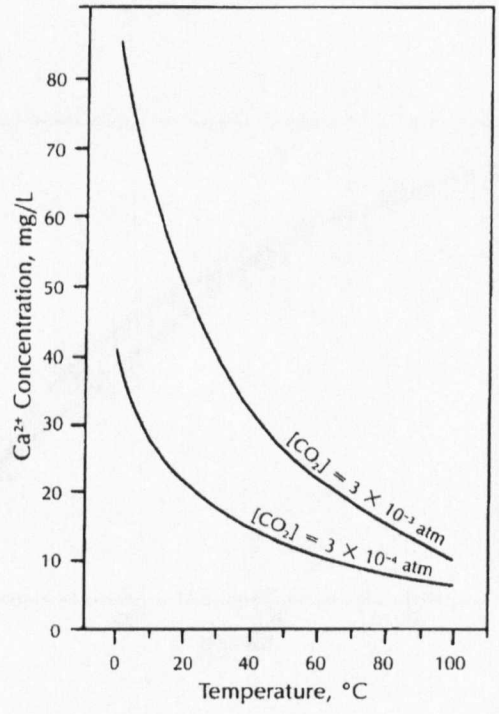

Figure 1.5. Decrease in Ca^{2+} concentration within increasing temperature in a saturated solution of calcite in pure water at two partial pressures of CO_2 (after Faure, 1998).

iv) Evaporation and Other Mechanisms for Increasing Ion Concentrations

Another process influencing the solubility and saturation state of carbonate minerals is evaporation. Evaporation causes an increase of Ca^{2+} and HCO_3^- (and other) ions and CO_2(g) may be released. As a result, calcite precipitation may occur. Similarly, ion concentration increases from sources other than the dissolution of calcite (e.g. $CaSO_4$ dissolution) could supersaturate the water with respect to calcite, resulting in its precipitation. This is referred to as the common ion effect (e.g. Langmuir, 1997).

v) Mixing

Mixing of two waters can lead to a mixed water that is either super- or under- saturated within respect to carbonate minerals. This effect is illustrated in Figure 1.6. In this figure,

calcite saturation is defined by the curve, while the straight line represents a mixing line between two saturated solutions, A and B. In Figure 1.6, *m* represents a mixture of approximately 65% solution A and 35% solution B. This mixture is undersaturated and will dissolve, for example, calcite until saturation (S) is reached. It is also feasible to mix undersaturated waters to obtain mixtures supersaturated with respect to carbonate mineral species.

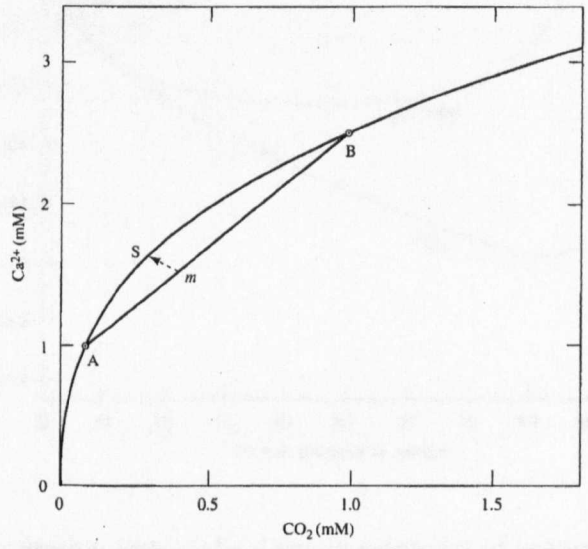

Figure 1.6 Solubility of calcite in pure water at 25°C and 1 bar total pressure as a function of Ca^{2+} and CO_2 (aq) concentrations. See text for further description. From Langmuir, 1984; 1997.

The mixing effect may be particularly important in driving calcite dissolution in coastal regions, where meteoric carbonate groundwaters mix with seawater, which is usually supersaturated with respect to calcite. Plummer (1975) mixed Yucatan Peninsula freshwaters with Caribbean seawater and showed calcite undersaturation should occur in mixtures of 5-70% seawater (Figure 1.7). It is important to note, however, that the degree of undersaturation generated from mixing is strongly dependent on the composition (and, in particular, the pCO_2) of the mixing end-members (Plummer, 1975; Wigley and Plummer, 1976).

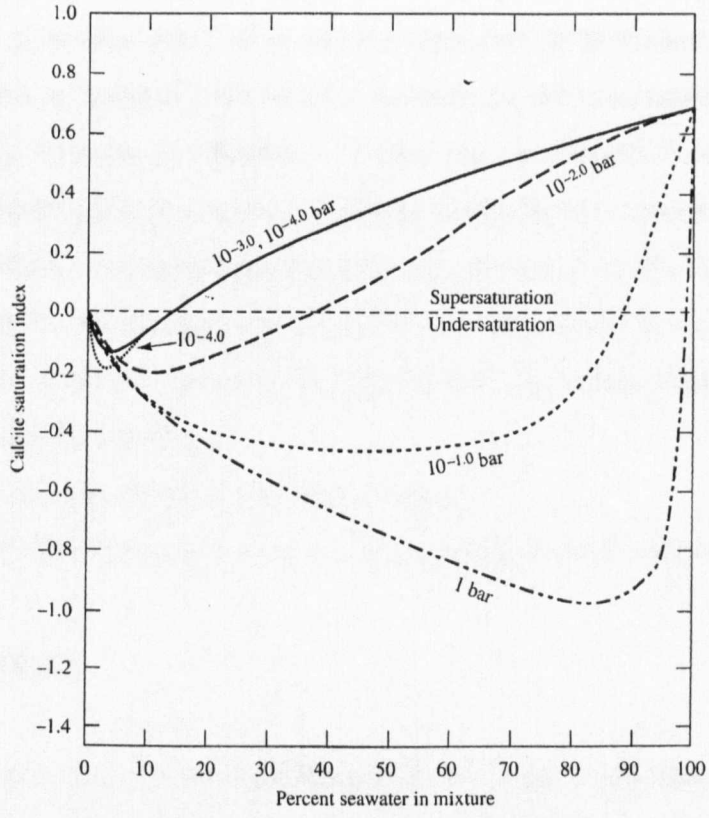

Figure 1.7 Saturation index of calcite in mixtures of seawater and freshwater in equilibrium with calcite at 25°C and different CO_2 pressures. From Plummer, 1975.

1.3 Research Objectives

The fundamental aim of this study is to investigate the geochemical and geomicrobiological processes driving carbonate diagenesis in the Yucatan Peninsula, Mexico. The Yucatan Peninsula is a modern carbonate platform which serves as a natural laboratory for examining modern carbonate diagenesis, and may provide a modern analogue for many major oil-bearing fossil carbonates (e.g. Middle East and Canada). The Yucatan Peninsula is an ideal study site as it hosts over 500 km of explored cave passage and enables unparalleled direct access to the subsurface and groundwaters within the interior of the platform.

Field results will be compared to those obtained from theoretical geochemical modeling in order to test the validity of such models. Of particular interest is to compare the potential of groundwater to dissolve aragonite and calcite and to precipitate dolomite. The

importance of inorganic geochemical processes will be considered alongside the influence of bacterial production of carbonic (and other) acid(s) and oxidation of organic matter. These bacterial processes likely play an important role in carbonate dissolution, but may also be involved in breaking the kinetic barriers to dolomitisation. A complementary investigation by Patricia A. Beddows (University of Bristol School of Geographical Sciences) of hydrological processes controlling groundwater circulation patterns will also be briefly described. The main research questions addressed in this thesis are:

- What are the main diagenetic processes (e.g. limestone dissolution/dolomitisation) occurring in the freshwater lens, mixing zone and saline zone along the east coast of the Yucatan Peninsula?
- At what rates are these processes occurring?
- What role do microorganisms play with respect to carbonate diagenesis?

1.4 Thesis Structure

Chapter One provides a brief introduction to the nature and importance of carbonate diagenesis, followed by a description of the Yucatan Peninsula study area. **Chapter Two** describes the methods employed in this study and includes error and analytical uncertainty calculations. **Chapter Three** considers carbonate diagenesis in the freshwater system. Within this chapter, the progressive geochemical evolution of fresh groundwaters is studied from the bedrock surface, through the vadose zone and into the freshwater lens. **Chapter Four** considers carbonate diagenesis in the fresh-salt water mixing zone. A brief investigation into the thickness of the Yucatan Peninsula mixing zones is followed by a detailed study of the geochemistry in the mixing zone of the Mayan Blue cave section of Sistema Naranjal. From this case study, a general conceptual model is proposed that describes the controls on mixing zone geochemistry and diagenesis. Wall rock diagenesis, as well as an *in situ* dissolution experiment carried out in Mayan Blue is compared to the aqueous geochemistry. The chapter ends by examining the role geomicrobiology plays in controlling the geochemistry and subsequent diagenesis. **Chapter Five** examines the geochemistry and carbonate diagenesis within the zone of saline groundwaters. Sub-surface evolution of these waters is examined relative to input waters (seawater). The role of microbiology is considered, particularly with respect to the apparent maintenance of undersaturation in the saline groundwaters. Finally, **Chapter Six** briefly reviews the objectives of this thesis and the extent to which they have been fulfilled. The importance

of the various geochemical processes driving diagenesis is reviewed and an assessment of spatial variation in the nature and rate of diagenetic processes throughout the upper part of the carbonate platform is presented.

1.5 Location of the Study Area

The Yucatan Peninsula is located in southeastern Mexico. The main study area is located along the east (Caribbean) coast of the peninsula, within the Holbox Fracture Zone-Xel Ha Zone (described, for example, by Perry et al., 2002) and comprises an area extending ~40 km along the east coast and a distance of ~12 km inland. A map of the field area showing its location and the location of the main study sites is presented in Figure 1.8.

1.6 Geology and topography

The Yucatan Peninsula is the emergent portion of the 300 000 km^2 Yucatan Platform (Lopez Ramos, 1975). On the Caribbean side, there is an abrupt drop to ~200 m depth at 2-10 km from the coast. Multiple phases of carbonate deposition have resulted in an interior core of Paleocene-Eocene age, surrounded by Miocene-Pliocene deposits (Weidie, 1985). The Caribbean coastal region of the Yucatan Peninsula is composed of upper Pleistocene limestone (Back et al., 1979; 1986), composed of a mixture of predominantly low-Mg calcite and aragonite. These have accumulated 65 m in a few thousand years (Ward, 1985b). Carbonate deposition continues today with reefs, lagoonal and shoal sediments being deposited at the platform margins (Ward and Weidie, 1985).

The underlying stratigraphy of the area has been inferred from PEMEX (Petroleos Mexicanos) exploration wells drilled across the peninsula (Figure 1.9; Socki, 1984; Ward et al., 1995). Late Cretaceous and underlying strata tilt gently to the west (Weidie, 1985), while the overlying Tertiary carbonates are sub-horizontal. The Cretaceous-Tertiary boundary in the northwestern coast of the peninsula is marked by the Chicxulub Impact Crater (Sharpton et al., 1993; Ward et al., 1995), around which a 'Ring of Cenotes' (sinkholes) has formed. While major structural disturbance of strata by the impact is limited to the northwestern region (to within about 100 km of the proposed impact center), breccia from the impact is present throughout the region (Ward et al., 1995).

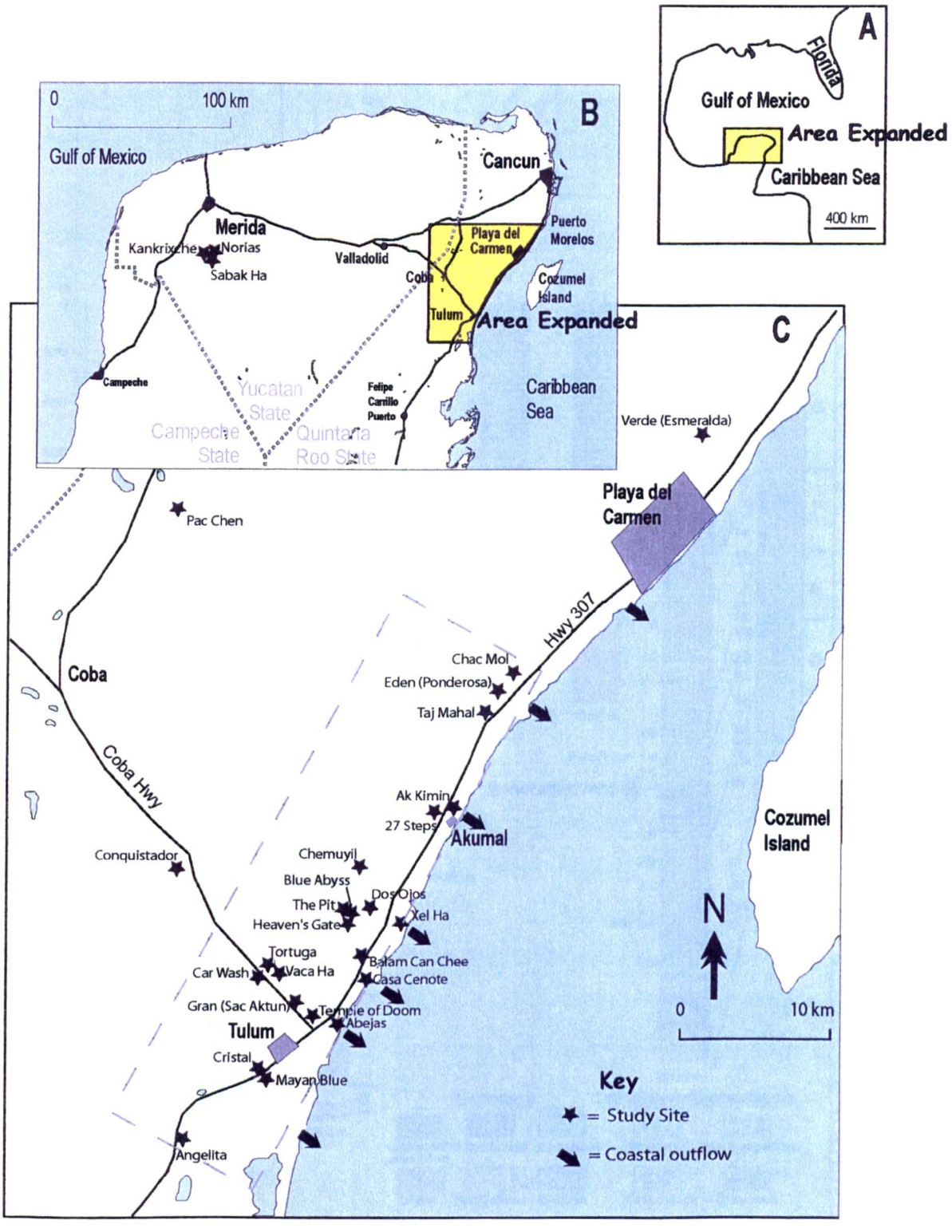

Figure 1.8 A) Map showing the location of the Yucatan Peninsula, Mexico. B) Map showing the location of the field area within the peninsula C) Map showing the location of the study area and principle sampling sites. Grey dashed box shows the location of the main focus of sampling and covers ~40 km along the coast and ~12 km inland from the Caribbean Sea (480 km^2). Modified from Beddows (2004).

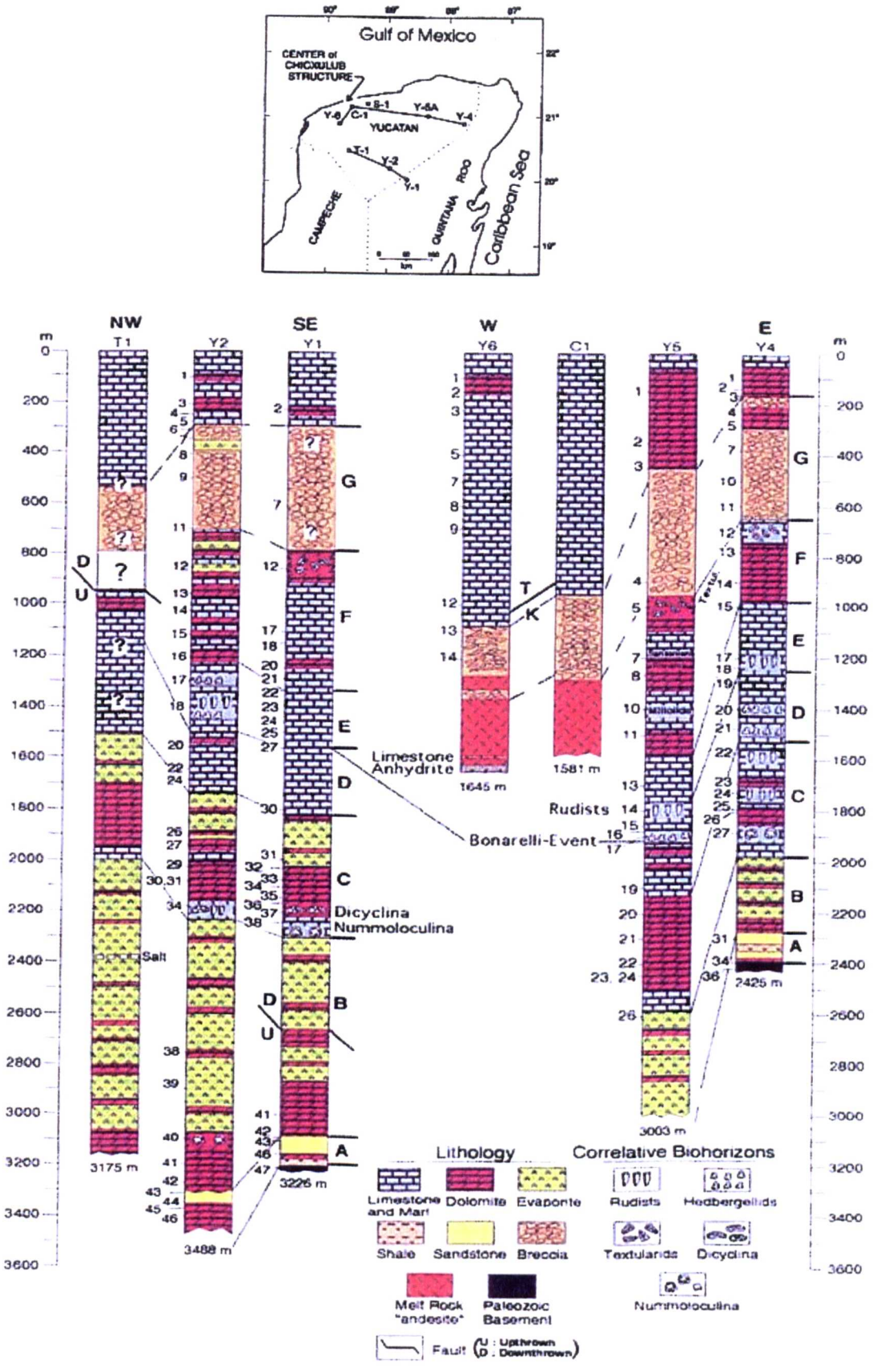

Figure 1.9 Correlation of PEMEX wells of the northern Yucatan Peninsula. Datum is ground level. Approximate age of units: A – Jurassic-Early Cretaceous, B – Albian, C – Albian-Cenomanian, D – Denomanian_Turonian, E – Turonian, F – Coniacian? – Masstrichtian, G – late Maastrichtian (Ward et al., 1995).

In Y4, the closest borehole to the sites examined in the present study, impact breccia is present at ~150 m to 650 m (Figure 1.9). The breccia is polymict, and is composed predominantly of clasts of dolomite, limestone and typically 15-20% anhydrite in a dolomitised carbonate mud matrix (Ward et al., 1995). An earlier interpretation of Y4 noted that evaporites were present slightly higher (~110 m) in Y4 (Socki, 1984).

The Yucatan Peninsula is characterised by low relief; a maximum of 30 m above sea level in the northern section, but more generally of around 5 m. A ridge and swale topography (5 to 10 m elevation is present on the Caribbean coast between Cancun and Xel Ha (Ward and Brady, 1979).

Above modern sea level, there are a few subaerial caves (e.g. Aktun Chen), but these are not extensive or common along the east coast. Below modern sea level, however, there is extensive cavernous development (trending southeast to northwest) with over 500 km of passage explored since the early 1980s, including the three longest underwater cave systems in the world (QRSS, 2004).

1.7 Climate

There are two main seasons in the Yucatan Peninsula: cool/dry and hot/wet. The cool/dry season runs from November to March and had a mean monthly air temperature of 25.11 ± 1.08°C and a mean monthly precipitation of 34.2 ± 22.4 mm throughout the study period (NOAA, 2002). The hot/wet season runs from May to September and had a mean monthly air temperature of 28.32 ± 0.52°C and a mean monthly precipitation of 109.6 ± 54.9 mm (NOAA, 2002). The months lying between these seasons (April and October) tend to be hot/dry (27.96 ± 0.35°C, 17.6 ± 17.6 mm precipitation) and cool/wet (26.61 ± 0.71°C, 135.1 ± 85.3 mm), respectively (NOAA, 2002).

1.8 Soils and Paleosoils

The Terra-Rosa soil that occurs within the study area is generally patchy and thin (Gmitro, 1986). The soil collects in dissolution pockets and depressions that are usually ~0.1 – 1 m wide and less than 20 cm deep. These thin soils are incapable of storing large amounts of water at the surface, although marshy areas do persist around some cenotes (e.g. Mayan

Blue, Tortuga). Generally, however, surface waters only occur where the bedrock surface intersects the water table (e.g. cenotes, which are water-filled depressions or collapse areas).

1.9 Vegetation and Land-use

The tree canopy is ~20 m high and is sufficiently open to allow an under-story composed of succulent plants, palms and immature trees developed at ~3 m height (Beddows, 2004). The ground is covered in desiccated decaying leaves. Phreatophyte trees and vines with deep rooting systems that penetrate the thick (~10 m) vadose zone are occasionally present, but these are rare. In general, the vegetation of the field area is observed to have many xerophytic characteristics such as waxy leaves and succulent stems. This suggests that the forest is adapted to a water-deprived environment despite high annual rainfall, and that only a limited number of forest species benefit from unlimited water access due to deep routing.

Many Mayan people still undertake subsidence 'milpa' agriculture with slash and burn farming to grow intermixed crops of corn, beans, squash and gourds. Despite the growing increase of chemical fertilizer use, a milpa field is usually exhausted after only three or four growing seasons (and is then used for grazing cattle for up to five years). Based on aerial photos and field observations, Beddows (2004) estimates that the proportion of land used for agriculture within the field area is only ~5%. Despite this low proportion, the rotating land-use associated with the milpa fields does result in the removal of a potentially significant amount of mature phreatophyte trees that would otherwise account for the majority of deep evapotranspirative withdrawals. In addition, the increasing use of fertilizers may pose a threat to the water quality of the area.

In the past, the Mayan people were reliant on the 'fresh' groundwater supply obtained *via* cenotes (Doehring and Butler, 1974; Back, 1985a; Veni, 1990; Fedick, 1996; Gill, 2000). This reliance continues to present day (Marin et al., 2000). However, a fast-growing tourism industry along the east coast of the peninsula increases the demands on water supply and water abstraction is now undertaken using boreholes and wells in addition to cenotes.

One of the principal problems currently facing the Mexican government is waste disposal and currently sewage treatment is limited and the majority of the sewage is returned untreated to the freshwater lens (Beddows, 2004). The government-mandated practice of sewage treatment plant effluent disposal is to pump the effluent into disposal wells that are 60-100 m deep (often located within or near the tourism developments and urban centers near the coast). Alternatively, a large portion of treated effluent is used for irrigation of golf courses and landscaped areas in some resorts.

1.10 Water and Site Types

Thirteen types of water were sampled from various sites throughout the course of this study:

i) Rainwater

Samples were taken both from the beginning and near the end of rainstorms. All rainwater samples were collected in Akumal (Figure 1.8), within 200 m of the coast. Due to a usually small sample volume, a complete suite of analyses for each sample was not always possible.

ii) Surface Runoff and Throughfall

Samples were obtained from a variety of bedrock and vegetated surfaces during and immediately after a rainstorm. One 'throughfall' sample was also obtained (rainfall that had percolated through waxy tree leaves). All samples were taken during periods of rainfall to minimize evaporitic effects.

iii) Surface Pools

There is very little surface retention of water within the Yucatan Peninsula (there are no surface rivers or streams). However, some rainwater is retained at the surface as bedrock pools (with a diameter generally no more than 2 m) and/or mangrove waters. Surface waters are subject to evaporation and direct inputs (e.g. rain, runoff, vegetation debris) from the surface.

iv) Vadose Drip Samples

Water samples from dripping stalactites were obtained from sites with subaerial cavernous porosity in attempts to characterise vadose zone processes. Drip samples were obtained from Aktun Chen, Heaven's Gate (Sistema Nohoch Nah Chich) and Tak Be Ha (Sistema Dos Ojos).

v) Wells – Static and Pumped

Samples were collected from both static (non-pumped) and pumped wells. The water level in the wells was generally ~9 m below the surface and the diameter of the wells was 0.5 – 1 m. Some well samples (i.e. surface samples taken from static wells) will have been subject to evaporation and degassing (and surface-derived inputs such as vegetation debris).

vi) Cenotes

With the exception of relatively localized and small diameter bedrock pools, the occurrence of surface water is generally restricted to areas where the land surface intersects the water table. This results in 'cenotes'; water-filled surface depressions or collapse zones. There are ~490 known cenotes within the study area (QRSS, 2004) and each have an average diameter of ~10 m. Cenotes serve as access points to the extensive cave systems of the subsurface. Cenotes are usually shallow (~6 m deep) and contain only freshwater (Temple of Doom is an exception). Cenote waters are susceptible to surface-derived inputs, evaporation and degassing. Due to the nature of their formation (collapse), cenotes often have rocky (blocks and boulders) floors covered with macrophytes and algae.

vii) Open Pit Cenotes

Open pit cenotes are vertical shafts that have a relatively large diameter and are usually 60 m (up to 119 m) deep. These have circular entrances (10 - 30 m+ in diameter) and tend to bell out with depth. Some have a small number of horizontal passages leading off from the main chamber, but more often than not, these are small in diameter and are not very long. Most of the deeper passages are blocked by boulder collapse or sediment infill comprised mostly of organic matter that has fallen in from the surface. As such, almost all sites have a maximum depth of 60 m (The Pit is an exception, with over 200 m of passage extending at depth from the bottom of the cenote). Within The Pit, the deepest rock (~≥110 m) is

extremely crumbly (divers can put their arms through the 'wall rock'), suggesting locally high rates of dissolution. The shallower rock tends to be hard and fretted with various colours and degrees of staining (e.g. Angelita wall-rock is stained with purple patches, while much of The Pit wall rock is stained light orange).

Because of the large surface diameter and depth, organic matter tends to accumulate on the bottom and sides of the pit cenotes. The degradation of this organic matter plays a key role in controlling the chemistry of these sites. All open pit cenotes have hydrogen sulfide layers associated with them, formed during the breakdown of this organic matter. In addition, due to their depth, all open pit cenotes penetrate the saline zone (and thus have a mixing zone).

Within the immediate field area, four open pit cenotes were sampled: Angelita, Chemuyil, The Pit and Verde (a.k.a. Esmeralda). One additional open pit cenote was sampled from the Merida region (Sabak Ha, Figure 1.8).

viii) Caverns

Caverns form the interface between the cenote and cave environments and are defined as the zone of cave within 40 m of a light/air source (Prosser and Grey, 1992). In this thesis, a cavern is defined as a site with a cave roof, but where there is an air pocket between the water and roof and/or some light is able to penetrate the sampling site. Three cavern sites were sampled in this study: Chac Mool, Taj Mahal and Temple of Doom. At Chac Mool, the site is completely dark, but there is an air dome above the study site. At Taj Mahal, there is no air pocket directly above the site, but some light does penetrate from the adjacent cenote. At Temple of Doom, both air and light are present.

ix) Caves

Caves are sites with limited direct input from the surface (the sites are at least 40 m from a light source or air space). 124 laterally-extensive submerged caves have been explored along the east coast of the Yucatan Peninsula, along the 40 km coastal stretch leading from south of Tulum to Playa del Carmen. These include the three longest underwater cave systems in the world (Sistemas Ox Bel Ha, Nohoch Nah Chich and Dos Ojos, which are 115, 61 and 57 km long, respectively)(QRSS, 2004). Two of the caves are known to discharge at the coast and all have formed along a southeast to northwest axis,

perpendicular to the coast (Figure 1.10). In these caves, the passages tend to be quite large (generally 10 m wide and over 2 m high). These are generally developed at one or sometimes two horizontal levels and some show dissolutional fretting on the cave walls. The passages are intercepted by chambers formed by collapse, which generates piles of platey to blocky collapse debris.

Passages that lie in freshwater are usually highly decorated by speleothem deposits. While passages containing mixing zones are often extremely fretted and have 'swiss cheese' weathering patterns (Back et al., 1979). These caves are most likely to have undergone dissolution at the water table and/or mixing zone over a prolonged period. Smart et al. (2002) proposed that almost all caves correspond to the present-day level of the mixing zone and suggested mixing zone dissolution (discussed in Chapter 4) as the primary mechanism for their formation.

x) Deep Saline Zone

The deep saline zone is defined as saline groundwaters $\geq$60 m water depth. This depth was chosen based on the maximum depth limit of most sites within the study area (notably the open pit cenotes) and was thought to be a possible divide between shallow and deep saline zones. Very few sites offer access into the 'deeper tier of cave development' and samples were obtained from The Pit (Dos Ojos), Blue Abyss (Nohoch Nah Chich) and Sabak Ha.

xi) Sulfide Layers

Sulfide layers persist where there is an accumulation and breakdown of surface-derived organic matter. The term 'layer' is used because a sulfide 'taste' experienced while diving often corresponds with a few meters of decreased visibility (the water is coloured white, orange or black-brown) and the sulfide taste is sudden and not continuous much beneath the coloured layer (although it is possible that the divers become anesthetized to the 'taste' and tingling sensations after a short period of exposure).

xii) Coastal Discharge Sites

Coastal discharge (or outflow) sites are defined here as sites within 200 m of the east coast of the peninsula and include the outflow points of Sistemas Nohoch Nah Chich (Casa Cenote), Ox Bel Ha and Abejas. In addition, samples were collected from Ak Kimin, Xel Ha, and Yalku Lagoon.

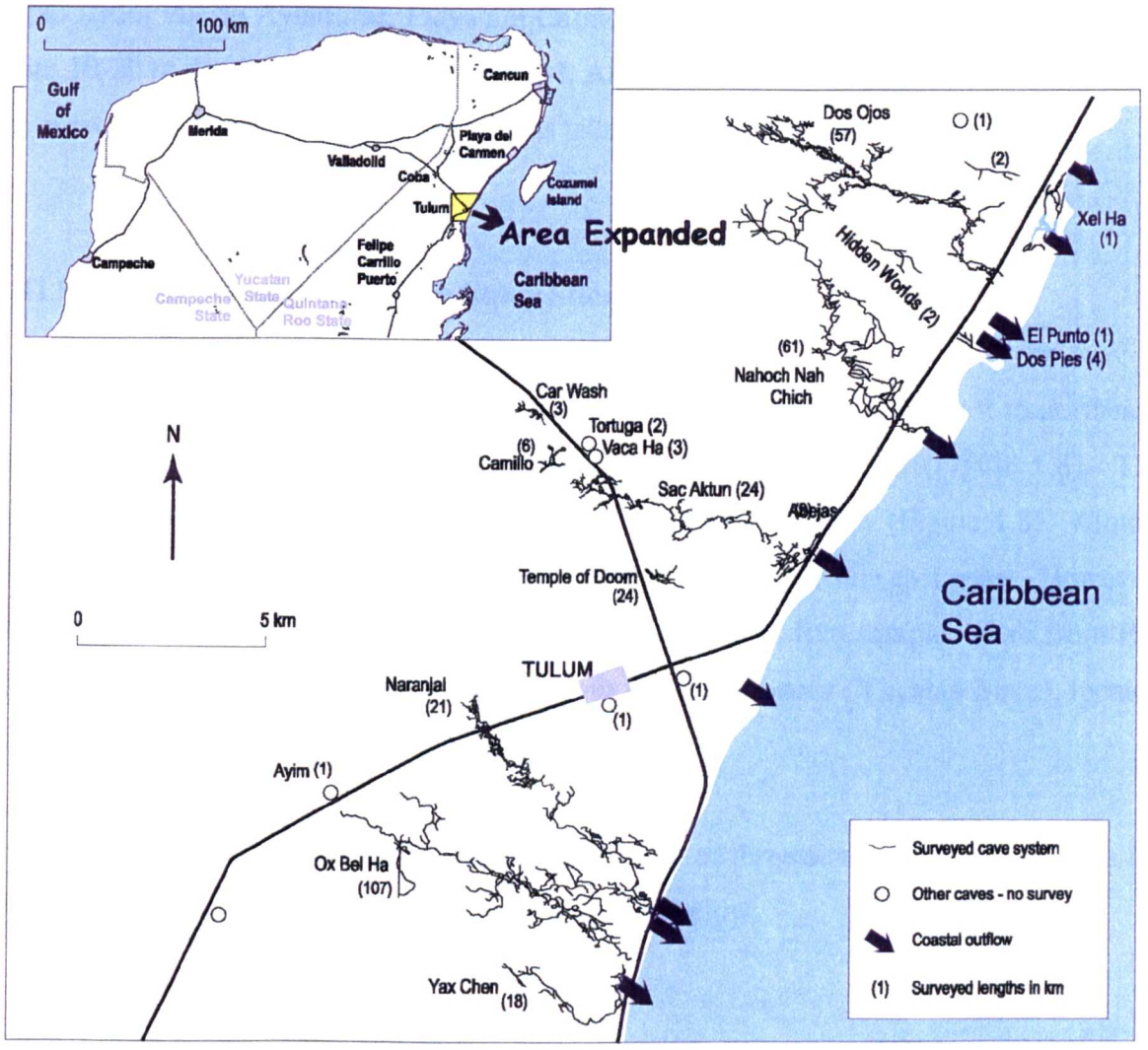

Figure 1.10 Map showing the location and line surveys of some of the main study sites, including the three longest underwater cave systems in the world (Ox Bel Ha, Nahoch Nah Chich and Dos Ojos). Note the southeast to northwest trajectory of the cave passages. Modified from Beddows (2004).

xiii) Seawater

Eight seawater samples were taken from the Caribbean Sea (although a complete suite of analysis was not conducted on all samples). Of these, four were taken from <5 m water depth (from Puerto Aventuras, Playa del Carmen, Tankah and Akumal). Two were taken from 10-20 m depth (both from Dick's Reef, Akumal), one was taken from 30 m depth off the west coast of Isla Cozumel and one was taken from 70 m outside Akumal.

1.11 Sampling Strategy and Main Study Sites

The samples were collected along two 'transects'. The first runs southwest to northeast, along Highway 307, which runs approximately parallel to the coast (Figure 1.8). The second transect runs roughly west to east, along the Coba Highway (Figure 1.8). Almost all samples were taken within 12 km inland of the Yucatan Peninsula east coast. However, one sample was taken from Conquistador (22.1 km inland), five samples were from Pac Chen (40 km inland) and 3 samples were from the Merida area (Yucatan State), located approximately 70-80 km west of the east coast.

In addition, this study involved the detailed sampling of three sites: Mayan Blue, The Pit and Ak Kimin. Descriptions of these sites are given below.

1.11.1 Mayan Blue Section of Sistema Naranjal

Surveyed in the early 1990s, Mayan Blue is a conduit (cave) site located 5.6 km inland and ~3 km south of Tulum (Figure 1.8). It comprises about one third of the total length of Sistema Naranjal, which has over 21 km of surveyed cave passage and is thought to be the upstream portion of Sistema Ox Bel Ha, currently the longest underwater cave system in the world (Figure 1.10). The system exhibits complex anastomosing passages and these are developed in at least two different phases. The average passage width is ~10-15 m and the average height is ~6-10 m. The maximum explored depth of this system is 34.7 m water depth (QRSS, 2004). There is only one cenote (15 x 45 m) within the Mayan Blue section of Sistema Naranjal and this is surrounded by a marshy depression. At the cenote,

the vadose zone is only ~2-3 m thick, although it is at least 8-9 m thick above the cave passages.

Stalactites occur in the shallower (freshwater) portions of the cave and these are covered with a black/brown coating (bacterial mats?). Fresh internal sedimentation of both fine limestone grains (released by dissolution of cements, a.k.a. 'percolation') and fretted and boulder breakdown appears to dominate the conditions found on the floor of the cave (Smart et al., 2002). In some areas, the beige to white percolation is underlain by dark brown sediment. Ledges are covered with a fine orange to brown layer of sediment, which is sometimes 'layered' in alternating colours of beige/white, orange and brown.

Mayan Blue is one of the few east coast sites to host passages containing fresh, mixed and saline water. As such, it is ideal for a detailed study of mixing zone geochemistry and geomicrobiology. The Mayan Blue mixing zone is ~4 m thick, occurring between ~15 and ~19 m water depth. Geochemical sampling site locations within the cave are shown in Figure 1.11 and these include 'Stal Dome' (2), 'Dog Leg' (3), 'FSI Passage' (4) and 'Death Arrow' (5). Locations 2, 3 and 4 occur within the B-Tunnel, while location 5 is within the A-Tunnel. Both A and B tunnels are accessible from the cenote and these run parallel to one another in an approximately north-south direction. The tunnels are connected to one another by three deeper (mostly saline) passages running east-west at a depths of ~20 m (Figure 1.11).

The majority of geochemical samples were obtained from location 2, although some additional mixing zone samples were taken from locations 3 and 5. Location 4 is an isolated saline zone passage (i.e. without an associated mixing zone) and one saline zone sample was obtained from this site. In addition, two samples were taken from the cenote.

Cave samples for geomicrobiological analysis were taken from location 2 only. One additional sample was obtained from the cenote. An *in situ* dissolution experiment (Chapter 4) was conducted at location 2 and this is also the site of the dye release summarised in Chapter 4.

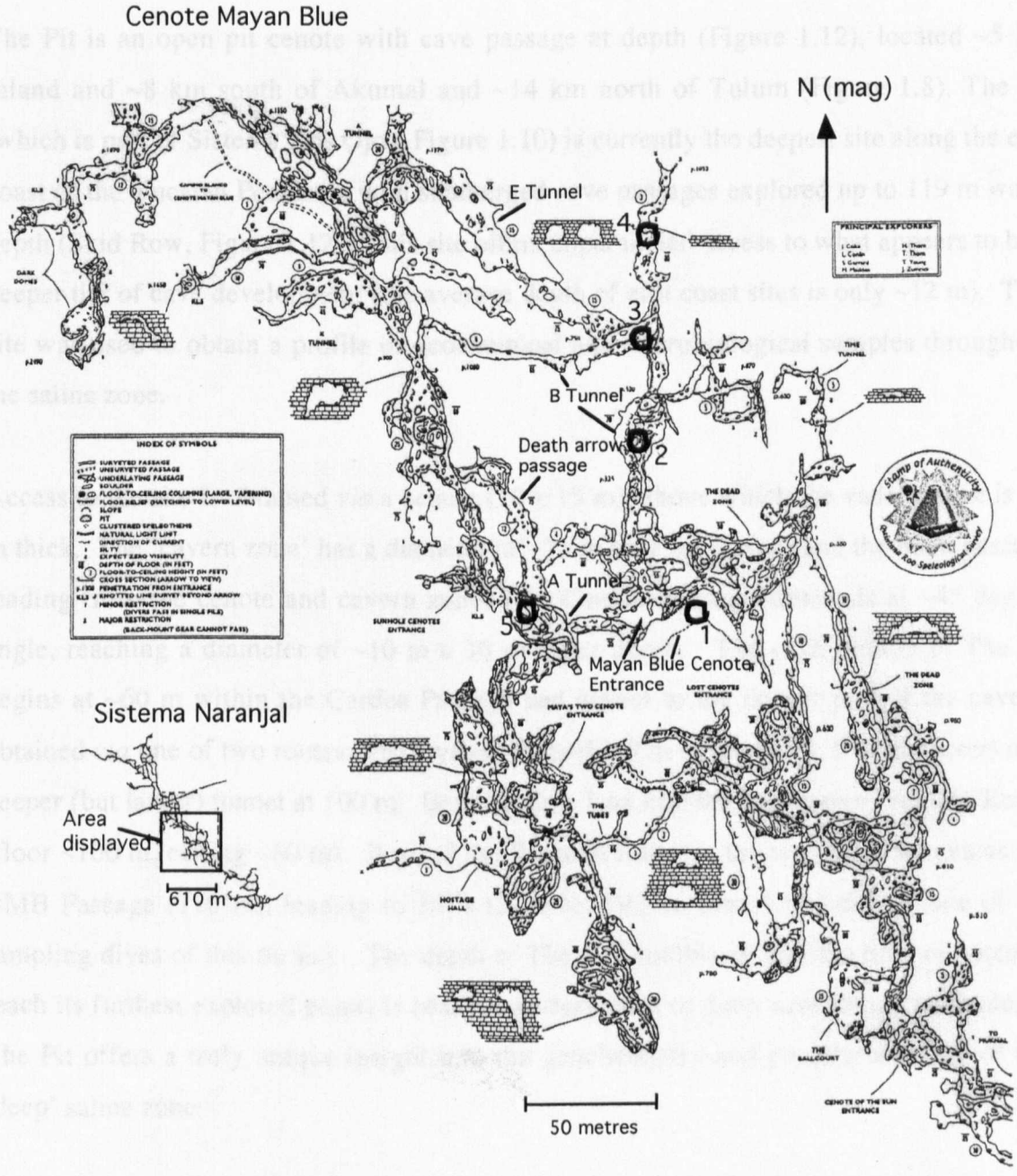

Figure 1.11 Map of the Mayan Blue section of Sistema Naranjal showing the location of the sampling and study sites. including Mayan Blue cenote (1), Stal Dome (2), Dog Leg (3), FSI Passage (4) and Death Arrow (5). Used with kind permission from J. Coke and the Qunitana Roo Speleological Survey.

1.11.2 The Pit, Sistema Dos Ojos

The Pit is an open pit cenote with cave passage at depth (Figure 1.12), located ~5 km inland and ~8 km south of Akumal and ~14 km north of Tulum (Figure 1.8). The Pit (which is part of Sistema Dos Ojos, Figure 1.10) is currently the deepest site along the east coast of the Yucatan Peninsula with submerged cave passages explored up to 119 m water depth (Skid Row, Figure 1.12). This site offers unparalleled access to what appears to be a deeper tier of cave development (the average depth of east coast sites is only ~12 m). This site was used to obtain a profile of geochemical and microbiological samples throughout the saline zone.

Access to the site is obtained *via* a cenote (10 x 15 m), above which the vadose zone is ~9 m thick. The 'cavern zone' has a diameter of ~33 m near the surface and the main passage leading from the cenote and cavern zones (the Cardea Passage) descends at ~45 degree angle, reaching a diameter of ~10 m a 30 m water depth. The cave section of The Pit begins at ~60 m within the Cardea Passage and access to the deeper part of the cave is obtained *via* one of two routes: The ByPass Tunnel (88 m water depth, 2 m diameter) or a deeper (but larger) tunnel at 100 m. Both of these lead into the impressive Wakulla Room (floor ~100 m, ceiling ~60 m). Beyond the Wakulla Room is the restriction known as the BMB Passage (110 m), leading to Jill's Chamber (92 m, discovered during one of the sampling dives of this thesis). The depth of The Pit (combined with the time required to reach its furthest explored point) is near the current limit of deep cave diving technology. The Pit offers a truly unique insight into the geochemistry and geomicrobiology of the 'deep' saline zone.

The locations of the sampling sites are shown in Figure 1.12. The mixing zone within The Pit is 6.8 m thick and occurs between 12.3 and 19.1 m water depth. Below this, two coloured layers within the water column exist, one at ~30 m water depth (white layer) and the second at ~50 m water depth (black layer). These coincide with an accumulation of organic matter, derived primarily from plant material that has fallen in from the surface. While diving, a faint sulfide 'taste' occurs beneath the white layer. Apart from the pile of organic matter (mostly restricted to the area directly underneath the cenote), the floor of the cenote, cavern zone and cave is comprised of boulder-sized breakdown (and it assumed that the breakdown underlies the organic sediment as well).

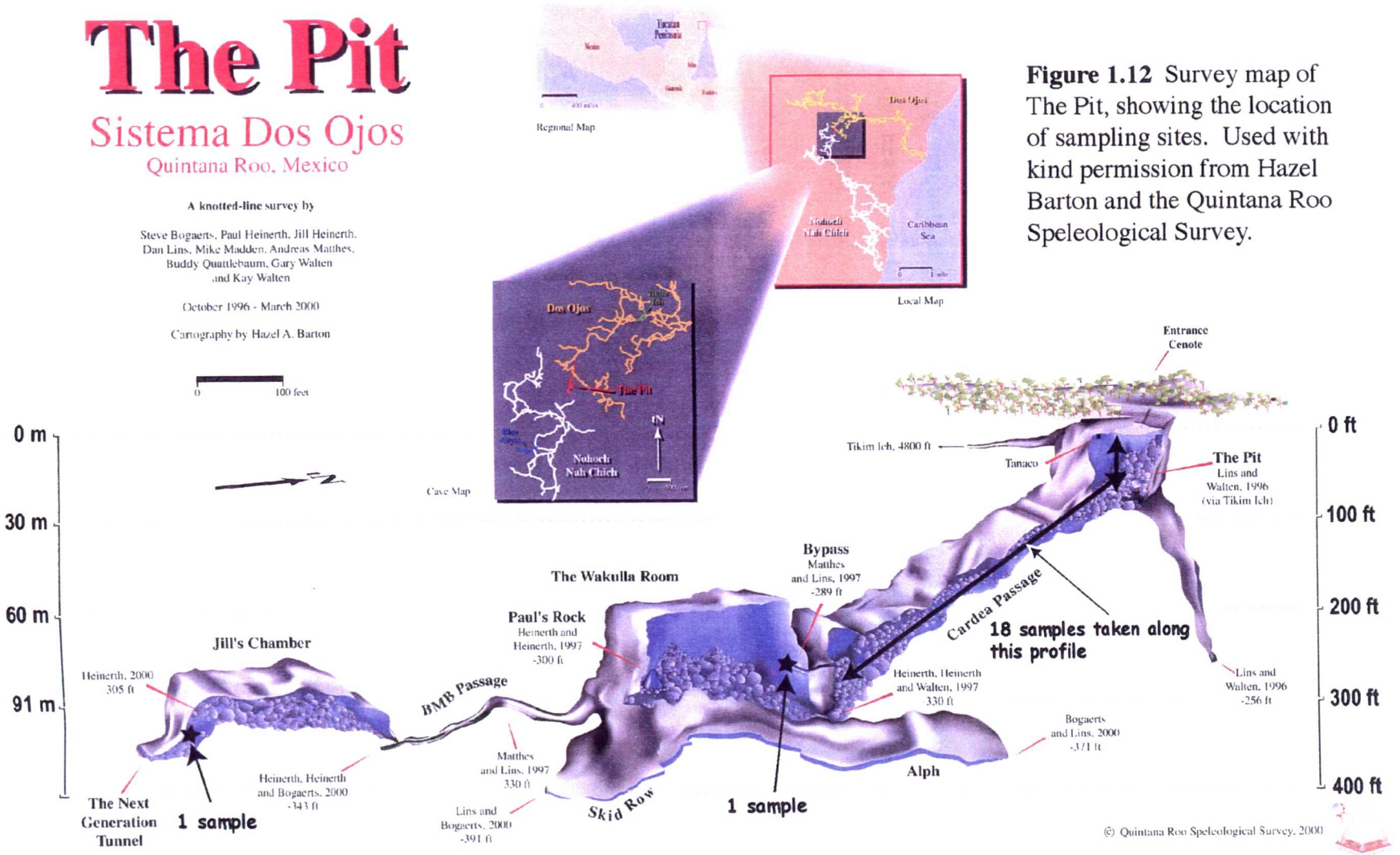

Figure 1.12 Survey map of The Pit, showing the location of sampling sites. Used with kind permission from Hazel Barton and the Quintana Roo Speleological Survey.

1.11.3 Ak Kimin

Ak Kimin is a coastal site that discharges into Yalku Lagoon in Akumal (Figure 1.8). Ak Kimin appears to have developed along fractures that run mostly parallel to the coast up to a maximum explored water depth of ~69 m. These fracture-guided passages occur below ~20 m depth, above which, extensive shallow (~<10 m water depth) horizontal passages have developed, reaching an explored distance of ~2 km inland. The survey data from this site is currently not published.

Sistema Ak Kimin comprises two cenotes. Due to constant exchange with seawater, its mixing zone position is variable, ranging in thickness from 0.8 to 8.6 m. In addition, Ak Kimin is subject to large amounts of surface-derived organic inputs, including those from mangrove swamps and nearby tourist developments. Thick (several meters) layers of sediment cover breakdown piles and when these are disturbed, sulfide can be tasted.

Chapter 2

Methodology

2.1 Introduction

The approach adopted in this study has been to combine field sampling and experiments with geochemical and microbiological analyses and numerical modeling to examine the geochemistry and geomicrobiology of the freshwater system (Chapter 3), the fresh-saltwater mixing zone (Chapter 4) and the zone of saline groundwaters (Chapter 5). In addition, some complementary hydrological research was carried out as part of this thesis, although most of the hydrological research conducted in the field area is reported in Beddows (2004). Finally, limited analysis of geological samples has been performed, specifically to investigate the effects of mixing zone and saline zone diagenesis.

The field-based portion of this study comprised four field seasons. These took place in January-May 2000, then November 2000, June-July 2001 and August-September 2002. An important aspect of this work was accessing the subsurface using cave diving techniques. Almost all work was conducted along the east coast of the Yucatan Peninsula, although more limited sampling was conducted in the Merida area (Figure 1.2) in November 2000.

This chapter describes the methods used to study the geochemistry and geomicrobiology of the salinity-stratified coastal carbonate aquifer of the Yucatan Peninsula. This is followed by a brief description of the hydrological techniques employed and methods of analyses of cave and cavern wall-rock samples, in addition to an *in situ* dissolution experiment.

2.2 GPS Co-ordinates

A Garmin 12XL GPS (12 satellites) was used to mark the co-ordinates of the sampling sites (and, in the case of caves, their entrances). These co-ordinates were later used to determine the location of the site relative to distance inland from the Caribbean (East) coast. Precision was generally better than ± 6 m.

2.3 Access to sampling sites

Permission to enter sites was granted by Ejidos/land-owners or by way of paying an entrance fee. A car was used to access near-road sites, while horses or off-road vehicles were used to access more remote sites. Cave diving techniques (Prosser and Grey, 1992) were used to access the submerged cave sampling sites. In almost all cases, open circuit SCUBA equipment was used to conduct the dives, although on occasion closed-circuit rebreathers were also used.

2.4 Aqueous Geochemistry

Water samples were collected from various geochemical environments including surface pools, drip samples, freshwater lens, mixing zone, saline zone, rainfall, throughfall, runoff and seawater. Descriptions of these water types are given in Chapter 1.

2.4.1 YSI Profiles

In situ profiles of specific conductance, temperature, pH, dissolved oxygen and depth were carried out using either a Yellow Springs International (YSI) 600 xlm or 6000 multi-parameter probes. The YSI 6000 was used for taking measurements in sites >60 m water depth.

The YSI multi-parameter probe was set to have a sampling interval no longer than 4 seconds (the time required for the stabilization of the dissolved oxygen probe) and was used to obtain profiles of the water column either by cave diving or by being lowered from

the surface on a rope. While cave diving, the profiles were conducted with the probe held out in front of the diver (horizontally so that the probes were at the same depth as the instrument's depth gauge). The profile was taken from cave ceiling to floor in order to minimize disturbance to the water column by exhaled bubbles. The oxygen probe was removed for sites suspected of having sulfide to avoid poisoning the electrode. The specifications of the YSI 600xlm and 6000 multi-parameter probes are summarised in Table 2.1.

Table 2.1 Specifications of the YSI 600xlm and 6000 multi-parameter probes.

Probe	Sensor Type	Range	Accuracy	Resolution
Depth	Stainless steel strain gauge	0-60 m (600 xlm) 60-200 m (6000)	± 0.12 m	0.001 m
Temperature	Thermistor	-5 to 45°C	± 0.15°C	0.01°C
Dissolved Oxygen	Rapid Pulse, Clark type, polarographic	0-500% air saturation	± 2-6% saturation	0.1% saturation
Conductivity	4 electrode cell with autoranging	0-100 mS/cm	± 0.05% + 0.001 mS/cm	0.001 mS/cm to 0.1 mS/cm (range dependent)
pH	Glass combination electrode	0-14 units	± 0.2 units	0.01 units

2.4.2 Sample Collection

2.4.2.1 Cenotes and Submerged Caverns and Caves

Samples from cenotes and submerged cavern and cave sites were collected using 1.5 L capacity 7 cm diameter PVC sampling tubes. The tubes were filled at the surface with cenote water (to make them negatively buoyant) and were then cleared of this water in exchange for sample water by the forward motion of the diver. Once filling was complete, the tubes were capped immediately at both ends. Sample depths were chosen from YSI

profiles and depths were determined underwater using UWATEC and Beauchat Aladin Pro dive computers (± 0.1 m).

For detailed discrete sampling within the mixing zone, ten pieces of ≥10 m long (4.5 mm diameter) PVC tubing were used (similar to the method described by Schwabe, 1999). Their length allowed sampling from an upstream portion of the cave whilst minimizing diver disturbance to the water at the point of sample intake. The tubes were used to obtain samples for both geochemical and microbiological analyses and thus were sterilized (washed three times with ethanol and rinsed three times and then filled with pressure-sterilised distilled water) before use. The tubes were clamped at both ends to prevent loss of sterile water during transport. The tubes were suspended from the ceiling of the cave using nylon line and zip ties and this line was secured to the floor in the saline zone. Following installation, the input ends of the tubes were unclamped and the water column was left to settle for three days before sampling commenced. Sampling of each tube was undertaken using a 50 ml sterile syringe affixed to a three-way sterile stopcock, which was in turn attached to a sterile (ethanol washed and sterile distilled water rinsed and then emptied) 0.5 L blood bag. The sterile water within the tube was extracted using the 50 ml syringe and discharged into the surrounding cave water. The tube was then flushed twice with cave water before dispelling the intake water into the blood bag using the three-way stopcock. The bag was rinsed with sample water twice (and this water was then discharged into the surrounding cave water) before filling the blood bag with sample. Three bags were filled per sample depth: one for microbiological analyses and two for geochemical analyses. The three-way stopcock was shut for transport of the bags out of the cave.

At all sites, shallow samples were collected first, and the depth of the sampling increased progressively in order to minimise the disturbance to the water column. For some sites with very sharp mixing zones (occurring over centimeters, e.g. Cristal), the main sampling methods used (i.e. a 7 cm diameter PVC tube) were not ideal. In these instances, the 4.5 mm diameter tubing described above would have been adequate, but this method was used at only one site due to the logistics involved in set-up dives.

2.4.2.2 Static and pumped wells

To sample waters from static wells or at sites where diving was not allowed (drinking water supply sites), either a bucket and rope or a VanDorne sampler was used to sample the groundwater.

Pumped wells were pumped for a minimum of 3 minutes (up to 10 minutes) prior to sampling. Samples were taken through PVC tubing into glass or Nalgene bottles.

2.4.2.3 Rainfall, Runoff, Throughfall and Vadose Drip Samples

Rainfall samples were collected using a funnel into a glass bottle. Run-off and throughfall samples were collected directly into glass or Nalgene bottles.

Drip water samples were collected over a period of between 2 and 48 hours, depending on the drip speed. For fast drips, a glass funnel and narrow-mouthed glass bottle were placed below the stalactites, while for slower drips the rim of a Nalgene bottle was placed over the end of the stalactite and was tied on, in order to reduce evaporation rates.

2.4.3 Field (on-site) Analyses and Sample Preservation

At the surface, the samples collected using the methods described in Section 2.4.2.1 were immediately flowed through a closed cell system (Figure 2.1), modified from Garske and Schock (1986), which allowed the measurement of pH and dissolved oxygen with minimal degassing of the sample.

Within the cell, pH was measured using a WPA high precision (± 0.02 pH units) digital pH meter calibrated (2 point calibration) before and after each batch of analyses with Fisher or Sigma high precision pH buffers (± 0.01 pH units). DO was measured using a WTW OX91 dissolved oxygen meter (±1 % saturation) and the meter was calibrated to 100% saturated air before each batch of analyses.

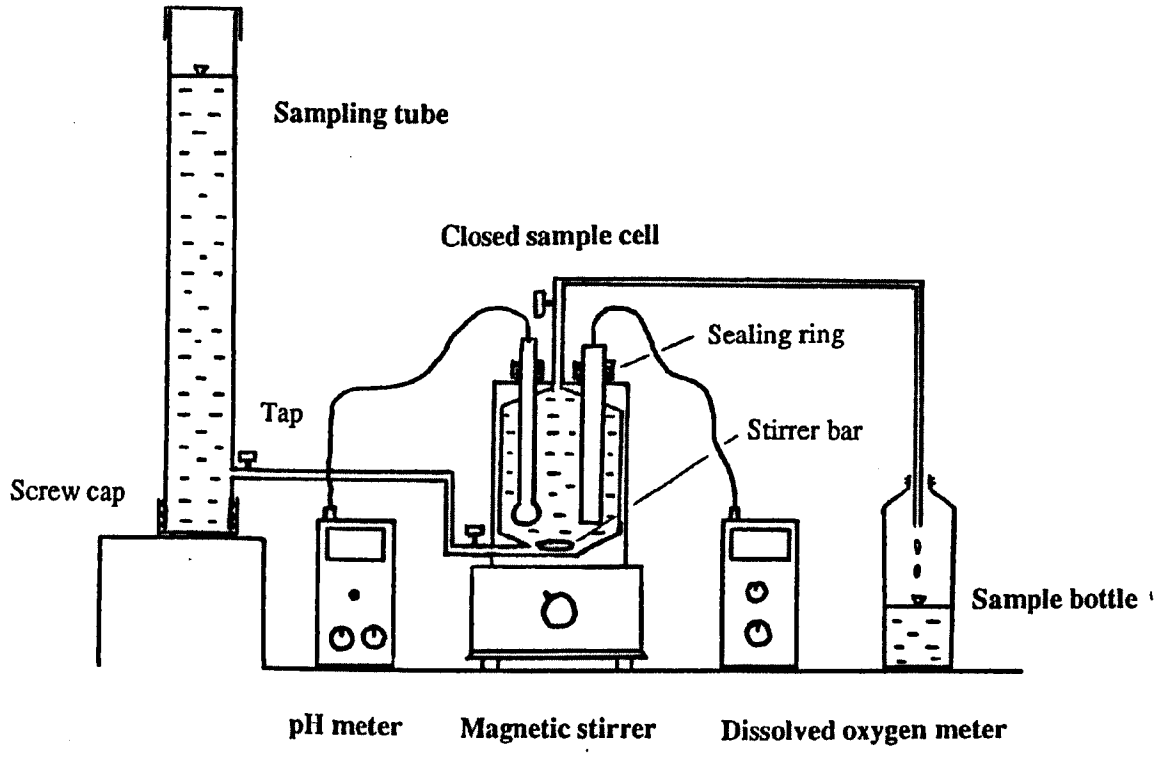

Figure 2.1 Flow-through cell used to measure pH and dissolved oxygen from collected samples with minimal degassing. Diagram from Whitaker (1992).

Once the sample had passed through the closed cell, samples were then split. The bulk of the sample was stored in 500-1000 ml Nalgene® bottles. A 125 ml sub-sample was stored in a glass bottle for analysis of alkalinity and a 60 ml sub-sample was stored in a Nalgene bottle with zinc acetate (final solution ~10% ZnAc) for later analysis of sulfide. Occasionally, samples for methane analysis were extracted from the sampling tubes using a small piece of PVC tubing and syringes. A needle was fitted to each syringe and a 20 ml sub-sample was injected into inverted 30 ml silicone-septa-sealed glass serum crimp vials that had previously been flushed with filtered oxygen-free nitrogen (OFN) inside a laminar flow cabinet. The samples were kept inverted during the entire course of the method so that any headspace remained on the non-septa side of the vials. The samples were immediately frozen in the field lab and were transported inverted and frozen from Mexico to the UK. Samples stored for later analysis of $\delta^{34}S$ of sulfate were kept in 500 or 1 L Nalgene bottles with a sample:copper acetate ratio of 10:1.

After running the sample through the closed cell, the specific conductance of the sample was verified using a WTW LF90 meter (±0.5 mS/cm). The YSI 600xlm and the WTW LF90 instruments were later cross-calibrated.

2.4.4 Field Laboratory Analysis

Upon returning to the field laboratory (Centro Ecologico Akumal), samples were immediately analysed for their alkalinity concentration by titration with 0.01 M HCl, using BDH 4.5 as an indicator. The different batches of HCl were standardized and, where permitted by sample volume, at least three determinations were made for each sample. Sample volume was measured using Grade A glass pipettes (pre-washed with sample) and the volume of HCl was measured using a Grade A 50 ml burette.

Samples for cation and anion analyses were filtered using a vacuum pump through a 0.45 μm cellulose nitrate membrane filter, cations were preserved in 1% HNO_3 and both sample types were stored in polypropylene Nalgene® bottles. 10 ml sub-samples for DOC analyses were filtered through combusted Whatman 0.45 μm glass fiber (GF/C) filters, acidified in concentrated HCl to pH 1-2 and stored in glass bottles which had been

combusted at 450°C overnight. The bottles were then capped with septa and lids that had been washed in dichloromethane (DCM).

Analytical techniques and their associated uncertainties are summarized in Table 2.2.

2.4.5 Laboratory Analysis in the UK

2.4.5.1 Cations

Apart from strontium, all other cations (Ca^{2+}, Mg^{2+}, Na^{+}, K^{+}) were analysed using a Jobin-Yvon JY 24 compact sequential inductively-coupled plasma atomic emission spectrometer. At least six standards (diluted with 1 % HNO_3 from universal stock solutions and made up in A grade volumetric flasks) were used to calibrate each instrument and a drift standard and a blank (1 % HNO_3) were run after every tenth sample. A few water samples were run repeatedly throughout the different runs in order to standardize the results. Each sample was run in at least triplicate.

Sr^{2+} was analysed using a VG PlasmaQuad Turbo 2 plus inductively coupled plasma mass spectrometer (ICP-MS) using indium as an internal standard and dilutions were made using 1% HNO_3 At least six standards (diluted with 1 % HNO_3 from universal stock solutions and made up in A grade volumetric flasks using calibrated pipettes) were used to calibrate the instrument and a drift standard and a blank (1 % HNO_3) were run after every tenth sample. A few water samples were run repeatedly throughout the different runs in order to standardize the results from the different runs. Each sample was run in at least triplicate.

2.4.5.2 Sulfate and Chloride

Sulfate and chloride were analysed using a Dionex DX500 ion chromatograph (IC) with an IonPac AG11-HC 4 x 50 mm guard column and IonPac AS11-HC 4 x 250 mm anion separator column. A 30 mM NaOH eluent was used, which was degassed with helium. Sodium sulfate and sodium chloride standards were used. Due to machine availability, samples were run only one time each. Dilutions were weighed ($\pm 10^{-5}$ g) rather than measured volumetrically, enabling higher precision to be attained (discussed below).

Table 2.2 Techniques used for aqueous geochemistry analyses and associated analytical uncertainties, expressed as percentage fractional error (fe) and the absolute error (E) expressed directly as units of measurement, for mean seawater (SW) and mean fresh ground water (FGW) samples from this study.

Element	Analytical Technique	fe (%)	Σ E(SW) ± 1σ (mM)*	Σ E(FGW) ± 1σ (mM)*
Calcium	ICP-AES	1.08	10.29 ± 0.11	2.76 ± 0.03
Magnesium	ICP-AES	1.39	54.9 ± 0.76	3.77 ± 0.05
Sodium	ICP-AES	1.51	496 ± 7.49	27.61 ± 0.42
Potassium	ICP-AES	1.61	10.55 ± 0.17	0.54 ± 0.00
Strontium	ICP-MS	8.31	0.099 ± 0.008	0.016 ± 0.001
Alkalinity	Titration with HCl	0.54	2.58 ± 0.01	6.69 ± 0.04
Chloride	IC	1.01	575 ± 5.81	32.51 ± 0.33
Sulfate	IC	0.87	29.05 ± 0.25	1.73 ± 0.02
Sulfide	Cline Method, Spectrophotometry	3.92	0	0.05 ± 0.002
pH	High Precision pH meter	0.28	8.32 ± 0.02	7.07 ± 0.02
DOC	Pyrolitic Oxidation	1.50	0.38 ± 0.01	0.81 ± 0.01
DO	Dissolved Oxygen Meter	-	<1 %	<1 %

*All absolute errors are expressed as mM, with the exception of pH and DO (%)

2.4.5.3 Sulfide

Sulfide was measured following the Cline method (Cline, 1969) using a Cecil Series 2/CE 292 digital UV spectrophotometer (tungsten lamp, 670 nm, absorbance). Sulfide was analysed colormetrically on samples preserved in 10% zinc acetate using the methylene blue method of Cline (1969). All samples were run in triplicate. The detection limit was 1 μmol/l.

2.4.5.4 Dissolved Organic Carbon (DOC)

DOC analyses were performed using the Shimadzu TOC-500 total organic carbon analyser using the high temperature catalytic oxidation method of Sugimura and Suzuki (1988). This involved pyrolitic oxidation of the DOC on the surface of a catalyst (0.5% platinum on alumina) to generate gaseous CO_2, which was determined by an infrared analyser. Due to the high alkalinity of the samples, the acidification step in the preservation method caused an unnaturally high level of CO_2 to be present in the sample. Thus, measurements of the acidified solution caused unrealistically high values of DOC. After the first field trip, subsequent samples were sparged for fifteen minutes using zero-grade air (BOC, UK) to eliminate this excess CO_2. Subsequent DOC results were believed to be much more accurate and precision was greatly improved (20% standard deviation became less than 3% for most samples). A minimum of three determinations were made for each sample. The "DOC" results from the sparging method are known as 'non-purgable organic carbon' or NPOC.

2.4.5.5 Methane

The 20 ml sub-samples collected for methane analysis were thawed, inverted, at 4°C. After thawing, 600 μl 10 M HCl was injected into each vial (using a needle and syringe) to convert the pH of the samples to ~1 and release any gases from the water. After the acid additions, the samples were shaken for 20 minutes using an automated shaker. The headspace gas was removed by replacing its volume with 10% KCl (pH 1) solution. Both the gas removal and KCl additions were performed using needles and syringes fitted with

3-way stopcocks. The syringe used for gas extraction was "washed" 3 times with helium prior to removing the headspace. $\geq$ 5 ml gas samples were injected into Carlo Erba HRGC5300 Mega Series Gas Chromatograph (GC). Air was run as a 'blank'. Peak areas were converted to concentrations using a standard of known CH_4 concentration as a reference (20.8 ppm CH_4, BOC). The standard was run at the beginning, middle and end of the run to enable drift corrections. One sample was run in triplicate to test the method for its reproducibility. Three replicates of air were also run through the GC to determine the minimum detection limit for this method (~2 ppm CH_4).

2.4.5.6 $\delta^{34}S$-SO_4

Analyses of $\delta^{34}S$-SO_4 were carried out at the University of Leeds (UK). The samples (preserved in copper acetate) were first filtered through 0.45 μm cellulose nitrate filters to remove suspended solids/CuS precipitates. The pH of the filtrates were adjusted to 2.5-3.0 using AnalaR grade HCl. Any overshoot was corrected using a 5% ammonia solution. The filtrates were then heated to 70°C ± 5°C on a hotplate, and a 10% (v/v) 100g/l $BaCl_2$ solution added to precipitate $BaSO_4$. Samples were left covered on the hotplate for 3 hours, then cooled slowly overnight. The $BaSO_4$ precipitates were filtered onto preweighed 0.45 μm cellulose nitrate filters (Nucleopore), rinsed thoroughly with distilled water and dried overnight at 70°C in preparation for isotope analysis. $BaSO_4$ was converted to SO_2 (Halas *et al.*, 1982) and cryogenically purified for isotopic analysis on a VG SIRA10 mass spectrometer. Raw data were corrected to $\delta^{34}S$ (precision ± 0.2 ‰ to ± 0.4 ‰, depending on run) relative to SMOW and CDT standards, using standard procedures (Craig, 1957).

Extraction of sulfur from solid residues

Known volumes of samples from hydrogen sulfide layers were pressure filtered through 0.45 μm cellulose nitrate membranes, and air-dried. Total sulfur (presumed to be predominantly elemental sulfur) from these filters was converted to sulfate by combustion with oxygen in a par-bomb apparatus at Leeds University. The sulfate was recovered as $BaSO_4$ and analysed for $\delta^{34}S$ as described in section above.

2.4.6 Data Quality and Calculation of Saturation Indices and pCO_2

Ion Balance Errors (IBEs) were calculated for all water samples as the difference between the equivalencies of the total of all cations and anions divided by the sum of the total anions plus cations. IBEs give an indication of the net charge balance error, which, without any analytical error, should be zero. IBE calculations included the major cations (Ca^{2+}, Mg^{2+}, Na^{+}, K^{+}) and anions (Cl^{-}, SO_4^{2-}, HCO_3^{-}) but excluded minor constituents such as strontium and sulfide, which do not contribute significantly to the total elemental composition of the waters of this study.

IBEs are larger for the more dilute samples, probably due to difficulties encountered in trying to obtain accurate and stable alkalinity measurements from low ionic-strength poorly buffered solutions such as rainwater and vadose drip samples. Apart from these samples, IBEs for all other water samples lie within ±10% of zero. Over 92% of the waters had an IBE smaller than ± 5% and more than 65% of the waters had an IBE less than ± 2% (Figure 2.2). The mean IBE was –0.22 ± 2.68%.

The chemical composition of most samples is dominated by the seawater-derived component and errors are largely driven by errors in chloride and sodium analyses. All analyses were replicated 3 times, except sulfate and chloride.

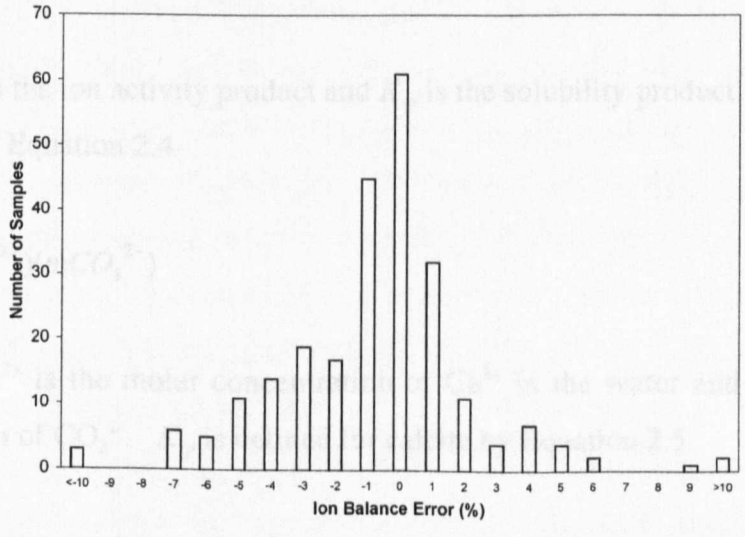

Figure 2.2 Frequency plot of ion balance errors for all geochemical samples with complete cation and anion analyses (n = 249).

The USGS geochemical modeling program PHREEQ-C 2.8 (Parkhurst, 1995) was used to calculate the partial pressure of carbon dioxide (pCO_2) with which the waters were in equilibrium and the degree of thermodynamic equilibrium with respect to the minerals aragonite, calcite, dolomite, disordered dolomite, anhydrite and gypsum. The partial pressure of carbon dioxide is expressed as $\%pCO_2$ at 1 atmosphere. The log CO_2 value derived from PHREEQ-C (x in Equation 2.1) is converted to % pCO_2 using Equation 2.1. For waters equilibrated with atmospheric CO_2 at 25°C, x is –3.5 and pCO_2 is 0.03%.

$$pCO_2(\%) = 10^x \cdot 100 \tag{2.1}$$

Saturation indices (SI) of water measure the extent of its deviation from equilibrium with respect to a particular mineral. A positive SI indicates supersaturation, while a negative SI indicates undersaturation. The reaction showing the relationship between calcite (or aragonite) precipitation-dissolution is shown in Equation 2.2.

$$Ca^{2+} + CO_3^{2-} \leftrightarrow CaCO_3 \tag{2.2}$$

To determine if a water is under- or super- saturated with, for example, calcite, Equation 2.3 is used.

$$SI_{calcite} = \log \frac{IAP}{K_{sp}} \tag{2.3}$$

where IAP is the ion activity product and K_{sp} is the solubility product. IAP is calculated for calcite using Equation 2.4.

$$IAP = (mCa^{2+})(mCO_3^{2-}) \tag{2.4}$$

where mCa^{2+} is the molar concentration of Ca^{2+} in the water and mCO_3^{2-} is the molar concentration of CO_3^{2-}. K_{sp} is defined for calcite by Equation 2.5.

$$K_{sp_{calcite}} = \frac{(Ca^{2+})^1(CO_3^{2-})^1}{(CaCO_3)_s^1} \tag{2.5}$$

where s = solid (thus the term $(CaCO_3)_s^1$ is equivalent to 1). $(Ca^{2+})^1$ and $(CO_3^{2-})^1$ are the molar concentrations of these constituents at equilibrium. Thus, K_{sp} is equal to the *IAP* at equilibrium (where $SI_{calcite}$ equals zero). The K_{sp} values for the different minerals discussed in this study are presented in Table 2.3.

Table 2.3 Equilibrium Constants (K) of dissolution reactions for aragonite, calcite, ordered dolomite and disordered dolomite and anhydrite and gypsum at 25°C.

Mineral	K
Aragonite	$10^{-8.34}$
Calcite	$10^{-8.48}$
Ordered Dolomite	$10^{-17.09}$
Disordered Dolomite	$10^{-16.54}$
Anhydrite	$10^{-4.36}$
Gypsum	$10^{-4.58}$

The results generated from geochemical modeling are very much dependant on the equilibrium constants used in the calculations (Table 2.3). Equilibrium constants used for calcite and aragonite are well constrained by experimental data and are considered dependable (Plummer and Busenburg, 1982). However, there is a large amount of uncertainty with respect to the equilibrium constant of dolomite and because of this, saturation indices were determined for both stoichiometric (ordered) and non-stoichiometric (disordered) dolomite. The equilibrium constant for ordered dolomite is the default of the modeling program PHREEQC (Parkhurst, 1995) and it, as well as the equilibrium constant for disordered dolomite is computed as a function of pressure and temperature (Helgeson et al., 1981) rather than being derived from experimental data, due to difficulties encountered in attempts to precipitate dolomite at near-earth surface temperatures and pressures (Lippmann, 1973). The equilibrium constants of dolomite and disordered dolomite, therefore, remain less exact than those of calcite and aragonite.

2.4.6.1 Analytical Precision and Accuracy

The precision for most cation analyses (Ca^{2+}, Mg^{2+}, Sr^{2+}, Na^{+}, K^{+}), alkalinity (as HCO_3^-), sulfide and DOC was determined by running each sample a minimum of three (up to twelve) times. The relative standard error (or fractional error, fe) is calculated by dividing the standard deviation by the mean and multiplied by one hundred, and thus, is expressed as percentage error. The mean fractional errors associated with these analyses are illustrated in Table 2.2.

Due to limited availability of the IC, chloride and sulfate samples were generally run only once. The errors associated with both chloride and sulfate analyses include those associated with making up the standard stock solutions (fe_{STOCK} = ± 0.06%), weighed dilutions (fe_{WEIGHT} = 0.25 ± 0.21%), sample density calculations ($fe_{DENSITY}$ = 0.30 %) and the error from the Dionex (IC) itself (fe_{DIONEX} = ± 0.23 % for sulfate and ± 0.46 % for chloride, based on six replicate analyses of the same solution). Calibration curves consistently produced r^2-values of 1.000 (n = 6) for both chloride and sulfate and it is assumed that no additional error was added when making weighed diluted standards from the stock standard solution. Combining the fractional errors results in a total fractional error of ± 0.87 % for sulfate and ± 1.10 % for chloride. Samples made up and analysed in triplicate produced fractional errors of $\leq$ 0.37 % for sulfate and $\leq$ 0.01 % for chloride, values well within the expected error of these analyses. In addition, there was no apparent bias (in terms of fractional error) towards fresh or saline samples, indicating that the error encountered when making weighed dilutions was insignificant (and is likely over-estimated). However, because the absolute error is defined as the product of the fractional error and the concentration of the sample, the absolute error of saline samples is greater than that of freshwater samples. All fractional errors are comparable with those expected from the methods used (Brown et al, 1970), and most values were <2% (Table 2.2).

The precision of derived variables such as pCO_2 and saturation indices of calcite, aragonite and ordered and disordered dolomite, are calculated using the probable error method, where the total fractional error (Σfe) of the derived variable is calculated as the square root of the sum of the squared individual errors (Equation 2.6).

$$\Sigma fe = \sqrt{fe_1^2 + fe_2^2 + fe_3^2 \ldots\ldots fe_n^2} \qquad (2.6)$$

The fractional errors of all parameters that are used to calculate the derived variable must be included in this calculation. This technique assumes all errors are randomly distributed and does not take into account possible multiplier effects within the calculations.

Probable error calculations produced a total fractional error of ± 1.83 % (precision is ± 0.006) for aragonite and calcite saturation indices and ± 2.48 % (precision is ± 0.015) for ordered and disordered dolomite saturation indices. The total probable error for pCO_2 is 0.020 % pCO_2, which is equivalent to a fractional error of around 0.85 %. Over 95% of the uncertainty involved with pCO_2 and saturation index calculations is due to pH. Well-buffered samples with high dissolved solid content resulted in more stable pH readings than samples of poorly buffered low ionic strength solutions (e.g. rainfall, runoff, vadose drips). The precision associated with the calculations of ΔpCO_2 and ΔSI (which are determined from the difference between sample values and values derived from geochemical modeling) are determined by combining errors. Thus, the precision of ΔSI-A and ΔSI-C is 0.012 (i.e. 2 x 0.006). Likewise, the precision of ΔSI-D and ΔSI-DD is 0.030. The fractional error of ΔpCO_2 is 1.70 %.

The accuracy of the geochemical analyses is determined using multiple runs on standard calibrations and running drift samples (both standards of known concentrations and water samples).

2.4.6.2 Drift Corrections and Blank Subtractions

A drift standard (of a representative concentration for the given run) and a blank were analysed every 10-15 samples during geochemical analyses. Any systematic instrument drifts were corrected and samples were blank subtracted for each element analysed. The formula used to calculate "actual" sample concentrations is shown in equation 2.7.

$$[Sample] = \frac{(Conc - Blank)}{(((D_1)(P_1/n+1))+((D_2)(P_2/n+1)))} \qquad (2.7)$$

D_1 and D_2 were the drift factors run before and after the sample in question, respectively. D was calculated by dividing the concentration obtained from the analytical instrument for

the drift standard by the actual concentration of that standard. The blank was made up from 0.2 μm-filtered deionised water containing any constituents used in making the matrix solution of the other standards and samples (for example, in the case of cation analyses, the matrix solution used was 1% HNO_3, thus the blank was solely 1% HNO_3). P_1 and P_2 were the positions of the sample from D_2 and D_1, respectively, while n was the number of samples between the drift standards.

In seawater samples, the absolute and relative concentrations of most of the parameters studied agree with those published for Caribbean seawater (i.e. Stoessell, unpublished; Whitaker, 1992; Marcella, 1994; Reeve and Perry, 1994) and with those predicted from the dilution or concentration of standard seawater (Nordstrom et al, 1979) (Table 2.4).

Table 2.4 Comparison of seawater concentrations derived from six different studies.

Seawater Sample	Ca^{2+} (mM)	Mg^{2+} (mM)	Sr^{2+} (mM)	K^+ (mM)	Na^+ (mM)	HCO_3^- (mM)	SO_4^{2-} (mM)	Cl^- (mM)
Nordstrom, 1979	10.28	53.2	0.099	10.20	468	2.33	28.23	546
Whitaker, 1992	10.60	54.9	0.099	10.56	484	2.41	10.56	565
Reeve and Perry, 1994	10.63	56.57	n.d.	10.51	495	n.d.	29.86	578
Stoessell, unpublished	10.50	55.5	n.d.	10.51	489	2.48	29.10	576
Marcella, 1994	10.50	54.9	n.d.	10.36	496	2.49	30.42	575
Caribbean; this study ±1σ, n = 6	10.29 ± 0.27	54.9 ± 0.62	0.099 ± 0.000	10.55 ± 0.07	496 ± 3.34	2.58 ± 0.03	29.05 ± 0.24	575 ± 5.46

2.4.7 Geochemical Modeling

The geochemical modeling program PHREEQ-C (Parkhurst, 1995) was used to investigate the dominant reactions controlling the geochemistry of the Yucatan waters. PHREEQ-C was developed from the Garrels-Thompson ion-association model for seawater (Garrels and Thompson, 1962) and given the elemental composition of the water, as well as its pH

and temperature, the program's basic function is to calculate solution speciation and saturation states of the aqueous phase with respect to numerous mineral phases. PHREEQ-C is also able to model evolution along one or more phase boundaries and can calculate the resultant pH and pe as well as speciation and mass-transfer, due in part by geochemical work of Garrels and Mackenzie (1967) and computer programming developed by Helgeson (1968) and Helgeson et al. (1970).

In addition to calculating pCO_2 and saturation indices, PHREEQ-C was used to model the following:

i) **Mixing** of two solutions with defined percentages of each was performed. Fresh and saline end-members were chosen to model the expected mixing zone chemistry. However, mixing calculations were also made to investigate the potential mixing of waters within the freshwater system.

ii) **Evaporation/evapotranspiration** can be simulated by titrating the system with minus H_2O by an amount calculated from the budgeting of chloride concentrations. In the Yucatan Peninsula, where the vadose zone is ~10 meters thick, the majority of the evaporation may occur before reaching the freshwater lens. However, some may evaporate directly from the lens.

iii) **Microbial oxidation of organic matter** under aerobic conditions was modelled by adding organic carbon to the system in an amount equal to that measured as DOC. This method assumes that all carbon is in the labile form and that particulate organic carbon does not play a significant role.

2.4.8 Calculation of Rates of Diagenesis

Different carbonate minerals have different amounts of calcium, magnesium and strontium incorporated into them. As a result, the ratios of these elements in groundwater may be used to identify where diagenetic reactions involving aragonite, high- and low-Mg calcite and dolomite have occurred. In addition, the concentration of these elements may be used, in combination with flow data (derived from Beddows, 2004), to estimate rates of

diagenesis. It is important to note that most of the magnesium, calcium and strontium found in all but very fresh groundwaters comes from seawater. Consequently, calculations are carried out to subtract the concentrations of these elements derived from seawater, using chloride as a conservative tracer. The result is a term called "excess" (XS) for each element.

Results from the calculation vary, depending on the make-up of the end-member solutions. In the case of the freshwater and saline systems, dilution is determined relative to Caribbean seawater concentrations. For the fresh-salt water mixing zone, however, diagenetically evolved (local) fresh and saline groundwaters are used as end-members.

The method by which these uncertainties are calculated for a fresh-saltwater mixing zone sample is summarized below, using Ca_{XS} as an example. The absolute value of Ca_{XS} is derived from the calcium content of the sample relative to that in the fresh (FW-EM) and saline (SZ-EM) end-members and fraction saline end-member (%SZ-EM) of the sample (Equations 2.8 and 2.9).

$$Ca_{XS} = Ca_{SAMPLE} - (Ca_{FW-EM} + (Ca_{SZ-EM} - Ca_{FW-EM})(\%SZ - EM)) \qquad (2.8)$$

and

$$\%SZ - EM = \frac{(Cl_{SAMPLE} - Cl_{FW-EM})}{(Cl_{SZ-EM} - Cl_{FW-EM})} \qquad (2.9)$$

In order to compute the uncertainties associated with Ca_{XS} calculations, it is necessary to combine elements for the uncertainties associated with the percentage saline end-member, as well as the combined uncertainties associated with the calcium determinations (Equation 2.10). Note that E refers to error, which is expressed as a unit of measurement (e.g. mM), while fe refers to fractional errors.

$$\sum E_{Ca_{XS}} = \sqrt{(E_{Ca_{SAMPLE}})^2 + (E_{Ca_{SZ-EM}})^2 + 2(E_{Ca_{FW-EM}})^2 + ([Ca_{SZ-EM} - Ca_{FW-EM}] \times \sum fe_{Cl})^2} \qquad (2.10)$$

where

$$\sum fe_{Cl} = \sqrt{4 \times (fe_{Cl})^2}$$

The second part of Equation 2.10, underlined, depends upon the magnitude of the difference between the fresh and saline end-member calcium concentrations. Consequently, a saline groundwater mixed with a very fresh water sample will result in greater uncertainty than a saline groundwater sample mixed with a brackish lens sample. In addition, the total error term is dependent on the concentration of calcium in the sample, which is in most part related to the salinity/chloride content of the sample (Table 2.5). Table 2.5 summarises the absolute errors for Ca_{XS}, Sr_{XS}, Mg_{XS}, SO_{4XS} and Ca_{XS}. An average value of these two estimates ($\bar{x}GW$), which is considered to be representative of the analytical uncertainty of all waters, is used where a single value is required (e.g. to indicate uncertainties on cross plots).

Table 2.5 Combined errors for mixing zone excess calculations (1σ).

Parameter	ΣE(FGW) (mM)	ΣE(SGW) (mM)	ΣE($\bar{x}$GW) (mM)
Ca_{XS}	± 0.16	± 0.18	± 0.17
Mg_{XS}	± 0.97	± 0.98	± 0.98
SO_{4XS}	± 0.58	± 0.64	± 0.61
Sr_{XS}	± 0.0091	± 0.0123	± 0.0106

Note: For individual calculations these values may be slightly different due to the variations in end-member compositions.

The method by which the uncertainty is computed for saline zone (and freshwater) XS calculations is summarized below, again using Ca_{XS} as the example. The absolute value of Ca_{XS} is determined by the difference between the actual calcium concentration of a sample and the calcium concentration predicted for that sample, based on the Ca:Cl ratio of seawater (Equation 2.11).

$$Ca_{XS} = Ca_{SAMPLE} - \left(\frac{Ca_{SEAWATER} \times Cl_{SAMPLE}}{Cl_{SEAWATER}} \right) \qquad (2.11)$$

The total probable error can then be defined using Equation 2.12 (where E refers to absolute error and fe refers to fractional errors).

$$\sum E_{Ca_{XS}} = \sqrt{\left(E_{Ca_{SAMPLE}}\right)^2 + \left(\frac{Ca_{SEAWATER} \times Cl_{SAMPLE}}{Cl_{SEAWATER}} \times fe_{Ca_{PREDICTED}}\right)^2} \quad (2.12)$$

where

$$fe_{Ca_{PREDICTED}} = \sqrt{(fe_{Ca_{SEAWATER}})^2 + (fe_{Cl_{SAMPLE}})^2 + (fe_{Cl_{SEAWATER}})^2}$$

Saline groundwater Ca_{XS} total error ($\sum E_{CaXS}$) is ± 0.35 mM (±14 mg/l), $\sum E_{MgXS}$ is ± 1.11 mM (± 27 mg/l), $\sum E_{SO4XS}$ is ± 0.53 mM (± 51 mg/l) and $\sum E_{SrXS}$ is ± 0.012 mM (± 1.05 mg/l).

Freshwater Ca_{XS} total error ($\sum E_{CaXS}$) is ± 0.04 mM, $\sum E_{MgXS}$ is ± 0.15 mM, $\sum E_{SO4XS}$ is ± 0.06 mM and $\sum E_{SrXS}$ is ± 0.003 mM.

2.5 Geomicrobiology

Methods in microbial ecology can be divided into those focusing on biodiversity, and those that study microbial activity. The enumeration of total or specific bacteria can lend valuable insight into the types of bacteria present in a particular environment and their potential for interacting with that environment (Madigan *et al.*, 2000).

It is important to note that the mere presence of organisms implies nothing about their activity and the effect they can have on their environment (Madigan et al., 2000). In order to determine the effects of bacteria in the environment, chemical concentrations of particular compounds (e.g. O_2, NO_3^{2-}, NH_4^+, SO_4^{2-}, HS^- and CH_4) in the water can often provide useful clues for determining which metabolic processes dominate. Rates of activity in flowing cave systems, however, can be difficult to measure because the cave waters are seldom (if ever) in "steady state". Thus, first-order Fickian diffusion models (Schultz, 2000) cannot easily be used to determine approximate rates of activity. Experiments to examine activity rates (e.g. oxygen consumption) may be designed in

situations such as these. In addition, stable isotopes can be useful in determining where redox reactions are taking place, and can provide clues for elucidating microbial activity.

Sample Collection and Preservation

Water samples for microbiological analyses were collected from submerged cave sites using either:

- autoclaved (pressure-sterilised) 125 ml red-topped glass Duran® bottles
- The PVC tubing and blood-bag set-up described above for obtaining a detailed profile of samples throughout a mixing zone

The capped Duran bottles were brought into the cave empty. Upon reaching the sampling location, the top of the bottle was faced (at arms reach) upstream of the diver and the lid was removed while the diver continued to swim slowly upstream. Subsequent samples were taken from progressively deeper depths within the cave to minimize disturbance from up-welling bubbles caused by the diver.

The tubing, blood-bag, syringe and three-way stopcock set-up used to sample cave waters is the same as that described for geochemical sampling in Section 2.4.2.1. However, prior to microbiological sampling, the tubing, blood-bags, syringes and three-way stopcocks were washed three times with ethanol and rinsed with pressure-sterilised distilled water before placement in the cave. The tubes were brought into the cave filled with sterile distilled water. All of the sampling equipment was rinsed three times with sample water (by drawing sample water through the sampling 'system') before sampling commenced. Blood bags were rinsed an additional three times with sample water before being filled with sample from the upstream site. The blood-bags were sealed with sterile three-way stopcocks for transport to the surface.

Bacterial mat and sediment samples were obtained using sterile syringes with the luer ends removed. The syringes had been sterilized by autoclaving with aluminum foil taped over the open ends. Just prior to sampling, the foil was removed. After sampling, the open ends of the syringes were capped with sterile (autoclaved and wrapped in foil) rubber caps.

Although sampling of drip waters was not carried out completely aseptically (the sample was exposed to the cave air during the two-hour sampling interval needed to obtain sufficient volume required for analyses), attempts were made to minimize contamination. Drip water samples were collected using a glass funnel placed in a glass Duran bottle. This set-up was wrapped in aluminum foil and autoclaved prior to use. The set-up (and Duran bottle lid) was brought to the sampling site wrapped in sterile aluminum foil. The Duran bottle and funnel were then placed under the dripping stalactite.

One pumped well was sampled using a sterile (autoclaved) glass Duran bottle, after pumping for 10 minutes. The bottle was overfilled and capped.

All samples were stored on ice in a cooler during transport from the sampling site to the field laboratory. Once at the laboratory, samples were stored in a fridge ($\leq$4°C) until preservation/inoculation. The time interval between sampling and preservation was never more than six hours (and was usually less than four hours).

Field anaerobic chamber

A field anaerobic chamber was constructed out of a modified gas-impermeable AtmosBag™ supplied by Sulpelco, UK. The bag was fitted with two heavy-duty rubber gloves attached to the bag using PVC 'cuffs' and duct tape. A plastic tray was placed in the interior of the bag to add stability. The interior of the bag, gloves and tray were washed with 70% ethanol prior to use. The samples, AODC and MPN vials, needles, syringes, ethanol and cotton wool were placed in the bag alongside Anaerocults supplied by Supelco, UK, and the bag was emptied of air and sealed using tape. The bag was then filled with 0.2 μm-filtered oxygen free nitrogen (OFN) gas (supplied by INFRA, Mexico) and the oxygen levels in the bag were measured using a Ceramatec Mini-OX I oxygen analyzer. Sample preservation and the preparation of MPN series commenced when oxygen levels reached less than 0.5%.

2.5.1 Total Counts

Sample preservation

Within the sealed field anaerobic chamber (described above), 9 ml of sample water was taken from the sample bottle using a sterile 10 ml syringe and needle and placed into sterile serum vials containing 1 ml of filter sterilised (0.1 μm) 4 % formaldehyde with 3.5 % NaCl (Fry, 1988). The serum vials had been furnaced overnight at 450°C to remove any organic carbon. Septa were sterilized by boiling in 20% HCl.

Counting

The methods used to count total cell numbers are based on those of Fry (1988). Fixed samples were vortex mixed, and a sub-sample (1 to 2 ml) was added to 10 ml of 2% filter-sterilised (0.1 μm) formaldehyde in 3.5% NaCl. 50 μl of acridine orange stain was added and left for three minutes. The solution was then filtered through a 25 mm Nucleopore black polycarbonate membrane with a pore size of 0.2 μm. The filter was rinsed with a further 10 ml of 2% filter-sterilised formaldehyde in 3.5% NaCl, and then mounted in paraffin oil under a coverslip. Filters were viewed using a Zeiss Axioskop microscope fitted with a 50 W mercury vapour lamp and a wide-band interference filter set for blue excitation. A 100x (numerical aperture = 1.3) Plan Neofluar lens and 10x eyepieces were used. Bacterially-shaped, green fluorescent objects with sharp outlines were counted as bacteria in a 10 by 10 grid (98 μm by 98 μm). Cells were classified as 'on particle' (bacteria in association with particulate matter), 'off particle' (stand-alone bacteria not associated with particulate matter), 'dividing' (those bacteria with a clear invagination) and 'divided' (closely adjacent and identical cells). A minimum of 200 cells and 20 fields of view were counted for each filter. All counts were performed in triplicate. 'On particle' bacteria were counted as two bacteria to account for hidden bacteria. Blanks were run at the end of each counting session and always produced a cell count of zero.

2.5.2 Viable bacteria

Most Probable Number (MPN) series

The presence and most probable numbers of populations of specific viable groups of bacteria were determined using the MPN method; the serial dilution of environmental samples in specific growth media (based on APHA, 1969; Hurley and Roscoe, 1982). Two methods were used to obtain estimates of Most Probable Numbers of bacteria. The first method described was used for samples taken between January and May 2000 during a reconnaissance fieldtrip. The second method described was used for samples taken between June and August 2001. The dates the samples were taken are mentioned in subsequent chapters. Media preparations were carried out aseptically in the Geomicrobiology Unit of the Department of Earth Sciences (University of Bristol, UK). Sample inoculations and preservations were carried out at the Centro Ecologico Akumal Field Lab (Akumal, Mexico).

MPN Method 1

MPN analyses of aerobic and anaerobic heterotrophs, sulfate reducers, iron reducers and iron oxidizers were carried out between January and May 2000. For each media type, two water types were prepared: brackish (8% seawater) and salt (90% seawater).

The 30 ml anaerobic media vials (anaerobic heterotrophs, sulfate reducers and iron reducers) contained 20 ml of media, while 50 ml vials were used to hold 20 ml 'aerobic media' (including aerobic heterotrophs and iron-oxidising bacteria). To these, 10 ml of 'sample solution' was added, described below.

Three different sample dilutions were made using the 10 ml 'sample solution'. For a total dilution of 3×, 10 ml sample was added to 0 ml sterile dilution media. For a total dilution of 30×, 1 ml sample was added to 9 ml sterile dilution media. For a total dilution of 300×, 0.1 ml sample was added to 9.9 ml sterile dilution media. The chosen dilutions were based on numbers of bacteria reported by Schwabe (1999) for the Blue Holes of the Bahamas. Four sterile dilution medias were prepared:

- Aerobic, 8% seawater
- Anaerobic, 8% seawater
- Aerobic, 90% seawater
- Anaerobic, 90% seawater

All samples were thoroughly shaken prior to obtaining an aliquot to ensure adequate mixing. 10, 1 or 0.1 ml of sample followed by 0, 9 or 9.9 ml sterile dilution media was added to the media vials using sterile needles and syringes. Each dilution for each media type was performed in duplicate.

Four different dilution media and five different specific growth media were used, as shown in Table 2.6. A full list of the dilution media and specific growth media is given in the Appendix.

MPN Method 2

MPN analyses of sulfate reducing and thiosulfate-oxidising bacteria were carried out between June and August 2001. For each media type, three water types were prepared: brackish (8% seawater), mixed (50% seawater) and salt (90% seawater). The serial dilution procedures for sulfate reducing bacteria (SRB) and thiosulfate oxidising bacteria (SOX) are described below.

SRB MPN Dilution Series

6 ml water samples, taken with sterile syringes and needles, were serially diluted 5 times in 24 or 27 ml dilution media (1:5 steps for the first dilution, followed by 1:173 steps for subsequent dilutions). Between every dilution, the samples were shaken. From the first, third and fifth dilution, three replicate 3 ml samples were taken aseptically and inoculated into 20 ml vials containing 15 ml of specific growth media. This resulted in dilutions of 3.3×10^{-2}, 2.8×10^{-5} and 2.3×10^{-8} for the first, third and fifth dilutions respectively.

SOX MPN Dilution Series

10 ml water samples, taken with sterile syringes and needles, were serially diluted 5 times in 40 or 48.5 ml dilution media (1:5 steps for the first dilution, followed by 1:163 steps for subsequent dilutions). Between every dilution, the samples were shaken. From the first, third and fifth dilution, three replicate 2 ml samples were taken aseptically and inoculated into 20 ml vials containing 10 ml of specific growth media. This resulted in dilutions of 3.3×10^{-2}, 3.2×10^{-5} and 3.0×10^{-8} for the first, third and fifth dilutions respectively. Six different dilution media and five different specific growth media were used, as shown in Table 2.6. A full list of the dilution media and specific growth media (recipes) is given in the Appendix.

Table 2.6 List of media used to make MPN series

MPN Series	Dilution Media*§	MPN Media*	Determination of positive/negative growth
Sulfate Reducing Bacteria	1, 2, 3, 4, 5, 6	1	Presence of black sulfide deposits indicate positive growth, determination of sulfide (Cline, 1969)
Sulfur Oxidising Bacteria	1, 2, 3, 4, 5, 6	2	Media colour change from pink to yellow (acid-producing), or pink to purple (base-producing), AODC counts, thiosulfate and sulfate analysis by IC
Anaerobic Heterotrophs	2,6	3	AODC counts (see above section)
Aerobic Heterotrophs	1,5	4	AODC counts (see above section)
Iron Reducing Bacteria	2,6	5	AODC counts and change in media colour from amber to green
Iron Oxidising Bacteria	1,5	6	AODC counts (see above section)

*See appendix for media recipes

§The choice of dilution media used was based on the salt content of the sample and whether or not the MPN specific growth media was for aerobic or anaerobic bacteria

All MPN series were incubated in the dark at ~26°C. Positive growth was assessed daily for the first month and then every other week for up to 24 months after collection.

2.5.3 Oxygen Consumption Experiments

Two sets of oxygen consumption experiments were carried out, with the following aims:

- Experiment 1: To compare oxygen consumption rates in fresh, mixed and saline groundwaters within the Mayan Blue cave system (site described in Section 2.x).

- Experiment 2: To determine the affect of adding a) thiosulfate as an electron donor and b) host rock on the rate of oxygen consumption in a mixing zone water sample. In addition, an abiotic control was created using formaldehyde.

Sampling Protocol

Samples were collected using a 10 L capacity PVC sampling tube with a 10 cm diameter opening at either end, which was capped at all times apart from when sampling. Each push-on cap was fitted with a tap with stopcock to allow excess sample water to escape when affixing the end-caps back on the tube after sampling and to allow dispensing of the sample water at the surface. Each end-cap was affixed to the sampling tube with a piece of bungee cord to prevent losing the caps during sampling. The tube was rinsed three times with ethanol, and then rinsed and filled with autoclaved (121°C, 30 minutes) sterile distilled water then capped at both ends. The YSI 600xlm multi-parameter probe (Section 2.4.1) was affixed to the side of the sampling tube and this data was used to confirm the sample depth. Once at a sampling site, the end caps were removed (care was taken not to touch the insides of the end-caps or tube) and the stopcocks were put in the 'open' position. To sample, the tube was held parallel to (but below) the diver's body to minimize disturbance from the diver's upwelling bubbles and to ensure control over the depth and stability of the tube. The sterile distilled water within the tube was displaced with sample water by the forward (swimming upstream) motion of the diver. Mixing between the distilled water and cave water was evident and once mixing no longer

occurred, the diver swam a further 5 m upstream before re-capping the tube with the end-caps and closing the stopcocks. Once at the surface, the sample was randomly dispensed into pressure-sterilised pre-numbered glass BOD bottles that were covered in aluminum foil and kept in a cardboard box to minimize light penetration. The samples were stored at 20-25°C at the field laboratory for the duration of the experiment. The remaining sample was run through the field cell apparatus (described above) to confirm the pH, dissolved oxygen and conductivity of the starting water.

Experimental Method

A time series experiment was performed to allow the determination of oxygen consumption rates over the course of five days. The following treatments were studied:

- Untreated freshwater sample
- Untreated mixing zone samples (various conductivities)
- Untreated saline zone sample
- Mixing Zone sample treated with 1 mM thiosulfate
- Mixing Zone sample treated with 10 g host rock (collected in an ethanol rinsed wine bag which was sealed underwater)
- Abiotic control (4% formaldehyde)

The rate of oxygen consumption was measured by taking oxygen readings at set intervals throughout the experiment. Up to nine 'kill times' were used in the experiment (including a "Time Zero") and each kill time for each treatment was done in triplicate. The samples were "killed" (i.e. oxygen consumption was stopped) by adding the first two reagents of the Winkler Titration. Oxygen was measured using the Winkler Titration (APHA, 1992) for all treatments except the thiosulfate additions. For these, oxygen was measured using the WTW OX91 probe described above and a corresponding untreated sample was run in parallel and dissolved oxygen was measured using the probe to ensure that the results were comparable to the results obtained from the Winkler titrations.

2.6 Groundwater Hydrology

Two simultaneous semi-quantitative dye traces were conducted in the Mayan Blue section of Sistema Naranjal. Rhodamine WT dye was released in the freshwater lens at 14.4 m (~0.5 m above the mixing zone) and fluorescein dye was injected into the saline zone at 20.5 m (~1.2 m below the mixing zone). The vertical and horizontal movements of the dyes were assessed by comparing the dyes' locations relative to fixed survey stations. Observations were made every 24 hours for the first week and then once more two weeks after the dye release.

2.7 Wall-Rock Analysis

Rock samples were collected from two sites (Ak Kimin and Mayan Blue) using a hammer. On returning to the surface, the rock samples were air dried and stored in plastic bags.

The preparation and analysis of rock samples was carried out jointly by the author and Miss Anna Goodwin of the University of Bristol (see Goodwin, 2002). In the laboratory, the samples were re-dried at 60^{0}C. All hand specimens were examined and their main features recorded. The rocks were then sliced using a rock saw to enable description of their interior. These sections were photographed, showing internal and external features, and had an area marked and removed for thin section preparation. Sub-samples were taken where the interior, exterior and any layers within the sample were observed to differ significantly from each other in density and/or colour, and were dried and crushed. Larger pieces were reduced to course sand size by crushing in a metal pestle and mortar crusher. All sub-samples were crushed in the Gyro-mill for two minutes (plus one further minute if deemed necessary) to a flour-like texture. Prior to crushing, all crushing implements were cleaned with acetone. Low iron sand and a small wash of each sample were ground and discarded before the sample was ground. The powder was used for XRD analysis and for acid digestion in progressive calcite dissolution and ICP-AAS trace element analysis (see below).

2.7.1 Thin-section analysis

Thin sections were prepared from rock samples at Southampton Oceanography Centre. The sections were set in blue epoxy resin and half the slide stained with Alazarin Red-S which stains calcite red but leaves dolomite unstained. The sections were examined under a standard light microscope. Dr. Jim Hendry of the University of Portsmouth aided with their interpretation.

2.7.2 XRD analysis

Powdered rocks were analysed on a Philips XRD. XRD slides were prepared for each powdered sample or sub-sample by finely crushing the powder in a clean agate pestle and mortar with excess acetone. This mixture was applied to a glass XRD slide using a disposable pipette, spread evenly over the slide, and allowed to dry. Each slide was analysed in turn using an analysis program running between 25θ and 32θ which encompasses the peak values for the minerals dolomite, calcite and aragonite. The percentage abundance of each carbonate phase was calculated from the relative peak areas (with background subtracted) of the principle peak for that phase. Results were standardized against four dolomites and limestones of known composition. The reproducibility of calcite percentages produced by XRD was 93.81% ± 8.03 (n=4).

2.7.3 Trace Element analysis

2-3 g sub-samples of powdered Mayan Blue rocks were dissolved following the method of Kemp and Brown, 1990. Strontium, magnesium and calcium were analysed by ICP-AES (method described above). Ak Kimin samples were dissolved in dilute HCl and strontium, magnesium, iron and manganese were determined by Atomic Adsorption Spectrophotometry (Goodwin, 2002).

2.7.4 C,H,N analysis

Carbon, hydrogen and nitrogen concentrations of powdered rocks were determined on a Carlo Erba EA1108 elemental analyser at the Department of Chemistry, University of Bristol. The detection limit for all three elements was 0.03%. The RSD was 0.3%.

2.8 Pill Dissolution Experiments

Sets of calcite, aragonite and dolomite tablets ('pills') were placed in various water and site types to study the relative rate of dissolution/precipitation over a ~2 year period. The sources of the pills are summarised in Table 2.7. The calcite pills were made with an 18 mm internal diameter drill and then cut transversely to produce cylinders approximately 6-7 mm thick and the aragonite and dolomite pills were cut into cubes. The edges were rounded very slightly and after polishing, the pills were washed with deionised water. The dimensions of the pills were measured using a micrometer (±0.1 mm) to allow calculations of surface area. For cylindrical pills, two measurements were taken of the diameter and 4 'height' measurements were made. For cube-shaped pills, two measurements were taken from each dimension (i.e. height, width and length). Following this, the pills were placed in 2 M HCl for one minute and then washed immediately with deionised water. The pills were dried at 105°C for 24 hours and placed in a desiccator to cool. The dessicator and balance were placed in an AtmosBag™ (described in the Geomicrobiology section above) along with six beakers of desiccant (silica gel). This set-up was left for three days before weighing (10^{-5} g). Handling of the pills was minimized and following weighing, the pills were placed in pre-labeled plastic mesh baggies (held together using plastic wire ties) and these were then placed in plastic Ziploc bags for transport. Several 'blanks' were also prepared. One set of blanks was left in Bristol for the duration of the experiment, while two sets were taken to Mexico and returned, unused. Thus, any weight loss that occurred during transport could be accounted for.

The pills were transported to the site in their sealed Ziploc bags and were installed by hanging the mesh baggies from the either tree branches (cenote sites) or the ceiling (cave sites) using knotted nylon line and zip ties. The pills were left *in situ* for ~2 years. Each set of pills was put into individual clean Ziploc bags for removal. At the surface, the pills were rinsed with deionised water to remove any salt residue. The pills (in their mesh bags) were hung to dry at ambient temperature (~25°C). Once dry the pills (and mesh baggie) were carefully wrapped in clean, dry (pre-labeled) aluminum foil and this was then placed in a clean and dry labeled plastic Ziploc bag for transport back to the UK.

The pills were dried at 105°C for 24 hours and left to cool in a desiccator. Once cool, the pills were weighed again in the manner described above (i.e. within an AtmosBag™ with

silica gel). The pills were weighed to five decimal places and the amount of weight change per unit of surface area was calculated.

Table 2.7 Descriptions of source rock for the pill dissolution experiment

Pill Type	Source	Site	Notes
Aragonite	Cave speleothem	Lamb Leer cave (Mendips, UK)	- pills have laminations
Calcite	Gravestone Marble	Source unknown	- consistent composition (Smart and Osmaston, unpublished data)
Dolomite	Late Precambrian dolomite	Central east Greenland	-described as collapse brecciated dolomite by Middleton (1961) and Herrington and Fairchild (1989) -55.5 Wt % $CaCO_3$

Chapter 3

Diagenesis in the Freshwater System

3.1 Introduction

The aim of this chapter is to describe and model the progressive evolution of waters within the fresh groundwater system of the east coast of the Yucatan Peninsula carbonate platform. The initial part of this chapter briefly reviews the present understanding of freshwater geochemistry. This is followed by a review of the field data collected during this study, including measurements of lens thickness and the role of hydrology. The majority of Chapter 3, however, is dedicated to the study of geochemistry, geomicrobiology and carbonate dissolution/precipitation reactions throughout the freshwater system and, in particular, in the freshwater lens. In addition, theoretical modeling using PHREEQC (Parkhurst, 1995) is undertaken in attempts to study processes that are difficult (or impossible) to measure directly.

3.1.1 Vadose Zone Hydrology and Geochemistry

Vadose zone geochemical processes begin with the infiltration of rainwater into the ground, either as runoff from the bedrock surface, or by direct infiltration into the soil/rock zone. A relatively fast flow of water through the soil/rock *via* fissure flow will maintain the water in approximate equilibrium with atmospheric pCO_2 (Esteban and Klappa, 1983), while during slower diffuse percolation flow, the water will equilibrate with higher ground air pCO_2 due to respiration in the soil zone (Harrison, 1975).

Important geochemical processes within the vadose zone include mineral stabilization, carbonic acid driven dissolution, and cementation in response to evapo(trans)piration.

i) Mineral stabilisation

After deposition, the mixture of heterogeneous carbonate particles will tend to evolve to form thermodynamically more stable minerals, *via* a combination of dissolution, reprecipitation and recrystallisation reactions (Robie et al., 1979). A dominant diagenetic reaction in the Upper Pleistocene rocks of the Yucatan Peninsula carbonate platform is the stabilisation of high magnesium calcite (HMC) to low magnesium calcite (LMC) (Ford, 1985). This process generates little new porosity (Harrison, 1975).

ii) Carbonic acid driven dissolution

CO_2 dissolves in water to form carbonic acid with the potential for carbonate dissolution (Ford and Williams, 1989; Thrailkill, 1976). Compared to an atmospheric pCO_2 content of ~0.03%, soil pCO_2 can be orders of magnitude higher due to plant root and microbial respiration. pCO_2 in soils tends towards maximum values of 4-6 % due to the inhibiting affect of high CO_2 concentrations on bacteria (Drake, 1980). The amount of carbonate dissolution due to carbonic acid will depend on the balance between the rate of CO_2 production and loss due to diffusion. The rate of CO_2 generation depends on the moisture content and temperature of the soil (Brook et al., 1983; White, 1984), while the rate of CO_2 loss depends on the soil permeability and thickness (De Jong and Schappert, 1972). Carbonate dissolution rates can be especially intense at the soil/bedrock interface (Esteban and Klappa, 1983).

iii) Cementation

Cementation can be driven both by evaporation and degassing. The difference between rainfall and 'evapo(trans)piration' rates determines the effective recharge for a carbonate platform. The thickness of the vadose zone is a critical parameter in determining the effective recharge; in thin or non-existent vadose zones (i.e. the water table intersects the surface) evapotranspiration rates can exceed rainfall, resulting in the formation of (hyper)saline lagoons, increasing the saturation indices of carbonate minerals, and eventually the formation of nodular or laminar caliche (Esteban and Klappa, 1983).

Degassing of high pCO_2 waters in fissures of caverns within the vadose zone can also lead to $CaCO_3$ cementation and the formation of speleothems (Frantz, 1971;White, 1976).

3.1.2 Freshwater Lens Hydrology and Geochemistry

Meteoric water from the vadose zone passes down to the water table, and drives groundwater flow in the freshwater lens. In comparison to the underlying saline zone, the hydrology of the freshwater lens in modern carbonate platforms is relatively well characterized due to its relative ease of access and importance in terms of potable water supplies. The three-dimensional from of the lens for carbonate islands has been modeled using Dupuit-Ghyben-Herzberg analysis (Bear, 1972; Vacher, 1978), and is a function of island width (Budd and Vacher, 1990), hydraulic conductivity (Vacher, 1978) and effective recharge (Cant and Weech, 1986). Both hydrological and diagenetic fluxes have been proposed to decrease below the water table, and stagnate below sea level (Longman, 1980).

The phreatic (water-saturated) zone may be of greater importance in the meteoric diagenesis of carbonate rocks compared to the vadose zone due to the longer residence time of water within the phreatic zone (Land, 1973). As in the vadose zone, mineral stabilisation to more thermodynamically stable forms is an important process in immature carbonates, and cementation often occurs where there is an airspace above the lens (due to degassing and evapotranspiration) (Goudie, 1983; Perry et al., 1989). However, in more mature carbonates, diagenesis within the freshwater lens has generally considered to be driven predominantly by mixing between high pCO_2 vadose water and degassed lens water (James and Choquette, 1984). *In situ* organic decomposition by microorganisms also has the potential for carbonate dissolution.

i) Freshwater mixing

As discussed in greater detail in Chapters 1 and 4, the mixing of two saturated (with respect to calcite) waters of differing ionic strength and composition can result in an undersaturated mixed water (Runnels, 1969; Plummer, 1975). The mixing of vadose waters (with high pCO_2) with degassed lens water can, in theory, create the potential for the dissolution of calcite, and it has been suggested that this process is critical in the initiation of cavernous porosity at the water table. However, extensive fieldwork in the Bahamas revealed that mixing of vadose and lens waters did little to promote enhanced dissolution (Whitaker, 1992).

ii) Organic mineralization

Organic matter may either be incorporated into carbonate sediments during deposition, or be transported into the freshwater lens either as dissolved organic carbon (DOC), or as particulate organic carbon (POC). The accumulation of organic carbon in sediments will be especially important in cenotes (and some caverns) where there is a direct route to the surface. The oxidation of organic matter, predominantly by microorganisms, takes place sequentially using a number of different electron acceptors (i.e. O_2, NO_3^-, Mn(IV), Fe(III), SO_4^{2-}, CO_2; Froelich et al., 1979), with the most thermodynamically favourable (O_2) being used first in aerobic respiration, producing CO_2.

As described earlier, the production of CO_2 in aerobic respiration results in the generation of acidity due to the formation of carbonic acid, which has the potential to dissolve carbonate minerals. Conversely, bacterial processes such as iron and sulfate reduction results in the production of alkalinity, which can enhance carbonate precipitation reactions (to be discussed in detail later).

3.2 Fresh Water Hydrology of the East Coast of the Yucatan Peninsula

The work presented in this chapter was carried out alongside the PhD thesis of Patricia Beddows (University of Bristol) entitled "The groundwater hydrology of a coastal conduit carbonate aquifer: Caribbean coast of the Yucatan Peninsula, Mexico". The main findings of this work as it pertains to freshwater lens hydrology are summarised in this section.

3.2.1 Velocity and Water Level Measurements

Beddows (2004) reports two long-term velocity measurements (2000-2001) made using:

- an Aanderra RCM9 2D acoustic Doppler current meter and
- an Aanderra RCM7 mechanical vane current meter

The first site studied was Heaven's Gate (Sistema Nohoch Nah Chich), an inland freshwater conduit located 3.17 km inland. The second site was Casa Cenote, the coastal discharge site of Sistema Nohoch Nah Chich (confirmed by dye tracing; Beddows, 1999).

A 132-day record was obtained from a second coastal discharge site (Xel Ha), which is located 6.7 km south of the Casa Cenote discharge site. In addition, records of cenote water levels were obtained from two inland conduit sites: Heaven's Gate (mentioned above) and Balam Can Chee (Sistema Nohoch Nah Chich, 1.58 km inland).

Beddows (2004) showed that the primary high frequency (daily time scale) control on both flow velocity and water level was the coastal tides. Analysis of the combined groundwater velocity and cenote water level data revealed semi-diurnal oscillations of both factors in response to the small amplitude (~30 cm) semi-diurnal tidal regime on the east coast. The small amplitude tides exert the dominant control on the water velocity because the aquifer hydraulic conductivity is very high due to the extensive conduit systems. The conduits and general karstification of the aquifer result in an exceptionally low hydraulic gradient on the east coast ranging from $5.19 \pm 2.17 \times 10^{-5}$ to $9.25 \pm 1.47 \times 10^{-5}$ (Beddows, 2004). Thus even small amplitude changes in sea level over the course of the semi-diurnal tides are the primary control on head differences between sites located several kilometers inland and the coastal discharge points. At low tide, the aquifer head may be several centimeters greater than sea level. At high tide, the aquifer head will be reduced, but it will still remain somewhat greater than sea level. Higher fresh water conduit velocities are therefore observed during low tide phases when the hydraulic gradient is greatest. It is noted by Beddows (2004), however, that even at high tide stages, there remains a head potential between the inland aquifer water levels and the sea level. Thus, the direction of flow within the freshwater lens is almost always continuously coastward (i.e. northwest to southeast), with only minor reversing periods occurring at times of very high sea level often associated with storms. Beddows suggests that these high-frequency sea level variations are the best predictor of conduit velocity, except during storm events (considered in more detail later).

The amplitude of the aquifer water table fluctuations decreases exponentially with distance inland (Beddows, 1999, 2004) while theoretically the time lag increases linearly (Fetter, 1988). Thus, it is expected that increased (turbulent) mixing occurs at the coast (and decreases with distance inland) due to tidal pumping.

The unconfined freshwater lens is replenished by meteoric recharge and recharge increases during times of (extended) high precipitation (i.e. during the wet season). Thus, the water

table level is expected to rise during wet seasons (May to October) and fall during dry seasons (December to March). This anticipated seasonal trend is supported by work by Marin (1990), who presented evidence from the northwest part of the peninsula showing the water table was 1.01 ± 0.29 m (n = 14) higher in the wet season (September 1988) compared to the dry season (April 1998). In addition, Marin et al. (1989) reported very rapid and significant water table responses to hurricanes for the northwest of the peninsula. However, the time series data presented by Beddows (2004) for the east coast indicates significant and rapid responses to individual events are relatively rare, suggesting there may be some water storage within the vadose zone.

The effects of six hurricanes and tropical storms were captured in the time series presented in Beddows (2004) and of these, only one (Hurricane Keith; 29 September to 6 October 2000) had any appreciable effect on the aquifer. This effect, however, was short lived with a return to preceding water level and conduit flow values within four days of the passing of the storm. In addition to the classified storms and hurricanes, one large rain event on 27 May 2001 (the first heavy rain after a dry season) also had substantial effect on the aquifer (i.e. an increase in water level and velocity occurred).

Although the aquifer seldom responds to individual events, Beddows (2004) showed that water velocity increases during the wet season (the current meter record from Heaven's Gate showed higher outflow occurs during the rainy season) with 'progressively decreasing mean flows with the advance of dry season'. The coastal discharge sites, however, showed no such pattern and flow rates were always dependent on mean sea level.

3.2.2 Water Budget/Evapotranspiration Rate

According to Hanshaw and Back (1980), surface runoff is non-existent along the east coast of the Yucatan Peninsula. This, combined with a lack of river or stream channels, means that most of the rainfall is routed back to the atmosphere by means of evapotranspiration and the rest percolates through the vadose zone to reach the water table.

The published evapotranspiration rate of the Yucatan Peninsula is 85% of the mean annual rainfall of 1325 mm/a (Lesser, 1976). This value, implying a recharge rate of 15%, is used

by Hanshaw and Back (1980) to calculate the freshwater outflow per kilometer of coastline for the entire Yucatan Peninsula as 8.6 x 10^6 m^3/year, equivalent to 0.27 m^3/s per kilometer. However, Beddows (2004) measured freshwater outflows from two sites (Casa Cenote and Xel Ha) and these results indicate average annual freshwater discharge rates of 0.99 and 1.83 m^3/s per kilometer of coastline, respectively. Calculations based on these rates, combined with the geographical limits of the peninsula indicate that the annual recharge rates must be between 30-60% of measured rainfall to allow such discharge rates to occur (Beddows, 2004). Thus, maximum estimates of evapotranspiration (excluding interception by trees and other foliage and human consumption, for which current estimates are not known) must be between 40 and 70%. Despite the wide range, the estimates by Beddows (2004) may be a more robust assessment of the recharge rate because they are based on extensive field observations and long-term monitoring of coastal discharge. In contrast, the previously published water budgets were based on theoretical calculations of potential evapotranspiration using energy balance equations and the mean annual air temperature. In this chapter, where calculations require an input of evapotranspiration rate, values of 40, 70 and 85% are used.

3.2.3 Types of Freshwater

Several types of freshwater were sampled from the east coast of the Yucatan Peninsula throughout this study. The water types were distinguished from one another based on their source and field chemistry. Eleven 'freshwater types' are recognized; rainwater, throughfall, runoff, surface pools, vadose cave drips, and from the freshwater lens: static and pumped wells, cenotes, caverns, caves, and coastal discharge. These are described in Chapter 1. Within the lens categories, there are a further four sub-categories, including coastal (<200 m from the east coast) and inland (>200 m from the east coast) sites and degassed and non-degassed sites (explained further in later sections).

All but eight samples were taken within ~12 km inland of the Yucatan Peninsula east coast. One sample was obtained from Conquistador (22.1 km inland), five samples were obtained from Pac Chen, a site located ~40 km inland from the east coast and two samples were collected from caves (Kankrixche, Norias) located near Merida (Yucatan State), approximately 70-80 km west of the east coast.

3.2.4 YSI profiles

Conductivity profiling permitted the identification of the base of the freshwater lens, allowing the study of the relationship between lens thickness and distance inland. The profiles showed that the thickness of the freshwater lens (determined from the position of the interface between the bottom of the freshwater lens and the top of the mixing zone, is thinner near the coast and increases linearly inland (Figure 3.1). In addition, temperature profiling allowed the collection of *in situ* temperature readings, required for the calculation of saturation indices and modeling using PHREEQC.

3.3 Soil pCO_2

Eleven gaseous CO_2 measurements were taken in June 2001 in litter and humus dominated soils in soil pockets up to 45 cm deep. The soil CO_2 readings range from 1.00 to >5% and the mean is 3.36 ± 1.34% (n = 11).

3.4 Aqueous Geochemistry of Fresh Waters

A total of 116 freshwater samples (including two from the Merida region) were taken from the Yucatan Peninsula, Mexico. In this section, the aqueous geochemistry of these samples is described, beginning with results obtained from field measurements. Following this, major ion chemistry, and calculations of 'XS', saturation indices and pCO_2 of the freshwaters are presented.

3.4.1 Field Measurements

This section describes the 'field chemistry' results and includes measurements of conductivity, *in situ* temperature, pH, and dissolved oxygen. The results are summarised in Table 3.1. Unless otherwise stated, depth refers to depth below the local water table.

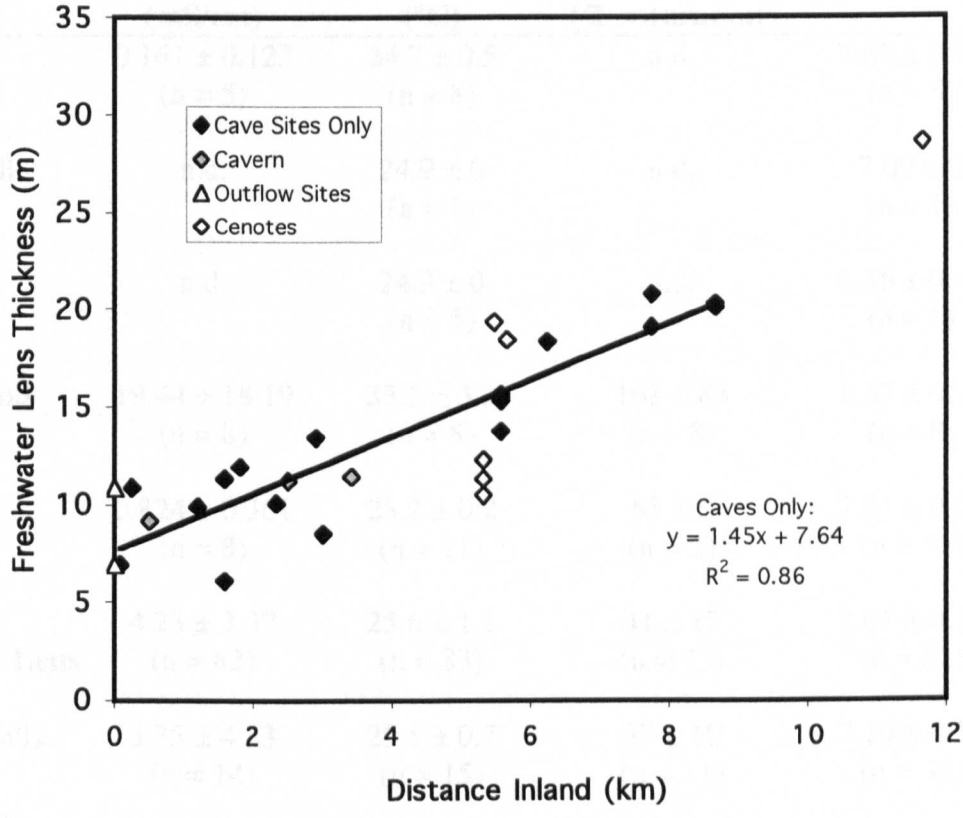

Figure 3.1 Freshwater lens thickness with distance inland from the east (Caribbean) coast of the Yucatan Peninsula. Data from YSI 600xlm conductivity profiles from caves, caverns, cenotes and coastal discharge (outflow) sites.

Table 3.1 Mean freshwater field chemistry (±1σ)

Water Type	Specific Conductance (mS/cm)	*in situ* Temperature (°C)	Dissolved Oxygen (% saturation)	pH
Rainwater	0.161 ± 0.123 (n = 5)	24.7 ± 0.5 (n = 8)	n.d.	7.80 ± 0.94 (n = 5)
Throughfall	n.d.	24.9 ± 0 (n = 1)	n.d.	7.09 ± 0 (n = 1)
Runoff	n.d.	24.9 ± 0 (n = 5)	n.d.	8.36 ± 0.44 (n = 5)
Surface Pools	19.44 ± 18.19 (n = 8)	33.2 ± 3.3 (n = 8)	163 ± 83 (n = 8)	8.37 ± 0.70 (n = 8)
Drips	0.824 ± 0.361 (n = 8)	25.2 ± 0.2 (n = 11)	63 ± 0 (n = 2)	7.81 ± 0.25 (n = 10)
Mean Freshwater Lens	4.23 ± 3.37 (n = 82)	25.6 ± 1.1 (n = 83)	41 ± 17 (n = 73)	7.07 ± 0.27 (n = 82)
Static Wells	5.75 ± 4.33 (n = 14)	25.5 ± 0.7 (n = 15)	37 ± 19 (n = 11)	7.19 ± 0.31 (n = 35)
Pumped Wells	7.37 ± 5.69 (n = 9)	27.7 ± 1.6 (n = 9)	42 ± 23 (n = 7)	7.20 ± 0.17 (n = 9)
Cenotes	2.72 ± 1.85 (n = 36)	25.3 ± 0.9 (n = 36)	45 ± 17 (n = 33)	7.10 ± 0.31 (n = 35)
Caverns	5.35 ± 1.52 (n = 3)	25.2 ± 0.4 (n = 3)	44 ± 11 (n = 3)	7.02 ± 0.27 (n = 3)
Caves*	4.29 ± 0.37 (n = 20)	25.3 ± 0.3 (n = 20)	34 ± 9 (n = 19)	6.89 ± 0.08 (n = 20)
Caves§	4.44 ± 0.37 (n = 2)	27.6 ± 0.1 (n = 2)	64 ± 0 (n = 1)	6.60 ± 0.28 (n = 2)
Coastal Q	19.74 ± 9.55 (n = 11)	26.2 ± 0.9 (n = 13)	47 ± 21 (n = 12)	7.07 ± 0.34 (n = 12)
Analytical Uncertainty	± 0.5	± 0.15	±1	±0.02

* = caves from main field area (east coast) § = caves from Merida area (Yucatan)

3.4.1.1 Specific Conductance

Rainwater has the lowest conductivity of all freshwaters, followed by drips (Table 3.1). Lens waters have a specific conductance ~5 times greater than the drip samples. Surface pools and coastal discharges have similar mean conductivities which are ~5 times greater than mean lens conductivity, indicating evaporation and seawater mixing, respectively.

The specific conductance of the freshwater lens decreases with increasing distance inland up to ~8 km (Figure 3.2a). Lens samples further than 8 km (up to ~40 km) do not show any further significant reductions in conductivity, possibly indicating the extent of mixing with saline groundwater.

3.4.1.2 *In situ* temperature

Rainwater has the coolest temperatures and these are not significantly different from throughfall, runoff or drip samples (Table 3.1). Coastal discharge waters have slightly elevated temperatures (26.2 ± 0.9°C, n = 13) compared to the mean of lens waters (25.6 ± 1.1°C, n = 83). Surface pools have the highest temperatures (33.2 ± 3.3°C, n = 8).

The temperature of the freshwater lens does not vary systematically with distance from the coast at distances greater than ~0.5 km inland (Figure 3.2b), suggesting that temperature is spatially consistent. This finding may indicate that the water has thermally equilibrated after infiltrating through the vadose zone. In coastal outflows and cave sites <0.5 km from the coast, the freshwater lens temperature increases with values up to 27.9°C. However, these warm fresh waters are also brackish (Figure 3.2), indicating mixing with warmer saline water.

3.4.1.3 Dissolved Oxygen

Dissolved oxygen (DO) data was not obtained for rainwater, throughfall or runoff samples. Surface pools are supersaturated with oxygen (163 ± 83%, n= 8, Table 3.1). Drip DO concentrations were measured as 63 ± 0% saturation (n = 2), although these measurements were difficult to make due to degassing and may indicate more oxygen than is actually present.

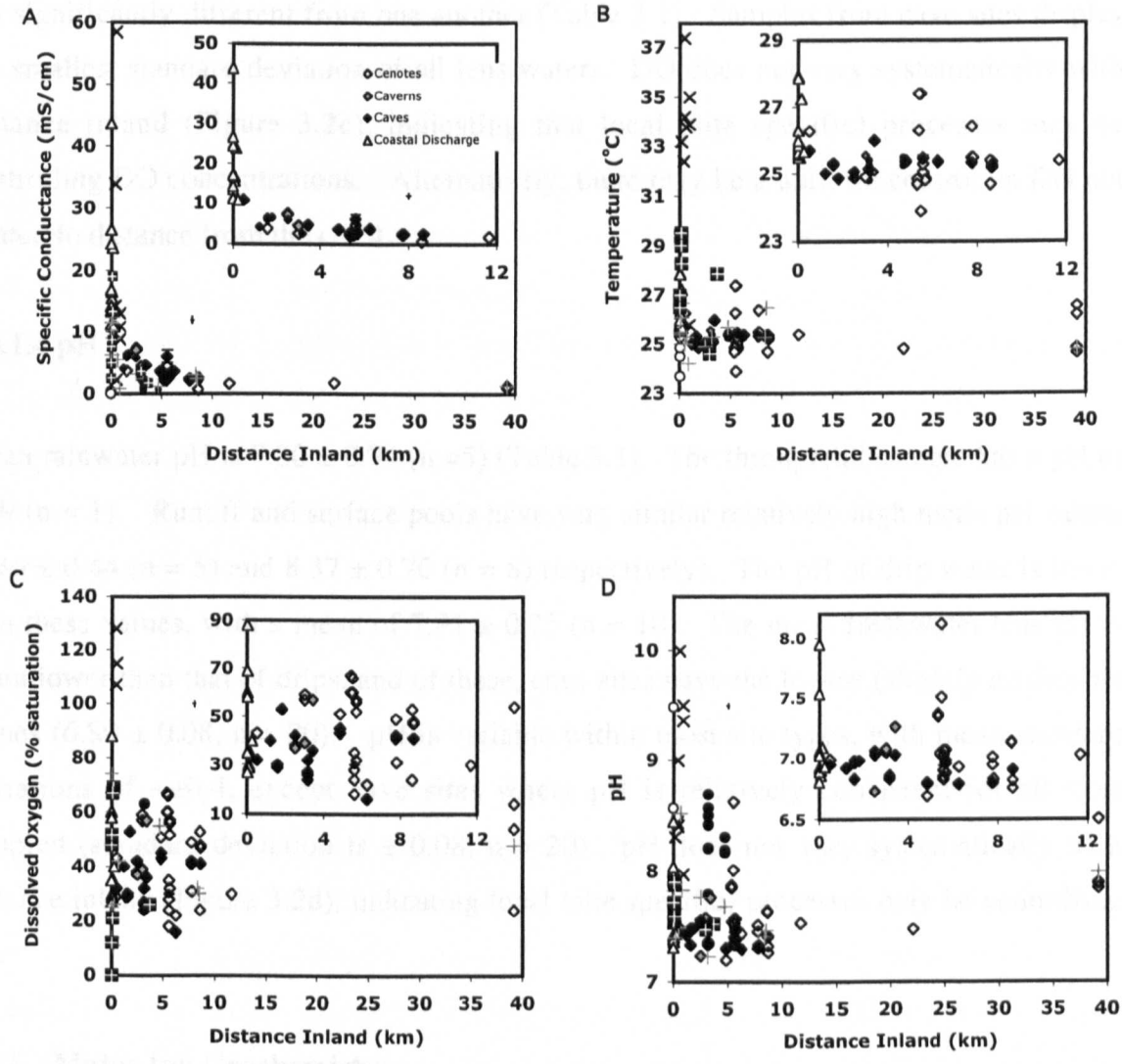

Figure 3.2 Specific conductance (A), Temperature (B), Dissolved Oxygen (C), pH (D) against distance inland from the east coast of the Yucatan Peninsula for the different freshwater sample types. Freshwater types include rainwater (open circles), throughfall (grey circles), Runoff (open squares), surface pools (black X), drips (closed circles), static wells (grey +), pumped wells (white + in black box), cenotes (open diamonds), caverns (grey diamonds), caves (black diamonds) and coastal discharge (open triangles). Insert graphs show cenote, cavern and cave lens water trends within the main study area (up to 12 km inland). Black crosses are representative analytical uncertainties (±1σ).

The mean lens (41 ± 17%, n = 73) and outflow (47 ± 21%, n = 12) DO concentrations are not significantly different from one another (Table 3.1). Samples from cave sites display the smallest standard deviation of all lens waters. DO does not vary systematically with distance inland (Figure 3.2c), indicating that local (site specific) processes may be controlling DO concentrations. Alternatively, there may be a uniform control on DO not related to distance from the coast.

3.4.1.4 pH

Mean rainwater pH is 7.80 ± 0.94 (n =5) (Table 3.1). The throughfall sample has a pH of 7.09 (n = 1). Runoff and surface pools have very similar relatively high mean pH values (8.36 ± 0.44 (n = 5) and 8.37 ± 0.70 (n = 8) respectively). The pH of drip water is lower than these values, with a mean of 7.81 ± 0.25 (n = 10). The mean freshwater lens pH is again lower than that of drips, and of these, cave sites have the lowest (slightly acidic) pH values (6.89 ± 0.08, n = 20). pH is variable within most site types, with mean standard deviations of ~±0.4, except cave sites where pH is relatively consistent for all sites sampled (standard deviation is ± 0.08, n = 20). pH does not vary systematically with distance inland (Figure 3.2d), indicating local (site specific) processes may be controlling pH.

3.4.2 Major Ion Geochemistry

This section examines the geochemistry of freshwater samples. First of all, the chloride budget for the east coast of the Yucatan Peninsula is considered. Following this, first approximations about which water-rock reactions are occurring are made with ion:chloride ratios. Following this, the results from calculations of XS and the saturation indices and pCO_2 with which the waters are in equilibrium are also presented.

3.4.2.1 Chloride

Five major processes potentially effect the chloride concentrations of a freshwater lens (Likens et al., 1977):

a) Wet deposition
b) Dry deposition

c) Evapotranspiration
d) Dissolution/precipitation reactions
e) Mixing with seawater

No evaporite (halite) minerals have been reported at shallow depth (<100 m) along the east coast of the Yucatan Peninsula and thus dissolution is assumed to have a negligible effect on the freshwater lens chloride concentrations. The remaining four processes, however, can be quantified by combining the chloride concentrations from various freshwater environments with the hydrological measurements of Beddows (2004). These calculations follow those made by Whitaker (1992) for the Bahamas.

Wet Deposition

The dominant source of chloride in rainfall is the sea surface, from which small droplets of seawater can be entrained in the air and evaporated, producing salt particles. Concentrations of rainfall vary spatially (i.e. with distance from the coast, see Matthess and Harvey, 1982) and temporally. However, it is beyond the scope of this study to fully characterize this variability. Five uncontaminated rainfall samples were collected from the study area, approximately 200-300 m inland from the east coast of the Yucatan Peninsula. Of these, four are from the early stages of a rainstorm and contain 0.48 ± 0.12 mM chloride. One sample was collected near the end of a heavy rainstorm and this contains 0.12 mM chloride. These values should represent the extremes of chloride in rainfall, and the difference in the samples suggests that during a storm, aerosols are 'washed out' of the atmosphere. As most of the rainfall in the study area occurs during heavy convective storms, the lower chloride figure may be a concentration representative of that due to wet deposition.

Dry Deposition

Surface runoff was sampled from a variety of bare rock and sparsely vegetated surfaces, prior to evapotranspiration, all within 500 m of the east coast. These samples have a mean chloride concentration of 4.82 ± 3.27 mM (n = 4). Chloride may be elevated because of the proximity of these samples to the coast, thus the direct contribution of salt spray is a factor in these measurements.

Evaporation and Evapotranspiration

Evapotranspiration causes conservative ions within a solution to become more concentrated. The mean annual rainfall of the study area is 1325 mm/a and evapotranspiration is thought to be between 40 and 70 or 85% (Section 3.2.2), resulting in evapotranspiration rates of 530, 928 or 1126 mm/a, respectively. These rates result in an increase in concentration by a factor of 1.66, 3.32 or 6.64, respectively.

Based on a chloride concentration for immediate recharge waters of 4.82 ± 3.27 mM Cl^- (n = 4), evapotranspiration should result in an average increase of 3.2, 11.8 or 27.2 mM Cl^- (40, 10, 85% ET, respectively), giving a predicted concentration of 8, 16 or 32 mM Cl^- in effective recharge. For these calculations, it is assumed that any surface detention caused by trees will evaporate, leaving salt residue on leaves. It is assumed that this residue is then washed down into the aquifer during the next rain event. It should be noted, however, that this process was not studied systematically in this thesis.

In this study, the majority of freshwater lens samples were taken between February-May 2000 (dry season) near the east coast of the Yucatan Peninsula and these samples have chloride concentrations (32.5 ± 31.7 mM, n = 77) not significantly different from that predicted from evapotranspirative concentration of runoff if evapotranspiration is 85%. It should be noted that with such high chloride concentrations, these 'freshwaters' are actually brackish. However, the term 'freshwater lens' is used throughout this thesis when referring to the brackish water lens.

Mixing

However, if evapotranspiration is between 40 and 70%, the fresh lens waters have significantly higher chloride concentrations than predicted from evapotranspirative concentration of runoff. This indicates that mixing between lens and saline waters could provide a considerable input of chloride into the lens (16.5 or 24.5 mM if ET is 40 or 70%, respectively). If ET is 85%, the input from mixing with saline water is only ~0.5 mM Cl^-.

Mixing between the lens and the saline zone should result in an increase in salinity with depth (due to salt dispersion) throughout the lens. However, YSI profiles indicate this gradient is small or non-existant (Figure 3.3).

Detailed modelling of the flux of salt through the mixing zone was not a major goal of this study (e.g. the processes of dispersion and advection are not well defined) – however, some constraints can be placed on the rate of salt transfer across the mixing zone. If it is assumed the system is in steady state, a minimum estimate of the upward diffusional flux of NaCl required to maintain the observed mixing zone chloride concentration gradient may be made.

Initial estimates assume diffusion is occurring through a static medium, and Fick's first law of diffusion (Equation 3.1) is used:

$$F_d = -D \bullet \frac{dC}{dz} \qquad \text{(units: mM•cm}^{-2}\text{•s}^{-1}\text{)} \qquad (3.1)$$

where F_d is the diffusional flux, D is the diffusion coefficient (1.474×10^{-5} cm^2/s for saline groundwater NaCl concentrations at 25°C; Lerman, 1979; Robinson and Stokes, 1970; Landolt-Bornsein, 1969) and dC/dz is the concentration gradient. The good relationship between salinity and chloride allows conversion of the detailed salinity with depth profile (Figure 3.3) to a chloride concentration profile. The chloride concentration profile at Mayan Blue yields an average concentration gradient of 1.26×10^{-3} mM Cl$^-$•cm^{-4}, resulting in a flux of about 1.86×10^{-8} mM•cm^{-2}•s^{-1} NaCl. This estimate ignores contributions from thermal diffusion (which would act to increase the flux given saline groundwater is warmer than the brackish water lens).

As per Bottrell et al. (1991), a more practical approach may be to consider vertical eddy diffusion (caused by tidal fluctuations) as the primary mechanism of mass transfer through the mixing zone. In this case, the flux required to maintain the observed chloride concentration gradient would be much greater than that derived from the static water model. Indeed, fairly rapid vertical diffusion upwards from the saline zone was inferred by an experiment involving the release of Fluorescein dye in Mayan Blue (see Section 4.4.1.5), which showed vertical movement of up to 3.2 m within 24 hours.

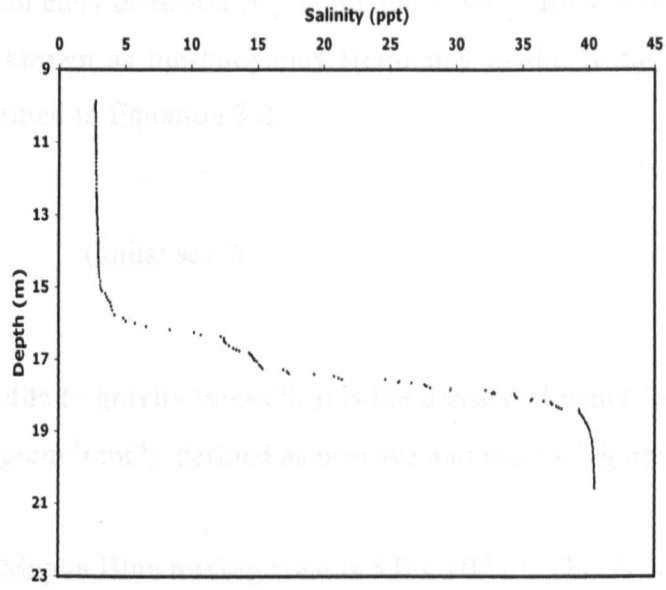

Figure 3.3 Vertical variation of salinity in Mayan Blue cave, showing that salinity (and, by inference, chloride) increases throughout the freshwater lens and mixing zone, to reach saline groundwater concentrations.

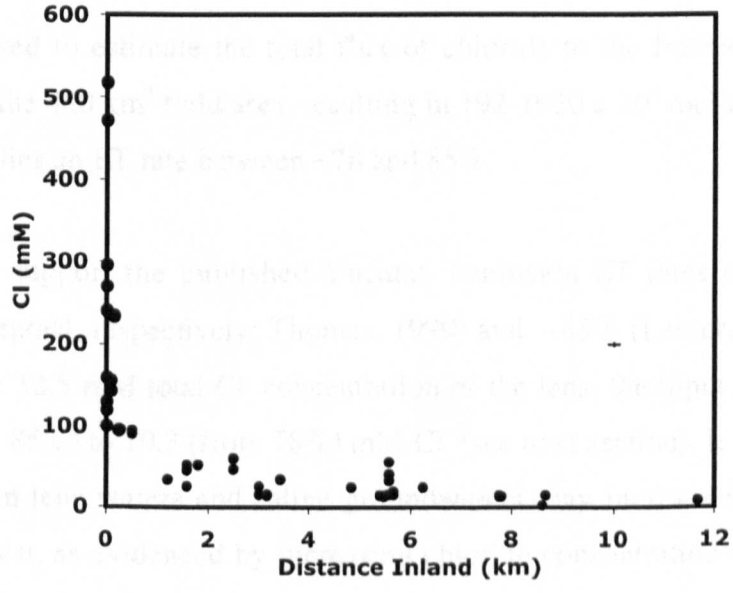

Figure 3.4 Chloride concentration of freshwater lens samples with distance inland from the east coast of the Yucatan Peninsula. Mean Caribbean seawater chloride concentration is 575 ± 5.46 mM (n = 6). Cross shows representative analytical uncertainties (±1σ).

The coefficient of vertical eddy diffusion (K_z) is related to the vertical stability of the water column, N (otherwise known as the buoyancy frequency or the Brunt-Väisälä stability frequency), which is defined in Equation 3.2:

$$N^2 = \left(\frac{g}{\rho}\right) \bullet \left(\frac{d\rho}{dz}\right) \qquad \text{(units: sec}^{-2}\text{)} \qquad (3.2)$$

where g is acceleration due to gravity ($cm \bullet s^{-2}$), ρ is the density of water ($g \bullet cm^{-3}$) and $d\rho/dz$ is the density gradient ($g \bullet cm^{-3} \bullet cm^{-1}$), defined as positive and increasing downward.

The value of N^2 for the Mayan Blue mixing zone is 5.0×10^{-2} s^{-2}. This N^2 value is large and suggests the Mayan Blue mixing zone is very stable and not very susceptible to turbulent mixing (Lerman, 1979). A plot of correlations between N^2 and K_Z is provided by Lerman (1979) and this shows that for $N^2 = 10^{-1.3}$ s^{-2}, K_Z is between 10^{-2} and 10^{-3} $cm^2 \bullet s^{-1}$. This would necessitate a salt (NaCl) flux of 1.26×10^{-6} to 1.26×10^{-5} $mM \bullet cm^{-2} \bullet s^{-1}$ or 0.4 to 4.0 $\times 10^3$ $mol \bullet m^2 \bullet a$ to maintain the concentration gradient of the Mayan Blue mixing zone.

This flux can be used to estimate the total flux of chloride to the freshwater lens from mixing throughout the 480 km^2 field area, resulting in 192-1920 x 10^9 mol/a or 5.42 – 54.2 x 10^9 g/a. This implies an ET rate between ~78 and 85%.

These calculations support the published Yucatan Peninsula ET rates of 77-79% (for Valladolid and Chetumal, respectively; Thomas, 1999) and ~85% (Lesser, 1976) and this indicates that of the 32.5 mM total Cl^- concentration of the lens, the input from mixing is between ~0.4 (from 85%) to 10.3 (from 78%) mM Cl^- (see next section). It is worth noting that mixing between lens waters and saline groundwaters may increase with increasing proximity to the coast, as evidenced by increasing chloride concentrations at coastal lens sites (Figure 3.4).

There are a few limitations with the above calculations that need to be addressed. The N^2 value determined in Equation 3.2 indicates the Mayan Blue mixing zone is not very susceptible to turbulent mixing. However, rapid horizontal and vertical movements of dye (Chapter 4) indicate processes other than simple diffusion are acting to increase the rate of salt transfer to the lens. These processes could include: turbulent shear flows and double

diffuse convection. For example, Beddows (2004) studied the mixing zone hydrodynamics in Balam Can Chee (a conduit site located ~1.6 km inland, approximately 18 km north of Mayan Blue) and found that double diffuse convection acts as a slow background process transferring salt across the mixing zone at all times (explained by fluid dynamics theory, given the contrast in specific conductance between the lens and saline water). Beddows (2004) notes the effects of double diffuse convection are most evident during low velocity phases (at or near 0 cm/s; e.g. at high tide), when warm saline water diffuses upwards into the base of the freshwater lens. In contrast, during high velocity phases (i.e. low tide), Beddows (2004) notes the top of the mixing zone appears to be "sheared away by turbulent flows", and the saline water that accumulated during the low flow periods becomes mixed into the freshwater lens. Thus, the rate of salt transfer into the lens is greatest during periods of turbulent shear flow, which occur at low tide.

In Mayan Blue, the visually observed water velocities (estimated at 0.03 – 0.09 cm/s) are thought to be less than those at Balam Can Chee, indicating double diffuse convection may be of greater importance at Mayan Blue due to reduced turbulent shear. However, during low tide, turbulent shear flows should occur, acting to increase the rate of salt transfer from the top of the mixing zone into the freshwater lens.

A very important observation of the dye movement was that the dye did not cross the entire mixing zone. Although the vertical rate of dye transfer was deemed fast compared to that expected from simple diffusion, the Fluorescein dye released in the saline zone was found only in the bottom of the mixing zone and the Rhodamine WT dye released in the freshwater lens was found only in the top of the mixing zone (details given in Chapter 4). Neither dye was observed in the middle part of the mixing zone. It is possible that different processes dominate the salt transfer across the various mixing zone strata. Double diffuse convection and/or turbulent shear flows may transfer saline water into the base of the mixing zone, then double diffuse convection and/or (vertical eddy?) diffusion may progressively move saline water upwards through the middle portion of the mixing zone. Finally, salt is transferred from the top of the mixing zone to the freshwater lens *via* turbulent shear flows. The complete progression of the saline water through the middle of the mixing zone may not have been observed in the field study because this multi-stepped processes is probably very slow, with net transfer times being longer than the observation period.

Assuming the above processes are occurring to increase the rate of salt transfer to the lens from mixing, the amount of salt required by ET to reach lens values will be less than that estimated above. This indicates ET is less than 78-85%. Thus, Beddows' (2004) ET estimates (40-70% of precipitation) are still considered in the following sections. For completeness, calculations are also carried out using the published 85% value.

Increased chloride concentrations may also be due to upconing of the base of the freshwater lens in response to over-pumping. Fresh water samples from pumped wells are enriched in chloride (63.0 ± 57.3 mM, n = 9) compared to static wells where pumping does not occur (41.6 ± 37.7 mM, n = 13), although the difference is not significant ($P > 0.05$).

3.4.2.2 The Chloride Budget

The chloride concentrations discussed above are combined with volumes of flow in the freshwater system (derived from Beddows, 2004) to develop a chloride budget for the study area. The study area comprises a 'length' of 40 km along the coastline and a 'width' of 12 km inland (Figure 1.2). Three chloride budgets are presented in Tables 3.2 to 3.4, based on 40, 70 and 85% ET, respectively, and these are described below.

Column 1 (Cl_1) summarises the concentration of chloride derived from various inputs to the freshwater system. Column 2 (Cl_2) is Cl_1 expressed as percent of the average freshwater lens chloride concentration. ~15% of the total chloride is derived from surface runoff. Of this, ~98% is due to dry deposition and ~2% is due to wet deposition. The input of chloride in effective recharge increases from ~15% to ~25, 49 or 99% due to 40, 70 or 85% ET respectively. The remaining fraction (75, 51 and 1%) is due to mixing with underlying saline groundwaters.

These values are converted into the total input of chloride to the freshwater system of the Yucatan Peninsula study area (Cl_3) by multiplying the chloride concentration in Cl_1 by the total recharge. The land area covered by the study area is approximately 480 km^2 and it is assumed that a freshwater lens underlies all of this and that no waters discharging at the coast are derived from lens waters located further inland than the western boundary of the study area.

With a mean annual rainfall of 1325 mm, the total volume of rainfall that could potentially recharge the lens is equal to 480 km^2 x 1325 mm/a, which computes to a total of 6.36 x 10^8 m^3/a. This has an estimated chloride concentration of 0.12 mM which is increased to an average 4.82 ± 3.27 mM in runoff waters by the addition of approximately 4.7 mM Cl- in the form of dry deposition. Thus, the total input to the freshwater lens from runoff is 1.08 x 10^{11} g/a (3 x 10^9 mols/a) chloride.

40% Evapotranspiration (Table 3.2)

Evapotranspiration of 40% reduces the volume of effective recharge to 60% of the mean annual rainfall (3.82 x 10^8 m^3/a). This increases the chloride concentration to 8 mM. The remaining 24.5 mM chloride (derived from the average chloride concentration of 32.5 mM for the freshwater lens) could be attributable to mixing with the underlying saline groundwaters. If it is assumed that the saline end-member is of seawater chloride composition, a maximum volumetric ratio of recharge water to saline water of 24:1 can be calculated, indicating a contribution of 1.6 x 10^7 m^3/a over the whole study area, and increasing the volumetric input to the lens to a minimum of 3.98 x 10^8 m^3/a. This annual input represents 5.97% of the total volume of the lens beneath the study area (calculated as 6.67 x 10^9 m^3) and suggests a residence time for waters in the lens of ~17 years.

70% Evapotranspiration (Table 3.3)

Evapotranspiration of 70% reduces the volume of effective recharge to 30% of the mean annual rainfall (1.91 x 10^8 m^3/a). This increases the chloride concentration to ~16 mM. The remaining 16.5 mM chloride (derived from the average chloride concentration of 32.5 mM for the freshwater lens) is attributable to mixing with the underlying saline groundwaters. If it is assumed that the saline end-member is of seawater chloride composition, a maximum volumetric ratio of recharge water to saline water of 35:1 can be calculated, indicating a contribution of 5.46 x 10^6 m^3/a over the whole study area, and increasing the volumetric input to the lens to a minimum of 1.96 x 10^8 m^3/a. This annual input represents 2.94% of the total volume of the lens beneath the study area (calculated as 6.67 x 10^9 m^3) and suggests a residence time for waters in the lens of ~34 years.

Table 3.2 Chloride Budget of the east coast of the Yucatan Peninsula (see map for area), with evapotranspiration of 40%

Source of Cl^-	Cl_1 (mM)	Cl_2 (%)	ΣRecharge (10^9 m^3/a)	Cl_3 (10^9 g/a)
Input from wet deposition	0.12	0.37	0.636	2.7
Input from dry deposition	4.7	14.5	-	106
Total input from runoff	**4.82 ± 3.27**	**14.8**	**0.636**	**108**
Concentration by ET (x1.66)	-	-	-0.254	-
Effective Recharge	8.03 ± 5.45	24.7	0.382	108
Mixing with saline water*	24.5	75.3	0.016	326
Total	**32.5 ± 31.7**	**100**	**0.398**	**434**

* assuming mixing with seawater composition end-member
Cl_1 = chloride concentration in mM
Cl_2 = chloride concentration as a percentage of total lens concentration
ΣRecharge = volumetric recharge to lens 10^9 m^3/a
Cl_3 = chloride input to system 10^9 g/a

Table 3.3 Chloride Budget of the east coast of the Yucatan Peninsula (see map for area), with evapotranspiration of 70%

Source of Cl^-	Cl_1 (mM)	Cl_2 (%)	ΣRecharge (10^9 m^3/a)	Cl_3 (10^9 g/a)
Input from wet deposition	0.12	0.37	0.636	2.7
Input from dry deposition	4.7	14.5	-	106
Total input from runoff	**4.82 ± 3.27**	**14.8**	**0.636**	**108**
Concentration by ET (x3.33)	-	-	-0.445	-
Effective Recharge	16.1 ± 10.9	49.4	0.191	108
Mixing with saline water*	16.5	50.6	0.0055	112
Total	**32.5 ± 31.7**	**100**	**0.196**	**220**

Table 3.4 Chloride Budget of the east coast of the Yucatan Peninsula (see map for area), with evapotranspiration of 85%

Source of Cl^-	Cl_1 (mM)	Cl_2 (%)	ΣRecharge (10^9 m^3/a)	Cl_3 (10^9 g/a)
Input from wet deposition	0.12	0.37	0.636	2.7
Input from dry deposition	4.7	14.46	-	106
Total input from runoff	**4.82 ± 3.27**	**14.83**	**0.636**	**108**
Concentration by ET (x6.66)	-	-	-0.541	-
Effective Recharge	32.1 ± 21.8	98.8	0.0954	108
Mixing with saline water*	0.4	1.2	0.0001	0
Total	**32.5 ± 31. 7**	**100**	**0.0955**	**108**

* assuming mixing with seawater composition end-member
Cl_1 = chloride concentration in mM
Cl_2 = chloride concentration as a percentage of total lens concentration
ΣRecharge = volumetric recharge to lens 10^9 m^3/a
Cl_3 = chloride input to system 10^9 g/a

85% Evapotranspiration (Table 3.4)

Evapotranspiration of 85% reduces the volume of effective recharge to 15% of the mean annual rainfall (0.95 x 10^8 m^3/a). This increases the chloride concentration to 32.1 mM, although the total input of chloride to the system remains the same. The remaining 0.4 mM chloride (derived from the average chloride concentration of 32.5 mM for the freshwater lens) is attributable to mixing with the underlying saline groundwaters. If it is assumed that the saline end-member is of near-seawater composition, a maximum volumetric ratio of recharge water to saline water of 1438:1 can be calculated, indicating a contribution of 6.63 x 10^4 m^3/a over the whole study area, and increasing the volumetric input to the lens to a minimum of 0.96 x 10^8 m^3/a. This annual input represents 1.43% of the total volume of the lens within the study area (calculated as 6.67 x 10^9 m^3) and suggests the average residence time of lens waters is ~70 years.

3.4.2.3 Ion/chloride ratios

Chloride should be conserved during both evapotranspiration and mixing. Thus, chloride can be used as a conservative tracer to model the contribution of seawater to the elemental composition of the lens waters. Chloride has a good positive linear relationship with sodium (Figure 3.5), confirming its conservative behaviour. Chloride also has a good positive linear relationship with conductivity (Figure 3.5), although it is possible two trends can be delineated (one for samples with < 30 mM Cl^-, where carbonate dissolution-precipitation reactions may be the major control on specific conductance and another for samples with > 30 mM Cl^-, where mixing with saltwater may be the major control on specific conductance). These processes (carbonate diagenesis and mixing with saltwater) and the effect they have on major ion chemistry are discussed further in this section.

If an ion from a freshwater sample has the same ratio with chloride as it does in seawater, it is assumed the source of that ion is seawater. A deviation from this ratio may lend insight into the water-rock interactions occurring in the Yucatan Peninsula platform. For example, $CaCO_3$ dissolution will result in elevated Ca/Cl and HCO_3/Cl ratios. If aragonite dissolution is occurring, Sr/Cl ratios are also expected to increase relative to seawater. In addition, if high-Mg calcite (HMC) or dolomite dissolution is occurring, an increase in Mg/Cl ratios is expected. A summary of ion/chloride ratios for all freshwaters and the various site types is given in Table 3.5.

From Table 3.5, it is apparent that calcium, alkalinity, strontium and magnesium ratios with chloride are consistently higher than those predicted from the dilution of seawater. The highest ratios occur in vadose drip samples, indicating a large amount of dissolution occurs within the vadose zone. In addition, Merida cave lens samples have elevated Ca/Cl, Mg/Cl, Sr/Cl, but not HCO_3/Cl, molar ratios compared to the east coast cave waters. SO_4/Cl ratios are also generally higher than expected from seawater (and are especially high in vadose drip and Merida cave samples). Na/Cl ratios, which are similar to the ratio found in seawater, indicate sodium is acting conservatively, although some elevated ratios are found in rain, runoff and some drip samples.

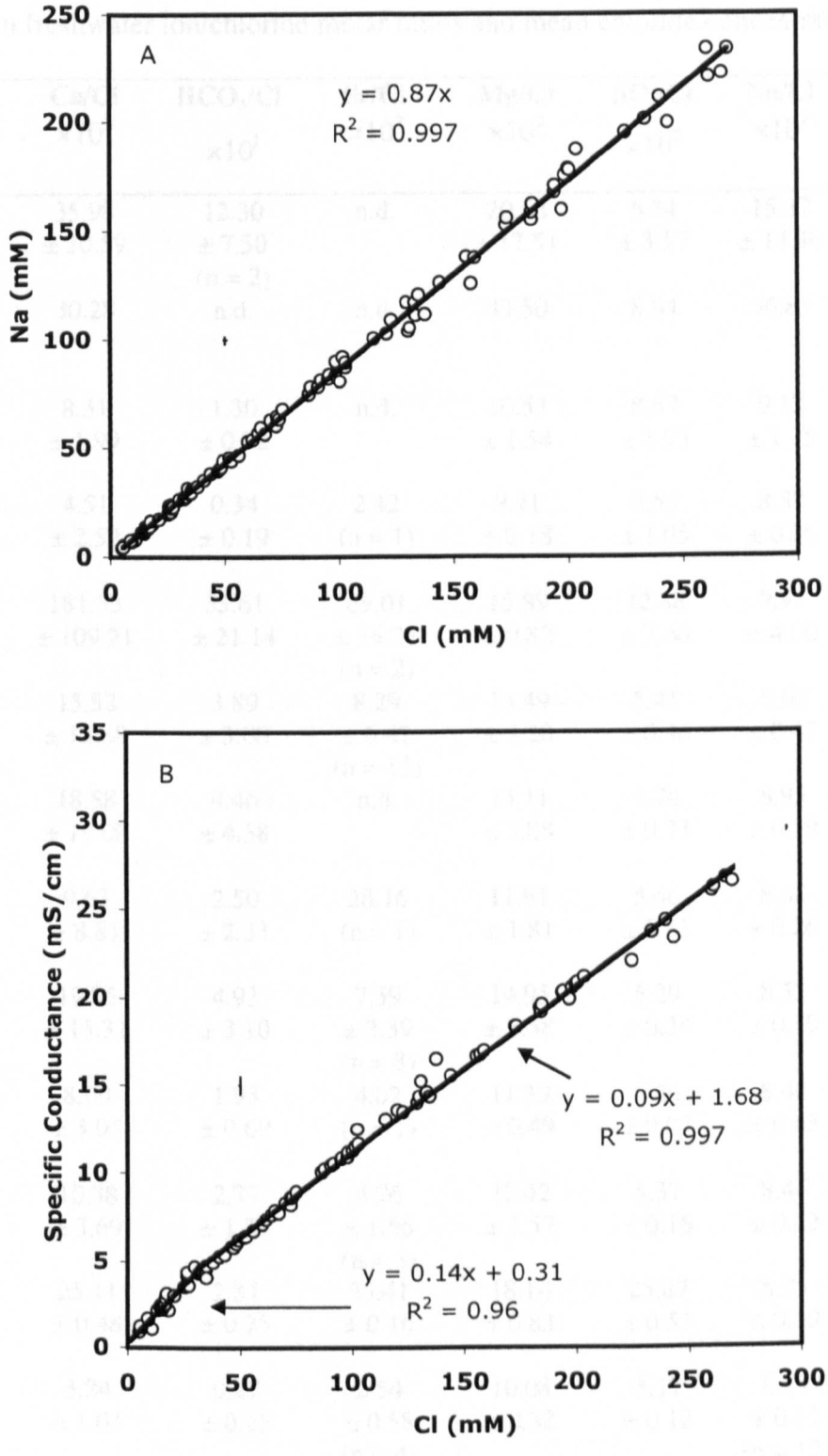

Figure 3.5 Chloride against sodium (A) and specific conductance (B). Crosses are representative analytical uncertainties (±1σ).

Table 3.5 Mean freshwater ion/chloride molar ratios and mean chloride concentrations (±1σ).

Water Type	Ca/Cl $\times 10^2$	HCO_3/Cl $\times 10^1$	Sr/Cl $\times 10^2$	Mg/Cl $\times 10^2$	SO_4/Cl $\times 10^2$	Na/Cl $\times 10^2$	Cl (mM)
Rainwater (n = 5)[¶]	35.98 ± 20.59	12.30 ± 7.50 (n = 2)	n.d.	20.58 ± 17.51	6.34 ± 3.57	15.37 ± 14.36	0.41 ± 0.19
Throughfall (n = 1)	30.28	n.d.	n.d.	43.50	8.84	36.85	1.28
Runoff (n = 4)	8.31 ± 1.99	1.30 ± 0.72	n.d.	10.53 ± 1.54	8.57 ± 1.93	9.12 ± 1.15	4.82 ± 3.27
Surface Pools (n = 7)[¶]	4.51 ± 2.52	0.34 ± 0.19	2.42 (n = 1)	9.91 ± 2.18	5.55 ± 1.05	8.88 ± 0.26	216 ± 222
Drips (n = 7)[¶]	181.33 ± 109.21	35.61 ± 21.14	69.01 ± 16.21 (n = 2)	15.89 ± 9.82	12.88 ± 7.66	9.91 ± 4.00	1.90 ±1.13
Mean Freshwater Lens[†] (n = 77)[¶]	15.52 ± 13.88	3.89 ± 3.08	8.29 ± 6.42 (n = 13)	13.49 ± 3.20	5.41 ± 0.46	8.60 ± 0.42	32.5 ± 31.7
Static Wells (n = 13)	18.58 ± 19.00	4.46 ± 4.58	n.d.	13.11 ± 3.88	5.74 ± 0.73	8.95 ± 0.59	41.6 ± 37.7
Pumped Wells (n = 9)[¶]	9.63 ± 8.81	2.50 ± 2.33	28.16 (n = 1)	11.91 ± 1.81	5.46 ± 0.83	8.68 ± 0.26	63.0 ± 57.3
Cenotes (n = 32)[¶]	19.85 ± 15.31	4.93 ± 3.10	7.59 ± 2.39 (n = 8)	14.95 ± 3.58	5.29 ± 0.24	8.53 ± 0.39	18.2 ± 29.6
Caverns (n = 3)[¶]	8.00 ± 3.05	1.93 ± 0.69	4.02 (n = 1)	11.39 ± 0.49	5.26 ± 0.07	8.45 ± 0.45	40.2 ± 17.4
Caves[*] (n = 20)[¶]	10.38 ± 3.69	2.77 ± 1.37	4.96 ± 1.56 (n = 3)	12.42 ± 1.57	5.37 ± 0.16	8.46 ± 0.22	32.8 ± 19.9
Caves[§] (n = 2)	25.11 ± 0.48	2.31 ± 0.25	25.41 ± 0.16	18.14 ± 0.83	25.87 ± 0.51	8.95 ± 0.19	27.9 ± 2.40
Coastal Q (n = 13)[¶]	3.24 ± 1.03	0.27 ± 0.15	2.54 ± 0.58 (n = 4)	10.08 ± 0.32	5.17 ± 0.12	8.59 ± 0.31 (n = 12)	225 ± 136
Caribbean Seawater	1.80 ± 0.03	0.04	1.72	9.53 ± 0.12	5.06 ± 0.05	8.63 ± 0.09	575 ± 5.46
Combined Analytical Uncertainty	± 0.51	± 0.09	± 1.20	± 0.32	± 0.11	±0.23	± 0.33

[¶] n value unless otherwise stated
[†] excluding coastal discharge samples/Merida sites
[*] = caves from main field area (east coast)
[§] = caves from Merida area (Yucatan State)
n.d. = no data

Plots of ion ratios with chloride against chloride show that Ca/Cl, HCO_3/Cl, Sr/Cl and Mg/Cl molar ratios increase with decreasing chloride concentration, indicating that the main source of these ions is the freshest waters (Figure 3.6). There is a continuum between these fresh waters and seawater (i.e. most samples fall along a conservative mixing line), confirming mixing between the freshest waters and saline water may be an important process controlling ion chemistry in lens waters, although there is some scatter in the data (especially with respect to Mg/Cl ratios) (Figure 3.6). Both SO_4/Cl and Na/Cl are acting conservatively; these molar ratios seldom deviate from the ratios measured in seawater (Figure 3.6).

Ca/Cl increases with increasing distance inland from the east coast, and there appear to be two significant trends of increase (Figure 3.7). The upper trend ($r = 0.97$, $P<0.01$, d.f. = 20) includes samples known to contain hydrogen sulfide layers (based on field observations). Measurements of sulfide are discussed in Section 3.5.3. The bottom trend includes all other lens samples, except pumped wells and samples from sites over 10 km inland ($r = 0.89$, $P< 0.01$, d.f. = 39). The decrease in Ca/Cl near the coast probably indicates increased mixing with seawater, but may also indicate precipitation is occurring at the coast or along the lens flow-path. There are no discernable trends with distance inland for HCO_3/Cl, Mg/Cl, SO_4/Cl or Na/Cl.

3.4.2.4 XS Calculations

As mentioned earlier, chloride can be used as a conservative tracer to model the contribution of seawater to the elemental composition of the lens waters. Seawater is also a major source of calcium (and other ions) and thus calcium derived solely from rock-water interactions can only be distinguished by reference to levels of calcium predicted from the chloride concentrations of seawater. Thus, the amount of calcium due to dissolution, here termed 'calcium excess' (Ca_{XS}) is defined relative to open seawater:

$$Ca_{XS} = Ca_{sample} - \left(\frac{Cl_{sample}}{Cl_{seawater}} \bullet Ca_{seawater} \right) \qquad (3.3)$$

Magnesium, strontium and sulfate excesses are calculated in a similar manner. The analytical uncertainties associated with these calculations are described in Chapter 2.

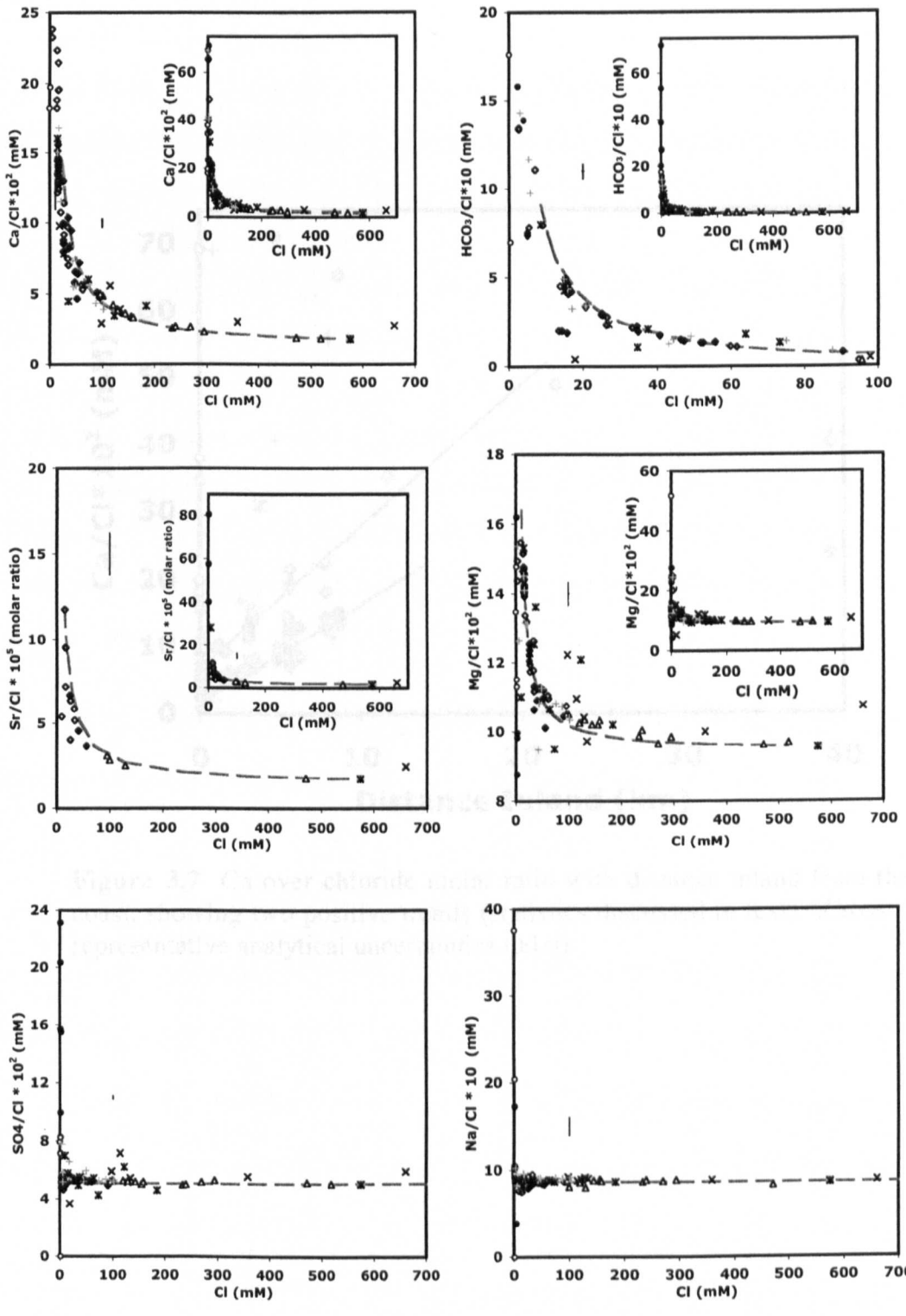

Figure 3.6 Ion over chloride molar ratios against chloride for Ca^{2+} (A), HCO_3^- (B), Sr^{2+} (C), Mg^{2+} (D), SO_4^{2-} (E) and Na^+ (F) for the different freshwater sample types. Freshwater types include rainwater (open circles), throughfall (grey circles), Runoff (open squares), surface pools (black X), drips (closed circles), static wells (grey +), pumped wells (black asterisk), cenotes (open diamonds), caverns (grey diamonds), caves (black diamonds) and coastal discharge (open triangles). Dashed line is conservative mixing line between seawater and a freshwater end-member. Black crosses are representative analytical uncertainties (±1σ).

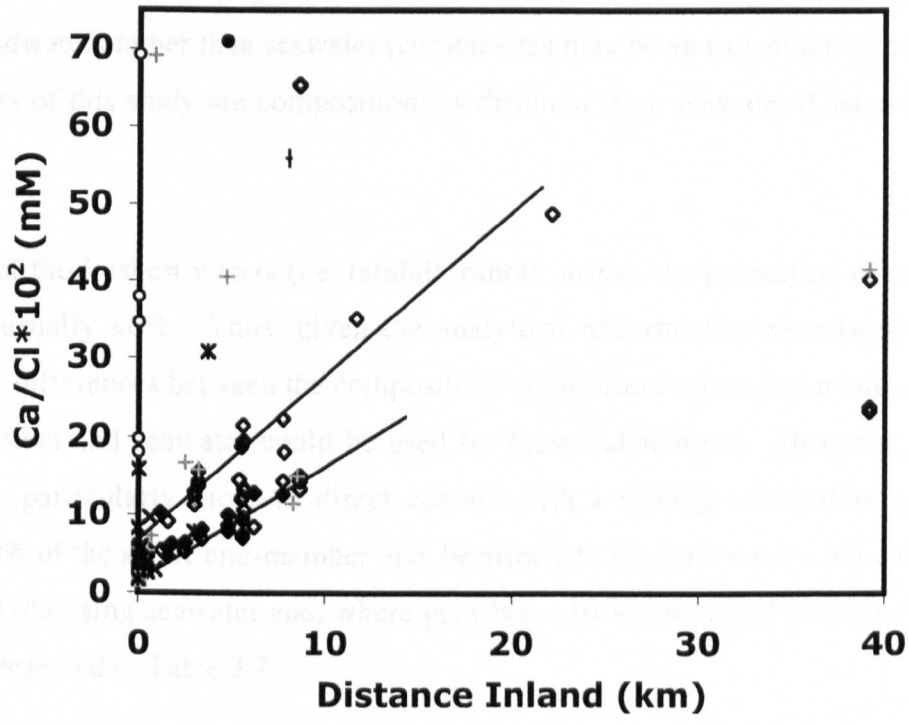

Figure 3.7 Ca over chloride molar ratio with distance inland from the east coast, showing two positive trends (statistics discussed in text). Cross shows representative analytical uncertainties (±1σ).

An important issue with this calculation is the choice of saline end-member. Most studies that have used this, or a similar, calculation use 'standard seawater' as the saline end-member, as described, for example, by Nordstrom et al. (1979) or a seawater sample taken from a local source is used (e.g. Stoessell, 1993). However, lens waters are mixing with saline groundwaters rather than seawater (coastal sites may be an exception) and the saline groundwaters of this study are compositionally different from seawater (Chapter 5, Table 3.6).

In the case of the freshest waters (i.e. rainfall, runoff, drips), the proportion of saline end-member is usually <6%. Thus, given the analytical uncertainties associated with XS calculations, differences between the compositions of different saline end-members should have little effect and seawater could be used for these calculations. However, brackish lens waters (particularly those in direct contact with a mixing zone/saline zone) that comprise >6% of the saline end-member may be affected. For lens waters, XS calculations were carried out using seawater and, where possible, a local saline end-member and these results are presented in Table 3.7.

Table 3.6 Composition of standard seawater (Nordstrom et al., 1979), compared to that of Caribbean Seawater from the eastern Yucatan Peninsula and saline groundwaters sampled in the study, as well as saline groundwaters sampled from the Bahamas (Whitaker, 1992) (±1σ).

Saline End-member	Cl (mM)	Ca (mM)	Mg (mM)	Sr (mM)
Standard Seawater	565	10.6	54.9	0.099
Caribbean Seawater (this study)	575 ± 5.46 (n = 6)	10.3 ± 0.27 (n = 6)	54.9 ± 0.62 (n = 6)	0.099 ± 0.000 (n = 2)
Saline Groundwater (Yucatan)	556 ± 27 (n = 48)	11.6 ± 3.01 (n = 48)	51.8 ± 1.78 (n = 48)	0.11 ± 0.04 (n = 21)
Saline Groundwater (Bahamas)	597 ± 48 (n = 30)	11.4 ± 0.6 (n = 30)	56.9 ± 3.9 (n = 30)	0.11 ± 0.01 (n = 11)

Table 3.7 Mean XS concentrations, calculated using seawater as the saline end-member. XS results in parentheses were, where possible, calculated using a local saline groundwater as the saline end-member (±1σ).

Water Type	Ca_{xs} (mM)	Mg_{xs} (mM)	Sr_{xs} (mM)	SO_{4xs} (mM)
Rainwater (n = 5)	+0.16 ± 0.13	+0.05 ± 0.10	n.d.	0.00 ± 0.02
Throughfall (n = 1)	+0.36	+0.43	n.d.	+0.05
Runoff (n = 4)	+0.44 ± 0.11	+0.05 ± 0.07	n.d.	+0.26 ± 0.14
Surface Pools (n = 7)[¶]	+3.23 ± 1.80	+2.03 ± 2.76	+0.046 (n = 1)	+1.59 1.98
Drips (n = 7)[¶]	+2.52 ± 0.33	+0.04 ± 0.13	+0.007 ± 0.000 (n = 2)	+0.09 ± 0.10
Mean Freshwater Lens[†] (n = 77)[¶]	+2.19 ± 0.55	+0.73 ± 0.37	+0.012 ± 0.005 (n = 13)	+0.08 ± 0.21
Static Wells (n = 13)	+2.24 ± 0.28	+0.65 ± 0.33	n.d.	+0.17 ± 0.13
Pumped Wells (n = 9)[¶]	+2.38 ± 0.93	+1.02 ± 0.92	+0.023 (n = 1)	+0.08 ± 0.62
Cenotes (n = 32)[¶]	+2.11 ± 0.56 (+2.10 ± 0.55)	+0.72 ± 0.19 (+0.73 ± 0.19)	+0.011 ± 0.004 (+0.010 ± 0.004) (n = 8)	+0.05 ± 0.04 (+0.04 ± 0.05)
Caverns (n = 3)[¶]	+2.20 ± 0.37 (+2.18 ± 0.38)	+0.70 ± 0.18 (+0.65 ± 0.08)	+0.006 (+0.006) (n = 1)	+0.07 ± 0.02 (+0.03 ± 0.03)
Caves[*] (n = 20)[¶]	+2.21 ± 0.50 (+2.20 ± 0.49)	+0.69 ± 0.14 (+0.66 ± 0.13)	+0.012 ± 0.001 (+0.011 ± 0.001) (n = 3)	+0.08 ± 0.05 (+0.05 ± 0.04)
Caves[§] (n = 2)	+6.51 ± 0.69 (6.02 ± 0.65)	+2.39 ± 0.03 (+2.96 ± 0.02)	+0.066 ± 0.006 (0.059 ± 0.006)	+5.81 ± 0.64 (5.73 ± 0.64)
Coastal Q (n = 13)[¶]	+2.12 ± 0.93	+0.84 ± 0.29	+0.009 ± 0.005 (n=4)	+0.22 ± 0.26
Analytical Uncertainty	± 0.04	± 0.15	± 0.003	± 0.06

[¶] n value unless otherwise stated
[†] excluding coastal discharge samples/Merida sites
[*] = caves from main field area (east coast)
[§] = caves from Merida area (Yucatan State)
n.d. = no data

In almost all cases, the choice of saline end-member makes little difference to the XS calculation (i.e. the difference is within analytical uncertainty ($\pm 2\sigma$)), except for the Merida cave sites (Table 3.7). The Merida lens waters are probably mixing with saline groundwaters of very different composition compared to those along the east coast (Chapter 5). For consistency, calculations of XS for all other freshwater samples are made using seawater as the common saline end-member.

The means of all water types for all XS calculations are positive, indicating enrichment of ions (Ca, Mg, Sr, SO_4) above that predicted from the dilution of seawater (Table 3.7). Ca_{XS} of the freshwater lens (excluding discharge and Merida sites) is $+2.19 \pm 0.55$ mM (n = 77). Thus, substantial calcium enrichment due to $CaCO_3$ dissolution has occurred as waters pass through the freshwater system. Similarly, there is a magnesium enrichment of +0.73 $\pm$ 0.37 mM (n = 77) and a strontium enrichment of $+0.012 \pm 0.005$ mM (n = 13) in lens waters. Although positive, lens water SO_{4XS} ($+0.08 \pm 0.21$, n = 77) is within two standard deviations of zero and is thus not significantly enriched nor depleted relative to the dilution of seawater. However, caves from the Merida region and static wells from the east coast region are significantly enriched in sulfate. No discernable systematic trend exists between XS and distance inland, although this is considered again later in Section 3.4.4.4.

Of the samples taken from the main study area, surface pools and drip samples have the highest Ca_{XS} concentrations (Table 3.7), suggesting $CaCO_3$ dissolution has occurred. Pumped wells and surface pools have elevated Mg_{XS} (and possibly Sr_{XS}, n = 1) concentrations, compared to other east coast samples, implying that HMC and aragonite dissolution may have occurred.

3.4.3 Saturation Indices (SI) and pCO_2

Saturation indices (SI) with respect to calcite (C), aragonite (A), ordered dolomite (D, $K_D = 10^{-17}$), disordered dolomite (DD, $K_{DD} = 10^{-16.5}$) and the carbon dioxide partial pressure (pCO_2) with which the water samples are in equilibrium were calculated using the geochemical modeling program PHREEQC (Parkhurst, 1995). These results are summarised for each water type in Table 3.8.

Table 3.8 Mean freshwater SI and pCO_2 ($\pm 1\sigma$)

Water Type	SI-A	SI-C	SI-D	SI-DD	pCO_2 (%)	$\bar{x}$IBE (%)
Rainwater	-1.65 ± 1.38 (n =4)	-1.51 ±1.38 (n = 4)	-4.98 ± 2.64 (n = 2)	-5.53 ± 2.64 (n = 2)	0.07 ± 0.09 (n = 5)	+21 ± 23
Throughfall (n = 1)	-2.16	-2.02	-3.74	-4.29	0.11	+60
Runoff (n = 4)	-0.34 ± 0.45	-0.20 ± 0.45	-0.15 ± 0.90	-0.70 ± 0.90	0.04 ± 0.04	-0.19 ± 3.11
Surface Pools (n = 7)	+0.90 ± 0.27	+1.04 ± 0.27	+2.68 ± 0.69	+1.99 ± 0.65	0.29 ± 0.36	+2.13 ± 0.81
Drips (n = 7)	+0.55 ± 0.20	+0.69 ± 0.20	+0.45 ± 0.43	-0.11 ± 0.43	0.66 ± 0.37	-0.71 ± 8.52
Mean Freshwater Lens[†] (n = 77)	-0.13 ± 0.29	+0.01 ± 0.29	+0.21 ± 0.63	-0.35 ± 0.62	3.68 ± 1.89	-1.47 ± 3.12
Static Wells (n = 13)	+0.02 ± 0.30	+0.16 ± 0.30	+0.50 ± 0.67	-0.06 ± 0.66	2.84 ± 2.23	-0.39 ± 2.91
Pumped Wells (n = 9)	+0.12 ± 0.37	+0.26 ± 0.36	+0.89 ± 0.81	+0.29 ± 0.79	2.85 ± 1.22	-1.28 ± 2.11
Cenotes (n = 32)	-0.17 ± 0.28	-0.03 ± 0.28	+0.04 ± 0.57	-0.52 ± 0.56	3.54 ± 1.93	-1.33 ± 3.72
Caverns (n = 3)	-0.15 ± 0.28	-0.01 ± 0.27	+0.30 ± 0.49	-0.25 ± 0.49	3.78 ± 2.20	-1.88 ± 2.60
Caves[*] (n = 20)	-0.28 ± 0.14	-0.14 ± 0.14	-0.02 ± 0.34	-0.58 ± 0.34	4.83 ± 1.27	-2.42 ± 2.57
Caves[§] (n = 2)	-0.25 ± 0.25	-0.11 ± 0.25	-0.21 ± 0.54	-0.80 ± 0.55	9.34 ± 5.44	+0.86 ± 0.36
Coastal Q (n = 12)	-0.23 ± 0.31	-0.09 ± 0.31	+0.50 ± 0.77	-0.07 ± 0.76	2.38 ± 1.57	+0.41 ± 1.28
Analytical Uncertainty	± 0.006	± 0.006	± 0.015	± 0.015	± 0.020	-

[*] = caves from main field area (east coast) [§] = caves from Merida area (Yucatan)
[†]excluding coastal discharge samples and Merida sites

3.4.3.1 pCO_2

The pCO_2 of rainwater, throughfall and runoff samples is slightly (but not significantly) higher than atmospheric (Table 3.8), but this is probably due to difficulties encountered while trying to obtain stable pH and alkalinity measurements from such poorly-buffered, low ionic strength solutions.

The pCO_2s of surface pools and drip waters are ~1 order of magnitude greater than atmospheric. Both sample types are subject to degassing (supported by the observed supersaturation). The pCO_2 of lens waters is significantly higher than the mean of all other sample types and at 3.68 ± 1.89% (n = 77), lens waters have pCO_2 values over two orders of magnitude greater than atmospheric. Within the lens, static and pumped wells have the lowest pCO_2 (and these samples are also supersaturated, indicating degassing has occured) while cenotes, caverns and caves especially have the highest pCO_2.

3.4.3.2 Saturation Indices of Calcite (SI-C) and Aragonite (SI-A)

Rainwater and runoff (including throughfall) samples are undersaturated with respect to both calcite and aragonite (Table 3.8). Surface pools and drip waters are both supersaturated with respect to calcite and aragonite, while the mean of lens waters approaches equilibrium with respect to calcite and is undersaturated with respect to aragonite. Of the lens waters, only waters from wells (both static and pumped) are supersaturated with respect to calcite and aragonite (although the mean of static wells approaches SI-A = 0). Cenote and cavern waters are equilibrated with respect to calcite, while caves from both the east coast and Merida region and coastal discharges are undersaturated with respect to both carbonate species.

3.4.3.3 Saturation Indices of Dolomite (D) and Disordered Dolomite (DD)

Although no dolomite is expected to be present in the freshwater lens (Ward, 1985), any modern dolomites that are present in the field area are likely to be disordered (Hardie,

1987), thus descriptions are given for SI-DD only. Only two sample types show supersaturation with respect to disordered dolomite: surface pools and pumped wells/boreholes. Two other sample types approach equilibrium with respect to SI-DD: static wells/boreholes and coastal discharge. All other samples are undersaturated with respect to disordered dolomite.

3.4.4 Geochemistry Discussion

The amount of dissolution/precipitation can be examined directly using calcium concentrations (i.e. Ca_{XS}), while the distribution of dissolution is assessed using measurements of soil air and water pCO_2, mineral saturation indices, and potential dissolution capability under open system conditions are calculated using PHREEQC (Parkhurst, 1995).

Two series of reactions are important in controlling dissolution and precipitation of $CaCO_3$ (James and Choquette, 1984):

- mineral-controlled reactions
- water-controlled reactions

3.4.4.1 Mineral vs. water-controlled reactions

The Yucatan Peninsula continues to accrete at the coastal margins (Ward, 1985) and Quaternary rocks have been identified at sites from 1 to potentially 10 km inland (Ward, 1985). A profile of wall rock samples from Casa Cenote (~200 m inland) were analysed by Ford (1985), who argued that the preferential dissolution of aragonite and stabilisation of HMC to LMC are the only active diagenetic processes taking place in the upper Pleistocene limestones (exposed to lens and mixed waters) along the eastern margin of the Yucatan Peninsula. Ford (1985) found that HMC occurs only in the vadose zone and is preserved in miliolid and red algal constituents. In the phreatic zone (below the modern water table) only LMC and aragonite are present (Ward and Halley, 1985; Ford, 1985; Ford et al., 1985; Back et al., 1986).

Additional wall-rock samples from below the water table in a coastal site (Ak Kimin, ~200 m from the east coast) support the finding of Ford (1985), showing an absence of HMC, but aragonite is present in samples to a maximum water depth of 18.4 m (Goodwin, 2002). Aragonite abundance is greatest in the shallowest sample (21.7 % of the bulk rock sample from 3.9 m water depth) and decreases fairly linearly to 0.49 % at 18.4 m (Goodwin, 2002). No dolomite has been found in rock samples in contact with modern lens waters or in the vadose zone of the Yucatan Peninsula.

Molar ratios of calcium, magnesium and strontium in solution are compared to those of high-magnesium calcite (HMC), aragonite and calcite to examine the possible mineral-controlled reactions occurring.

Mg_{xs}:Ca_{xs}

The means of all water types are enriched with respect to both calcium and magnesium (i.e. Ca_{xs} and Mg_{xs} are positive, Table 3.7). HMC dissolution results in an Mg:Ca ratio of 0.12:0.88 (Garrels and Wollast, 1978), while calcite dissolution results in an Mg:Ca ratio of 0.04:0.96 (Budd, 1988). If the waters have dissolved HMC and precipitated calcite, a ratio greater than 0.12:0.88 is expected (Figure 3.8). If HMC dissolution is not accompanied by calcite precipitation, the ratio should be equal to 0.12:0.88. However, if the waters have dissolved both HMC and LMC, the samples should fall below the 0.12:0.88 line. The mean of all lens samples fall above this line, indicating that HMC dissolution and calcite precipitation has occurred. Drip samples fall on the calcite dissolution line. The variability of these relationships with distance inland is considered in Section 3.4.4.4.

Sr_{xs}:Ca_{xs}

Dissolved strontium and calcium concentrations can be used in a similar manner to indicate aragonite stabilization. The molar ratio of Sr:Ca in aragonite (0.011:0.989) is higher than it is in calcite (0.0017:0.9983) (Budd, 1988). Although strontium was not analysed routinely, the data available for freshwaters indicates samples have a range of Sr:Ca ratios (Figure 3.9). Pumped wells (n = 1), surface pools and Merida lens waters have mean compositions approaching the aragonite dissolution line. Both the pumped well and surface pool samples contain water in contact with shallow (less mature) rock.

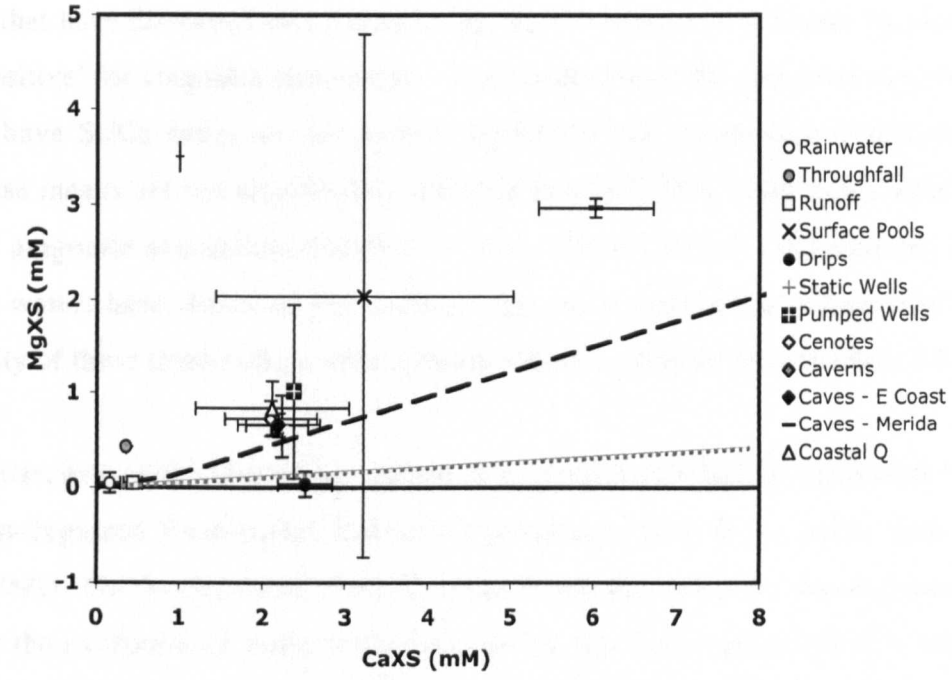

Figure 3.8 Relationship between Mg_{XS} and Ca_{XS} plotted as sample means ± 1σ. Black dashed line is the Mg/Ca ratio expected from high-Mg calcite dissolution and the grey dashed line is the Mg/Ca ratio expected from calcite dissolution.

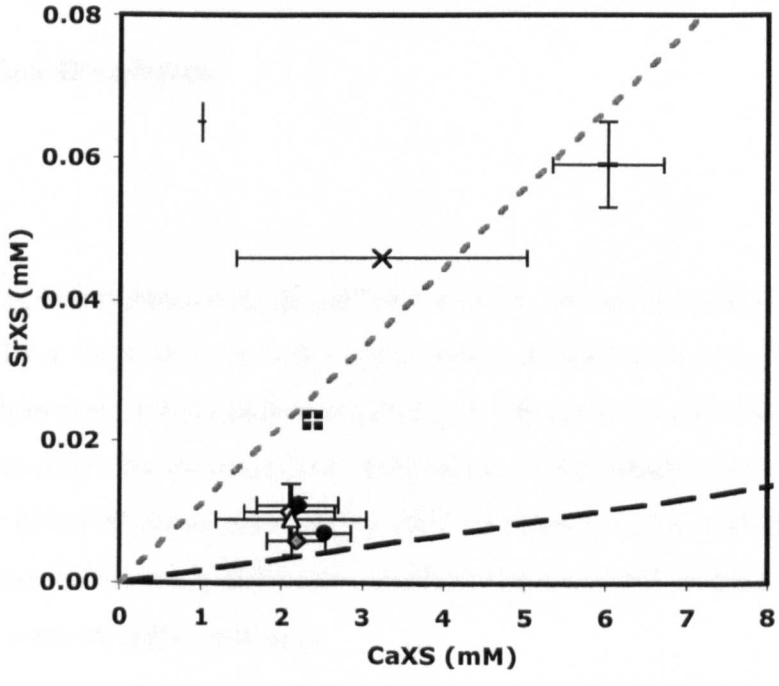

Figure 3.9 Relationship between Sr_{XS} and Ca_{XS} plotted as sample means ±1σ. Black dashed line is Sr/Ca ratio expected from calcite dissolution and the grey dashed line is the Sr/Ca ratio expected from aragonite dissolution. Symbols as in Figure 3.8.

Lens waters from Merida caves (which were sampled from >50 m depth) may be mixing with waters that have dissolved strontium-rich gypsum or anhydrite (Chapter 5), resulting in a 'false positive' for aragonite dissolution. Lens waters from the east coast caverns and drip waters have Sr/Ca ratios nearest to that expected from simple calcite dissolution, although these means are not significantly different from all other water types which fall between the aragonite and calcite dissolution lines. These 'mixed' compositions could indicate that waters have dissolved both mineral species at some stage in their evolution. The variability of these relationships with distance inland is considered in Section 3.4.4.4.

In the Bahamas, aragonite controls the carbonate equilibrium, which is supported by the fact that non-degassed freshwaters maintain equilibrium with SI-A, rather than SI-C (Whitaker, 1992). On the east coast of the Yucatan Peninsula, however, non-degassed lens waters (with the exception of static wells) are equilibrated with calcite (SI-C = +0.01 ± 0.29, n = 77) rather than aragonite (SI-A = -0.13 ± 0.29, n = 77). In subsequent geochemical modeling, calcium carbonate is dissolved until the solution comes to equilibrium with respect to calcite.

3.4.4.2 Surface Dissolution

Rainwater

Before coming into contact with the bedrock surface, rain samples have dissolved calcium (Ca_{XS} = +0.16 ± 0.13 mM, n = 5), presumably derived primarily from $CaCO_3$ dust. Rainwaters, however, remain undersaturated with respect to calcite (SI-C = -1.51 ± 1.38, n = 4) and thus have the potential for dissolution. The samples have pCO_2 values not significantly different from atmospheric (0.07 ± 0.09, n = 5), with the relatively large standard deviation reflecting difficulties in obtaining stable pH readings from these poorly buffered low ionic strength solutions.

Runoff

It is assumed that dry deposition has the Ca/Cl ratio of seawater and thus it should have no effect on the Ca_{XS} calculations of runoff waters (+0.44 ± 0.11 mM, n = 4). These are

maximum estimates of dissolution at the bed-rock surface as a substantial contribution may be from the dissolution of $CaCO_3$ dust rather than the dissolution of the bedrock surface. Despite the dissolution of ~0.28 mM calcium compared to rainwater, runoff samples are still undersaturated with respect to calcite.

Surface Waters

Some runoff water remains at the surface in pools and as mangrove waters and these show evidence of considerable calcium enrichment (Ca_{XS} surface pools = +3.17 ± 2.10 mM, n = 5; Ca_{XS} mangrove waters = +3.37 ± 1.37 mM, n = 2).

Both surface pools and mangrove waters are supersaturated with respect to both calcite and aragonite (Table 3.8). This supersaturation, combined with calcium enrichment indicates that these waters were once moderately enriched in CO_2 and have since degassed. However, pCO_2 is still greater than atmospheric in both of these environments.

Although surface pools and mangroves may contribute to significant dissolution locally, they are neither continuous nor extensive along the east coast of the peninsula. In addition, the main process occurring in surface pools is evaporation (evidenced by high chloride concentrations) and these waters are thought to be largely isolated from the vadose zone and freshwater lens and thus, they are unlikely to contribute significantly to the total amount of dissolution occurring. Surface pools may play a larger role in dissolution of the bed-rock surface in the northern part of the Yucatan Peninsula, where the bedrock surface is characterised by a 'pock-marked' terrain (Perry et al., 2002 and others). Similarly, such a terrain occurs in the Bahamas, where banana holes, which comprise ~20% of the total surface area, are thought to contribute significantly to the dissolution occurring at the bedrock surface (Whitaker, 1992).

Soil Zone

Eleven gaseous CO_2 measurements taken in June 2001 give a soil CO_2 concentration of 3.36 ± 1.34 % (Section 3.3). Carbonic acid, formed primarily from the hydration of CO_2 provides the potential for dissolution at the bedrock surface. The balance between

production (microbial and root respiration) and removal (diffusion/degassing) governs the concentration of CO_2. The rate at which CO_2 is produced is controlled predominantly by biological activity, which is, in turn, controlled by soil temperature and moisture content.

Brook et al. (1983) demonstrated a relationship between mean annual temperature and the mean annual pCO_2 of groundwaters from North American sites. For a mean annual temperature of 25°C, pCO_2 is expected to be 3.6%. This is not significantly different from the mean of the soil pCO_2 measurements taken during this study. The mean pCO_2 of lens waters is higher, but not significantly different than the pCO_2 of the soil zone (Table 3.8), suggesting surface waters do not by-pass soils on their way to the lens and/or soil CO_2 is similar to that in the vadose zone and/or some CO_2 is generated in the lens.

The dissolution potential in the subaerial environment is generated by high soil and/or lens pCO_2. But, the effect soil pCO_2 has on dissolution rates depends on the routing and residence times of recharge waters. This is considered in the next section.

3.4.4.3 Vadose Zone Dissolution

Due to the very low hydraulic gradient, the thickness of the vadose zone in the Yucatan Peninsula is controlled by topographic elevation and is generally ~10 m thick (although it can be $\leq$ 2 m thick in the vicinity of cenotes). Runoff waters entering the vadose zone are undersaturated with respect to both aragonite and calcite (Table 3.8), indicating their potential for dissolution. However, the degree to which this dissolution potential can be realised will depend on hydrological routing of these waters, which is the primary control on residence time, which in turn determines whether or not the waters can equilibrate with ground air pCO_2. In addition, the locus of evapotranspiration will play a role in governing the amount of dissolution that can occur within the vadose zone.

Direct sampling of vadose zone waters was not a major focus of this study. However, seven samples from cave drips were obtained in attempts to quantify some of the dissolution occurring in the vadose zone (although drips might provide over-estimates). The vadose zone above where the drip samples were sampled was generally 3-6 m thick and although vadose drips were sampled at different times of year, these samples are not necessarily representative of all recharge waters (as discussed below).

Drip samples are enriched in calcium, with a mean Ca_{XS} of +2.52 ± 0.33 mM (n = 7), some 2.08 mM greater than runoff, indicating substantial shallow dissolution has occurred. The drip water samples are also supersaturated with respect to calcite (SI-C = +0.69 ± 0.20, n= 7), indicating these waters were once enriched in CO_2 but have subsequently degassed. This is expected given the samples were collected after dripping through the cave void and 2 to 24 hours were required to fill the sample bottle with drip water (i.e. degassing occurs during sampling). Note, however, that drip water pCO_2 is still one order of magnitude greater than atmospheric (0.66 ± 0.37%, n = 7). The relatively low pCO_2 value may also reflect difficulties encountered when attempting to obtain accurate pH and alkalinity readings from degassed samples. PHREEQC was used to drive an average drip water sample to equilibrium with respect to calcite (i.e. to remove the effect of degassing). This produces a solution with a pCO_2 of 1.10% and a Ca_{XS} of 2.11 mM. This may provide an estimate of the 'real' vadose drip water conditions.

In addition, the amount of vadose zone dissolution can be estimated indirectly using PHREEQC (Parkhurst, 1995). Geochemical modeling was used to model the evolution of a mean runoff sample passing through the vadose zone under open system conditions.

Rapid Percolation

If runoff waters are directed from the surface and through the vadose zone by fractures, fissures and/or root holes, their residence time in the vadose zone will be extremely short and equilibration with ground pCO_2 will not occur (if these routings have a large diameter, it is entirely plausible that the pCO_2 within them will not be significantly elevated compared to atmospheric). However, some dissolution may occur, allowing percolating waters to evolve and achieve equilibration with respect to calcite. These two possibilities suggest that rapid percolation may be responsible for the dissolution of 0 (no rock-water interaction) to 0.12 mM Ca^{2+} (assuming equilibration with respect to calcite and that atmospheric pCO_2 is maintained).

Diffuse Percolation

Alternatively, the infiltrating waters may take a less direct route (*via* inter-granular and linked vug porosity) to reach the freshwater lens. Reardon et al. (1979) showed that pore spaces within the vadose zone of an inter-granular calcareous sand aquifer had elevated

concentrations of CO_2, thus this less-direct-routing may involve the evolution of runoff water under CO_2-enriched conditions.

Along the east coast of the Yucatan Peninsula, there are various sources of CO_2 within vadose zone air, including:

- downward diffusion of CO_2 from the soil zone
- root respiration within the vadose zone
- bacterial oxidation of organic matter within the vadose zone
- diffusion of CO_2 upwards from the freshwater lens

Vadose zone air pCO_2 can be estimated from the mean pCO_2 of lens surface waters sampled from static wells, which should have degassed to reach equilibrium with the over-lying vadose zone air. The mean pCO_2 of lens top waters sampled from static wells is 1.18 ± 0.19% (n = 5). This is very close to the estimate obtained by driving drip waters to equilibrium with respect to calcite, resulting in a pCO_2 of 1.10% (see above). Assuming drip waters have representative chemistries of waters that have passed through the vadose zone, this suggests at least 93% of recharge water is recharging the lens *via* diffuse percolation. If it is assumed that air in the vadose zone maintains this high pCO_2 (1.18%) year-round, waters recharging the aquifer via diffuse percolation could dissolve an additional 1.67 mM Ca^{2+} compared to runoff waters.

The residence time of most waters percolating through the vadose zone is probably sufficient to allow equilibration with both calcite and ground air pCO_2. Water level measurements from Heaven's Gate indicate the main control on water level is tidal and sometimes barometric fluctuations, not rainfall (Beddows, 2004), suggesting some storage within the vadose zone must occur. Individual rainfall events only appear to affect cenote levels when large rain events occur after several months of dry periods (Section 3.2; Beddows, 2004).

Evapotranspiration

Given that the vadose zone is generally 10 m thick and that at least some vadose zone storage does appear to take place (see above), most evapotranspiration will likely occur

above and within the vadose zone, rather than at the surface of the lens. Combined with the assumption that the residence time of water within the vadose zone is sufficient to allow equilibrium with ground air pCO_2, the path of runoff water through the vadose zone can be modeled using PHREEQC. Here, an average runoff water (Ca_{XS} = +0.44 mM, SI-C = -0.20) undergoes evapotranspiration and equilibration with ground air pCO_2 and calcite. This route is modeled with 40, 70 and 85% evapotranspiration. A flow diagram, summarising the results, is presented in Figure 3.10.

Evapotranspiration of 40% causes an increase in calcium of 0.32 mM (Ca_{XS} = +0.76 mM) and supersaturation with respect to calcite (SI-C = +0.14). After equilibration with ground air pCO_2 and calcite, the waters recharging the lens have a Ca_{XS} of +1.97 mM, suggesting that *via* this mechanism, 1.53 mM Ca^{2+} can be dissolved in the vadose zone.

Evapotranspiration of 70% causes an increase in calcium of 1.11 mM (Ca_{XS} = +1.55 mM) and supersaturation with respect to both calcite (SI-C = +0.56) and aragonite. After equilibration with ground air pCO_2 and calcite, the waters recharging the lens have a Ca_{XS} of +2.13 mM, suggesting that under this mechanism, 1.69 mM Ca^{2+} can be dissolved in the vadose zone. This Ca_{XS} value is very similar to the Ca_{XS} calculated for non-degassed drip water samples (i.e. +2.11 mM, see above).

Evapotranspiration of 85% causes an increase in calcium of 2.69 mM (Ca_{XS} = +3.13 mM) and supersaturation with respect to both calcite (SI-C = +0.95) and aragonite. After equilibration with ground air pCO_2 and calcite, the waters recharging the lens have a Ca_{XS} of +2.38 mM, which is 1.94 mM Ca^{2+} greater than runoff waters.

The Ca_{XS} value derived from using the 85% estimate for evapotranspiration exceeds that measured in lens waters. Thus, if this simulation is correct, additional processes must be active to decrease the Ca_{XS} by ~0.18 mM to reach mean lens values.

If either the 40 or 70% evapotranspiration estimates are correct, there is still ~0.07 – 0.23 mM calcium unaccounted for in the lens. This additional dissolution may be derived from mixing or the oxidation of organic matter, which produces CO_2 and subsequently acidity (discussed in the next section).

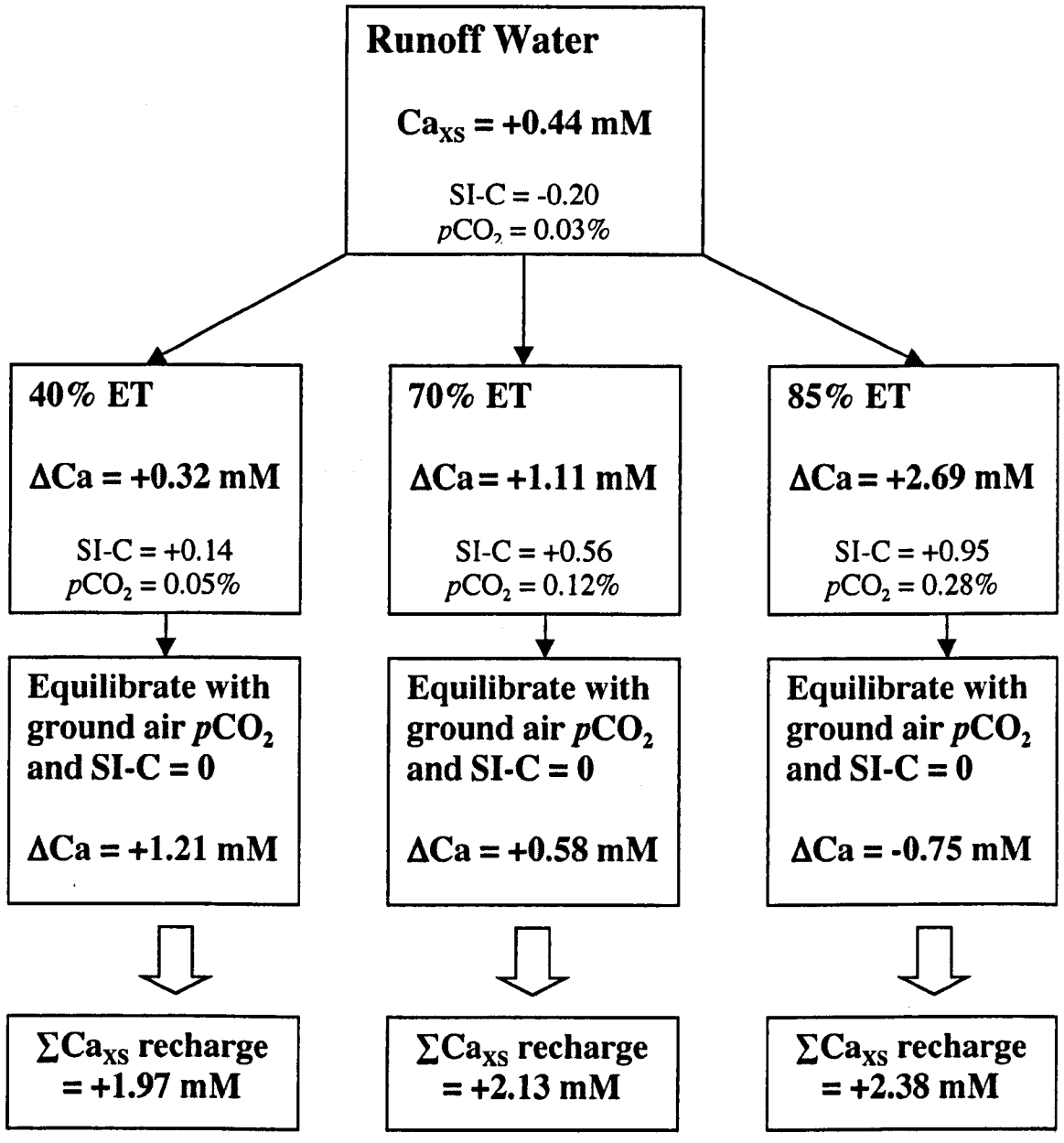

Figure 3.10 Summary of PHREEQC modelling results, showing the path of an average runoff water through the vadose zone. Three potential paths are modelled, with 40, 70 and 85% evapotranspiration, respectively. The waters then undergo equilibration with respect to ground air pCO_2 (1.18%) and calcite. The total Ca_{XS} of waters thought to be recharging the lens (ΣCa_{XS} recharge) are shown in the bottom boxes.

Depending on where evapotranspiration occurs (i.e. above or at the water table), this process could result in a cemented zone in the upper part of the lens, a groundwater caliche at the water table, vadose cementation and/or a case-hardened micritised surface crust (Whitaker, 1992).

3.4.4.4 Diagenesis in the Freshwater Lens

Rainwater and runoff can reach the lens directly *via* cenotes. There are at least 490 cenotes within the study area (QRSS, 2004). Assuming an average diameter of 10 m per cenote, the total surface area covered by cenote openings is 0.15 km^2, equivalent to 0.03% of the total study area. Thus, the effect of unaltered rainfall and rapid runoff on fresh groundwater chemistry *via* this route to the lens is considered to be insignificant.

The majority of waters recharging the freshwater lens have Ca_{XS} values of +1.97, +2.13 or +2.38 mM if evapotranspiration is 40, 70 or 85%, respectively. In comparison, the mean Ca_{XS} of all fresh lens waters is +2.19 ± 0.55 mM (n = 77). This suggests dissolution of 0.06 to 0.22 mM calcium must occur in the freshwater lens to obtain the observed lens Ca_{XS} values if evapotranspiration is 40-70%. Alternatively, precipitation of 0.19 mM Ca^{2+} must occur in the lens if recharge waters have undergone 85% evapotranspiration.

The carbonate geochemistry of the freshwater lens samples is summarised in Table 3.9. From the assumption that pCO_2 is the main control on the geochemical evolution of these waters, two main types of waters can be identified:

- low (0.26 – 2.34%) pCO_2
- high (2.57 – 8.32%) pCO_2

Low pCO_2 samples were obtained from depths between 0.2 and 3.0 m from the surface of the lens, although low pCO_2 waters were present up to 20 m water depth in some cenote sites. Low pCO_2 at these depths is probably attributable to lower production rates, combined with a large surface area and possibly more efficient mixing of lens waters due to wind (Whitaker, 1992). The low pCO_2 waters are also supersaturated with respect to both aragonite and calcite (Table 3.9) and Ca_{XS} ranges from +2.16 ± 0.51 mM (n = 12) for

low pCO_2 wells to +1.94 ± 0.56 mM (n = 12) for low pCO_2 cenote and cave waters. This implies that these waters have evolved under elevated pCO_2 conditions but have since degassed. Despite this degassing, pCO_2 remains significantly higher than atmospheric and are higher than ground air, although the values are significantly less than soil air.

Table 3.9 Carbonate geochemistry of samples from the freshwater phreatic zone (±1σ).

Water Type	pCO_2 (%)	SI-C (A)	Ca_{xs} (mM)	Mg_{xs} (mM)	Sr_{xs} (mM)	SO_{4xs} (mM)
Non-degassed Cenotes/Caves (n = 43)	4.74 ± 1.28	-0.08 (-0.23) ± 0.14	+2.21 ± 0.51	+0.72 ± 0.12	+0.011 ± 0.003	+0.07 ±0.04
Non-degassed Wells (n = 11)	4.43 ± 1.54	+0.11 (-0.04) ± 0.27	+2.46 ± 0.73	+0.84 ± 0.37	+0.023 (n = 1)	+0.05 ± 0.32
Degassed Cenotes/Caves (n = 12)	1.52 ± 0.59	-0.32 (-0.46) ± 0.16	+1.94 ±0.56	+0.65 ± 0.27	n.d.	+0.04 ± 0.05
Degassed Wells (n = 12)	1.75 ± 0.36	+0.28 (+0.14) ±0.35	+2.16 ± 0.51	+0.77 ± 0.83	n.d.	+0.20 ± 0.45
Analytical Uncertainty (±1σ)	± 0.02	± 0.01	± 0.04	± 0.15	± 0.027	± 0.06

The mean pCO_2 of non-degassed cenote and cave waters is 4.74 ± 1.28% (n = 43), while the mean pCO_2 of non-degassed wells is 4.43 ± 1.54% (n = 11). The majority of non-degassed lens waters are enriched in pCO_2 relative to soil air (Figure 3.11), indicating an *in situ* production of CO_2, likely from the bacterial oxidation of organic matter. The means of non-degassed cenotes and caves approach equilibrium with respect to calcite, while non-degassed wells appear to approach equilibrium with respect to both aragonite and calcite. It is somewhat surprising that degassed cenote and cave waters maintain undersaturation, despite degassing.

Examining Figure 3.11, a plot of pCO_2 against SI-C(A), shows that the degassed sample data points display a larger degree of scatter than do the data points of the non-degassed samples. 60% of the main outliers (in ovals) show evidence of sulfate reduction (i.e. measurable (>0.01 μM) sulfide and/or negative SO_{4XS} values). The effects of sulfur redox reactions on carbonate geochemistry are discussed further in the Geomicrobiology section of this chapter.

The Ca_{XS} of non-degassed waters is, on average, 0.29 mM higher than degassed waters. This difference may indicate that precipitation (of ~29 mg/l $CaCO_3$) has occurred in the upper part of the lens following degassing. Alternatively, continued dissolution may occur in the lower part of the lens, increasing Ca_{XS} concentrations.

Examining a plot of Ca_{XS} against pCO_2 (Figure 3.12) indicates that there is no clear relationship between the two variables for the majority of the samples. The only significant ($P < 0.05$) positive relationship involves samples that show evidence of sulfate reduction (i.e. measurable sulfide and/or negative SO_{4XS} values). The presence of sulfide indicates that bacterial sulfate reduction is occurring. Subsequent oxidation of these reduced sulfur species will produce acidity (see Section 3.5), driving the potential for enhanced calcium carbonate dissolution, which would subsequently result in increased Ca_{XS} values. Most other (non-sulfidic) samples have a higher pCO_2 than expected for a given Ca_{XS} (or a lower Ca_{XS} for a given pCO_2). This may be explained by calcite precipitation. Calcite precipitation does occur at some sites, as evidenced by mounds of 'calcite rafts'. However, these only occur in sites where the freshwater lens is not directly mixing with an underlying saline zone (Smart et al., 2002) and no systematic geochemical differences are found between sites with and sites without an associated saline zone.

Distance from the coast may also play a role in controlling the carbonate geochemistry of lens waters. Table 3.10 shows that non-degassed coastal sites (i.e. sites located within 200 m of the Caribbean coastline) have higher Ca_{XS} ($P<0.01$) and, in particular, Mg_{XS} ($P<0.001$) concentrations compared to inland sites (i.e. sites located >200 m from the coast). This may reflect the different rock types that the waters are interacting with, and/or that mixing between the freshwater lens and saline water is more active near the coast.

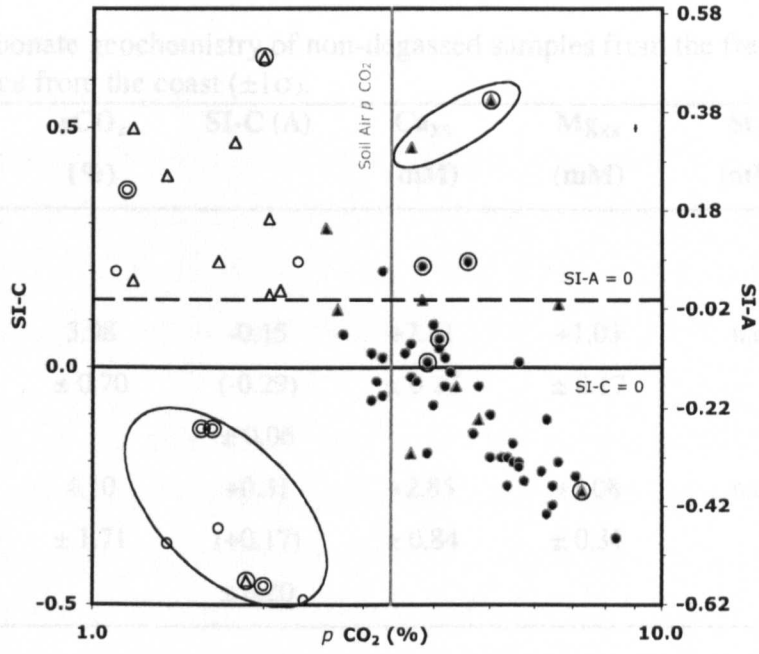

Figure 3.11 Relationship between pCO_2 and aragonite and calcite saturation in freshwater lens samples from degassed wells (open triangles), degassed caves/cenotes (open circles), non-degassed wells (closed triangles) and non-degassed caves/cenotes (closed circles). Samples within ovals are considered 'outliers' from the main trend. Circled sample points had measurable sulfide (>0.01 μM/L) and/or negative SO_{4XS} values, indicating sulfate reduction. Cross shows representative analytical uncertainties (±1σ).

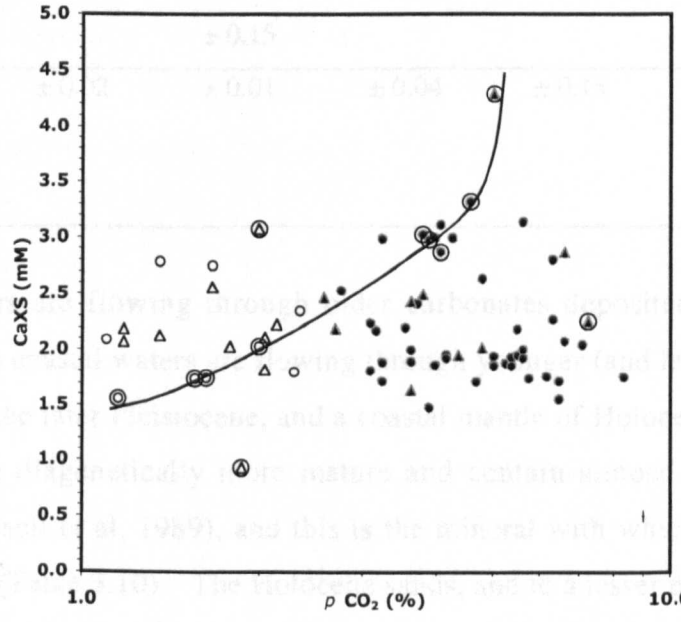

Figure 3.12 Relationship between pCO_2 and Ca_{XS} in freshwater lens samples from degassed wells (open triangles), degassed caves/cenotes (open circles), non-degassed wells (closed triangles) and non-degassed caves/cenotes (closed circles). Circled sample points had measurable sulfide (>0.01 μM/L) and/or negative SO_{4XS} values, indicating sulfate reduction. Solid black line shows main trend through these samples (statistics discussed in text). Cross shows representative analytical uncertainties (±1σ).

Table 3.10 Carbonate geochemistry of non-degassed samples from the freshwater phreatic zone with distance from the coast (±1σ).

Water Type	pCO_2 (%)	SI-C (A)	Ca_{xs} (mM)	Mg_{xs} (mM)	Sr_{xs} (mM)	SO_{4xs} (mM)
Coastal Sites						
(0-200 m)						
Cave Outflows	3.98	-0.15	+2.51	+1.03	n.d.	+0.12
(n = 5)	± 0.70	(-0.29)	± 0.27	± 0.17		± 0.18
		± 0.06				
Wells	4.10	+0.31	+2.85	+1.08	n.d.	+0.00
(n = 5)	± 1.71	(+0.17)	± 0.84	± 0.31		± 0.47
		± 0.20				
Inland Sites						
(>200 m)						
Cenotes/Caves	4.74	-0.08	+2.21	+0.72	+0.011	+0.07
(n = 43)	± 1.28	(-0.23)	± 0.51	± 0.12	± 0.003	± 0.04
		± 0.14				
Wells	4.77	-0.09	+2.07	+0.61	+0.023	+0.09
(n = 11)	± 1.46	(-0.24)	± 0.32	± 0.27	(n = 1)	± 0.04
		± 0.15				
Analytical Uncertainty (±1σ)	± 0.02	± 0.01	± 0.04	± 0.15	± 0.027	± 0.06

Inland lens waters are flowing through older carbonates deposited largely before the Pleistocene, while coastal waters are flowing through younger (and less stable) carbonates deposited during the later Pleistocene, and a coastal mantle of Holocene sands. The older rocks, inland, are diagenetically more mature and contain almost exclusively low-Mg calcite (e.g. Stoessell et al, 1989), and this is the mineral with which inland lens waters have equilibrated (Table 3.10). The Holocene sands, and to a lesser extent the Pleistocene deposits, contain a significant fraction of the less stable carbonate minerals high-Mg calcite (HMC) and aragonite (Ford, 1985; Goodwin, 2002). Thus, the increases in Ca_{xs} and Mg_{xs} that occurs near the coast may reflect the dissolution of these carbonate species.

Although both Ca_{xs} and Mg_{xs} concentrations are higher in coastal sites compared to inland sites, the ratios of these ions imply the major processes occurring in each location are the same: HMC dissolution followed or accompanied by the precipitation of LMC (Figure

3.13). Two inland cave sites fall between the HMC and calcite lines, indicating the dissolution of both carbonate species, while one inland well site indicates the dissolution of calcite (although these three data points are within analytical uncertainty of one another). Examining a plot of Ca_{xs} against Sr_{xs} (Figure 3.14) does not lend any further insight into whether it is calcite or aragonite that is predominantly dissolving (all samples but one fall between the aragonite and calcite dissolution lines).

It is worth nothing that coastal outflows (cave sites) are undersaturated with respect to both calcite and aragonite and this may reflect enhanced dissolution due to mixing between out-flowing fresh lens water and inflowing seawater. Sulfate is also in excess in coastal outflows, suggesting that the re-oxidation of reduced sulfur species may also play a role in acidity generation and undersaturation at these sites (this is discussed further in the Geomicrobiology section of this chapter).

There are four main water-controlled processes that may be important in generating dissolution or precipitation in the freshwater lens (Whitaker, 1992):

- Evapotranspiration (considered above)
- Mixing
- Equilibration with ground air CO_2
- Oxidation of organic matter

Mixing

The mixing of two waters with different salinities, saturation state, pCO_2, temperature and ionic strength can generate the potential for dissolution or precipitation due to the non-linearity of mineral solubility (Runnels, 1969). In this section, mixing is simulated using PHREEQC between:

- Vadose percolation and lens-top waters
- Different lens waters (i.e. top of lens and base of lens)

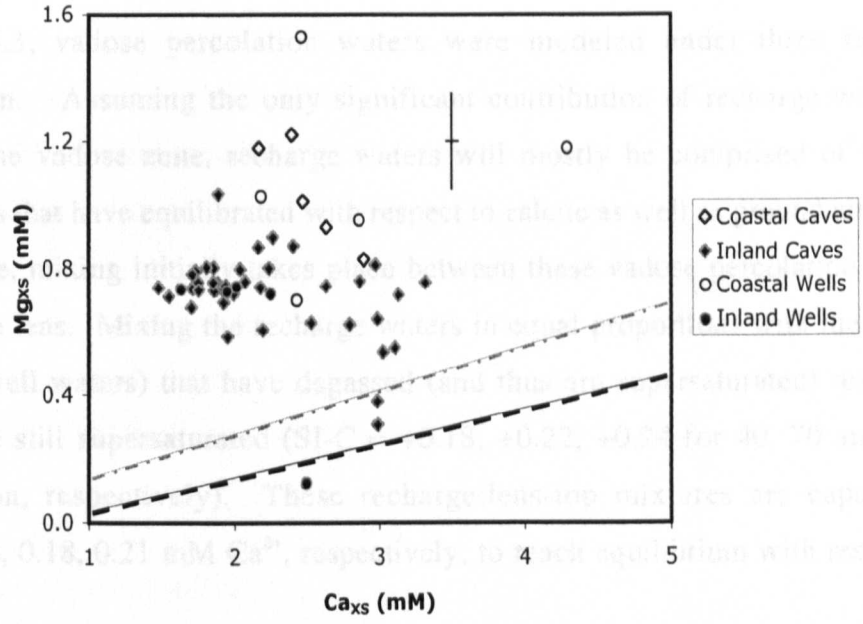

Figure 3.13 Relationship between Ca_{XS} and Mg_{XS} for non-degassed lens waters. Dashed grey line is HMC dissolution line. Dashed black line is calcite dissolution line. Cross shows representative analytical uncertainties (±1σ).

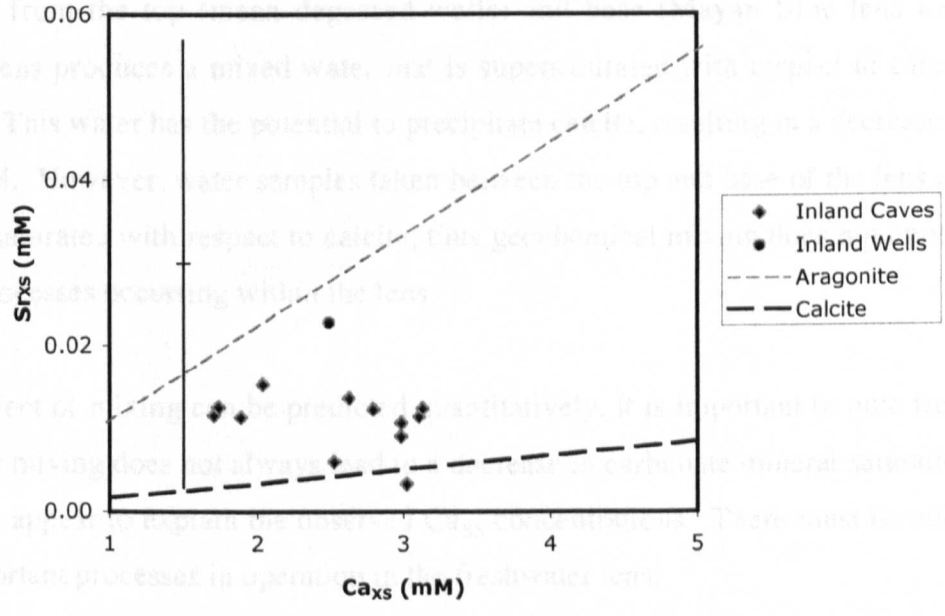

Figure 3.14 Relationship between Ca_{XS} and Sr_{XS} for non-degassed lens waters. Dashed grey line is aragonite dissolution line. Dashed black line is calcite dissolution line. Cross shows representative analytical uncertainties (±1σ).

In Section 3.4.4.3, vadose percolation waters were modeled under three rates of evapotranspiration. Assuming the only significant contribution of recharge waters is routed through the vadose zone, recharge waters will mostly be comprised of diffuse percolation waters that have equilibrated with respect to calcite as well as ground air pCO_2. At the water table, mixing initially takes place between these vadose percolation waters and the top of the lens. Mixing the recharge waters in equal proportions with mean lens top waters (i.e. well waters) that have degassed (and thus are supersaturated) results in solutions that are still supersaturated (SI-C = +0.18, +0.22, +0.24 for 40, 70 and 85% evapotranspiration, respectively). These recharge:lens-top mixtures are capable of precipitating 0.14, 0.18, 0.21 mM Ca^{2+}, respectively, to reach equilibrium with respect to calcite.

In addition, mixing occurs between the degassed lens-top waters and waters at the base of the freshwater lens. Compared to lens-top waters, the waters at the base of the lens have higher pCO_2s and they are at or near equilibrium with respect to calcite. A 50:50 mix between waters from the top (mean degassed wells) and base (Mayan Blue lens base sample) of the lens produces a mixed water that is supersaturated with respect to calcite (SI-C = +0.11). This water has the potential to precipitate calcite, resulting in a decrease in Ca_{XS} of 0.13 mM. However, water samples taken between the top and base of the lens are generally undersaturated with respect to calcite, thus geochemical mixing does not appear to explain the processes occurring within the lens.

Although the effect of mixing can be predicted quantitatively, it is important to note from these results that mixing does not always lead to a decrease in carbonate mineral saturation state, nor does it appear to explain the observed Ca_{XS} concentrations. There must be other much more important processes in operation in the freshwater lens.

Equilibration with Ground Air pCO_2

As shown in the previous sections, lens-top waters are degassed relative to deeper lens waters and thus degassing to reach equilibrium with respect to ground air pCO_2 may be an important control on lens top CO_2 concentrations. Driving the mean of non-degassed cave

and cenote lens waters (SI-C = -0.08, pCO_2 = 4.57%) to equilibrium with ground air pCO_2 (1.18%) results in supersaturation with respect to calcite (SI-C = +0.50) and aragonite (SI-A = +0.35). This water is then capable of precipitating 0.45 mM Ca^{2+} to reach equilibrium with respect to SI-C.

The occurrence of this process is supported by Ford (1985), who reports minor precipitation of sparry calcite and aragonite cements at the present-day Yucatan water table, apparently formed by CO_2 degassing.

In situ oxidation of organic matter

The high pCO_2 of lens waters (3.68 ± 1.89%, n = 77), and in particular cave waters (4.83 ± 1.27%, n = 20), suggests the *in situ* production of CO_2 by root respiration and/or bacterial decomposition of organic matter is an important process in this environment. Occasionally, roots can penetrate the water table (e.g. Heaven's Gate; Kankrixche; Chac Mool), but based on field observations, this is thought to be quite rare and root respiration is unlikely to effect more than a small proportion of the total lens volume. However, the breakdown of organic matter by bacteria *in situ* is probably of greater significance in controlling lens pCO_2. The role bacteria play in carbonate diagenesis within the freshwater system is discussed in the next section.

3.5 Geomicrobiology of the Freshwater System

Acridine Orange Direct Counts (AODC), and Most Probable Number (MPN) analyses were performed on the samples taken from microbiological analyses. In addition, analyses of nitrogen species, phosphorus, sulfur chemistry, and dissolved organic carbon are considered in attempts to elucidate the activity and impact of bacteria within fresh waters. Conductivity readings were taken from each sample (after microbial work was complete) to confirm its location within the water column.

3.5.1 Microbiological Analyses

Total Counts

15 samples from the freshwater system were counted by Acridine Orange Direct Counts (AODC, Chapter 2). Of these, one was from a vadose drip sample (Aktun Chen), seven were from the freshwater lens environment, including one pumped well (Rancho Tranquillo), three cenotes (The Pit, Mayan Blue and Cristal), one cavern site (Chac Mool) and two caves (Mayan Blue and Cristal). In addition, one sample was taken from a bacterial mat located on the cave (Cristal) wall within the freshwater lens. Cell count results are summarised in Table 3.11. The greatest numbers of cells occurred in the cavern sample, followed by the pumped well and bacterial mat samples. Caves and vadose drip samples had the lowest cell counts.

When counting the total numbers of bacteria, the numbers of bacteria in the process of cell division were noted. The fraction of the total number of cells that were dividing indicates where the bacteria have the fastest growth rates, and by inference, activity. The data, summarised in Table 3.11, shows that freshwater samples can be split into two groups; those with a high (>2.5%) proportion of dividing cells and those with a low (<1%) proportion of dividing cells. Sample types with a low proportion of dividing cells include vadose drip water and cave lens samples, which also had the lowest cell counts. Sample types with a high proportion of dividing cells include pumped wells, caverns, cenotes and bacterial mats.

Viable Counts

Populations of bacteria within specific functional groups were measured using MPN (Most Probable Number) techniques (described in Chapter 2):

- Aerobic Heterotrophs (HOX)
- Anaerobic Heterotrophs (HAN)
- Thiosulfate-oxidising bacteria (SOX)
- Sulfate-reducing bacteria (SRB)
- Iron-oxidising bacteria (Fe-OX)
- Iron-reducing bacteria (Fe-R)

Table 3.11 Mean freshwater microbiology (AODC and MPN) results (±1σ).

Water Type	AODC‡	% Dividing Cells	HOX‡	HAN‡	MPN – SOX ‡ (Acid)	MPN – SOX‡ (Base)	MPN - SRB ‡	MPN – Fe-R‡
Drips	170	0.85	>23	>23 ± 0	n.d.	n.d.	0.01	>23
Mean Freshwater Lens†	1170 ± 1210 (n = 7)	3.09 ± 2.36 (n = 7)	>23 ± 0 (n = 5)	>23 ± 0 (n = 5)	7.68 ± 1.33 (n = 3)	64.0 ± 111 (n = 3)	83 ± 150 (n = 6)	18.4 ± 10.3 (n = 5)
Pumped Wells (n = 1)	1940	6.81	>23	>23	n.d.	n.d.	>23	>23
Cenotes	820 ± 930 (n = 3)	3.75 ± 1.31 (n = 3)	>23 (n = 1)	>23 (n = 1)	11.5 ± 16.3 (n = 2)	96.0 ± 136 (n = 2)	204 ± 255 (n = 2)	>23 (n = 1)
Caverns (n = 1)	3263	2.79	>23	>23	n.d.	n.d.	0.02	0.02
Caves*	270 ± 330 (n = 2)	0.40 ± 0.58 (n = 2)	>23 ± 0 (n = 2)	>23 ± 0 (n = 2)	0.03 (n = 1)	0.16 (n = 1)	33.0 ± 46.7 (n = 2)	>23 ± 0 (n = 2)
Bacterial mat (n = 1)	1210	3.46	>23	>23	n.d.	n.d.	0.23	>23

‡numbers represent number of cells/ml and have been multiplied by 10^{-2} †excluding coastal discharge samples

* = caves from main field area (east coast)

Heterotrophs

All waters from the freshwater environment (and all MPN dilutions) tested positive for the presence of both aerobic (HOX) and anaerobic (HAN) heterotrophs, indicating that their minimum concentration is 2300 cells/ml. Table 3.12 summarises the minimum proportion of the total count that these numbers represent.

Thiosulfate-oxidising Bacteria

MPN analyses of thiosulfate oxidising bacteria (SOX), indicated that thiosulfate oxidation proceeded by one of two reactions: i) complete oxidation from thiosulfate to sulfate with acidity produced (Equation 3.4), and ii) incomplete oxidation of thiosulfate to an intermediary species of oxidised sulfur (e.g. polythionates, such as tetrathionate), rather than sulfate (Equation 3.5), with an increase in pH.

$$S_2O_3^{2-} + 2O_2 + H_2O \leftrightarrow 2SO_4^{2-} + 2H^+ \quad (3.4)$$

$$S_2O_3^{2-} + \tfrac{1}{2}O_2 + H^+ \leftrightarrow \tfrac{1}{2}S_4O_6^{2-} + OH^- \quad (3.5)$$

Aerobic acid-producing thiosulfate-oxidising bacteria (capable of complete oxidation to sulfate) were present in all samples where attempts were made to enumerate them. Numbers range from 3 cells/ml in the cave lens water to 1.15 ± 1.63 x 10^3 cells/ml in cenote lens waters (n = 2). These numbers represent 0.01 and 2.07 ± 2.92% of the total number of cells counted by AODC, respectively. The final pH of the freshwater SOX media was 3.25 ± 0.33 (n = 2), compared to a starting pH of 7.3.

Aerobic base-producing incomplete thiosulfate-oxidisers were, in general, one order of magnitude more abundant than the complete oxidisers in all samples. Numbers of base-producing SOX range from 16 cells/ml in the cave water to 9.6 ± 13.6 x 10^3 cells/ml in cenote waters (n = 2). These numbers represent 0.03 and 5.20 ± 7.35% of the total number of cells counted by AODC, respectively.

Table 3.12 Mean proportion of the total count of bacteria cells comprised by different functional groups for the freshwater system, based on MPN analysis (±1σ).

Water Type	HOX	HAN	SOX (Acid)	SOX (Base)	SRB	Fe-R
Drips	>13	>13	n.d.	n.d.	0.01	>13
Mean Freshwater Lens[†]	>25 ± 32	>25 ± 32	1.4 ± 2.4	3.5 ± 6.0	17 ± 22	25 ± 32
Pumped Wells (n = 1)	>1.2	>1.2	n.d.	n.d.	>1.2	>1.2
Cenotes	>48	>48	2.1 ± 2.9	5.2 ± 7.4	34 ± 19	>48
Caverns (n = 1)	>0.71	>0.71	n.d.	n.d.	0.001	0.001
Caves[*]	>37 ± 46	>37 ± 46	0.01	0.03	6.6 ± 9.2	>37 ± 46
Bacterial mat (n = 1)	>1.9	>1.9	n.d.	n.d.	0.02	>1.9

[†]excluding coastal discharge samples

[*] = caves from main field area (east coast)

Sulfate-Reducing Bacteria

Sulfate-reducing bacteria (SRB) are present in numbers that range from 1 cell/ml in the drip sample to >2300 cells/ml in the pumped well sample (Table 3.11). Lens waters have a mean SRB number of 8.3 ± 15 x10^3 cells/ml (n = 6), while the bacteria mat sample had only 23 cells/ml.

Iron-Oxidising Bacteria (Fe-OX)

The media used to obtain an Fe-OX MPN series required a pH of 2-3 to ensure that chemical oxidation of Fe^{2+} did not occur. The bacteria within the freshwaters were probably not acidophilic and thus were unlikely to survive at such low pH values. Although direct counts were made from the Fe-OX MPN series, no bacteria were found. Thus, no results were obtained from the enrichment of Fe-OX media.

Iron-Reducing Bacteria (Fe-R)

MPN analyses of iron reducing bacteria (Fe-R) illustrated that iron reduction was possible by bacteria residing in all fresh waters tested for their growth. The greatest numbers of Fe-R occurred in the drip water, pumped wells, cenotes, caves and bacterial mat samples, with numbers exceeding 2300 cells/ml (the cavern sample was the only sample that did not demonstrate positive growth of Fe-R at all dilutions of the media).

3.5.1 Oxygen Consumption

Oxygen consumption was not measured systematically in waters from the freshwater environment. However, the results from one cave lens sample (measured during the mixing zone oxygen consumption experiment detailed in Chapter 4) indicate rates in the freshwater lens are in the order of 38 μM/L/day. This is equivalent to ~14 mM O_2/year per litre of lens water.

3.5.2 Chemical evidence for Microbial Activity

Analyses of nitrogen species, phosphorus, sulfide, dissolved organic carbon (DOC) are considered in attempts to elucidate the activity and impact of bacteria within the freshwater system. The results of these analyses are presented in Table 3.13. None of these parameters showed significant relationships with either distance inland from the east coast or chloride concentration. This indicates that these parameters reflect local conditions rather than cumulative concentrations along a flow path or due to mixing. These parameters (and their relationships) are considered in more detail in the following discussion.

3.5.3 Geomicrobiology Discussion

As discussed in Section 3.4.4.4, the oxidation of organic matter may play an important role in the generation of pCO_2 and Ca_{XS} in lens waters. Regions of increased pCO_2 may represent areas where the chemistry is dominated by heterotrophic bacteria, which consume organic matter and produce CO_2 (Equation 3.3, to follow).

AODC and % Dividing Cells

AODC analyses demonstrate significant populations (1.70×10^4 to 3.26×10^5 cells/ml) of bacteria throughout the freshwater system. The maximum proportion of dividing cells (inferring bacterial reproduction rates and relative activities) was ~4% of the total population.

Evidence for Heterotrophic Activity

Heterotrophs are organisms that gain energy from the oxidation or fermentation of organic compounds (Madigan et al., 2000). A simplified heterotrophic metabolism is illustrated in Equation 3.6, where one mole of carbon dioxide is produced for every mole of oxygen consumed. The carbon dioxide then combines with water to form carbonic acid (Equation 3.7), which drives carbonate dissolution.

Table 3.13 Mean freshwater results for chemical indicators of biological activity (±1σ).

Water Type	NO_3^- (μM)	NH_4^+ (μM)	PO_4^{3-} (μM)	DOC (mM)	HS^- (μM)
Rainwater	35 ± 57 (n = 6)	10.0	n.d.	1.87 ± 1.64 (n = 3)	n.d.
Throughfall	1 (n = 1)	n.d.	n.d.	n.d.	n.d.
Runoff	13 ± 9 (n = 4)	n.d.	n.d.	6.68 ± 4.35 (n = 2)	n.d.
Surface Pools	112 ± 44 (n = 7)	10.9 ± 6.4 (n = 7)	0.50 ± 0.46 (n = 4)	1.06 ± 0.25 (n = 2)	0.0 ± 0.01 (n = 8)
Drips	780 ± 895 (n = 9)	8.7 ± 5.7 (n = 5)	0.95 (n = 1)	0.84 ± 0.44 (n = 8)	n.d.
Mean Freshwater Lens[†]	146 ± 107 (n = 71)	17.3 ± 3.6 (n = 60)	2.01 ± 1.94 (n = 23)	0.81 ± 0.99 (n = 56)	0.04 ± 0.23 (n = 57)
Static Wells	171 ± 135 (n = 13)	12.8 ± 11.1 (n = 9)	2.40 ± 1.44 (n = 4)	0.53 ± 0.24 (n = 10)	0.02 ± 0.06 (n = 7)
Pumped Wells	262 ± 215 (n = 9)	42.3 ± 57.0 (n = 5)	4.56 ± 4.37 (n = 3)	1.89 ± 2.33 (n = 6)	0.34 ± 0.76 (n = 5)
Cenotes	110 ± 37 (n = 29)	21.0 ± 46.8 (n = 27)	1.59 ± 1.29 (n = 7)	0.71 ± 0.72 (n = 26)	0.00 ± 0.01 (n = 26)
Caverns	115 ± 9 (n = 3)	5.6 ± 4.8 (n = 3)	1.47 (n = 1)	1.56 ± 1.65 (n = 2)	0.00 ± 0.00 (n = 2)
Caves[*]	134 ± 14 (n = 17)	8.0 ± 6.2 (n = 16)	1.29 ± 0.60 (n = 8)	0.58 ± 0.32 (n = 12)	0.01 ± 0.03 (n = 17)
Caves[§]	n.d.	n.d.	n.d.	0.28 ± 0.04 (n = 2)	n.d.
Coastal Q	80 ±29 (n = 9)	12.2 ± 13.6 (n = 7)	n.d.	0.58 ± 0.43 (n = 11)	0.00 ± 0.01 (n = 7)
Analytical Uncertainty	± 9 to 18	± 2.2	± 0.20	± 0.02	± 0.05

[*] = caves from main field area (east coast) [§] = caves from Merida area (Yucatan)
[†]excluding coastal discharge samples n.d. = no data

$$CH_2O + O_2 \leftrightarrow CO_2 + H_2O \quad (3.6)$$

$$CO_2 + H_2O \leftrightarrow H_2CO_3 \quad (3.7)$$

All freshwater samples (and all MPN dilutions) tested positive for the presence of both aerobic (HOX) and anaerobic (HAN) heterotrophic bacteria, indicating that their minimum concentration within all solutions is 2300 cells/ml. It is important to note that although only minimum cell numbers could be reported for heterotrophs, these numbers represent a minimum of 1 to 48% of the total bacterial population counted by AODC, suggesting their importance in the freshwater environment. These percentages are substantial and unexpected, given that, usually, less than 1% of the total prokaryotic population in natural habitats can be cultivated (Amann et al., 1995). These large percentages of viable populations demonstrate the potential for significant activity.

Oxygen is present in all freshwaters (Table 3.1), and because oxygen is the preferred electron acceptor for many bacteria (Madigan et al., 2000), it can be assumed that the rate at which oxygen is consumed will give a good overall estimate of bacterial activity (e.g. Jorgensen, 1989). The oxygen consumption rate measured from a freshwater lens sample was 38 μM/day per litre of water.

As stated above, oxygen consumption by heterotrophic bacteria leads to the production of carbonic acid (Equations 3.6 – 3.7). Ideally, each mole of carbonic acid is capable of dissolving one mole of calcium carbonate (Equation 3.8). From this assumption, the oxygen consumption rate measured from a freshwater lens sample indicates maximum CO_2 generation of ~14 mM/L/year and maximum calcium carbonate dissolution at a rate of 1.39 g $CaCO_3$/yr per litre of water. Thus, despite their relatively low numbers and proportion of dividing cells, bacteria in cave lens waters could be responsible for significant carbonate dissolution.

$$H_2CO_3 + CaCO_3 \rightarrow Ca^{2+} + 2HCO_3^- \quad (3.8)$$

The importance of heterotrophic bacteria in driving carbonate diagenesis is further supported by relationships between 'indicators of bacterial activity' and carbonate geochemistry (some of which overlap). Most 'bacterial indicators' (including pCO_2,

dissolved oxygen, pH and nitrate) have a relationship with Sr_{XS} (Figure 3.15). Increases in Sr_{XS} are associated with:

- Decreases in dissolved oxygen (indicating oxygen consumption)
- Increases in nitrate (indicating organic matter breakdown, followed by nitrification)
- Increases in pCO_2 (indicating CO_2 production during heterotrophic activity)
- Decreases in pH (indicating acidity generation from the production of carbonic – and other – acids)

These relationships confirm that the breakdown of organic matter by heterotrophic bacteria, which consumes oxygen, producing CO_2 and acidity, leads to the dissolution of strontium-containing carbonates (aragonite). If the aragonite dissolution is accompanied by precipitation of calcite, this may explain why the relationships between bacterial indicators and strontium are not apparent for calcium.

Drive for Heterotrophy

Where the breakdown of organic matter by heterotrophic bacteria occurs, ammonia and phosphate are expected to increase (Equation 3.9, modified from Bender and Heggie, 1984).

$$(CH_2O)_{106}(NH_3)_{16}(H_3PO_4) + 1060_2 \leftrightarrow 106CO_2 + 16NH_3 + H_3PO_4^{3-} + 106H_2O \qquad (3.9)$$

In the presence of nitrosifying and nitrifiying bacteria in oxygenated waters, the ammonia from Equation 3.9 may be oxidised to nitrate in a 3-step process (Equations 3.10 to 3.13).

Step 1. $NH_3 + O_2 + 2e^- + 2H^+ \rightarrow NH_2OH + H_2O$ (3.10)

Step 2. $NH_2OH + H_2O + \frac{1}{2}O_2 \rightarrow NO_2^- + 2H_2O + H^+$ (3.11)

SUM of Steps 1 and 2: $NH_3 + 1\frac{1}{2}O_2 + 2e^- + H^+ \rightarrow NO_2^- + 2H_2O$ (3.12)

Step 3. $NO_2^- + \frac{1}{2}O_2 \rightarrow NO_3^-$ (3.13)

Nitrate has a strong inverse relationship with dissolved oxygen (Figure 3.16) and most site types (except pumped wells) demonstrate a strong positive association between nitrate and pCO_2 (Figure 3.17).

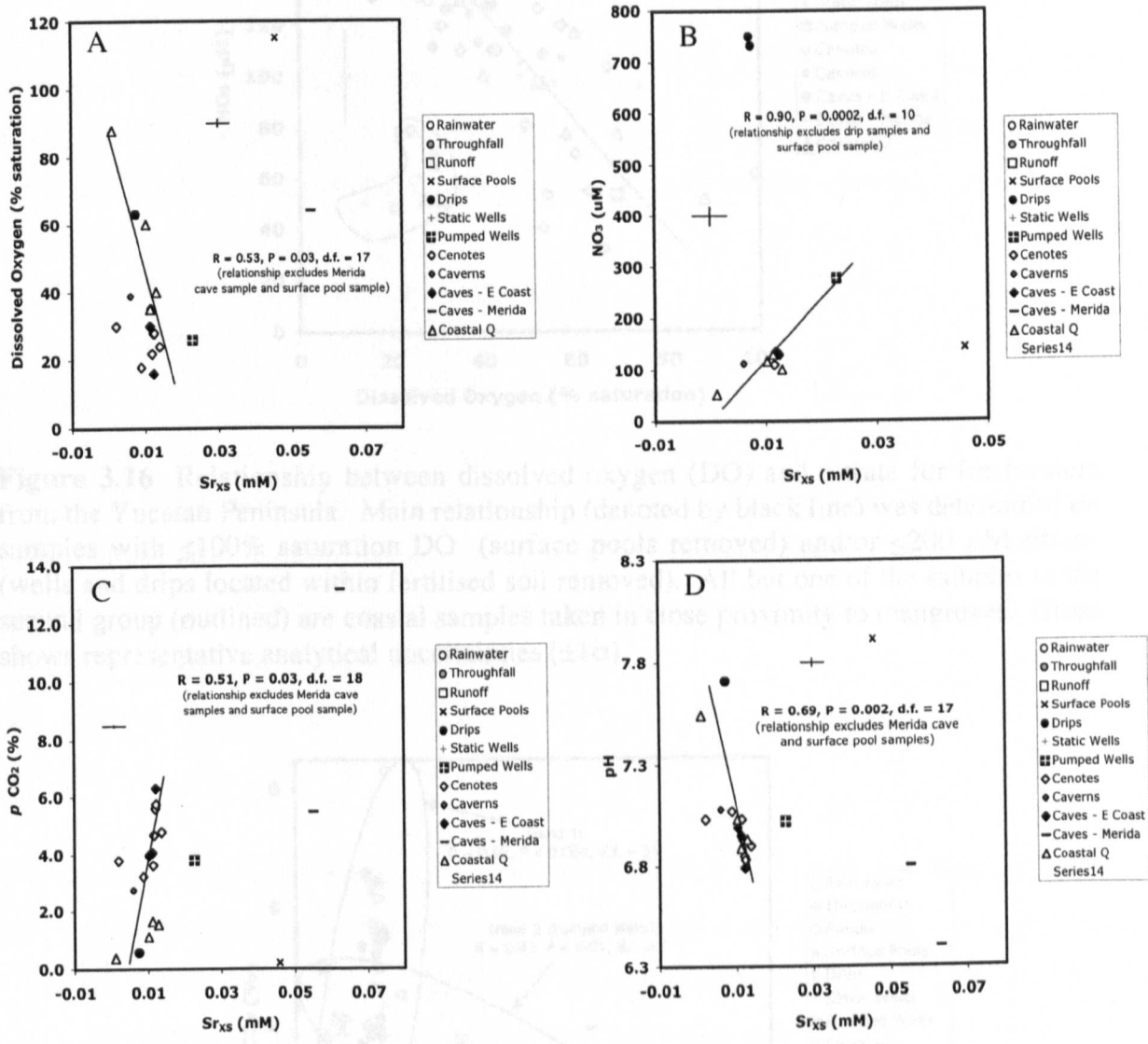

Figure 3.15 Sr_{XS} against various 'indicators' of bacterial activity (discussed in text), including dissolved oxygen (A), nitrate (B), pCO_2 (C), and pH (D). Crosses are representative analytical uncertainties (±1σ).

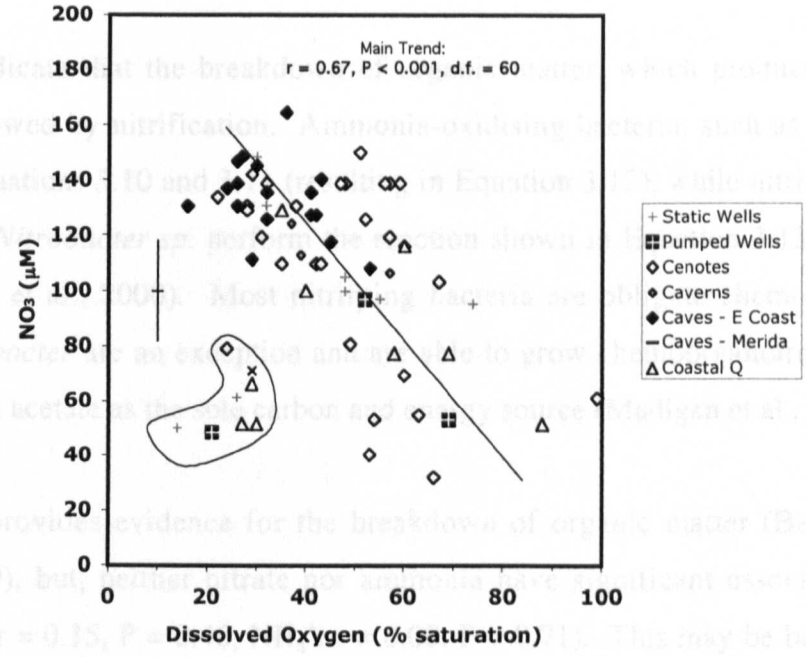

Figure 3.16 Relationship between dissolved oxygen (DO) and nitrate for freshwaters from the Yucatan Peninsula. Main relationship (denoted by black line) was determined on samples with ≤100% saturation DO (surface pools removed) and/or ≤200 μM nitrate (wells and drips located within fertilised soil removed). All but one of the samples in the second group (outlined) are coastal samples taken in close proximity to mangroves. Cross shows representative analytical uncertainties (±1σ).

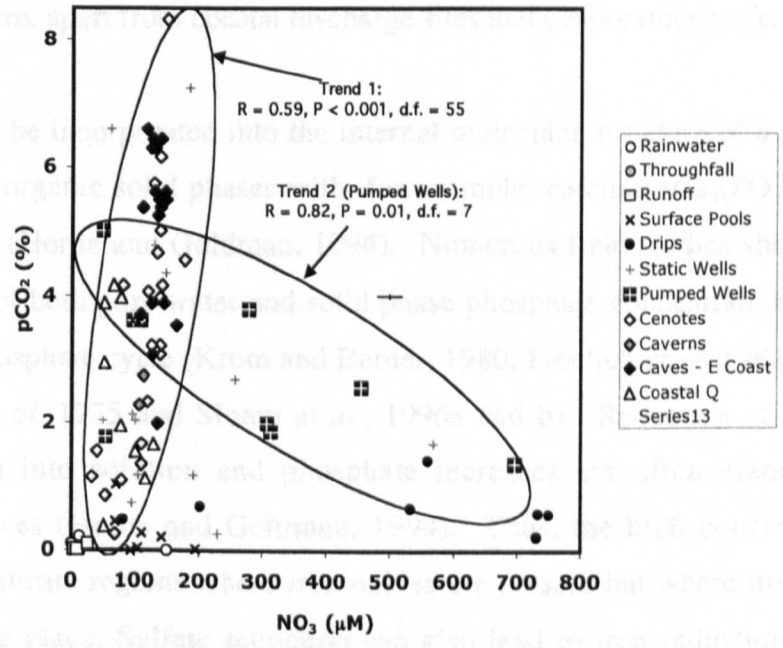

Figure 3.17 Relationship between pCO_2 and nitrate for freshwaters from the Yucatan Peninsula. Main (Trend 1) was determined for all non-degassed lens samples. Trend 2 was determined from pumped well sites only. Cross shows representative analytical uncertainties (±1σ).

These results indicate that the breakdown of organic matter, which produces CO_2 and ammonia is followed by nitrification. Ammonia-oxidising bacteria, such as *Nitrosomas sp.*, carry out Equations 3.10 and 3.11 (resulting in Equation 3.12), while nitrite-oxidising bacteria such as *Nitrobacter sp.* perform the reaction shown in Equation 3.13, producing nitrate (Madigan et al., 2000). Most nitrifying bacteria are obligate chemolithotrophs. Species of *Nitrobacter* are an exception and are able to grow chemoorganotrophically on substrates such as acetate as the sole carbon and energy source (Madigan et al., 2000).

Phosphate also provides evidence for the breakdown of organic matter (Berner, 1974; Rosenfield, 1979), but, neither nitrate nor ammonia have significant associations with phosphate (NO_3^-:r = 0.15, P = 0.46, NH_4^+: r = 0.08, P = 0.71). This may be because most (90-95%) phosphorus is held within sediments and is in a biologically unavailable form (Horne and Goldman, 1994). Soluble reactive phosphorus (SRP) concentrations may indicate locations where the release of phosphorus from particulate matter into a free, biologically available form occurs. Phosphate adsorbed onto the surface layers of particulate matter can be released where direct mixing with saltwater occurs, but salt concentrations thought to be associated with this process are unlikely to be encountered in the freshwater system, apart from coastal discharge sites and evaporating surface pools.

Phosphate can also be incorporated into the internal molecular structure of a particle and phosphate forms inorganic solid phases with, for example, calcium ($Ca_3(PO_4)_2$) and iron ($Fe_3(PO_4)_2$, $FePO_4$) (Horne and Goldman, 1994). Numerous field studies show that iron oxides likely control both pore water and solid phase phosphate concentrations and drive the sedimentary phosphate cycle (Krom and Berner, 1980, Froelich *et al*, 1982, Sundby *et al*, 1992, Jensen *et al*, 1975 and Slomp *et al.*, 1996a and b). Reduction of iron oxides releases phosphate into solution and phosphate increases are often associated with anoxic/oxic interfaces (Horne and Goldman, 1994). Thus, the high concentrations of phosphate might indicate regions where iron oxides are present but where iron reduction reactions are taking place. Sulfate reduction can also lead to iron reduction (Canfield, 1989) and the phosphate data might indicate where sulfate reduction is occurring. Sample means exhibiting the highest phosphate concentrations (pumped and static wells and boreholes) also have the highest sulfide concentrations (Table 3.13).

The Role of Phosphate in Carbonate Diagenesis

Phosphate been shown experimentally to both decrease dissolution (≥ 3 μM PO_4^{3-}; e.g. Morse et al., 1979; Walter and Burton, 1986) and inhibit precipitation (≥ 10 μM PO_4^{3-}; Raistrick, 1949; Simkiss, 1964 a, b; Reddy and Noncollas, 1973; Reddy, 1977, 1978; Berner et al., 1978) of carbonate minerals. Although the maximum phosphate concentration measured from freshwaters is only ~2 μM (Table 3.13), increases in phosphorus have a positive relationship with SI-C (Figure 3.18). This suggests phosphorus is inhibiting dissolution directly, or that phosphorus is associated with a process (such as sulfate reduction, which increases alkalinity, Equation 3.14) that causes SI-C to increase (Figure 3.18).

Sulfur and Iron Cycling

MPN analyses provide further insight into the potential cycling of sulfur and iron within the freshwater system of the Yucatan Peninsula.

Sulfur oxidisers

MPN analyses of thiosulfate-oxidising bacteria (SOX), indicated that thiosulfate oxidation proceeded by one of two reactions: i) complete oxidation from thiosulfate to sulfate with acidity produced (Equation 3.4), and ii) incomplete oxidation of thiosulfate to intermediary species of oxidised sulfur (e.g. polythionates, such as tetrathionate), rather than sulfate, (Equation 3.5), with an increase in pH. These results indicate the presence of two distinct populations.

Aerobic acid-producing thiosulfate-oxidising bacteria (capable of complete oxidation to sulfate) were present in all freshwater samlpes, with maximum numbers occurring in the cenotes (Table 3.11). The final pH of the freshwater SOX media was 3.25 ± 0.33 ($n = 2$), compared to a starting pH of 7.3, indicating that these bacteria can have a massive impact on the pH of their environment. In the field, the increases in acidity will be buffered by the carbonate system itself. Acidic SOX are probably autotrophic and will occur where they can gain greatest energy for autotrophic growth (i.e. at the steepest redox gradients).

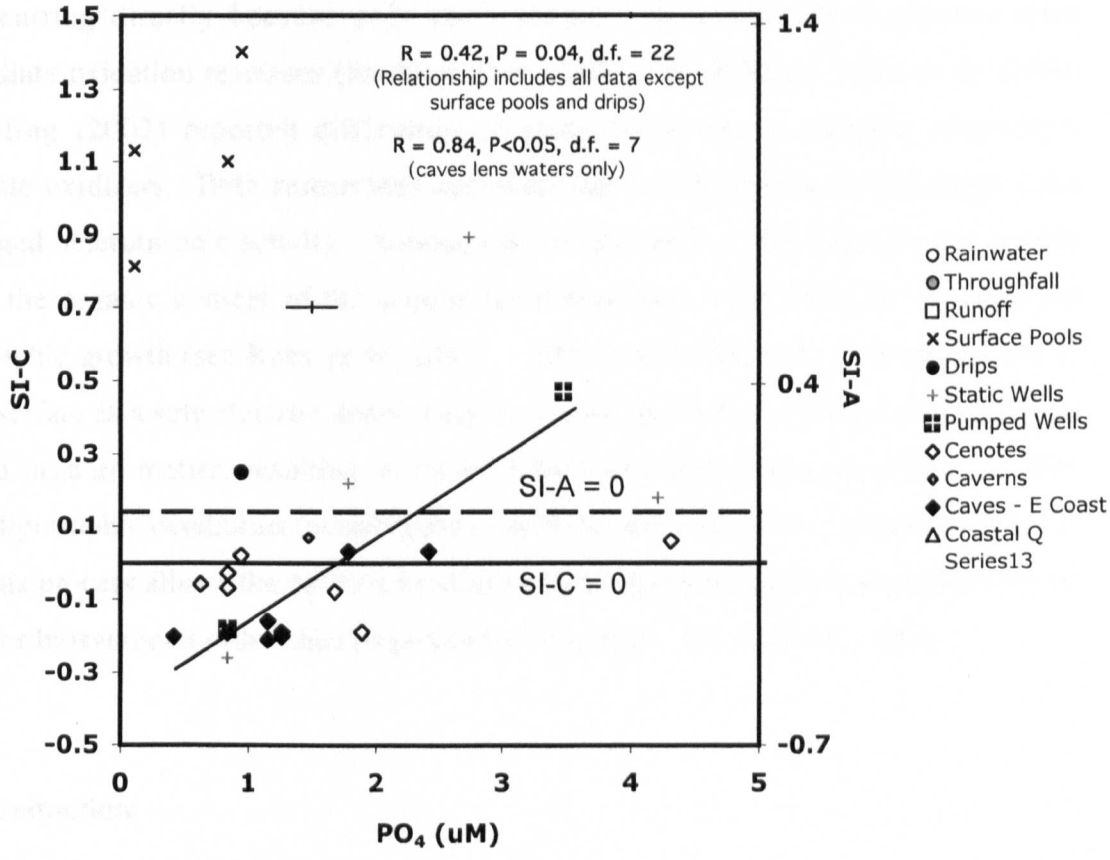

Figure 3.18 Relationship between phosphate and the saturation index of calcite in the freshwater system of the Yucatan Peninsula. Black cross shows representative analytical uncertainties (±1σ).

Aerobic base-producing incomplete thiosulfate-oxidisers were more abundant than the complete oxidisers in all freshwater samples. Maximum numbers of base-producing incomplete thiosulfate-oxidisers also occur in cenotes. Incomplete oxidation of thiosulfate to polythionates was likely the result of a side reaction from heterotrophic activity rather than occurring directly because only small amounts of energy can be grained from intermediate oxidation reactions (Madigan et al., 2000). In addition, Teske et al. (2000) and Telling (2002) reported difficulties in interpreting base-producing incomplete thiosulfate oxidisers. Both researchers added acetate to their media, which might have encouraged heterotrophic activity. Although the media used in this study did not include acetate, the organic content of the sample itself may have been sufficient to stimulate heterotrophic growth (see Ruby *et al.*, 1981). Mixotrophic bacteria, although unable to use thiosulfate as a sole electron donor, may have used thiosulfate as an auxiliary electron donor to organic matter, resulting in mixed lithotrophy and autotrophy (Tuttle, 1980). Under oligotrophic conditions (possibly the conditions within the more diluted MPN series vials), this process allows the bacteria to utilise a larger proportion of the available organic carbon for biosynthesis rather than respiration (Tuttle et al., 1974; Tuttle, 1980).

Sulfate reduction

MPN analyses of SRB demonstrated that all fresh waters sampled contained bacteria capable of sulfate reduction, which, in turn, indicates that anoxia (likely in association with microbial micro-environments) is possible in the freshwater system, despite the presence of oxygen. As mentioned previously, and shown by Equation 3.11, sulfate reduction adds alkalinity to the system and, as a result, SRB might play a role in carbonate precipitation/dissolution reactions.

$$2CH_2O + SO_4^{2-} \leftrightarrow 2HCO_3^- + H_2S \qquad (3.14)$$

A comparison of the distributions of incomplete and complete sulfur oxidisers with sulfate reducers (Table 3.11) demonstrates that SRB were more abundant than SOX in all fresh waters. The greatest numbers of SRB (>2300 cells/ml in pumped wells) are associated with the greatest concentrations of sulfide (Table 3.13), although SO_{4XS} values are within analytical uncertainty (±2σ) of zero.

The alkalinity produced by SRB could stimulate $CaCO_3$ precipitation reactions (and cause a decrease in Ca_{XS}). However, all of the freshwaters contain some level of oxygen (Table 3.1), thus the majority (if not all) sulfide produced will eventually be oxidised. Sulfur oxidation reactions, which may be catalysed by SOX, will contribute to acidity production, enhancing $CaCO_3$ dissolution (and subsequent increases in Ca_{XS}). The interplay of these two reactions may be important in driving the Ca_{XS} concentration at a given site. For example, the acidity produced by sulfur re-oxidation reactions, if spatially separated from the alkalinity produced by sulfate reducing bacteria, may be responsible for the elevated Ca_{XS} values seen at some sulfidic sites within the freshwater lens (Figure 3.12).

Iron (II) oxidation

Despite the inability to culture acidophilic Fe-OX, the activity of neutrophilic iron-oxidising bacteria, which would only reside at oxic/anoxic interfaces (Madigan et al., 2000) may be indicated by orange encrustations ($Fe(OH)_3$?) found on some wall-rock surfaces within the caves (e.g. see Figure 4.21), implying that the pore water within the rock matrix is anoxic. The crusts may indicate the presence of *Gallionella ferruginea*, *Sphaerotilus natans*, and/or *Leptothrix ochracea*, (Madigan et al., 2000) which could produce $Fe(OH)_3$ by Equation 3.15. Iron oxides may provide an energy gain in later reducing reactions.

$$Fe^{2+} + \tfrac{1}{4}O_2 + \tfrac{5}{2}H_2O \leftrightarrow Fe(OH)_3 + 2H^+ \qquad (3.15)$$

Iron oxidising bacteria also produce acidity and thus they may play a role in carbonate dissolution. This may be supported by the fact that the orange staining on the wall-rock occurs only where the wall-rock appears significantly weathered (Figure 4.21).

Iron (III) reduction

MPN analyses of iron-reducing bacteria (Fe-R) demonstrated that all samples taken from fresh waters contained bacteria capable of iron reduction, producing alkalinity (Equation 3.16). The presence of Fe-reducers suggests, again, that anoxic (or sub-oxic) micro-

environments may have been present, despite the presence of oxygen throughout the water column.

$$4Fe(OH)_3 + CH_2O + 7H^+ \leftrightarrow 4Fe^{2+} + HCO_3^- + 10H_2O \quad (3.16)$$

It is within the freshwater lens that black-brown crusts, similar in texture and density to those precipitated by the Fe-R MPNs, were found covering stalactites and part of the cave walls. One of these 'crusts' was sampled for microbiological analysis (i.e. the 'bacterial mat' sample, taken from Cristal) and was found to contain >2300 cells/ml Fe-R, but only 23 cells/ml SRB, suggesting iron reduction is the dominant process. Bottrell *et al.* (1991) and Smart *et al.* (1998) reported similar black-brown encrustations on submerged stalactites found in Stargate Blue Hole and Evelyn Green's Blue Hole, respectively, both located on South Andros in the Bahamas. These crusts were analysed and were found to contain iron sulfide compounds, including pyrite (FeS_2). FeS generally converts to FeS_2 when oxic waters are in contact with sediments that become anoxic with depth (likely the case in this study) or when anoxic water 'overlies' anoxic sediments (Boesen and Postma, 1988) and this conversion might take place in a matter of years (Berner, 1970; Equation 3.17), or days (Rickard and Luther, 1997; Equation 3.18).

$$FeS + S^\circ \leftrightarrow FeS_2 \quad (3.17)$$

$$FeS + H_2S \leftrightarrow FeS_2 + H_2 \quad (3.18)$$

When conducting MPN analyses for various functional groups, it is possible that the same bacteria are capable of two or more metabolisms. For example, bacteria capable of iron reduction may also reduce sulfate, given the right conditions (Coleman et al., 1993). This may be the case for the pumped well sample, where numbers of Fe-R equal numbers of SRB, but for all other samples, Fe-R outnumber SRB. This might indicate that two physiologically distinct microbial communities are present; one with the ability to reduce iron, and a second, which is more inclined to reduce sulfate. Due to the fact that the media contained acetate, the Fe-R bacteria are likely very closely related to (or may be) *Geobacter sp.* (Lovley et al., 1986).

3.6 Modeling the Effect of Heterotrophy on Freshwater Carbonate Diagenesis

The potential of organic matter oxidation in driving dissolution can be examined by modeling (using PHREEQC) the effect of organic carbon oxidation on the saturation indices and pCO_2 of lens waters.

SI-C may be expected to decrease following the oxidation of organic matter (due to acidity production). However, whether or not SI-C increases or decreases following the oxidation of organic matter is critically dependant on the calcium concentration of the initial solution, which is in turn very much dependant on:

- the rate (and locus) of evapotranspiration (which is currently not well defined)
- the ground air pCO_2 with which the waters are in equilibrium

In addition, the amount of organic matter that is oxidised will determine whether or not sufficient acidity is generated to 'overcome' the calcium concentrations in SI-C calculations (explained below).

At constant pressure, temperature and ionic strength, SI-C is defined using Equation 3.19 and it is the interplay of these variables that determines the calcite saturation index of a solution (Ford and Williams, 1989; see Chapter 1).

$$SI-C = \log\frac{(Ca^{2+})(HCO_3^-)K_2}{(H^+)(K_c)} \qquad (3.19)$$

During the oxidation of organic matter, CO_2 is produced which dissolves in water to produce carbonic acid (H_2CO_3). At circumneutral pH, this dissociates into HCO_3^- and H^+ ions. In a solution with a high (defined below) calcium concentration, this increase in HCO_3^- ions causes the SI-C to increase despite the decrease in pH caused by the formation of H^+ ions. Where there is insufficient Ca^{2+} to counteract the effects of increased acidity, the saturation index of calcite will decrease.

For example, if a solution has a starting chemistry similar to the Yucatan Peninsula runoff waters (Ca_{XS} = +0.44 mM), 70% evapotranspiration will cause an increase of 1.11 mM

Ca^{2+}. If this water then equilibrates with a ground air pCO_2 of 2.82% (mean of all static wells), the amount of calcium in the solution is increased to 2.90 mM. However, Figure 3.19 demonstrates that, under these pCO_2 conditions, if a sample has a concentration of calcium over 2.47 mM, oxidising 0.81 mM DOC (mean DOC of lens waters) will produce a positive SI-C value and the precipitation of calcite could occur, causing a decrease in Ca_{XS}.

PHREEQC Modeling

The modeling was performed on an average runoff water that has undergone evapotranspirative concentration, has a pCO_2 of ground air and is at equilibrium with respect to calcite. Due to the uncertainty associated with evapotranspiration estimates for the Yucatan Peninsula, three values of evapotranspiration were simulated: 40, 70 and 85%. Each of these solutions was equilibrated with the minimum and maximum estimates of ground air pCO_2 and was driven to equilibrium with respect to SI-C. The minimum ground air pCO_2 estimate (1.18 ± 0.19%) was obtained from the lens top waters form static wells, assumed to have equilibrated with ground air. The maximum ground air pCO_2 estimate (1.82%) was derived from driving the lens top static well waters to calcite equilibrium (after Whitaker, 1992). The oxidation of organic matter was then simulated under aerobic conditions at a constant pressure of 1.1 atm.

The following calculations assume that all of the organic carbon is in a labile form. The refractory portion of organic carbon may be substantial and thus these figures may overestimate the production of CO_2 and the resultant impact on Ca_{XS}. In attempts to account for this, three concentrations of organic matter were oxidised, based on DOC measurements taken from field samples:

- 0.81 mM (the mean DOC concentration of lens waters)
- 1.89 mM (the mean DOC concentration of pumped wells)
- 1.08 mM (the difference between pumped well and lens mean values)

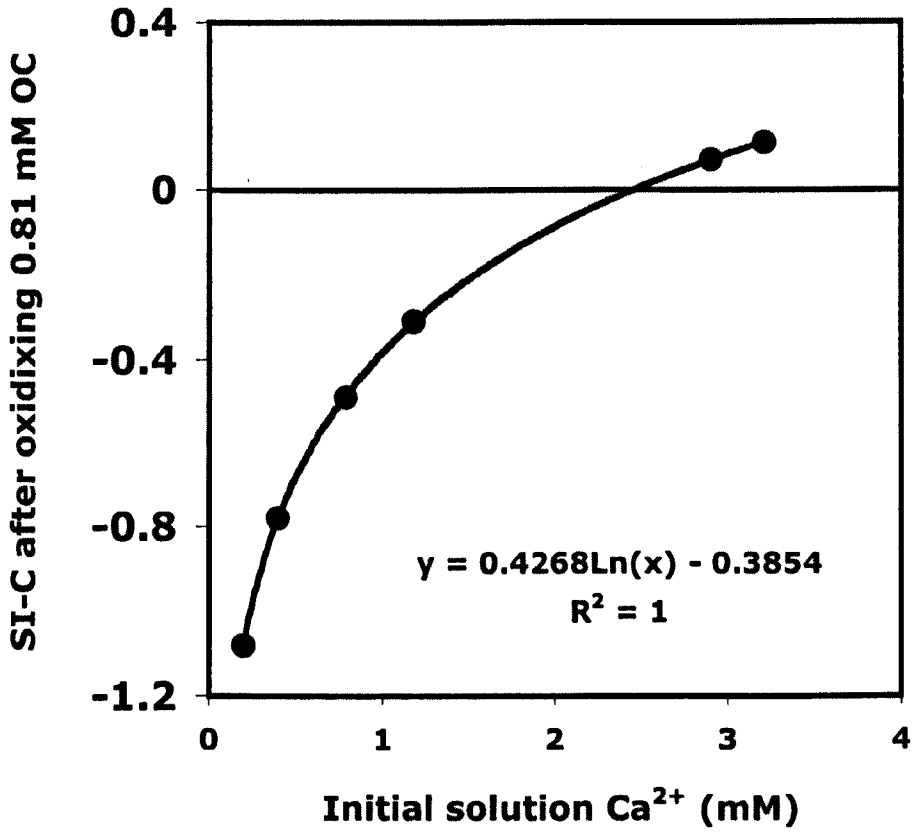

Figure 3.19 PHREEQC modelling results showing the effect of calcium concentration in the initial solution on the SI-C value obtained after oxidising 0.81 mM organic carbon (OC). The initial solution had a pCO_2 of 2.82% and modelling was performed under open-system (aerobic) conditions at 1.1 atm.

The results of this modeling are summarised in Figures 3.20 – 3.22. Evapotranspiration of 85% produces a Ca_{XS} concentration of +3.13 mM. To achieve the +2.19 mM Ca_{XS} measured in lens waters, the oxidation of organic matter (combined with all other processes) would have to cause precipitation of ~94 g $CaCO_3$ to decrease Ca_{XS} by ~0.94 mM. Only one scenario (scenario number 85d, Figure 3.20) is modeled (under 85% evapotranspiration) in which a decrease in Ca_{XS} is achieved. This involves the oxidation of 0.81 mM DOC in a water equilibrated with the estimated maximum pCO_2 of ground air. The oxidation of 0.81 mM organic carbon and subsequent equilibration with calcite causes a decrease in Ca_{XS} (Ca_{XS} = 2.64 mM), but this is insufficient to reach lens values. These results indicate if the 85% evapotranspiration estimate is correct, other mechanism(s) must be active which involves the precipitation of ~0.45 mM calcium to achieve lens Ca_{XS}. Lens waters could achieve this by degassing to reach equilibrium with the minimum estimate of ground air pCO_2 (Section 3.4.4.4).

Of the 18 simulations, there is only one 'pathway' (scenario number 70a, Figure 3.21) that approximates both the Ca_{XS} and pCO_2 of lens waters. This is mean runoff water that has undergone:

- 70% evapotranspiration
- equilibration with a ground air pCO_2 of 1.18% and calcite
- oxidation of 0.81 mM organic carbon
- dissolution of 0.09 mM Ca^{2+} to reach SI-C = 0

This 'pathway' produces a water with a Ca_{XS} of +2.22 mM and pCO_2 of 2.88%. These values are almost exactly the means measured in static and pumped wells (Tables 3.7 and 3.8).

The mean pCO_2 of all lens waters (3.68 ± 1.89%) was best predicted using simulation 70d (Figure 3.21), resulting in a pCO_2 of 3.72% in the final solution. However, in this case, the oxidation of organic matter did little to effect the Ca_{XS} concentration, which was in fact decreased by 0.01 mM, bringing the total Ca_{XS} to +2.46 mM, which is 0.27 mM higher than that measured in the lens.

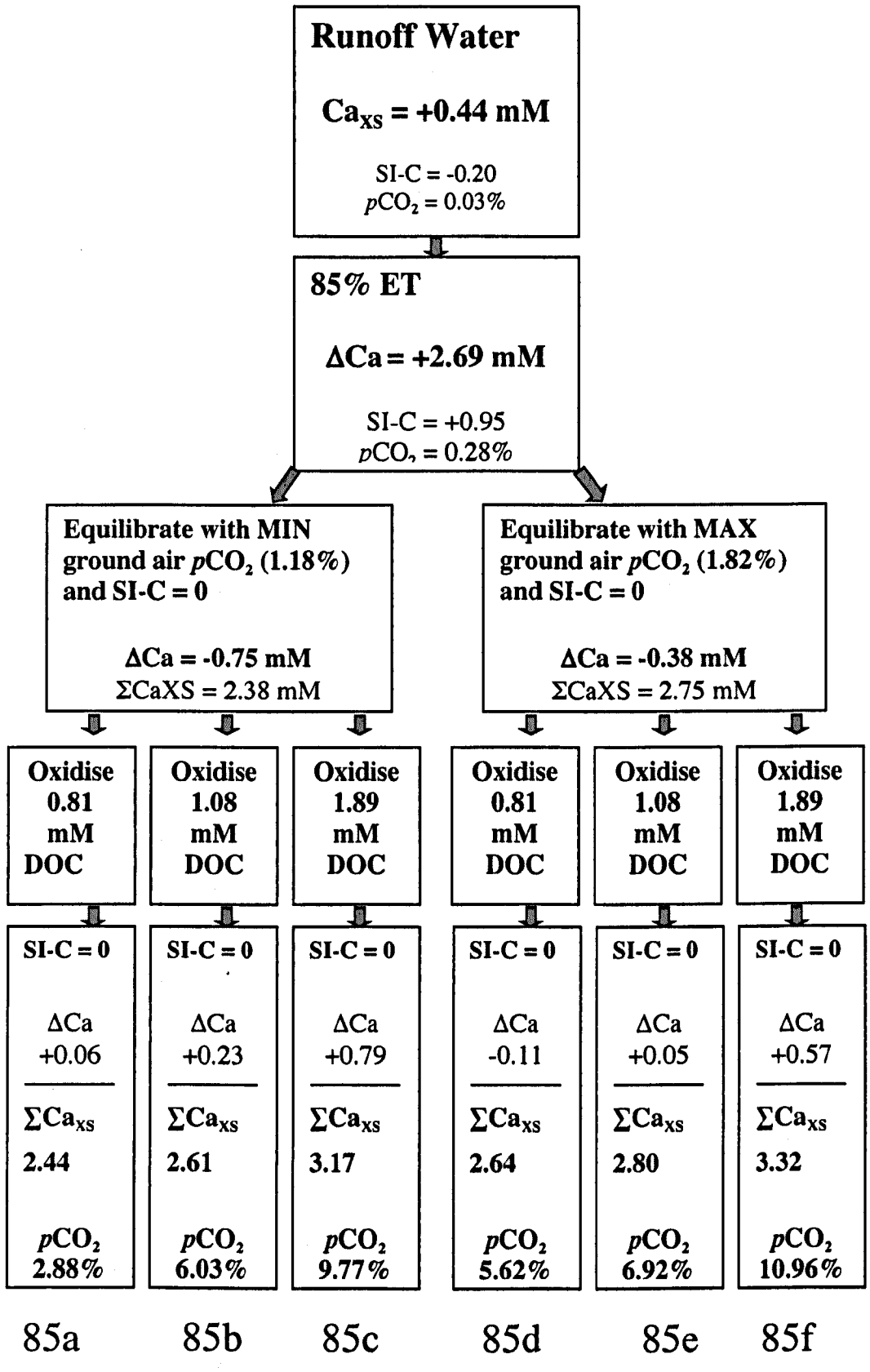

Figure 3.20 Flow diagram, summarising PHREEQC modelling results, showing six possible pathways (scenarios 85a – 85f) a recharge water may take under 85% evapotranspiration. Two ground air pCO_2 values and three estimates of organic carbon are used in attempts to reproduce mean lens water Ca_{XS} (+2.19 ± 0.55 mM) and pCO_2 (3.68 ± 1.89%).

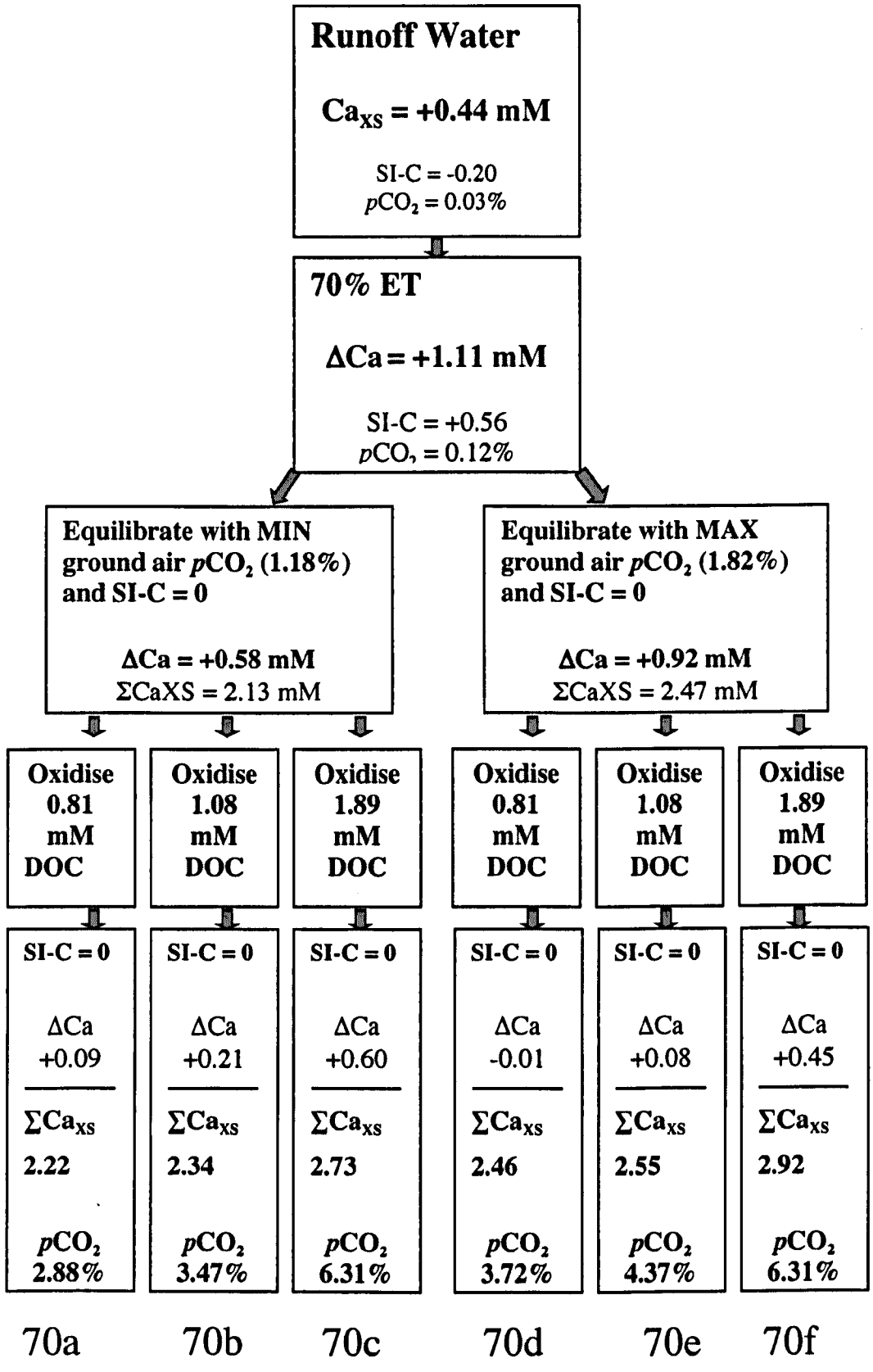

Figure 3.21 Flow diagram, summarising PHREEQC modelling results, showing six possible pathways (scenarios 70a – 70f) a recharge water may take under 70% evapotranspiration. Two ground air pCO_2 values and three estimates of organic carbon are used in attempts to reproduce mean lens water Ca_{XS} (+2.19 ± 0.55 mM) and pCO_2 (3.68 ± 1.89%).

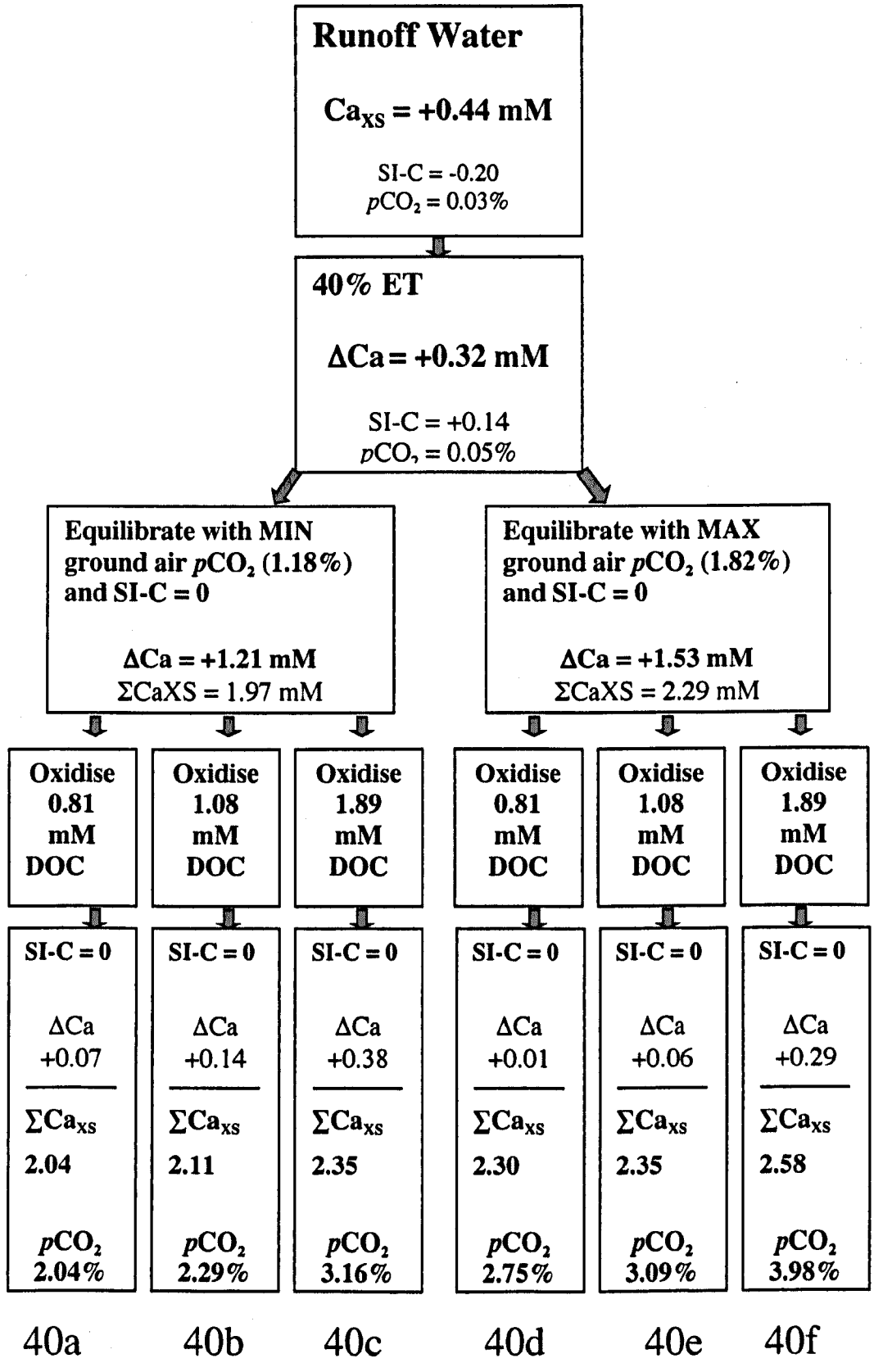

Figure 3.22 Flow diagram, summarising PHREEQC modelling results, showing six possible pathways (scenarios 40a – 40f) a recharge water may take under 40% evapotranspiration. Two ground air pCO_2 values and three estimates of organic carbon are used in attempts to reproduce mean lens water Ca_{XS} (+2.19 ± 0.55 mM) and pCO_2 (3.68 ± 1.89%).

The pCO_2 of cave waters (4.83 ± 1.27%, n =20) is much higher than the mean of lens waters, indicating:

- increased CO_2 production compared to other lens waters and/or
- less CO_2 removal and/or
- cave waters may be equilibrating with a higher ground air pCO_2 than indicated by estimates obtained from static wells

The high soil pCO_2 (3.36 ± 1.34%, n = 11) and the fact that similar (and slightly higher) values were calculated for lens waters (3.68 ± 1.89%, n = 77) indicate that cave waters may be equilibrating with soil air pCO_2 (and/or that a high pCO_2 is maintained throughout the vadose zone).

An average runoff water that has undergone 70% evapotranspiration, and equilibration with calcite and a ground air pCO_2 of 3.36% will have a calcium concentration of 3.08 mM. Upon oxidation of 0.81 (1.89) mM organic carbon, SI-C (SI-A) will become +0.09 (-0.09) and pCO_2 will increase to 5.13 (8.91) %. In the sample in which 0.81 mM organic carbon was oxidised, calcite could precipitate (0.17 mM Ca^{2+} will be lost) to reach calcite equilibrium, resulting in a final pCO_2 of 5.50%. In the sample in which 1.89 mM organic carbon was oxidised, calcite could dissolve (0.23 mM Ca^{2+} will be gained) to reach calcite equilibrium, resulting in a final pCO_2 of 8.32%. Clearly, these values over-estimate the pCO_2 of the east coast cave waters (although they underestimate Merida cave pCO_2), however, other processes (such as degassing) may also occur to decrease the pCO_2 of the east coast waters.

3.7 Rates of Diagenesis in the Freshwater System

Combined with estimated freshwater discharge rates, Ca_{XS} of the freshwater lens can be used to calculate the $CaCO_3$ dissolution rate in the Yucatan Peninsula (Hanshaw and Back, 1980). Hanshaw and Back (1980) multiplied the estimated annual recharge of the Yucatan Peninsula (9800 x 10^6 m^3/a; calculated from rainfall and an estimated 85% evapotranspiration rates; Lesser, 1976) by the mean Ca_{XS} value of the freshwater lens (2.5 mM) to give 24,500 x 10^6 moles calcite (24,500 x 10^5 kg calcite) dissolved per year,

equivalent to ~37.5 metric tons of calcite removed by solution for each square kilometer of the peninsula per year.

However, there are a few possible flaws in the calculations of Hanshaw and Back (1980):

1) It is not clear whether discharge rates measured for the east coast of the Yucatan Peninsula can be extrapolated to the peninsula as a whole;
2) The present study suggests that no evaporites are dissolving in the freshwater lens, hence sulfate should not be subtracted from the calcium concentration to estimate Ca_{XS};
3) A recharge rate of 15% (i.e. 100 - 85% evapotranspiration) may be insufficient to support outflows measured on the east coast of the Yucatan Peninsula (Beddows, 2004). Recharge may be closer to ~30% (based on the modeling performed in Sections 3.4.4.3 and 3.6, whereby the use of 70% ET gave a good prediction of the Ca_{XS} and pCO_2 of both non-degassed vadose zone drip waters and subsequently lens waters);
4) The effect of evapotranspiration on Ca_{XS} was not taken into account

These oversights can be addressed using the data from the present study. The chosen recharge area comprises 40 x 12 km of the eastern peninsula, encompassing all main study sites (Figure 1.8). Recharge is calculated as the difference between annual rainfall (1325 mm/a; NOAA, 2002) and evapotranspiration (70% of rainfall), equivalent to 397.5 mm/a. Multiplying this by the study area (4.8×10^5 m^2) gives the total recharge of 1.9×10^8 m^3/a. The choice of both the recharge area and the evapotranspiration rate are supported by Beddows (2004). Long-term discharge measurements from two major outflow sites on the east coast (Xel Ha and Casa Cenote) were 7 and 3 times greater than the values used by Hanshaw and Back (1980). As such, Beddows (2004) calculated that at least 30% of mean annual rainfall must recharge and consequently, the recharge areas of Xel Ha and Casa Cenote must be 580 and 235 km^2, respectively. These areas are within the same order of magnitude as the 480 km^2 recharge area used here.

In the following calculations, the Ca_{XS} of runoff waters is derived from field measurements, while the vadose zone and freshwater lens values were calculated by modeling (Section 3.6; Model 70a, Figure 3.21). The final Ca_{XS} of the modeled lens water

is 2.22 mM. Of this, 50% can be attributed to evapotranspiration rather than $CaCO_3$ dissolution. Of the remaining 50%, 12.6% of the total Ca_{XS} is due to dissolution at the bedrock surface, 26.1% is due to dissolution within the vadose zone and only 4.1% is due to dissolution occurring in the freshwater lens.

Dissolution rates of the various freshwater zones were calculated by multiplying the effective recharge of the area by the Ca_{XS} concentration of each zone. For example, the $CaCO_3$ dissolution rate of the vadose zone is determined by multiplying the total discharge (1.9×10^8 m^3/yr^1) by the Ca_{XS} (0.58 mM) to give 1.1×10^8 moles of $CaCO_3$ dissolution, equivalent to 1.1×10^7 kg of $CaCO_3$ (Column 3, Table 3.14). Dividing this mass by the recharge area (480 km^2) and by 1000 (to convert kilograms to metric tons) gives the mass of calcite removed per km^2 per year (Column 4, Table 3.14). Converting mass to volume by dividing by the density of calcite (2.65 g/cm^3), gives 8.64 m^3 calcite removed by solution in the vadose zone each year. Given that the average depth of the vadose zone is 10 m, each km^2 of vadose zone has a volume of 10^6 m^3, and therefore the porosity of the vadose zone increases by 8.64×10^{-4}% every year (Column 5, Table 3.14).

Table 3.14 Calculated $CaCO_3$ dissolution rates and % porosity generation in the vadose zone

Process	Contribution (mM) to lens Ca_{XS}	Contribution (%) to lens Ca_{XS}	Moles of $CaCO_3$ dissolution	Metric tons calcite removed (per km^2/a)	% Porosity generation in vadose zone (10 m depth)
(Rainfall)	0.16	7.2	-	-	-
Run-off	0.28	12.6	5.3×10^7	11.1	4.17×10^{-4}
Evapotranspiration	1.11	50.0	-	-	-
Vadose Zone $CaCO_3$ dissolution	0.58	26.1	1.1×10^8	22.9	8.64×10^{-4}
Freshwater Lens $CaCO_3$ dissolution (possibly derived from the oxidation of organic matter)	0.06	4.1	1.7×10^7	3.6	-
Totals	**2.19**	**100**	**1.8×10^8**	**37.6**	**1.42×10^{-3}**

The total dissolution rate value of 37.6 metric tons of calcite removed/km^2/year for a 480 km^2 area of the eastern Yucatan Peninsula is almost identical to the value of 37.5 metric tons of calcite removed/km^2/year for the entire Yucatan Peninsula calculated by Hanshaw and Back (1980). This is due to the corrected (lower) Ca_{XS} values of the present study

canceling out increases in recharge due to the lower evapotranspiration rates used in these calculations. This dissolution rate is geomorphologically extremely significant, capable of completely dissolving a 1 km^2 and 1 m thick block of limestone in 10,000 years.

Further dissolution in the underlying mixing zone is considered in Chapter 4.

Chapter 4

Diagenesis in the Fresh-Salt Water Mixing Zone: A Case Study from Sistema Naranjal (Mayan Blue Section)

4.1 Introduction

Carbonate diagenesis, and in particular dolomitisation, in the mixing zone between fresh and salt water has been the subject of a number of geological and geochemical studies (e.g. Ward and Halley, 1985, Back et al., 1986, Smart et al., 1988, Sanford and Konikow, 1989, Stoessell et al., 1989 and Wicks et al., 1995). The mixing of two waters saturated with respect to calcite but with different salinities and pCO_2 values can produce a mixed water that is calcite undersaturated (Bölgi, 1964; Runnels, 1969; Plummer, 1975), giving rise to the enhancement of limestone dissolution in the mixing zone. In a study using freshwater lens and seawater end-members from the Yucatan Peninsula, Plummer (1975) demonstrated that calcite undersaturation should occur in mixtures of 5-70% seawater. Field studies confirm that the meteoric-marine mixing zone is the site of extensive cave development (Vernon, 1969; Mylroie and Carew, 1995; Smart et al., 1988) and extensive carbonate dissolution features (e.g. "swiss cheese" rock) have been reported in a coastal fresh-salt water mixing zone of the Yucatan Peninsula (Back et al., 1979).

In addition, Hanshaw et al. (1971) suggested a model for mixing zone dolomitisation whereby dolomite can replace calcite where calcite is undersaturated and dolomite is supersaturated. This 'Dorag' model of dolomitisation (Badiozamani, 1973) predicts the dolomitisation of limestone within the dilute parts (5-30 % seawater) of the mixing zone. Stoessell et al. (1989) used field (water chemistry) evidence from the Yucatan Peninsula to suggest that this range could be extended to 70% seawater. In addition, seawater sulfate concentrations may inhibit dolomitisation and the dilution of these concentrations in mixed waters, combined with still relatively high magnesium concentrations, may allow dolomite to form (Baker and Kastner, 1981). Highly porous replacement dolomites have been

reported in several Pleistocene rocks within the Caribbean area (Ward and Halley, 1985; González et al., 1997). However, many studies have presented field evidence from modern mixing zones that suggest the Dorag model cannot be used to explain large-scale dolomitisation of carbonate platforms (e.g. Gebelien, 1977; Budd, 1984; Halley and Harris, 1979; Smart et al., 1988).

Smart et al. (1988) reported major calcite undersaturation rather than dolomitisation in mixing zone waters and suggested that this was due to organic processes within the mixing zone. Subsequent work has confirmed that acid-producing (e.g. sulfur oxidizing) bacteria may play an important role in carbonate dissolution (e.g. Stoessell et al., 1992; Stern et al., 2002). In addition, sulfate-reducing bacteria may facilitate dolomite formation by reducing kinetic barriers to its precipitation (Vasconcelos et al., 1995; Vasconcelos and McKenzie, 1997; Wright, 1999; Warthmann et al., 2000). Communities of these bacteria may be focused around and within the mixing zone, where sharp density interfaces act to 'trap' organic matter and/or bacteria.

The initial part of this chapter reviews the types of mixing zones observed in the Yucatan Peninsula and briefly examines the role of hydrology in shaping these. The majority of Chapter Four, however, is dedicated to the detailed study of geochemistry, geomicrobiology and carbonate diagenesis occurring in the mixing zone of one site, Sistema Naranjal, Mayan Blue Section, where a detailed study of the mixing zone was undertaken.

4.2 Mixing Zone Site Types

In this study, the mixing zone is defined as a body of water where the overall chemistry is the result of mixing between the fresh/brackish and saline groundwaters. There are several site types containing mixing zone waters within the Yucatan Peninsula. These were distinguished from one another based on differences in location (e.g. coastal vs. inland) and on geomorphological observations made in the field. The mixing zone samples from this study are split into four categories. These are: open pit cenotes, caverns, caves and coastal (outflow) sites. Full site descriptions are given in Chapter 1.

4.2 Hydrology of Yucatan Peninsula Mixing Zones

4.3.1. Flow Meter Records and Dye Traces

No direct measurements of flow direction or velocity using recording current meters or dye traces were conducted in any mixing zone waters. However, some data obtained from two dye traces performed simultaneously in the freshwater lens and saline zone at one site may lend insight in to the mixing zone flow dynamics (Section 4.4.1.5).

4.3.2 Mixing Zone General Physio-Chemical Trends

The Yucatan Peninsula mixing zones were characterised using conductivity, temperature, dissolved oxygen and pH depth profiles, obtained *in situ* using YSI 600xlm and YSI 6000 submersible probes. 141 YSI profiles were obtained from 26 unique mixing zone sites throughout the Yucatan Peninsula, although not all have complete profiles through the freshwater lens, mixing zone and saline zone. The profiles obtained from five representative cave sites are shown in Figures 4.1 and 4.2. The sites were chosen based on the presence of fresh, mixed and saline groundwater within a single passage and completeness of data. YSI profiles throughout the water column helped to define the location and thickness of the mixing zone. *In situ* conductivity, temperature, pH and dissolved oxygen data obtained from YSI profiles will be described next.

4.3.2.1 Specific Conductance (SpCond)

In this thesis, the mixing zone is defined as the zone of water between the freshwater lens and the saline zone, where conductivity increases (with depth) from fresh/brackish to saltwater values (Figure 4.3). *In situ* conductivity profiling showed that the Yucatan Peninsula mixing zones are 4.4 ± 4.2 m thick (n = 26). The profiles show that the freshwater lens thickness increases with distance west from the east coast ($r^2 = 0.86$), while the top interface of the saline zone becomes deeper inland ($r^2 = 0.96$) (Figure 4.4). The thickness of the mixing zone does not vary systematically with distance inland from the coast.

i) Vaca Ha:

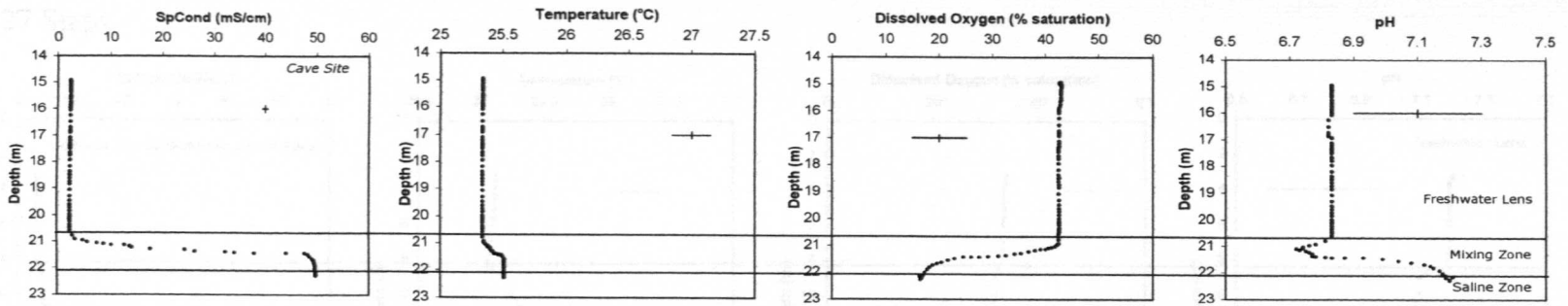

ii) Temple of Doom:

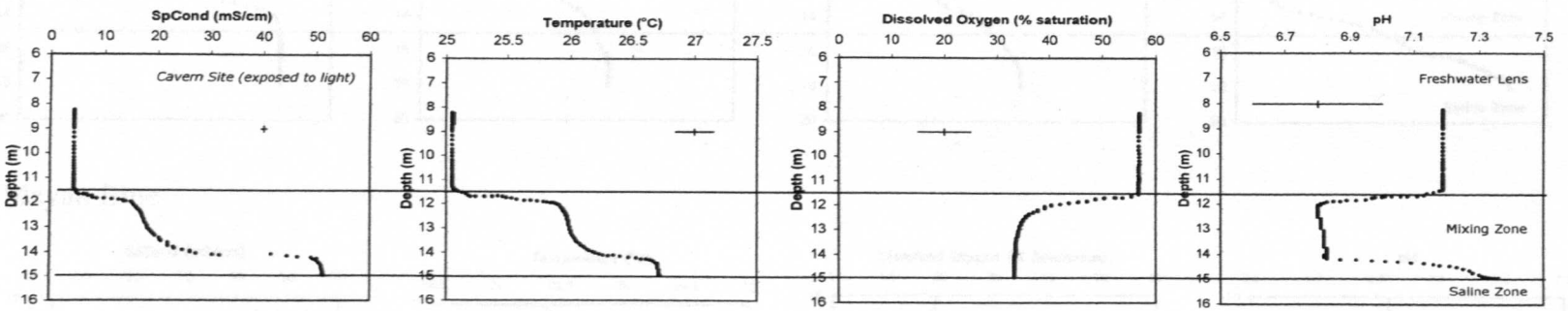

iii) Balam Can Che:

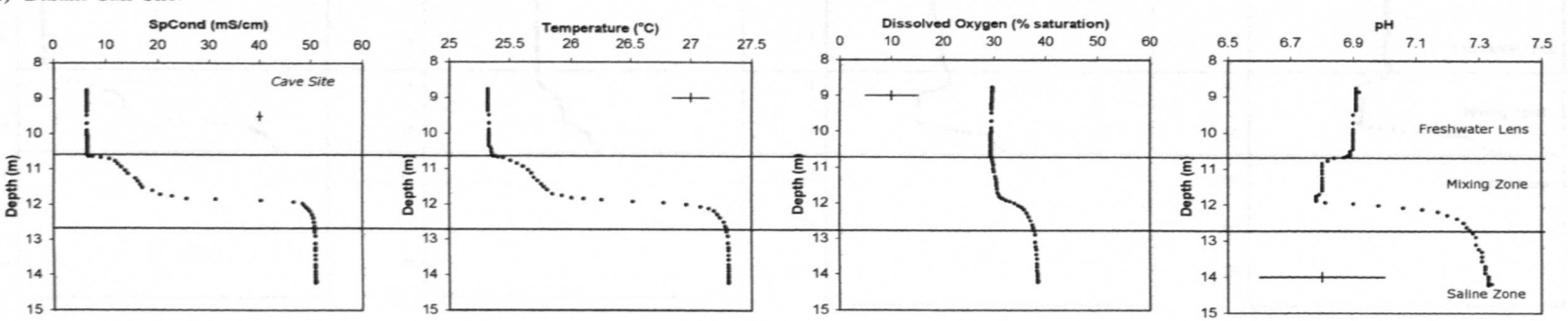

Figure 4.1 Specific Conductance (SpCond), Temperature, Dissolved Oxygen and pH depth profiles from three mixing zone sites within the Yucatan Peninsula. The profiles were taken with a YSI 600xlm multi-parameter probe. Horizontal black lines mark the extent of the mixing zone. Crosses are representative analytical uncertainties (±1σ).

i) 27 Steps

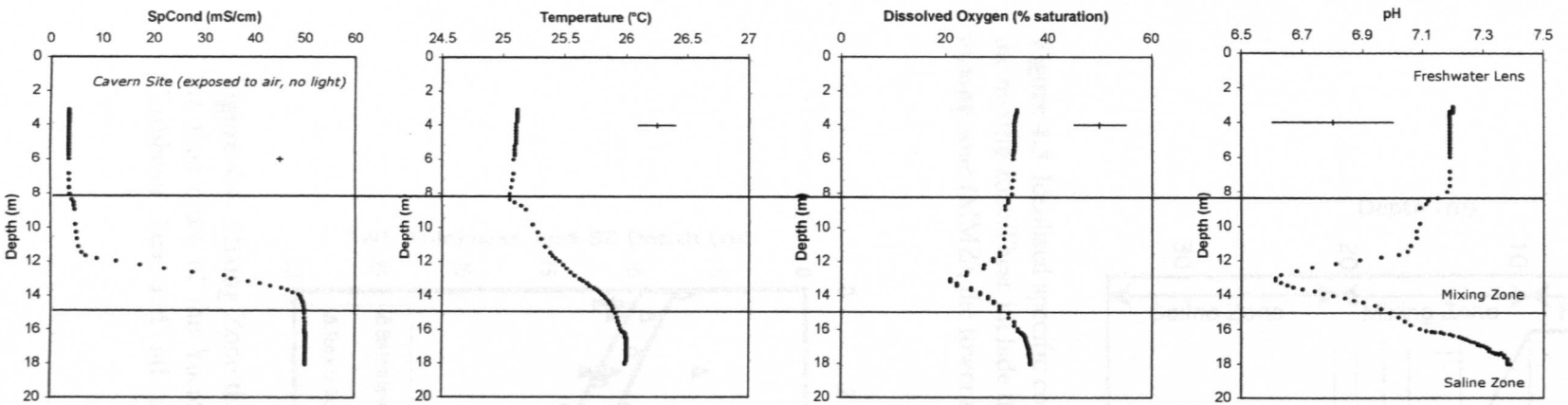

ii) Mayan Blue

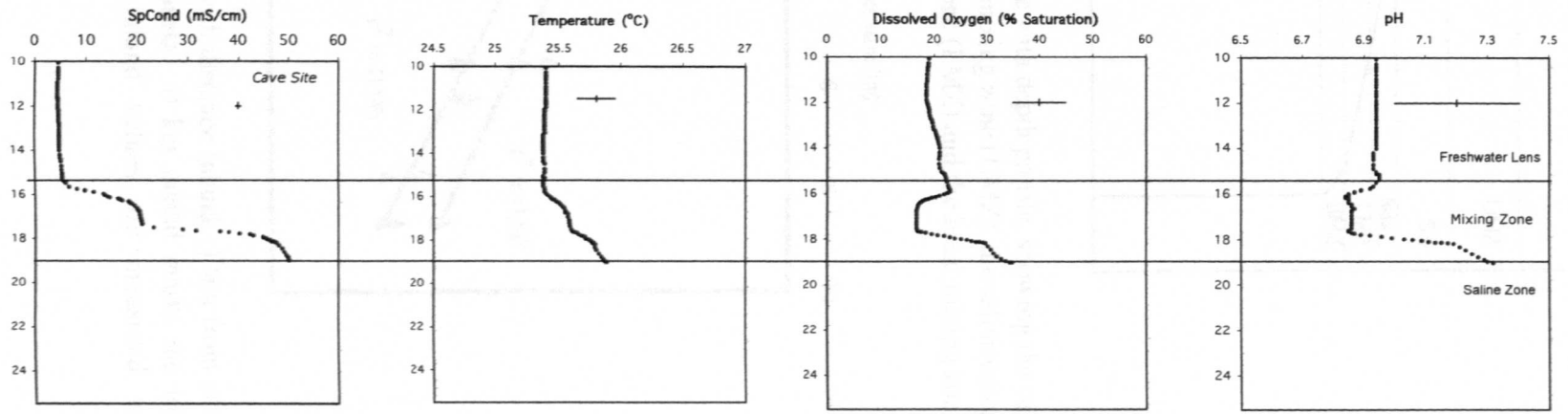

Figure 4.2 Specific Conductance (SpCond), Temperature, Dissolved Oxygen and pH depth profiles from two mixing zone sites within the Yucatan Peninsula. The profiles were taken with a YSI 600xlm multi-parameter probe. Horizontal black lines mark the extent of the mixing zone. Crosses are representative analytical uncertainties (±1σ).

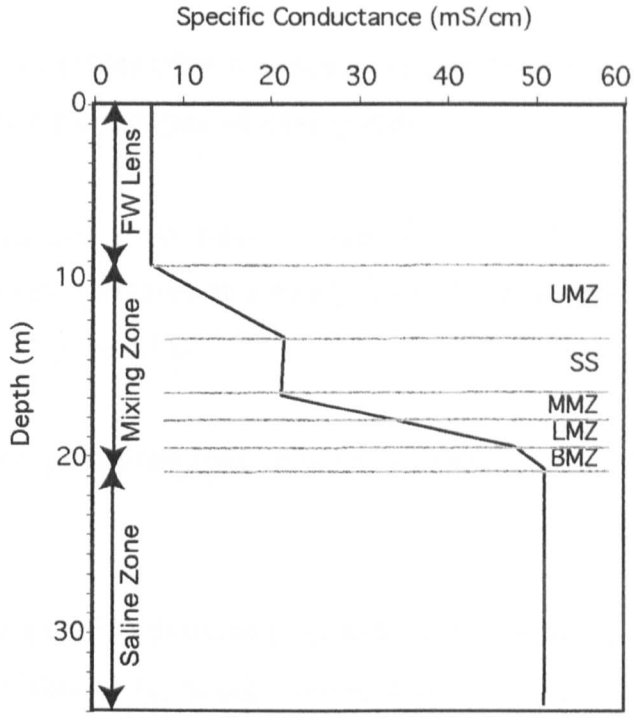

Figure 4.3 Idealised specific conductance with depth profile, showing the subzones within the mixing zone.These include the upper mixing zone (UMZ), the salinity step (SS), the middle mixing zone (MMZ), the lower mixing zone (LMZ) and the basal mixing zone (BMZ).

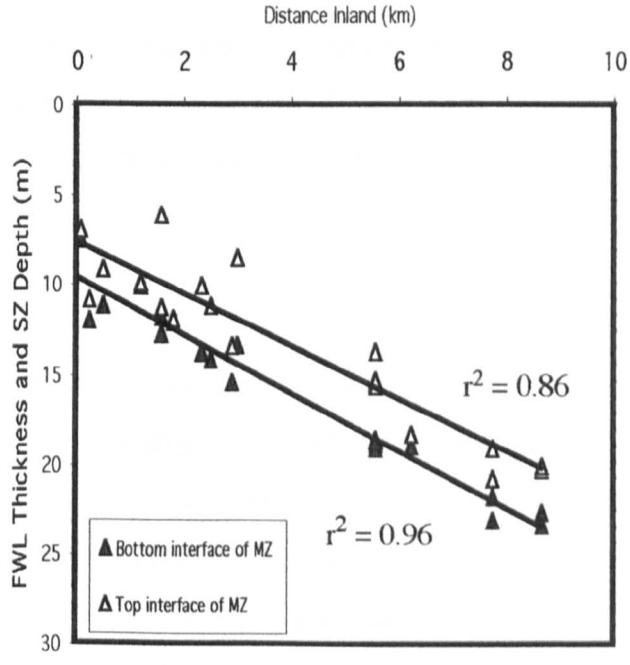

Figure 4.4 Mixing Zone thickness with distance inland. Data from cave sites along the East coast of the Yucatan Peninsula. 0 km inland marks the location of the Caribbean Sea and all distance inland values are measured west of this.

The conductivity profiles (five representative profiles are shown in Figure 4.1 and 4.2) show there are two main 'types' of mixing zones:

a) The transition from fresh to salt water is relatively linear with depth and conductivity increases at a constant rate between the freshwater lens and saline zone (e.g. Figure 4.1.i)

a) The transition contains one or more "conductivity steps" (e.g. Figure 4.1.ii, iii and 4.2.ii)

Using Whitaker's (1992) definitions of sub-zones within the mixing zone (derived for Evelyn Green's Blue Hole, South Andros, Bahamas), the stepped mixing zone can be divided into five sub-zones, distinguished by conductivity (Figure 4.3). The Upper Mixing Zone (UMZ) is the zone of first increase in conductivity beneath the freshwater lens (FWL). The Salinity Step (SS) is found below the UMZ and is an area of relatively uniform water in terms of conductivity. Beneath the SS is a zone of water with rapidly increasing conductivity with depth, divided equally (in terms of depth) into the Middle Mixing Zone (MMZ) and Lower Mixing Zone (LMZ). The inflection occurring between the LMZ and Saline Zone (SZ) is termed the Basal Mixing Zone (BMZ).

4.3.2.2 Temperature

The mean freshwater lens temperature is 25.34 ± 0.53°C (n = 55), while the mean saline groundwater temperature is slightly higher, although more variable (25.80 ± 3.94°C, n = 48). The increase in mixing zone temperature with increasing depth reflects the mixing between the relatively cool freshwater lens and the warmer saline zone (Figures 4.1 and 4.2). If the conductivity profile is stepped, then the temperature profile is also stepped (e.g. Figure 4.1.ii). A more detailed description of Yucatan Peninsula temperature profiles is presented elsewhere (Beddows et al., 2002; Beddows, 2004).

4.3.2.3 Dissolved Oxygen

Representative dissolved oxygen (DO) profiles from five different sites are shown in Figures 4.1 and 4.2. Dissolved oxygen profiles are highly variable in their patterns. Some

profiles show that DO decreases (e.g. Figures 4.1.i, ii) or increases (e.g. Figure 4.1.iii) systematically with depth through the mixing zone from freshwater lens to saline zone values. Other profiles (e.g. Figures 4.1.2.iv, v) show that DO may reach a minimum in the mixing zone that cannot be explained by fresh-salt water mixing.

4.3.2.4 pH

Mixing zone pH does not generally increase or decrease systematically with depth. Representative profiles from five different sites are shown in Figures 4.1 and 4.2. In the upper parts of the mixing zone, all profiles show a decrease in mixing zone pH relative to freshwater lens values (6.99 ± 1.16, $n = 59$). An increase in pH occurs in the lower parts of the mixing zone towards saline groundwater values (7.24 ± 0.18, $n = 49$). The zone of pH minimum appears to be 'sharp' when the mixing zone is relatively thin (e.g. Figure 4.1.i) and is thicker when mixing zone thickness increases (e.g. Figure 4.1.ii).

4.3.2.5 YSI profiles - Discussion of General Trends

Conductivity is largely a function of salinity and within the mixing zone, conductivity is not impacted by diagenesis except in the freshwater zone. Thus, increases in conductivity from freshwater lens values should only reflect mixing with saline groundwaters or dissolution of evaporites.

Conductivity data from YSI profiles showed that the thickness of the mixing zone does not vary systematically with distance inland from the east coast ($P = 0.279$, d.f. = 25). It should be noted that the mixing zone is expected to thicken near the coast where tidal dispersion dominates mixing between fresh and saline groundwaters (Whitaker, 1992). Other factors controlling the mixing zone thickness may be the permeability of the bedrock (Whitaker, 1992) and passage morphology, the details of which are beyond the scope of this thesis and are presented elsewhere (Beddows, 2004).

The steps present in many of the conductivity profiles of the mixing zones likely reflect sites with lower flow velocity. The steps may also indicate zones of differing bedrock permeability (Little et al., 1975), an input of mixed water (Whitaker, 1992) or thermally-

driven mixing, developed in response to greater absorbance of solar radiation by water with increased turbidity. The latter may be a valid point for open pit cenotes, but it is probably not relevant for the majority of the caves of this study.

Temperature and conductivity data indicate mixing between fresh and saline groundwaters is responsible for the temperatures and conductivities observed in the mixing zone. In contrast, dissolved oxygen and pH data indicate site-specific (localised) conditions are occurring. Increases in dissolved oxygen in the mixing zone may indicate an input of oxygen-rich water, an increase in photosynthesis (relevant for open pit cenotes and some cavern zones only), or that oxygen is not being consumed. Decreases in dissolved oxygen, on the other hand, may indicate regions where bacterial oxygen consumption is occurring. The oxidation of organic matter, producing acidity, could also explain the marked decrease in pH observed in all mixing zones studied.

4.4 Case study: Mixing Zone in Mayan Blue, Sistema Naranjal

Introduction

A case study of detailed groundwater mixing zone geochemistry and geomicrobiology was performed at Mayan Blue (part of the Naranjal cave system). Mayan Blue is situated ~5.8 km west of the Caribbean Sea, approximately halfway between the coast and the limit of the zone in which extensive submerged cave systems are currently known to exist. Mayan Blue is one of the few caves in the Yucatan Peninsula region that hosts passages containing fresh, mixed and saline waters at sites relatively far from cenote openings (minimising organic matter and/or photosynthetic input and allowing the collection of non de-gassed samples) and yet is accessible to divers. In addition, YSI profiling demonstrated that the Mayan Blue mixing zone is 3.7 ± 0.3 m thick (Figure 4.2.ii). This allowed the detailed collection of samples throughout the mixing zone, which enabled the characterization of small vertical variations in mixing zone chemistry. A map of Mayan Blue, showing the location of sampling sites within the cave, is presented in Figure 1.5. Site descriptions are given in Chapter 1.

4.4.1 Field Results

This section describes the field chemistry results obtained from the mixing zone of Mayan Blue and includes measurements of conductivity, *in situ* temperature, pH and dissolved oxygen. Unless otherwise stated, depth refers to depth below the modern water table. The data is compiled from measurements taken by YSI profiling and from individual samples.

Thirty-three YSI profiles from Mayan Blue cave were collected between January 2000 and September 2002 during five field seasons. Of these, only twenty-three extend completely from the freshwater lens and into the saline zone. Conductivity profiles are used to study the seasonal variations in the thickness and position of the Mayan Blue mixing zone. Seasonal variations in temperature profiles are also considered. In addition, vertical sequences of water samples were collected in Spring 2000, Autumn 2000, Summer 2001 and Summer 2002, resulting in a total of thirty-five samples. Of these, two were from the fresh/brackish water lens, twenty-seven samples were taken throughout the mixing zone, and six were from the saline water underlying the mixing zone. Conductivity measurements from individual samples were made in the field to confirm the location of the samples throughout the water column. pH and dissolved oxygen were also measured from individual samples because YSI measurements of these variables are associated with relatively low accuracy (± 0.2 pH units, ± 2-6% saturation for dissolved oxygen) compared with measurements taken from a closed flow-through cell (Chapter 2) immediately after the samples arrived at the surface (± 0.02 pH units, ± 1% saturation for dissolved oxygen). Thus, only sample measurements of these variables are considered in this section.

4.4.1.1 Specific Conductance (SpCond)

Conductivity profiling and sampling at Mayan Blue showed that the 15.5 ± 0.7 m-thick freshwater lens is actually relatively brackish (4.81 ± 0.76 mS/cm). The mixing zone, which extends from ~15.5 – 18.7 m, underlies this brackish water lens. Below the mixing zone, at depths greater than 18.7 ± 0.5 m (n= 24), the saline zone is comprised of diagenetically-altered seawater (discussed in detail in Chapter 5). The specific conductance of the Mayan Blue saline zone is 49.8 ± 1.2 mS/cm, which is slightly less than, but not significantly different, from seawater ($\bar{x}$ = 50.9 ± 0.5, n = 8).

The mean mixing zone thickness was calculated for each field season and this was compared to the precipitation of the previous month. Mixing zone thickness has a strong inverse relationship with the amount of precipitation of the preceding month ($r = -0.92$, $P = 0.03$, d.f. =4), indicating that mixing zone thickness decreases following periods of increased rainfall. Mixing zone thickening may correlate with decreasing freshwater lens thickness although the P value suggests this relationship is not significant ($r = -0.77$, $P = 0.13$, d.f. = 4) and mixing zone thickness is independent of the depth of the saline zone ($r = 0.07$, $P = 0.90$, d.f. = 4).

The conductivity profiles from Mayan Blue were stepped during four of the five field seasons (Spring 2000, Summer 2001, Winter 2001, Summer 2002) and a representative stepped profile is shown in Figure 4.5. Using Whitaker's (1992) subdivisions (Section 4.3.2.1, above), the steps can be divided into five sub-zones (Table 4.1; Figure 4.5). The bottom part of the UMZ, the MMZ and the LMZ have relatively steep (22 ± 9 $mScm^{-1}m^{-1}$) conductivity (and density) gradients, while the top part of the UMZ, the SS and BMZ have relatively low (3 ± 2 $mScm^{-1}m^{-1}$) conductivity gradients (Figure 4.6).

Table 4.1 Sub-zones of Mayan Blue Mixing Zone, defined using Specific Conductance

Sub-Zone	Abbr.	Approx. Depth Range (m)	(% SZ-EM)*
Upper Mixing Zone	UMZ	15.2– 16.3/4	0-29
Salinity Step	SS	16.3/4 – 17.2/3	29-37
Middle Mixing Zone	MMZ	17.2/3 – 17.8	37-70
Lower Mixing Zone	LMZ	17.8 - 18.3	70-95
Basal Mixing Zone	BMZ	18.3– 19.3	95-100

*% SZ-EM = % Saline End-Member. The Mayan Blue saline zone (SZ) is the Saline End-Member and %SZ-EM is calculated from conductivity (i.e. $\%SZ\text{-}EM = SpCond_{sample}/SpCond_{SZ\text{-}EM}*100$).

The only non-stepped profiles (Autumn 2000) occurred following a month of rainfall almost four times greater (~250 mm) than the average observed throughout this study (63 ± 61 mm). In addition, the mixing zone was 0.61 m thinner during the Autumn 2000 field season compared to the mean of all other dates.

As the position and thickness of the mixing zone varies with season, in the following sections, mixing zone temperature, dissolved oxygen, pH and alkalinity are considered with conductivity (rather than depth).

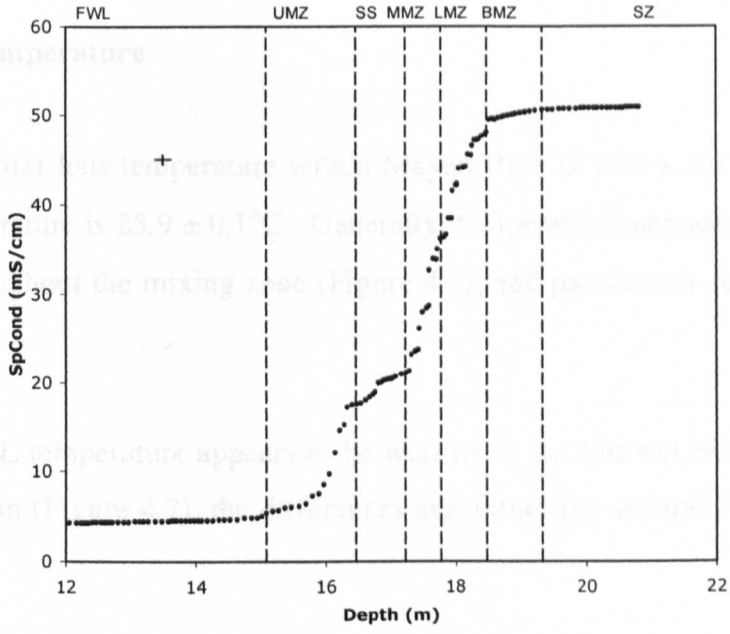

Figure 4.5 A representative profile of specific conductance against depth from Mayan Blue cave (Sistema Naranjal). Dashed lines mark the boundaries between the different water types within the water column, including the freshwater lens (FWL), upper mixing zone (UMZ), middle mixing zone (MMZ), lower mixing zone (LMZ), basal mixing zone (BMZ) and saline zone (SZ). Analytical uncertainties are represented by the cross.

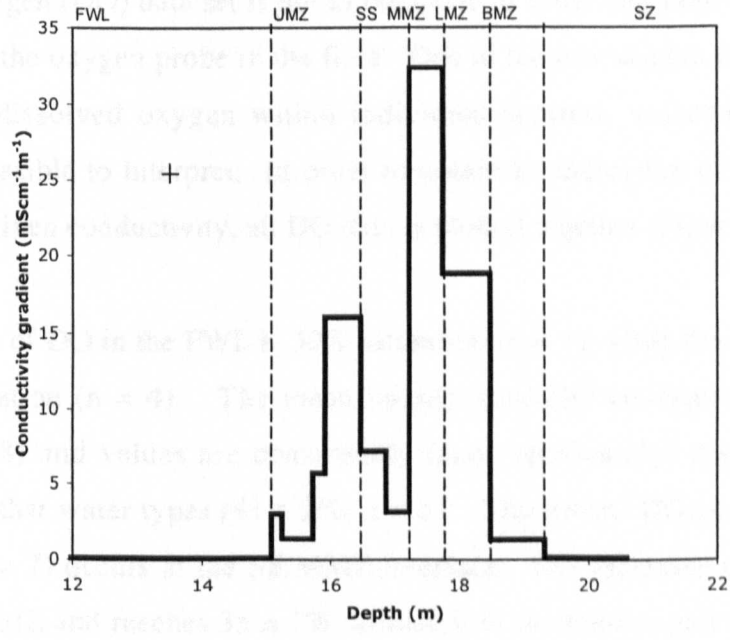

Figure 4.6 Conductivity gradient against depth determined from a representative specific conductance with depth profile (Figure 4.x) taken from Mayan Blue cave (Sistema Naranjal). Dashed lines mark the boundaries between the different water types within the water column, including the freshwater lens (FWL), upper mixing zone (UMZ), middle mixing zone (MMZ), lower mixing zone (LMZ), basal mixing zone (BMZ) and saline zone (SZ). Analytical uncertainties are represented by the cross.

4.4.1.2 *in situ* Temperature

The mean freshwater lens temperature within Mayan Blue is 25.4 ± 0.1°C and the mean saline zone temperature is 25.9 ± 0.1°C. Generally, temperature increases with increasing conductivity throughout the mixing zone (Figure 4.7), and particularly towards the saline zone.

Although the FWL temperature appears to be warmer in the hot/wet season compared to the cool/dry season (Figure 4.7), the differences are within the accuracy and precision of the YSI.

4.4.1.3 Dissolved oxygen (DO)

The dissolved oxygen (DO) data set is not as complete as other analyses due to difficulties encountered with the oxygen probe in the field. Due to the low sample frequency, as well as variations in dissolved oxygen within individual seasons, seasonal differences (if present) are impossible to interpret. In order to obtain an indication of the range of DO encountered at a given conductivity, all DO data is plotted together (Figure 4.8).

The concentration of DO in the FWL is 30% saturation (n = 1), while the SZ concentration is 35 ± 2% saturation (n = 4). The mean mixing zone DO concentration is 30 ± 8% saturation (n = 18) and values are consistently (and significantly) higher in the UMZ compared to all other water types (41 ± 2%, n = 3). The lowest DO concentration (19 ± 1% saturation, n = 2) occurs at the SS/MMZ interface. DO increases with conductivity throughout the MMZ and reaches 35 ± 1% saturation in the bottom part of the MMZ (n = 3). DO may decrease with increasing conductivity throughout the LMZ, although there is only limited data (31 ± 3% saturation, n = 2). DO increases with conductivity throughout the BMZ and SZ.

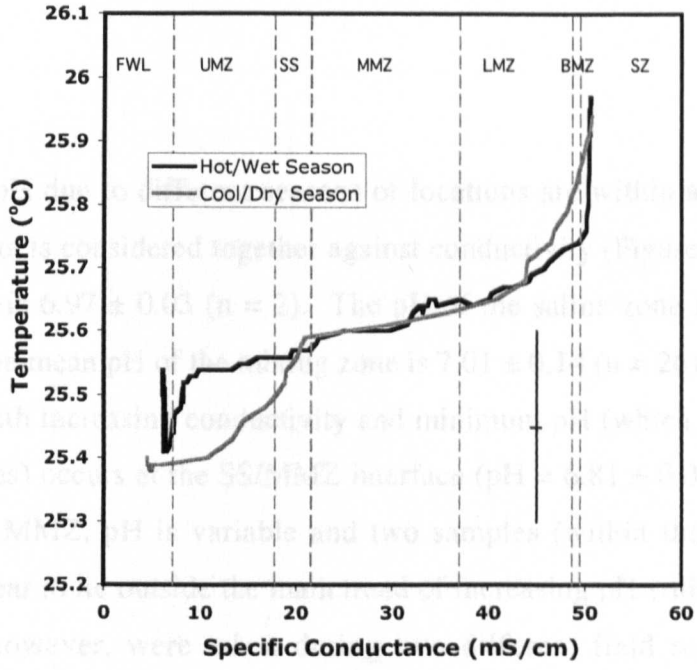

Figure 4.7 *in situ* temperature against conductivity throughout the mixing zone of Mayan Blue for the hot/wet (black line) and cool/dry (grey line) seasons. Data collected with a YSI 600xlm multi-parameter probe. Dashed lines mark the boundaries between the different water types within the water column, including the freshwater lens (FWL), upper mixing zone (UMZ), middle mixing zone (MMZ), lower mixing zone (LMZ), basal mixing zone (BMZ) and saline zone (SZ). Analytical uncertainties are represented by the cross (±1σ).

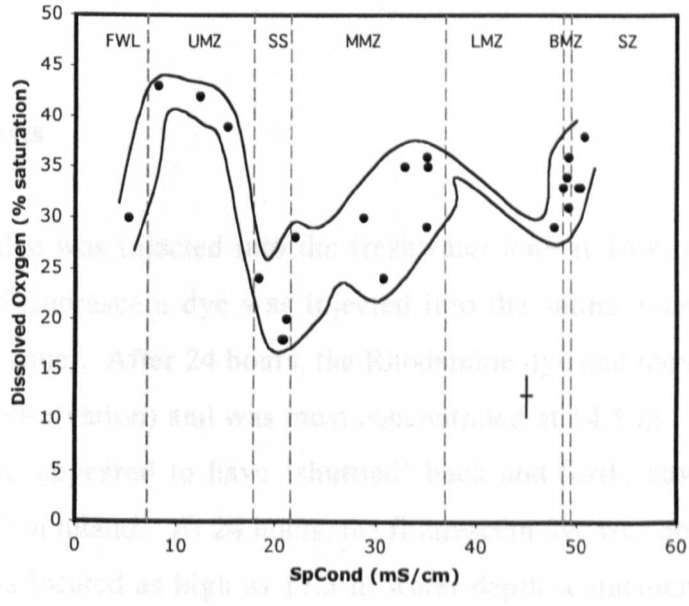

Figure 4.8 Dissolved oxygen against conductivity throughout the mixing zone of Mayan Blue. Data collected from individual samples. Dashed lines mark the boundaries between the different water types within the water column, including the freshwater lens (FWL), upper mixing zone (UMZ), middle mixing zone (MMZ), lower mixing zone (LMZ), basal mixing zone (BMZ) and saline zone (SZ). Analytical uncertainties are represented by the cross (±1σ).

4.4.1.4 pH

Differences in pH due to different seasons or locations are within analytical uncertainty. Thus, all pH data is considered together against conductivity (Figure 4.9). The pH of the freshwater lens is 6.97 ± 0.03 (n = 2). The pH of the saline zone is more basic (7.31 ± 0.05, n = 4). The mean pH of the mixing zone is 7.01 ± 0.14 (n = 26). pH in the UMZ and SS decreases with increasing conductivity and minimum pH (which is significantly lower than FWL values) occurs at the SS/MMZ interface (pH = 6.81 ± 0.01, n = 3). Within the top part of the MMZ, pH is variable and two samples (within the dashed markings in Figure 4.9) appear to lie outside the main trend of increasing pH with conductivity. These two samples, however, were taken during two different field seasons and from two different locations within the cave, suggesting that their values are real. Mixing zone pH reaches a maximum in the bottom part of the MMZ (7.07 ± 0.03, n = 7). LMZ pH may increase with conductivity towards saline zone values. However, one low (and possibly spurious) value (pH = 7.02) occurs near the LMZ/BMZ interface and does not follow this trend. The validity of this sample is discussed in later sections. BMZ pH (7.25 ± 0.04, n = 3) approaches saline zone values.

4.4.1.5 Tracer Tests

Rhodamine WT dye was injected into the freshwater lens at 14.4 m (~0.5 m above the mixing zone) and fluorescein dye was injected into the saline zone at 20.5 m (~1.2 m below the mixing zone). After 24 hours, the Rhodamine dye had moved ~80 m coastward (based on visual observation) and was most concentrated at 14.5 m. The fluorescein dye, on the other hand, appeared to have 'shuttled' back-and-forth, having traveled ~20 m coastward and ~43 m inland. At 24 hours, the flourescein dye was now most concentrated at 19.5 m, but was located as high as 17.3 m water depth (coincident with the SS/MMZ interface). Within 48 hours, the visible Rhodamine WT front had traveled a further 40 m towards the coast (although some dye was still evident at the point of injection) and was now most concentrated within the UMZ at 15.8 m water depth (although the dye cloud extended from 15.7 to 15.9 m). No fluorescein dye was found during the 48 hour (or subsequent) observation dive(s). Observations were made up to a week (at which point a major tropical storm hit the study area and diving was not possible) after the injection.

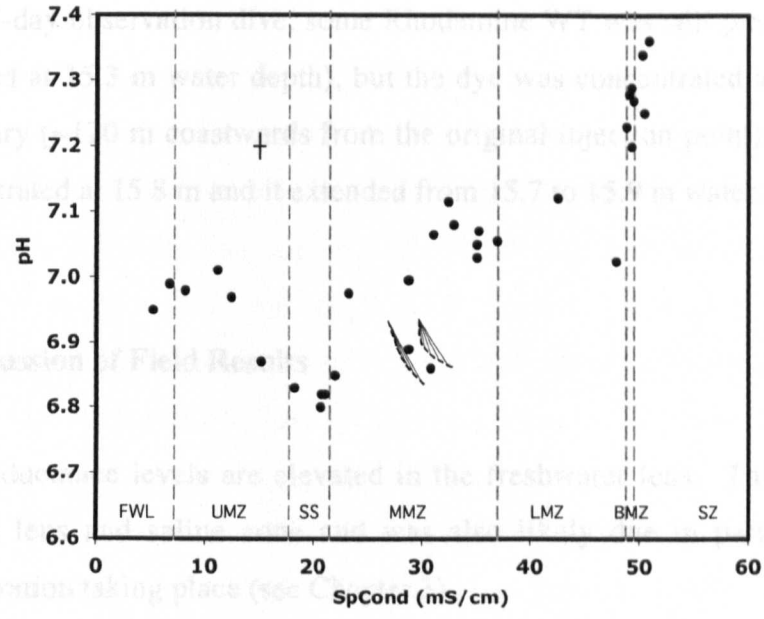

Figure 4.9 pH against conductivity throughout the mixing zone of Mayan Blue. Data collected from individual samples. Dashed lines mark the boundaries between the different water types within the water column, including the freshwater lens (FWL), upper mixing zone (UMZ), middle mixing zone (MMZ), lower mixing zone (LMZ), basal mixing zone (BMZ) and saline zone (SZ). Analytical uncertainties are represented by the cross (±1σ).

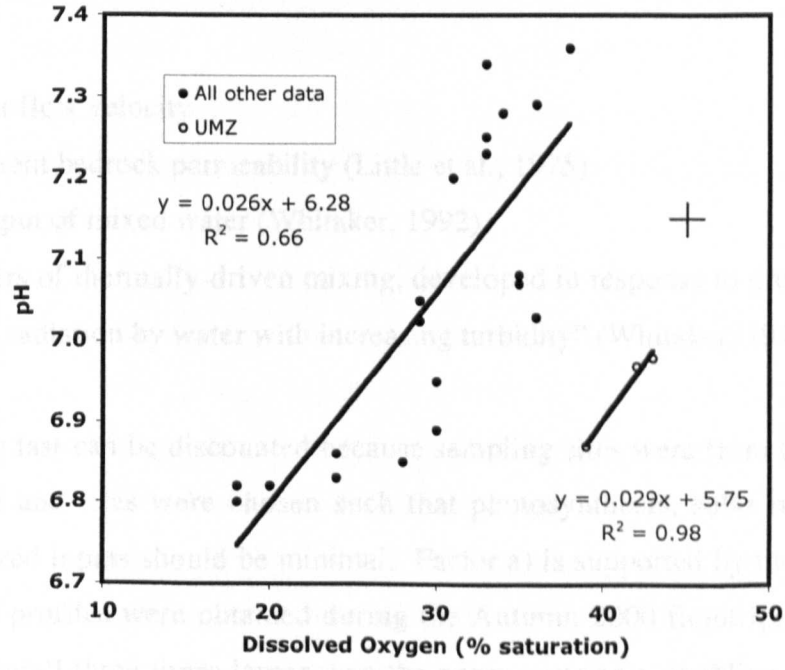

Figure 4.10 pH against dissolved oxygen for Mayan Blue mixing zone samples. Open circles are measurements taken from the upper mixing zone only, while closed circles represent all other data. Data collected from individual samples. Analytical uncertainties are represented by the cross (±1σ).

During the 7-day observation dive, some Rhodamine WT was still present at the injection point (located at 15.3 m water depth), but the dye was concentrated at the cenote/cavern zone boundary (~120 m coastwards from the original injection point). The dye was still most concentrated at 15.8 m and it extended from 15.7 to 15.9 m water depth.

4.4.1.7 Discussion of Field Results

Specific conductance levels are elevated in the freshwater lens. This is due to mixing between the lens and saline zone and was also likely due in part to the amount of evapotranspiration taking place (see Chapter 3).

Mixing between the freshwater lens and saline groundwater is the main control governing mixing zone conductivity and temperature. The conductivity profiles at Mayan Blue reveal a stepped structure during four out of five field seasons. In the discussion of general profile trends (Section 4.3.2.5), it was suggested that stepped profiles might be the result of:

a) lower flow velocity
b) different bedrock permeability (Little et al., 1975)
c) an input of mixed water (Whitaker, 1992)
d) "layers of thermally-driven mixing, developed in response to greater absorbance of solar radiation by water with increasing turbidity" (Whitaker, 1992).

Of these, the last can be discounted because sampling sites were from the cave portion of Mayan Blue and sites were chosen such that photosynthesis, solar radiation and other surface-derived inputs should be minimal. Factor a) is supported by the fact that the only non-stepped profiles were obtained during the Autumn 2000 fieldtrip, which followed a month of rainfall three times larger than the norm, causing a doubling of freshwater lens flow velocities (Beddows, 2004), possibly preventing conductivity steps from forming in the water column. Different bedrock permeability may play a role in step formation during times of lower flow (but this influence may be masked during periods of higher flow) and warrants further investigation. An input of mixed water may also stimulate step formation, but there is no evidence of such an input (e.g. another water source) at Mayan Blue.

Conductivity profiles were used to determine the thickness of the freshwater lens, mixing zone, and depth of the saline zone (i.e. base of the mixing zone). Following times of increased precipitation, the freshwater lens thickness may increase, although the P-value is greater than 0.05 ($r = +0.84$, $P = 0.08$, d.f. = 4), the mixing zone thickness decreases ($r = -0.92$, $P < 0.05$, d.f. = 4), but the base of the mixing zone appears to be stable and independent of precipitation ($r = +0.23$, $P = 0.71$, d.f. = 4). Although not significant to the 95% confidence level (probably due to the small number of observations), the data suggests increases in freshwater lens volume may cause mixing zone thickness to decrease ($r = -0.77$, $P>0.05$, d.f. = 4) and this may be due to:

a) the expanding freshwater lens pushes down the top interface of the mixing zone and/or
b) the increase (i.e. doubling of) freshwater flow velocity that occurred during wet seasons (Beddows, 2004) acted to constrain the mixing zone, preventing it from mixing vertically upwards.

Temperature increases with conductivity throughout the mixing zone, indicating that mixing zone temperature (within a cave site) is primarily a function of mixing between cooler fresh and warmer saline groundwaters. Any seasonal differences with respect to *in situ* temperature could not be established given the relatively large uncertainties associated with the YSI temperature probe.

As mentioned above, dissolved oxygen and pH, although in part controlled by the mixing of fresh and saline groundwaters, are also the result of site-specific (localised) conditions. Increases in dissolved oxygen in the mixing zone may indicate an input of oxygen-rich water or regions where oxygen is not being consumed. Decreases in dissolved oxygen, on the other hand, may indicate regions where oxygen consumption (perhaps due to the oxidation of organic matter by heterotrophic bacteria) is occurring. A significant positive relationship between dissolved oxygen and pH ($r = +0.81$, $P <0.001$, d.f. = 19, Figure 4.10) supports the hypothesis that as oxygen is consumed, acidity is produced. Although the UMZ values are offset from the other samples (due to increased DO concentrations), the quantitative relationship (i.e. slope) between pH and DO is similar (Figure 4.10). The lowest dissolved oxygen content (indicating the greatest oxygen consumption) occurs at the SS/MMZ interface and may indicate that heterotrophic bacterial activity is greatest

here.

Decreases in pH and DO also occur at the LMZ/BMZ interface and may indicate a second zone of increased heterotrophic activity. The role of bacteria in controlling mixing zone geochemistry and their oxygen consumption rates within the mixing zone of Mayan Blue are considered further in Section 4.4.8.2. In addition, the increase in DO in the SZ likely indicates the active circulation of relatively oxygen-rich saline groundwater, with the Caribbean Sea as the source.

Simultaneous dye traces in the freshwater lens and saline zone of Mayan Blue showed that these flows are largely decoupled from one another. Beddows et al. (2002) and Beddows (2004) report the same finding from another Yucatan Peninsula east coast cave site (Ponderosa). At Mayan blue, the freshwater lens dye moved coastward, but also appeared to mix vertically downwards, reaching a maximum depth of 15.9 m, within the UMZ. The saline groundwater shuttled back and forth (but most flow was directed inland) and some vertical mixing upwards also occurred. The minimum depth reached by the fluorescein dye was 17.3 m, which is coincident with the SS/MMZ interface. Water flow within the SS may be relatively static, while flow in the UMZ may be coastward and waters below the SS may shuttle with the saline groundwater, while traveling mostly inland.

4.4.2 Major ions

Chloride is considered to be conservative throughout the groundwaters of this study and it has a good linear relationship with conductivity and sodium (Figure 4.11). In the following section, geochemical results are plotted against chloride concentration. It is worth noting that although chloride content increases with depth as a function of increasing conductivity, the relation is not uniform. For example, samples taken within the salinity step will plot closely together in terms of their chloride content, even though they were not all from the same depth (rather, the salinity step, when present, extended over a range of 0.85 m). Although every care was taken to obtain a very detailed profile of water samples over a wide range of chloride concentrations, there are some instances where the sample distribution is irregular. This is particularly true of samples taken from a region within the profile where large changes in chloride content occur over very small vertical distances.

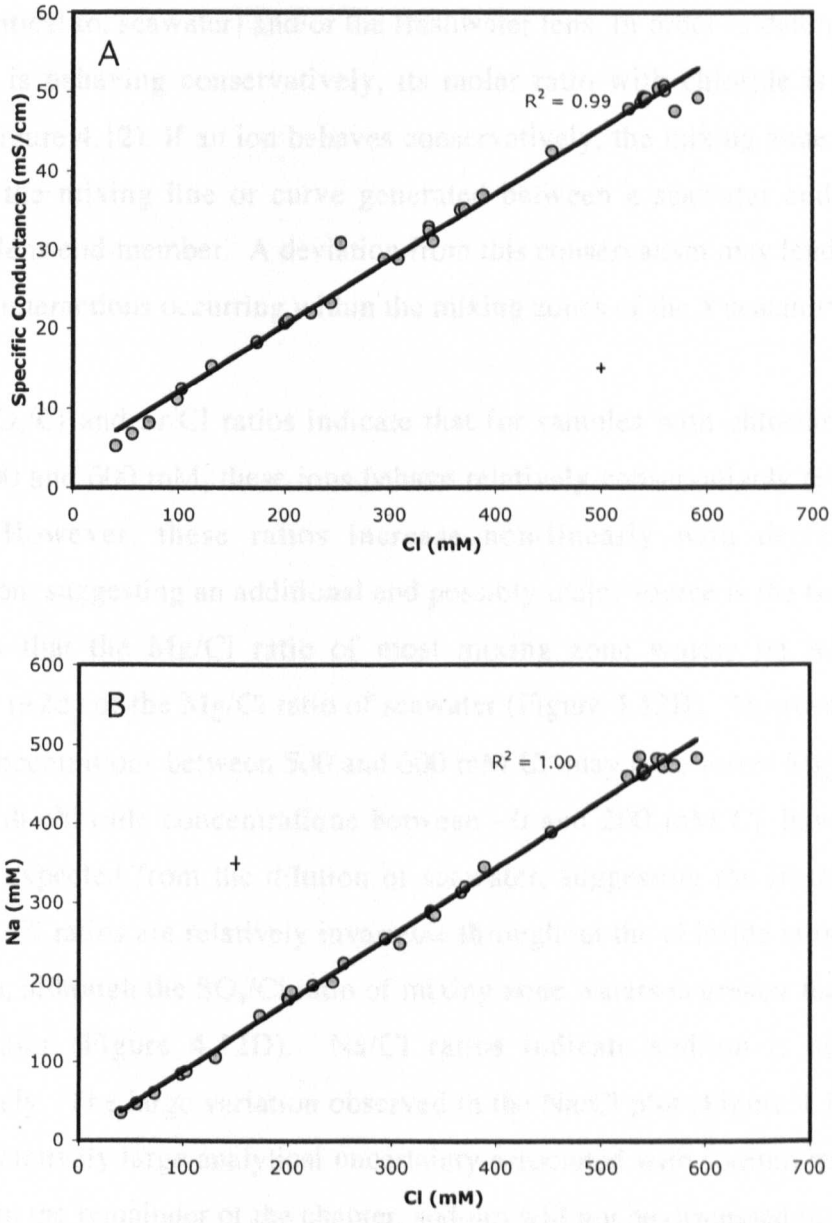

Figure 4.11 Specific conductance (A) and sodium (B) against chloride for Mayan Blue mixing zone samples. Crosses are representative analytical uncertainties (±1σ).

4.4.2.1 Ion relationships with chloride.

The source of ions within the mixing zone will be the saline groundwaters (derived from, but not identical to, seawater) and/or the freshwater lens. In order to determine whether or not an ion is behaving conservatively, its molar ratio with chloride is plotted against chloride (Figure 4.12). If an ion behaves conservatively, the mixing zone samples should plot along the mixing line or curve generated between a seawater end-member and a freshwater lens end-member. A deviation from this conservatism may lend insight into the water-rock interactions occurring within the mixing zones of the Yucatan Peninsula.

Ca/Cl, HCO_3/Cl and Sr/Cl ratios indicate that for samples with chloride concentrations between 400 and 600 mM, these ions behave relatively conservatively (Figure 4.12 A, C and E). However, these ratios increase non-linearly with decreasing chloride concentration, suggesting an additional and possibly major source is the freshwater lens. It is apparent that the Mg/Cl ratio of most mixing zone waters lie within analytical uncertainty ($\pm 2\sigma$) of the Mg/Cl ratio of seawater (Figure 4.12B). However, samples with chloride concentrations between 500 and 600 mM Cl^- may have lower Mg/Cl ratios, while samples with chloride concentrations between ~0 and 200 mM Cl^- have higher Mg/Cl ratios than expected from the dilution of seawater, suggesting the freshwater lens as a source. SO_4/Cl ratios are relatively invariable throughout the chloride range of the mixing zone waters, although the SO_4/Cl ratio of mixing zone waters is greater than that expected from seawater (Figure 4.12D). Na/Cl ratios indicate sodium is acting relatively conservatively. The large variation observed in the Na/Cl plot (Figure 4.12F) is probably due to the relatively large analytical uncertainty associated with sodium measurements (fe = 2.06%). In the remainder of the chapter, sodium will not be discussed in detail.

4.4.3 Excess (XS) Calculations

The effect of geochemical processes on the concentration of a particular element is established by its deviation from the concentration predicted from conservative mixing between fresh and saline end-members. The calculation of this deviation, termed 'excess concentration' (XS), for the mixing zone waters is illustrated in Equation 4.1 for calcium excess (Ca_{XS}).

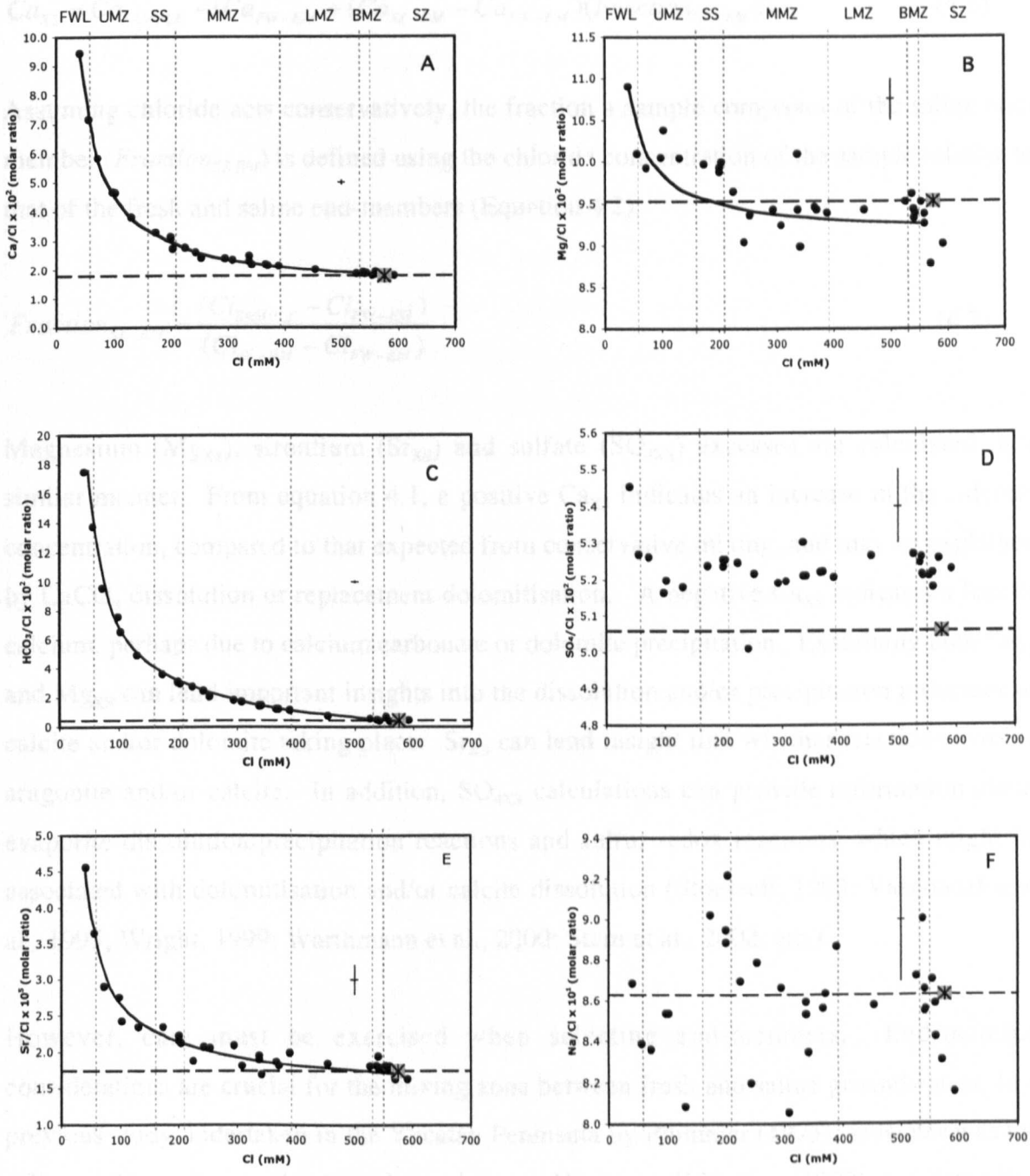

Figure 4.12 Ion molar ratios with chloride [Ca/Cl (A), Mg/Cl (B), HCO_3/Cl (C), SO_4/Cl (D), Sr/Cl (E), and Na/Cl] against chloride throughout the mixing zone of Mayan Blue. Mayan Blue data is plotted as closed circles. Seawater data is plotted as an asterisk surrounded by a grey square. Dashed black line marks the seawater ratio. Curved black line marks the conservative mixing curve between the fresh and saline end-members. Dotted lines mark the boundaries between the different water types within the water column, including the freshwater lens (FWL), upper mixing zone (UMZ), middle mixing zone (MMZ), lower mixing zone (LMZ), basal mixing zone (BMZ) and saline zone (SZ). Crosses are representative analytical uncertainties ($\pm 1\sigma$).

$$Ca_{XS} = Ca_{SAMPLE} - (Ca_{FW-EM} + (Ca_{SZ-EM} - Ca_{FW-EM})(Fraction_{SZ-EM})) \quad (4.1)$$

Assuming chloride acts conservatively, the fraction a sample comprises of the saline end-member ($Fraction_{SZ-EM}$) is defined using the chloride concentration of the sample relative to that of the fresh and saline end-members (Equation 4.2):

$$Fraction_{SZ-EM} = \frac{(Cl_{SAMPLE} - Cl_{FW-EM})}{(Cl_{SZ-EM} - Cl_{FW-EM})} \quad (4.2)$$

Magnesium (Mg_{XS}), strontium (Sr_{XS}) and sulfate (SO_{4XS}) excesses are calculated in a similar manner. From equation 4.1, a positive Ca_{XS} indicates an increase in the calcium concentration, compared to that expected from conservative mixing, and may be explained by $CaCO_3$ dissolution or replacement dolomitisation. A negative Ca_{XS} indicates a loss of calcium, perhaps due to calcium carbonate or dolomite precipitation. Examining both Ca_{XS} and Mg_{XS} can lend important insights into the dissolution and/or precipitation processes of calcite and/or dolomite taking place. Sr_{XS} can lend insight into whether reactions involve aragonite and/or calcite. In addition, SO_{4XS} calculations can provide information about evaporite dissolution/precipitation reactions and sulfur redox reactions, which might be associated with dolomitisation and/or calcite dissolution (Stoessell, 1993; Vasconcelos et al., 1995; Wright, 1999; Warthmann et al., 2000; Stern et al., 2002; etc.).

However, care must be exercised when selecting end-members. End-member considerations are crucial for the mixing zone between fresh and saline groundwaters. In a previous study undertaken in the Yucatan Peninsula by Plummer (1975), seawater was the saline end member used to simulate mixing. However, Whitaker (1992) suggested that end-members used for mixing should be site specific due to the variability of 1) the fresh/brackish lens waters and 2) saline groundwaters (specifically, saline groundwater chemistry is considerably different than that of seawater, Chapter 5).

Mayan Blue end-members

In order to minimize the effect of degassing, neither Mayan Blue cenote nor cavern waters were used as the freshwater end-member. Instead, a freshwater lens water sampled from

the cave was used. This sample was sufficiently above the mixing zone (>1 m) that mixing influences should be minimal, and it was located sufficiently below the cave roof (>1 m) to ensure that percolation was not sampled with the lens water. Difficulties were encountered when selecting a saline end-member due to variability in Mayan Blue saline groundwater chemistry. However, an end-member was chosen which was sufficiently below the mixing zone and yet above the cave floor to minimise mixing and sediment influences, respectively. The chosen saline end-member approximated the mean chemistry encountered in the Mayan Blue saline zone samples (although the sulfate concentration was slightly lower than other saline samples, it is not significantly different from the mean saline groundwater sulfate concentration).

XS calculations were confirmed using sodium and conductivity as well as chloride to calculate XS. The results of these analyses indicated that there are two outliers within the data set (where chloride is probably reading too low, causing a significant increase in the XS result). These two outliers have therefore not been included in the following descriptions and discussion and appear as open squares in the XS figures.

4.4.3.1 Ca_{xs}

On average, mixing zone waters are enriched in calcium relative to the linear mixing between fresh and saline end-members ($\bar{x}$ mixing zone Ca_{xs} = +0.11 ± 0.23 mM, n = 25) (Table 4.2), however only two samples within the mixing zone have Ca_{xs} values significantly greater than zero (±2σ) (Figure 4.13). The significant enrichments occur at the SS/MMZ interface and in the lower part of the MMZ. In addition, there is one sample in the upper part of the MMZ where calcium may be significantly depleted (Figure 4.13).

Seasonal differences in mixing zone Ca_{xs} are within analytical uncertainty and a two-tailed t-test demonstrated that there is no significant difference in Ca_{xs} for samples taken during dry and wet seasons (P-value = 0.191). Likewise, a one-way ANOVA demonstrated that there were no significant differences in Ca_{xs} between samples (of a given chloride concentration) taken at different sites within the cave (sites tested were: Dog Leg, Death Arrow, Stal Dome, P-value = 0.423). In addition, no differences in Ca_{xs} were found between samples taken with 7 cm diameter PVC tubes compared to samples taken with 1.5 cm diameter PVC tubing (P-value = 0.520).

Table 4.2 Mean XS of Mayan Blue cave waters (±1σ).

Water Type	Ca_{xs} (mM)	Mg_{xs} (mM)	SO_{4xs} (mM)	Sr_{xs} (mM) ($x10^{-2}$)
Freshwater Lens (FWL) (n = 2)	+0.02 ±0.03	+0.09 ±0.13	+0.03 ±0.04	+0.03 ±0.04
$\bar{x}$ Mixing Zone (n = 25, excluding two outliers)	+0.11 ±0.23	+0.57 ±0.76	+0.12 ±0.19	-0.08 ±0.30
Upper Mixing Zone (UMZ) (n = 4)	+0.08 ±0.07	+0.43 ±0.31	-0.03 ±0.03	-0.17 ±0.12
Salinity Step (SS) (n = 4)	+0.18 ±0.33	+0.99 ±0.13	+0.09 ±0.03	+0.03 ±0.10
Middle Mixing Zone (MMZ) (n = 11)	+0.17 ±0.35	+0.51 ±1.28	+0.07 ±0.19	-0.17 ±0.37
Lower Mixing Zone (LMZ) (n = 3)	+0.26 ±0.31	+2.04 ±1.58	+0.35 ±0.12	-0.05 ±0.02
Basal Mixing Zone (BMZ) (n = 3)	+0.06 ±0.09	+0.68 ±0.28	+0.27 ±0.15	+0.16 ±0.46
Saline Zone (SZ) (n = 6)	+0.07 ±0.36	-0.32 ±1.49	+0.22 ±0.15	-0.44 ±0.52
Analytical uncertainty (±1σ)	±0.17	±0.98	±0.61	±1.06

4.4.3.2 Mg_{xs}

On average, mixing zone waters are enriched in magnesium relative to linear mixing between fresh and saline end-members ($\bar{x}$ mixing zone Mg_{xs} = +0.57 ± 0.76 mM, n = 25), although only one sample within the mixing zone had an Mg_{xs} value significantly greater than zero (±2σ) (Figure 4.13B). This sample was taken from the MMZ. No mixing zone samples were significantly depleted of magnesium. Seasonal differences are within analytical uncertainty.

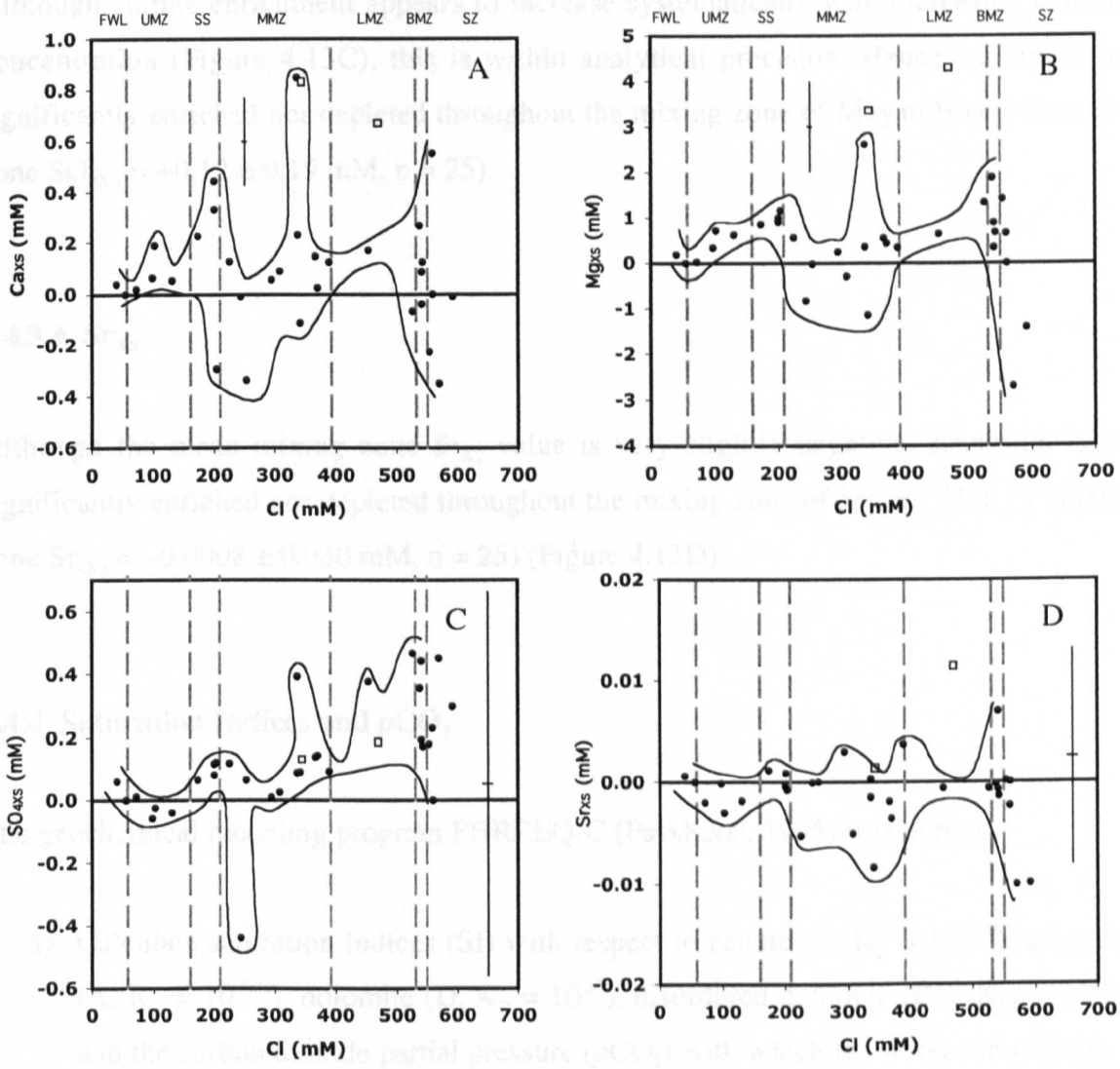

Figure 4.13 Variation in (A) Ca_{XS}, (B) Mg_{XS}, (C) SO_{4XS} and (D) Sr_{XS} with chloride concentration through the mixing zone of Mayan Blue cave. Dashed grey lines show the location of the different parts of the water column, including the freshwater lens (FWL), upper mixing zone (UMZ), salinity step (SS), middle mixing zone (MMZ), lower mixing zone (LMZ), basal mixing zone (BMZ) and saline zone (SZ). Outliers (confirmed by calculating XS with sodium) are shown as squares. Crosses are representative analytical uncertainties (±1σ).

4.4.3.3 SO_{4XS}

Although sulfate enrichment appears to increase systematically with increasing chloride concentration (Figure 4.13C), this is within analytical precision. Hence, sulfate is not significantly enriched nor depleted throughout the mixing zone of Mayan Blue ($\bar{x}$ mixing zone SO_{4XS} = +0.12 ± 0.19 mM, n = 25).

4.4.3.4 Sr_{XS}

Although the mean mixing zone Sr_{XS} value is very slightly negative, strontium is not significantly enriched nor depleted throughout the mixing zone of Mayan Blue ($\bar{x}$ mixing zone Sr_{4XS} = -0.0008 ± 0.030 mM, n = 25) (Figure 4.13D).

4.4.4 Saturation Indices and pCO_2

The geochemical modeling program PHREEQ-C (Parkhurst, 1995) was used to:

a) Calculate saturation indices (SI) with respect to calcite (C, $K_C = 10^{-8.50}$), aragonite (A, $K_A = 10^{-8.36}$), dolomite (D, $K_D = 10^{-17}$), disordered dolomite (DD, $K_{DD} = 10^{-16.5}$) and the carbon dioxide partial pressure (pCO_2) with which the water samples are in equilibrium
b) Predict theoretical geochemical profiles from the mixing of freshwater and saline zone end-members, to allow comparison with actual field data.

4.4.4.1 Calcite (SI-C) and Aragonite (SI-A) Saturation Indices

All Mayan Blue water samples are undersaturated with respect to aragonite (Table 4.3 and Figure 4.14). Given the consistent offset between SI-A and SI-C, only SI-C data is described in detail here. The freshwater lens is only marginally supersaturated with respect to calcite (SI-C = +0.07 ± 0.04, n = 2) and saline groundwaters are at equilibrium (SI-C = -0.02 ± 0.07, n = 6). The mean mixing zone saturation is –0.10 ± 0.09 (n = 27).

Table 4.3 Mean saturation indices and pCO_2 of Mayan Blue cave waters (±1σ).

Water Type	SI-C	SI-A	SI-D	SI-DD	pCO_2 (%)
Freshwater Lens (FWL) (n = 2)	+0.07 ±0.04	-0.08 ±0.04	+0.39 ±0.13	-0.17 ±0.13	4.03 ±0.07
Mean Mixing Zone waters (n = 27)	-0.10 ±0.09	-0.25 ±0.09	+0.54 ±0.20	-0.02 ±0.20	2.27 ±1.30
Upper Mixing Zone (UMZ) (n = 4)	-0.01 ±0.09	-0.16 ±0.09	+0.46 ±0.14	-0.10 ±0.14	3.60 ±0.26
Salinity Step (SS) (n = 4)	-0.21 ±0.03	-0.36 ±0.03	+0.25 ±0.02	-0.32 ±0.02	4.05 ±0.16
Middle Mixing Zone (MMZ) (n = 12)	-0.08 ±0.08	-0.23 ±0.08	+0.61 ±0.19	+0.04 ±0.19	2.14 ±0.75
Lower Mixing Zone (LMZ) (n = 3)	-0.16 ±0.09	-0.31 ±0.09	+0.54 ±0.15	-0.02 ±0.15	0.96 ±0.13
Basal Mixing Zone (BMZ) (n = 4)	-0.09 ±0.05	-0.23 ±0.05	+0.71 ±0.09	+0.15 ±0.09	0.52 ±0.04
Saline Zone (SZ) (n = 6)	-0.02 ±0.07	-0.17 ±0.07	+0.84 ±0.14	+0.28 ±0.14	0.51 ±0.17
Analytical uncertainty (±1σ)	±0.006	±0.006	±0.015	±0.015	±0.020%

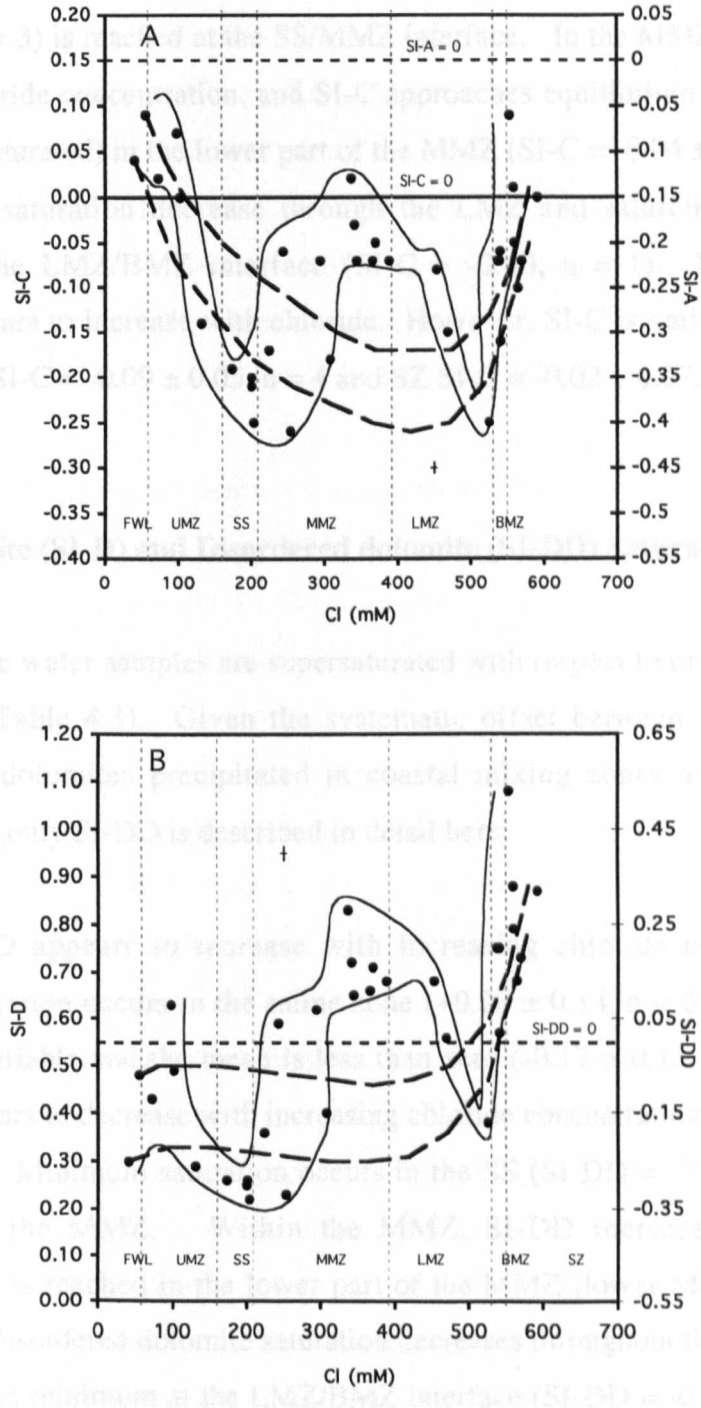

Figure 4.14 Variations in saturation with respect to calcite (SI-C) and aragonite (SI-A) (A) and dolomite (SI-D) and disordered dolomite (SI-DD) (B) against chloride throughout the mixing zone of Mayan Blue cave. Observed saturation indices (individual data points) are compared to those predicted from inorganic mixing simulations using fresh and saline end-members (black dashed curves show the range of saturation expected from modeling). Black dotted lines show where SI-A (A) and SI-DD (B) = 0. Dotted grey lines show the locations of the different parts of the water column, including the freshwater lens (FWL), upper mixing zone (UMZ), salinity step (SS), middle mixing zone (MMZ), lower mixing zone (LMZ), basal mixing zone (BMZ) and saline zone (SZ). Crosses are representative analytical uncertainties (±1σ).

In the UMZ, the mean SI-C is near equilibrium (SI-C = -0.01 ± 0.09, n = 4), and saturation appears to decrease with increasing chloride concentration. Minimum saturation (SI-C = -0.22 ± 0.03, n = 3) is reached at the SS/MMZ interface. In the MMZ, SI-C increases with increasing chloride concentration, and SI-C approaches equilibrium (and two samples are slightly supersaturated) in the lower part of the MMZ (SI-C = -0.04 ± 0.02, n = 7). Calcite and aragonite saturation decrease through the LMZ and saturation reaches a second minimum at the LMZ/BMZ interface (SI-C = -0.40, n = 1). Below this interface, saturation appears to increase with chloride. However, SI-C is variable in both the BMZ and SZ (BMZ SI-C = -0.09 ± 0.05, n = 4 and SZ SI-C = -0.02 ± 0.07, n = 6) (Figure 4.14).

4.4.4.2 Dolomite (SI-D) and Disordered dolomite (SI-DD) Saturation Indices

All Mayan Blue water samples are supersaturated with respect to ordered dolomite (SI-D) (Figure 4.14, Table 4.3). Given the systematic offset between SI-D and SI-DD and because most dolomites precipitated in coastal mixing zones are non-stoichiometric (Hardie, 1987), only SI-DD is described in detail here.

Overall, SI-DD appears to increase with increasing chloride concentration and the maximum saturation occurs in the saline zone (+0.28 ± 0.14, n = 6) (Figure 4.14). FWL saturation is variable and the mean is less than zero (-0.17 ± 0.13, n = 2). In the UMZ, saturation appears to decrease with increasing chloride concentration (UMZ SI-DD = -0.10 ± 0.14, n = 4). Minimum saturation occurs in the SS (SI-DD = -0.32 ± 0.02, n = 4) and upper part of the MMZ. Within the MMZ, SI-DD increases with chloride and supersaturation is reached in the lower part of the MMZ (lower MMZ SI-DD = +0.34 ± 0.34, n = 6). Disordered dolomite saturation decreases throughout the LMZ and saturation reaches a second minimum at the LMZ/BMZ interface (SI-DD = -0.18, n=1). Below this interface, saturation appears to increase with chloride. However, SI-DD is variable in both the BMZ and SZ (BMZ SI-DD = +0.15 ± 0.09, n = 4 and SZ SI-DD = +0.28 ± 0.14, n = 6).

4.4.4.3 pCO_2

Freshwater lens pCO_2 is 4.03 ± 0.07% (n = 2), while saline zone has a mean of 0.51 ±

0.17% (n = 6) (Table 4.3). In general, pCO_2 decreases with increasing chloride concentration throughout the mixing zone of Mayan Blue (Figure 4.15) and the mean mixing zone value is 2.27 ± 1.30% pCO_2 (n = 27). The highest pCO_2 values occur in the lower part of the UMZ, in the SS and in the top part of the MMZ (pCO_2 = 3.99 ± 0.18%, n = 6). Throughout the MMZ and top part of the LMZ, pCO_2 decreases with increasing chloride concentration at a rate of -0.01% pCO_2/mM Cl^-. A slight increase in pCO_2 occurs at the LMZ/BMZ interface (pCO_2 = 1.05%, n = 1). BMZ pCO_2 is 0.52 ± 0.04 (n = 4), which is not significantly different from saline zone values.

4.4.5 Comparison of theoretical geochemical mixing profiles with actual field data.

Geochemical modeling with PHREEQ-C (Parkhurst, 1995) was used to simulate mixing between Mayan Blue fresh and saline end-members. Several simulations were carried out using various end-members in order to obtain a range of expected saturation and pCO_2 concentrations. The results of this modeling are presented with the field data in Figure 4.14. It is apparent that there are distinct regions where saturation and pCO_2 are greater or less than that predicted from fresh-salt water mixing. In order to better quantify these increases and decreases, calculations of ΔSI and Δ pCO_2 were carried out. ΔSI and Δ pCO_2 are calculated by subtracting the theoretically predicted values (as defined by modeling the mixing of two waters) from the observed values from field measurements.

4.4.5.1 Differences between observed and predicted mineral saturation indices (ΔSI)

Differences between the observed IAP and predicted saturation indices (ΔSI) of aragonite (A), calcite (C), and disordered (DD) and ordered dolomite (D), are plotted in Figure 4.16. ΔSI was calculated using the most conservative estimate (i.e. the predicted SI value nearest that of the actual value was used to calculate ΔSI). A positive ΔSI value indicates an increase in saturation compared to fresh-salt water mixing, while a negative ΔSI indicates a decrease in saturation compared to mixing. The change in magnitude of ΔSI-C was equal to that of ΔSI-A.

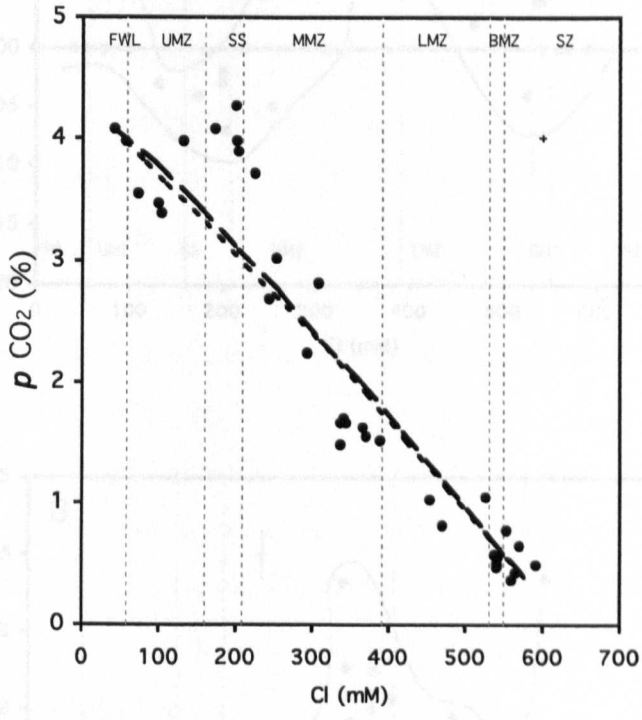

Figure 4.15 Distribution of $p\ CO_2$ measured in the mixing zone samples (individual data points) compared to that predicted by fresh-salt water mixing (dashed black lines) against chloride concentration through the mixing zone of Mayan Blue. Dotted lines show the locations of the different parts of the water column, including the freshwater lens (FWL), upper mixing zone (UMZ), salinity step (SS), middle mixing zone (MMZ), lower mixing zone (LMZ), basal mixing zone (BMZ) and saline zone (SZ). Crosses are representative analytical uncertainties ($\pm 1\sigma$).

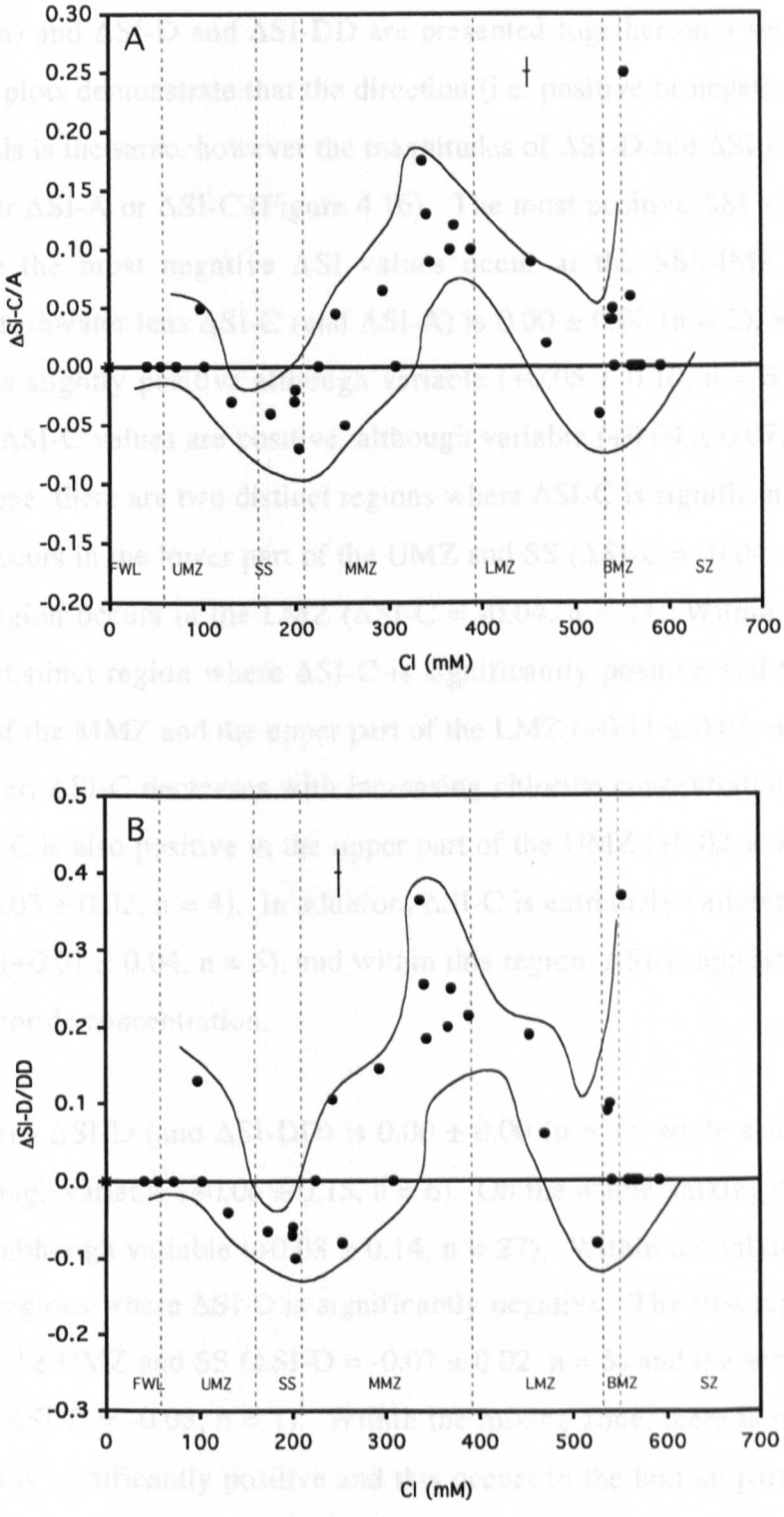

Figure 4.16 Variations in Δsaturation indices with respect to calcite and aragonite (A) and dolomite and disordered dolomite (B) against chloride throughout the mixing zone of Mayan Blue cave. Δsaturation indices are calculated from the difference between observed and predicted saturation indices. Dotted lines show the locations of the different parts of the water column, including the freshwater lens (FWL), upper mixing zone (UMZ), salinity step (SS), middle mixing zone (MMZ), lower mixing zone (LMZ), basal mixing zone (BMZ) and saline zone (SZ). Solid black line marks ΔSI = 0. Crosses are representative analytical uncertainties (±1σ).

Likewise, ΔSI-D = ΔSI-DD. Thus, ΔSI-C and ΔSI-A are presented together on one plot (Figure 4.16.a) and ΔSI-D and ΔSI-DD are presented together on a second plot (Figure 4.16.b). ΔSI plots demonstrate that the direction (i.e. positive or negative) of ΔSI change for all minerals is the same, however the magnitudes of ΔSI-D and ΔSI-DD are larger than those of either ΔSI-A or ΔSI-C (Figure 4.16). The most positive ΔSI values occur in the MMZ, while the most negative ΔSI values occur at the SS/MMZ and LMZ/BMZ interfaces. Freshwater lens ΔSI-C (and ΔSI-A) is 0.00 ± 0.00 (n = 2), while mean saline zone ΔSI-C is slightly positive although variable (+0.05 ± 0.10, n = 6). On the whole, mixing zone ΔSI-C values are positive, although variable (+0.04 ± 0.07, n = 27). Within the mixing zone, there are two distinct regions where ΔSI-C is significantly negative. The first region occurs in the lower part of the UMZ and SS (ΔSI-C = -0.04 ± 0.02, n = 5) and the second region occurs in the LMZ (ΔSI-C = -0.04, n = 1). Within the mixing zone, there is one distinct region where ΔSI-C is significantly positive and this occurs in the bottom part of the MMZ and the upper part of the LMZ (+0.11 ± 0.05, n = 9). Within the LMZ, however, ΔSI-C decreases with increasing chloride concentration. Although very variable, ΔSI-C is also positive in the upper part of the UMZ (+0.02 ± 0.03, n = 3) and in the BMZ (+0.03 ± 0.02, n = 4). In addition, ΔSI-C is extremely variable in the upper part of the MMZ (+0.01 ± 0.04, n = 5), and within this region, ΔSI-C appears to increase with increasing chloride concentration.

Freshwater lens ΔSI-D (and ΔSI-DD) is 0.00 ± 0.00 (n = 2), while saline zone ΔSI-D is positive although variable (+0.06 ± 0.15, n = 6). On the whole, mixing zone ΔSI-D values are positive, although variable (+0.08 ± 0.14, n = 27). Within the mixing zone, there are two distinct regions where ΔSI-D is significantly negative. The first region occurs in the lower part of the UMZ and SS (ΔSI-D = -0.07 ± 0.02, n = 5) and the second region occurs in the LMZ (ΔSI-D = -0.08, n = 1). Within the mixing zone, there is one distinct region where DSI-D is significantly positive and this occurs in the bottom part of the MMZ and the upper part of the LMZ (+0.23 ± 0.09, n = 9). Within the LMZ, however, ΔSI-D decreases with increasing chloride concentration. Although very variable, ΔSI-D is also positive in the upper part of the UMZ (+0.04 ± 0.08, n = 3) and in the BMZ (+0.07 ± 0.05, n = 4). In addition, ΔSI-D is extremely variable in the upper part of the MMZ (+0.03 ± 0.09, n = 5), and within this region, ΔSI-D appears to increase with increasing chloride concentration.

4.4.5.2 Differences between observed and predicted pCO_2 (ΔpCO_2)

Freshwater lens ΔpCO_2 is negative (–0.15 ± 0.01%, n=2) (Figure 4.17). ΔpCO_2 values in the saline zone are variable, although the mean is not significantly different from zero (+0.01 ± 0.18%, n = 6). Mixing zone ΔpCO_2 values are variable, although the mean is positive (+0.06 ± 0.04%, n = 27). Within the mixing zone, there are two distinct regions where ΔpCO_2 is significantly positive, indicating a gain in pCO_2 compared to that expected from fresh-salt water mixing. The first positive ΔpCO_2 region occurs in the lower part of the UMZ and in the SS (ΔpCO_2 = -0.88 ± 0.27%, n = 5) and the maximum mixing zone ΔpCO_2 occurs at the SS/MMZ interface (where ΔpCO_2 = +0.98 ± 0.17%, n =4). The second region of positive ΔpCO_2 values occurs at the LMZ/BMZ interface (ΔpCO_2 = 0.27%, n = 1). In addition, ΔpCO_2 is generally positive but variable in the upper part of the MMZ (+0.31 ± 0.41%, n = 5), but within this region, ΔpCO_2 appears to decrease with increasing chloride concentration (Figure 4.17). Also, within the mixing zone, there are three distinct regions where ΔpCO_2 is significantly negative (implying a loss of pCO_2). These occur in the top part of the UMZ (-0.31 ± 0.05%, n = 3), in the bottom part of the MMZ and the upper part of the LMZ (-0.35 ± 0.12%, n = 9) and ΔpCO_2 is also negative in the BMZ (-0.16 ± 0.04%, n = 4).

4.4.6 Aqueous Geochemistry Discussion

Table 4.4 summarises the main sources and sinks expected for calcium and magnesium in carbonate groundwaters. The main processes expected to be occurring in the mixing zone waters are the enhancement of calcium carbonate ($CaCO_3$) dissolution (Bölgi, 1964; Runnels, 1969; Plummer, 1975) and possibly replacement dolomitisation (Hanshaw et al., 1971; Badiozamani, 1973). If $CaCO_3$ dissolution has occurred, an increase in calcium and alkalinity is expected. Both HCO_3/Cl and Ca/Cl ratios are explained by mixing between fresh and saline end-members (Figure 4.12), however the primary source of these ions is the freshwater lens. A similar result was obtained for Sr/Cl, indicating the dissolution of aragonite may be occurring in fresher waters. In addition, Mg/Cl ratios increase with decreasing chloride concentration, suggesting HMC or dolomite dissolution has occurred in the fresher waters. Na/Cl and SO_4/Cl are behaving conservatively and are not dynamic components of the system.

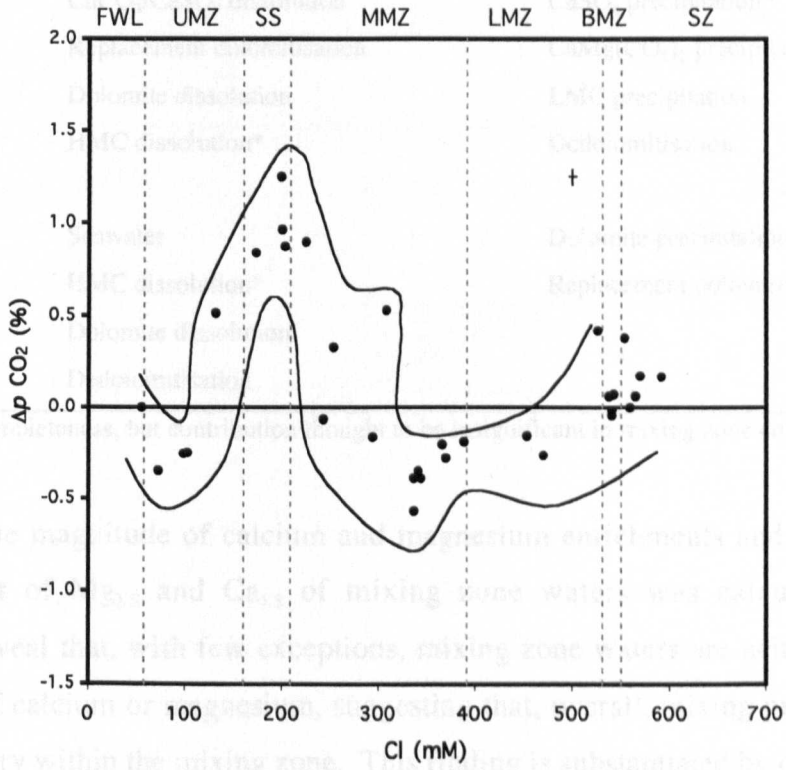

Figure 4.17 Variations in $\Delta p\ CO_2$ against chloride throughout the mixing zone of Mayan Blue cave. $\Delta p\ CO_2$ is calculated from the difference between observed and predicted $p\ CO_2$. Dotted lines show the locations of the different parts of the water column, including the freshwater lens (FWL), upper mixing zone (UMZ), salinity step (SS), middle mixing zone (MMZ), lower mixing zone (LMZ), basal mixing zone (BMZ) and saline zone (SZ). Crosses are representative analytical uncertainties ($\pm 1\sigma$).

Table 4.4 Summary of the main sources and sinks for calcium and magnesium in carbonate groundwaters (LMC = low magnesium calcite, HMC = high magnesium calcite)

Ion	Possible Sources	Possible Sinks
Calcium	Seawater	$CaCO_3$ precipitation
	$CaCO_3/CaSO_4$ dissolution	$CaSO_4$ precipitation*
	Replacement dolomitisation	$CaMg(CO_3)_2$ precipitation
	Dolomite dissolution	LMC precipitation
	HMC dissolution*	Dedolomitisation
Magnesium	Seawater	Dolomite precipitation
	HMC dissolution*	Replacement dolomitisation
	Dolomite dissolution	
	Dedolomitisation	

*Included for completeness, but contribution thought to be insignificant in mixing zone environment

To calculate the magnitude of calcium and magnesium enrichments and depletions, the excess amount of Mg_{xs} and Ca_{xs} of mixing zone waters was calculated. Excess calculations reveal that, with few exceptions, mixing zone waters are neither enriched in nor depleted of calcium or magnesium, suggesting that, overall, mixing processes control the ion chemistry within the mixing zone. This finding is substantiated by other work from the Yucatan Peninsula mixing zone waters (Ford, 1985; Stoessell et al., 1989). Only two samples (occurring at the UMZ/SS interface and in the lower MMZ) are significantly enriched in calcium. In addition, one sample is depleted of calcium (upper MMZ) and one sample (in the lower part of the MMZ) is significantly enriched in magnesium.

Despite generally insignificant depletions and enrichments, a good positive relationship between Ca_{xs} and Mg_{xs} may exist in the mixing zone waters ($r = +0.54$, $P = 0.001$, d.f. = 31) (Figure 4.18). A better correlation is found when MMZ waters are considered alone ($r = +0.84$, $P = 0.001$, d.f. = 10) (Figure 4.18). In the MMZ, the Ca_{xs}:Mg_{xs} ratio is ~1:3, implying that dolomite dissolution may have occurred in addition to calcite dissolution.

Overall, the trend between Ca_{xs} and the saturation indices of both calcite and disordered dolomite in the MMZ is a weakly positive one (Figure 4.19 A and B), suggesting increases in Ca_{xs} (from dissolution reactions) may be driving increases in saturation state. Due to the analytical uncertainties associated with Mg_{xs} calculations, no patterns are easily discernable when examining plots of Mg_{xs} against saturation index (Figure 4.19 C and D).

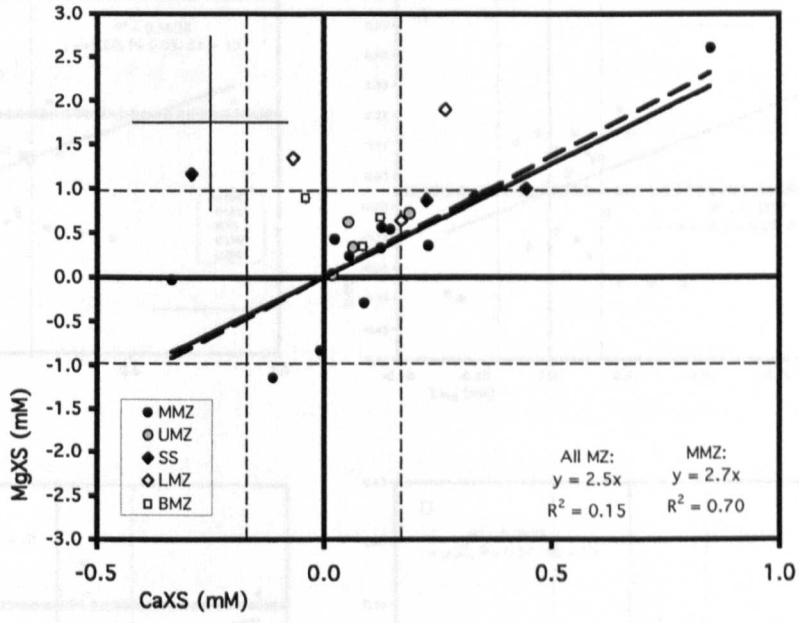

Figure 4.18 Cross plot showing Ca_{xs} against Mg_{xs} for Mayan Blue mixing zone samples. Regression lines are shown for all mixing zone samples (solid) and for middle mixing zone (MMZ) samples only (dashed line). Thin dashed lines show concentrations significantly greater or less than zero (1σ) and crosses are representative analytical uncertainties ($\pm 1\sigma$).

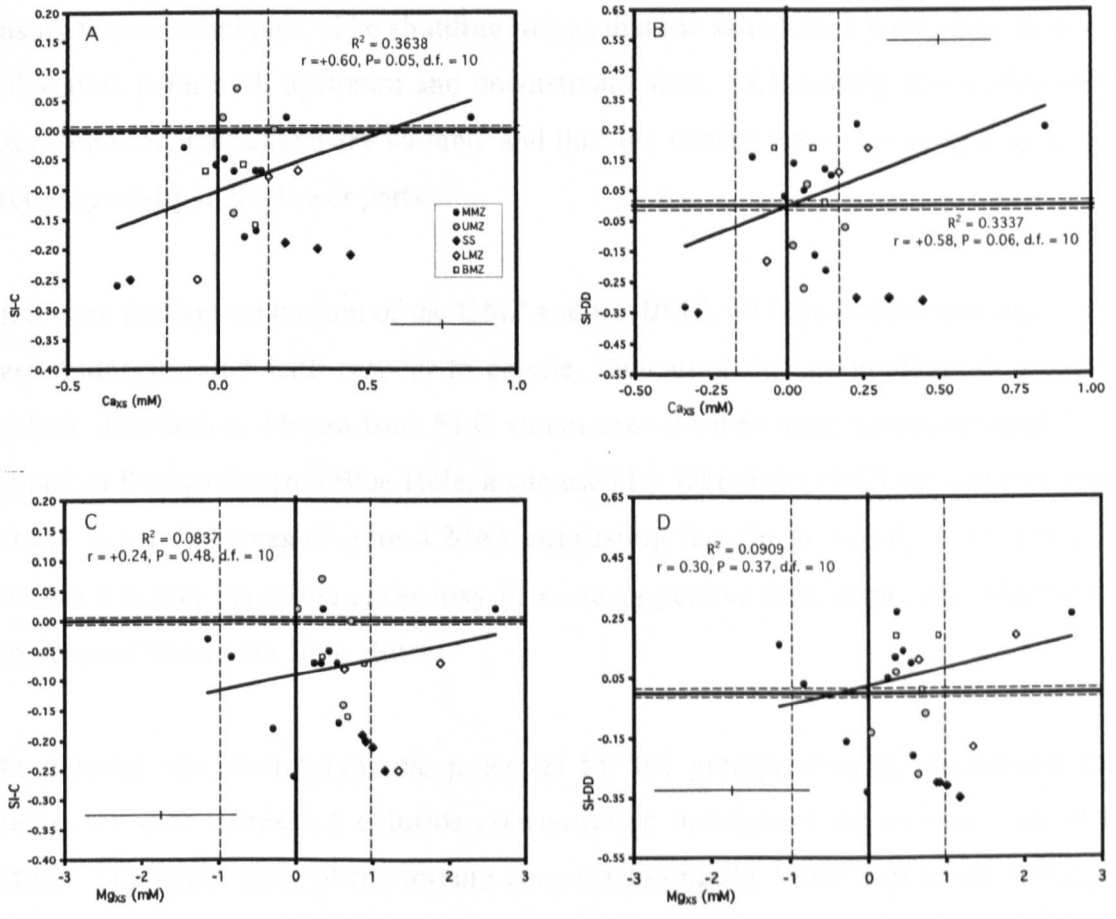

Figure 4.19 Saturation indices against XS plots for Mayan Blue mixing zone waters: A) Ca_{XS} vs SI-C, B) Ca_{XS} vs SI-DD, C) Mg_{XS} vs SI-C and D) Mg_{XS} vs SI-DD. Samples are divided into water type: upper mixing zone (UMZ), salinity step (SS), middle mixing zone (MMZ), lower mixing zone (LMZ) and basal mixing zone (BMZ). Line of best fit and statistics pertain to MMZ samples. Thin dashed lines show concentrations significantly greater or less than zero ($\pm 1\sigma$) and crosses ae representative analytical uncertainties ($\pm 1\sigma$).

It should be noted that the source of the freshwater lens end-member is located further inland, while the source of the saline zone end-member is probably closer to the coast compared to the location of Mayan Blue. Although upstream end-members were considered for the predictive mixing, it is virtually impossible to estimate how far upstream the end-members should be taken. Thus, local waters were used as end-members. In addition, the saline zone chemistry is probably variable because of shuttling observed using tracer techniques. The shuttling means that the saline zone water may be comprised of waters from both upstream and downstream sites. Ultimately, this makes the saline zone end-member chemistry variable and thus the mixing zone chemistry may be variable too, especially in the lower parts.

Between the bottom portion of the UMZ and the BMZ, all Mayan Blue mixing zone waters are undersaturated with respect to calcite, indicating the thermodynamic potential for calcite dissolution. Mayan Blue SI-C values are ~2 times more undersaturated than those found in Evelyn Green's Blue Hole, a site used by Whitaker (1992) for a mixing zone case study in the Bahamas (Figure 4.20A), suggesting that the fresh-salt water mixing zones within Yucatan Peninsula caves may be more aggressive with respect to calcite compared to those of Bahamian Blue Holes.

In general, the thermodynamic potential for the precipitation of disordered dolomite increases with increasing chloride concentration throughout the mixing zone of Mayan Blue. The upper parts of the mixing zone (including the lower part of the UMZ, SS and upper part of the MMZ) are undersaturated with respect to disordered dolomite, indicating that dolomite dissolution (rather than precipitation) is favoured in these waters. Below the MMZ, all mixing zone waters except one are saturated or supersaturated with respect to disordered dolomite, providing the potential for dolomite precipitation. The exception (where SI-DD = -0.18) occurs at the LMZ/BMZ interface. These findings are very different from those found in Evelyn Green's Blue Hole, where all mixing zone waters are supersaturated with respect to disordered dolomite (Whitaker, 1992). This indicates that the thermodynamic drive for mixing zone dolomitisation in Bahamian Blue Holes may exceed that found in the Yucatan Peninsula caves (Figure 4.20B).

The Yucatan Peninsula groundwaters may be more aggressive with respect to carbonate minerals due to a greater predominance of oxidation reactions compared to the Bahamas,

where sulfate reduction may dominate (Bottrell et al., 1991; Whitaker, 1992). Heterotrophy and sulfur oxidation (supported by relatively high oxygen concentrations in the Yucatan Peninsula, compared to the Bahamas, Figure 4.20C) produce acidity, which increases pCO_2 and drives carbonate mineral undersaturation.

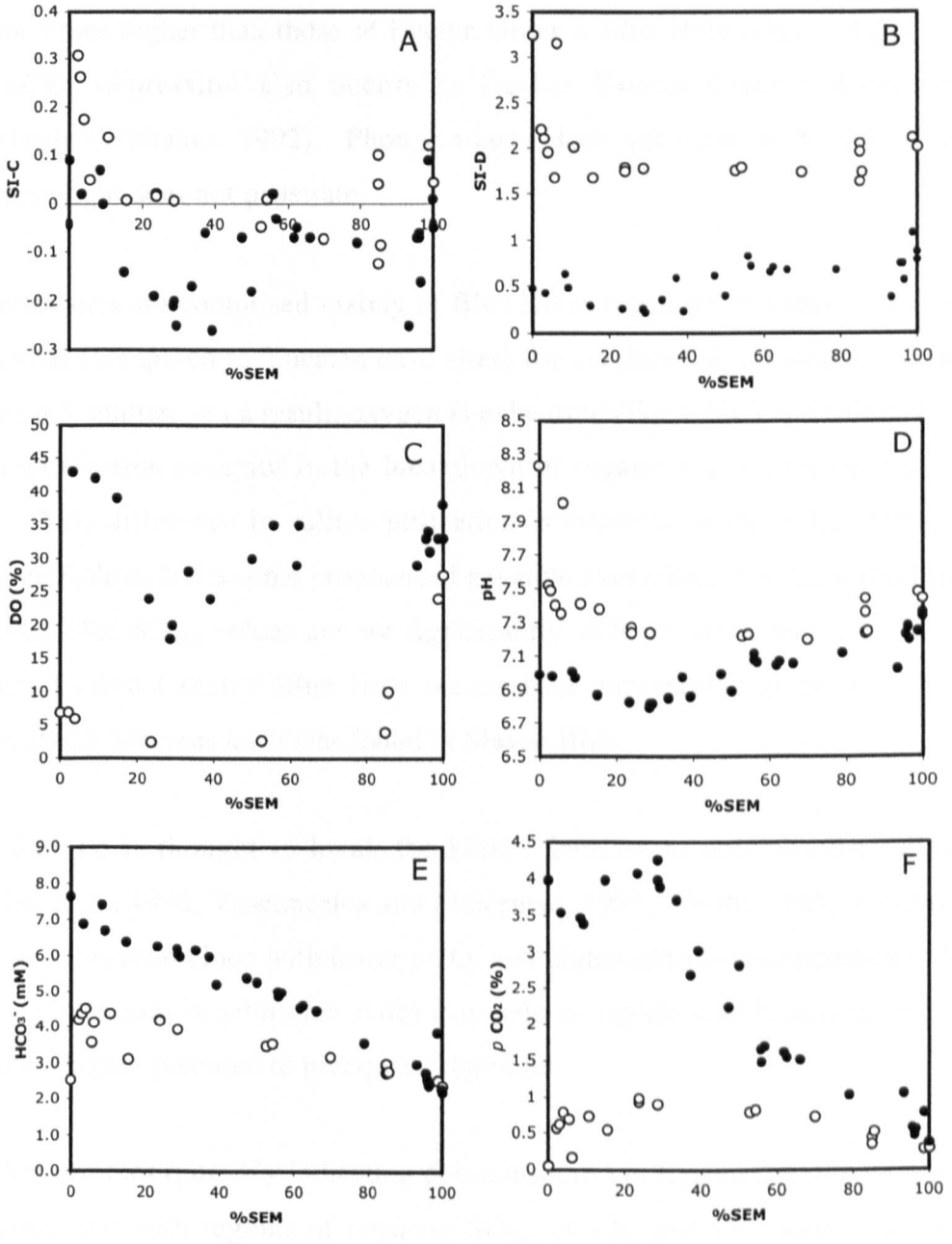

Figure 4.20 A comparison of carbonate chemistry between Mayan Blue (Yucatan Peninsula, closed circles, this study) and Evelyn Green's Blue Hole (Bahamas, open circles, data from Whitaker, 1992). Plots show changes in SI-C (A), SI-D (B), Dissolved Oxygen (C), pH (D), HCO_3^- (E) and $p\ CO_2$ (F) with % saline end-member (%SEM).

Evidence for greater acidity production in Mayan Blue is supported by the pH data (Figure 4.20D), where pH values are much lower than Evelyn Green values (where pH does not fall below 7.0), particularly in fresher waters.

This low pH, combined with higher HCO_3^- concentrations (Figure 4.20E) in Mayan Blue (presumably due to large amounts of prior carbonate dissolution) result in pCO_2 values almost four times higher than those of Evelyn Green's Blue Hole (Figure 4.20F). Some (~0.2%) pCO_2 depression also occurs in fresher Evelyn Green's waters due to photosynthesis (Whitaker, 1992). Photosynthesis does not occur in Mayan Blue cave waters, where light does not penetrate.

The Bahamas sites are comprised mainly of Blue Holes (open pit cenotes), where there is more potential (compared to Yucatan cave sites) for continual direct loading of surface-derived organic matter. As a result, oxygen is exhausted (Fig 4.20C) and sulfate becomes the preferred electron acceptor in the breakdown of organic matter, resulting in sulfate reduction. This difference in sulfate utilization is apparent in the SO_{4XS} data; Evelyn Green's Blue Hole exhibits some pronounced negative excursions in SO_{4XS} concentrations, while Mayan Blue SO_{4XS} values are not significantly different from zero (Figure 4.21A). In addition, Evelyn Green's Blue Hole waters have measurable quantities of sulfide (Whitaker, 1992), whereas none was found in Mayan Blue.

Sulfate reduction is thought to break the kinetic barriers to dolomite formation (e.g. Vasconcelos et al., 1995; Vasconcelos and McKenzie, 1997; Wright, 1999; Warthmann et al., 2000) and this (combined with lower pCO_2 and higher pH values compared to Mayan Blue, driving increases in saturation state) may help to explain why Bahamian Blue holes demonstrate a higher potential to precipitate dolomite.

Depleted Mg_{XS} values (possibly indicating dolomitisation) in Evelyn Green's Blue Hole do indeed correspond with regions of negative SO_{4XS} at ~20 and 85% saline end-member (Whitaker, 1992; Figures 4.21A and C). In Mayan Blue, the most depleted Mg_{XS} values occur between 40 and 60% saline end-member (% S-EM). Despite these differences, the mean Mg_{XS} concentrations of the two sites are not significantly different from one another ($P>0.05$, type 3 two-tailed t-test).

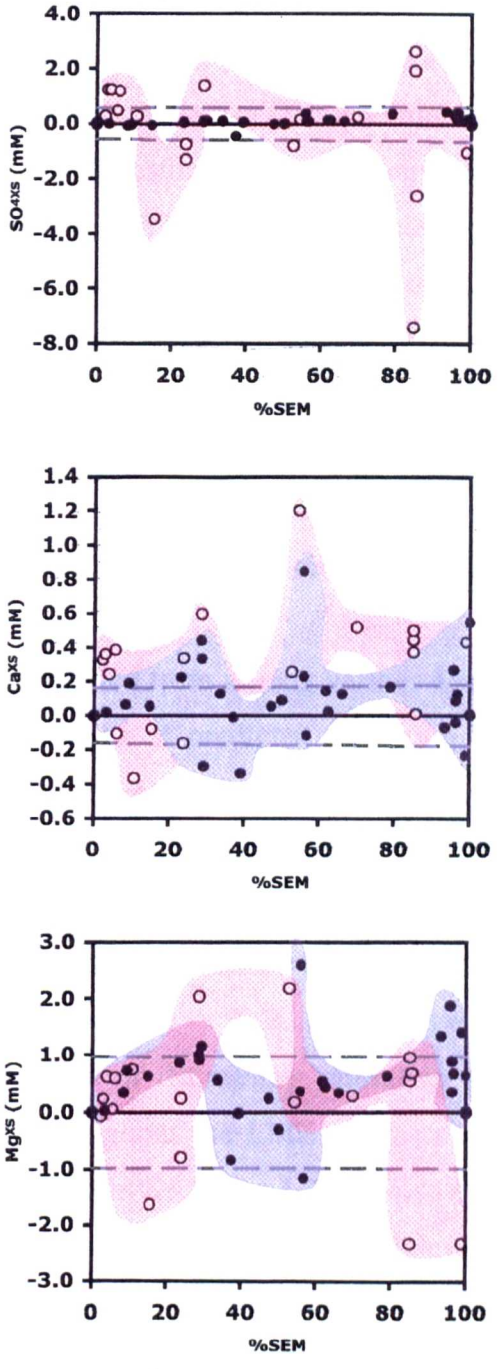

Figure 4.21 A comparison of SO_{4XS} (A), Ca_{XS} (B) and Mg_{XS} (C) between Mayan Blue (Yucatan Peninsula, closed circles with grey outline, this study) and Evelyn Green's Blue Hole (Bahamas, open circles with red outline, data from Whitaker, 1992).

Ca_{XS} concentrations from both sites are relatively similar (P = 0.05, type 2 two tailed t-test) and plots of % S-EM against Ca_{XS} show similar patterns (Figure 4.21B), with possible peaks occurring in both sites at ~30 and 55% S-EM. More detailed comparisons are difficult to make given differences in sampling frequencies.

Potential for Dolomitisation in Mayan Blue

The saturation indices of the Mayan Blue MMZ, LMZ and BMZ (where SI-C < 0, SI-DD > 0) indicate that these waters have the potential for Dorag dolomitisation (Hanshaw et al., 1971; Badiozamani, 1973). Assuming that Dorag dolomitisation is possible, the diagenetic potential of these waters can be estimated by geochemical modeling under closed system conditions. Within the MMZ, LMZ and BMZ, the most aggressive waters (at ~240, 470, 540 mM Cl-, respectively) are capable of dissolving 6.20 ± 1.10 x 10^{-3} g calcite to reach equilibrium with respect to calcite, increasing Ca_{xs} of the water by only 0.062 ± 0.011 mM. If these solutions are then driven to equilibrium with respect to disordered dolomite, 7.37 ± 1.84 x 10^{-3} g dolomite will be formed, producing a magnesium depletion of 0.040 ± 0.10 mM, accompanied by a reduction of Ca_{xs} of 0.038 ± 0.07 mM. These values are within the analytical uncertainties associated with Mg_{xs} and Ca_{xs} calculations.

Saturation indices were predicted from mixing various Mayan Blue fresh and saline end-members. From these, a range of predicted saturation indices can be calculated and compared with field data. There are two regions within the Mayan Blue mixing zone where undersaturation is significantly greater than that predicted from mixing:

a) the bottom part of the UMZ, the SS and the upper part of the MMZ, with the greatest undersaturation at the SS/MMZ interface
b) the LMZ/BMZ interface - N.B. this observation is based on one sample, however, the trend of decreasing saturation state with increasing chloride concentration throughout the LMZ suggests it is real. The validity of this sample is evaluated in Section 4.4.7.6, which examines the *in situ* dissolution rates of carbonate tablets throughout the mixing zone.

The coincidence of these regions with positive ΔpCO_2 values (pCO_2 up to 1.5 times greater than predicted from mixing, Figure 4.17) strongly suggests that pCO_2 inputs are not just maintaining, but are in fact driving, undersaturation beyond that predicted from fresh-salt water mixing. ΔpCO_2 increases are probably the result of heterotrophic bacterial activity, where carbon dioxide is produced (and oxygen is consumed) during aerobic respiration, which involves the oxidation of organic matter (Equation 4.3).

$$CH_2O + O_2 \rightarrow CO_2 + H_2O \qquad (4.3)$$

This is supported by a significant negative relationship between dissolved oxygen and pCO_2 within the mixing zone waters ($r = -0.80$, $P < 0.001$, d.f. = 19) (Figure 4.22). Increases in carbon dioxide will lead to increases in carbonic acid production (Equation 4.4), which will ultimately lower the pH of the water.

$$CO_2 + H_2O \rightarrow H_2CO_3 \qquad (4.4)$$

Although not directly linked, there is a significant positive relationship ($r = +0.81$, $P = 0.00001$, d.f. = 19) between dissolved oxygen and pH, confirming that as oxygen is consumed, acidity is produced (Figure 4.10). pCO_2 and pH cannot be directly compared because pH is a major control on (and is used to calculate) pCO_2.

The maintenance of undersaturation beyond that predicted from linear mixing indicates that geochemical evolution is proceeding under open (rather than closed) system conditions with the continual renewal of dissolution potential. Undersaturation appears to be maintained by the local (*in situ*?) production of CO_2 and under open system conditions, rates of diagenesis will be controlled by the rate at which CO_2 (and subsequent undersaturation) is generated and by the residence time of the waters within a given site. Regions where undersaturation is maintained may indicate where bacterial activity is greatest. These regions appear to coincide with areas where waters of a high conductivity gradient meet waters of a low conductivity gradient (Figure 4.6). Changes in conductivity (density) gradients may act to 'trap' bacteria and/or particulate (including organic) matter and could explain why their activity may appear greatest there. Oxygen consumption rates and the role bacteria play in influencing geochemistry and water-rock interactions within the fresh-salt water mixing zone are considered further in Section 4.4.8.

The double peak in undersaturation in the Mayan Blue mixing zone is the first to be reported for the Yucatan Peninsula, but has been reported elsewhere. A double peak saturation curve occurs in Evelyn Green's blue hole in the Bahamas, where "two pronounced maxima of unexplained reduced saturation" occur in the UMZ and BMZ (Whitaker, 1992). Both of these regions coincided with areas of relatively low salinity gradients compared to surrounding waters, which also is a similar finding to the present study.

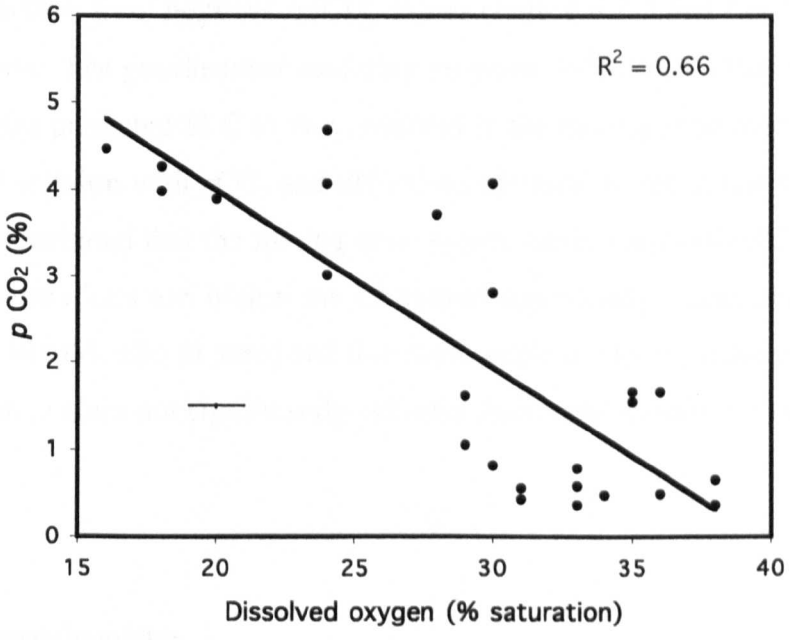

Figure 4.22 *p* CO_2 against dissolved oxygen for mixing zone waters from Mayan Blue. Cross shows representative analytical uncertainties (±1σ).

There are also three regions in the Mayan Blue mixing zone where saturation indices are greater than those predicted from fresh-salt water mixing (Figure 4.16):

a) The top part of the UMZ (one sample)
b) The lower part of the MMZ and upper part of the LMZ (ten samples)
c) The BMZ (three samples)

In addition, these waters have negative ΔpCO_2 values (Figure 4.17) that can be explained by calcite dissolution. The geochemical modeling program, PHREEQC (Parkhurst, 1995), was used to bring the predicted SI-C to that observed in the mixing zone waters, resulting in a new predicted solution with pCO_2 and pH values identical to the actual values. This modeling also demonstrated that the mixing zone waters have dissolved 0.02 – 0.22 mM Ca^{2+}. These concentrations are within the analytical uncertainty associated with Ca_{XS} calculations (= ±0.34 mM, ±2σ of zero) and this could explain why the majority of mixing zone waters had Ca_{XS} values not significantly different from zero, despite the occurrence of $CaCO_3$ dissolution.

4.4.7 Wall rock geochemistry

4.4.7.1 Wall rock observations

The gross morphology of the wall-rock observed in the cave is summarised in Figure 4.23. There appears to be a systematic variation in surface morphology and staining of the cave walls that may be related to the position of the mixing zone (Figure 4.23). In the freshwater lens, from ~0.5 to 2 m below the cave ceiling, the wall rock is crumbly, brittle and 'powdery' (a residue was left on fingers/wetsuits after touching the wall rock). This rock displayed intense 'swiss cheese' fretting (described by Back et al., 1979). Below this (but still in the freshwater lens), the wall-rock becomes harder, but more 'pockets' appear to have developed within the rock. The wall-rock in contact with the bottom ~1 m of the freshwater lens and top of the UMZ is weathered, displaying 'swiss cheese' fretting. The rock is crumby and contains numerous 'pockets'. A decrease in the amount of pocketing occurs at the conductivity inflection point in the UMZ.

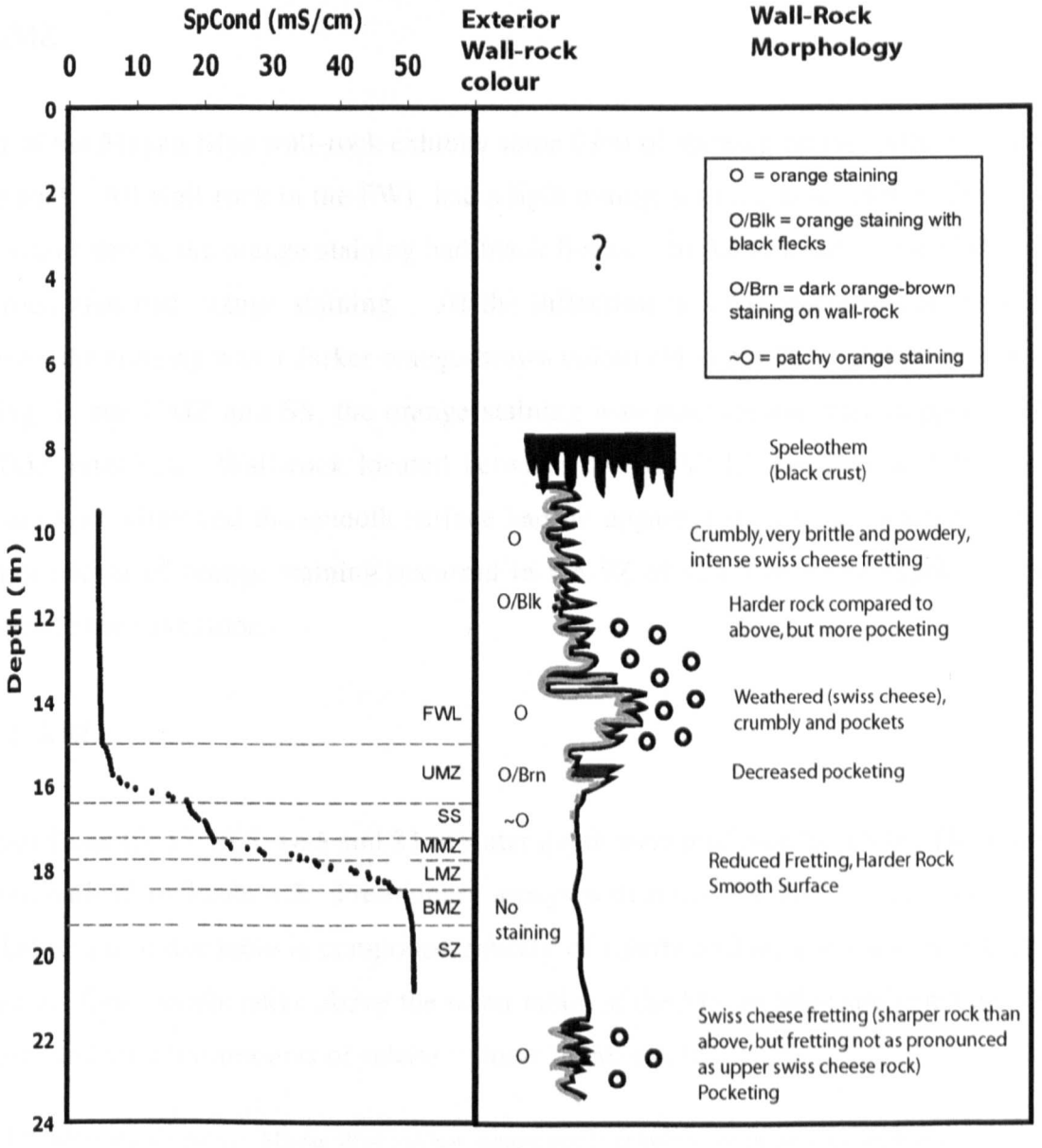

Figure 4.23 Gross wall-rock morphology within the cave at Mayan Blue. Observations from 'B Tunnel' (Stal Dome site). The floor of the cave occurs at ~24 m water depth. Specific conductance (SpCond) depth profile shows the location of the various water types, including the freshwater lens (FWL), upper mixing zone (UMZ), salinity step (SS), middle mixing zone (MMZ), lower mixing zone (LMZ), basal mixing zone (BMZ) and saline zone (SZ).

The wall-rock is relatively smooth throughout the SS, MMZ, LMZ, BMZ and top part of the SZ. This rock is harder and there is very little fretting. A second zone of 'swiss cheese' fretting was observed in the SZ, at ~21.5 – 23 m water depth. This rock was sharper, but the swiss cheese fretting was less pronounced than that observed in the FWL and UMZ.

Much of the Mayan Blue wall-rock exhibits some form of staining on the exterior surface of the rock. All wall-rock in the FWL had a light orange staining associated with it. At 12 m water depth, the orange staining had black flecks. In the top part of the UMZ, the wall-rock also had orange staining. At the inflection in UMZ specific conductance, however, the staining was a darker orange-brown colour (Figure 4.23). Below the brown staining, in the UMZ and SS, the orange staining was patchier and this stopped at the SS/MMZ interface. Wall-rock located between the SS/MMZ interface and BMZ/SZ interface was white and the smooth surface had no apparent staining associated with it. Another region of orange staining occurred in the SZ at ~21.5 m water depth and this extended to the cave floor.

4.4.7.2 XRD

Samples from 12, 17-17.5, 18.5 and 23 m water depth were analysed by XRD. The results are summarised in Table 4.5. Preliminary analyses demonstrate that Mayan Blue wall-rock below the water table is comprised entirely of calcite and no aragonite or dolomite was found. One sample taken above the water table at the Mayan Blue site contained 0% dolomite and variable amounts of calcite ('Unsat.', Table 4.5).

Table 4.5 XRD results for one Mayan Blue surface sample and four submerged wall-rock samples.

		Exterior Sample (5 mm)			Interior Sample		
Depth (m)	Water Type	Aragonite (%)	Calcite (%)	Dolomite (%)	Aragonite (%)	Calcite (%)	Dolomite (%)
	Unsat.	7.6	92.4	0	12.3	87.7	0
12	FWL	0	100	0	0	100	0
17-17.5	SS-MMZ	0	100	0	0	100	0
18.5	LMZ-BMZ	0	100	0	0	100	0
23	SZ	0	100	0	0	100	0
	fe (%)	8.0	2.0	7.5	-	2.0	7.5

4.4.7.3 Acid Digestion

Only three Mayan Blue cave wall-rock samples were analysed by ICP-AES following acid digestion: 1) freshwater lens (12 m water depth) 2) mixing zone (17.5 m water depth) 3) saline zone (21 m water depth). The results are summarised in Table 4.6.

Table 4.6 Acid Digestion Results from Mayan Blue Wall-Rock samples

Location	CaO (%)	MgO (%)	SrO (%)
Freshwater lens	57.1	0.34	0.09
Mixing Zone	50.9	0.58	0.08
Saline Zone	54.8	0.37	0.09
Analytical Uncertainty	± 2.5	± 0.03	± 0.01

The results indicate that the rocks are calcitic, with small amounts of magnesium (0.34 to 0.58 % MgO), with the highest magnesium content in the mixing zone sample. Strontium concentrations were an order of magnitude lower than magnesium.

4.4.7.4 Thin Section Analysis

Thin sections of Mayan Blue wall-rock from five depths (surface, 12 m, 16.8 m, 17.5 m, 18.5 m, 23 m) stained with Alazarin Red S, suggest that there is no dolomite within the Mayan Blue wall-rock exposed to the present-day mixing zone (Goodwin, pers. comm., 2002). Also, no dolomite was found in the Mayan Blue wall-rock exposed to fresh or saline groundwaters. In addition, no dolomite was found in the mixing zone of another (coastal) site (Chapter 5).

4.4.7.5 Carbon, Hydrogen and Nitrogen (C,H,N) Analyses of Wall Rock

Preliminary results show that most wall-rock exposed to groundwater within Mayan Blue does not contain significant amounts of organic carbon. Of the eight wall-rock samples analysed for C,H,N, only one had a significant amount of organic carbon. This sample was a cutting from the outer 5 mm of the rock at 17.5 m water depth (MMZ) at Mayan Blue and it contained 0.40 ± 0.01% organic carbon. The interior of this rock sample contained 0.00 % organic carbon. No hydrogen or nitrogen was found in the rock samples.

4.4.7.6 *in situ* "Pill" Dissolution Experiment

15 sets of dolomite, aragonite and calcite pills were hung throughout the water column of Mayan Blue for 46 months. From these, dissolution rates per unit surface area ($g/m^2/year$) were calculated. All pills lost weight, suggesting that all pills (and wall-rock) at all depths were at some point subjected to water aggressive with respect to all three carbonate species.

Aragonite Dissolution

Aragonite dissolution rates in the freshwater lens and saline zone were 116 (n = 1) and 103 ± 11 (n = 2) $g/m^2/yr$, respectively. These rates are not dissimilar to the rates measured throughout the mixing zone (118 ± 16 $g/m^2/yr$, n = 11). The rate of aragonite dissolution in the mixing zone was variable, although aragonite dissolution may decrease with increasing depth. The greatest amount of aragonite dissolution (149 $g/m^2/yr$) occurred in the MMZ, near the MMZ/LMZ interface, while the least dissolution occurred in the BMZ (85.9 $g/m^2/yr$) (Figure 4.24). Examining the pills under SEM revealed that most aragonite dissolution occurred preferentially along veins within the pill and variability in veins may account for the observed scatter in the data.

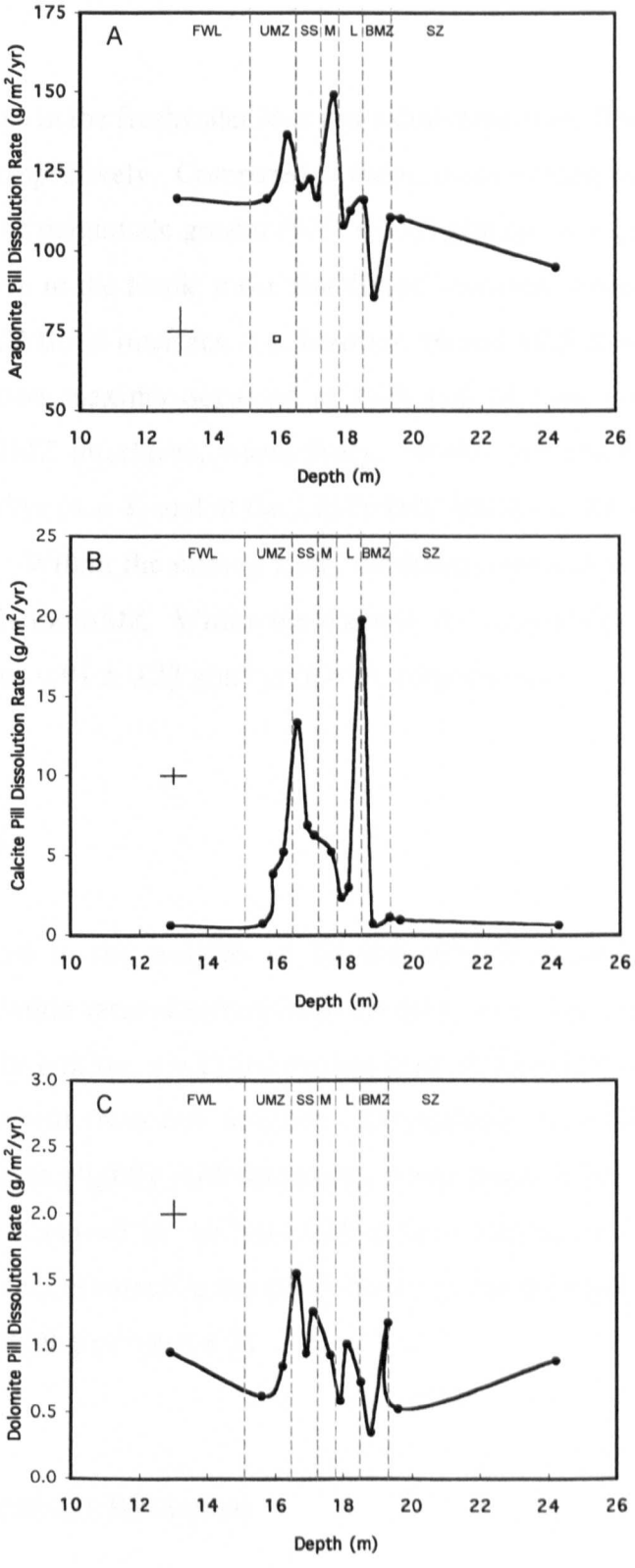

Figure 4.24 Aragonite (A), Calcite (B) and Dolomite (C) dissolution rates against depth throughout the water column in Mayan Blue cave. Dashed lines represent the average location of the different water types within the water column, including the freshwater lens (FWL), upper mixing zone (UMZ), salinity step (SS), middle mixing zone (M), lower mixing zone (L), basal mixing zone (BMZ) and saline zone (SZ). The aragonite plot includes one outlier (represented by white square) - discussed in text. Analytical uncertainties (±1 σ) are represented by the crosses (and the uncertainty associated with depth includes that due to seasonal variations with respect to the position of the mixing zone and its sub-zones).

Calcite Dissolution

Calcite dissolution rates in the freshwater lens and saline zone were 0.62 (n = 1) and 0.79 ± 0.22 (n = 2) g/m^2/yr, respectively. Compared to these, mean mixing zone dissolution rates were almost an order of magnitude greater (5.71 ± 5.65 g/m^2/yr, n = 12). Although all the pills lost weight relative to the blank, most dissolution occurred between the lower part of the UMZ and the LMZ/BMZ interface (i.e. between 16 and 18.5 m water depth) (Figure 4.24). Two dissolution maxima occurred at 16.6 and 18.5 m, corresponding to the UMZ/SS and LMZ/BMZ interfaces, respectively. Within the SS, the dissolution rates were 8.84 ± 3.94 g/m^2/yr (n = 3) and at the LMZ/BMZ interface, the dissolution rate was 19.8 g/m^2/yr (n = 1). Within the mixing zone, minimum dissolution occurred in the top part of the UMZ and in the BMZ. Within these zones, the rates of calcite dissolution were 0.74 g/m^2/yr (n = 1) and 0.91 ± 0.28 g/m^2/yr (n = 2), respectively.

Dolomite Dissolution

Little change occurred in the weights of the dolomite pills over the course of the experiment and dissolution rates obtained from the freshwater lens (0.96 g/m^2/yr, n = 1), saline zone (0.71 ± 0.26 g/m^2/yr, n = 2) and mixing zone (0.91 ± 0.34 g/m^2/yr, n = 11) were not significantly different from one another. Throughout the mixing zone, dolomite dissolution may decrease slightly with increasing water depth (Figure 4.24). Maximum dolomite dissolution occurred in the SS (1.26 ± 0.30 g/m^2/yr, n = 3) and minimum dissolution (0.35 g/m^2/yr) occurred in the BMZ, although the dissolution rates in the BMZ were variable (0.77 ± 0.59 g/m^2/yr, n = 2).

4.4.7.7 Solid Geochemistry Discussion

Wall-rock morphology observations indicate that the 'swiss cheese' morphology often associated with modern mixing zones (e.g Back et al., 1979) is present only in the FWL, UMZ and SZ. The locations of the 'swiss cheese' fretting may indicate where present-day dissolution of cave rock is particularly active (perhaps due to shear zones between waters with different flow rates or directions), or the locations of past mixing zone levels. Within

the mixing zone, orange and orange-brown staining on the surface of the wall-rock was noted in the UMZ and SS only. These colourations may indicate where iron or manganese oxidation is occurring, either abiotically or by bacterial oxidation.

XRD analyses revealed that there was no dolomite in the wall-rock samples associated with the water column at Mayan Blue. In addition, stained thin sections of the same samples showed that the wall-rock is comprised entirely of calcite and that no dolomite was present (Goodwin, pers. comm., 2002). Analysis of acid-digested samples demonstrated that the wall-rock is calcitic, with only small amounts of magnesium (~0.4 % MgO). A study performed by Ford (1985) which examined a profile of core rock samples from Tancah (a site located only a few kilometers north of Mayan Blue), showed that only LMC and aragonite were present in the rocks. Ford (1985) found no evidence of HMC or dolomite in rock samples taken below the vadose zone. Thus, despite the thermodynamic potential for Dorag dolomitisation by mixing zone waters, no significant amounts of (if any) dolomite are present within the wall-rock currently exposed to mixing zone waters. The only substantial amounts of dolomite found in this study were from the saline zone of a coastal site (see Chapter 5). Thus, some doubt is cast on the mixing zone model for dolomitisation (although further detailed analysis of the Mayan Blue rocks would undoubtedly be useful).

In addition, the waters most undersaturated with respect to calcite (bottom of UMZ, SS, top part of MMZ and LMZ/BMZ interface) do not correspond with wall-rock that displays the characteristic 'swiss-cheese' fretting thought to be associated with rock having undergone chemical dissolution in mixed waters. The pill experiment was used to determine where present-day dissolution was occurring. It is important to note that the 'pills' used in this experiment were not comprised of host rock. Thus, the data can only represent relative, rather than actual, rates of dissolution expected from Mayan Blue wall rock.

Throughout the mixing zone, aragonite pills lost the most weight (118 ± 16 $g/m^2/yr$, n = 11), followed by calcite (5.71 ± 5.65 $g/m^2/yr$, n = 12), then dolomite (0.91 ± 0.34 $g/m^2/yr$, n = 11) (Figure 4.24). This sequence reflects the relative solubility of the three minerals. Beyond this, the data obtained from the aragonite pills is difficult to interpret due to variations within and between individual pills and the small number of pills in some zones.

All aragonite pills were veined and dissolution proceeded preferentially along these veins. Thus, the more veins (or the larger the veins) a pill contained, the more likely it was to undergo dissolution. Also, some pills became extremely "powdery" and soft throughout the experiment and although every care was taken to minimise weight loss during transport, inevitably, some 'powder' was left in the sample bags used for transport. In addition, aragonite, being a much less stable mineral than either calcite or dolomite, is much more susceptible to dissolution. As discussed in Section 4.4.3.1, the chemistry at a given chloride concentration is the same, regardless of when the sample is taken, as long as it was taken within the Mayan Blue cave. However, the position and thickness of the mixing zone is variable, depending on the season (Section 4.4.1.1) and, thus, the chloride content and resulting chemistry at a given depth also varied. The pill data reflects the sum effects of the various water types the pill was exposed to throughout the course of the experiment. An aragonite pill, even if exposed to an aggressive water for a fairly short period of time, was much more likely to show the effect of that water than either the calcite or dolomite pills. Aragonite pill dissolution shows no relationship with SI-A (most dissolution occurred in the MMZ, where SI-A is greatest).

Calcite weathering rates, on the other hand, varied systematically throughout the mixing zone (Figure 4.24). The calcite pills' greater hardness compared to aragonite and the fact that they were not veined and that they were much more consistent in their size and shape and structure (i.e. they were much more homogeneous), made their weight change a much more reliable measure of the dissolution/precipitation processes occurring within the mixing zone of Mayan Blue. Although all the pills lost weight relative to the blank, the most dissolution occurred between 16 and 18.5 m water depth. There was a 'double peak' in the dissolution rates and most weight loss occurred in the SS and at the LMZ/BMZ interface. Both of these regions correspond to areas where undersaturation is greatest (and the single negative ΔSI value at the LMZ/BMZ interface is now supported by the pill evidence). Mixing zone calcite pill dissolution was lowest in the bottom part of the MMZ and top part of the LMZ, corresponding to positive ΔSI values and negative ΔpCO_2 values. This suggests that SI-C data can be used to describe the relative diagenetic potential of waters with respect to calcite. In addition, the pill placed in the freshwater lens of Mayan Blue demonstrated very little weight loss compared to the mixing zone pills, despite this being where swiss cheese fretting was greatest according to wall-rock morphology observations.

The dissolution peak occurring in the upper parts of the mixing zone is broader than that occurring at the LMZ/BMZ interface. This may be because the depth of the FWL/UMZ interface is more variable than that between the BMZ and SZ (Section 4.4.1.1). Thus, the pills in the upper part of the mixing zone are subjected to more variable chemistry than the pills at the base of the mixing zone. This may also explain why greatest dissolution appears to be occurring at the LMZ/BMZ interface (i.e the pills there were continually exposed to a more undersaturated water).

All dolomite pills lost weight, suggesting that despite the thermodynamic potential to precipitate disordered dolomite in some mixing zone waters (top part of UMZ, bottom part of MMZ, top part of LMZ and BMZ) dolomite may be dissolving, indicating the K value used in SI-DD calculations may be inaccurate for this setting. However, it is important to note that the dolomite pills were not pure dolomite and most had thin white calcite veins running through them and these may have been preferentially dissolved (as evidenced by SEM). The maximum dissolution (of ~1.5 $g/m^2/yr$) occurred within the SS, coincident with the upper maximum in calcite dissolution (Figure 4.24), which supports the idea that, unfortunately, the data may represent calcite vein dissolution, rather than dolomite dissolution. However, there is some further evidence to support dolomite dissolution: the rate of dolomite dissolution decreases with increasing depth throughout the mixing zone, a pattern expected from the SI-DD data (i.e. saturation state increases with depth).

4.4.8 Geomicrobiology of the Mayan Blue Mixing Zone

4.4.8.1 Microbiological Analyses

On the samples taken for microbiological analyses, acridine orange direct counts (AODC), and Most Probable Number (MPN) analyses (aerobic and anaerobic heterotrophs, sulfur oxidisers, sulfate reducers, iron oxidisers and iron reducers) were performed. In addition, oxygen consumption experiments were carried out on separate samples to estimate the rate of organic carbon utilization and acidity generation throughout the mixing zone, of particular relevance to carbonate dissolution.

Conductivity readings were taken from each sample to confirm its location within the mixing zone and the geomicrobiology data is plotted against conductivity.

Total Counts (AODC)

The total number of bacterial cells in the freshwater lens and saline zone are 8.77 ± 10.35 x 10^3 (n = 3) and 2.84 ± 0.28 x 10^3 (n = 2) cells/ml, respectively. Total counts revealed that bacteria within the mixing zone at Mayan Blue were present in numbers ranging between 4.90 x 10^3 and 1.74 x 10^6 cells/ml ($\bar{x}$ = 1.40 ± 4.03 x 10^5 cells/ml, n = 18) (Table 4.7). Cell counts against conductivity throughout the mixing zone are illustrated in Figure 4.25. Maximum cell counts occur near the MMZ/LMZ interface.

When counting the total numbers of bacteria, the numbers of bacteria in the process of dividing, or having recently divided, were counted. The fraction of the total number of cells that were dividing indicates where the bacteria had the fastest growth rates, and by inference, activity. The data show two peaks of maximum cell division (up to 21% of the total population): one at the interface between the UMZ and SS and the other near the LMZ/BMZ interface (Figure 4.26) (Table 4.7). Within the mixing zone, the least cell division occurred in the lower part of the MMZ and upper part of the LMZ.

Viable Bacteria (MPN)

Populations of bacteria within specific functional groups were measured using MPN (Most Probable Number) techniques (described in Chapter 2). Anaerobic and aerobic heterotrophs as well as sulfate-reducing, iron-reducing and iron-oxidising bacteria MPNs were measured in Spring 2000. MPNs of thiosulfate-oxidising and sulfate-reducing bacteria were measured in Summer 2001.

Heterotophs (Chemoorganotrophs)

All Mayan Blue samples (and all MPN dilutions) tested positive for the presence of both aerobic (HOX) and anaerobic (HAN) heterotrophs, indicating that their minimum concentration within all solutions throughout the freshwater lens, mixing zone and saline zone is 2300 cells/ml.

Table 4.7 Summary of cell counts, dividing cells and DOC throughout the Mayan Blue mixing zone (±1σ).

Water Type	No. cells/ml ($x10^3$)	% Dividing Cells	DOC (mM)
Freshwater Lens	8.77 ± 10.35 (n = 3)	0.52 ± 0.90 (n = 3)	0.61 ± 0.34 (n = 2)
Mean Mixing Zone	140 ± 403 (n = 18)	2.84 ± 4.74 (n = 18)	1.25 ± 1.55 (n = 21)
Upper Mixing Zone	65.6 ± 43.5 (n = 5)	6.13 ± 8.19 (n = 5)	3.19 ± 2.40 (n = 4)
Salinity Step	89.1 ± 117 (n = 2)	4.37 ± 1.91 (n = 5)	0.27 ± 0.25 (n = 3)
Middle Mixing Zone	394 ± 754 (n = 5)	0.73 ± 1.23 (n = 5)	0.77 ± 0.78 (n = 10)
Lower Mixing Zone	6.43 ± 3.72 (n = 5)	1.86 ± 2.28 (n = 5)	1.95 ± 1.69 (n = 2)
Basal Mixing Zone	5.03 (n = 1)	1.26 (n = 1)	0.57 ± 0.01 (n = 2)
Saline Zone	2.84 ± 0.28 (n = 2)	0.74 ± 1.04 (n = 2)	0.49 ± 0.25 (n = 3)

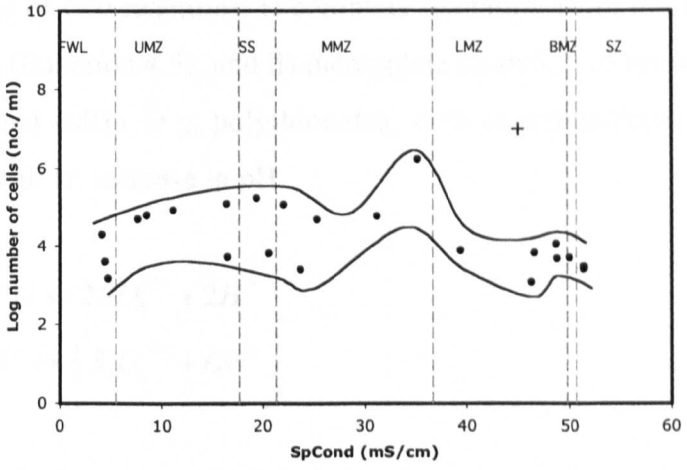

Figure 4.25 Total numbers of bacteria cells against specific conductance throughout the mixing zone of Mayan Blue cave. Dashed grey lines mark the divisions between different water types throughout the water column, including the freshwater lens (FWL), upper mixing zone (UMZ), salinity step (SS), middle mixing zone (MMZ), lower mixing zone (LMZ), basal mixing zone (BMZ) and saline zone (SZ). Analytical uncertainties are represented by the cross (±1σ).

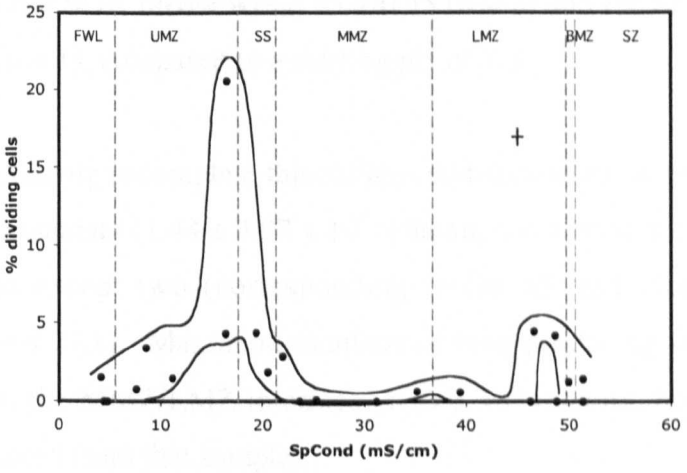

Figure 4.26 Specfic conductance (SpCond) against the percentage of bacteria cells that are undergoing cell division throughout the mixing zone of Mayan Blue cave. Dashed grey lines mark the divisions between different water types throughout the water column, including the freshwater lens (FWL), upper mixing zone (UMZ), salinity step (SS), middle mixing zone (MMZ), lower mixing zone (LMZ), basal mixing zone (BMZ) and saline zone (SZ). Analytical uncertainties are represented by the cross (±1σ).

Thiosulfate-oxidising Bacteria (SOX)

MPN analyses of thiosulfate-oxidising bacteria (SOX), indicated that thiosulfate oxidation proceeded by one of two reactions: i) complete oxidation from thiosulfate to sulfate with acidity produced (Equation 4.5), and ii) incomplete oxidation of thiosulfate to intermediary species of oxidised sulfur (e.g. polythionates, such as tetrathionate), rather than sulfate, (Equation 4.6), with an increase in pH.

$$S_2O_3^{2-} + 2O_2 + H_2O \leftrightarrow 2SO_4^{2-} + 2H^+ \quad (4.5)$$

$$S_2O_3^{2-} + \tfrac{1}{2}O_2 + H^+ \leftrightarrow \tfrac{1}{2}S_4O_6^{2-} + OH^- \quad (4.6)$$

Aerobic acid-producing thiosulfate-oxidising bacteria (capable of complete oxidation to sulfate) were present at all chloride concentrations sampled through the Mayan Blue mixing zone ($1.44 \pm 3.66 \times 10^2$ cells/ml, n = 8), with maximum numbers occurring in the SS (1.05×10^3 cells/ml, representing 0.02% of the total, n = 1) (Figure 4.27A). The final pH of the freshwater SOX media was 3.25 ± 0.33 (n = 2) and the final pH of the saltwater media was 5.35 (n = 1), compared to a starting pH of 7.3.

Aerobic base-producing incomplete thiosulfate-oxidisers were, in general, three orders of magnitude more abundant ($1.44 \pm 3.97 \times 10^5$ cells/ml, n = 8) than the complete oxidisers at all conductivities except two (corresponding to the SS and close to the LMZ/BMZ interface) (Figure 4.27A). Maximum numbers of base-producing incomplete thiosulfate-oxidisers occur at the MMZ/LMZ interface (1.13×10^6 cells/ml, representing 65% of the total bacteria counted from that sample).

Sulfate-Reducing Bacteria (SRB)

Two sets of MPN analyses for sulfate-reducing bacteria (SRB) were performed in the Mayan Blue mixing zone: one in April 2000 and the other in June 2001. In both years, the greatest numbers of SRB were found in the upper parts of the water column (Figure 4.27B) with numbers up to 2.30×10^3 cells/ml in April 2000 and up to 6.6×10^3 cells/ml in June 2001, representing 55 and 13% of the total number of cells counted in the respective samples by AODC.

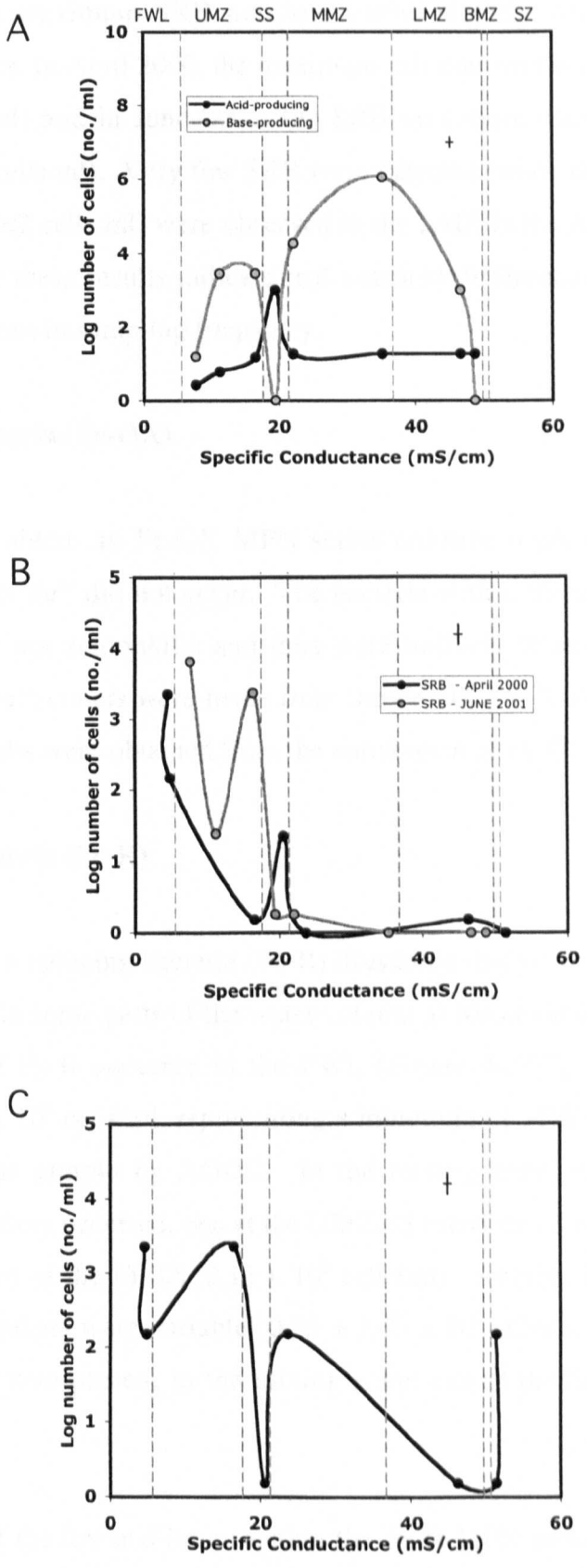

Figure 4.27 Most probable numbers of SOX (A), SRB (B) and Fe-R (C) against specific conductance throughout the mixing zone of Mayan Blue. Dashed grey lines mark the interfaces between the different water types throughout the water column, including the freshwater lens (FWL), upper mixing zone (UMZ), salinity step (SS), middle mixing zone (MMZ), lower mixing zone (LMZ), basal mixing zone (BMZ) and saline zone (SZ). Crosses are representative analytical uncertainties (±1σ).

The location of the maximum SRB numbers varied slightly within the mixing zone between the two years. In April 2000, the maximum cell numbers occurred at the SS/MMZ interface (23 cells/ml) and in June 2001, the SRB maximum occurred at the UMZ/SS interface (2.4 x 10^3 cells/ml). Very few SRB were detected below the SS/MMZ interface, and small numbers (<2 cells/ml) were observed in the LMZ in the April 2000 samples. It is unknown whether these results indicate real seasonal differences or if the differences resulted from variations in sampling frequency.

Iron-Oxidising Bacteria (Fe-OX)

The media used to obtain an Fe-OX MPN series required a pH of 2-3 to ensure that chemical oxidation of Fe^{2+} did not occur. The bacteria within the mixing zone of Mayan Blue were probably not acidophilic and thus were unlikely to survive at such low pH values. Although direct counts were made from the Fe-OX MPN series, no bacteria were found. Thus, no results were obtained from the enrichment of Fe-OX media.

Iron-Reducing Bacteria (Fe-R)

MPN analyses of iron reducing bacteria (Fe-R) illustrated that iron reduction was possible by bacteria residing in some parts of the water column at Mayan Blue (Figure 4.27C). The greatest numbers of Fe-R occurred in the FWL (Figure 4.27C), where concentrations reached up to 2.30 x 10^3 cells/ml, representing a minimum of 55% of the total number of cells counted in that sample by AODC. In the mixing zone, two possible peaks of maximum Fe-R numbers occurred, one at the UMZ/SS interface (2.30 x 10^3 cells/ml) and a second in the top part of the MMZ (0.15 x 10^3 cells/ml). Another Fe-R high occurred in the SZ, although numbers were variable (0.75 ± 1.05 x 10^3 cells/ml). Two minimums of Fe-R numbers were also present in the mixing zone: one at the SS/MMZ interface and another in the LMZ.

In some samples (of the lower dilution within the Fe-R MPN series), a black precipitate formed. The black precipitate was likely FeS, created by the reduction of both iron and sulfur (and thus would only occur where there was a large sulfur concentration in the original sample), *via* Equation 4.7.

$$H_2S + Fe^{2+} \leftrightarrow FeS + 2H^+ \quad (4.7)$$

In addition, some samples (again of the lower dilutions of the MPN series) formed a white granular precipitate, which is probably siderite ($FeCO_3$). The production of siderite would probably not occur in the natural environment, and is instead an artifact that formed due to a large building-up of CO_2 within the sealed MPN vials.

4.4.8.2 Oxygen Consumption Experiment

Oxygen consumption rates in the freshwater lens and saline zone were 38 μM/L/day (n = 1) and 9 μM/L/day (n = 1), respectively. Oxygen consumption rates throughout the mixing zone are 37 ± 12 μM/L/day (n = 11) and are variable, ranging from 17-51 μM/L/day.

Throughout the mixing zone, there are four peaks of oxygen consumption (42-51 μM/L/day) (Figure 4.28). These peaks occur close to the interface between the UMZ and SS, two peaks occur in the MMZ, and one peak is present at the interface between the LMZ and BMZ. A minimum of 17 μM/L/day occurs between the two peaks of increased oxygen consumption rates in the MMZ, demonstrating that the oxygen consumption rates within the MMZ are extremely variable (39 ± 15, n = 5). Two other minima occur: the first in the SS and the second near the interface between the MMZ and LMZ.

In addition, an increase in oxygen consumption in a sample from the mixing zone (16.7 m water depth) was stimulated by the addition of i) host rock and ii) thiosulfate and was completely inhibited by the addition of formaldehyde (hence there was no chemical oxygen uptake). The oxygen consumption rate measured in the unammended sample was 10 μM/L/day. This rate increased to 61 μM/L/day and 23 μM/L/day with the addition of host rock and thiosulfate, respectively. For both 'substrates', the uptake was stimulated within 6-18 hours of the start of the experiments, suggesting these substrates are used *in situ*.

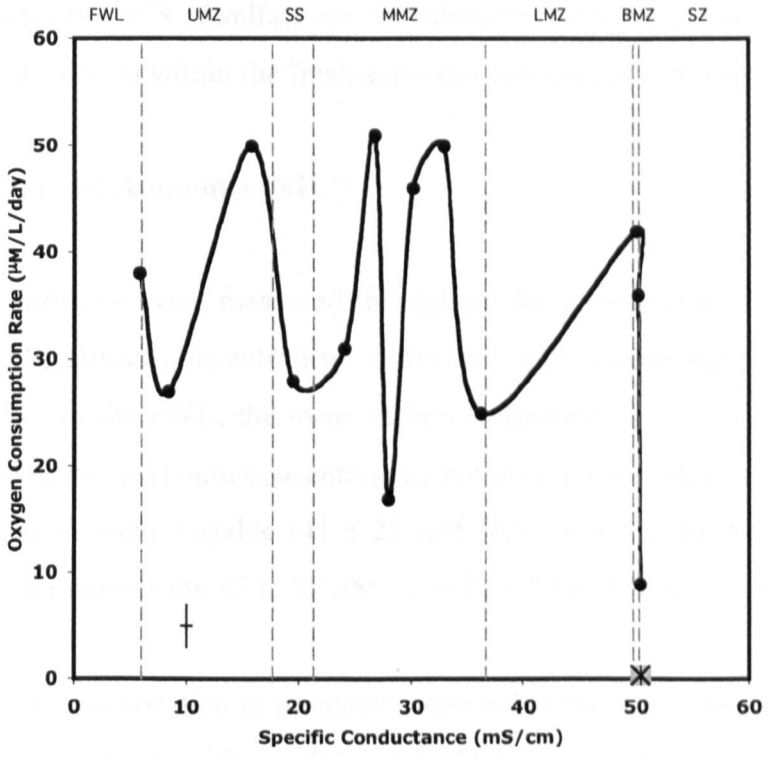

Figure 4.28 Oxygen consumption rates against specific conductance throughout the mixing zone of Mayan Blue (black circles). Ocean oxygen consumption rates depicted by the star surrounded by grey square. Dashed grey lines mark the interfaces between the different water types throughout the water column, including the freshwater lens (FWL), upper mixing zone (UMZ), salinity step (SS), middle mixing zone (MMZ), lower mixing zone (LMZ), basal mixing zone (BMZ) and saline zone (SZ). Analytical uncertainties are represented by the cross ($\pm 1\sigma$).

4.4.8.3 Chemical Evidence for Microbial Activity

In this section, analyses of nitrogen species, phosphorus, sulfide, methane, dissolved organic carbon, and $\delta^{34}S$ of sulfate are considered in attempts to help elucidate the activity and impact of bacteria within the fresh-saltwater mixing zone of Mayan Blue.

Nitrate (NO_3^-) and Ammonia (NH_4^+)

Nitrate and ammonia were measured throughout the mixing zone at Mayan Blue (Figure 4.29). Overall, nitrate concentrations decreased with increasing chloride concentration (Figure 4.29). In the FWL, the mean nitrate concentration is 116 ± 25 μM (n = 2), and these represent the maximum concentrations measured in the Mayan Blue cave. In the SZ, the nitrate values were variable (41 ± 22 μM NO_3^-, n = 3). In the mixing zone, nitrate concentrations ranged from 47 to 98 μM ($\bar{x}$ = 77 ± 28 μM NO_3^-, n = 9).

The maximum concentration of ammonia occurred in the FWL (24 ± 9.4 μM NH_4^+, n = 2) and the mean saline zone value is 6.5 ± 1.2 μM NH_4^+ (n = 3). Below the FWL, ammonia decreased with increasing chloride concentration and reached zero near the interface between the SS and MMZ. In the mixing zone, the maximum ammonia concentration (23 μM NH_4^+) occurred in the MMZ at 308 mM Cl^-. A second low value (0.6 μM NH_4^+) occurred at 366 mM Cl^- (also within the MMZ). The mean mixing zone ammonia concentration is 9.6 ± 7.3 μM (n = 9).

Soluble Reactive Phosphorus (SRP, as PO_4^{3-})

The concentration of soluble reactive phosphorus (SRP) varies systematically throughout the mixing zone at Mayan Blue (Figure 4.29B). In the FWL, SRP is variable and has a mean concentration of 2.4 ± 1.8 μM PO_4^{3-}, (n = 2), while in the SZ, SRP is 0.67 ± 0.44 μM (n = 3). In the mixing zone, SRP is variable (2.67 ± 3.03 μM, n = 9) and two peaks occur: the first near the interface between the SS and MMZ (7.8 ± 1.0 μM PO_4^{3-}, n = 2) and the second in the lower part of the MMZ (2.3 ± 0.5 μM PO_4^{3-}, n = 2, between 337 and 344 mM Cl^-).

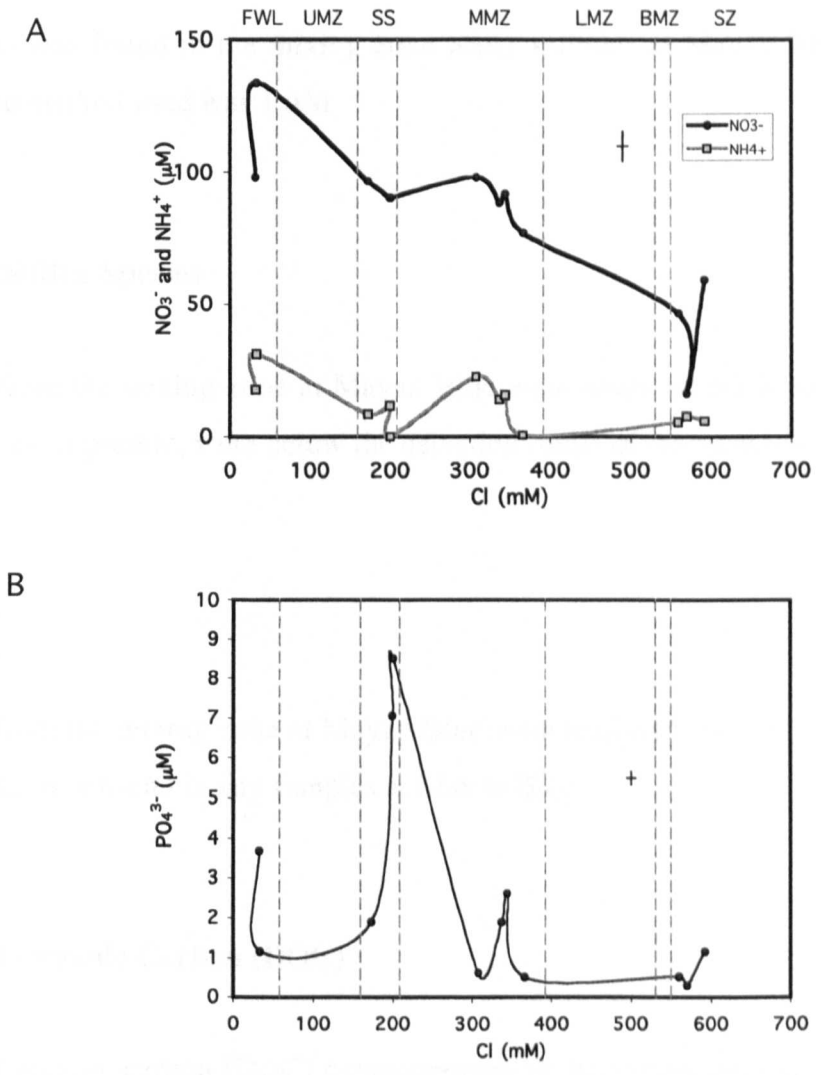

Figure 4.29 Nitrate, Ammonia (A) and Phosphate (B) concentrations against chloride throughout the mixing zone of Mayan Blue. Dashed grey lines mark the interfaces between the different water types throughout the water column, including the freshwater lens (FWL), upper mixing zone (UMZ), salinity step (SS) middle mixing zone (MMZ), lower mixing zone (LMZ), basal mixing zone (BMZ) and the saline zone (SZ). Crosses are representative analytical uncertainties (±1σ).

Acetate

No acetate was found in the mixing zone water samples at Mayan Blue. The detection limit of the method used was 1 μM.

Reduced Sulfur Species

Samples from the mixing zone at Mayan Blue were analysed for sulfide and thiosulfate. Both species, if present, were below the detection limits of the techniques used (1 μM).

Methane

Samples from the mixing zone at Mayan Blue were analysed for the presence of methane. No methane was found in any samples at Mayan Blue.

Dissolved Organic Carbon (DOC)

Dissolved organic carbon (DOC) concentrations in the freshwater lens and saline zone of Mayan Blue are not significantly different from one another (FWL DOC = 0.61 ± 0.34 mM, n = 2 and SZ DOC = 0.49 ± 0.25, n = 3) (Table 4.7). The mean DOC concentration in the mixing zone is 1.25 ± 1.55 (n = 21). There are two main peaks in elevated DOC concentration, and these occur in the UMZ (DOC = 3.19 ± 2.40, n = 4) and LMZ (DOC = 1.95 ± 1.69, n = 3) (Figure 4.30). In the UMZ, the highest concentrations are found in the top part of the UMZ and in the LMZ, the highest concentration occurs at the base of the LMZ. Within the mixing zone, the lowest concentrations occur in the SS, MMZ and upper part of the LMZ. One high value (2.89 mM DOC) occurs in the MMZ. This sample has a DOC concentration almost four times higher than the mean of all other MMZ values and may be a spurious result.

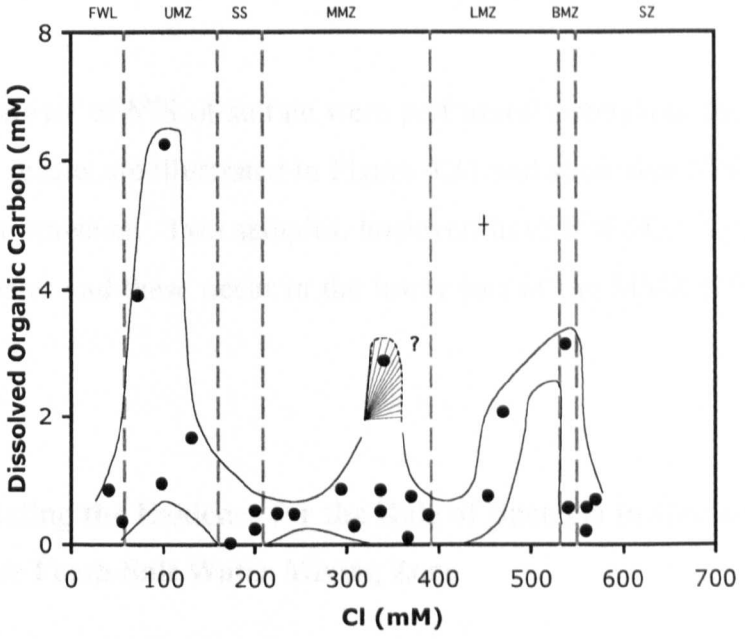

Figure 4.30 Dissolved organic carbon (DOC) against chloride throughout the mixing zone of Mayan Blue. Dashed lines mark the interfaces between the different water types throughout the water column, including the freshwater lens (FWL), upper mixing zone (UMZ), salinity step (SS), middle mixing zone (MMZ), lower mixing zone (LMZ), basal mixing zone (BMZ) and saline zone (SZ). Question mark indicates MMZ samlpe with a DOC concentration three times greater than the mean of all other MMZ samples, possibly indicating it is a spurious result. Analytical uncertainties represented by the cross (±1σ).

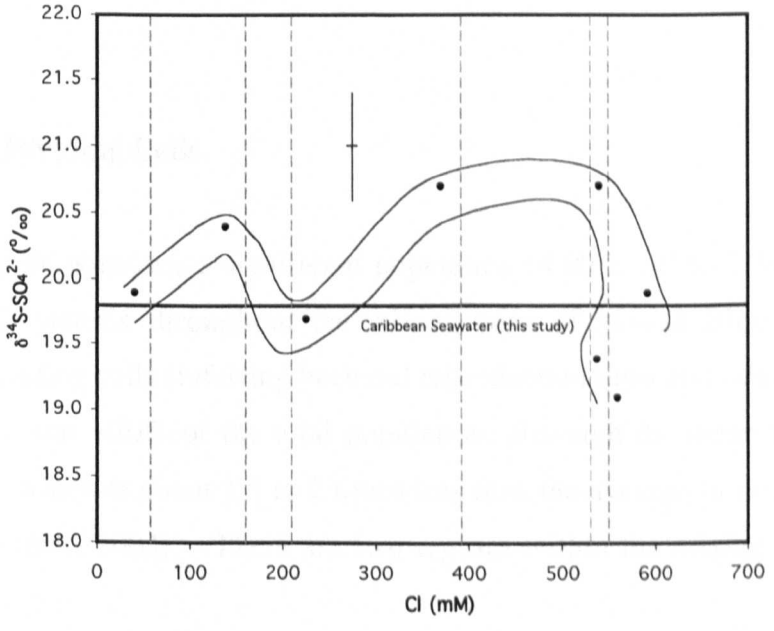

Figure 4.31 $\delta^{34}S$ of sulfate against chloride throughout the mixing zone of Mayan Blue. Solid black line indicates the Caribbean seawater value. Dashed lines mark the interfaces between the different water types throughout the water column, including freshwater lens (FWL), upper mixing zone (UMZ), salinity step (SS), middle mixing zone (MMZ), lower mixing zone (LMZ), basal mixing zone (BMZ) and saline zone (SZ). Representative analytical uncertainties are shown by the cross (±1σ).

$\delta^{34}S\text{-}SO_4^{2-}$

Stable isotope analyses of $\delta^{34}S$ of sulfate were performed throughout the mixing zone of Mayan Blue. The results are illustrated in Figure 4.31 and show that $\delta^{34}S\text{-}SO_4^{2-}$ values are very near those of seawater. Two samples, however, have $\delta^{34}S\text{-}SO_4^{2-}$ values significantly greater than seawater and these occur in the lower part of the MMZ (20.7‰) and in the BMZ (20.7‰).

4.4.8.4 Consolidating the Evidence for the Role of Bacteria in Carbonate Diagenesis in the Mayan Blue Fresh-Salt Water Mixing Zone

As discussed in Section 4.4.6, pCO_2 enrichments in waters cannot be explained by geochemical mixing alone, nor could they be explained by carbonate dissolution/precipitation kinetics. Regions of positive ΔpCO_2 may represent areas where the chemistry was dominated by heterotrophic bacteria, which consume organic matter and produce CO_2 (Equation 4.3). In fact, any reaction generating acidity (e.g. sulfur oxidation, which also consumes oxygen) will increase pCO_2. In order to investigate the role of bacteria in carbonate diagenesis, the geomicrobiology of mixing zone waters was studied.

AODC and % Dividing Cells

AODC analyses demonstrate a significant population (4.90×10^3 to 1.74×10^6 cells/ml; Figure 4.25) of bacteria throughout the mixing zone of Mayan Blue. The maximum proportion of dividing cells (inferring bacterial reproduction rates and relative activities) in the mixing zone was ~20% of the total population, although the mean was only 2.84 ± 4.74% (n = 18), which is about 1.5 to 2 times less than the average in deep-sea sediments (Cragg, pers. comm., 2003). There are two regions within the mixing zone where cell division is greatest:

a) the UMZ, SS and top part of the MMZ (greatest value at or near the UMZ/SS interface)
b) the lower portion of the LMZ (up to and including the LMZ/BMZ interface)

Both of these regions correspond to areas of increased pCO_2 (Figure 4.17) and undersaturation (Figure 4.16) compared to fresh-salt water mixing. Statistical analyses using Spearman's rank correlation coefficient (r_s-value) calculations reveal that the proportion of dividing cells has a strong positive relationship with $\Delta\, pCO_2$ ($r_s = +0.66$) and an even stronger negative relationship with ΔSI-C ($r_s = -0.85$), suggesting increases in general bacterial and presumably significant heterotrophic activity results in increases in pCO_2 production and (subsequent) decreases in saturation. The fact that ΔSI-C has a stronger relationship with percent dividing cells than does $\Delta\, pCO_2$ may indicate that acids other than carbonic acid (e.g. sulfuric acid and/or organic acids other than acetate) may play a role in maintaining the undersaturation with respect to calcite observed throughout the mixing zone. These other acids may also be products of bacterial metabolism. Both regions of increased bacterial activity correspond to where calcite pill dissolution was greatest (Figure 4.24), further substantiating the importance of bacteria in carbonate dissolution.

Evidence for Heterotrophic Activity

Heterotrophs are organisms that gain energy from the oxidation or fermentation of organic compounds (Madigan et al., 2000). A simplified heterotrophic metabolism is illustrated in Equation 4.3 (repeated), where one mole of carbon dioxide is produced for every mole of oxygen consumed. The carbon dioxide then combines with water to form carbonic acid (Equation 4.3, repeated), which plays a role (as inferred above) in carbonate dissolution.

$$CH_2O + O_2 \leftrightarrow CO_2 + H_2O \qquad \text{(4.3, repeated)}$$

$$CO_2 + H_2O \leftrightarrow H_2CO_3 \qquad \text{(4.4, repeated)}$$

All mixing zone samples (at all MPN dilutions) tested positive for the presence of both aerobic (HOX) and anaerobic (HAN) heterotrophic bacteria, indicating that their minimum concentration within all solutions is 2300 cells/ml. It is important to note that although only minimum cell numbers could be reported for heterotrophs, these numbers represent a minimum of 31 ± 46% of the total bacterial population counted by AODC, suggesting their importance in the mixing zone environment. These percentages are substantial and unexpected, given that, usually, less than 1% of the total prokaryotic population in natural

habitats can be cultivated (Amann et al., 1995), hence these large percentages of viable populations demonstrate the potential for significant activity.

Oxygen is present throughout the mixing zone (Figure 4.8), and because oxygen is the preferred electron acceptor for many bacteria (Madigan et al., 2000), it can be assumed that the rate at which oxygen is consumed will give a good overall estimate of bacterial activity (e.g. Jorgensen, 1989). The oxygen consumption rates are variable throughout the water column of Mayan Blue (35 ± 13 μM O_2/L/day, n = 13) and mixing zone rates range from 9 to 51 μM O_2/L/day. Due to the variability of these rates (Figure 4.28), systematic changes with increasing conductivity are difficult to interpret. Two possible reasons for the variability are:

a) low sampling frequency
b) lack of very discrete samples

The second point is probably the most relevant in this case. In order to obtain a uniform water for all samples (and their triplicates) required for the time series experiment, ~7.5 L of sample water was needed. A 10 L PVC sampling tube was constructed (Chapter 2) and the mouth of this tube extended over a 10 cm depth range. Thus, discrete sampling of regions with steep conductivity gradients (i.e. lower part of the UMZ, the MMZ and LMZ, Figure 4.6) was not always possible. The variability observed in the data indicates that, rather than providing oxygen consumption rates for specific parts of the mixing zone, these values may only be useful in indicating a *range* of mixing zone oxygen consumption rates. Despite this, the location of maximum oxygen consumption may be indicated by the lowest DO concentration, which corresponds to the SS/MMZ interface (Figure 4.8).

As stated above, oxygen consumption by heterotrophic bacteria leads to the production of carbonic acid (Equations 4.3 - 4.4). Ideally, each mole of carbonic acid is capable of dissolving one mole of calcium carbonate (Equation 4.8). From this assumption, the mixing zone oxygen consumption rates indicate calcium carbonate dissolution at a rate of 0.33 – 1.86 g $CaCO_3$/yr per litre of water.

$$H_2CO_3 + CaCO_3 \rightarrow Ca^{2+} + 2HCO_3^- \qquad (4.8)$$

Oxygen consumption was also increased by six times by the addition of host rock and it was doubled by the addition of thiosulfate. Some organic carbon was found in association with the exterior surface of one wall-rock sample (Section 4.4.7). This organic carbon could have stimulated heterotrophic activity, causing the increase in oxygen consumption.

Drive for Heterotrophy: DOC and Nutrients

Organic matter (represented as CH_2O in Equation 4.3, above) will support (and could stimulate) heterotrophic activity. Dissolved organic carbon (DOC) was measured to provide an estimate of the total amount of organic matter available to heterotrophic bacteria. DOC data, however, can be difficult to interpret. An increase in DOC (or a high DOC value) may indicate where bacterial communities are supported, or it may indicate a lack of bacterial activity (i.e. the DOC is not being used).

Two peaks of increased DOC concentration (indicated by a minimum of two samples occurring above the mean for a given water type) occur:

a) in the UMZ
b) in the bottom part of the LMZ, including the LMZ/BMZ interface (Figure 4.30).

The upper peak in DOC (a) occurs just above the upper maximum in % dividing cells (Figure 4.26), suggesting that the bacteria at the SS/MMZ interface may have consumed DOC. The minimum dissolved oxygen concentration also occurs at the SS/MMZ interface, supporting the idea that organic matter oxidation is occurring. The lower DOC peak (b) corresponds with the lower peak in the proportion of dividing cells (Figure 4.26), indicating that DOC may stimulate bacterial activity in the bottom part of the LMZ and LMZ/BMZ interface. These relationships between DOC and % dividing cells may also reflect different sources of organic matter within the different water types; more refractory terrigenous organic matter in the fresher waters, and more labile marine organic matter in the saline zone and hence lower parts of the mixing zone (Rullkotter, 2000).

Nutrient Cycling

Where the breakdown of organic matter by heterotrophic bacteria occurs, ammonia and phosphate are expected to increase (Equation 4.9, modified from Bender and Heggie, 1984).

$$(CH_2O)_{106}(NH_3)_{16}(H_3PO_4) + 1060_2 \leftrightarrow 106CO_2 + 16NH_3 + H_3PO_4^{3-} + 106H_2O \qquad (4.9)$$

Ammonia concentrations do not correspond with increases or decreases in dissolved oxygen ($r = 0.13$, d.f. = 11, $P = 0.68$) or pCO_2 ($r = 0.42$, d.f. = 11, $P = 0.17$). In the presence of nitrosifying and nitrifiying bacteria in oxygenated waters, the ammonia from Equation 4.9 may be oxidised to nitrate in a 3-step process (Equations 4.10 to 4.13).

Step 1. $NH_3 + O_2 + 2e^- + 2H^+ \rightarrow NH_2OH + H_2O$ (4.10)

Step 2. $NH_2OH + H_2O + \frac{1}{2}O_2 \rightarrow NO_2^- + 2H_2O + H^+$ (4.11)

SUM of Steps 1 and 2: $NH_3 + 1\frac{1}{2}O_2 + 2e^- + H^+ \rightarrow NO_2^- + 2H_2O$ (4.12)

Step 3. $NO_2^- + \frac{1}{2}O_2 \rightarrow NO_3^-$ (4.13)

Nitrate has a strong inverse relationship with dissolved oxygen ($r = 0.614$, d.f. = 11, $P = 0.03$) and a strong positive association with pCO_2 ($r = 0.79$, d.f. = 11, $P = 0.002$). The fact that nitrate, rather than ammonia, has these relationships with DO and pCO_2 indicate that nitrification is probably occurring in the mixing zone of Mayan Blue.

Ammonia-oxidising bacteria, such as *Nitrosomas sp.*, carry out Equations 4.10 and 4.11, while nitrite-oxidising bacteria such as *Nitrobacter sp.* perform the reaction shown in Equation 4.13, producing nitrate (Madigan et al., 2000). Most nitrifying bacteria are obligate chemolithotrophs. Species of *Nitrobacter* are an exception and are able to grow chemoorganotrophically on substrates such as acetate as the sole carbon and energy source (Madigan et al., 2000). The significant positive association between nitrate and ammonia ($r = 0.62$, d.f. = 11, $P = 0.03$) supports the idea that the oxidation of ammonia is occurring and that nitrifying bacteria are active. Pohlman et al. (2000) also suggested nitrification was occurring in the mixing zone waters of Mayan Blue, as evidenced by a nitrite peak,

coincident with peak in nitrate and a decrease in dissolved oxygen.

Based on nitrogen ($^{15}N/^{14}N$) and carbon ($^{13}C/^{12}C$) isotope studies, Pohlman et al. (2000) concluded that the soil zone overlying the carbonate rock was the primary source of organic matter in the Mayan Blue mixing zone. This may explain why concentrations of nitrate and ammonia are highest in the freshwater lens and decrease with increasing chloride concentration (Figure 4.29A).

In addition, there are two samples (from the SS and lower MMZ) where the ammonia concentration is zero, with no resultant increase in nitrate. This suggests that, here, the oxidation may be incomplete (i.e. only Equations 4.10 to 4.11 are occurring), producing nitrite. Nitrite was not analysed in this study.

There are thought to be four possible processes responsible for the two phosphate peaks in the mixing zone: a) breakdown of organic matter *via* heterotrophy; b) breakdown of organic matter *via* sulfate reduction; c) release from inorganic iron minerals; d) the salt content of the water.

A) Breakdown of Organic Matter *via* Heterotrophy

Like nitrate and ammonia, phosphate also provides evidence for the breakdown of organic matter (Berner, 1974; Rosenfield, 1979) and, overall, phosphate has a strong inverse relationship with dissolved oxygen ($R = -0.71$, d.f. = 11, $P = 0.01$) suggesting oxygen consumption yields increases in phosphate. However, neither nitrate nor ammonia have significant associations with phosphate (NO_3^-:$R = +0.28$, d.f. = 11, $P = 0.3$, NH_4^+: $R = +0.22$, d.f. = 11, $P = 0.49$) and phosphate has only a weak positive association with pCO_2 ($R = +0.57$, d.f. = 11, $P = 0.05$), indicating that perhaps not all phosphate increases are the result of heterotrophic activity.

The breakdown of organic matter *via* hetertrophy (Equation 4.9) could explain the phosphate peak at the SS/MMZ interface, where a decrease in oxygen and pH and an increase in pCO_2 also occurs (see Figures 4.8, 4.9 and 4.15, respectively). It is worth noting, however, that any process consuming oxygen and producing acidity (such as sulfur

oxidation, discussed later) would produce these results.

Heterotrophy in an unlikely source of phosphate in the lower MMZ because this region coincides with increased dissolved oxygen and pH and decreased pCO_2 values (see Figures 4.8, 4.9 and 4.15 respectively).

B) Breakdown of Organic Matter *via* Sulfate Reduction

Phosphorus may be released from organic matter decomposition *via* sulfate reduction, where sulfate, rather than oxygen, is used as an electron acceptor and where alkalinity (as HCO_3^-), rather than CO_2, is produced.

At the SS/MMZ interface, this process is supported by the location of the maximum numbers of SRBs counted in 2001 (Figure 4.27B). However, SO_{4XS} values are not significantly less than zero, sulfide is below detection and $\delta^{34}S\text{-}SO_4^{2-}$ is equivalent to seawater values, indicating significant sulfate reduction has not occurred. It is possible, however, that any sulfide produced is re-oxidised back to sulfate.

In the lower MMZ, $\delta^{34}S\text{-}SO_4^{2-}$ is high (above seawater values), indicating sulfate reduction has occurred. The pH is also high (relative to other mixing zone waters), which could be explained by alkalinity production. However, SO_{4XS} is not significantly different from zero, sulfide is below detection and SRB MPN counts are zero in lower MMZ waters (Figure 4.27B).

C) Phosphate Release from Iron Minerals

Besides liberation from the microbial breakdown of phosphorus-containing organic matter, phosphate can also be liberated from adsorption sites on ferric oxyhydroxides during anoxic reduction of iron, either by iron reducing bacteria or possibly by H_2S formed during sulfate reduction (Krom and Berner, 1981). Numerous field studies show that iron oxides likely control both pore water and solid phase phosphate concentrations and drive the sedimentary phosphate cycle (Krom and Berner, 1980; Froelich *et al*, 1982; Sundby *et al*,

1992; Jensen *et al*, 1975; and Slomp *et al.*, 1996a and b). Reduction of iron oxides releases phosphate into solution and phosphate increases are often associated with anoxic/oxic interfaces (Horne and Goldman, 1994). Thus, the peaks in phosphate observed in Mayan Blue might indicate regions where iron oxides are present but where iron and/or sulfate reduction reactions are taking place.

The large peak in phosphate that occurs near the SS/MMZ interface (Figure 4.29B) coincides with a transition from wall-rock stained with orange precipitates (probably iron oxides) to non-stained wall-rock (possibly indicating iron reduction) (Figure 4.23). Iron-reducing bacteria numbers are at a minimum at this interface (Figure 4.27). However, the occurrence of sulfate reduction is supported by the MPN data. Evidence for and against sulfate reduction occurring at the SS/MMZ interface is given in the previous section. It is plausible that sulfide is below detection due to the reduction of iron minerals, which consumes sulfide by producing iron sulfides. However, no evidence for iron sulfides was found on wall-rock between the SS/MMZ interface and the lower MMZ.

Fe-R MPN data suggest iron reducing bacteria are probably present in the lower MMZ possibly inferring dissimilatory iron oxide reduction by bacteria. This is substantiated in part by the white colouration of the wall-rock in this region; all orange iron oxides appear to have been reduced. Reasons for and against sulfate reduction are given above and it is thought the phosphate peak in the lower MMZ could arise from the reduction of iron minerals containing phosphate, either by dissimilatory bacterial iron reduction and/or sulfide.

D) Salt content of the water

Another possible explanation for peaks in phosphate is the salt content of the water. Phosphate is often released in estuaries where fresh/brackish groundwaters mix with seawater (Froelich, 1988). The salt concentration at which this process occurs is uncertain and would likely explain only one of the two peaks.

The Role of Phosphate in Carbonate Diagenesis

Phosphate has been shown experimentally to both decrease dissolution (≥ 3 μM PO_4^{3-}; e.g. Morse et al., 1979; Walter and Burton, 1986) and inhibit precipitation (≥ 10 μM PO_4^{3-}; Raistrick, 1949; Simkiss, 1964 a, b; Reddy and Noncollas, 1973; Reddy, 1977, 1978; Berner et al., 1978) of carbonate minerals. Although the maximum phosphate concentration in Mayan Blue is only 8.5 μM, increases in phosphate may cause decreases in SI-C ($r = -0.62$, d.f. = 11, $P = 0.03$). The relationship between phosphate and SI-DD, on the other hand, is not significant ($r = -0.55$, d.f. = 11, $P = 0.06$). The 'release' of phosphate by iron and/or sulfate reduction may therefore play a part in maintaining calcite undersaturation, possibly inhibiting carbonate mineral precipitation.

Sulfur and Iron Cycling

MPN analyses provide further insight in to the potential cycling of sulfur and iron within the Mayan Blue water column.

Sulfur oxidisers

MPN analyses of thiosulfate-oxidising bacteria (SOX), indicated that thiosulfate oxidation proceeded by one of two reactions: i) complete oxidation from thiosulfate to sulfate with acidity produced (Equation 4.5), and ii) incomplete oxidation of thiosulfate to intermediary species of oxidised sulfur (e.g. polythionates, such as tetrathionate), rather than sulfate, (Equation 4.6), with an increase in pH. These results indicate the presence of two distinct populations.

Aerobic acid-producing thiosulfate-oxidising bacteria (capable of complete oxidation to sulfate) were present at all chloride concentrations sampled thought the Mayan Blue mixing zone, with maximum numbers occurring in the SS (Figure 4.27). The final pH of the freshwater SOX media was 3.25 ± 0.33, $n = 2$ and the final pH of the saltwater media was 5.35 ($n = 1$), compared to a starting pH of 7.3, indicating that these bacteria can have a massive impact on the pH of their environment. In the case of Mayan Blue, the increases in acidity will be buffered by the carbonate system. Acidic SOX are probably autotrophic

and will occur where they can gain greatest energy for autotrophic growth (i.e. at the steepest redox gradients).

Aerobic base-producing incomplete thiosulfate-oxidisers were, in general, more abundant than the complete oxidisers at all conductivites except two (corresponding to the SS and LMZ/BMZ interface) (Figure 4.27). Maximum numbers of base-producing incomplete thiosulfate-oxidisers occur at the MMZ/LMZ interface. Incomplete oxidation of thiosulfate to polythionates was likely the result of a side reaction from heterotrophic activity rather than occurring directly because only small amounts of energy can be grained from intermediate oxidation reactions (Madigan et al., 2000). In addition, Teske et al. (2000) and Telling (2002) reported difficulties in interpreting base-producing incomplete thiosulfate oxidisers. Both researchers added acetate to their media, which might have encouraged heterotrophic activity. Although the media used in this study did not include acetate, the organic content of the sample itself may have been sufficient to stimulate heterotrophic growth (see Ruby *et al.*, 1981). Mixotrophic bacteria, although unable to use thiosulfate as a sole electron donor, may have used thiosulfate as an auxiliary electron donor to organic matter, resulting in mixed lithotrophy and autotrophy (Tuttle, 1980). Under oligotrophic conditions (possibly the conditions within the more diluted MPN series vials), this process allows the bacteria to utilise a larger proportion of the available organic carbon for biosynthesis rather than respiration (Tuttle et al., 1974; Tuttle, 1980).

Heterotrophic/mixotrophic activity seems to dominate the MPN samples taken from the water column of Mayan Blue, except those from the SS and LMZ/BMZ interface, where they appear to out-competed by sulfur-oxidising bacteria capable of complete oxidation to sulfate. In these locations, acidity generation would be increased, contributing to undersaturation and $CaCO_3$ dissolution. Maximum numbers of SOX (SS) correspond to where pH is lowest (Figure 4.9) and where SI-C is most undersaturated (Figure 4.16).

Clearly, the oxygen consumption experiment results demonstrated that bacterial activity in Mayan Blue would be stimulated by S_2O_3 (and possibly other reduced sulfur species), if present (Section 4.4.8.2). This is further evidence for the importance of sulfur cycling in this environment.

Sulfate reduction

MPN analyses of SRB demonstrated that some Mayan Blue bacteria were capable of sulfate reduction, which, in turn, indicates that anoxia (likely in association with microbial micro-environments) is possible in the water column of Mayan Blue, despite the presence of oxygen. As mentioned previously, and shown by Equation 4.14, sulfate reduction adds alkalinity to the system and, as a result, SRB might play a role in dolomitisation and/or carbonate precipitation/dissolution.

$$2CH_2O + SO_4^{2-} \leftrightarrow 2HCO_3^- + H_2S \qquad (4.14)$$

A comparison of the distributions of incomplete and complete sulfur oxidizers with sulfate reducers (Figure 4.27) demonstrates that SRB were similar to SOX in waters with chloride concentrations $\leq$ 200 mM Cl^- (SS/MMZ interface), while SOX were more abundant than SRB at chloride concentrations $\geq$ 200 mM Cl^-. Despite this, $\delta^{34}S$ analyses reveal that sulfate reduction (evidenced by a $\delta^{34}S$-SO_4^{2-} signature significantly heavier than seawater) had occurred. However, no sulfide could be measured and SO_{4XS} values were within analytical uncertainty of zero, indicating subsequent re-oxidation (or FeS precipitation) had probably also occurred.

Iron (II) oxidation

Despite the inability to culture acidophilic Fe-OX, the activity of neutrophilic iron-oxidising bacteria, which would only reside at oxic/anoxic interfaces (Madigan et al., 2000) may have been indicated by orange encrustations ($Fe(OH)_3$) found on some of the wall-rock surfaces within the cave (Figure 4.23), implying that the pore water within the rock matrix is anoxic. In Mayan Blue, the orange encrustations are confined to two distinct zones: above the MMZ (i.e. throughout the FWL, UMZ and SS) and in the SZ. The crusts may indicate the presence of *Gallionella ferruginea*, *Sphaerotilus natans*, and/or *Leptothrix ochracea*, (Madigan et al., 2000) which could produce $Fe(OH)_3$ by Equation 4.15. Iron oxides may provide an energy gain in later reducing reactions.

$$Fe^{2+} + \tfrac{1}{4}O_2 + \tfrac{5}{2}H_2O \leftrightarrow Fe(OH)_3 + 2H^+ \quad (4.15)$$

Iron oxidising bacteria also produce acidity and thus they may play a role in carbonate dissolution. This may be supported by the fact that the orange staining on the wall-rock occurs only where the wall-rock appears significantly weathered (Figure 4.23).

Iron (III) reduction

MPN analyses of iron-reducing bacteria (Fe-R) demonstrated that some mixing zone bacteria were capable of iron reduction (Equation 4.16), producing alkalinity. The presence of Fe-reducers suggests, again, that anoxic (or sub-oxic) micro-environments may have been present, despite the presence of oxygen throughout the water column.

$$4Fe(OH)_3 + CH_2O + 7H^+ \leftrightarrow 4Fe^{2+} + HCO_3^- + 10H_2O \quad (4.16)$$

Within the Mayan Blue cave environment, it was within the FWL (and FWL/UMZ interface) that black-brown crusts, similar in texture and density to those precipitated by the Fe-R MPNs, were found covering stalactites and part of the cave walls. Bottrell *et al.* (1991) and Smart *et al.* (1998) reported similar black-brown encrustations in Stargate Blue Hole and Evelyn Green's Blue Hole, respectively, both located on South Andros in the Bahamas. These crusts were analysed and were found to contain iron sulfide compounds, including pyrite (FeS_2). FeS generally converts to FeS_2 when oxic waters are in contact with sediments that become anoxic with depth (likely the case in this study) or when anoxic water 'overlies' anoxic sediments (Boesen and Postma, 1988) and this conversion might take place in a matter of years (Berner, 1970; Equation 4.17), or days (Rickard, 1997; Equation 4.18).

$$FeS + S^\circ \leftrightarrow FeS_2 \quad (4.17)$$

$$FeS + H_2S \leftrightarrow FeS_2 + H_2 \quad (4.18)$$

When conducting MPN analyses for various functional groups, it is possible that the same bacteria are capable of driving two or more reactions/metabolisms. For example, bacteria capable of iron reduction may also reduce sulfate, given the right conditions (Coleman et

al., 1993). This may be the case with respect to the bacteria in the FWL, where the numbers of Fe-R equaled those of SRB. However, the data obtained for Fe-R and SRB (taken from the same samples, i.e. April 2000) within the mixing zone, illustrated that the numbers of Fe-R had an almost entirely inverse relationship to the numbers of SRB (Figure 4.27). These results indicate that, in the mixing zone, two physiologically distinct microbial communities are present; one with the ability to reduce iron, and a second, which is more inclined to reduce sulfate. The acetate-utilsing Fe-R bacteria are likely very closely related to (or may be) *Geobacter sp.* (Lovley et al., 1986).

4.4.9 Estimating Rates of Dissolution

In order to calculate the average amount of $CaCO_3$ dissolution in the mixing zone, estimates of mixing zone volume and discharge must first be made. In addition, the amount of $CaCO_3$ in contact with mixing zone waters must also be approximated.

Dye traces at Mayan Blue demonstrated that the top part of the mixing zone flowed with the freshwater lens (indicating a coastward flow rate of ~80 m/day) and the bottom part of the mixing zone 'shuttled' with the underlying saline water (indicating a net inland flow rate of ~23 m/day). The flow regime within the 1.4 m thick salinity step remains enigmatic and for now it is assumed the top 0.7 m flows with the top part of the mixing zone and the bottom 0.7 m flows with the bottom part of the mixing zone, resulting in thicknesses of 1.10 and 2.10 m for the top and bottom parts of the mixing zone, respectively. Mixing zone thickness does not vary systematically with distance inland (Figure 4.4) and it is assumed that these thicknesses are approximately representative of the mixing zone underlying the 480 km^2 study area. Multiplying thickness by study area gives volumes of 5.28 x 10^8 m^3 and 10.08 x 10^8 m^3 for the top and bottom parts of the mixing zone, respectively. Given calcite density of 2.65 g/cm^3, and assuming an average porosity of ~20% within the study area (e.g. Worthington et al., 2002), the masses of calcite in 'contact' with the top and bottom parts of the mixing zone are 1.12 and 2.14 x 10^{15} g, respectively.

As mentioned in Section 4.4.8.4, the mixing zone oxygen consumption rates indicate calcium carbonate dissolution at a rate of 0.33 – 1.86 g $CaCO_3$/a per litre of water

(assuming each mole of consumed oxygen produces one mole of carbonic acid, capable of dissolving one mole of calcium carbonate; Equations 4.3, 4.4 and 4.8), with a mean rate of 1.35 g $CaCO_3$/L/a. Multiplying by volume results in $CaCO_3$ removal of 0.71 and 1.36 x 10^{12} g/a in the top and bottom parts of the mixing zone, respectively. These values equate to 0.06 and 0.12% porosity generation/a (with a mean mixing zone rate of 0.10%/a) by bacterial oxygen consumption.

This mean rate indicates total dissolution of the mixing zone portion of this part of the platform within ~1000 years, which is one to two orders of magnitude greater than the rates estimated by Sanford and Konikow (1989) for mixing corrosion of a coastal carbonate aquifer with similar flow velocities (~1 – 13% porosity generation in 10,000 years; based on Sanford and Konikow's Figures 11 and 12).

The calcite 'pill' porosity generation rate, determined from % weight loss, was 0.08 ± 0.07%/a (n=12). This is lower than the rates predicted above, probably due to a different rock source than the host rock. The pills were comprised of high-density marble (the density of the pills was very high compared to the Yucatan bedrock) and thus the rates measured from the pills are more likely to reflect surface lowering rates rather than internal porosity generation – thus, pill dissolution rates would be expected to be lower than host rock dissolution rates. Nevertheless, the values are within the same order of magnitude, supporting the calculations made above and these results indicate bacteria could be responsible for 100% of present-day dissolution in this modern mixing zone.

Chapter 5

Diagenesis in the Zone of Saline Groundwaters

5.1 Introduction

The majority of platform carbonates spend most of their pre-burial history exposed to waters of near-seawater salinity. Saline groundwaters are widely recognized for their potential to precipitate marine calcite cements (MacIntyre, 1977) and the active circulation and composition of saline groundwaters may be a critical drive for dolomitisation (Land, 1985; Whitaker, 1992; Whitaker et al., 1994). In addition, there is increasing recognition of the ubiquity of bacteria and the crucial role they have in sediment diagenesis (Parkes et al., 1994). In particular, recent studies show that sulfate-reducing bacteria play an important role in dolomite formation (Vasconcelos et al., 1995; Wright, 1999), while sulfur-oxidising bacteria may play a significant role in carbonate dissolution (e.g. Stern et al., 2002). However our understanding of the hydrology and geochemistry of saline groundwaters has been limited by the inaccessibility of the interior of carbonate platforms, without resorting to costly and time-consuming drilling. In this study, cave diving techniques are used to access the submerged caves hosting saline groundwater within the Yucatan Peninsula carbonate platform.

The first part of this chapter briefly describes the hydrology of saline groundwaters in general, and then specifically within the Yucatan Peninsula carbonate platform where direct measurements of groundwater flow (using current meters and dye tracer tests) were used to estimate saline groundwater circulation patterns. The causes and detailed descriptions of these circulation patterns are outside the scope of this thesis and are described elsewhere (Beddows, 2004). The majority of Chapter 5 is dedicated to the detailed study of the geochemistry and geomicrobiology of saline groundwaters. Caribbean seawater samples (from 0.5 – 70 m water depth), from which the saline groundwaters

originate, are also characterised. Geochemical modeling is used to predict the geochemistry of the saline groundwaters, and the effects of mixing and rock-water interaction are considered. These predictions are then compared to the observed water chemistry within the saline zone, with emphasis on the influence of bacterially mediated processes on diagenesis.

5.2 Hydrology of Saline Groundwaters

The controls on saline groundwater circulation are less well understood than those on freshwater circulation due to access limitations and the logistics associated with studying waters below the freshwater lens. However, Whitaker and Smart (1990) and Whitaker (1992) suggest four primary mechanisms for saline water circulation, based on extensive field observations made in the Bahamas:

- Sea Surface Elevation (Elevation Head)
- Buoyant Circulation (Density Driven)
- Reflux (Density Driven)
- Temperature (Geothermal Heat)

Sea Surface Elevation

Differences in the sea surface elevation across a carbonate platform could drive subsurface flow of saline groundwater from an area of relatively high sea surface elevation to an area of relatively low sea surface elevation (Whitaker and Smart, 1990). Tides, local wave conditions, or ocean currents control the sea surface elevation (Whitaker and Smart, 1990).

Buoyant Circulation

The process of buoyant circulation involves mixing between fresh and saline water, producing a lower density water that rises along the mixing zone and contributes to coastal discharge. This loss of saline water results in a compensatory inflow of seawater at depth flowing landward (Cooper, 1959; Cooper, 1964; Fetter, 1988). Whitaker and Smart (1990) estimate that this saline influx occurs at depths of 10s to 100s of meters below the mixing

zone in the Bahamas, while Moore (1992) and Stoessell (1995) suggest that this saline influx occurs at depths >100 m below the water table in the Yucatan Peninsula. However, Beddows (2002, 2004) discounts buoyant circulation as a principal drive for saline circulation due to observations made in the Yucatan Peninsula where shallow saline groundwater flow observed in Sistema Ponderosa (which shuttled back and forth) was decoupled from the flow of the freshwater lens (which flowed constantly towards the coast).

Reflux

Reflux involves the downward and lateral flow of dense (evaporated) water from the surface of the platform, replacing less-dense waters below (Whitaker, 1992). This process was originally proposed by Adams and Rhodes (1960) for isolated bodies of hypersaline water. However, Simms (1984) showed that reflux might also be applicable to waters of only slightly elevated salinity (37 – 42‰). Thus, the reflux process may be more widespread than previously thought (Whitaker and Smart, 1990).

Temperature

Thermal convection may be induced by a horizontal density gradient between relatively cold seawater and warmer saline groundwaters (Kohout et al., 1977; Aahron et al., 1987). Under this mechanism, saline groundwater that has been heated by the geothermal gradient will become less dense and will subsequently rise within the platform, discharging at the platform margins (Whitaker and Smart, 1990). In turn, this may cause an inflow of cooler, denser seawater at depth (which is then heated and rises, etc., repeating the process).

5.3 Hydrology of east coast Yucatan Peninsula saline groundwaters

In a parallel study (Beddows, 2004), the circulation of saline water within the Yucatan Peninsula carbonate platform was investigated by direct measurements of flow velocity using recording current meters (RCMs) and tracer tests. Beddows (2004) describes two types of saline groundwater flow occurring within the east coast of the Yucatan Peninsula platform: i) a shallow saline zone located within 5 m below the mixing zone-saline zone interface and ii) a deep saline zone located deeper than 5 m below the mixing zone.

The shallow saline zone appears to shuttle back and forth along a southeast-northwest axis. This shuttle is controlled by changes in (mean) sea level (Beddows, 2004). During periods of higher than mean sea level, there is net inflow of saline groundwater, while during periods of lower than mean sea level, there is a net outflow.

The deep saline groundwater flow, on the other hand, is consistently unidirectional (from the coast towards inland, i.e. cardinal direction of 283°). The difference in elevation head between the Gulf of Mexico (lower) and Caribbean (higher) coasts of the Peninsula has been proposed by Beddows (2004) as a potentially major drive for this the east-to-west cross-platform sub-surface saline groundwater flow. However, velocity records show semi-diurnal tidal signals, with maximum inflow rates occurring at low tide and minimum inflow rates at high tide. This phenomenon has yet to be adequately explained (Beddows, 2004).

5.3.1 RCM data

Two long-term measurements of deep saline groundwater flow were made using FSI recording current meters (Beddows, 2004). The sites studied were: The Pit (Sistema Dos Ojos) and Mayan Blue (Sistema Naranjal). Both records showed semi-diurnal tidal signals, with maximum inflow rates occurring during low tide and minimum inflow rates occurring at high tide (Figure 5.1). In addition, both records show that the deep saline groundwater flow is uni-directional; it always flows from the southeast (coast) to the northwest (inland) (Beddows, 2004). The mean velocity of the saline groundwaters within The Pit is ~1.6 cm/s, while the mean velocity of Mayan Blue saline groundwaters is ~3 cm/s.

5.3.2 Tracer tests

As part of the detailed geochemical work of the present study, a qualitative dye trace was conducted in Mayan Blue, Sistema Naranjal, in September 2002. 500 ml of diluted 10% Fluorescein dye was released at 20.5 m water depth (~ 1 – 2 m below the mixing zone/saline zone interface) in the saline zone of the B Tunnel, Mayan Blue.

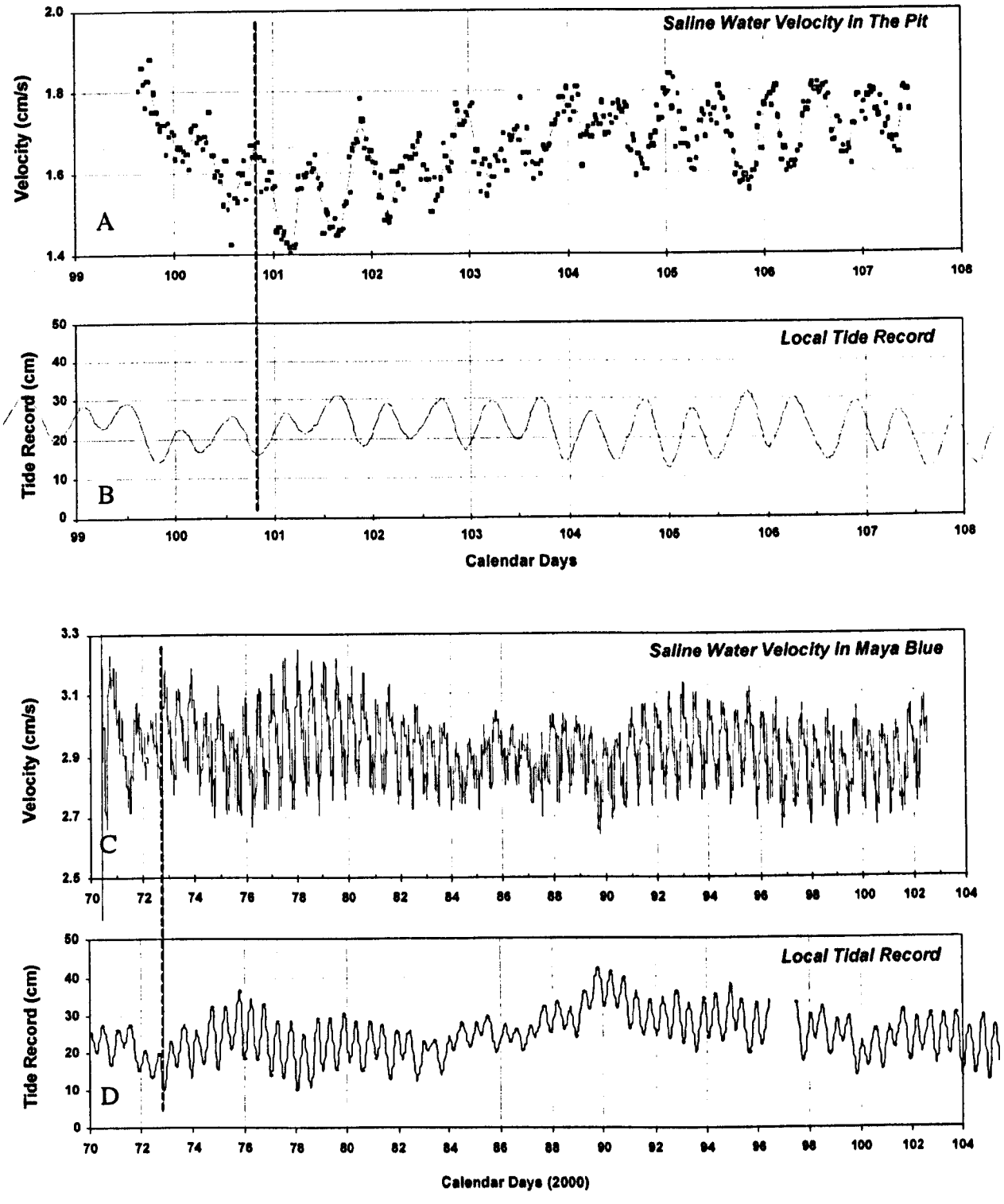

Figure 5.1 Velocity measurements from The Pit (A) and Mayan Blue (C) against time, shown with the corresponding local tide records (B and D, respectively). Note that high velocities measured in the saline groundwaters correspond with low tide at the coast (dashed lines). Direction of flow at both sites was continuous (towards the NW) (data from Beddows, 2004).

The point of release was approximately 100 m from the cenote entrance. The dye was released by shaking bottles within the cave, resulting in the horizontal distribution of dye over ~5 m. After one hour, the dye had moved a further 6 m north (into the cave) and about 10 m south (towards the cenote). After 24 hours, the dye had traveled 220 m north/northwest and 20 m south of the injection point. During 24 hour and 48 hour observation dives, it was noted that the dye was most concentrated at 19.5 m water depth, but it was present as shallow as 17 m water depth. At 7 and 14 days, all signs of Fluorescien dye were gone from the cave (searches were made in A, B, E and "flow meter" tunnels) (Figure 1.5). From this data, a net flow velocity of 0.23 cm/s (0.2 km/day) can be calculated. In addition, this dye trace demonstrates that the saline groundwater within Mayan Blue may "shuttle' back and forth, along a SE-NW axis, supporting the observation made by Beddows (2002, 2004) in Sistema Ponderosa. In Mayan Blue, the net saline groundwater flow direction was from the southeast to the northwest over the two-week-long observation period.

5.3.3 YSI profiles

Profiles of specific conductance (obtained from YSI data) through the water column were used to define the location of the saline zone. In this thesis, the saline zone (a.k.a. saline groundwater) is defined as a groundwater of near-seawater conductivity in which there is little variation in conductivity with depth (Figure 5.2). In addition, the profiles showed that the position of the top interface of the saline zone (determined from the position of the interface between the bottom of the mixing zone and top of the saline zone) is higher near the coast and becomes progressively deeper with distance inland (Figure 5.3).

5.4 Geochemistry of Saline Groundwater

5.4.1 Sampling distributions and site types

On the basis of field geochemistry and site morphology, the sampled saline groundwaters can be split into six site categories: open pit cenotes, caverns, caves, coastal sites, deep (60 m+) saline zone and hydrogen sulfide layers. Full site descriptions are given in Chapter 1.

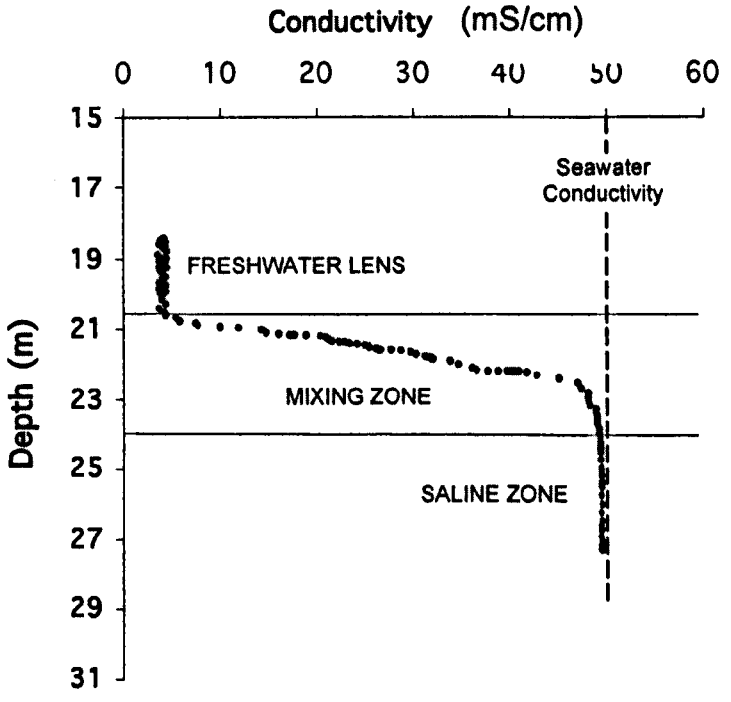

Figure 5.2 Conductivity with depth data obtained from a YSI profile taken from a Yucatan Peninsula submerged cave site, showing the location of the saline zone relative to the mixing zone and freshwater lens. Dashed line shows seawater conductivity.

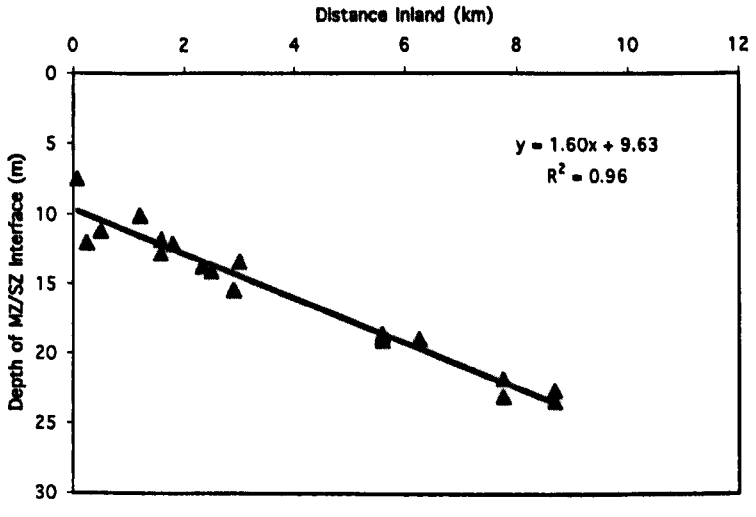

Figure 5.3 Saline zone thickness with distance inland (data from cave sites only). The Caribbean Sea is located at 0 km inland, while all other distances are measured west of this.

48 samples were taken from the saline groundwaters of the Yucatan Peninsula, Mexico, up to ~12 km inland and 110 m water depth. Of these, 9 were from open pit cenotes, 3 were from cavern sites (exposed to some light and/or air), 21 were from caves, 7 were from coastal sites, 4 were from sites that extended into the deeper (60 m+) saline zone and 3 were from sulfide layers. An additional one sample (taken from the deep saline zone of Sabak Ha) was from a site located on the Ring of Cenotes, located ~70 km west of the main study area and ~30 km south of Mérida in Yucatan State. Eight samples of Caribbean seawater were also taken.

5.4.2 Saline Groundwater Sample Field Measurements

This section describes the field chemistry results and includes measurements of specific conductance, *in situ* temperature, pH, dissolved oxygen and alkalinity. Unless otherwise stated, depth refers to water depth.

5.4.2.1 Specific Conductance

The specific conductance of Caribbean seawater is 50.9 ± 0.5 mS/cm (n = 8). The mean saline groundwater conductivity was not significantly less than that of seawater (49.8 ± 1.4 mS/cm, n = 47) (Table 5.1). Saline groundwater within caverns had the lowest mean specific conductance (48.9 ± 2.1 mS/cm, n = 3), while the deep saline zone had the highest specific conductance, with a mean greater than that of seawater (51.5 ± 0.3 mS/cm, n = 5).

There were no significant changes in saline groundwater specific conductance with distance inland from the Caribbean Sea (Figure 5.4). In general, conductivity increases with depth below the mixing zone/saline zone interface (Figure 5.5). This is shown clearly in a profile of samples obtained from the saline zone of an individual site (Figure 5.6). At The Pit, for example, saline groundwater conductivity increases at a rate of ~0.02 mS/m (23.2 μS/m). It is interesting to note that there is an inflection in the data at or near seawater specific conductance (at ~42 m depth) and other inflections are observed at 30 and 55 m. The data suggests that the maximum specific conductance within the saline zone at a given site will coincide with the maximum known depth of the cave system (Figure 5.7). This is particularly obvious for sites with cave passage extending below 60 m water depth (Figure 5.7).

Table 5.1 Summary of mean saline water sample field measurements (±1σ).

Site Type	Conductivity (mS/cm)	*in situ* Temperature (°C)	Dissolved Oxygen (% saturation)	pH	Alkalinity (mM HCO_3^-)
Mean Seawater	50.9 ± 0.5 (n=8)	27.96 ± 0.03 (n = 2)	94 ± 2 (n = 3)	8.32 ± 0.14 (n = 8)	2.58 ± 0.03 (n = 3)
Mean Saline Groundwaters	49.8 ± 1.4 (n = 47)	25.80 ± 3.94 (n= 48)	27 ± 12 (n = 44)	7.24 ± 0.18 (n = 49)	2.63 ± 0.65 (n = 47)
Open Pit Cenotes	49.7 ± 1.3 (n = 8)	25.65 ± 0.58 (n = 9)	22 ± 12 (n = 7)	7.11 ± 0.24 (n = 9)	2.60 ± 0.61 (n = 8)
Caverns	48.9 ± 2.1 (n = 3)	26.08 ± 0.59 (n = 3)	38 ± 12 (n = 3)	7.22 ± 0.08 (n = 3)	2.45 ± 0.12 (n = 3)
Cave Sites	49.3 ± 1.0 (n = 21)	25.99 ± 0.53 (n = 20)	31 ± 8 (n = 19)	7.27 ± 0.07 (n = 21)	2.56 ± 0.37 (n = 20)
Coastal Sites	49.8 ± 1.3 (n =7)	27.34 ± 0.96 (n = 7)	31 ± 9 (n = 7)	7.35 ± 0.12 (n = 7)	2.43 ± 0.24 (n = 7)
Deep Saline Zone	51.5 ± 0.3 (n = 5)	27.35 ± 0.67 (n = 5)	15 ± 1 (n = 4)	7.23 ± 0.20 (n = 5)	2.44 ± 0.04 (n = 5)
Sulfide layers	50.6 ± 0.6 (n = 3)	27.10 ± 2.44 (n = 3)	9 ± 9 (n = 3)	7.36 ± 0.20 (n = 3)	3.57 ± 1.97 (n = 3)
Analytical Uncertainty (±1σ)	±0.5	±0.02	±1	±0.02	± 0.01

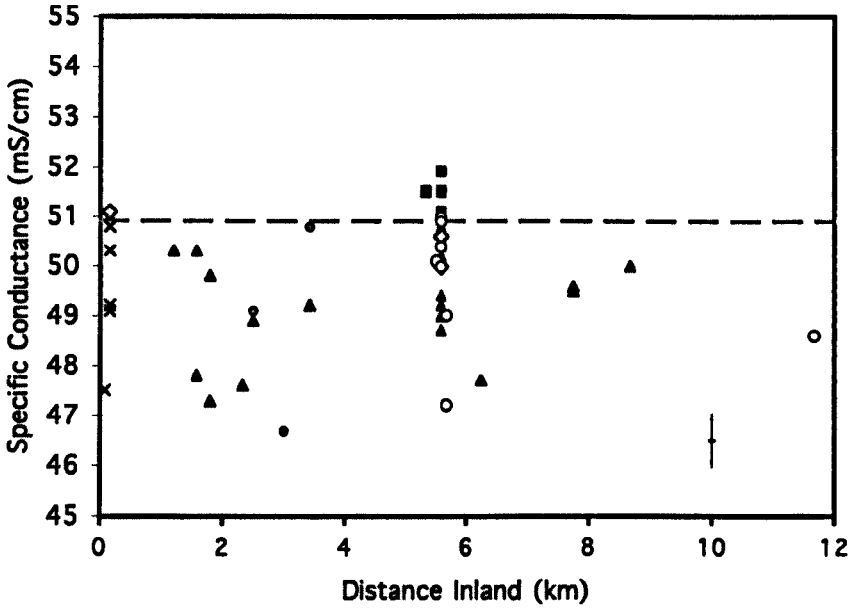

Figure 5.4 Saline groundwater conductivity against distance inland for sites within the deep saline zone (grey squares), caves (black triangles), caverns (grey circles), coastal sites (crosses), sulfide layers (open diamonds), and open pit cenotes (open circles). Mean Caribbean Seawater specific conductance represented by dashed grey line. The Caribbean Sea is located at 0 km inland, while all other distances are measured west of this. Cross represents analytical uncertainties of $\pm 1\sigma$.

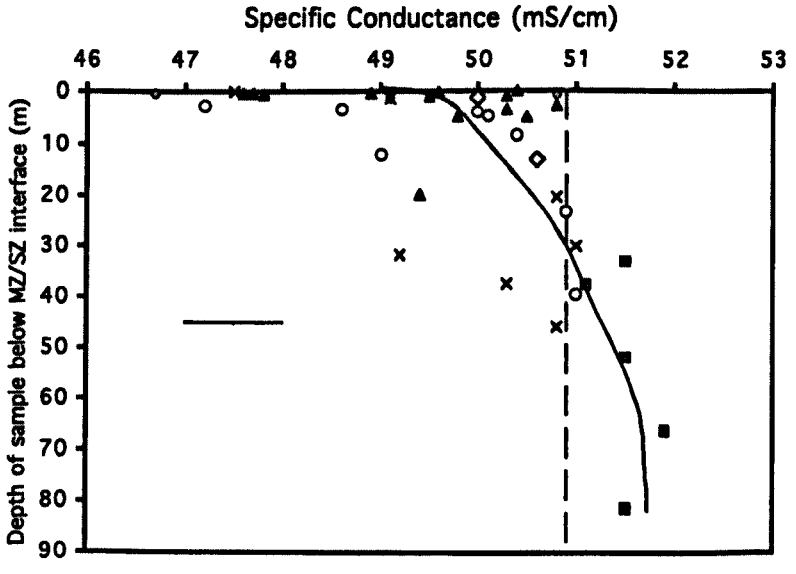

Figure 5.5 Saline groundwater conductivity against depth below the mixing zone (MZ) - saline zone (SZ) interface for sites within the deep saline zone (grey squares), caves (black triangles), caverns (grey circles), coastal sites (crosses), sulfide layers (open diamonds), open pit cenotes (open circles). Dashed grey line represents mean Caribbean Seawater specific conductance. Cross represents analytical uncertainties of $\pm 1\sigma$.

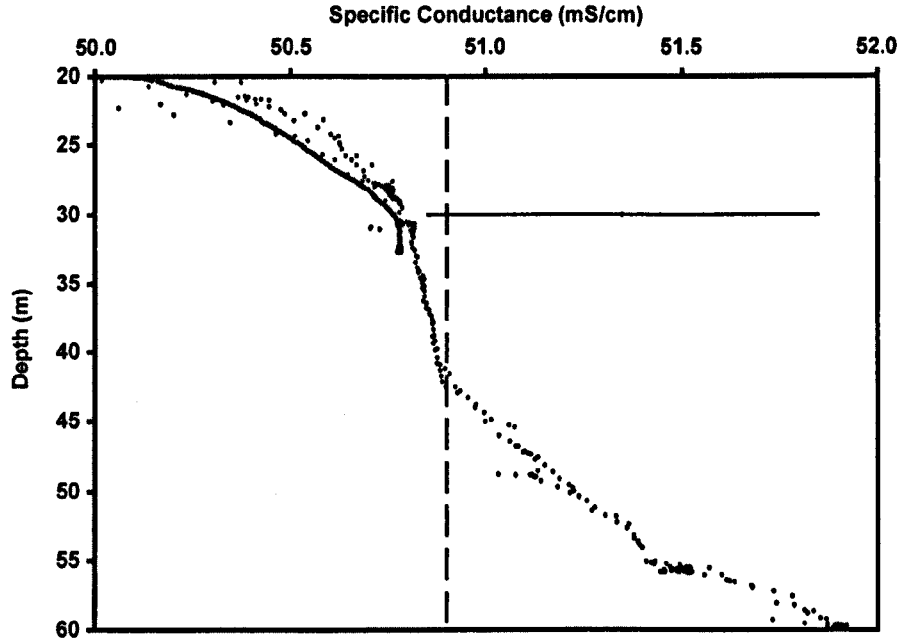

Figure 5.6 Specific conductivity against depth. Data from the saline zone of The Pit (Sistema Dos Ojos) plotted in black. Dashed grey line shows seawater value. Cross is representative analytical uncertainties (±1σ).

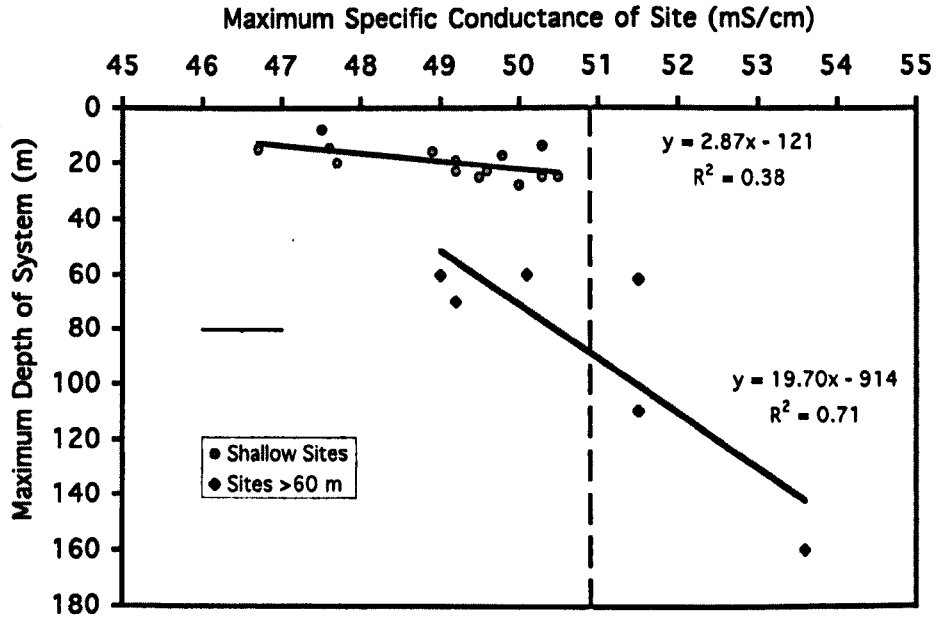

Figure 5.7 Maximum specific conductivity observed at a site against the maximum known (water) depth of that site. Dashed grey line shows seawater conductivity value, solid lines are best-fit regression lines for the two trends (shallow and > 60 m deep). Cross shows representative analytical uncertainties (±1σ).

5.4.2.2 Temperature

The *in situ* temperature of Caribbean seawater is 27.96 ± 0.03°C (n = 2). The mean *in situ* saline groundwater temperature is not significantly less than that of seawater (25.80 ± 3.94°C, n = 48) (Table 5.1). Saline groundwater sites with temperatures significantly less than that of seawater include open pit cenotes, caverns and caves, while saline groundwaters within the deep saline zone, coastal and sulfide sites had the highest temperatures, with means of each type approaching that of seawater (Table 5.1).

Saline groundwater temperature does not significantly decrease with distance inland from the Caribbean Sea (Figure 5.8) ($r^2 = 0.34$). This relationship is stronger (although still not significant) when samples taken from cave sites are considered on their own ($r^2 = 0.57$).

In general, saline groundwater temperature increases with depth and a profile of samples taken throughout the saline zone of The Pit demonstrates that the overall rate of temperature increase is ~39°C/km, which is similar to the geothermal gradient of the Straits of Florida (40°C/km) (Figure 5.9). Interestingly, there are inflections in the temperature data at ~29 and ~41 and 55 m depth, similar to those observed in specific conductance. Also, temperature may increase with increasing specific conductance (Figure 5.10), although the r^2 value is only 0.18 when all site types are examined together and no clear trends are apparent when site types are examined individually (Figure 5.10).

5.4.2.3 Dissolved Oxygen

The dissolved oxygen (DO) concentration of Caribbean seawater is 94 ± 2% saturation (n = 3). The mean saline groundwater DO content is 27 ± 12% saturation (n = 44) (Table 5.1). Saline groundwaters containing sulfide had the lowest mean DO concentration (9 ± 9% saturation, n = 3), and deep saline zone DO was also low (15 ± 1%, n = 4), while caverns, caves and coastal sites had the highest DO concentrations in the saline groundwaters (Table 5.1). Only one measurement of 0% DO was obtained throughout this study; from the sulfide zone within a coastal site (Ak Kimin, 50 m water depth).

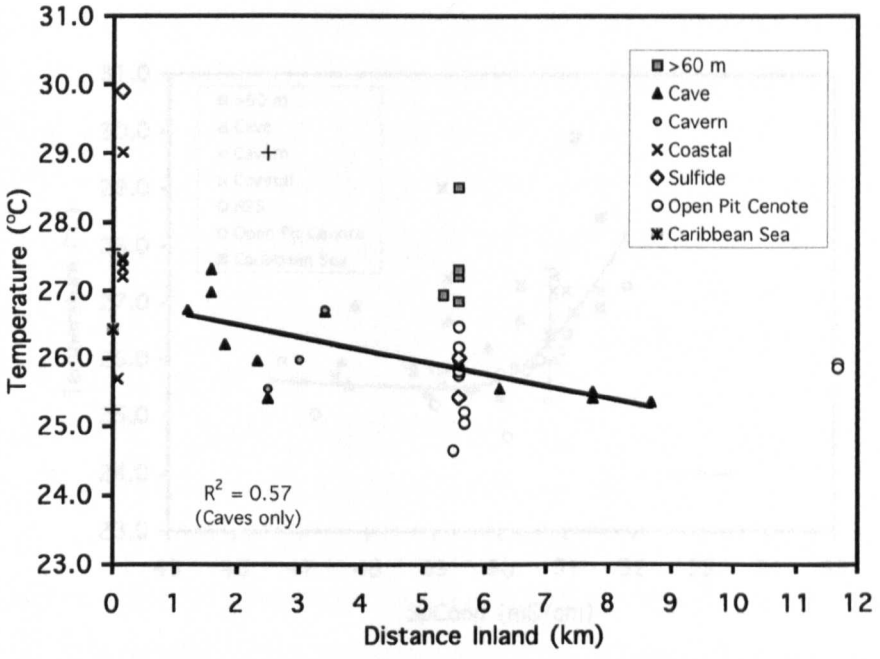

Figure 5.8 Saline groundwater temperature against distance inland. The Caribbean Sea is located at 0 km inland, while all other distances are measured west of this. Cross shows representative analytical uncertainties (±1σ).

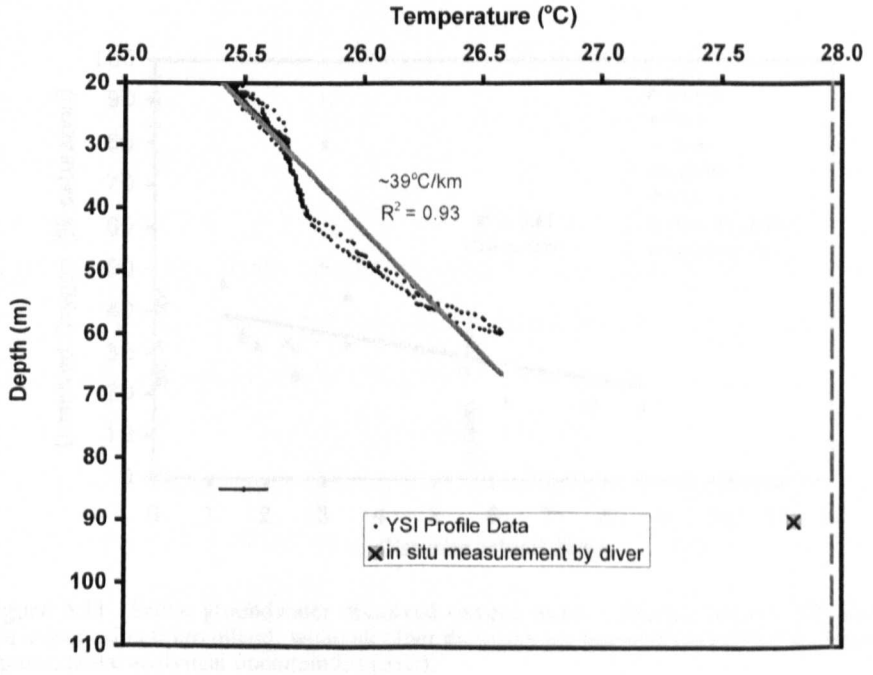

Figure 5.9 Temperature profile with depth from the saline zone of The Pit. Dashed grey line shows seawater temperature value, solid grey line is the best-fit regression line. Deepest data point (cross in grey square) is from an *in situ* measurement made by divers (data corrected to YSI readings). Cross shows representative analytical uncertainties (±1σ).

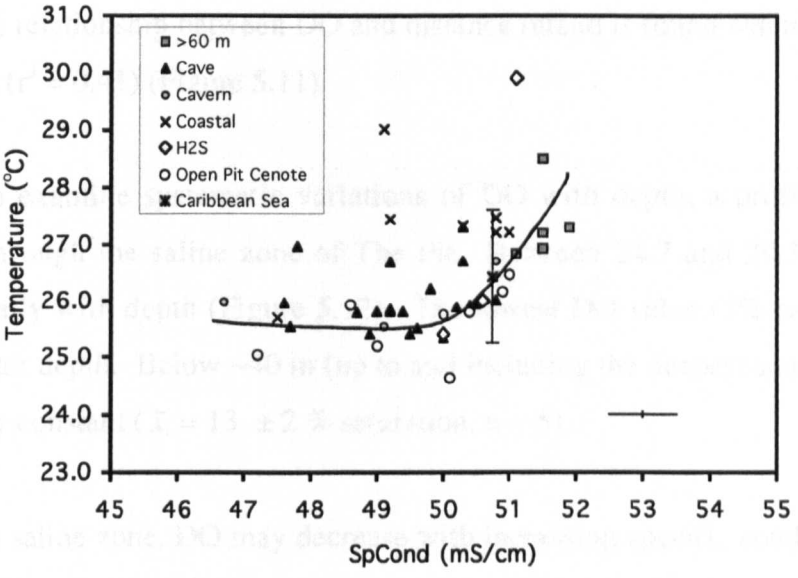

Figure 5.10 Saline groundwater temperature against specific conductivity. Crosses are representative analytical uncertainties (±1σ).

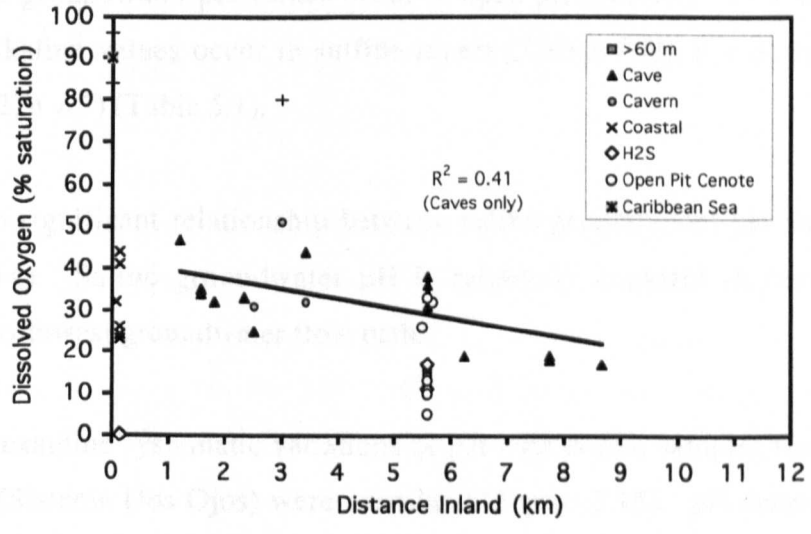

Figure 5.11 Saline groundwater dissolved oxygen against distance inland. The Caribbean Sea is located at 0 km inland, while all other distances are measured west of this. Crosses are representative analytical uncertainties (±1σ).

Saline groundwater DO concentrations do not significantly decrease with distance inland from the Caribbean Sea (r^2 = 0.10) (Figure 5.11). A stronger (although still not significant) relationship between DO and distance inland is found when only cave sites are considered (r^2 = 0.41) (Figure 5.11).

In order to examine systematic variations of DO with depth, a profile of samples was obtained through the saline zone of The Pit. Between 24.7 and 29.3 m, DO decreases systematically with depth (Figure 5.12). The lowest DO value (5% saturation) occurs at 29.3 m water depth. Below ~40 m (up to and including the deepest sample at 105 m), DO is relatively constant ($\bar{x}$ = 13 ± 2 % saturation, n = 5).

In the deep saline zone, DO may decrease with increasing specific conductance (r^2 = 0.88) (Figure 5.13). No other obvious relationships exist between these two variables.

5.4.2.4 pH

The pH of Caribbean Seawater is 8.32 ± 0.14 (n=8), while the mean pH of saline groundwaters is significantly lower than this (7.24 ± 0.18, n = 49) (Table 5.1). The lowest mean saline groundwater pH values occur in open pit cenotes (7.11 ± 0.24, n = 9), while the most alkaline values occur in sulfide layers (7.36 ± 0.20, n = 3) and at coastal sites (7.35 ± 0.12, n = 7) (Table 5.1).

There is no significant relationship between saline groundwater pH and distance inland (Figure 5.14). Saline groundwater pH is relatively constant in cave sites along the southeast-northwest groundwater flow path.

In order to examine systematic variations of pH with depth, samples from the saline zone of The Pit (Sistema Dos Ojos) were examined (Figure 5.15). pH decreases from 7.35 to 7.16 between 24.7 and 28.4 m depth. pH then increases from 7.16 to 7.36 between 28.4 and 33.8 m. Below 34 m, pH decreases systematically with depth (at a rate of 5.84 x 10^{-3} pH units/m), although an increase in 0.10 pH units occurs between the deepest two samples. pH remains relatively constant with increasing conductivity (Figure 5.16). However, pH may decrease with increasing conductivity in deep saline zone sites (Figure 5.16).

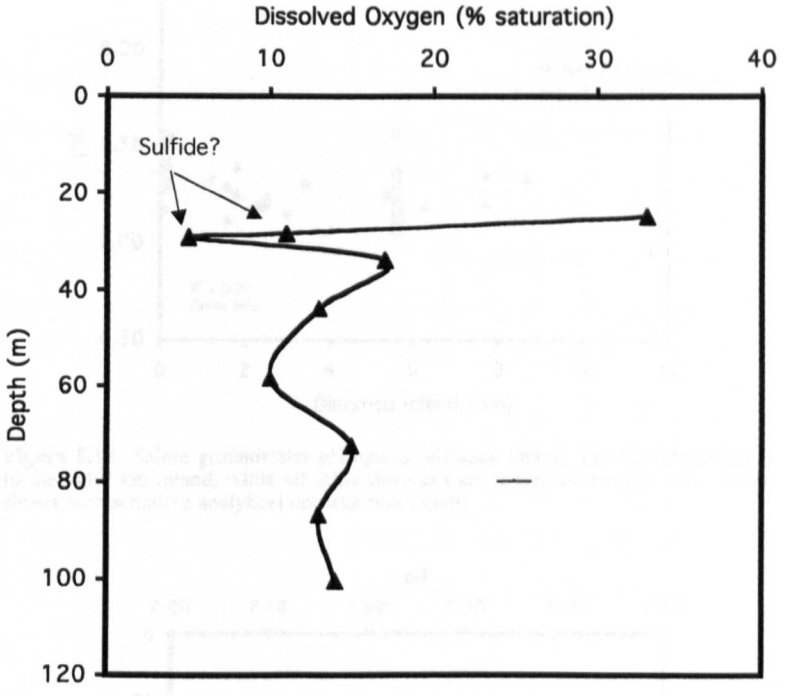

Figure 5.12 Dissolved oxygen profile with depth from the saline zone of The Pit. Measurements are from individual samples run through a flow-through cell at the surface. Cross shows representative analytical uncertainties (±1σ).

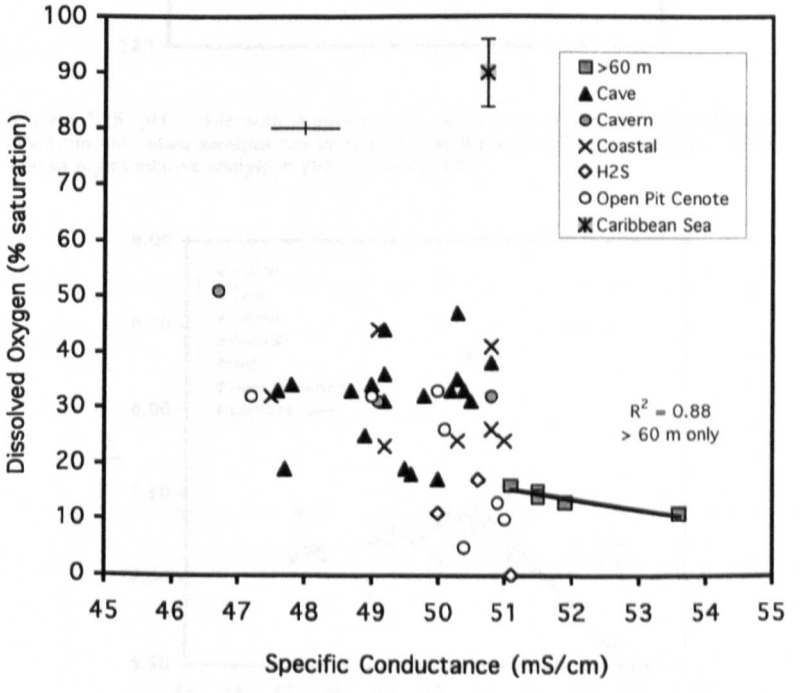

Figure 5.13 Saline groundwater and seawater dissolved oxygen against specific conductivity. Cross shows representative analytical uncertainties (±1σ).

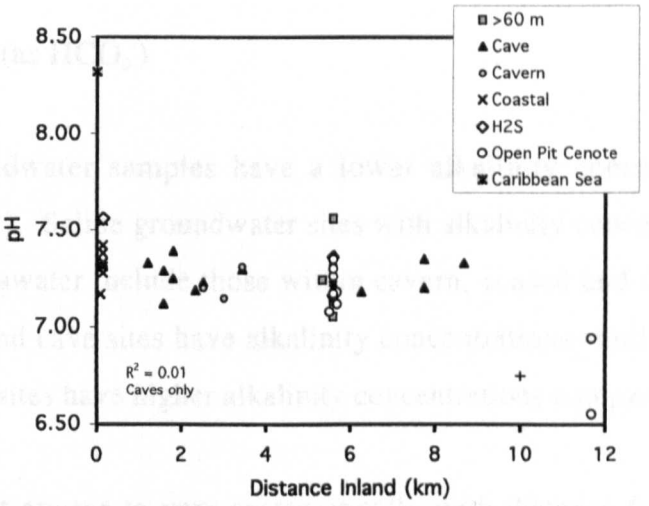

Figure 5.14 Saline groundwater pH against distance inland. The Caribbean Sea is located at 0 km inland, while all other distances are measured west of this. Cross shows representative analytical uncertainties (±1σ).

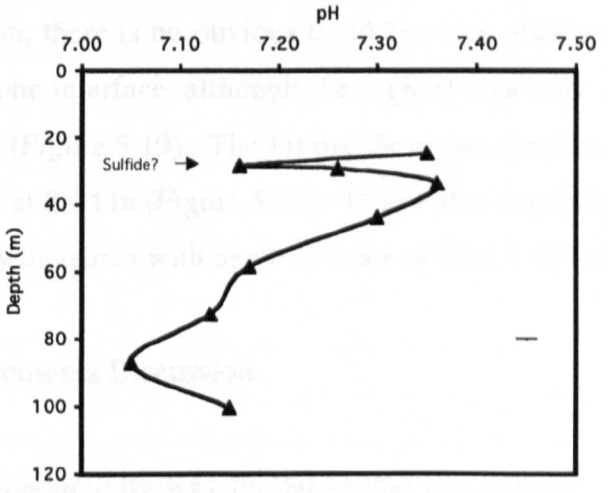

Figure 5.15 pH profile with depth from the saline zone of The Pit. Measurements are from individual samlpes run through a flow-through cell at the surface. Cross shows representative analytical uncertainties (±1σ).

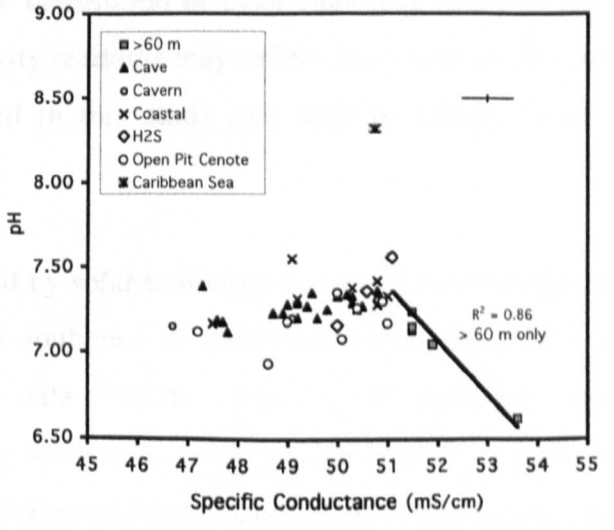

Figure 5.16 Saline groundwater pH against specific conductance. Crosses Cross shows representative analytical uncertainties (±1σ).

5.4.2.5 Alkalinity (as HCO_3^-)

Most saline groundwater samples have a lower alkalinity concentration than that of seawater (Table 5.1). Saline groundwater sites with alkalinity concentrations significantly less than that of seawater include those within cavern, coastal and deep saline zone sites. Open pit cenotes and cave sites have alkalinity concentrations similar to that of seawater, while sulfide layer sites have higher alkalinity concentrations compared to seawater.

Alkalinity does not appear to vary systematically with distance from the coast (Figure 5.17) but alkalinity decreases with increasing conductivity (Figure 5.18) and samples from sites with associated sulfide layers have the highest concentrations (e.g. The Pit, Angelita, Sabak Ha). In addition, there is no obvious trend between alkalinity and depth below the mixing zone/saline zone interface, although the highest alkalinity values seem to occur at the shallowest depths (Figure 5.19). The Pit profile shows that the highest alkalinity (5.84 mM HCO_3^-) occurred at 28.4 m (Figure 5.20). Below this depth, between 24.7 and 105 m water depth, alkalinity increases with depth at a rate of 2.11×10^{-3} mM/m (Figure 5.20).

5.4.3 Field Measurements Discussion

Saline groundwater conductivity was similar to that of seawater. Some sites have lower values than seawater, suggesting dilution from mixing with the overlying freshwater lens. Other sites (specifically, deep saline zone sites) have conductivities higher than seawater, possibly indicating the dissolution of evaporites (e.g. Perry et al., 1989). Alternatively, these higher conductivity readings may reflect true (undiluted) seawater conductivity (i.e. the seawaters sampled in this study may still be diluted from coastal discharges of fresh/brackish water).

Warm seawater (heated by solar radiation) enters the caves at the coast. This water cools as it travels along the southeast to northwest groundwater flow path, as evidenced by temperature and flow data. Sulfide layers (within open pit cenotes) also have higher temperatures, probably because they are associated with an increase in particulate matter (evidenced by field observations) that absorbs heat from the sun. In addition, temperature increases with water depth at a rate expected from geothermal heating (~40°C/km).

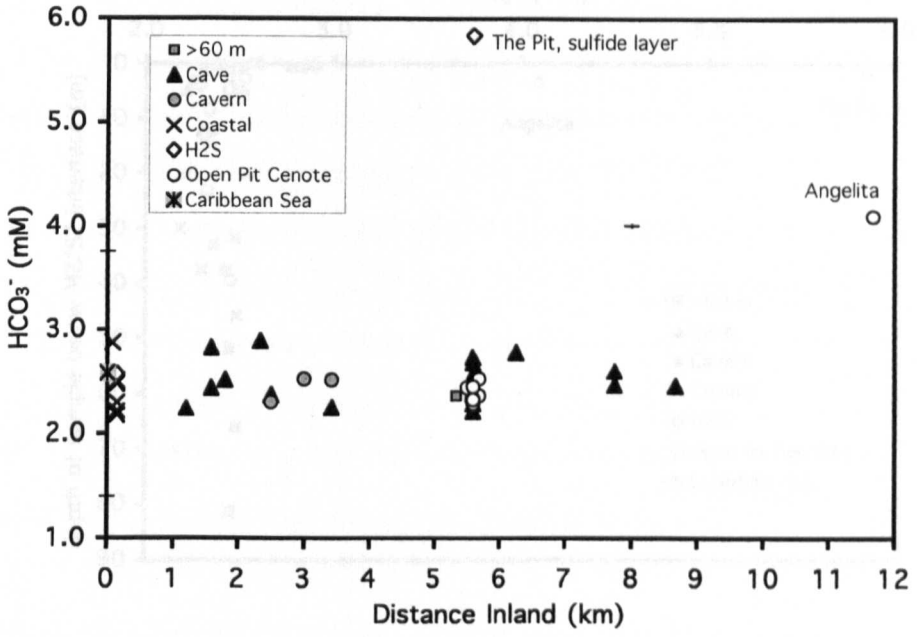

Figure 5.17 Saline groundwater alkalinity (as HCO_3^-) against distance inland. The Caribbean Sea is located at 0 km inland, while all other distances are measured west of this. Crosses are representative analytical uncertainties (±1σ).

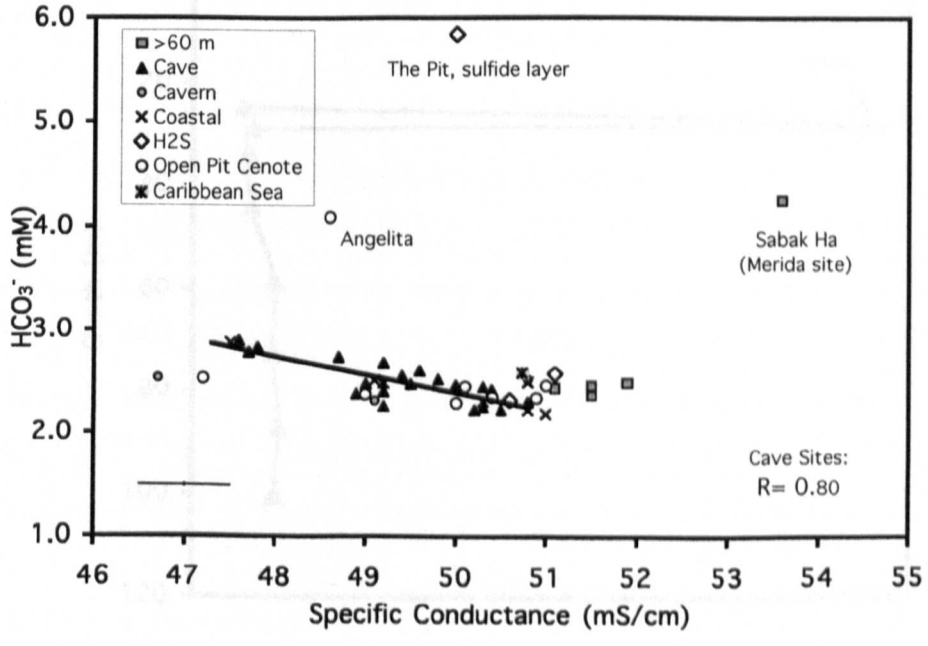

Figure 5.18 Saline groundwater alkalinity (as HCO_3^-) against specific conductance. Cross shows representative analytical uncertainties (±1σ).

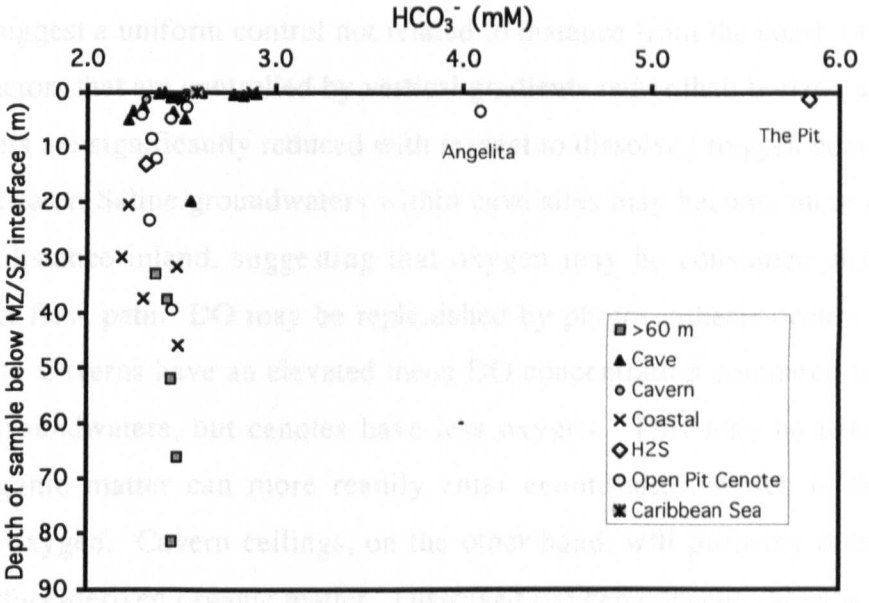

Figure 5.19 Saline groundwater alkalinity (as HCO_3^-) against depth below the mixing zone (MZ) - saline zone (SZ) interface. Crosses are representative analytical uncertainties (±σ)

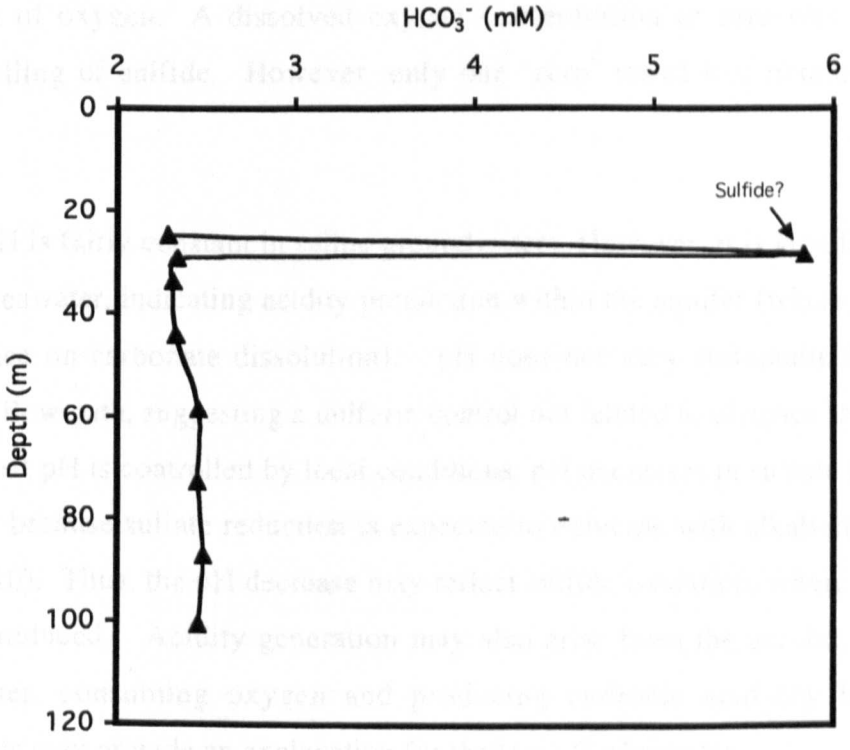

Figure 5.20 Alkalinity (as HCO_3^-) profile with depth from the saline zone of The Pit. Measurements are from individual samples. Cross shows representative analytical uncertainties (±1σ).

When considered on a larger scale, the data may be deemed to be very evenly distributed. This may suggest a uniform control not related to distance from the coast, or possibly that these are factors that are controlled by vertical gradients rather than horizontal ones. Saline groundwaters are significantly reduced with respect to dissolved oxygen content compared to open seawater. Saline groundwaters within cave sites may become more depleted with increasing distance inland, suggesting that oxygen may be consumed along the saline groundwater flow path. DO may be replenished by photosynthesis occurring in cenotes and caverns. Caverns have an elevated mean DO concentration compared to the mean of all saline groundwaters, but cenotes have less oxygen. This may be because surface-derived organic matter can more readily enter cenote sites, which is then oxidised, consuming oxygen. Cavern ceilings, on the other hand, will probably reduce the direct input of surface-derived organic matter. Dissolved oxygen concentrations within the deep saline zone are significantly reduced compared to shallower cave sites. This may be evidence for a geochemically distinct deeper saline groundwater body, which may have a longer residence time. In addition, low dissolved oxygen concentrations were observed in sulfide layers, and this is likely due to organic matter oxidation, resulting in the consumption of oxygen. A dissolved oxygen concentration of zero was expected for samples smelling of sulfide. However, only one 'zero' result was obtained (from Ak Kimin).

In general, pH is fairly constant in saline groundwaters. However, it is significantly lower than that of seawater, indicating acidity production within the aquifer (which could have a large influence on carbonate dissolution). pH does not vary systematically along the groundwater flow path, suggesting a uniform control not related to distance from the coast, or possibly that pH is controlled by local conditions. pH decreases in sulfide layers, which is interesting because sulfate reduction is expected to coincide with alkalinity production (Equation 5.10). Thus, the pH decrease may reflect sulfide oxidation, where sulfuric acid (H_2SO_4) is produced. Acidity generation may also arise from the aerobic oxidation of organic matter, consuming oxygen and producing carbonic acid (by heterotrophic bacteria). This may provide an explanation for the low pH of cenotes.

Alkalinity also does not vary with distance inland, suggesting that alkalinity is controlled locally, rather than being enriched or depleted systematically along the saline groundwater flow path. Alkalinity inputs could be from sulfate reduction or carbonate dissolution (e.g.

Stoessell et al., 1993). The high alkalinity observed in the shallowest samples may reflect mixing with fresher water that has dissolved calcium carbonate (Chapter 3). In The Pit (below the sulfide layer), alkalinity increases with depth (Figure 5.20). This may indicate increasing dissolution and/or sulfate reduction with depth. Alternatively (or in addition), alkalinity may be consumed at shallower depths by dolomitisation or calcite precipitation.

5.4.4 Major ion chemistry

5.4.4.1 Chloride

Chloride is considered to be conservative throughout the saline groundwaters of this study. There is a general trend of increasing chloride concentration with depth below the mixing zone/saline zone interface (Figure 5.21), with a significant difference (2σ) between the shallowest and deepest samples at individual sites (Figure 5.22). The maximum chloride concentration at a given site is in part dependent on the maximum depth of that site (Figure 5.23). There is no significant change in saline groundwater chloride concentrations with distance inland (Figure 5.24), although in general saline groundwater chloride concentrations are lower than that of seawater.

5.4.4.2 Ion ratios with chloride

The source of most major ions within the saline groundwaters is seawater. If an ion behaves conservatively, the ratio of that ion to chloride in the saline groundwaters should be the same as that found in the seawater samples. A deviation from this conservative behaviour may lend insight into the water-rock interactions occurring within the Yucatan Peninsula platform. A summary of these ion/chloride ratios for the various site types is given in Table 5.2. From this, it is apparent that the mean Mg/Cl ratio of saline groundwaters is lower than that of seawater, although the only significant overall depletion is found in the deep saline zone sites. Ca/Cl ratios are higher in saline groundwaters compared to open seawater, but this is only significant within the deep saline zone and hydrogen sulfide layers. SO_4/Cl ratios are high in the saline groundwaters compared to seawater and this is a significant increase within cave sites, coastal sites and within the deep saline zone.

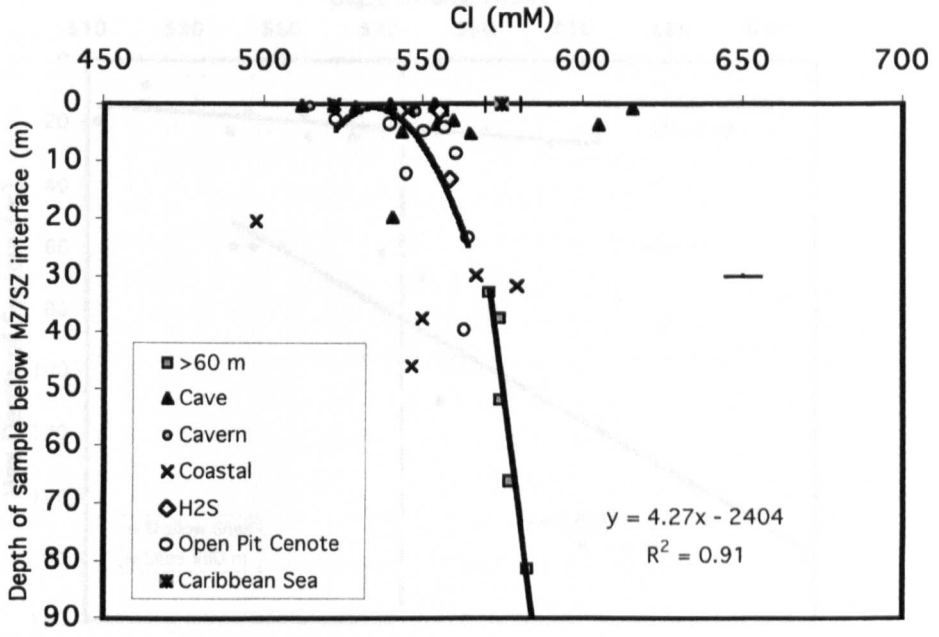

Figure 5.21 Saline groundwater chloride against depth below the mixing zone (MZ) - saline zone (SZ) interface for sites within the deep saline zone (grey squares), caves (black triangles), caverns (grey circles), coastal sites (crosses), sulfide layers (open diamonds), open pit cenotes (open circles) and the Caribbean Sea (asterisk with grey square). Crosses are representative analytical uncertainties (±1σ)

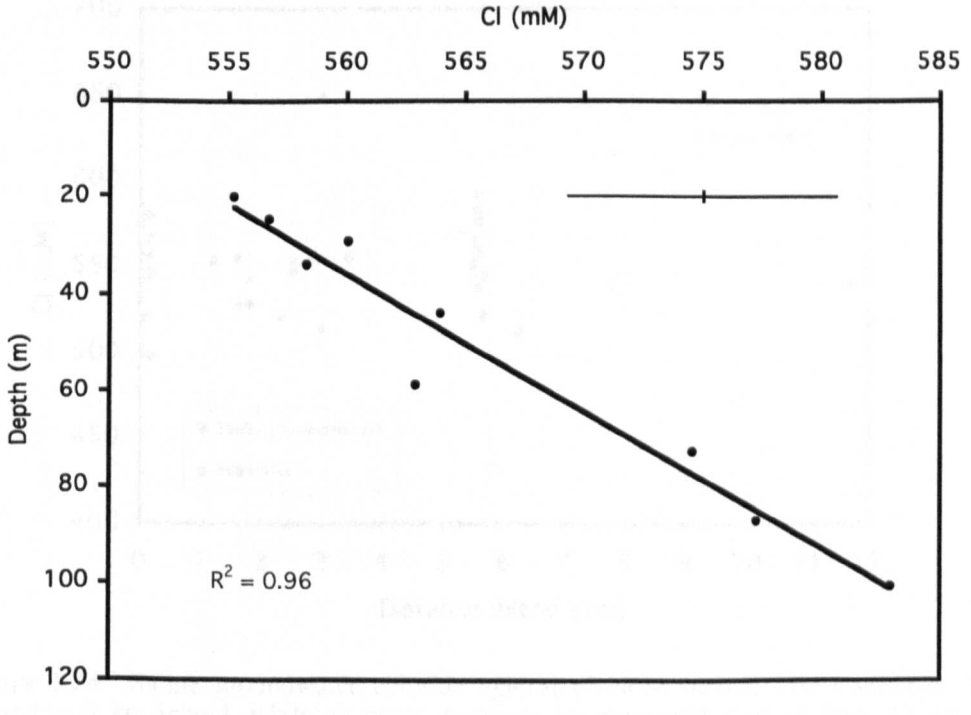

Figure 5.22 Chloride with depth from the saline zone of The Pit. Measurements are from individual samples. Crosses are representative analytical uncertainties (±1σ).

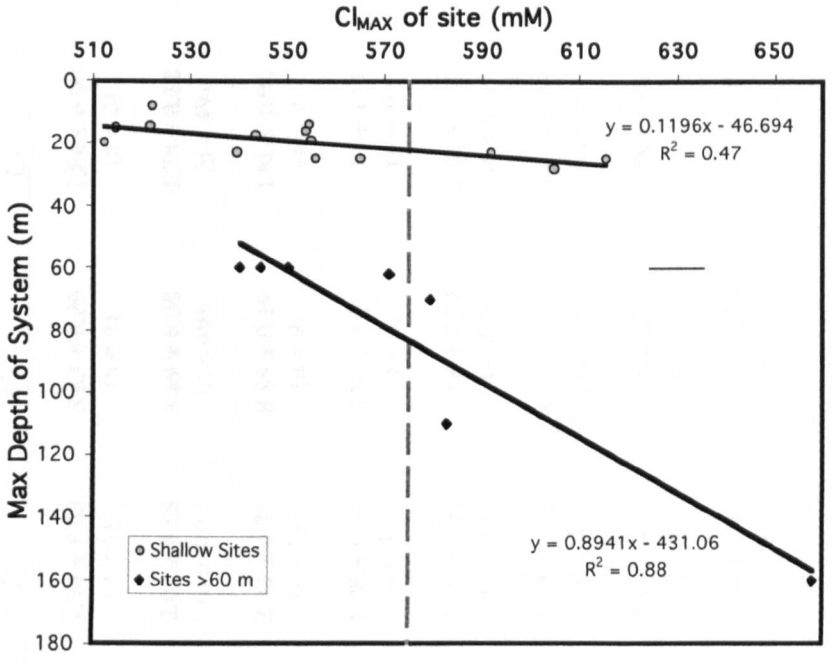

Figure 5.23 Maximum chloride concentration observed at a site against the maximum known (water) depth of that site. Dashed grey line shows seawater chloride concentration, solid lines are best-fit regression lines for the two trends (shallow and > 60 m deep). Crosses are representative analytical uncertainties (±1σ).

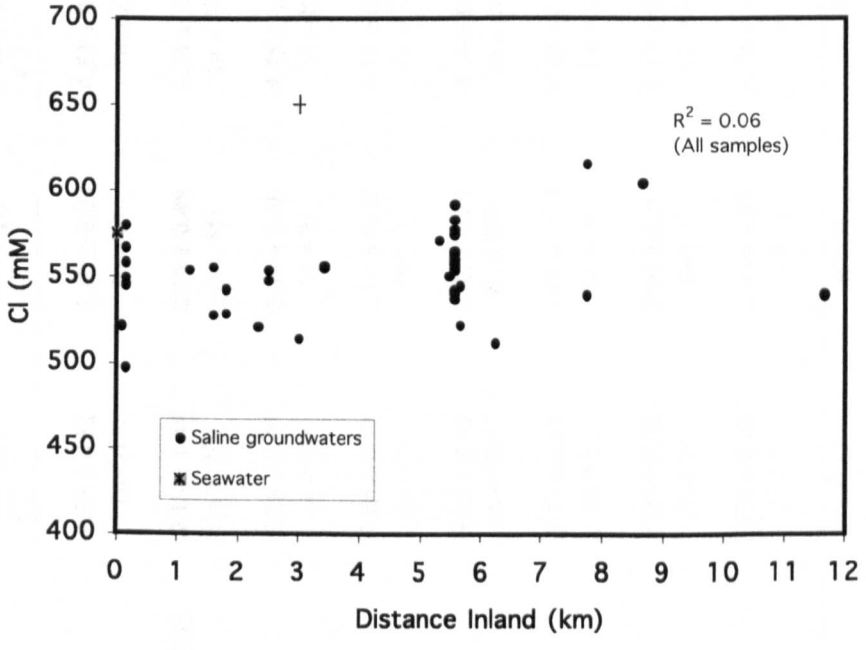

Figure 5.24 Saline groundwater chloride against distance inland. The Caribbean Sea is located at 0 km inland, while all other distances are measured west of this. Crosses are representative analytical uncertainties of ±1σ.

Table 5.2 Summary table showing the mean molar ratios of major ions with chloride for seawater and saline groundwater samples (±1σ).

Site Type	$\frac{Mg}{Cl}\times10^{2}$	$\frac{Ca}{Cl}\times10^{2}$	$\frac{HCO_3}{Cl}\times10^{3}$	$\frac{SO_4}{Cl}\times10^{2}$	$\frac{Sr}{Cl}\times10^{4}$	$\frac{Na}{Cl}\times10^{1}$	$\frac{K}{Cl}\times10^{2}$
Mean Seawater	**9.53 ± 0.12** (n=5)	**1.80 ± 0.03** (n = 5)	**4.53 ± 0.07** (n = 2)	**5.06 ± 0.05** (n = 4)	**1.74 ± 0.03** (n = 5)	**8.63 ± 0.09** (n = 4)	**1.84 ± 0.00** (n = 2)
Mean Saline Groundwaters	**9.18 ± 1.44** (n = 50)	**2.08 ± 0.49** (n= 48)	**4.74 ± 1.15** (n = 47)	**5.28 ± 0.22** (n = 51)	**2.02 ± 0.55** (n = 40)	**8.69 ± 0.38** (n = 49)	**1.78 ± 0.12** (n = 49)
Open Pit Cenotes	9.23 ± 0.39 (n = 9)	2.39 ± 0.78 (n = 9)	4.75 ± 1.17 (n = 8)	5.44 ± 0.43 (n = 9)	2.33 ± 0.71 (n = 8)	8.85 ± 0.19 (n = 9)	1.80 ± 0.08 (n = 9)
Caverns	9.63 ± 0.17 (n = 3)	1.84 ± 0.02 (n = 3)	4.55 ± 0.34 (n = 3)	5.17 ± 0 (n = 3)	1.78 ± 0.01 (n = 3)	8.74 ± 0.27 (n = 3)	1.75 ± 0.13 (n = 3)
Cave Sites	9.10 ± 2.10 (n = 22)	1.88 ± 0.09 (n = 20)	4.65 ± 0.75 (n = 20)	5.23 ± 0.06 (n = 23)	1.79 ± 0.09 (n = 17)	8.58 ± 0.39 (n = 21)	1.76 ± 0.12 (n = 21)
Coastal Sites	9.47 ± 0.67 (n =7)	1.86 ± 0.13 (n = 7)	4.49 ± 0.52 (n = 7)	5.19 ± 0.02 (n = 7)	1.69 ± 0.16 (n = 4)	8.89 ± 0.58 (n = 7)	1.83 ± 0.18 (n = 7)
Deep Saline Zone	8.90 ± 0.06 (n = 5)	2.60 ± 0.16 (n = 5)	4.23 ± 0.06 (n = 5)	5.54 ± 0.08 (n = 5)	2.31 ± 0.17 (n = 5)	8.68 ± 0.13 (n = 5)	1.78 ± 0.03 (n = 5)
H_2S layers	9.50 ± 0.23 (n = 3)	1.90 ± 0.03 (n = 3)	6.42 ± 3.55 (n = 3)	5.09 ± 0.09 (n = 3)	1.85 ± 0.16 (n = 2)	8.76 ± 0.14 (n = 3)	1.85 ± 0.07 (n = 3)
Combined Analytical Uncertainty (±1σ)	± 0.32	± 0.51	± 0.09	± 0.11	± 1.20	± 0.23	± 0.63

Sr/Cl ratios are higher in the saline groundwaters compared to seawater, and this is significant in caverns and the deep saline zone. As expected, Na/Cl and K/Cl saline groundwater ratios are not significantly different from those found in the seawater samples, bar one exception in the deep saline zone, where K/Cl ratios are slightly lower than that of seawater). In the remainder of this chapter, Na and K will not be discussed in detail.

5.4.5 Excess (XS) Calculations

The effect of geochemical processes on the concentration of a particular element is established by its deviation from the concentration predicted from the dilution of Caribbean seawater (this assumes that the effect of mixing with fresh lens waters is negligible in the saline groundwater environment). The calculation of this deviation, termed 'excess concentration' (XS) is shown in Equation 5.1.

$$Ca_{XS} = Ca_{ACTUAL} - Ca_{PREDICTED} \tag{5.1}$$

Chloride is used as a conservative tracer to predict the elemental composition of a sample with a given chloride content. For example, calcium is predicted by multiplying the chloride concentration of the sample by the Ca/Cl ratio of seawater, as shown in Equation 5.2.

$$Ca_{PREDICTED} = \frac{(Ca_{SEAWATER})(Cl_{SAMPLE})}{Cl_{SEAWATER}} \tag{5.2}$$

Magnesium (Mg_{XS}), sulfate (SO_{4XS}) and strontium (Sr_{XS}) excesses are calculated in a similar manner. From Equation 5.1, a positive Ca_{XS} indicates an increase in calcium concentration above that expected from seawater, and may be explained by $CaCO_3$ dissolution or replacement dolomitisation. A negative Ca_{XS} indicates a loss of calcium, perhaps due to calcium carbonate or dolomite precipitation. Examining both Ca_{XS} and Mg_{XS} can lend important insights into the dissolution and/or precipitation processes of calcite and/or dolomite taking place. In addition, SO_{4XS} calculations can provide information about anhydrite and gypsum dissolution/precipitation reactions and sulfur redox reactions, the latter of which might be associated with dolomitisation and/or calcite dissolution (e.g. Stoessell, 1993, Vasconcelos et al., 1995, Wright, 1999, Warthmann et al.,

2000, Stern et al., 2002). In addition, strontium is incorporated into the structure of many carbonate species, and its ratio with calcium can lend insight into which minerals are dissolving or precipitating. High Sr_{XS} values may indicate the dissolution of aragonite (not expected in saline groundwater environment), calcite or evaporite minerals, while low Sr_{XS} values imply the precipitation of these minerals (Garrels and Wollast, 1978; Budd, 1988).

It should be noted that end-member consideration is crucial. XS calculations were initially carried out using:

a) seawater as the sole end-member
b) seawater and freshwater lens (from a passage also containing salt water) end-members
c) seawater and freshwater lens (from a passage containing only freshwater) end-members

Although the results for Ca_{XS} varied slightly depending on the end-member combination used (fresh lens waters are considerably enriched in calcium, Chapter 3), all differences were within analytical uncertainty and no significant differences were found (Figures 5.25-5.28). For simplicity, seawater was used as the sole end-member.

5.4.5.1 Ca_{XS}

In general, saline groundwaters are enriched in calcium ($\bar{x}$ Ca_{XS} = + 1.24 ± 3.01 mM, n = 48) relative to the dilution of seawater. Ca_{XS} increases with increasing chloride concentration and from Figure 5.29, two trends emerge (the independent reason(s) for this separation will be considered in the discussion). The first of these trends includes samples taken from the deep saline zone, open pit cenotes and possibly some cave sites. Most of the saline groundwaters within this trend are significantly enriched in calcium, relative to the dilution of seawater, and ~1 mM of calcium enrichment is observed for every ~10 mM increase in chloride.

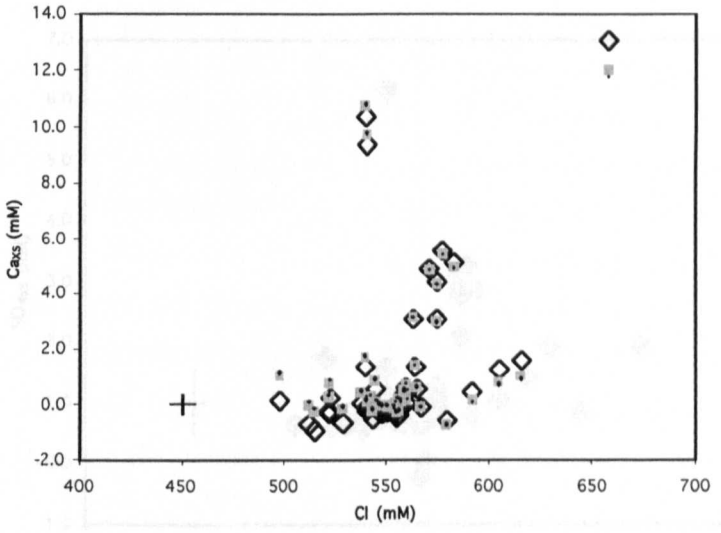

Figure 5.25 Ca_{XS} of saline groundwaters against chloride. Three end-member combinations were used in the calculations: a) seawater as the only end-member (open diamonds), b) seawater as the saline end-member with a freshwater lens sample (from a passage containing a mixing zone) as a freshwater end-member (grey squares) and c) seawater as the saline end-member with a freshwater lens sample (from an isolated freshwater lens passage - i.e. with no seawater) as the freshwater end-member (closed circles). Crosses are representative analytical uncertainties (±1σ)

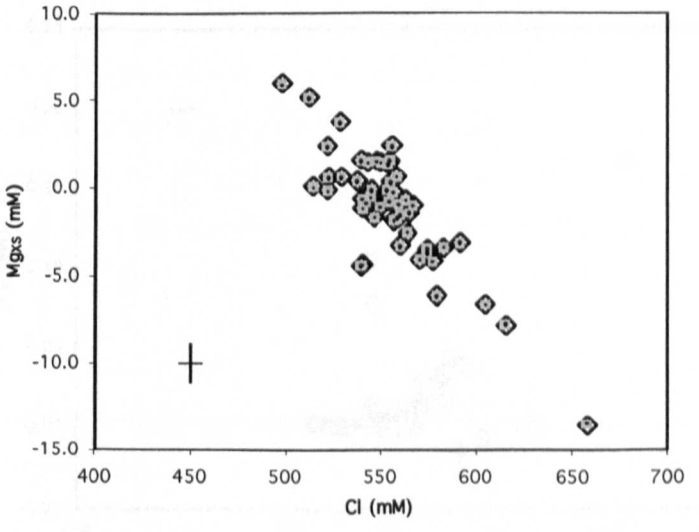

Figure 5.26 Mg_{XS} of saline groundwaters against chloride. Three end-member combinations were used in the calculations: a) seawater as the only end-member (open diamonds), b) seawater as the saline end-member with a freshwater lens sample (from a passage containing a mixing zone) as a freshwater end-member (grey squares) and c) seawater as the saline end-member with a freshwater lens sample (from an isolated freshwater lens passage - i.e. with no seawater) as the freshwater end-member (closed circles). Crosses are representative analytical uncertainties (±1σ)

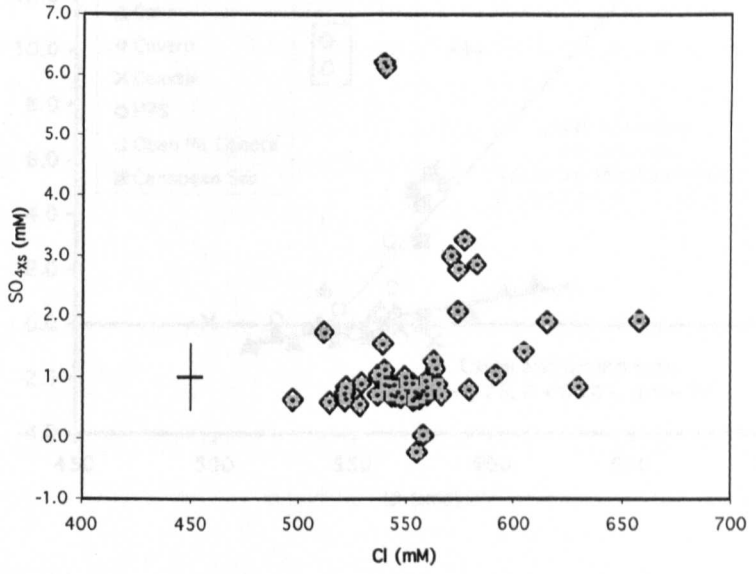

Figure 5.27 SO_{4XS} of saline groundwaters against chloride. Three end-member combinations were used in the calculations: a) seawater as the only end-member (open diamonds), b) seawater as the saline end-member with a freshwater lens sample (from a passage containing a mixing zone) as a freshwater end-member (grey squares) and c) seawater as the saline end-member with a freshwater lens sample (from an isolated freshwater lens passage - i.e. with no seawater) as the freshwater end-member (closed circles). Crosses are representative analytical uncertainties (±1σ)

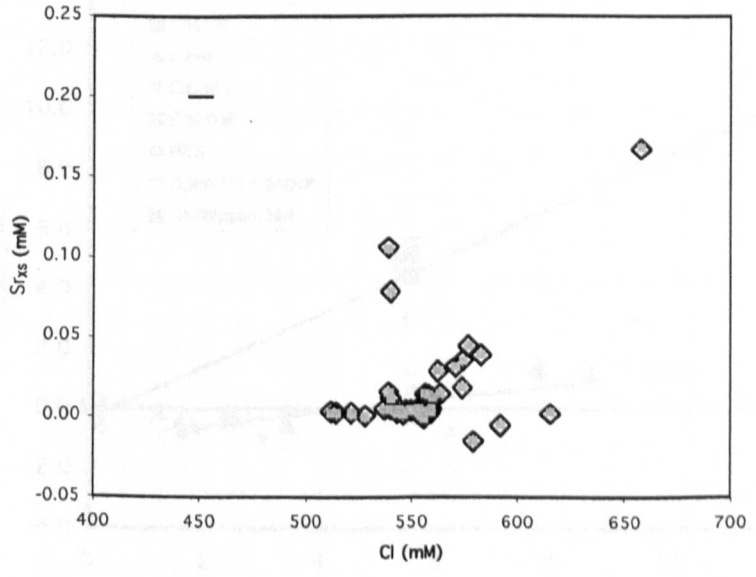

Figure 5.28 Sr_{XS} of saline groundwaters against chloride. Two end-member combinations were used in the calculations: a) seawater as the only end-member (open diamonds), b) seawater as the saline end-member with a freshwater lens sample (from a passage containing a mixing zone) as a freshwater end-member (grey squares). Crosses are representative analytical uncertainties (±1σ)

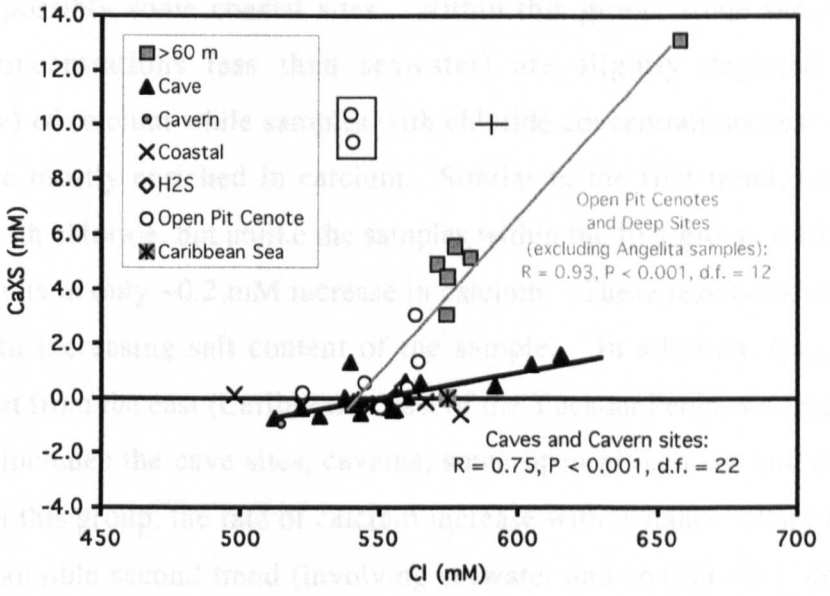

Figure 5.29 Ca_{XS} of saline groundwaters against chloride, showing two possible trends within the data set. Boxed samples are from Angelita and are considered outliers. Cross shows representative analytical uncertainties (±1σ).

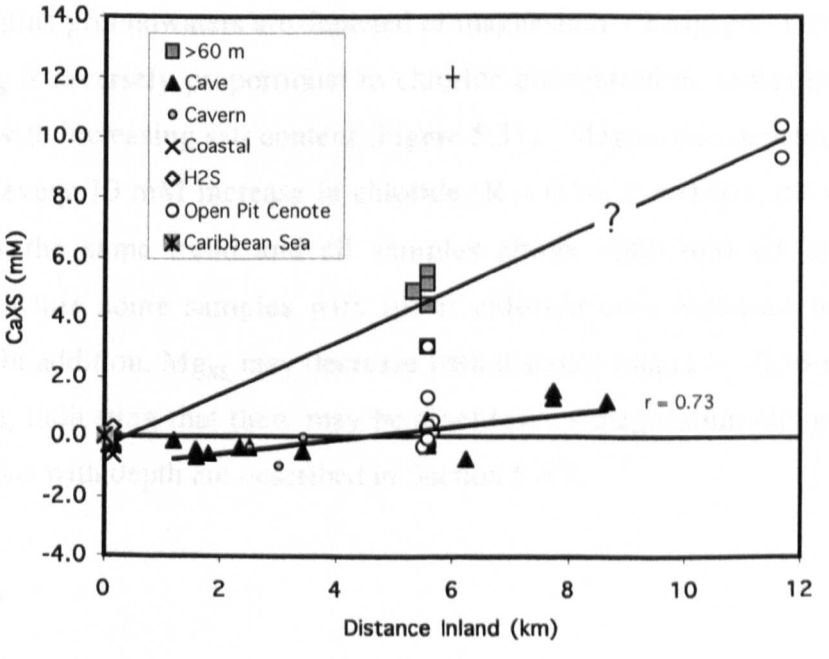

Figure 5.30 Ca_{XS} of saline groundwaters with distance inland, showing two possible trends within the data set. The Caribbean Sea is located at 0 km inland and all other distances are measured west of this. Crosses are representative analytical uncertainties (±1σ).

The second trend includes samples from caves, caverns, some open pit cenotes, sulfide layers and possibly some coastal sites. Within this group, some samples (those with chloride concentrations less than seawater) are slightly depleted (although not significantly) of calcium while samples with chloride concentrations near or above that of seawater are mostly enriched in calcium. Similar to the first trend, Ca_{xs} is positively correlated with chloride, but unlike the samples within the first group, a 10 mM increase in chloride results in only ~0.2 mM increase in calcium. These results indicate a net gain in calcium with increasing salt content of the sample. In addition, Ca_{xs} increases with distance west from the east (Caribbean) coast of the Yucatan Peninsula (Figure 5.30). The main trend includes the cave sites, caverns, some open pit cenotes and one sulfide layer site. Within this group, the rate of calcium increase with distance inland is ~0.2 mM/km. There is a possible second trend (involving seawater and coastal sites, deep sites and an open pit cenote) with a ~0.6 mM/km calcium enrichment. However, this relationship is dependant on two samples from cenote Angelita (which were considered to be outliers in the previous plot). Ca_{xs} variations with depth are described in Section 5.4.7.

5.4.5.2 Mg_{xs}

In general, saline groundwaters are depleted of magnesium ($\bar{x}Mg_{xs}$ = -1.16 ± 3.31 mM, n = 49). Mg_{xs} is inversely proportional to chloride concentration, indicating a net loss of magnesium with increasing salt content (Figure 5.31). Magnesium depletion increases by ~ 1 mM for every 10 mM increase in chloride ($R = 0.84$, $P < 0.001$, d.f = 47). All site types follow the same trend and all samples above ~560 mM Cl^- are depleted of magnesium, while some samples with lower chloride concentrations are enriched in magnesium. In addition, Mg_{xs} may decrease with distance inland (~ -0.75 mM Mg_{xs}/km), (Figure 5.32), indicating that there may be a net loss of magnesium along the flow path. Mg_{xs} variations with depth are described in Section 5.4.7.

5.4.5.3 SO_{4xs}

Saline groundwater samples are enriched in sulfate ($\bar{x}SO_{4xs}$ = + 1.26 ± 1.22 mM, n = 51). No saline zone samples had sulfate concentrations significantly less that that of seawater, including sulfide layers (Figure 5.33), indicating that there is no net loss of sulfate from the saline groundwater.

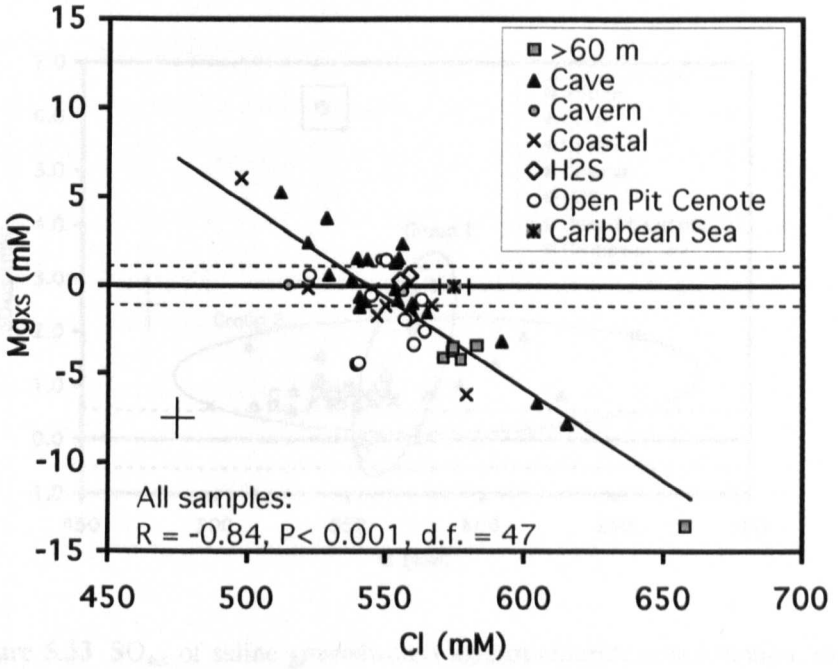

Figure 5.31 Mg_{xs} of saline groundwaters against chloride concentration. Dashed lines mark significance greater or less than zero. Cross shows representative analytical uncertainties (±1σ).

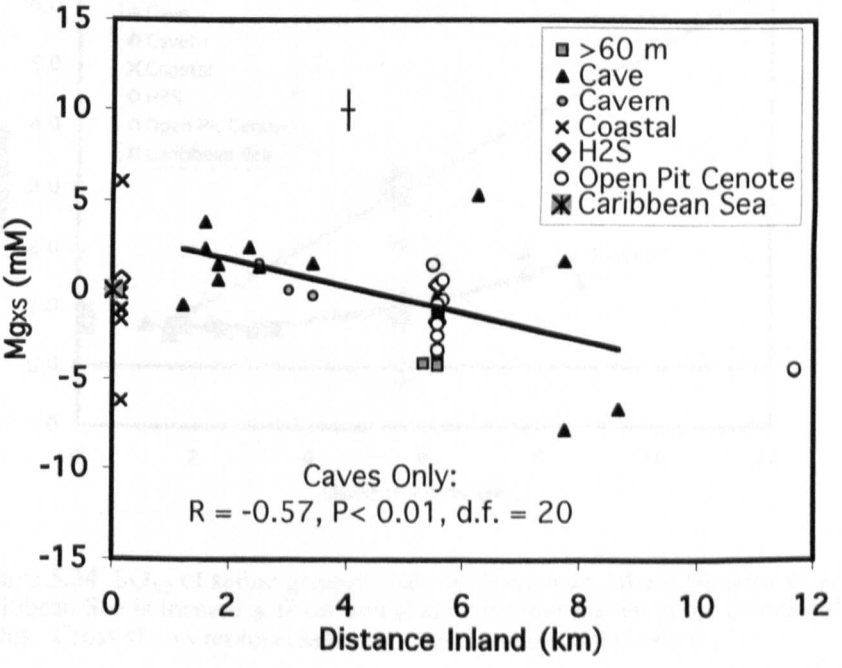

Figure 5.32 Mg_{xs} of saline groundwaters with distance inland from the coast. The Caribbean Sea is located at 0 km inland and all other distances are calculated West of this. Dashed lines mark significance greater or less than zero. Cross shows representative analytical uncertainties (±1σ).

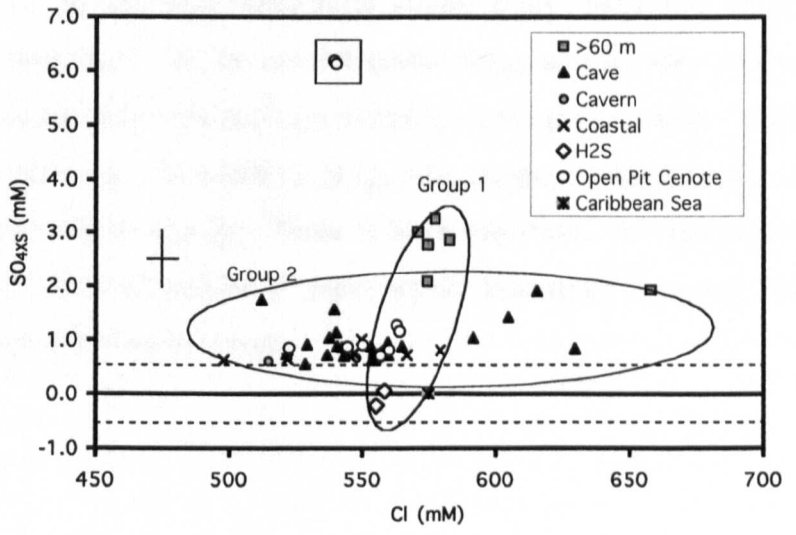

Figure 5.33 SO_{4xs} of saline groundwaters against chloride concentration, showing two possible trends within the data set (circled), one where SO_{4XS} is relatively constant with increasing chloride and another where SO_{4XS} increases with chloride. Dashed lines mark significance greater or less than zero (±1 σ). Boxed samples are from Angelita and are considered outliers. Cross shows representative analytical uncertainties (±1σ).

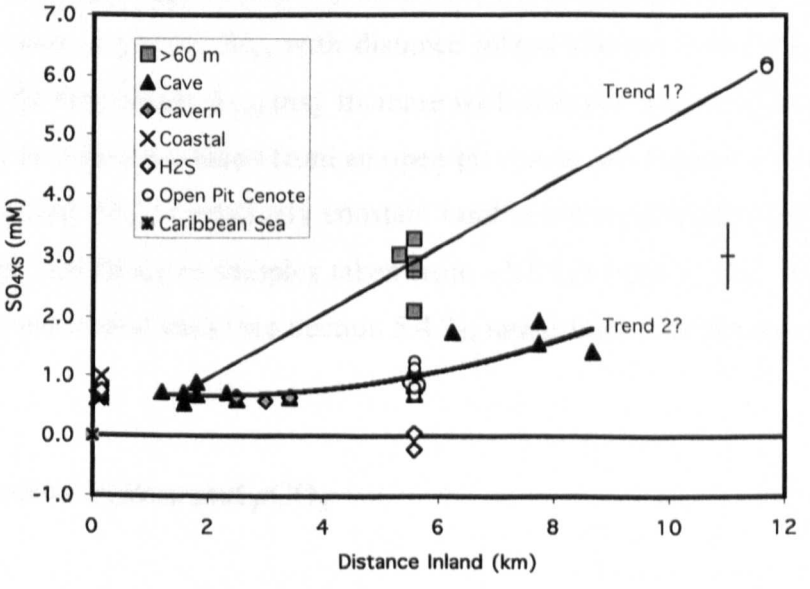

Figure 5.34 SO_{4xs} of saline groundwaters with distance inland from the coast. The Caribbean Sea is located at 0 km inland and all other distances are calculated West of this. Cross shows representative analytical uncertainties (±1σ).

From Figure 5.33, two groups of samples emerge. Within the first group, there is a trend of increasing SO_{4XS} with increasing chloride concentration and samples within this group include those from the deep saline zone, sulfide layers, some cave, some coastal and some open pit cenote sites. In the second group SO_{4XS} is relatively constant with increasing chloride concentration and includes samples from caves, caverns, some open pit cenotes and the coastal sites. In addition, SO_{4XS} may increase with distance inland (Figure 5.34) and again two trends emerge. There is high variability in samples taken from ~5.8 km inland. But, this is a function of depth within individual sites (see Section 5.4.7), rather than with distance from the coast.

5.4.5.4 Sr_{XS}

Saline groundwaters are enriched in strontium (Sr_{XS} = +0.017 ± 0.033 mM, n= 40), relative to the dilution of seawater. However, the only samples with Sr_{XS} concentrations significantly greater than zero (±2σ) include those from the deep saline zone and some open pit cenotes (Figure 5.35). As with Ca_{XS} and SO_{4XS}, two groups of samples are present. Within the first group, Sr_{XS} increases with increasing chloride concentration and in the second group, Sr_{XS} is relatively constant (and is not significantly greater or less than zero). Likewise, a plot of Sr_{XS} with distance inland (Figure 5.36) shows two groups of samples. In the first group, Sr_{XS} may increase with distance inland (although the trend may be biased by two samples taken from an open pit cenote site located ~12 km inland) and in the second group, Sr_{XS} is relatively constant (and is not significantly different from zero). There is high variability in samples taken from ~5.8 km inland. But, this is a function of depth within individual sites (see Section 5.4.7), rather than with distance from the coast.

5.4.6 Saturation Indices and pCO_2

Saturation indices (SI) with respect to calcite (C), aragonite (A), dolomite (D), disordered dolomite (DD), gypsum (G) and anhydrite (AN) and the carbon dioxide partial pressure (pCO_2) with which the water samples are in equilibrium were calculated using the geochemical modeling program PHREEQ-C (Parkhurst et al., 1995). These results are summarised for each water type in Table 5.3.

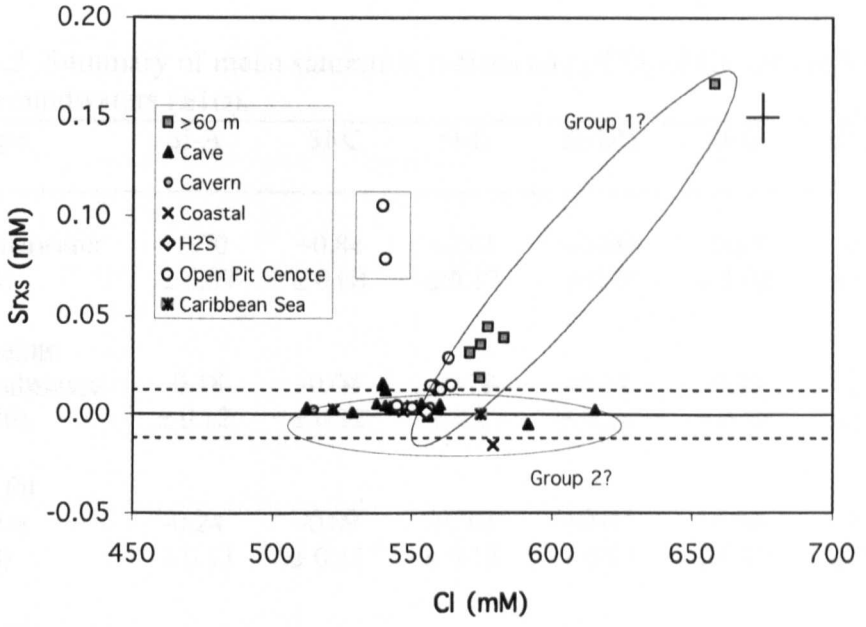

Figure 5.35 Sr_{xs} of saline groundwaters against chloride concentration, showing two possible trends/groups within the data set (circled), one where Sr_{xs} is relatively constant with increasing chloride and another where Sr_{xs} increases with chloride. Outliers (from Angelita Cenote) are boxed. Dashed lines mark significance greater or less than zero (±1σ). Cross shows representative analytical uncertainties (±1σ).

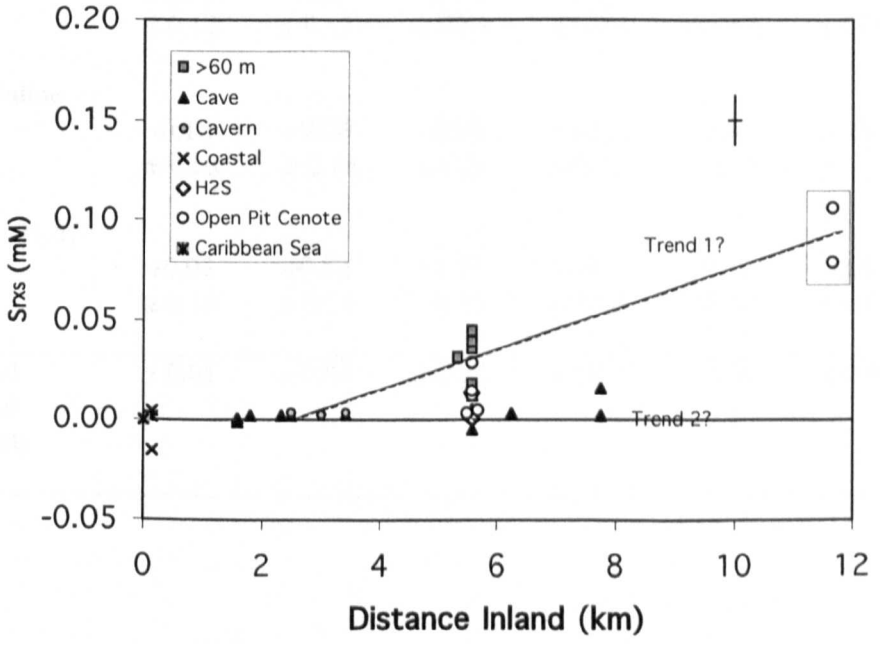

Figure 5.36 Sr_{xs} of saline groundwaters with distance inland from the coast. The Caribbean Sea is located at 0 km inland and all other distances are calculated West of this. Samples from Angelita Cenote are boxed. Cross shows representative analytical uncertainties (±1σ).

Table 5.3 Summary of mean saturation indices and pCO_2 of Caribbean Seawater and saline groundwaters (±1σ).

Site Type	SI-A	SI-C	SI-D	SI-DD	SI-G	SI-AN	pCO_2 (%)
Mean Seawater (n = 3)	+0.70 ± 0.09	+0.84 ± 0.08	+2.61 ± 0.17	+2.00 ± 0.18	-0.67 ± 0.02	-0.87 ± 0.02	0.05 ± 0.02
Mean Saline Groundwaters (n = 46)	-0.18 ± 0.12	-0.04 ± 0.12	+0.78 ± 0.25	+0.21 ± 0.24	-0.59 ± 0.10	-0.79 ± 0.11	0.62 ± 0.54
Open Pit Cenotes (n = 8)	-0.24 ± 0.13	-0.09 ± 0.13	+0.63 ± 0.18	+0.07 ± 0.17	-0.56 ± 0.12	-0.71 ± 0.19	0.69 ± 0.43
Caverns (n = 3)	-0.28 ± 0.11	-0.14 ± 0.11	+0.63 ± 0.22	+0.06 ± 0.21	-0.66 ± 0.03	-0.86 ± 0.03	0.54 ± 0.11
Cave Sites (n = 20)	-0.21 ± 0.07	-0.06 ± 0.07	+0.77 ± 0.12	+0.20 ± 0.12	-0.62 ± 0.04	-0.82 ± 0.04	0.51 ± 0.13
Coastal Sites (n = 7)	-0.14 ± 0.12	0.00 ± 0.12	+0.92 ± 0.25	+0.33 ± 0.23	-0.65 ± 0.02	-0.85 ± 0.02	0.42 ± 0.14
Deep Saline Zone (n = 5)	-0.10 ± 0.16	+0.04 ± 0.16	+0.81 ± 0.35	+0.23 ± 0.35	-0.44 ± 0.04	-0.64 ± 0.04	0.56 ± 0.22
Sulfide (H_2S) layers (n = 3)	+0.01 ± 0.14	+0.16 ± 0.14	+1.21 ± 0.31	+0.63 ± 0.28	-0.64 ± 0.02	-0.84 ± 0.02	0.69 ± 0.66
Combined Analytical Uncertainty (±1σ)	± 0.01	± 0.01	± 0.02	± 0.02	± 0.02	± 0.02	± 0.02

5.4.6.1 SI-C and SI-A

All saline groundwater samples are significantly less saturated than Caribbean seawater with respect to calcite and aragonite (Table 5.3), although saturation within caves may increase with increasing chloride concentration ($R = 0.66$, $P = 0.001$, d.f. = 19) (Figure 5.37). The means of samples from caverns, open pit cenotes and caves are undersaturated, while the means from deep sites and sulfide layers are supersaturated with respect to calcite. The mean SI-C of coastal sites is zero. In addition, there is no relationship between SI-C/SI-A and distance inland.

5.4.6.2 SI-D and SI-DD

There is a significant decrease in the saturation indices of dolomite (SI-D) and disordered dolomite (SI-DD) in saline groundwaters compared to Caribbean seawater (Table 5.3). The means of all saline groundwater samples are supersaturated with respect to dolomite and most are at equilibrium or supersaturated with respect to disordered (non-stoichiometric) dolomite. A few (six) individual samples from deep sites, cavern sites and open pit cenotes have SI-DD values less than zero and SI-D/DD may increase with increasing chloride concentration in cave sites (Figure 5.38). There is no convincing trend between SI-D or SI-DD with distance inland.

5.4.6.3 SI-G and SI-AN

There is a significant increase in the mean saline groundwater saturation indices of gypsum (SI-G) and anhydrite (SI-AN) compared to Caribbean Seawater (Table 5.3). However, the means of all saline groundwater samples remain undersaturated with respect to both SI-G and SI-AN. Open pit cenotes and deep sites have SI-G and SI-AN values significantly higher than that of seawater, while all other site types have values not significantly different from seawater. SI-G/AN may, in general, increase with increasing chloride concentration (Figure 5.39). There is a positive correlation between cave SI-G and SI-AN with distance inland ($R_{caves} = 0.77$, $P < 0.001$, d.f. = 19) (Figure 5.40).

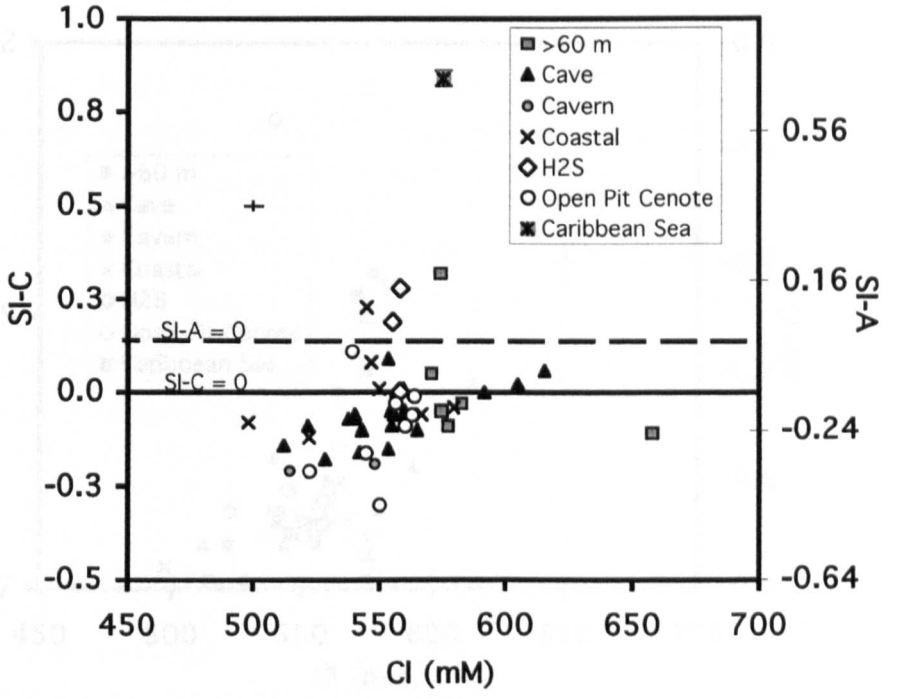

Figure 5.37 Saline groundwater aragonite (SI-A) and calcite (SI-C) saturation indices against chloride. Cross shows representative analytical uncertainties (±1σ).

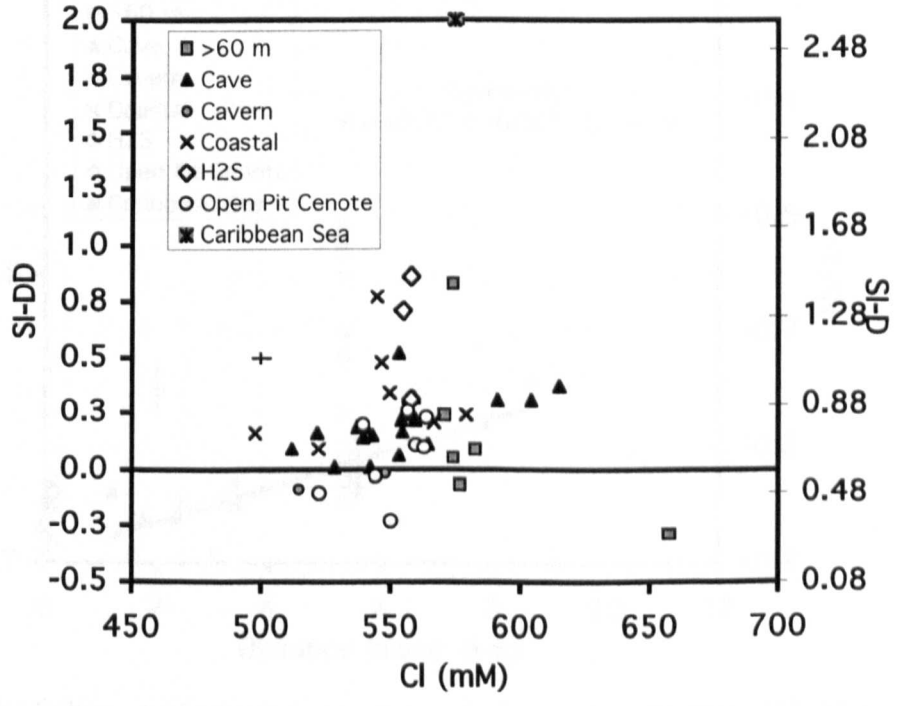

Figure 5.38 Saline groundwater dolomite (SI-D) and dissordered dolomite (SI-DD) saturation indices against chloride. Cross shows representative analytical uncertainties (±1σ).

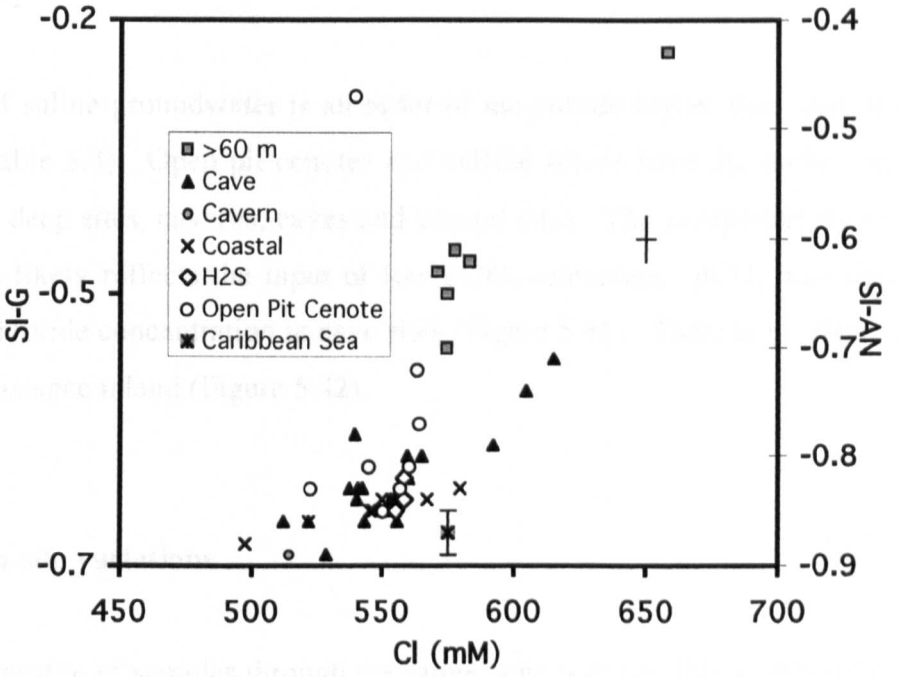

Figure 5.39 Saline groundwater gypsum (SI-G) and anhydrite (SI-AN) saturation indices against chloride. Cross shows representative analytical uncertainties (±1σ).

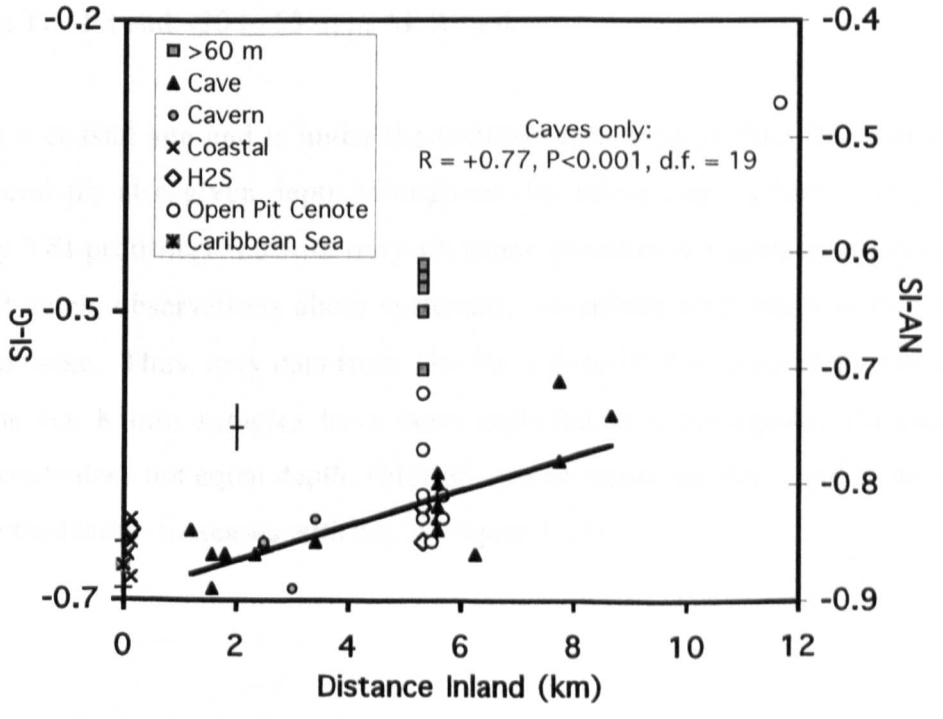

Figure 5.40 Saline groundwater gypsum (SI-G) and anhydrite (SI-AN) saturation indices with distance inland. The Caribbean Sea is located at 0 km inland and all distances are measured west of this. Cross shows representative analytical uncertainties (±1σ).

5.4.6.4 pCO_2

The pCO_2 of saline groundwater is an order of magnitude higher than that of Caribbean seawater (Table 5.3). Open pit cenotes and sulfide layers have the highest mean pCO_2, followed by deep sites, caverns, caves and coastal sites. The comparatively low pCO_2 of coastal sites likely reflects the input of low pCO_2 seawaters. pCO_2 may decrease with increasing chloride concentration in cave sites (Figure 5.41). There is no clear variation of pCO_2 with distance inland (Figure 5.42).

5.4.7 Within-site variations

Obtaining a profile of samples through the saline zone was possible within only a few sites (very often the depth of the cave floor limited access to the saline zone). Attempts to study systematic variations of chemistry with depth were made in two sites: The Pit (located ~6 km inland) and Ak Kimin (~0.15 km inland). Water samples were obtained from depths of ~25-105 m in The Pit and ~20 to 55 m in Ak Kimin.

Ak Kimin is a coastal site and is under the constant influence of tidal fluctuations. As such, the chemistry at a given depth throughout the saline zone is highly variable (as evidenced by YSI profiling) and with only six saline groundwater samples obtained from two different dates, observations about systematic variations with depth at this site are impossible to make. Thus, only data from The Pit is described with depth in this section. However, the Ak Kimin samples have been included in plots against chloride (and although chloride does not equal depth, chloride concentration usually – and in the case of The Pit, systematically - increases with depth, Figure 5.22).

5.4.7.1 XS

Mean calcium and sulfate enrichments and magnesium depletions are greater at The Pit compared to Ak Kimin (Table 5.4).

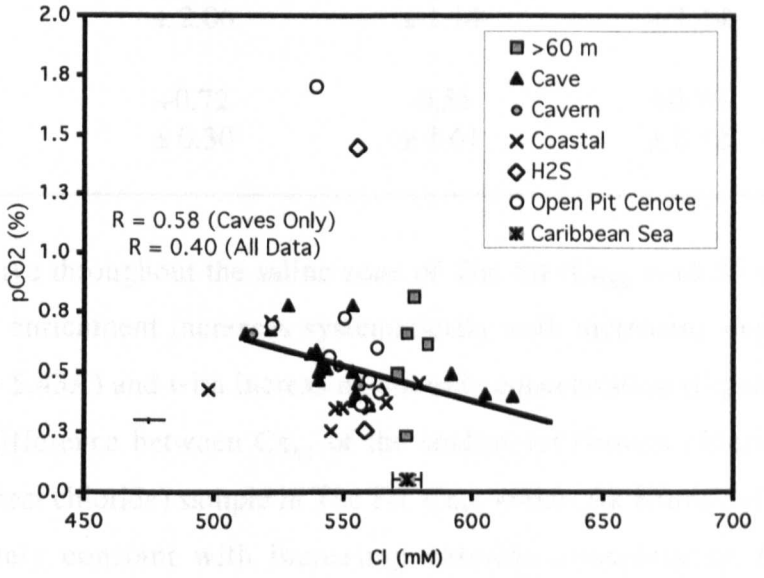

Figure 5.41 Saline groundwater $p\ CO_2$ against chloride. Crosses are representative analytical uncertainties (±1σ).

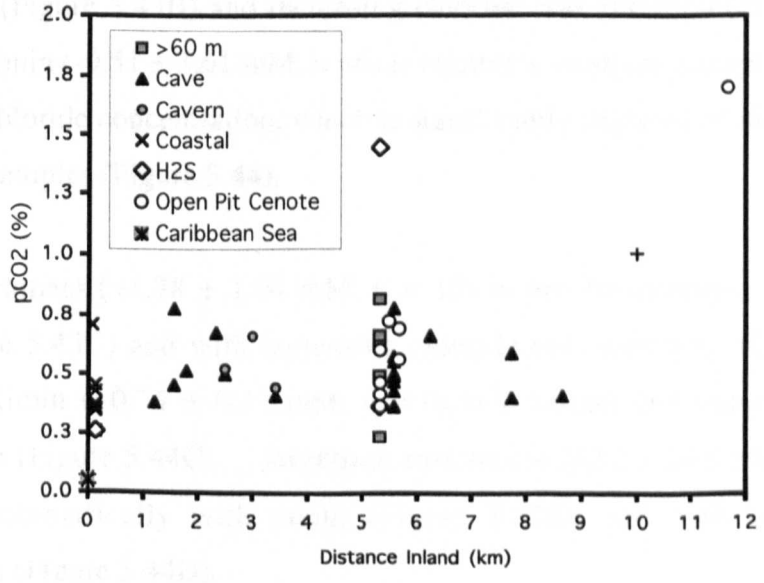

Figure 5.42 Saline groundwater $p\ CO_2$ with distance inland. The Caribbean Sea is located at 0 km inland and all distances are measured west of this. Crosses are representative analytical uncertainties (±1σ).

Table 5.4 Mean saline groundwater XS concentrations from The Pit and Ak Kimin (±1σ).

Site	Ca_{XS} (mM)	Mg_{XS} (mM)	SO_{4XS} (mM)	Sr_{XS} (μM)
The Pit (n = 10)	+3.80 ± 2.06	-2.91 ± 1.14	+1.78 ± 1.14	+22.2 ± 14.0
Ak Kimin (n = 6)	+0.72 ± 0.30	-0.51 ± 3.61	+0.75 ± 0.12	-3.1 ± 10.7 (n=3)

Ca_{XS} is positive throughout the saline zone of The Pit (Ca_{XS} = +3.80 ± 2.06 mM, n = 10) and calcium enrichment increases systematically with increasing depth below the water table (Figure 5.43A) and with increasing chloride concentration (Figure 5.44A). There is a significant difference between Ca_{XS} of the shallowest (lowest chloride) sample and the deepest (highest chloride) sample in The Pit. Ca_{XS} within Ak Kimin (+0.72 ± 0.30 mM, n = 6) is relatively constant with increasing chloride concentration (although the least enrichment coincides with the highest chloride concentration) (Figure 5.44A).

The mean magnesium depletion in The Pit is –2.91 ± 1.14 mM (n = 10) and Mg_{XS} decreases (although less systematically compared to the other parameters) with increasing water depth (Figure 5.43B) and increasing chloride concentration (Figure 5.44B). Mg_{XS} within Ak Kimin (-0.51 ± 3.61 mM, n =6) is relatively constant, except for the sample with the highest chloride concentration, which is significantly depleted of magnesium compared to the other samples (Figure 5.44).

Sulfate enrichment (+1.78 ± 1.14 mM, n = 10) in the Pit increases systematically with depth (Figure 5.43C) and with increasing chloride concentration (Figure 5.44C). SO_{4XS} within Ak Kimin (+0.75 ± 0.12 mM, n = 6) is invariant and independent of chloride concentration (Figure 5.44C). Strontium enrichment (22.2 ± 14.0 μM, n = 10) in the Pit increases systematically with depth (Figure 5.43D) and with increasing chloride concentration (Figure 5.44D).

5.4.7.2 Saturation Indices and pCO_2

Saline groundwater samples from The Pit are less saturated (and have higher pCO_2 values) compared to those from Ak Kimin (Table 5.5), suggesting undersaturation is generated along the saline groundwater flow path.

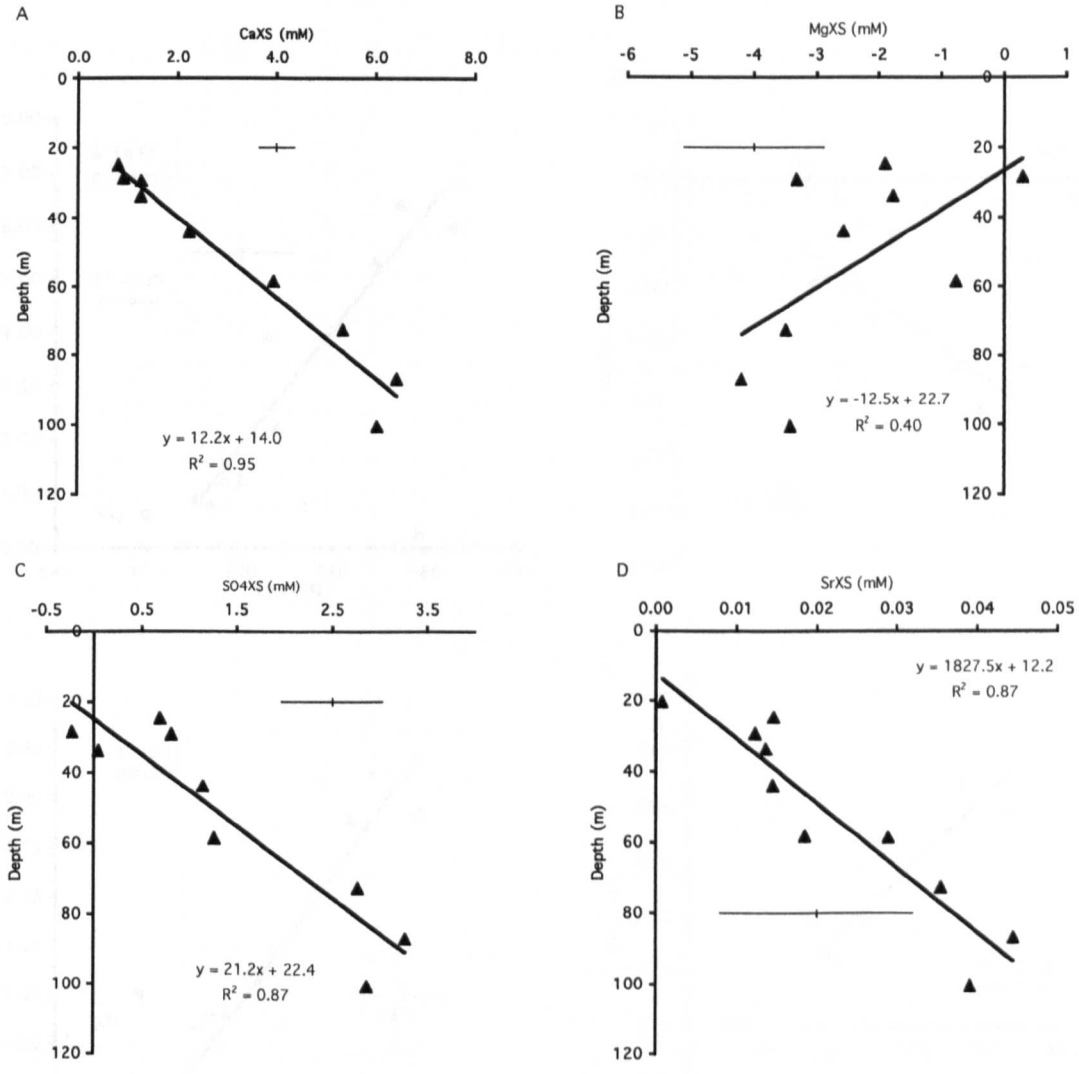

Figure 5.43 Saline groundwater Ca_{XS} (A), Mg_{XS} (B), SO_{4XS} (C), Sr_{XS} (D) with depth in The Pit, Sistema Dos Ojos. Solid black line is line of best fit for all data. Crosses are representative analytical uncertainties ($\pm 1\sigma$).

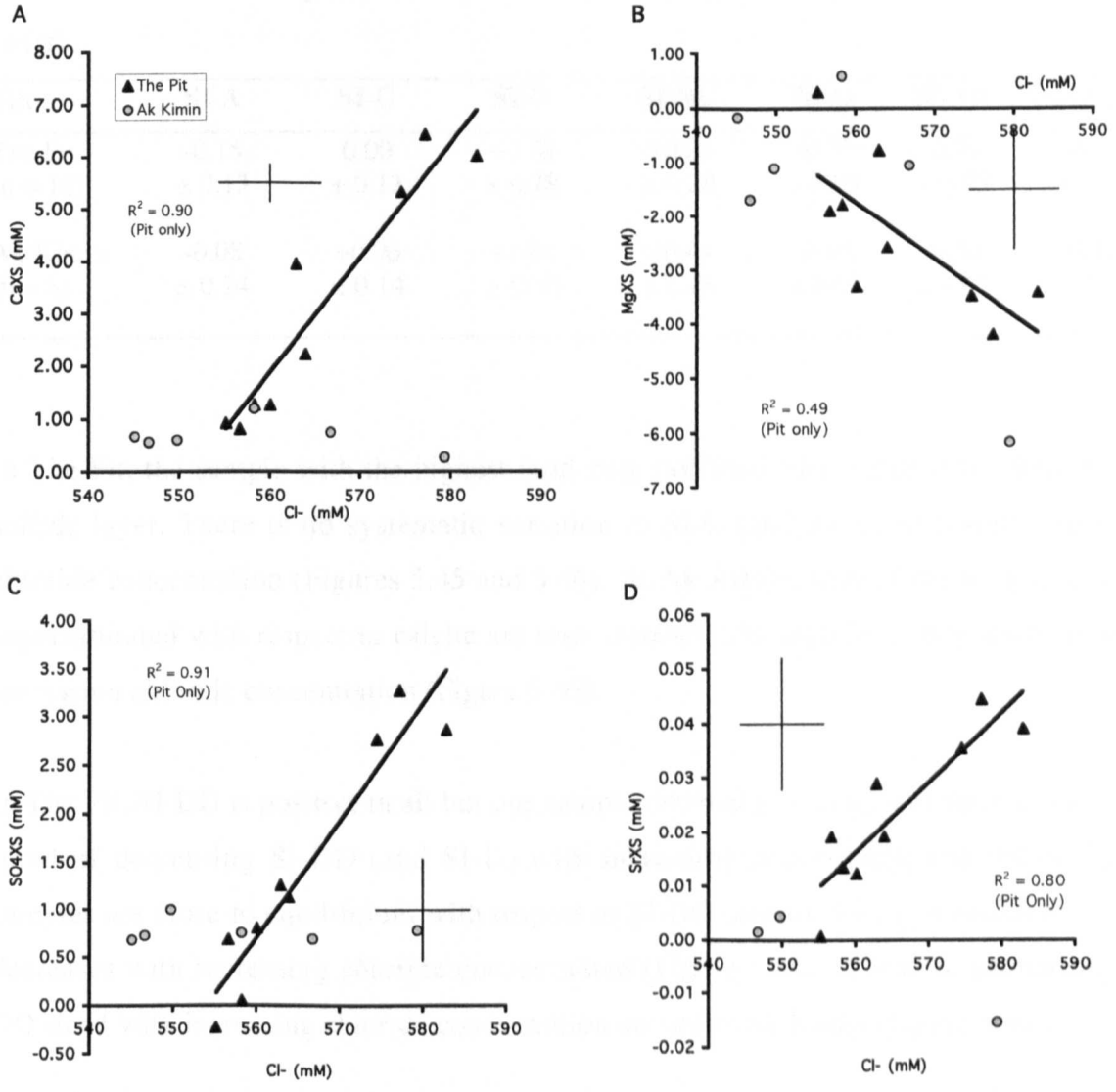

Figure 5.44 Ca_{XS} (A), Mg_{XS} (B), SO_{4XS} (C), Sr_{XS} (D) against chloride. Data from the saline zone of a site located ~6 km inland from the Caribbean Sea (The Pit, black triangles) and from a site located ~150 m from the coast (Ak Kimin, grey circles). Crosses are representative analytical uncertainties (±1σ).

Table 5.5 Mean saline groundwater chemistry (SI and pCO_2) from The Pit and Ak Kimin ($\pm 1\sigma$).

Site	SI-A	SI-C	SI-D	SI-DD	SI-G	SI-AN	pCO_2(%)
The Pit (n = 10)	-0.15 ± 0.13	0.00 ± 0.13	+0.78 ± 0.28	+0.21 ± 0.28	-0.51 ± 0.09	-0.71 ± 0.09	0.52 ± 0.19
Ak Kimin (n = 8)	-0.08 ± 0.14	+0.06 ± 0.14	+1.04 ± 0.30	+0.44 ± 0.28	-0.65 ± 0.01	-0.83 ± 0.01	0.35 ± 0.08

In The Pit, the sample with the highest (and only positive) SI-C value was taken from a sulfide layer. There is no systematic variation in SI-C (and SI-A) with water depth or chloride concentration (Figures 5.45 and 5.46). At Ak Kimin, four of the six samples are supersaturated with respect to calcite are also variable, although SI-C may decrease with increasing chloride concentration (Figure 5.46).

In The Pit, SI-DD is positive in all but one sample (located at ~86 m) and there is a general trend of decreasing SI-DD (and SI-D) with increasing water depth and below 70 m, samples are close to equilibrium with respect to SI-DD (Figure 5.45). In addition, SI-DD decreases with increasing chloride concentration (Figure 5.46). A similar decreasing SI-DD trend with increasing chloride concentration occurs at Ak Kimin (Figure 5.46).

In The Pit, SI-G and SI-AN increase systematically with increasing depth (Figure 5.45) and chloride concentration (Figure 5.46). At Ak Kimin, SI-G and SI-AN are independent of chloride concentration and the values are generally lower than those from The Pit (Figure 5.46).

In The Pit, the sample with the highest pCO_2 concentration is from a sulfide layer, corresponding to the highest SI-C. Apart from this sample, there appears to be a general trend of increasing pCO_2 with increasing water depth (Figure 5.47) and chloride concentration (Figure 5.48). There is no clear trend between pCO_2 and chloride concentration at Ak Kimin and the values are generally lower than those from The Pit (Figure 5.48).

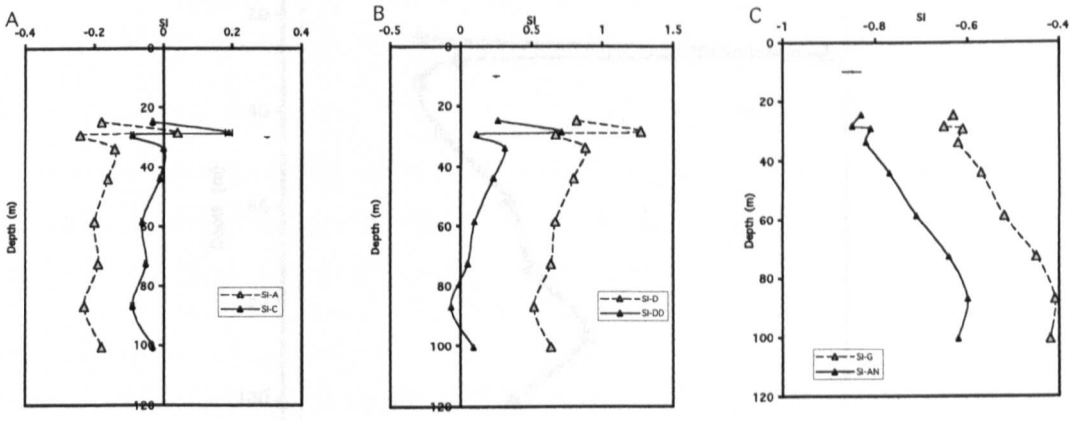

Figure 5.45 Depth profiles of SI-A and SI-C (A), SI-D and SI-DD (B) and SI-G and SI-AN (C) from The Pit (Sistema Dos Ojos). Crosses are representative analytical uncertainies (±1σ).

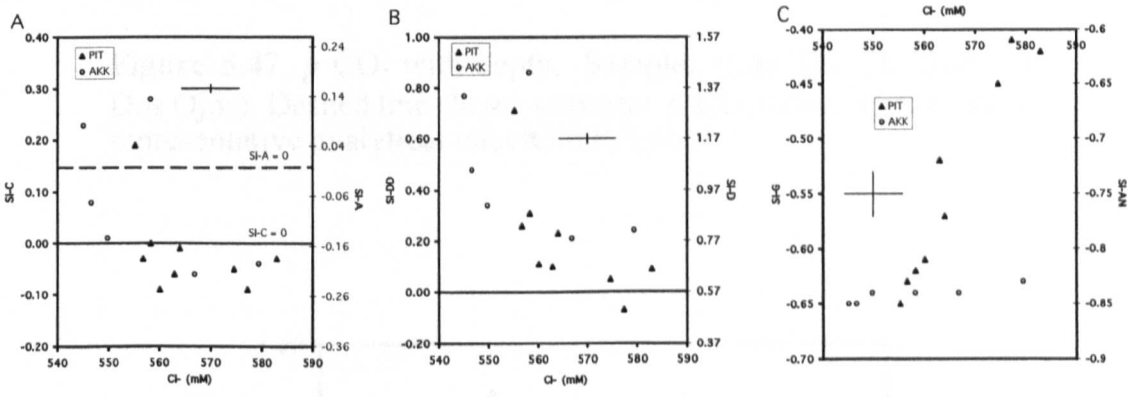

Figure 5.46 SI-A and SI-C (A) and SI-D and SI-DD (B) and SI-G and SI-AN (C) against chloride. Samples are from The Pit (PIT, circles) and Ak Kimin (AKK, squares). Crosses are representative analytical uncertainies (±1σ).

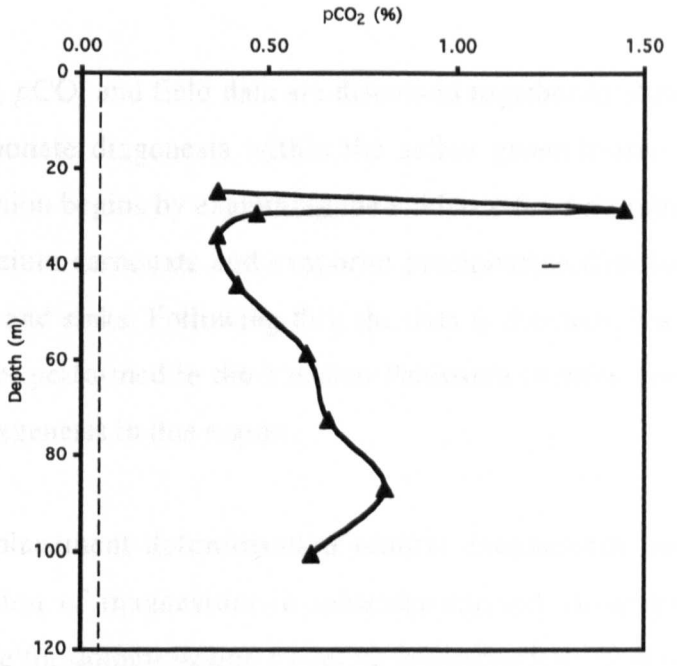

Figure 5.47 *p* CO_2 with depth. Samples from The Pit (Sistema Dos Ojos). Dashed line shows seawater *p* CO_2 value. Cross shows representative analytical uncertainies (±1σ).

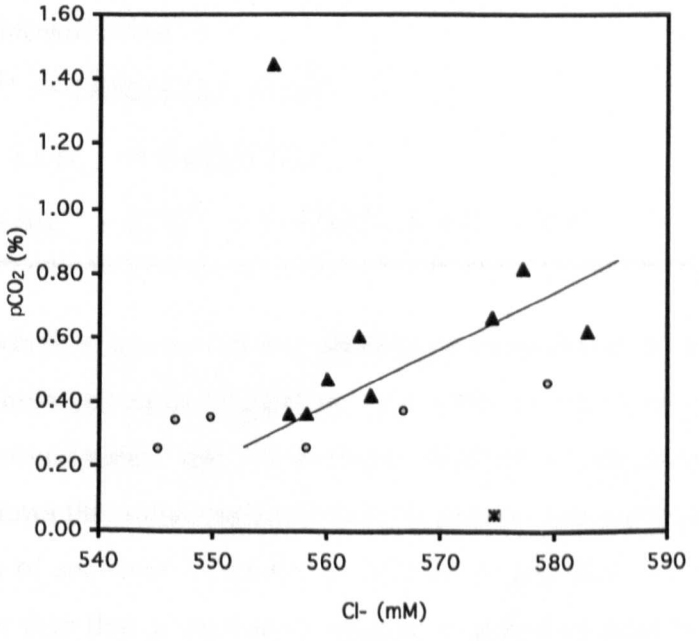

Figure 5.48 *p* CO_2 against chloride. Samples from The Pit (black triangles) and Ak Kimin (grey circles). Grey square with asterisk shows seawater value. Cross shows representative analytical uncertainies (±1σ).

5.4.8 Geochemistry Discussion

In this section, XS, SI, pCO_2 and field data are discussed together in attempts to reconcile the evidence for carbonate diagenesis within the saline groundwaters of the Yucatan Peninsula. The discussion begins by examining the evidence for dolomitisation, but brings into consideration calcium carbonate and evaporite precipitation-dissolution reactions as additional ion sources and sinks. Following this, the data is considered within the broader context of other studies performed in the Yucatan Peninsula to draw general conclusions regarding carbonate diagenesis in this region.

Both primary and replacement dolomitisation remove magnesium ions from solution (Table 5.6). Depletion of magnesium in seawater-derived saline groundwaters can provide direct evidence for dolomitisation by saline groundwaters. It is important to keep in mind, however, that other magnesium sinks could also cause magnesium depletion.

Table 5.6 Main dolomitisation reactions (From Whitaker et al., 1994).

1. *Primary precipitation of dolomite*

$$Ca^{2+} + Mg^{2+} + 2CO_3^{2-} \rightarrow CaMg(CO_3)_2$$

2. *Replacement dolomitisation*

A. $$2CaCO_3 + Mg^{2+} \rightarrow CaMg(CO_3)_2 + Ca^{2+}$$

B. $$CaCO_3 + Mg^{2+} + CO_3^{2-} \rightarrow CaMg(CO_3)_2$$

C. $$(2-x)CaCO_3 + Mg^{2+} + xCO_3^{2-} \rightarrow CaMg(CO_3)_2 + (1-x)Ca^{2+}$$

Using Mg/Cl ratios, which accounts for any dilution or evaporation (chloride should be conserved in both of these processes and during rock-water interactions), it is possible to determine if saline groundwaters are, on average, depleted of magnesium relative to seawater. Table 5.2 shows that saline groundwaters, in general, are depleted of magnesium relative to the dilution of seawater. Concurrent calcium enrichment (i.e. Ca/Cl of saline groundwaters is greater than that of seawater), suggests that replacement dolomitisation by either reaction 2A or 2C has occurred (Table 5.6). An increase in calcium relative to the dilution of seawater implies that the decrease in saline groundwater magnesium is probably not from the precipitation of HMC, which would result in an overall decrease in Ca/Cl ratios. However, calcium enrichment may be from a number of processes other than

dolomitisation, including $CaCO_3$ or $CaSO_4$ dissolution. SO_4/Cl ratios demonstrate that saline groundwaters are enriched in sulfate relative to seawater, indicating that sulfate has been added to the saline groundwater system through $CaSO_4$ dissolution and/or from the re-oxidation of reduced sulfur species. In order to elucidate the source of additional sulfate and to identify where redox reactions involving sulfur are taking place, $\delta^{34}S$ of sulfate analyses were carried out on some saline groundwater samples and these results are presented in Section 5.5.2.5. Saline groundwater Sr/Cl ratios are higher than those observed in seawater (Table 5.2). Strontium may be incorporated into the crystal structure of $CaCO_3$ or $CaSO_4$ and strontium enrichment may indicate dissolution of either (or both) of these minerals. The geochemical impact of water-rock interactions is further elucidated by the magnitude of magnesium depletion and calcium, sulfate and strontium enrichments.

Saline groundwaters are, on average, depleted of magnesium relative to the dilution of seawater (Mg_{XS} = -1.16 ± 3.31 mM, n = 49). Concurrent calcium enrichment (Ca_{XS}= +1.24 ± 3.01 mM, n = 48) suggests that replacement dolomitisation may be occurring *via* Equations 2A or 2C (Table 5.6). When Ca_{XS} is plotted against Mg_{XS} (Figure 5.49), two trends within the data set are revealed. The samples within the first group are from the shallow saline zone (<40 m) and the samples of group two were taken below 40 m water depth. Thus, 40 m (rather than the 60 m used previously in defining the deep saline zone) may mark the geochemical interface between the shallow and deep saline zones. Interestingly, 40 m corresponds to where there were inflections in both the temperature (Figure 5.9) and specific conductance (Figure 5.6) profiles from The Pit (and 40 m corresponds to where saline groundwater specific conductance had the same value as seawater).

Before the type, amount or rates of dolomitisation can be quantified (determined using the relationship between Mg_{XS} and Ca_{XS}), other sources of Ca_{XS} must first be considered. Calcium can become enriched, not only from replacement dolomitisation, but also from the dissolution of $CaCO_3$ and/or $CaSO_4$. Although positive SO_{4XS} values may be due to the re-oxidation of reduced sulfur species, a strong positive relationship between Ca_{XS} and SO_{4XS} (Figure 5.50) indicates a shared source and this implies that the source of sulfate is from the dissolution of $CaSO_4$. However, the ratio of Ca_{XS}:SO_{4XS} is ~2:1 (Figure 5.50), whereas $CaSO_4$ dissolution (Equation 5.3) should produce a 1:1 ratio between Ca_{XS} and SO_{4XS}.

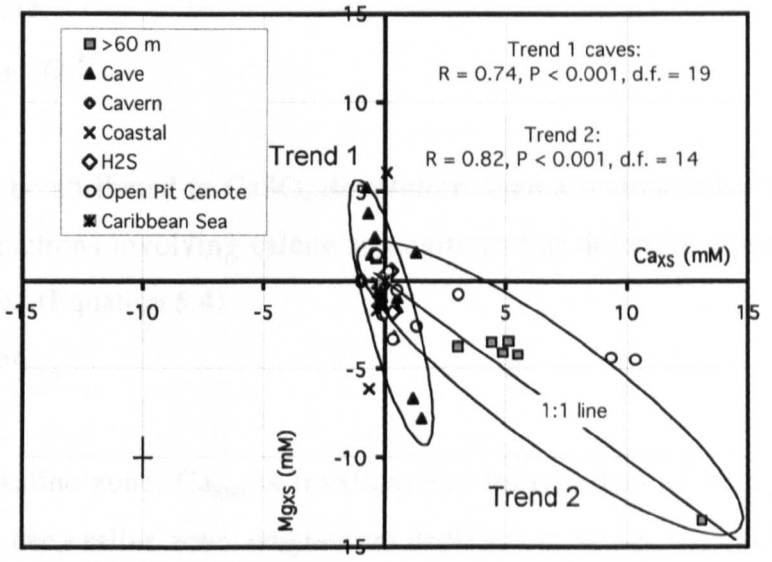

Figure 5.49 Saline groundwater Ca_{XS} (x axis) vs Mg_{XS} (y axis). Two trends within the data set are circled. Cross shows representative analytical uncertainties (±1σ).

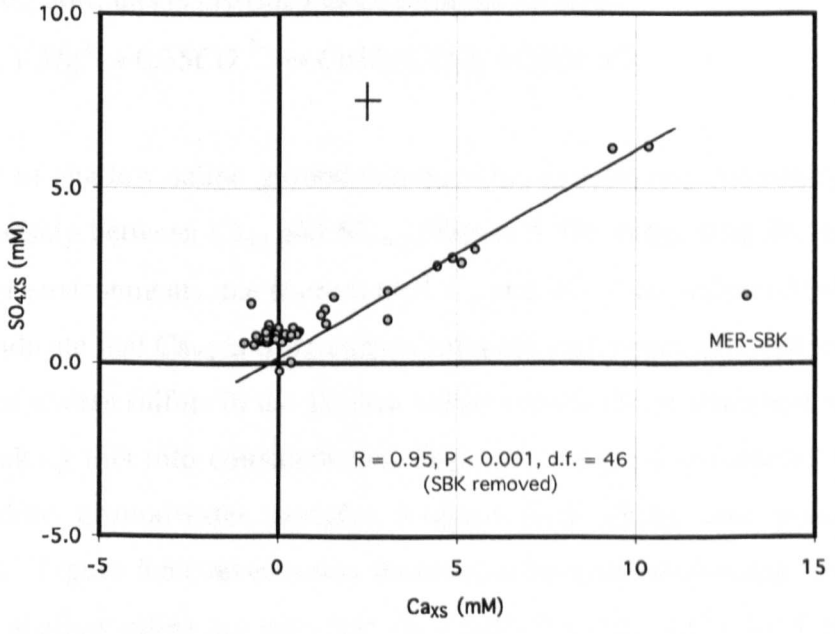

Figure 5.50 Saline groundwater Ca_{XS} vs SO_{4XS} (all samples). Cross shows representative analytical uncertainties (±1σ).

As stated above, Ca_{XS} may also be from calcite or aragonite dissolution and/or reactions involving dolomite.

$$CaSO_4 \rightarrow Ca^{2+} + SO_4^{2-} \quad (5.3)$$

If all SO_{4XS} can be attributed to $CaSO_4$ dissolution, then a revised value for Ca_{XS} (due to water-rock interactions involving calcite/aragonite and/or dolomite alone, termed Ca_{XS2}) can be determined (Equation 5.4).

$$Ca_{XS_2} = Ca_{XS} - SO_{4_{xs}} \quad (5.4)$$

In the shallow saline zone, Ca_{XS2} is invariant and independent of Mg_{XS} values (± 1σ). However, in the deep saline zone, magnesium depletion increases with increasing calcium (Ca_{XS2}) enrichment (Figure 5.51), indicating that the Ca_{XS} in the deep saline zone can be attributed to both $CaSO_4$ dissolution and dolomitisation. For samples taken below 40 m depth, the ratio between Ca_{XS2} and Mg_{XS} is ~ 1.00 : -1.53, suggesting that replacement dolomitisation is occurring via Equation 2C, in which alkalinity is consumed and where x = 0.35, resulting in Equation 5.5. It is worth noting that the data plotted in Figure 5.51 does not go through the origin, indicating the relationship may not be as straightforward as implied here. Still, this is provided as an estimate for now.

$$1.65CaCO_3 + Mg^{2+} + 0.35CO_3^{2-} \rightarrow CaMg(CO_3)_2 + 0.65Ca^{2+} \quad (5.5)$$

In the zone of shallow saline groundwaters, SO_{4XS} is relatively invariant and there is no clear relationship between Ca_{XS} and SO_{4XS} (Figure 5.52), suggesting that in shallow saline groundwater environments, the sources for Ca_{XS} and SO_{4XS} are independent of one another. This may indicate that Ca_{XS} is from calcite/dolomite water-rock interactions alone and that the source of excess sulfate in the shallow saline zone is the re-oxidation of reduced sulfur species. Taking this into consideration, Ca_{XS} and Mg_{XS} are considered together for the shallow saline groundwater samples without first taking into account SO_{4XS}-Ca_{XS} interactions. Figure 5.53 reveals that there is an inverse relationship between Ca_{XS} and Mg_{XS} in the shallow saline groundwaters ($R = 0.88$, $P < 0.01$, d.f. = 34, 4 outliers removed; identified using a type 2 two-tailed t-test on Ca_{XS}:Mg_{XS} ratios). The samples that lie around the centre of the plot are neither significantly enriched in, nor depleted of, calcium nor magnesium relative to the dilution of seawater. Most samples fall into the upper left or bottom right quadrants of the plot, although the trend is continuous.

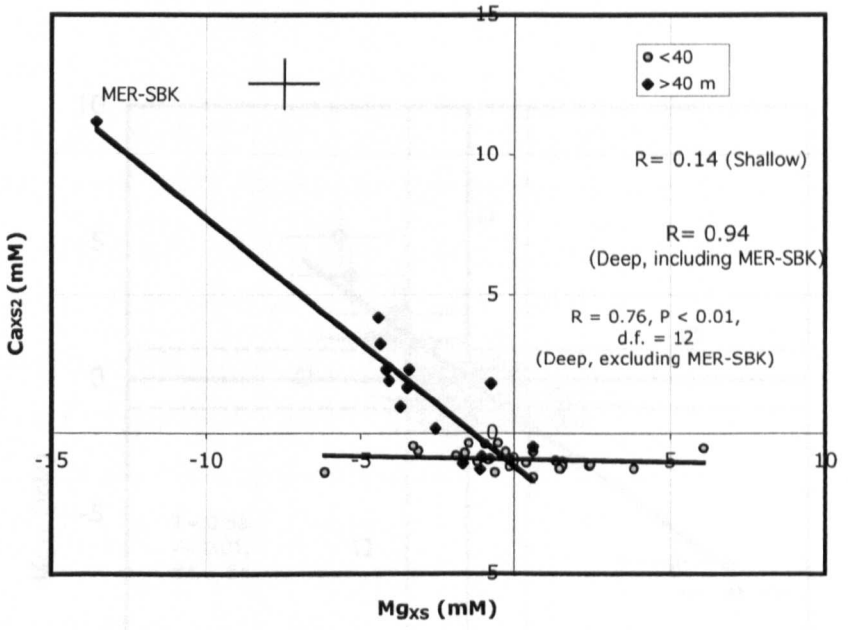

Figure 5.51 Saline groundwater Mg_{XS} against Ca_{XS2}. Grey circles represent the shallow (<40 m water depth) saline groundwater samples, while the black diamonds represent the deep (>40 m water depth) saline groundwater samples. Crosses are representative analytical uncertainties (±1σ).

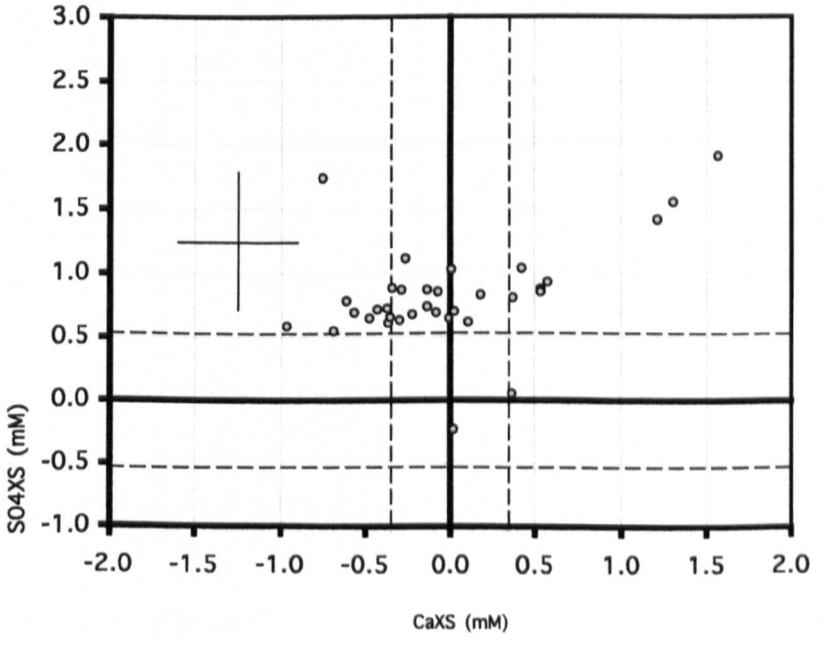

Figure 5.52 Saline groundwater Ca_{XS} against SO_{4xs} for shallow saline groundwater samples only. Dashed lines represent significance greater or less than zero. Crosses are representative analytical uncertainties (±1σ).

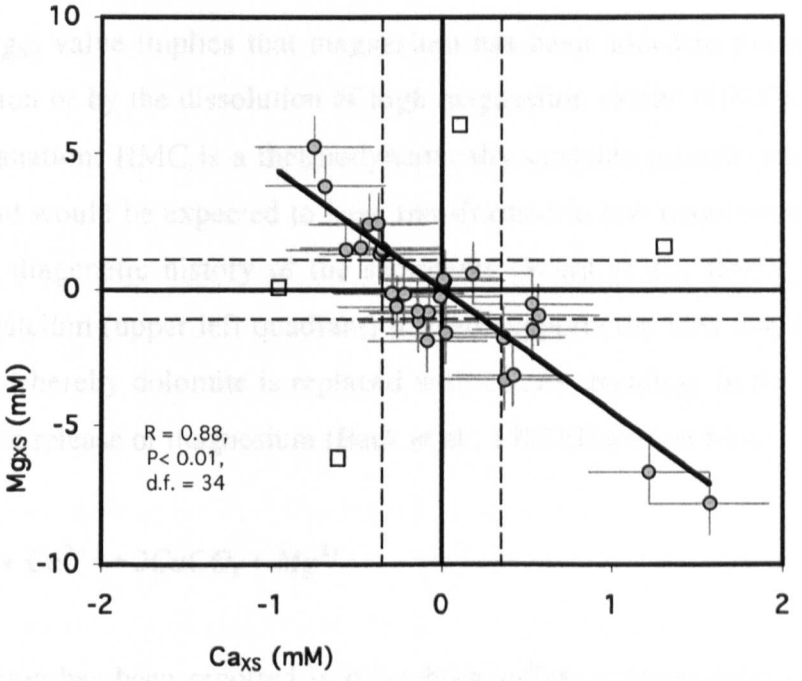

Figure 5.53 Mg_{xs} against Ca_{xs} for shallow saline groundwater samples (<40 m). Four outliers have been removed from the trend (open squares). Dashed lines represent signicance greater or less than zero (±1 σ). Error bars show analytical uncertainties (±1σ).

In the upper left quadrant, samples are depleted of calcium and enriched in magnesium. In the bottom right quadrant, samples are enriched in calcium and depleted of magnesium.

A positive Mg_{XS} value implies that magnesium has been added to the water, either *via* dedolomitisation or by the dissolution of high magnesium calcite (HMC). The latter is an unlikely explanation; HMC is a thermodynamically unstable mineral under near surface conditions, and would be expected to have transformed to low magnesium calcite (LMC) earlier in the diagenetic history of the sediments (Ward et al., 1995). The concurrent depletion in calcium (upper left quadrant) instead supports the idea that dedolomitisation has occurred, whereby dolomite is replaced with calcite, resulting in the consumption of calcium and the release of magnesium (Back et al., 1983)(Equation 5.6).

$$CaMg(CO_3)_2 + Ca^{2+} \rightarrow 2CaCO_3 + Mg^{2+} \qquad (5.6)$$

Dedolomitisation has been reported in other high-sulfate groundwaters of other aquifers containing gypsum (Buck et al., 1993; Plummer, 1990; Perry et al., 2002). However, the shallow saline groundwaters of the Yucatan Peninsula are saturated and supersaturated with respect to ordered and disordered dolomite (SI-DD = +0.19 ± 0.21), thus dedolomitisation is unlikely to be thermodynamically favoured (unless the dolomite is very disordered and the K value used to calculate SI-DD is inaccurate for this system).

Samples that are depleted of magnesium and enriched in calcium (bottom right quadrant of Figure 5.53) indicate that replacement dolomitisation has occurred. Replacement dolomitisation by Equation 2A (Table 5.6) results in the loss of one mole of magnesium for every one mole of calcium gained. However, there is not enough calcium to account for the amount of magnesium lost. Some calcium may have been lost to calcite precipitation, but this is unlikely given that SI-C is undersaturated in these waters. Alternatively, replacement dolomitisation could be occurring by reaction 2B, where there is an expected loss of magnesium with no change in calcium concentration. The calcium gain could then be attributed to calcite dissolution. However, the good relationship between Mg_{XS} and Ca_{XS} suggests a shared source. Thus, replacement dolomitisation has probably occurred by equation 2C, and the Ca_{XS}:Mg_{XS} ratio of 1 : -4.5 results in $x = 0.78$ (this is not dissimilar to the geochemistry observed in Bahamian blue holes where $x = 0.75$,

Whitaker et al., 1994). Equation 2C (from Table 5.6) then becomes Equation 5.7 for the shallow saline groundwater sites:

$$1.22CaCO_3 + Mg^{2+} + 0.78CO_3^{2-} \rightarrow CaMg(CO_3)_2 + 0.22Ca^{2+} \quad (5.7)$$

Evaporite ($CaSO_4$) dissolution as an explanation for calcium and sulfate enrichments in the deep saline zone is supported by Sr_{XS} data. Strontium inputs into the saline groundwater system may be derived from $CaCO_3$ or $CaSO_4$ dissolution, where strontium has been incorporated into the crystal structure. Although the Sr_{XS}:Ca_{XS} ratios are similar to that expected from aragonite dissolution (0.011:0.989; Budd, 1988)(Figure 5.54), aragonite is an unlikely source as it is thermodynamically unstable and unlikely to be present at depth in the carbonate sediments (this is supported by petrographic analyses by Ward et al., 1995). Instead, strong positive relationships between Sr_{XS}, SO_{4XS} and Ca_{XS} (Figures 5.54, 5.55) suggest that the source of strontium is from the dissolution of either gypsum or anhydrite. This is confirmed by the strong positive relationship between Sr_{XS} and the saturation indices of both gypsum and anhydrite (Figure 5.56), while Sr_{XS} and SI-A show no correlation (Figure 5.57).

In shallow saline groundwater sites, there is no relationship between Ca_{XS} and Sr_{XS} and most of these samples are within $\pm 1\sigma$ of zero (Figure 5.54). In addition, there is no relationship between Ca_{XS2} and Sr_{XS} for shallow saline groundwater sites (Figure 5.58).

Perry et al. (2002) suggest gypsum dissolution as the source of strontium enrichment in the fresh/brackish groundwaters of the northwest Yucatan Peninsula and that the evaporite source lies above the present-day freshwater lens. However, data from The Pit suggests a deep source of evaporites ($CaSO_4$) in the eastern part of the peninsula, evidenced by incremental increases in Ca_{XS}, SO_{4XS} and Sr_{XS} with depth (Figure 5.43). Evaporite-bearing waters, heated by the geothermal gradient (Figure 5.9), may be rising and potentially mixing with the shallower saline groundwaters above. The evaporite source is probably anhydrite clasts within impact breccias reported between ~100-160 m (Socki, 1984; Ward et al., 1995) in PEMEX borehole Y4.

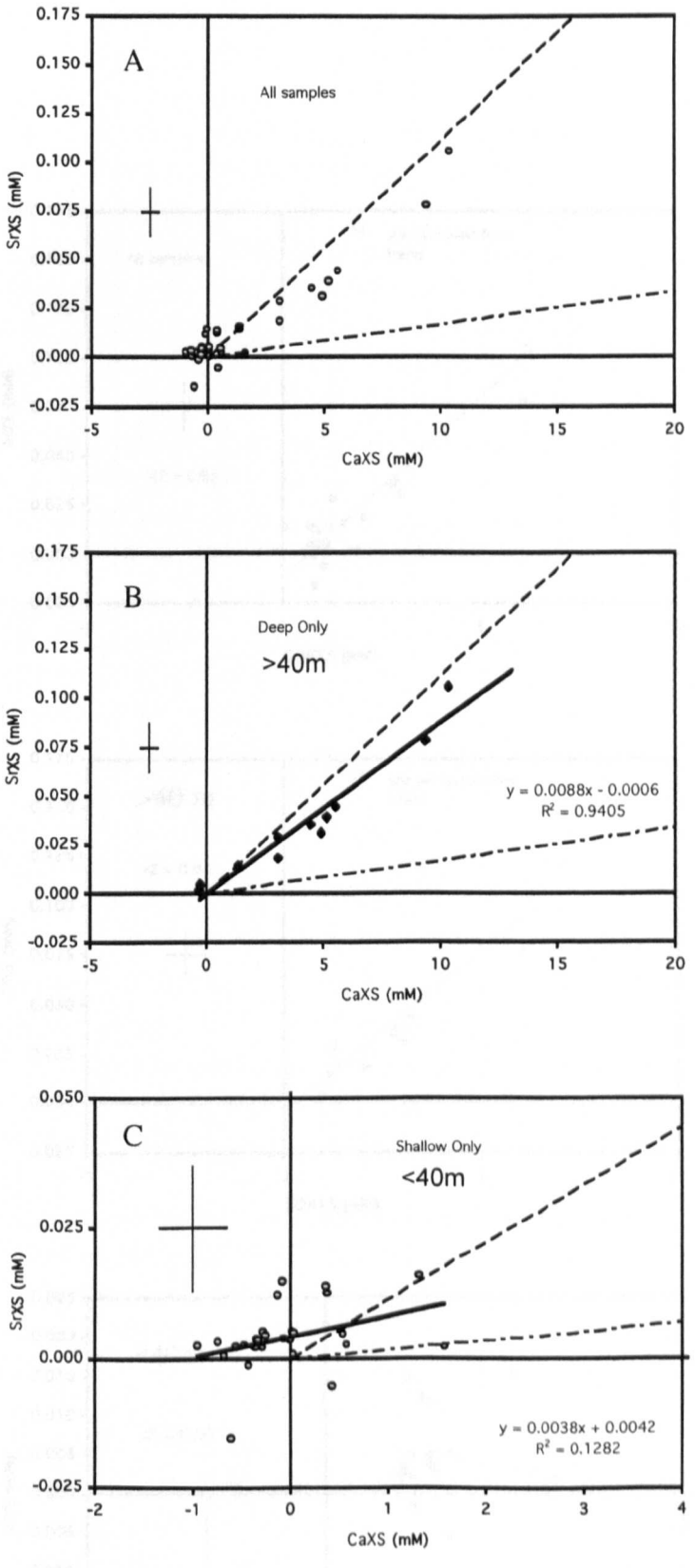

Figure 5.54 Ca_{XS} against Sr_{XS} for all saline groundwater samples (A), for deep saline groundwater samples only (B) and for shallow saline groundwater samples only (C). Dashed line represents the Ca_{XS}:Sr_{XS} ratio expected from aragonite dissolution, while the dash-dot line represents the ratio from calcite dissolution. Crosses are representative analytical uncertainties (±1σ).

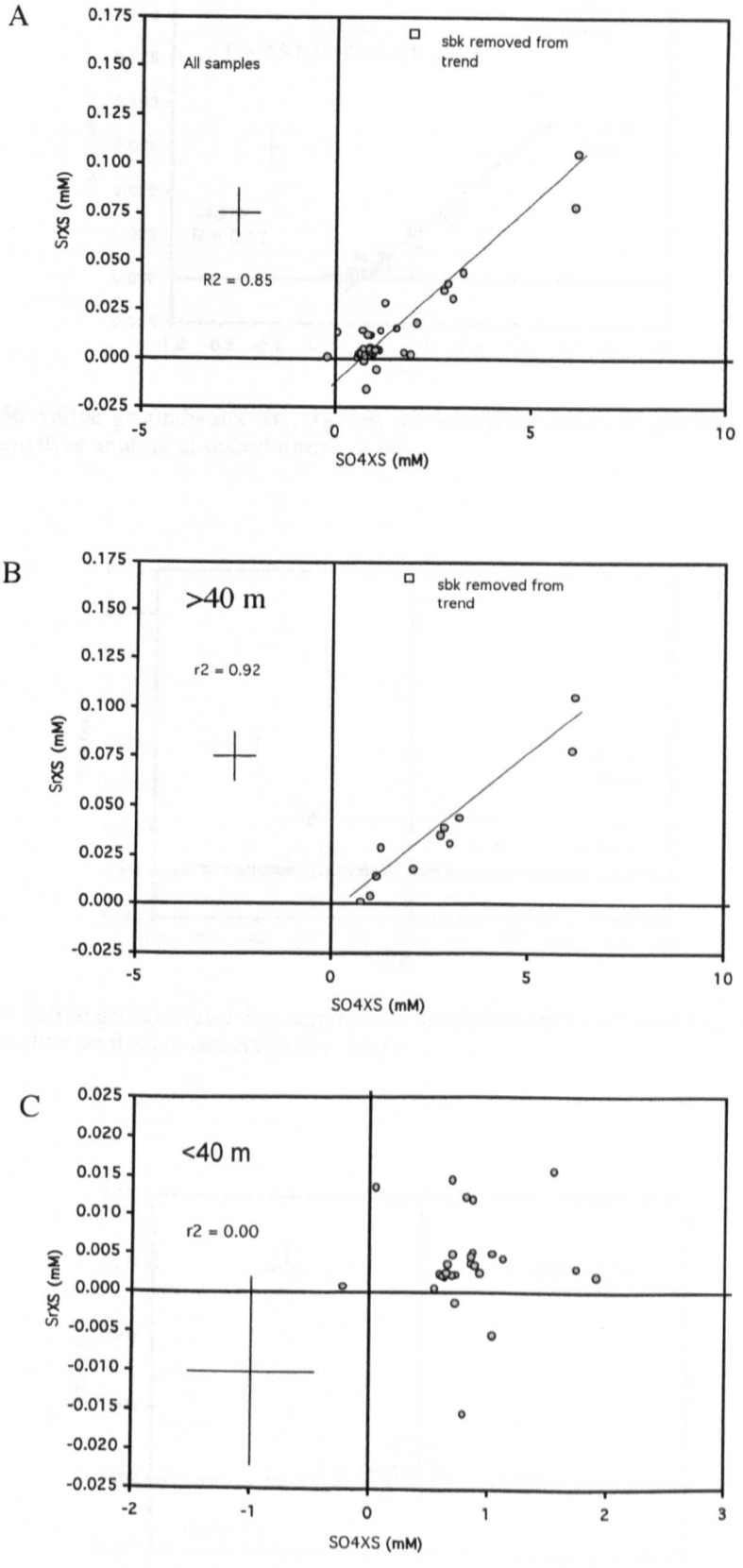

Figure 5.5 SO_{4XS} against Sr_{XS} for all saline groundwater samples (A), for deep saline groundwater samples only (B) and for shallow saline groundwater samples only (C). Crosses are representative analytical uncertainties ($\pm 1\sigma$).

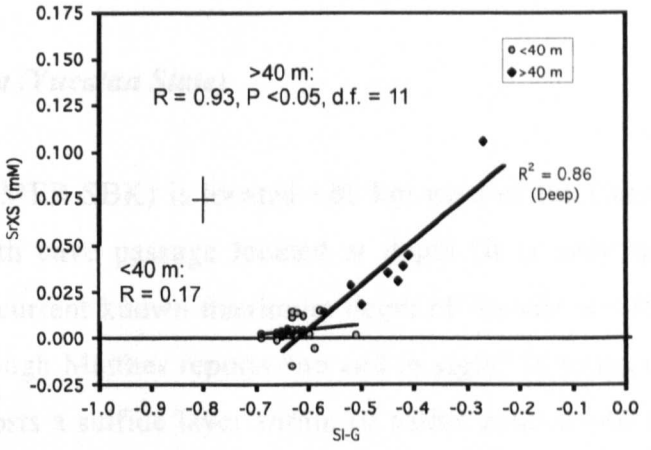

Figure 5.56 Saline groundwater Sr_{XS} against the saturation index of gypsum (SI-G). Crosses are representative analytical uncertainties (±1σ).

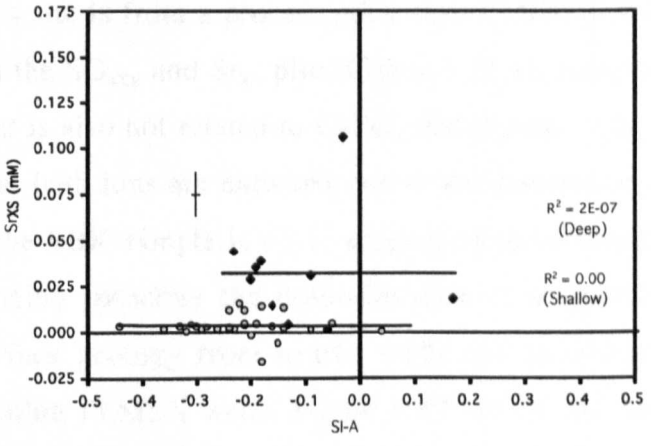

Figure 5.57 Saline groundwater Sr_{XS} against the saturation index of aragonite (SI-A). Crosses are representative analytical uncertainties (±1σ).

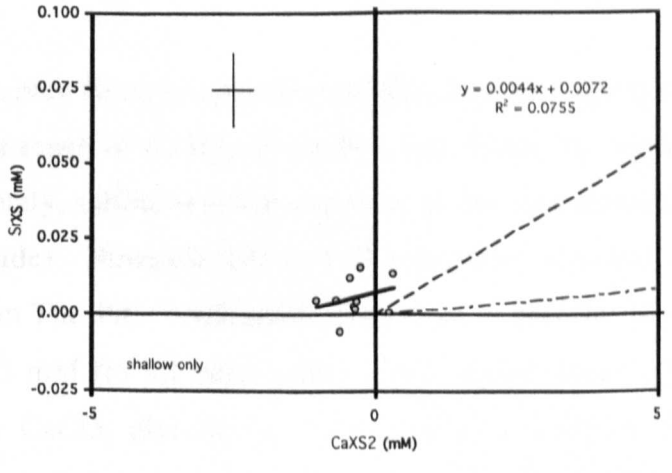

Figure 5.58 Ca_{XS2} against Sr_{XS} for shallow saline groundwater samples. Dashed line represents the Ca_{XS2}:Sr_{XS} ratio expected from aragonite dissolution, while the dash-dot line represents the ratio from calcite dissolution. Crosses are representative analytical uncertainties (±1σ).

5.4.8.1 Dataset Outliers: Implications for Saline Groundwater Hydrology

a) Sabak Ha (Yucatan State)

Sabak Ha (SBK or MER-SBK) is located ~80 km west of the Caribbean coast. It is an open pit cenote with cave passage located at depth (it is very similar to The Pit in morphology). The current known maximum depth of the site is ~150 m (Matthes, pers. comm., 2003), although Matthes reports "no end in sight" in terms of the site's possible floor depth. SBK hosts a sulfide layer within its saline zone at ~67 m water depth. The saline groundwater sample described in this study is from 74 m water depth. In many respects, SBK fits well within the east coast deep saline zone data set (e.g Ca_{XS}:Mg_{XS}). However, SBK is an outlier in the Ca_{XS} vs SO_{4XS} plot (Figure 5.50), which may indicate the source of Ca_{XS} at this site is from a process other than $CaSO_4$ dissolution. In addition, SBK is an outlier in the SO_{4XS} and Sr_{XS} plot (Figure 5.55A), indicating the source of the strontium enrichment is also not related to $CaSO_4$ dissolution. The ratio of Sr_{XS}:Ca_{XS} at this site suggests that both ions are enriched due to the dissolution of aragonite and the Mg_{XS}:Ca_{XS} ratio of the SBK sample is ~1:1, suggesting dolomitisation via equation 2A (Table 5.6) is occurring (possibly the dolomitisation of aragonite has occurred). In addition, the subsurface geology from nearby wells and boreholes (i.e. Borehole Y6, Merida 2 and Chicxulub PEMEX wells, Figure 5.59) shows the breccia deposits occur much deeper (~1000 m) than at the location of Y4 (the borehole associated with the main east coast study area). Thus, the saline groundwaters of Sabak Ha may not be in contact with (and may not be dissolving) $CaSO_4$. This suggests the saline groundwater at this site is not sourced from the east coast and this indicates a separate hydrological system.

However, the system may be more complex than this. It is also possible that the low SO_{4XS} at SBK is in part the result of $CaSO_4$ dissolution, but it may be 'depleted' due to sulfate reduction. Unfortunately, sulfide was not measured at this site (although the sample smelt very slightly of sulfide). However, DO is 11% saturation, which is similar to the non-sulfidic samples from The Pit. Alkalinity at this site is high (4.24 mM, compared to a mean of 2.58 ± 0.03 mM for all other saline groundwater sites), which could be from sulfate reduction or $CaCO_3$ dissolution. The continual addition of sulfate from the dissolution of gypsum/anhydrite, may mask any sulfate depletion due to sulfate reduction.

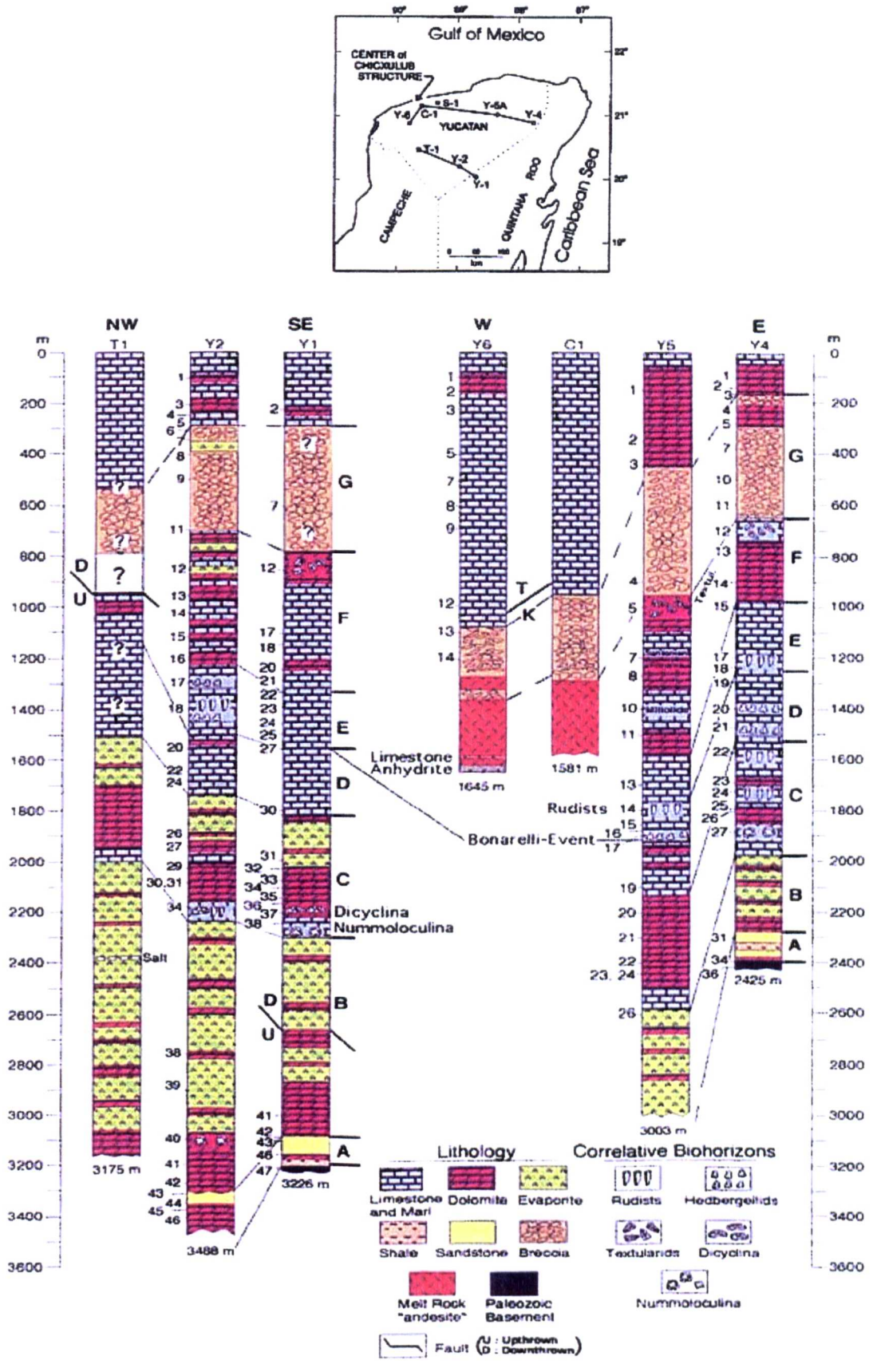

Figure 5.59 (Figure 1.9, repeated) Correlation of PEMEX wells of the northern Yucatan Peninsula. Datum is ground level. See Figure 1.9 for approximate age of units. Borehole Y4 is closest to the main east coast sites. Borehole Y6 is closest to Sabak Ha. From Ward et al., 1995.

This process may also help to explain why no SO_{4XS} values from this study are significantly less than zero.

b) East coast saline groundwater outliers

There is no relationship between Ca_{XS} and SO_{4XS} in shallow saline groundwater samples (Figure 5.52, R = 0.45, all samples), indicating the sources of Ca_{XS} and SO_{4XS} are independent of one another. However, within the data set, there are 6 outliers shown to have Ca_{XS}:SO_{4XS} ratios significantly different to the main data set using a type 2 two-tailed t-test ($P < 0.01$) (Figure 5.60). Of the 6 outliers, 5 have a Ca_{XS}:SO_{4XS} ratio of ~1:1 (R= 0.99, Figure 5.60). Unlike the majority of shallow saline groundwater samples, the increase in SO_{4XS} with increasing Ca_{XS} is significant for these 5 samples and the implication is that $CaSO_4$ dissolution does control the Ca_{XS} and SO_{4XS} increases within these sites. Of the 5 samples represented in this trend, two are from a site connected to the deeper saline zone (The Pit). The other three 'outliers' are from Sistemas Aktun Ha (a.k.a. Carwash), Tortuga and Vaca Ha. These three samples come from sites that are in very close proximity to one another, located at ~8-9 km inland from the east coast, which is the inland limit of known diver-sized cave passage along the Caribbean coast of the Yucatan Peninsula. The relatively large Ca_{XS} and SO_{4XS} values of these shallow saline groundwater samples (and two of the three sites have magnesium depletions similar in magnitude to those observed in the deep saline zone) indicate that these are the most diagenetically evolved of the shallow saline groundwater sites and their location may indicate the extent of local seawater circulation (and/or the extent of the shallow saline groundwater 'shuttle'). However, the chemistries (i.e. Ca_{XS} and SO_{4XS}) of Aktun Ha, Tortuga and Vaca Ha have a striking similarity to that of the deep saline zone (Figure 5.61) and a type 2 two-tailed t-test showed that Ca_{XS}:SO_{4XS} ratios of the 5 shallow outliers are not significantly different from those from main deep saline groundwater trend ($P = 0.91$). This, combined with a lack of shallow gypsum deposits in the immediate field area, implicates the deep saline groundwaters as their source. These sites may therefore represent the location of deep saline groundwater upwelling through relatively high porosity rock.

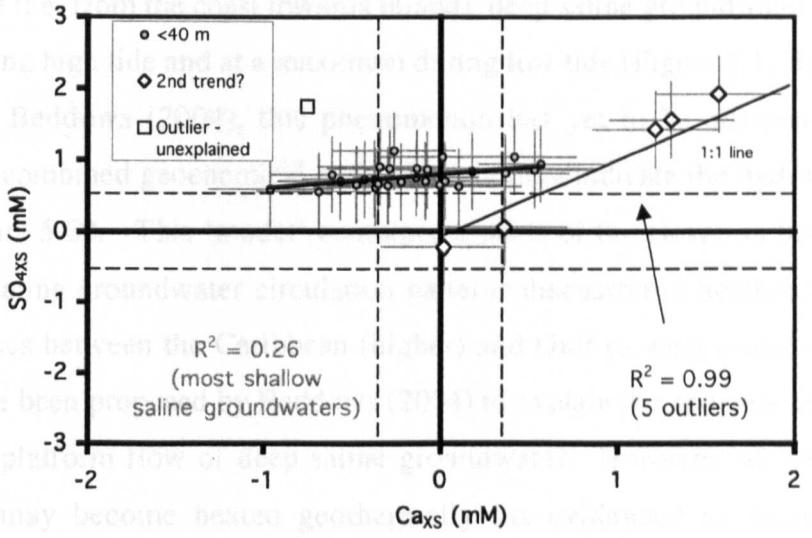

Figure 5.60 Shallow saline groundwater Ca_{XS} against SO_{4XS}. Dashed lines indicate XS values significantly less or greater than zero. Error bars are representative analytical uncertainties (±1σ).

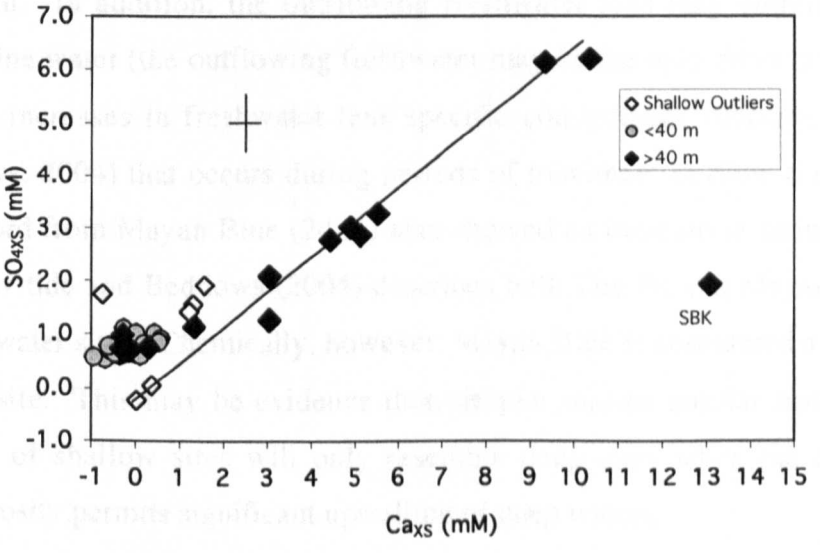

Figure 5.61 Saline groundwater Ca_{XS} against SO_{4XS}, demonstrating that five of the six shallow saline groundwater outliers fit the deep saline groundwater trend and that four deep saline groundwater samples fit the shallow saline groundwater data. Cross shows representative analytical uncertainties (±1σ).

The flow record from The Pit shows that although the inflow of salt water is consistently uni-directional (i.e. from the coast towards inland), deep saline groundwater velocity is at a minimum during high tide and at a maximum during low tide (Figure 5.1; Beddows, 2004). According to Beddows (2004), this phenomenon has yet to be adequately explained. However, the combined geochemical and flow data may indicate the hydrological regime shown in Figure 5.62. This 'model' combines aspects of the elevation head, geothermal and buoyant saline groundwater circulation patterns discussed in Section 5.2. Elevation head differences between the Caribbean (higher) and Gulf (lower) coasts of the Yucatan Peninsula have been proposed by Beddows (2004) to explain the apparent continuous east-to-west cross-platform flow of deep saline groundwater. However, at depth, this saline groundwater may become heated geothermally (as evidenced by temperature depth profiles) and some may consequently rise upwards towards the surface. This upward flow is aided in regions of extensive cavernous porosity (which may be limited to ~9 km inland based on the lack of diver-sized voids beyond this distance from the coast). At low tide, the velocities of both outflowing fresh lens waters and inflowing saline water are at a maximum, suggesting the outflow of freshwater drives a compensatory inflow of saline water at depth. In addition, the outflowing freshwater lens may entrain some of the upwelling saline water (the outflowing freshwater may be the only drive needed). This is supported by increases in freshwater lens specific conductance (observed at Heaven's Gate, Beddows, 2004) that occurs during periods of maximum outflow (i.e. at low tide). The flow record from Mayan Blue (24 m) also showed an increase in saline groundwater velocity at low tide and Beddows (2004) describes both The Pit and Mayan Blue as deep saline groundwater sites. Chemically, however, Mayan Blue is considered a shallow saline groundwater site. This may be evidence that, despite sharing similar flow regimes, the geochemistry of shallow sites will only resemble deep sites when the distribution of cavernous porosity permits significant upwelling of deep waters.

In addition, four of the deep saline zone samples fit the geochemical (i.e. Ca_{XS}:SO_{4XS}) data from the shallow saline zone (Figure 5.61) and this was confirmed statistically using a type 2 two-tailed t-test ($P = 0.73$) . In addition, a type 3 two-tailed t-test showed that these samples are outliers from the main deep saline zone trend ($P < 0.01$). All four samples were from Ak Kimin (a coastal site), indicating the water is not very diagenetically altered and/or that the deep saline zone is deeper than 60 m (the maximum sample depth) at the coast (see right hand side of Figure 5.62).

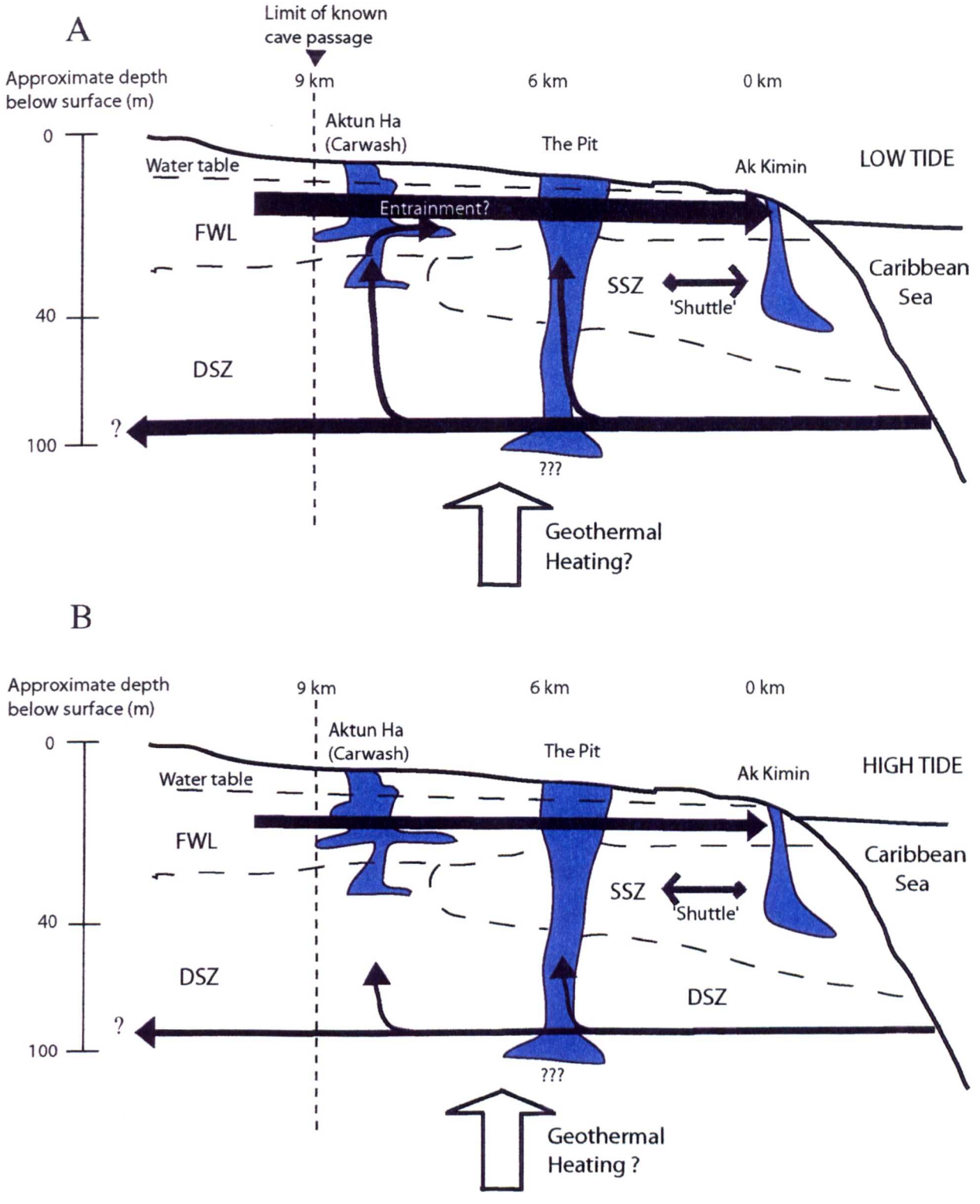

Figure 5.62 Schematic diagram of the proposed saline groundwater flow regime of the Caribbean coast of the Yucatan Peninsula, during low tide (A) and high tide (B). FWL = freshwater lens, SSZ = shallow saline zone, and DSZ = deep saline zone. Note extreme vertical exaggeration. Blue regions indicate cavernous porosity. Detailed description given in text.

Maintaining Undersaturation of Carbonate Minerals

With net northwesterly groundwater flow through the conduits (caves), the degree of alteration of locally derived seawater is expected to increase from southeast to northwest. However, the lack of strong relationships between distance inland and saturation index (Section 5.4.6) indicates that local (site-specific) conditions may have a major control in influencing saline groundwater saturation state and/or there is a uniform control acting on the aquifer to maintain saturation at a particular level.

Saline groundwater calcite and dolomite saturation indices are significantly lower than those predicted from chloride concentration and saturation indices of input waters (seawater), indicating that a reduction in saturation occurs within the platform. The reduction in calcite saturation observed in the saline groundwaters can be created by a decrease in calcium (most likely due to calcite precipitation) or an increase in acidity (potentially due to bacterial activity). Caribbean seawater is supersaturated with respect to SI-C and thus has the potential to precipitate calcite to bring the waters to equilibrium and calcite precipitation may explain the SI-C values observed in coastal, deep saline zone and sulfide layer sites. However, this process would result in a depletion of calcium of 0.35 mM (calculated using PHREEQC) and saline groundwaters are, on average, enriched in calcium, as discussed in Section 5.4.5.1. In addition, calcite precipitation cannot explain the undersaturation observed in many of the saline groundwater sites (e.g. open pit cenotes, caverns and cave sites). This suggests that the reduction of SI-C is due to an increase in acidity, probably as a result of oxidation reactions involving heterotrophic bacteria.

The saline groundwater pCO_2s are an order of magnitude greater than seawater. Increases in pCO_2 can be from increases in alkalinity and/or decreases in pH. In general, alkalinity concentrations in the saline groundwaters are lower than that of seawater (perhaps consumed by dolomitisation), implying that pCO_2 is controlled by pH, rather than by alkalinity. Acidity or carbon dioxide generation may be indicative of bacterial heterotrophic activity. The role bacteria play in influencing geochemistry and rock-water interactions is considered in the next section.

5.5 Geomicrobiology of Saline Groundwaters of the Yucatan Peninsula

5.5.1 Microbiological Analyses

On the samples taken for microbiological analyses, acridine orange direct counts (AODC), and Most Probable Number (MPN) analyses (aerobic and anaerobic heterotrophs, sulfur oxidisers, sulfate reducers, iron oxidisers and iron reducers) were performed. Both methods are described in Chapter 2.

5.5.1.1 Total Counts (AODC) and Most Probable Numbers (MPN) of Bacteria

A. Saline Groundwaters

a) Total Counts (AODC)

Bacteria were detected in all samples. Total bacterial counts using the Acridine Orange Direct Count (AODC) method showed that saline groundwaters have total bacterial cell numbers of 5.76 ± 6.95 x 10^4 (n=13) cells/ml. In addition, 2.77 ± 2.68 % of the saline groundwater bacterial community are undergoing cell division (Table 5.7).

b) Viable Counts - Most Probable Numbers (MPN) of Bacteria

i. Heterotrophs

All MPN dilution vials aimed at enumerating aerobic heterotrophic bacteria (HOX) and anaerobic heterotrophic bacteria (HAN) showed positive growth for all dilutions, indicating that the minimum numbers of both HOX and HAN is 2300 cells/ml (n = 5) in all saline groundwaters tested.

ii. Thiosulfate-oxidising bacteria (SOX)

All samples tested for the presence of SOX demonstrated positive growth. Thiosulfate-oxidising bacteria are present in numbers ranging from 1 to >2300 cells/ml ($\bar{x}$ = 294 ± 811 cells/ml, n = 8) in the saline groundwaters. Thiosulfate and sulfate measured from acidic SOX MPN vials showed that the molar ratio of thiosulfate oxidised:sulfate produced

was 2.03:1.00 (n = 3). The final pH of the media was 5.35 ± 0.02, 1.68 pH units lower than the initial media pH of 7.30.

iii. Sulfate reducing bacteria

Sulfate reducing bacteria (SRB) numbers range from 0 - 6600 cells/ml, although only two samples exhibited numbers greater than 1 cell/ml (n = 11).

iv. Iron-oxidising bacteria

Attempts to grow iron-oxidising bacteria (Fe-OX) were unsuccessful.

v. Iron-reducing bacteria (Fe-R)

Iron reducing bacteria (Fe-R) are present in numbers ranging from 1.54 to >2300 cells/ml ($\bar{x}$ = 614 ± 1127 cells/ml, n = 4), representing 2.05 ± 2.64 % of the total bacterial population.

Table 5.7 Summary of AODC and MPN results for saline zone environments. Numbers are in cells/ml except the mean number of dividing cells (which are in percent) (±1σ). n.d. = no data.

	Total Cell Numbers ($x10^4$)	**Mean % Dividing Cells**	**MPN HOX ($x10^3$)**	**MPN HAN ($x10^3$)**	**MPN SOX ($x10^3$)**	**MPN SRB ($x10^3$)**	**MPN Fe-R ($x10^3$)**
Saline Ground-waters	5.76 ± 6.95 (n = 13)	2.77 ± 2.68 (n = 13)	>2.3 (n = 5)	>2.3 (n = 5)	0.29±0.81 (n = 8)	0.60±1.99 (n = 11)	0.61±1.13 (n = 4)
Saline Zone Sediments	147 (n = 1)	0.94 (n = 1)	0 (n = 1)	>2.3 (n = 1)	n.d.	0.05 (n = 1)	>2.3 (n = 2)

B. Saline Zone Sediments

AODC and MPN analysis was carried out on one sediment (23 m water depth in Mayan Blue) sample from the saline zone. Total counts were 1.48 ± 0.04 x 10^6 cells/ml, 0.94 % of which were dividing. Attempts to enumerate aerobic heterotrophic bacteria from the sediment sample resulted in no positive growth within any of the MPN vials. However, all MPN vials showed positive growth (indicating a minimum of 2300 cells/ml) for both anaerobic heterotrophic and iron reducing bacteria. Sulfate reducing bacteria (SRB) were present in numbers of 48 cells/ml. MPN analyses of SOX were not performed.

5.5.1.2 Oxygen Consumption Rates

Oxygen consumption rates were only studied in detail throughout the mixing zone (Chapter 4). However, three measurements taken from the saline zone of one site (Mayan Blue) indicate that mean saline groundwater oxygen consumption rates are 0.03 ± 0.02 mM O_2/L/day. This translates to annual oxygen consumption rates of 10.60 ± 6.39 mM O_2/L/year, about 29 times faster than the rate published for the open ocean (0.363 mM O_2/L/year, Morita, 1986).

5.5.1.3 Bacterial Variations with Depth (Case Study from The Pit, Dos Ojos)

A profile of samples for microbiological analyses (AODC, SOX and SRB) was taken throughout the saline zone of The Pit. Six samples were obtained from the saline groundwaters of The Pit, four of which were from the deep (>40 m) saline zone. There is a general trend of decreasing bacterial numbers with depth, except for the deepest sample (91 m), which has cell numbers similar to those found in the freshwater lens and mixing zone of this site (Figure 5.63).

With respect to MPN analyses, only SOX and SRB were studied at The Pit. SOX were enriched from all water samples taken throughout The Pit. The highest numbers of SOX were found in the freshwater lens and at the top interface of the mixing zone (Figure 5.64). SOX numbers became drastically reduced at the top interface of the hydrogen sulfide layer, which is located in the saline zone between ~30 and 50 m water depth. The mean SOX concentration within the saline zone of the Pit is 7.07 ± 8.01 cells/ml.

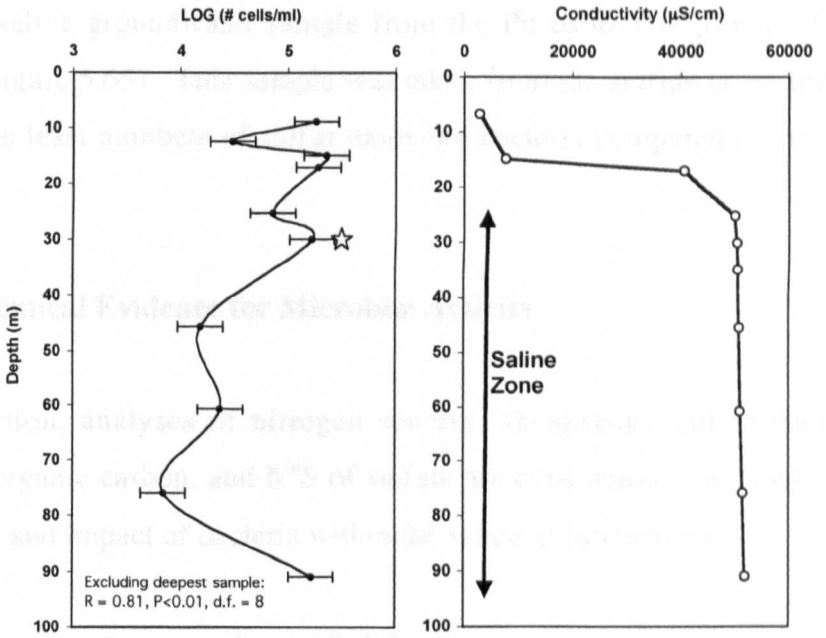

Figure 5.63 Depth profile of bacterial numbers from The Pit (left), shown with conductivity readings taken from the samples (right). Error bars show representative analytical uncertainties (±1 σ). Star denotes sample from sulfide layer.

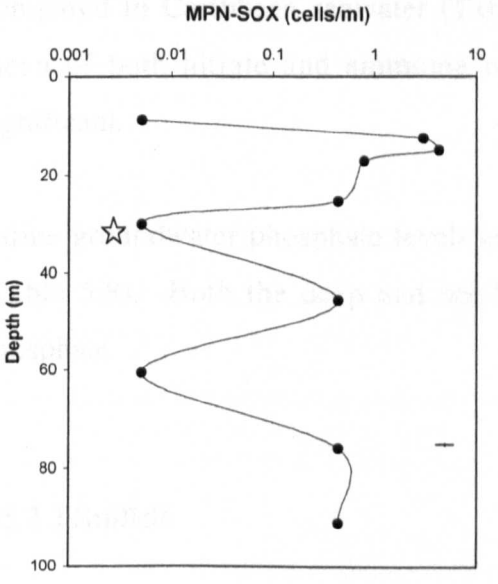

Figure 5.64 Depth profile of sulfur-oxidising bacteria (SOX) MPNs from The Pit. Cross shows representative analytical uncertainties (±1σ). Star denotes sample from sulfide layer.

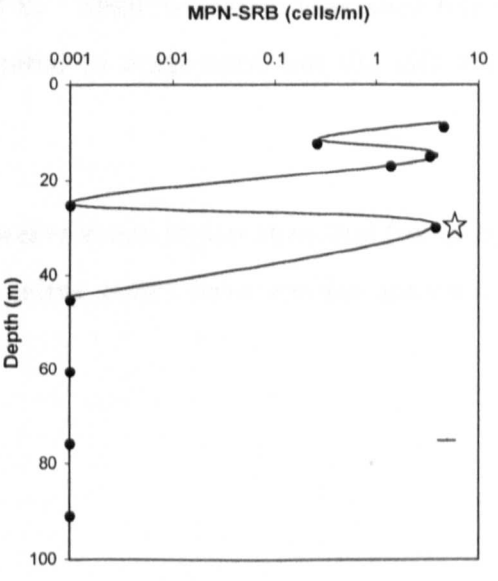

Figure 5.65 Depth profile of sulfate-reducing bacteria (SRB) MPNs from The Pit. Cross shows representative analytical uncertainties (±1σ). Star denotes sample from sulfide layer.

Only one saline groundwater sample from the Pit exhibited growth of sulfate reducing bacteria (Figure 5.65). This sample was taken from the sulfide layer and it is this sample that had the least numbers of sulfur oxidising bacteria compared to the other saline zone samples.

5.5.2 Chemical Evidence for Microbial Activity

In this section, analyses of nitrogen species, phosphorus, sulfur chemistry, methane, dissolved organic carbon, and $\delta^{34}S$ of sulfate are considered in attempts to help elucidate the activity and impact of bacteria within the saline groundwaters.

5.5.2.1 Nitrate and Ammonia and Soluble Reactive Phosphorus (as PO_4^{3-})

Saline groundwaters have significantly higher concentrations of nitrate and ammonia compared to Caribbean seawater (Table 5.8). Shallow saline zone sites have a higher mean of both nitrate and ammonia compared to deep sites, but the difference is not significant.

Saline groundwater phosphate levels are twelve times higher than that found in seawater (Table 5.8). Both the deep and shallow saline zones have similar amounts of "free" phosphate.

5.5.2.2 Sulfide

Despite some saline groundwater samples smelling strongly of sulfide (i.e. they had a "rotten egg' odour), very few samples had sulfide concentrations above the detection limit of the Cline method (Chapter 2). Samples taken from sulfide layers (detected by taste/mild burns while diving) within saline groundwaters had sulfide concentrations ranging from <0.01 (i.e. below detection) to 0.49 μM as HS^-. There is no relationship between sulfide and absolute water depth. Instead, sulfide layers appear to be restricted to areas where there is a visible build up of surface-derived organic matter.

Table 5.8 Summary of mean saline water ammonia, nitrate and phosphate concentrations (±1σ).

	NH_4^+ (μM)	NO_3^- (μM)	PO_4^{3-} (μM)
Seawater	0.004	0.22	0.16
(Merino and Otero, 1991;			
Stoessell et al., 1993)			
Mean Saline Groundwaters	10 ± 30	52 ± 34	1.9 ± 3.2
	(n = 22)	(n = 29)	(n = 14)
Shallow Saline Groundwaters	14 ± 34	63 ± 26	2.0 ± 3.8
	(n = 16)	(n = 21)	(n = 10)
Deep Saline Groundwaters	1 ± 2	23 ± 35	1.8 ± 0.9
	(n = 6)	(n = 8)	(n = 4)

5.5.2.3 Methane

Methane analyses were conducted on a few saline groundwater sites. Of the 24 samples tested, four had measurable quantities of methane, all of which were from deep saline zone sites associated with sulfide layers. Methane concentrations range from 0.23 to 1.03 mM.

5.5.2.4 Dissolved Organic Carbon (DOC)

Caribbean seawater samples had a DOC concentration of 0.38 ± 0.10 mM (n = 3). Saline groundwater DOC concentration is ~ 4 times higher with a mean of 1.61 ± 2.23 mM (n = 34, one value removed). Shallow saline groundwaters have a DOC concentration of 1.41 ± 2.33 mM (n = 24), while deep saline groundwaters have a slightly higher, but not significantly different, mean of 2.10 ± 2.01 mM DOC (n = 10). The lowest saline groundwater DOC value was observed in a shallow saline groundwater sample from a coastal site (0.04 ± 0.00 mM from Nahoch Nah Chich outflow point, 7.5 m water depth). The highest saline groundwater DOC value was measured from the deepest sample obtained in this study (DOC = 490 ± 14 mM at The Pit, 105 m water depth).

5.5.2.5 $\delta^{34}S\text{-}SO_4^{2-}$

In attempts to elucidate the source of excess sulfate (and to identify where redox reactions involving sulfur are taking place), analyses of $\delta^{34}S$ of sulfate were carried out on nineteen saline groundwater samples. Of these, ten were from the shallow (<40 m) saline zone (including samples from three cave, four coastal, one sulfide and two open pit cenote sites) and nine were from the deep (>40 m) saline zone. Within the deep saline zone, four samples were from sites >60 m water depth (including three cave, two coastal and one open pit cenote) and additional samples were taken from one sulfide and two open pit cenote sites.

Caribbean seawater has a mean $\delta^{34}S\text{-}SO_4^{2-}$ value of 19.8 ± 0.4 ‰ (n = 4, this study). Saline groundwaters have a mean $\delta^{34}S\text{-}SO_4^{2-}$ value of 20.1 ± 0.5 ‰ (n = 19), which is not significantly different from that of seawater. However, values obtained for saline groundwaters range from 19.0 to 20.8 ‰, indicating that some samples are significantly different from seawater. Six samples (two coastal, two cave, one open pit cenote, and one deep (>60 m) saline zone sample) have significantly higher $\delta^{34}S\text{-}SO_4^{2-}$ values compared to seawater (Figure 5.66). One sample (from a coastal site) has a $\delta^{34}S\text{-}SO_4^{2-}$ signature significantly lower than seawater. In addition, sulfur residues from filtered waters taken from the oxygenated zones around sulfide layers had a mean $\delta^{34}S\text{-}SO_4^{2-}$ value of –6.7 ± 3.0 ‰ (n = 3).

5.5.3 Consolidating the Evidence for the Role of Bacteria in Carbonate Diagenesis in the Zone of Saline Groundwaters

At the end of the geochemistry section of this chapter, it was suggested that heterotrophic bacteria are probably responsible for the high pCO_2 concentrations (and SI-C undersaturation) observed in the saline groundwaters. Heterotrophs are organisms that gain energy from the oxidation of organic compounds (Madigan *et al.*, 2000). A simplified heterotrophic metabolism is illustrated in Equation 5.8, where one mole of carbon dioxide is produced for every mole of oxygen consumed. The carbon dioxide then combines with water to form carbonic acid (Equation 5.9), which will play a role in carbonate dissolution.

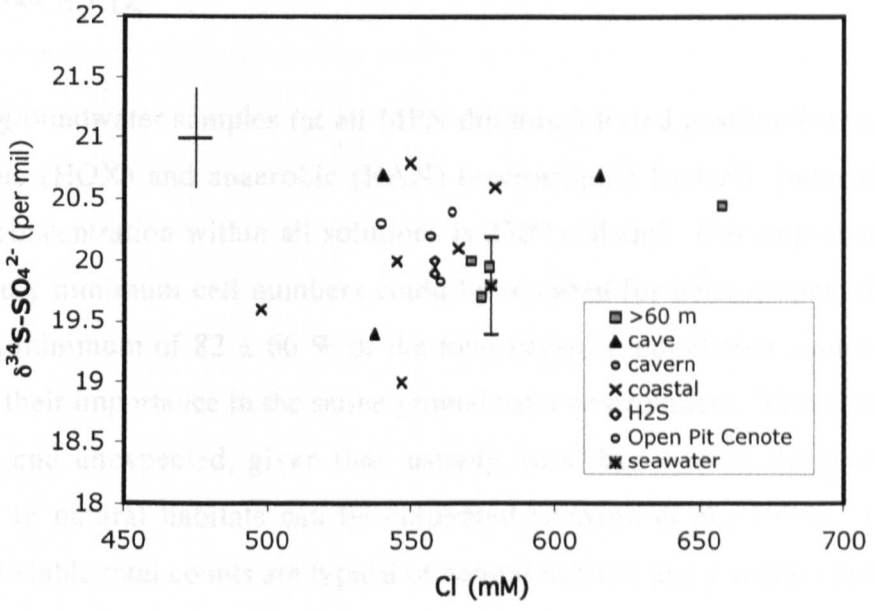

Figure **5.66** Saline groundwater $\delta^{34}S\text{-}SO_4$ against chloride. Cross shows representative analytical uncertainties (±1σ).

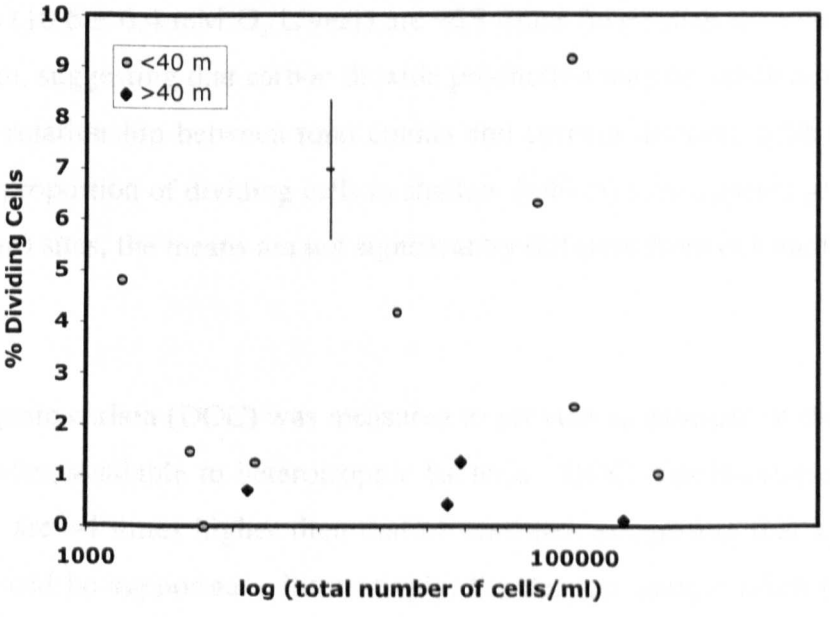

Figure 5.67 A semi-log plot of the total number of cells/ml against the proportion of the bacterial poplution undergoing cell division (% dividing cells) for shallow (grey circles) and deep (black diamonds) saline groundwaters. Crosses are representative analytical uncertainties (±1σ).

$$CH_2O + O_2 \leftrightarrow CO_2 + H_20 \quad (5.8)$$

$$CO_2 + H_2O \leftrightarrow H_2CO_3 \quad (5.9)$$

All saline groundwater samples (at all MPN dilutions) tested positive for the presence of both aerobic (HOX) and anaerobic (HAN) heterotrophic bacteria, indicating that their minimum concentration within all solutions is 2300 cells/ml. It is important to note that although only minimum cell numbers could be reported for heterotrophs, these numbers represent a minimum of 82 ± 66 % of the total bacterial population counted by AODC, suggesting their importance in the saline groundwater environment. These percentages are substantial and unexpected, given that, usually, less than 1 % of the total prokaryotic population in natural habitats can be cultivated (Amann et al., 1995). Indeed, small fractions of viable:total counts are typical of natural habitats and a smaller ratio is observed for most of the other functional groups that were enumerated from the saline groundwaters.

Despite total numbers of bacteria in the saline groundwaters ($5.76 \pm 6.95 \times 10^4$) being an order of magnitude lower than typical open ocean water (5×10^5 to 3×10^6 cells/ml; Hobbie et al., 1977; Porter and Feig, 1980), oxygen consumption rates in the saline groundwaters (10.6 ± 6.4 mM O_2/L/year) are ~29 times faster than the rate published for the open ocean, suggesting that carbon dioxide production may be substantial. In addition, there was no relationship between total counts and percent dividing cells (Figure 5.67). Although the proportion of dividing cells in shallow (<40 m) sites appears greater than that of deep (>40 m) sites, the means are not significantly different from one another (2 tailed t-test; P= 0.22).

Dissolved organic carbon (DOC) was measured to provide an estimate of the total amount of organic matter available to heterotrophic bacteria. DOC concentrations in the saline groundwaters are ~4 times higher than that of seawater, suggesting that a heterotrophic community could be supported. Interestingly, the deepest sample taken (from The Pit, 105 m water depth) had the highest DOC concentration (490 mM), perhaps indicating that a "deep cave biosphere" could be supported (unfortunately, there is no microbiology data from this depth), or that organic matter is being released from the dissolution of organic-rich sediments. DOC data can be difficult to interpret. An increase in DOC (or a high DOC value) may indicate where bacterial communities could be supported, or it might indicate a lack of bacterial activity (i.e. the DOC is not being used).

DOC data does not display a relationship with total cell numbers or with any MPN (although a correlation with numbers of heterotrophic bacteria was not possible because their concentrations could only be reported as >2300 cells/ml). In addition, there were no significant relationships between DOC and nitrate, ammonia, phosphate, Ca_{xs}, Mg_{xs}, SO_{4xs}, Sr_{xs}, pCO_2 or saturation index. This finding is dissimilar to the data from Bahamian blue holes where DOC had an inverse relationship with Mg_{xs} (Whitaker, 1992).

The only parameter that appears to have a relationship with DOC in the Yucatan Peninsula saline groundwaters is the proportion of the bacterial population that is undergoing cell division (i.e. % dividing cells). However, this relationship appears only to be true for samples taken from the deep saline zone, where the proportion of dividing cells decreases with decreasing DOC concentration (Figure 5.68). Direct counts do not differentiate between active and inactive cells, while % dividing bacterial cells is a measure of the growth rate of a bacterial community. Thus, the decrease in numbers of cells undergoing cell division in the deep saline zone may imply that deep saline groundwaters are nutrient limited compared to shallow saline ground waters. This may be supported by nitrate and ammonia data, which shows that the deep saline groundwaters are not as nutrient-rich as the shallow saline groundwaters (Table 5.8).

% dividing cells appear to be independent of DOC in the shallow saline groundwaters (perhaps indicating that DOC is non-limiting there). However, in the shallow saline groundwaters, the proportion of cells undergoing cell division has a positive relationship with pCO_2 (Figure 5.69) and an inverse relationship with both SI-C (Figure 5.70) and pH (Figure 5.71). Importantly, the sample in which none of the cells were undergoing cell division has an SI-C of zero, (and the regression has a zero intercept) thus suggesting that without an active bacterial population, SI-C does not become undersaturated. These findings indicate that the bacteria in the shallow saline groundwaters play an important role in increasing pCO_2 concentrations, decreasing pH and in maintaining undersaturation with respect to SI-C (and, by extension, SI-A). These relationships do not exist in the deep saline groundwaters.

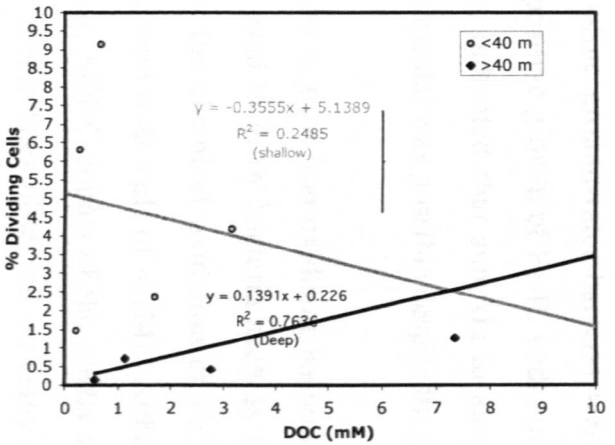

Figure 5.68 Saline groundwater DOC against percent dividing cells. Cross shows representative analytical uncertainties (±1σ).

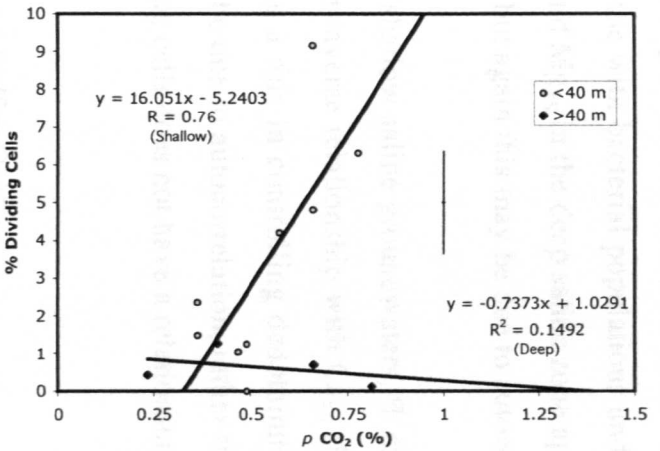

Figure 5.69 Saline groundwater $p\ CO_2$ against percent dividing cells. Cross shows representative analytical uncertainties (±1σ).

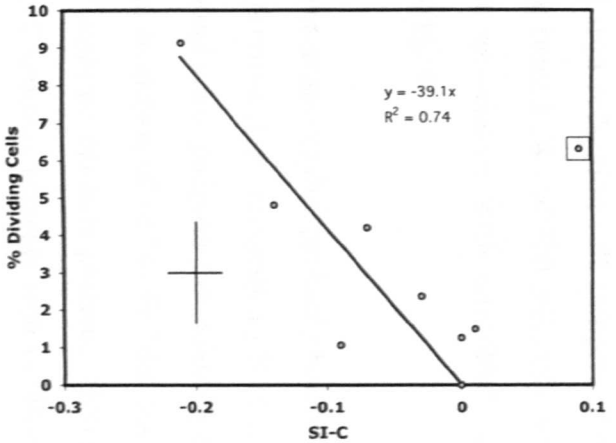

Figure 5.70 Shallow (<40 m) saline groundwaterSI-C against percent dividing cells. One outlier (boxed) removed for the regression. Cross shows representative of analytical uncertainties (±1σ).

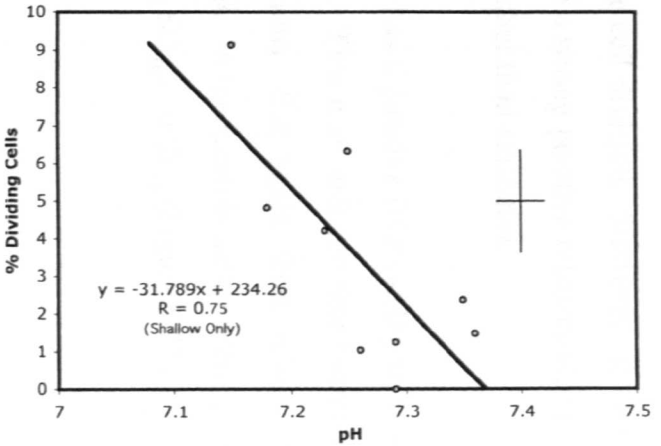

Figure 5.71 Shallow (<40 m) saline groundwater pH against percent dividing cells. Cross shows representative analytical uncertainties (±1σ).

In the deep saline groundwaters, where there is probable $CaSO_4$ dissolution (a process which is independent of pH), an inverse relationship exists between % dividing cells and Ca_{XS}, SO_{4XS} and Sr_{XS} (Figure 5.72). Rather than being a causal relationship, however, this is probably an autocorrelation between saline groundwater sites that are dissolving $CaSO_4$ and those with bacterial populations undergoing little cell division. Similarly, % dividing cells and Mg_{XS} in the deep saline zone appear to have a strong positive relationship (Figure 5.72), but again this may be due to autocorrelation, rather than causation.

In the shallow saline groundwaters, % dividing cells has a positive relationship with Mg_{XS} and an inverse relationship with Ca_{XS} (Figure 5.72). This may indicate that bacteria are playing a role in controlling dedolomitisation reactions. But, again, these relationships could be due to autocorrelation, rather than causation. In the shallow saline zone, percent dividing cells does not have a relationship with either SO_{4XS} or Sr_{XS} (Figure 5.72).

Iron and Sulfur Cycling

MPN analyses provide further insight into the potential cycling of iron and sulfur within the saline groundwaters. MPN analyses of iron-reducing bacteria (Fe-R) demonstrated that some saline groundwater bacteria were capable of iron reduction (all samples showed some positive growth of Fe-R, with numbers ranging from 1.54 - >2300 cells/ml), which, in turn, indicated that suboxia to anoxia (likely in association with microbial micro-environments) was possible despite the presence of oxygen.

Attempts to grow iron-oxidising bacteria (Fe-OX) were unsuccessful, probably because the media used to grow bacteria such as *Thiobacillus ferrooxidans* requires a pH of 2-3 to prevent the chemical oxidation of Fe^{2+} (saline groundwater bacteria are adapted to an environment with a pH of ~7.24). Although chemical oxidation of Fe^{2+} to Fe^{3+} did occur in the vials, AODC counts of the media showed there were no bacteria present. However, orange precipitates observed on many cave wall-rock samples indicate iron oxidation is occurring at the rock-water interface. But, it is unknown whether this oxidation is chemical or bacterially-controlled.

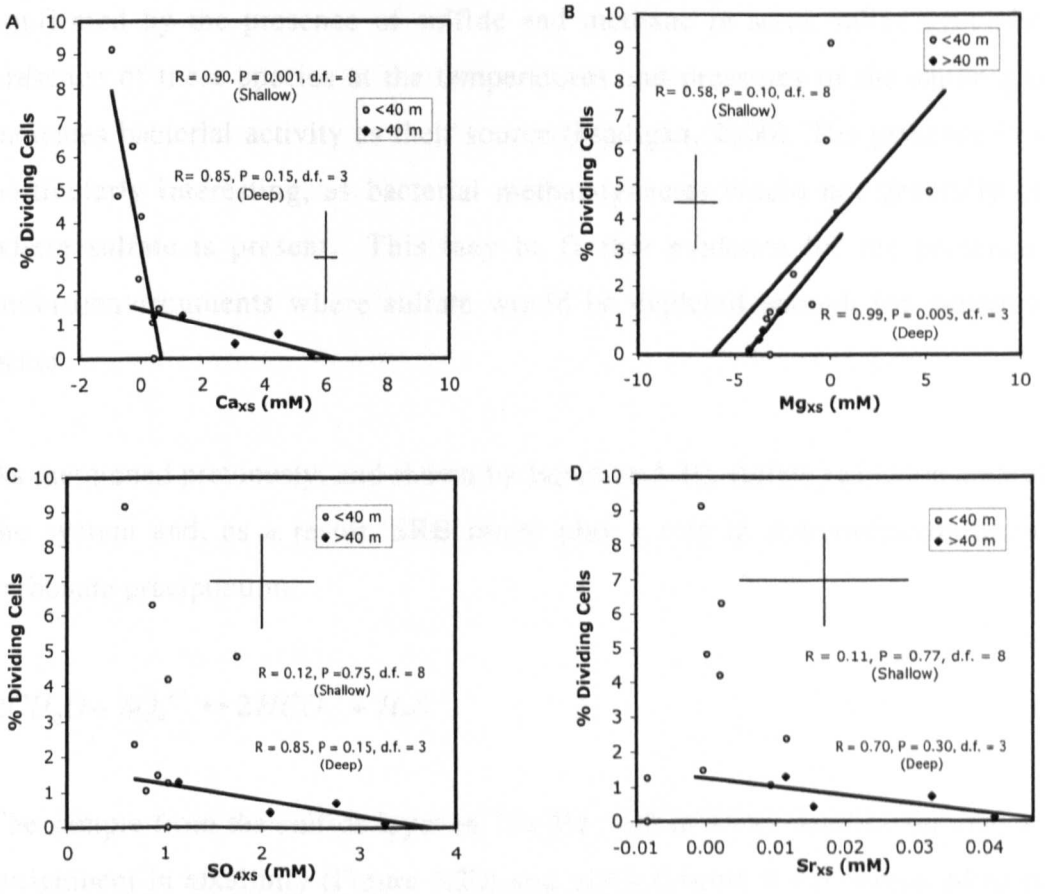

Figure 5.72 % Dividing Cells against Ca_{xs} (A), Mg_{xs} (B), SO_{4xs} (C) and Sr_{xs} (D). Shallow (<40 m) saline groundwaters are represented by grey circles, while deep (>40 m) saline groundwater samples are represented by black diamonds. Crosses are representative analytical uncertainties (±1σ).

MPN analyses of SRB demonstrated that some saline groundwater bacteria were capable of sulfate reduction, which, in turn, indicated that anoxia (likely in association with microbial micro-environments) was possible despite the presence of oxygen. This was confirmed by the presence of sulfide and methane in some saline groundwaters. The presence of these species at the temperatures and pressures of the saline groundwaters indicates bacterial activity as their source (Madigan, 2000). The presence of methane is particularly interesting, as bacterial methanogenesis would not generally be expected where sulfate is present. This may be further evidence for the presence of anoxic (micro)environments where sulfate would be depleted enough for methanogenesis to occur.

As mentioned previously, and shown by Equation 5.10, sulfate reduction adds alkalinity to the system and, as a result, SRB might play a role in dolomitisation and/or calcium carbonate precipitation.

$$2CH_2O + SO_4^{2-} \leftrightarrow 2HCO_3^- + H_2S \qquad (5.10)$$

The sample from the sulfide layer in The Pit (~30 m water depth) exhibited a significant enrichment in alkalinity (Figure 5.20) and pCO_2 (Figure 5.47) compared to surrounding waters, causing an increase in saturation, especially with respect to SI-C/A and SI-DD/D (Figure 5.45). Despite the increase in thermodynamic potential to precipitate calcite and/or dolomite, the major ion chemistry of the sulfide layer sample was not significantly affected (Figure 5.43).

MPN analyses of thiosulfate-oxidising bacteria (SOX) indicated that bacteria capable of thiosulfate oxidation were present in all saline groundwaters. Thiosulfate and sulfate measured from SOX MPN vials showed that the molar ratio of thiosulfate oxidised:sulfate produced is 2.03:1.00 (n = 3), confirming that complete oxidation to sulfate had occurred *via* Equation 5.11.

$$S_2O_3^{2-} + 2O_2 + H_2O \rightarrow 2SO_4^{2-} + 2H^+ \qquad (5.11)$$

This reaction generates acidity and the final pH of the saline groundwater SOX media was 5.35 ± 0.02, compared to a starting pH of 7.2-7.3, inferring that the bacteria are capable of

significant pH reductions within the saline groundwaters. Although buffering from the open carbonate system will dampen these pH changes, SOX may play a significant role in carbonate dissolution through acidity generation.

While MPN analyses give information about the potential for biological activity, geochemical evidence can provide information regarding their actual activity. The presence of sulfide in some of the saline groundwaters indicates that bacterial sulfate reduction is active in localized environments. Significant sulfate reduction is expected to cause a decrease in sulfate concentrations. However, the situation is complicated in the saline groundwaters by the probable dissolution of evaporites (Section 5.4.8), providing an additional source of sulfate. $\delta^{34}S\text{-}SO_4^{2-}$ analyses can help separate chemical from bacterially-controlled sulfur reactions.

$\delta^{34}S$ of Sulfate

As mentioned above, the source of excess sulfate could be from the dissolution of evaporites (i.e. $CaSO_4$) and/or from the re-oxidation of reduced (bacterially produced) sulfur species. An evaporite (gypsum) deposit will carry a slightly heavier $\delta^{34}S$ signature (+1.65 ± 0.12 ‰ : Thode and Monster, 1965; Faure, 1986) compared to the seawater from which it originally precipitated and upon dissolution, there is no fractionation (Faure, 1986). Over the past 65 Ma, the $\delta^{34}S$ signature of seawater sulfate has ranged from 17.3 to 22.5 ‰ (Paytan et al., 1998). Thus, gypsum deposited during this time would carry a $\delta^{34}S\text{-}SO_4^{2-}$ signature of ~19.0 – 24.2 ‰, corresponding to maximum changes from present-day seawater ranging from –0.8 to +4.4 ‰. If all SO_{4XS} is due to the dissolution of $CaSO_4$, a mass balance equation can be used to determine the expected $\delta^{34}S\text{-}SO_4^{2-}$ value of a given saline groundwater sample (Equation 5.12). The left-hand side of the equation calculates the $\delta^{34}S$ value expected from the seawater component of a sample's sulfate concentration and this is added to the $\delta^{34}S$ value expected from the 'XS' component of a sample's sulfate concentration.

$$\delta^{34}S_{SGW(expected)} = \left(\frac{SO_{4SW}}{SO_{4SW} + SO_{4XS}} \times \delta^{34}S_{SW}\right) + \left(\frac{SO_{4XS}}{SO_{4_{SW}} + SO_{4XS}} \times \delta^{34}S_{sourceSO4XS}\right) \qquad (5.12)$$

where:

$\delta^{34}S_{SGW(expected)}$ is the expected saline groundwater $\delta^{34}S$ value

SO_{4SW} is the concentration of sulfate in Caribbean Seawater (~29 mM SO_4^{2-})

SO_{4XS} is the concentration of saline groundwater sulfate above that of Caribbean Seawater

$\delta^{34}S_{SW}$ is the $\delta^{34}S$ value of seawater (19.8 ‰)

$\delta^{34}S_{sourceSO4XS}$ is the $\delta^{34}S$ value of the expected source of SO_{4XS}

If all saline groundwater SO_{4XS} is from the dissolution of $CaSO_4$, the $\delta^{34}S_{SGW(expected)}$ is 19.8 - 20.6‰. Taking into account the analytical uncertainty (±0.2‰), gypsum dissolution could explain the $\delta^{34}S$-SO_4^{2-} values observed in 17 of the 19 samples analysed. $\delta^{34}S$-SO_4^{2-} values significantly above that of seawater could also be explained by sulfate reduction by bacteria such as *Desulfovibrio desulfuricans*. However, positive SO_{4XS} values and the lack of reduced sulfur species make this an unlikely explanation.

The ubiquitous presence of sulfur-oxidising bacteria (and the potential for abiotic sulfide oxidation) provides the opportunity for the re-oxidation of any reduced sulfur species that may be present. Oxidation of reduced sulfur species results in little or no fractionation (see, for example, Fry et al., 1986). Thus, it is expected that sulfate from sulfur re-oxidation reactions will carry the negative signature of the reduced sulfur compounds. The average fractionation factor due to bacterial sulfate reduction has been measured as -28‰ in natural populations at 25°C where sulfate concentrations are non-limiting (Habicht and Canfield, 1987; Canfield, 2001). A fractionation of –28 ‰ from bacterial sulfate reduction within Caribbean seawater would produce a $\delta^{34}S$-SO_4^{2-} of –8.2 ‰. Using a simple mass balance equation (Equations 5.12), it can be demonstrated that the expected saline groundwater $\delta^{34}S$-SO_4^{2-} signature would be 14.9 – 19.8 ‰ ($\bar{x}$ = 18.4 ± 1.2‰, n = 19) if the source of SO_{4XS} is the re-oxidation of reduced sulfur species. Of the 19 samples analysed, 10 fall within this range. Of these, only one has a $\delta^{34}S$-SO_4^{2-} value significantly less than that of seawater, suggesting that only one sample is from an area where significant re-oxidation of reduced sulfur species is taking place (other samples from this site had higher $\delta^{34}S$ values). Although sulfide analyses wait to be run for this sample, the adjacent sediment smelled strongly of sulfide (and the author's arms were burned from handling the

sediment at the surface). This low $\delta^{34}S$ value (19 ‰) is similar to that reported by Bottrell et al. (1991) for Cousteau's Blue Hole in the Bahamas ($\delta^{34}S\text{-}SO_4^{2-}$ = 19.0 ± 0.5 ‰, n = 2), indicating the re-oxidation of reduced sulfur species (possibly derived from the overlying mixing zone) may be an important process there too.

The only other negative $\delta^{34}S\text{-}SO_4^{2-}$ signatures found in the saline groundwaters were obtained from sulfur residues collected from filtered samples taken from the vicinity of sulfide layers, further indicating that re-oxidation reactions, although present, are probably confined to small (localised) areas within the platform. Interestingly, the negative signatures obtained from the sulfur precipitates (-6.7 ± 3.0 ‰) imply a fractionation factor of -26.5 ± 3.0‰, which is not significantly different from that published from other natural environments (i.e. –28 ‰: Habicht and Canfield, 1987; Canfield, 2001). Colloidal S° from Cousteau's Blue Hole (Bahamas) had an average $\delta^{34}S$ value of –0.1 ± 0.5 ‰, indicating a fractionation of –22 ‰.

Overall, however, the saline groundwaters do not exhibit a negative $\delta^{34}S\text{-}SO_4^{2-}$ signature compared to that of Caribbean seawater. It is therefore likely that the dissolution of evaporites, rather than the re-oxidaton of reduced sulfur species, is the major source of the excess sulfate in most of the saline groundwaters.

There were two orders of magnitude more bacteria in the sediment sample compared to all groundwater samples. Lack of aerobic heterotrophic growth (and large numbers of anaerobic heterotrophs) in the sediment indicates that it is anoxic and capable of supporting anaerobic respiration/fermentation. Large numbers of iron reducing bacteria indicate that iron reduction (in addition to sulfate reduction) may be an important metabolism in the cave sediment environments.

5.6 Wall-rock analysis

Samples of cave wall rock were collected from sites up to 6 km inland and 105 m water depth. Although wall-rock analyses are on-going, preliminary results suggest only wall-rock exposed to saline groundwaters at the coast contain significant amounts of dolomite. Thus, data from a coastal site (Ak Kimin) are the focus of this section. XRD analyses are

from this study, with some values (including stoichiometry calculations) from Goodwin (2002). Thin section descriptions and AAS trace element data in this section are also from Goodwin (2002).

5.6.1 XRD Analyses

XRD analysis of a profile of wall-rock samples from a coastal site (Ak Kimin) indicates an increase in dolomite content (up to 75%) with water depth (Figure 5.73). No dolomite was found outside the saline zone.

5.6.1.1 Stoichiometry

XRD analysis was used to determine the Ca:Mg ratio of six Ak Kimin dolomites. The Ak Kimin dolomites are non-stoichiometric (39-43 mol % Mg). Duplicate analyses of three of these dolomites separated by digestion in 0.27 M di-Na EDTA (pH 6.0 – 6.5) and analysed by AAS demonstrated that the mol % Mg results were within ±2.64 % of those obtained using XRD analysis.

5.6.2 Thin Section Analyses

Ten wall-rock samples were examined using stained thin sections. The samples have variable porosity (5-40%), most of which is due to secondary dissolution. Goodwin (2002) notes that the dissolution is selective and that the bioclasts that have undergone dissolution are predominantly algae and corals, which may have been composed of HMC (Scholle, 1978). Aragonite dissolution or replacement (with dolomite) is evident in some samples. The dolomites predominantly occur as fabric preserving grain replacement and as cements which line inter- and intra-granular pores (Figure 5.74). The cements mostly replace original meteoric sparry calcite, but isolated dolomite rhombs also are evident (Figure 5.74 iv). However, subhedral shapes dominate. The amount of dolomite appears to increase with depth and may be confined to areas of inter-connected porosity (Goodwin, 2002).

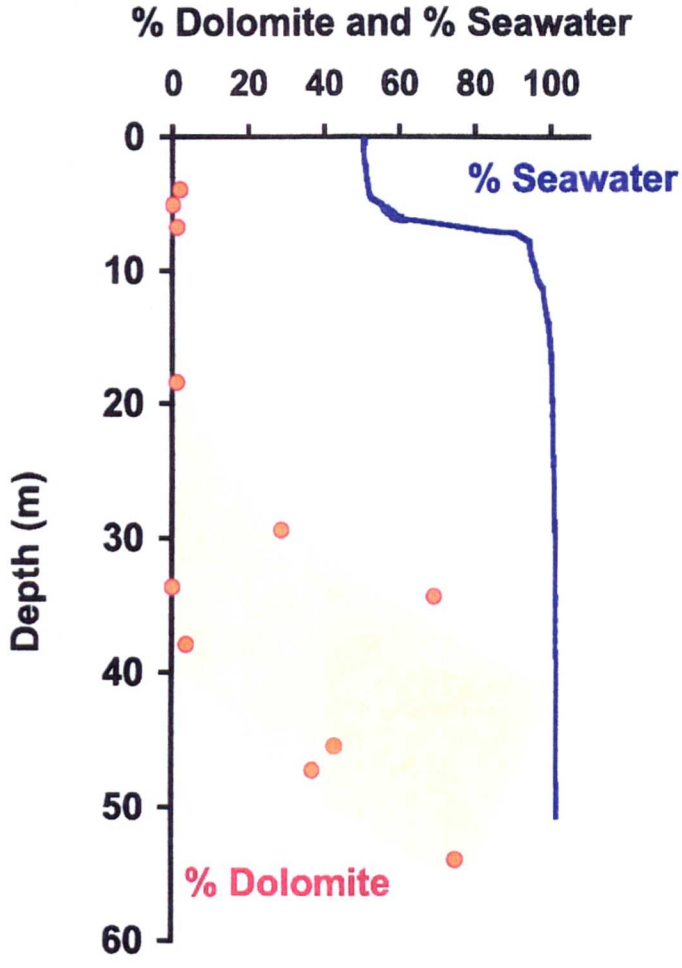

Figure 5.73 % Dolomite (circles) and % seawater (solid line) against depth for a profile of wall-rock samples taken from Ak Kimin.

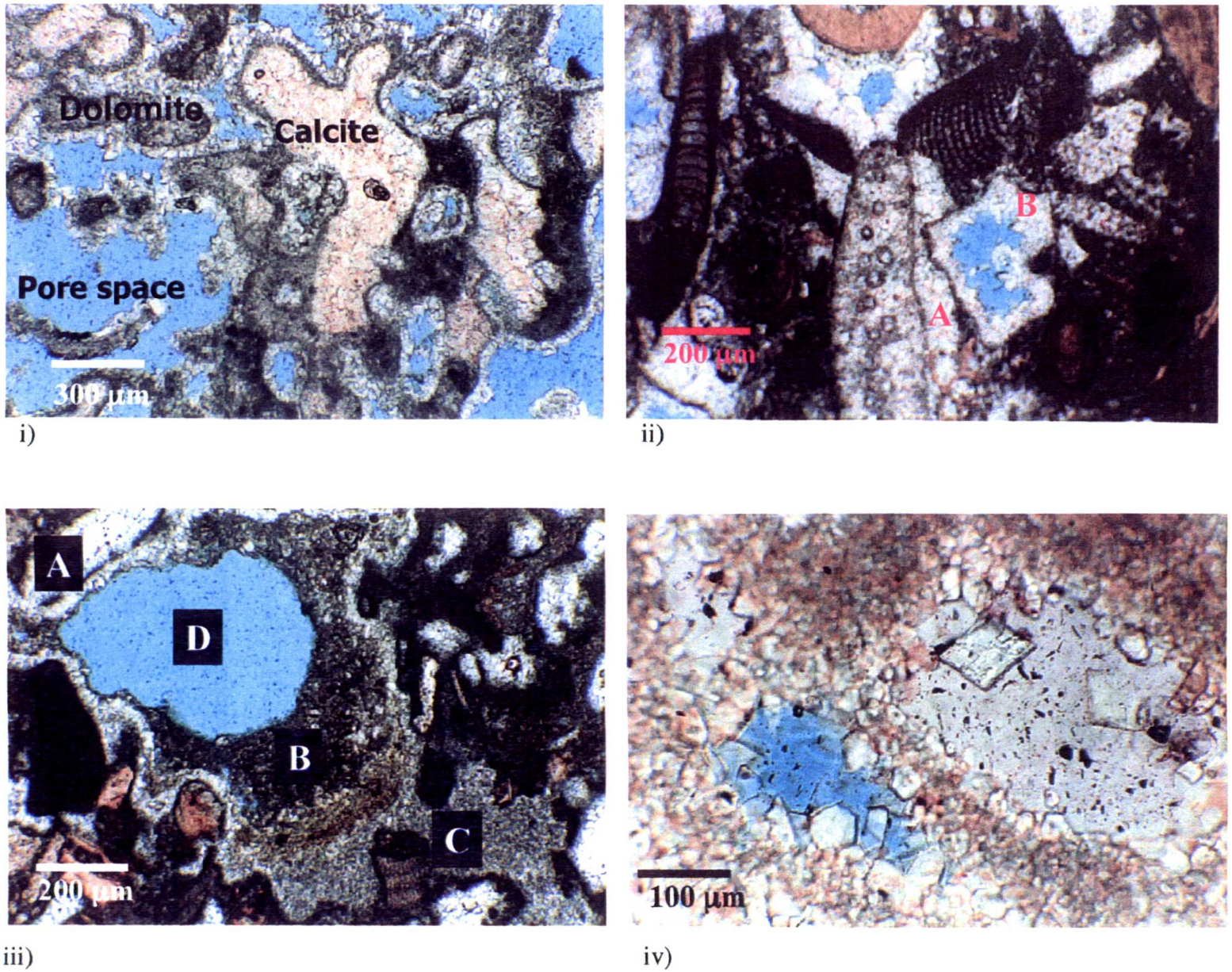

Figure 5.74 Thin section photomicrographs of wall-rock samples taken from Ak Kimin. Calcite is stained pink with alazarin red-S and dolomite appears grey to white. Interconnected pore spaces are filled with a blue plastic resin. In i), two types of dolomitisation are present: coarse limpid crystals lining the voids and replacement of fine-grained allochems. ii) shows the allochems, corals, algae and forams that typically dominate. Sample shows inter (A) and intra (B)- granular dolomite cementation. Sample iii) contains limpid dolomite crystals lining a void (A). (B) is a result of dolomitisation of a fine-grained matrix, (C) is mixed grain-sized dolomite, possibly in-filling the void (D). Sample (iv) shows a dolomite rhomb (A) growing freely within a void. Modified from Goodwin, 2002.

5.6.3 ICP-AAS Analyses

ICP-AAS techniques were used to measure the calcium, magnesium, iron, manganese and strontium concentrations of the Ak Kimin wall rock. Dolomite from three samples (isolated by digestion in 0.27 M di-Na EDTA, pH 6.0 - 6.5) was also examined. The concentrations of these elements with depth are shown in Figure 5.76. Wall-rock magnesium, iron and manganese concentrations increase with water depth (Goodwin, 2002). The data for calcium is less clear. Wall-rock strontium concentrations appear to be relatively constant with depth throughout the saline zone. The strontium concentrations of the isolated dolomites range from 199-290 ppm and strontium concentration decreases with increasing mol % Mg and indicate the dolomites have a strontium concentration of 185 ppm (Goodwin, 2002). These values indicate a marine origin of the dolomite if dolomite is formed by the replacement of calcite.

5.6.4 Wall-Rock Discussion

Wall-rock samples from the zone of saline groundwater at a coastal site (Ak Kimin) are partially dolomitised (up to 75%) with both fabric-preserving dolomitisation of grains and dolomite cements lining inter- and intra-granular pores. Preliminary analysis indicates that these dolomites are characteristically non-stoichiometric (~41 mol% Mg). In addition, the Sr/Ca molar ratio of the fluids from which the dolomites precipitated has been calculated as 0.0079 – 0.0463 (Goodwin, 2002). This suggests that seawater, which has a Sr/Ca molar ratio of 0.0097, was the dolomitising fluid. Low concentrations of iron and manganese (< 300 and < 50 ppm, respectively) within the wall-rock samples suggest that the dolomites formed under oxidizing conditions (Budd, 1997). Incremental increases of both elements with depth may suggest an increase in reducing conditions with depth. However, the proposed dolomitising fluid is seawater (which has very low iron and manganese concentrations), thus large amounts of either element may not be expected within the wall-rock. No dolomites were found outside the saline zone and dolomite content increases with depth, due to slow incremental dolomitisation over time or dissolution at shallower depths. Dolomitisation is more prevalent where there is interconnected porosity, confirming the importance of active circulation of magnesium-rich fluids.

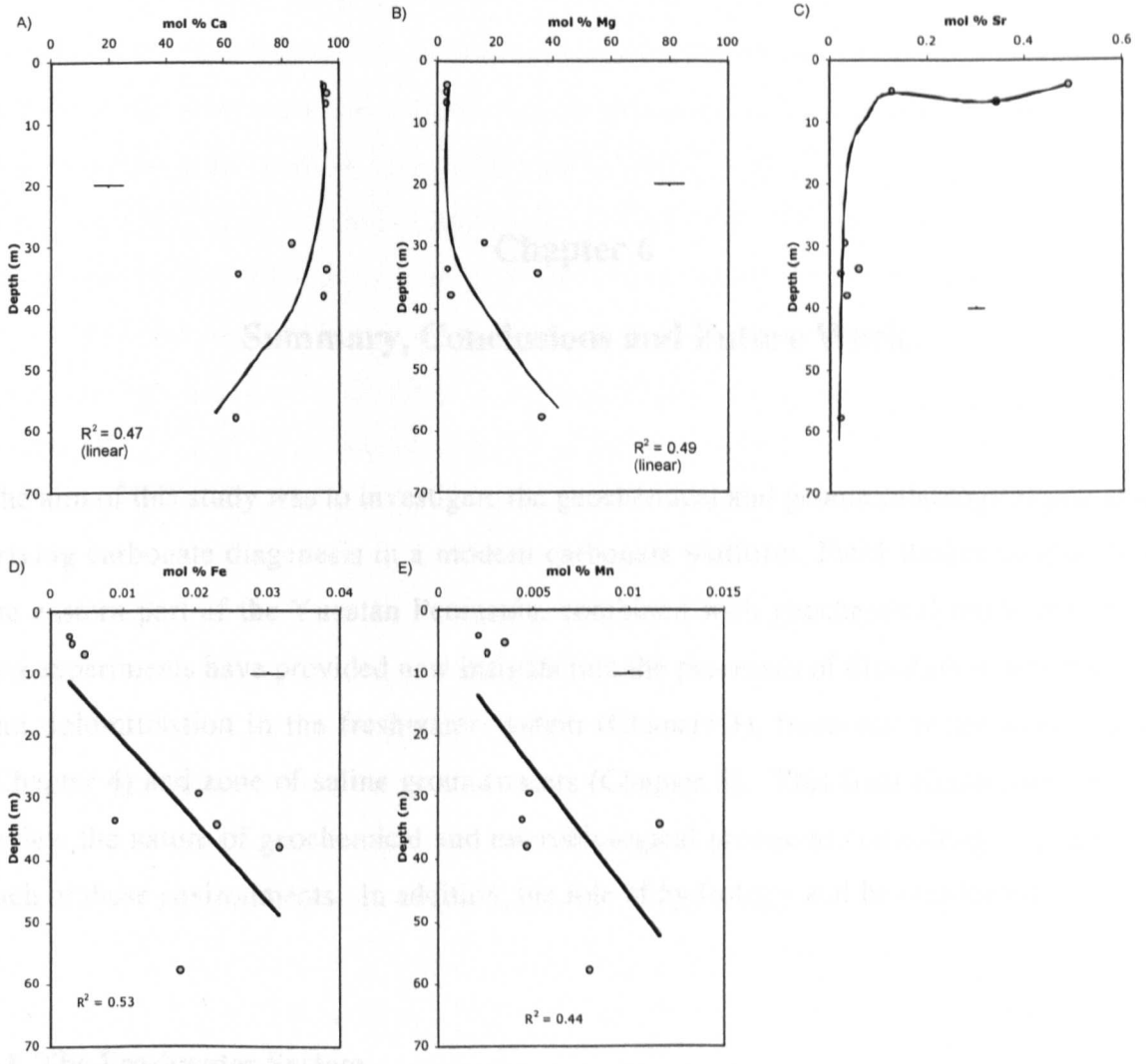

Figure 5.75 mol % calcium (A), magnesium (B), strontium (C), iron (D) and manganese (E) obtained from a profile of wall-rock samples taken from the saline zone of a coastal site. Crosses are represetative analytical uncertainties (±1σ). Modified from Goodwin, 2002.

Chapter 6

Summary, Conclusions and Future Work

The aim of this study was to investigate the geochemical and geomicrobiological processes driving carbonate diagenesis in a modern carbonate platform. Field studies conducted in the eastern part of the Yucatan Peninsula, combined with geochemical modeling and *in situ* experiments have provided new insights into the processes of dissolution, precipitation and dolomitisation in the freshwater system (Chapter 3), fresh-salt water mixing zone (Chapter 4) and zone of saline groundwaters (Chapter 5). This final chapter will briefly review the nature of geochemical and microbiological processes controlling diagenesis in each of these environments. In addition, the role of hydrology will be considered.

6.1 The Freshwater System

Conductivity profiles demonstrate that the thickness of the freshwater lens in the east Yucatan Peninsula increases linearly with distance inland ($R^2 = 0.86$; Figure 3.1), while the specific conductance decreases up until 8 km inland indicating the probable limit of mixing with saline groundwater. The decrease in freshwater lens conductance with distance inland may also be a result of decreasing aerosol inputs with distance away from the coast. Freshwater lens temperatures are warmest near the coast due to mixing with warmer saline water. Freshwater lens temperatures decrease within the first 0.5 km of the coastline but beyond 0.5 km, the lens waters appear to have thermally equilibrated, possibly *via* a common process (e.g. during infiltration through the vadose zone). There are no systematic variations in pH or dissolved oxygen with distance inland, suggesting local (site specific) processes control these parameters (Figures 3.2C and 3.2D) or that the processes controlling these parameters are evenly distributed.

Specific conductance has a strong positive relationship with chloride for all freshwater samples ($R^2 = 0.98$; Figure 3.5), indicating that mixing with saline water controls the ionic strength of the freshwater lens compared to carbonate diagenetic reactions. However, ratios of Ca^{2+}, HCO_3^-, Sr^{2+} and Mg^{2+} with chloride are higher than that predicted from mixing with seawater, and increase with decreasing chloride concentration (Figure 3.6), demonstrating that the main source of these ions is derived from the freshwater system. The highest ratios were from vadose samples, indicating significant dissolution in this zone. The decrease in the Ca/Cl ratio near the coast (Figure 3.7) may be due to calcite precipitation in addition to seawater dilution, while relatively high Ca/Cl ratios at sulfidic sites may be due to acidity produced by the re-oxidation of reduced sulfur species (see below).

Run-off water entering the vadose zone is undersaturated with respect to both aragonite and calcite (Table 3.8), with a Ca_{XS} of +0.44 ± 0.11 mM (n=4). Drip samples (having percolated through 3-6 m of the vadose zone) are enriched in calcium, with a mean Ca_{XS} of +2.52 ± 0.33 mM (n=7) (equivalent to a mean of +2.13 mM when degassing is back-calculated). When compared to the mean Ca_{XS} of all freshwater lens samples from the eastern Yucatan Peninsula of +2.19 ± 0.55 mM, this indicates that the bulk of $CaCO_3$ dissolution in the freshwater system occurs in the vadose zone rather than the underlying freshwater lens, and that $CaCO_3$ precipitation may take place in the lens through degassing, mixing or production of alkalinity by sulfate reduction (see below).

The mean Ca_{XS} of all freshwater lens samples from the eastern Yucatan Peninsula is +2.19 ± 0.55 mM (n=77), and mean Mg_{XS} is +0.73 ± 0.37 mM, indicating substantial $CaCO_3$ and/or HMC dissolution. The Mg_{XS}:Ca_{XS} ratios at all non-degassed freshwater lens sites indicate the dominant diagenetic processes are HMC dissolution followed by the precipitation of LMC (Figure 3.13). The mean saturation index of non-degassed lens waters approaches equilibrium with respect to calcite and is undersaturated with respect to aragonite and disordered dolomite (Table 3.8). Furthermore, petrographic analysis of wall-rock samples from below the water table at Ak Kimin (a coastal site) showed both an absence of HMC and the presence of aragonite to a maximum depth of 18.4 m water depth (Goodwin, 2002). No dolomite was found in any rock sample in contact with lens water or in the vadose zone. In addition, a positive relationship between SI-C and phosphate

concentrations (Figure 3.18), suggests that phosphate may be inhibiting calcite dissolution in the freshwater lens.

The majority of non-degassed lens waters are enriched in pCO_2 relative to soil air (Figure 3.11), indicating an *in situ* production of CO_2, likely from the bacterial oxidation of organic matter. This is supported by relationships between increases in Sr_{XS} and increases in nitrate, pCO_2 and decreases in dissolved oxygen and pH (Figure 3.15) indicating that the production of carbonic acid during the heterotrophic breakdown of organic matter leads to the dissolution of strontium-containing aragonite. Concurrent or subsequent calcite precipitation could explain why these relationships occur with Sr_{XS} and not Ca_{XS}. In addition, there is a strong negative relationship between nitrate and dissolved oxygen (Figure 3.16), suggesting that nitrification may also be an important process in the freshwater lens.

The Ca_{XS} of lower lens non-degassed waters is, on average, 0.29 mM higher than degassed upper lens waters, suggesting either carbonate dissolution in the lower lens or precipitation of $CaCO_3$ in the upper lens. The latter appears likely at non-sulfidic sites as these have a higher pCO_2 than expected for a given Ca_{XS} (Figure 3.12), indicating calcite precipitation, evidenced at some sites by the presence of calcite rafts. However, sites with evidence for sulfate reduction have a positive relationship ($P<0.05$) between Ca_{XS} and pCO_2. Most of these sulfidic sites show little or no significant SO_4^{2-} depletion indicating that most sulfide is rapidly recycled to sulfate by sulfur oxidizing bacteria. The acidity produced by this re-oxidation, if spatially separated from the alkalinity produced by sulfate reducing bacteria, may be responsible for the dissolution of carbonate minerals and elevated Ca_{XS} values (Figure 3.12).

Sites located within 200 m of the Caribbean coast have higher Ca_{XS} ($P<0.01$) and Mg_{XS} ($P<0.001$) concentrations compared to inland sites, probably due to the more thermodynamically unstable nature of the younger carbonate sediments near the coast, with a higher proportion of HMC and aragonite (Ford, 1985).

Bacteria were present in all freshwater samples tested (1.70×10^4 to 3.26×10^5 cells/ml), with a minimum of 2300 cell/ml of viable heterotrophic bacteria (comprising a minimum of 1-48% of the total bacteria present). Viable Fe(III)-reducing (Fe-R), sulfate reducing

bacteria (SRB) and thiosulfate oxidizing bacteria (SOX) were also present in all samples tested, with sulfate reducers more abundant than SOX in all samples. The numbers of Fe-R were, in all but one sample, greater than SRBs, indicating that these are two different physiological groups. The greatest numbers of sulfate reducing bacteria (> 2300 cells/ml) were associated with the greatest concentration of sulfide (Table 3.13), indicating that despite the presence of oxygen (Table 3.1), active bacterial sulfate reduction was taking place in anoxic microenvironments within the freshwater lens.

Modeling the geochemical evolution of run-off waters through the vadose zone to produce the geochemistry of drip waters (back-calculated to remove the effects of degassing) indicates that at least 93% of recharge water enters the lens by diffuse rather than rapid percolation. The residence time of these percolating waters is probably sufficient to allow equilibration with both calcite and the relatively high ground air pCO_2 of 1.18% produced by the respiration of microorganisms and plant roots. An evapotranspiration rate of 70% combined with oxidation of 0.81 mM DOC in the freshwater lens resulted in correct predictions of the actual chemistry in drip samples (after run-off, evapotranspiration and percolation through the vadose zone) and freshwater lens (after oxidation of organic matter).

The Ca_{XS} values of the vadose zone and freshwater lens calculated from the modeling were combined with recharge rates to estimate rates of $CaCO_3$ (high magnesium calcite and aragonite) dissolution. This demonstrated that the combined total freshwater zone dissolution rate was 37.6 metric tons of calcite removed/km^2/year for a 480 km^2 area of the eastern Yucatan Peninsula. 29.5% of this dissolution takes place at the bedrock surface, 61% in the vadose zone, and just 9.5 % occurs in the freshwater lens (Table 3.14). The combined dissolution rate is geomorphologically extremely significant, capable of completely dissolving a 1 km^2 and 1 m thick block of limestone in 10,000 years. These results are very similar to the findings made by Hanshaw and Back (1980).

6.2 The Fresh-Salt Water Mixing Zone

The mixing zone geochemistry of Mayan Blue showed that concentrations of calcium, magnesium, sulfate and strontium could be explained almost entirely by chemical mixing

between cooler fresh (or brackish) lens water and a warmer saline groundwater. Temperature and conductivity profiling confirmed that exchange between the two water types is occurring, and that profiles could be divided into 2 types: stepped and non-stepped. It is likely (based on multiple profiles taken over various seasons at a particular site) that steps are mainly controlled by flow velocity and recharge. Stepped profiles occur when flow velocity is relatively low (dry season) and non-stepped profiles occur when flow velocity is high (wet season).

Based on conductivity, the stepped mixing zone profiles were split into five sections. In order of increasing depth, these are: the upper mixing zone (UMZ), salinity step (SS), middle mixing zone (MMZ), lower mixing zone (LMZ) and basal mixing zone (BMZ) (Figure 4.5). The UMZ lies beneath the freshwater lens and the BMZ is located above the zone of saline groundwater. Dye tracing showed that the UMZ likely flows coastward with the freshwater lens, while the lower parts of the mixing zone may flow mostly landward with the underlying saline zone (although some back-and-forth shuttling may occur). The results of the tracer tests may also suggest that the water within the SS is relatively stagnant.

Saturation indices and pCO_2 were calculated using the geochemical modeling program PHREEQC (Parkhurst, 1995) and these results were compared to predicted values (Section 4.4.5). This work demonstrated that there are two distinct regions where pCO_2 is significantly higher and where SI (of calcite and aragonite) is significantly lower compared to that predicted from fresh-salt water mixing:

a) Lower part of the UMZ, SS, and top part of the MMZ interface, with greatest undersaturation occurring at the SS/MMZ interface
b) LMZ/BMZ interface

All mixing zone waters had significant populations of viable heterotrophic bacteria (> 2300 cells/ml), however the greatest bacterial activity (as determined by the proportion of dividing cells) were within these two high pCO_2 regions. Furthermore, the lowest dissolved oxygen content (indicating the greatest oxygen consumption) was at the SS/MMZ interface (Figure 4.8) and may indicate where heterotrophic bacterial activity was greatest. It is therefore likely that heterotrophic bacteria were responsible for maintaining the

undersaturation of carbonate minerals in these zones. This is supported by calcite pill dissolution rates, which were also greatest in these zones (Figures 4.22 and 4.24). Bacteria (and/or organic matter) may concentrate in these two zones due to sharp density differences, as both regions correspond to where an area of high conductivity gradient meets and area with a low conductivity gradient (Figure 4.6.).

Despite there being two peaks in DOC (Figure 4.28) similar to that observed for most other analyses mentioned so far, there is a not a consistent coincidence between the proportion of dividing cells and DOC (see below). However, without data on DOC production and consumption rates, DOC concentration data can be difficult to interpret. The upper peak in DOC (UMZ) is coincident with a decrease in dissolved oxygen and decrease in pH, and lies above the upper maximum in the proportion of dividing cells, suggesting the consumption of DOC at the SS/MMZ interface. However, the lower peak in the proportion of dividing cells (LMZ to LMZ/BMZ interface) corresponds with the lower peak in DOC, suggesting that organic matter stimulates bacterial activity there. This, in turn, may indicate that the lower parts of the mixing zone are relatively electron donor poor, hence limiting where bacterial activity can occur. This relationship between DOC and % dividing cells may also reflect the different sources of organic matter within the different water types; more refractory terrigenous organic matter in the freshwater zone, and more available marine organic matter in the saline zone (e.g. Rullkotter, 2000).

The relatively low oxygen concentration of the SS/MMZ interface suggests suboxic conditions and the location of a redox boundary. $\delta^{34}S\text{-}SO_4$ data suggests that sulfate reduction was active below the SS/MMZ interface, presumably in anoxic microenvironments. In addition, the lack of orange staining on the wall-rock between the SS/MMZ interface and the saline zone, combined with a peak in phosphate concentration at the SS/MMZ interface, suggests that iron oxides have been reduced in this region. This may be indirect by reaction with sulfide produced from bacterial sulfate reduction, or directly by bacterial iron reduction (viable iron(III)-reducing bacteria are present throughout the mixing zone, Figure 4.25C).

A peak of acid-producing sulfur-oxidising bacteria (SOX) occurs near the SS/MMZ interface (Figure 4.25A), corresponding to a minimum in dissolved oxygen. Acidic SOX are probably autotrophic and will occur where they can gain greatest energy for autotrophic growth (i.e. at the steepest redox gradients). Their presence also suggests the

location of a redox boundary. By producing H_2SO_4, SOX will contribute to increases in acidity observed at the SS/MMZ interface (i.e. the lowest pH of the system, pH = ~6.8), and therefore SOX have an important role in maintaining undersaturation there. Some of the variability observed in the XS, SI, and pCO_2 data in the top part of the MMZ (Figures 4.13 - 4.17) may be due to the balance between oxic/suboxic processes controlling water chemistry.

In addition, iron-oxidising bacteria, indicated by orange-staining on the wall-rock, coincide with rock that appears the most weathered (Figure 4.21). This suggests iron-oxidising bacteria may contribute to carbonate dissolution at the water-rock interface above the SS/MMZ interface and within the saline zone (Figure 4.21).

Bacterial activity was lowest in the bottom part of the MMZ to the upper part of the LMZ, which corresponds to regions of negative ΔpCO_2 and positive ΔSI (both of which are explained by calcite dissolution), suggesting that waters without a highly active bacterial population will be driven towards equilibrium and that only waters with an active bacterial population can maintain undersaturation. However, actual equilibrium (with respect to SI-C) is not achieved and supersaturation occurred only in one sample. In this region, SI-DD was positive, suggesting the thermodynamic potential for Dorag dolomitisation. However, no significant amounts of dolomite were found in the wall rock (evidenced by XRD and thin section analyses), although wall rock in contact with mixing zone waters did have slightly elevated magnesium concentrations compared to the rock associated with fresh and saline groundwaters (Section 4.4.7). As mentioned earlier, phosphate may play a role in inhibiting carbonate mineral precipitation/dissolution reactions and may help to explain why dolomite is not precipitating, despite the thermodynamic potential for it. In addition, Ca_{XS} and Mg_{XS} had a positive relationship and the ratio of Ca_{XS}:Mg_{XS} is 1:3, implying that dolomite (rather than Mg-calcite) dissolution as the likely source. All dolomite pills lost weight in the dissolution experiment (Section 4.4.7), suggesting the potential for dolomite dissolution.

Oxygen consumption rates in the water column of Mayan Blue ranged from 9 to 51 μM O_2/L/day. Oxygen consumption by heterotrophic bacteria leads to the production of carbonic acid, and each mole of carbonic acid is capable of dissolving one mole of calcium carbonate. Therefore the mixing zone oxygen consumption rates indicate an enhanced

calcium carbonate dissolution rate due to heterotrophic bacterial respiration of 0.33 – 1.86 g $CaCO_3$/L/a of water. Oxygen consumption was also increased by six times by the addition of host rock, possibly due to associated increases in organic carbon, and was doubled by the addition of thiosulfate. The positive effect of thiosulfate on oxygen consumption rates suggests that reduced sulfur species are actively used by bacterial populations *in situ*.

The calculation of rates of $CaCO_3$ dissolution in the mixing zone is made difficult by lack of suitable flow volume data for the underlying shallow saline water. However, the mean Ca_{XS} of the mixing zone of +0.11 mM, with only two data points significantly different to zero, suggests that despite the thermodynamic potential for the dissolution of $CaCO_3$ by mixing corrosion, actual dissolution rates in the eastern Yucatan Peninsula may be less important in porosity generation than previously suggested (Hanshaw and Back, 1980). This may be due to inhibition by phosphate concentrations.

6.3 Diagenesis in the Zone of Saline Groundwaters

This is the first study to carry out detailed research into the geochemistry of the relatively inaccessible saline zones of the Yucatan Peninsula. Plots of Ca_{XS} against Mg_{XS} (Figure 5.49) delineate two sub-zones within the saline zone: a shallow' saline zone at depth < 40 m water depth, and a deeper saline zone at > 40 m.

6.3.1 Shallow Saline Zone (< 40m water depth)

A semi-quantitative dye trace in Mayan Blue confirmed observations in Ponderosa (Beddows, 2004) that shallow saline zone water shuttles back and forth along a SE-NW trajectory. However, some vertical movement upwards towards the mixing zone was also noted. This shuttling probably makes the chemistry of shallow saline groundwaters variable, as the waters may be derived from either an upstream or downstream site at a given sampling time.

Diagenetic processes within the shallow saline zone are greatly influenced by the activity of microorganisms. A positive relationship between the proportion of bacterial cells undergoing cell division with pCO_2 (r = 0.76; Figure 5.69) combined with the inverse relationship with the saturation index of calcite (r = 0.89; Figure 5.70) suggests that without an active bacterial population to increase pCO_2 and lower pH, the shallow saline groundwaters would not maintain calcite undersaturation. These relationships do not exist in the deep saline groundwaters (see below).

The importance of microbial activity in shallow saline zone diagenesis is further supported by the relatively fast oxygen consumption rates (and consequent carbon dioxide production rates) measured within shallow saline waters at Mayan Blue; ~29 times faster than the rate published for the open ocean. This is initially surprising, given that total numbers of bacteria in the saline groundwaters ($5.76 \pm 6.95 \times 10^4$; combined shallow and deep saline zone data) are an order of magnitude lower than typical open ocean water (5×10^5 to 3×10^6 cells/ml; Hobbie et al., 1977; Porter and Feig, 1980). However, the saline groundwaters contain a far higher proportion of viable bacteria (a minimum of 82 ± 66% of total counts are viable heterotrophic bacteria) than is usually reported for natural environments (e.g. < 1% viable bacteria; Amann et al., 1995), indicative of a healthy and potentially active bacterial population.

There were two orders of magnitude more bacteria in the sediment sample analysed compared to all groundwater samples. Lack of aerobic heterotrophic growth (and large numbers of anaerobic heterotrophs) in the sediment indicates that it is anoxic and capable of supporting anaerobic respiration/fermentation. Large numbers of iron reducing bacteria indicate that iron reduction (in addition to sulfate reduction) may be an important metabolism in the cave sediment environments.

Dedolomitisation may be taking place at some shallow saline sites, as indicated by low Ca_{XS} values and high Mg_{XS} values. Replacement dolomitisation is suggested in other shallow saline groundwaters by depleted Mg_{XS} and higher Ca_X (Figure 5.53), perhaps in association with localised re-oxidation of reduced sulfur species.

Five shallow saline groundwater samples have almost 1:1 relationship between Ca_{XS} and SO_{4XS} ($r^2 = 0.99$; Figure 5.60), suggesting the dissolution of $CaSO_4$. Four of these samples

also have magnesium depletions similar in magnitude to those observed in the deep saline zone (see below). As there are no known shallow gypsum/anhydrite deposits in the region (no gypsum or anhydrite present above 100 m beneath the surface; Socki, 1984), these sites may therefore represent the location of deep saline groundwater upwelling through higher porosity rock (see below).

6.3.2 Deep Saline Zone (> 40m water depth)

Dissolved oxygen concentrations within the deep saline zone are significantly reduced compared to shallower cave sites, and may be evidence for the circulation of a deeper saline groundwater body. In addition, low dissolved oxygen concentrations were observed in sulfide layers, and this is likely due to organic matter oxidation, resulting in the consumption of oxygen. Despite the presence of sulfide, all waters had positive SO_{4XS} values, due to evaporite dissolution (see below). The presence of methane (0.23 to 1.03 mM CH_4) in samples associated with sulfide layers is indicative of highly reduced mircoenvironments allowing bacterial methanogenesis to take place.

Strong positive relationships between SO_{4XS}, Ca_{XS} and Sr_{XS} (Figures 5.54 and 5.55) indicate that $CaSO_4$ is dissolving and these ions also increase linearly with depth (Figure 5.43). A possible source of $CaSO_4$ is anhydrite clasts within brecciated deposits at ~ 110-160 m below the surface (Figure 1.3; Socki, 1985; Ward et al., 1995). $CaSO_4$ dissolution as the source of SO_{4XS} is supported by the $\delta^{34}S$ values of the sulfate (Figure 5.66), although some sulfate reduction and re-oxidation of reduced sulfur species is occurring in localized areas (predominantly associated with build-ups of surface-derived organic matter). At some sites, bacterial sulfate reduction may be responsible for decreasing SO_{4XS} and 'masking' $CaSO_4$ dissolution. Sulfate-reducing and sulfur-oxidising bacteria may play a role in localized dolomitisation (due to the increased alkalinity from sulfate reduction) and/or carbonate dissolution (from increased acidity). However, samples from the sulfide layer of The Pit show not only an increase in SI-DD, but also SI-C, suggesting calcite precipitation may be favoured over (or as well as) dolomite precipitation.

Decreases in magnesium and increases in calcium (above that calculated to be due to $CaSO_4$ dissolution; Figure 5.51) suggest that replacement dolomitisation is also taking place. This is supported by petrographic evidence: dolomite was present in the saline

groundwater region of a coastal site (Ak Kimin), and the amount of dolomite found in the wall rock increased with depth. In addition, the amount of dolomite was higher in regions of interconnected porosity (Goodwin, 2002), reinforcing the importance of saline water composition and circulation.

In contrast to the shallow saline groundwaters, there is no relationship between % dividing cells and pCO_2. There is, however, a relationship between dissolved organic carbon (DOC) and the proportion of dividing cells (again in contrast to the shallow saline groundwaters where there is no such relationship). This suggests that the deeper saline zone is relatively electron donor limited.

As mentioned above, the Ca_{XS} and SO_{4XS} and (in four cases) Mg_{XS} of five shallow saline groundwaters have a striking similarity to that of the deep saline zone (Figure 5.61). Two of these samples are from a site connected to the deeper saline zone at The Pit. The other three (Sistemas Aktun Ha, Tortuga and Vaca Ha) are located at ~8-9 km inland from the east coast, and represent the inland limit of known diver-sized cave passage along the Caribbean coast of the Yucatan Peninsula. The geochemistry is therefore suggestive of the thermal upwelling of deeper $CaSO_4$-rich saline water at these sites.

Although flow within the deeper saline groundwater of the Yucatan Peninsula is uni-directional (SE-NW), there are semi-diurnal tidal signals, with previously unexplained maximum inflow rates at low tide and minimum inflow rates (recorded at the Pit) at high tide (Beddows, 2004). This flow data, combined with the geochemically anomalous shallow sites described above (Figure 5.60) suggests that the saline groundwater becomes geothermal heated (as evidenced by temperature depth profiles) and rises towards the surface. Upward flow will be aided in regions of extensive cavernous porosity (limited to 9 km inland). At low tide, the outflow of freshwater causes a compensatory inflow of saline water at depth, and may also entrain some of the upwelling saline water. This entrainment is supported by an increase in freshwater lens conductivity during low tide (Beddows, 2004).

6.4 Future Work

Hydrology

Better characterization of the flow regime within the Yucatan Peninsula is a priority. A knowledge of the volume of flow within the mixing zone and saline groundwaters would enable the calculation of diagenetic rates within these environments. In the mixing zone, this would be aided by the injection of dyes (and in particular the salinity step) to determine the flow regime.

The installation of long term flow meters in the region of Vaca Ha/Tortuga/Carwash would help confirm the coupled freshwater:deep saline flow regime suggested in Figure 5.62.

Finally, future work should also be directed towards determining the extent of saline groundwater flow towards the Gulf of Mexico – i.e. is it cross peninsula, and can outflows be found on the west coast?

Geochemistry

Using samples collected during the present study, additional strontium analyses (particularly in the freshwater lens) would allow the determination of the amount and rate of aragonite dissolution. In addition, further detailed petrographic work on wall-rock samples would help elucidate the type and extent of dolomitisation.

$\delta^{34}S$ analysis of anhydrite samples from the breccia underlying the region would help constrain the source of SO_{4XS} in deep saline groundwaters.

Geomicrobiology

Field and laboratory experiments could be used to specifically investigate the direct role of physiologically different bacteria (sulfate reducers/oxidisers, iron reducers/oxidisers, heterotrophs) on carbonate diagenesis ($CaCO_3$, dissolution, dolomitisation).

Reference List

Aahron, P., Socki, R.A. and Chan, L. 1987. Dolomitization of atolls by sea water convection flow: test of a hypothesis at Niue, South Pacific. Journal of Geology 95: 187-203

Adams, J.E. and Rhodes, M.L. 1960. Dolomitisation by seepage refluxion. Bulletin of the American Association of Petroleum Geologists 44: 1912-1920

Amann, R.I., Ludwig, W. and Schleifer, K.H. 1995. Phylogenetic identification and in situ detection of individual microbial cells without cultivation. Microbial Review 59: 143-169

APHA (American Public Health Association), 1969. Standard methods for the examination of water and wastwater, including bottom sediments and sludge. American Public Health Association, Washington D.C., p. 604-609

Back, W. 1985a. Historical development of water use and management. In: W.C. Ward, A.E. Weidie and W. Back (Eds.), Geology and Hydrogeology of the Yucatan and Quaternary Geology of Northeastern Yucatan Peninsula. Pp. 120-124. New Orleans Geological Society Publications, New Orleans.

Back, W., Hanshaw,, B.B., Pyle, T.E., Plummer, L.N. and Weide, A.E. 1979. Geochemical significance of groundwater discharge and carbonate solution to the formation of Caleta Xel Ha, Quinta Roo, Mexico. Water Resources Research 15: 1521-1535

Back, W., Hanshaw, B.B., Plummer, L.N., Rahn, T.H., Rightmire, C.T. and Rubin, M. 1983. Process and rate of dolomitization: Mass transfer and ^{14}C dating in a regional carbonate aquifer. Geological Society of America Bulletin 94: 1415-1429

Back, W., Hanshaw, B.B., Herman J.S. and Van Driel, J.N. 1986. Differential dissolution of a Pleistocene reef in the groundwater mixing zone of Coastal Yucatan, Mexico. Geology 14: 137-140

Badiozamani, K.1973. The Dorag dolomitization model – application to the middle Ordovician of Winconsin. Journal of Sedimentary Petrology 43(4): 965-984

Baker, P.A. and Kastner, M. 1981. Constraints on the formation of sedimentary dolomite. Science 213: 214-216

Bathurst, R.G.C. 1975. Carbonate Sediments and Their Diagenesis. Elsevier Scientific Publishing Co., Amsterdam, 658 p.

Bear, J. 1972. Dynamics of fluids in porous media. Elsevier, New York, 764 p.

Beddows, P.A. 1999. Conduit hydrogeology of a tropical coastal carbonate aquifer: Caribbean coast of the Yucatan Peninsula. MSc Thesis, McMaster University, Canada. 162 p.

Beddows, P.A. 2004. Groundwater Hydrology of a Coastal Conduit Carbonate Aquifer: Caribbean Coast of the Yucatan Peninsula, Mexico. PhD thesis, School of Geographical Sciences, University of Bristol. 303 p.

Beddows, P.A., Smart, P.L., Whitaker, F.F. and Smith, S.L. 2002. Density stratified groundwater circulation on the Caribbean coast of the Yucatan Peninsula, Mexico. In: J.B. Martin, C.M. Wicks and I.D. Sasowsky (Eds.), Hydrogeology and Biology of Post-Paleozoic Carbonate Aquifers, Special Publication 7. pp. 129-134. Karst Waters Institute.

Bender, M.L. and Heggie, D.T. 1984. Fate of organic carbon reaching the deep sea floor: a status report. Geochimica et Cosmochimica Acta 48: 977-986

Berner, R.A. 1970. Sedimentary pyrite formation. American Journal of Science 268: 1-23

Berner, R.A. 1974. The role of magnesium in the crystal growth of calcite and aragonite from seawater. Geochimica et Cosmochimica Acta 39: 489-504

Berner, R.A., Westrich, J.T., Graber, J., Smith, J. and Martens, C.S. 1978. Inhibition of aragonite precipitation from supersaturated seawater: a laboratory and field study. American Journal of Science 278: 816-837

Boesen, C. and Postma, D. 1988. Pyrite formation in anoxic environments of the Baltic. American Journal of Science 288: 575-603

Bogli , A. 1965. The role of corrosion by mixed water in cave forming. In: Stekl O. (Ed.) Problems of Speleological Research Czechoslovak Academy of Science, Prague p. 125-131

Bottrell, S., Smart, P.L., Whitaker, F.F. and Raiswell, R. 1991. Geochemistry and isotope systematics of sulphur in the mixing zone of Bahamian blue holes. Applied Geochemistry 6: 97-103

Brook, G.A., Folkoft, M.E. and Box, E.O. 1983. A world model of soil carbon dioxide. Earth Surface Processes and Landforms 8: 79-88

Brown, E., Skovgstad, M.W. and Fishman, M.J. 1970. Methods of collection and analysis of water samples for dissolutional minerals and gasses. Techniques for Water Resource Investigation of United States Geological Survey, Book 5, Chapter A1, 160 p.

Budd, D.A. 1984. Freshwater diagenesis of Holocene ooid sands, Schooner Cays, Bahamas, M.A. thesis, University of Texas, Austin. 491 p.

Budd, D.A. 1988. Aragonite-to-calcite transformation during fresh-water diagenesis of carbonates: insights from pore-water chemistry. Geological Society of America Bulletin 100: 1260-1270

Budd, D.A. 1997. A Cenozoic dolomites of carbonate islands: Their attributes and origin. Earth Science Reviews 42(1-2): 1-47

Canfield, D.E. 1989. Reactive iron in marine sediments. Geochimica et Cosmochimica Acta. 53: 619-632

Canfield, D.E., Raiswell, R., Bottrell, S.H. 1992. The reactivity of sedimentary iron minerals towards sulfide. American Journal of Science. 292: 659-683.

Canfield, D.E. 2001. Isotope fractionation by natural populations of sulfate-reducing bacteria. Geochimica et Cosmochimica Acta 65(7): 1117-1124

Cant, R.V. and Weech,P.S. 1986. A review of the factors affecting the development of Ghyben-Hertzberg lenses in the Bahamas, Journal of Hydrology 84: 333-343

Chillingar, G.V., Zenger, D.H., Bissel, H.J. and Wolf, K.H. 1979. Dolomites and dolomitisation. In: Karsen, G. and Chillingar, G.V. (Eds.), Diagenesis in Sediments and Sedimentary Rocks, Elsevier, Amsterdam, p. 423-536

Cline, J.D. 1969. Spectrophotometric determination of hydrogen sulfide in natural waters. Limnology and Oceanography 14(3): 454-458

Cloud, PE. 1962. The behviour of calcium carbonate in seawater. Geochimica et Cosmochimica Acta 26:867.

Coleman, M.L., Hedrick, D.B., Lovley, D.R., White, D.C. and Pye, K. 1993. Reduction of Fe(III) in sediments by sulphate-reducing bacteria. Nature 361:436-438

Cooper, H.H. 1959. A hypothesis concerning the dynamic balance of fresh water and salt water in a coastal aquifer. Journal of Geophysical Research 64: 461-467

Cooper, H., Kohout, F., Henry, H. and Glover, R. 1964. Sea Water in Coastal Aquifers. Geologic Water-Supply Paper 1613-C, 84 pp. US Government Printing Office.

Coke, J., Perry, E.C. and Long, A. 1991. Charcoal from a probable fire pit on the Yucatan Peninsula, Mexico: Another point on the glacio-eustatic sea level curve. Nature 353: 25-25

Craig, H., 1957. Isotopic standards for carbon and oxygen and correction factors for mass spectrometric analysis of carbon dioxide. Geochimica et Cosmochimica Acta, v. 12, p. 133-149

De Jong, E. and Schappert,, H.J.V. 1972. Calculation of soil respiration and activity from CO_2 profiles in the soil. Soil Science 113: 328-333

Doehring, D.O. and Butler, J.H. 1974. Hydrogeologic constraints on Yucatan's development. Science 186(416): 591-595

Drake, J.J. 1980. The effect of soil activity on the chemistry of carbonate groundwater. Water Resources Research 16(2): 381-386

Eberhard, C., Wirsen, C.O., Jannasch, H.W. 1995. Oxidation of ploymetallic sulfides by chemolithoautotrophic bacteria from deep-sea hydrothermal vents. Geomicrobiology Journal 13: 145-164

Esteban, M. and Klappa, C.F. 1983. Subaerial exposure. American Association of Petroleum Geologists Memoir 33: 1-54

Fairbanks, R.G. 1989. A 17,000-year glacio-eustatic sea level record: Influence of glacial melting rates on the Younger Dryas event and deep-ocean circulation. Nature 342: 637-642

Faure, G.1986. Principles of Isotope Geology. Wiley and Sons, New York, 589 p.

Faure, G. 1998. Principles and Applications of Geochemistry. Prentice-Hall, New Jersey, 600 p.

Fedwick, S.L. (Ed.) 1996. Managed mosaic: Ancient Maya Agriculture and Resource Use. Salt Lake City, University of Utak Press, 424 p.

Fetter, C.W. 1988. Applied Hydrogeology. Columbus, Ohio. Merrill Publishing Company, 592 p.

Ford, B.H. 1985. Geochemistry of Water in a Coastal Mixing Zone, Northeastern Yucatan Peninsula. MSc thesis, Faculty of the Graduate School, University of New Orleans.

Ford, D.C. and Williams,P.W. 1989. Karst Geomorphology and Hydrology, London, Chapman and Hall, 601 p.

Ford, B.H., Schuffert, J.D., Stoessell, R.K. and Ward, W.C. 1985. Fluid geochemistry in a coastal mixing zone on the Yucatan Peninsula. Geological Society of America Abstracts with Programs 17: 598-585

Frantz, J.D. 1971. Bermudian ground and cave waters. Bermuda Biological Station for Research Special Publication 7: 47-55

Froelich, P.N., Klinkhammer, G.P., Bender, M.L., Luedtke, N.A., Heath, G.R., Cullen, D., Dauphin, P., Hammond, D., Hartman, B. and Maynard, V. 1979. Early oxidation of organic matter in pelagic sediments of the eastern equatorial Atlantic: suboxic diagenesis. Geochinica et Cosmochimica Acta 43: 1075-1090

Froelich, P.N., Bender, M.L., Luedtke, N.A., Heath, G.R. and DeVries, T. 1982. The marine phosphorus cycle. American Journal of Science 282: 474-511

Froelich, PN. 1988. Kinetic control of dissolved phosphate in natural rivers and estuaries. Limnology and Oceanography. 33 (4, part 2): 649-668.

Fry, F.C. 1988. Determination of biomass. In: Austin, B. (Ed), Methods in Aquatic Bacteriology. Chichester (Wiley), p. 27-72

Fry, B. Cox, J. Gest, H. and Hayes, J.M. 1986. Discrimination between ^{34}S and ^{32}S during bacterial metabolism of inorganic sulfur compounds. Journal of Bacteriology 165: 328-330

Garrels, R.M. and Thompson, M.E. 1962. A chemical model for sea water at 25oC and atmospheric total pressure. American Journal of Science 260: 57-60

Garrels, R.M. and Makenzie, F.T. 1967. Origin of the chemical composition of some springs and lakes. In: Equilibrium Concepts in Natural Water Systems, American Chemical Society Advances in Chemistry 67 pp. 222-242

Garrels, R.M. and Wollast, R. 1978. Discussion of equilibrium criteria for 2-component solids reacting with fixed composition in an aqueous phase – example, the magnesian calcites. American Journal of Science 278: 1469-1474

Garske, E.E. and Schock, M.R. 1986. An inexpensive flow-through cell and measurement system for monitoring selected geochemical parameters in groundwater. Groundwater Monitoring Review, Summer 1986: 79-84

Gebelien, C.D. 1977. Mixing-zone dolomitisation of Holocene tidal flat sediments, South West Andros Island, Bahamas (Abs.). Bulletin of the American Association of Petroleum Geologists 61: 787-788

Gill, R.B. 2000. The Great Maya Droughts: Water, Life and Death. Albuquerque, University of New Mexico Press, 464 p.

Gmitro, D.A. 1986. The Interactions of Waters with Carbonate Rock in Yucatan, Mexico. MSC Thesis. Department of Geology, Northern Illinois University, 111 p.

Goodwin, A. 2002. The Origins of Secondary Dolomites: East Coast, Yucatan Peninsula, Mexico. Undergraduate Thesis, Dept. of Earth Sciences, University of Bristol.

Goudie, A.S. 1983. Calcrete. In: Goudie, A.S. and Pye, K. (Eds). Chemical Sediments and Geomorphology, Academic Press, London. p. 93-132

Habicht, K.S. and Canfield, D.E. 1997. Sulfur isotope fractionation during bacterial sulphate reduction in organic-rich sediments. Geochimica et Cosmochimica Acta 24: 5351-5361

Haese, R.R. 2000. The Reactivity of Iron. In: Schultz, H.D. and Zabel, M. (Eds), Marine Geochemistry, Springer-Verlag, Berlin, p. 233-262

Halas, S., Shakur, A. and Krouse, H.R. 1982. A modified method of SO_2 extraction from sulphates for isotopic analysis using $NaPO_3$. Isotopenpraxis 18: 11-13

Halley, R.B. and Harris, P.M. 1979. Freshwater cementation of a 1000-year old oolite. Journal of Sedimentary Petrology 49: 969-988

Hanshaw, B.B. and Back, W. 1980. Chemical mass-wasting of the northern Yucatan Peninsula by groundwater dissolution. Geology 8: 222-224

Hanshaw, B.B., Back, W. and Deike, R. 1971. A geochemical hypothesis for dolomitisation by groundwater. Economic Geology 66: 710-724

Harrison, R.S. 1975. Porosity in Pleistocene grainstones from Barbados: some preliminary observations. Bulletin of Canadian Petroleum Geologists 23: 383-392

Helgeson, H.C. 1968. Evaluation of irreversible reactions in geochemical processes involving minerals and aqueous solutions: I. Thermodynamic relations. Geochimica et Cosmochimica Acta 34: 569-592

Helgeson, H.C., Brown, T.H., Nigrina, A. and Jones, T.A. 1970. Calculation of mass transfer in geochemical processes involving aqueous solutions. Geochimica et Cosmochimica Acta 34: 569-592

Helgeson, H.C., Kirkham, D.H. and Flowers, G.C. 1981. Theoretical prediction of the thermodynamic behavior of aqueous-electrolytes at high-pressures and temperatures. 4. Calculation of activity-coefficients, osmotic coefficients, and apparent molal and standard and relative partial molal properties to 600 degrees C. American Journal of Science 281(10): 1249-1516

Horne, A.J. and Goldman, C.R. 1994. Limnology, Second Edition. McGraw-Hill, Inc., New York. 576 p.

Hurley, M.A. and Roscoe, M.E. 1982. Automated statistical analysis of microbial enumeration by dilution series. Journal of Applied Bacteriology 55: 159-164

James, N.P. and Choquette,P.W. 1984. Diagenesis 9-Limestones, the meteoric diagenetic environment. Geoscience Canada 11: 161-194

Jensen, H.S., Mortensen, P.B., Andersen, F.O., Rasmussen, E. and Jensen, A. 1995. Phosphorus cycling in a coastal marine sediment, Aarhus Bay, Denmark. Limnology and Oceanography 40: 908-917

Karl, D.M. 1995. The ecology of free-living bacteria at deep-sea hydrothermal vents. In: Karl, D.M. (ed.). The Microbiology of Deep-Sea Hydrothermal Vents,. Springer-Verlag, New York.

Kemp, A.J. and Brown, C.J. 1990. Microwave digestion of carbonate rock samples for chemical analysis. Analyst 115: 1197-1199

Kohout, F.A., Henry, H.R. and Banks, J.E. 1977. Hydrogeology related to the geothermal conditions of the Floridan Plateau. In: Smith, D.I. and Griffin, G.M. (eds.), The Geothermal Nature of the Floridan Plateau, Special Publication No. 21 p. 1-40

Krom, M.D. and Berner, R.A. 1980. Adsorption of phosphate in anoxic marine sediments. Limnology and Oceanography 25: 797-806

Krom, M.D. and R.A. Berner. 1981. The diagenesis of phosphorus in a nearshore marine sediment. Geochimica et Cosmochimica Acta 45: 207-216.

Land, L.S. 1973. Holocene meteoric dolomitisation of the Pleistocene limestones, north Jamaica. Sedimentology 20: 411-424

Land, L.S. 1985. The origin of massive dolomite. Journal of Geological Education 33: 112-125

Landolt-Börnstein. 1969. Zahlenwerte und Funktionen. Transportphänomene I, Vol. 2, Part 5, Sect. A. Springer-Verlag, Heidelberg, Germany.

Langmuir, D. 1984. Physical and chemical characteristics of carbonate water. In *Guide to the hydrology of carbonate rocks*, P.E. Lamoreaux, M.Bm Wilson and B.A. Memeon, eds. Paris:UNESCO, pp. 60-105, 116-30.

Langmuir, D. 1997. Aqueous Environmental Geochemistry. Prentice-Hall, New Jersey, 600 p.

Lerman, A. 1979. *Geochemical Processes in Water and Sediment Environments.* Wiley Interscience. Toronto, Canada. 481 p.

Lesser, J.M. 1976. Estudio hidrogeologico y hidrogeoquimico de la peninsula de Yucatan. Proyecto Conacyt-NSF 704, Secretaria de Recursos Hidraulicos, Direccion de Geohidologia y Zonas Aridas, Mexico. 64 p. (Unpublished Technical report).

Lesser, J.M. and Weidie, A.E. 1988. Region 25, Yucatan Peninsula. In: W. Back, J.S. Rosenshein and P.R. Seaber (Eds.), Hydrogeology, pp. 237-242. Boulder, CO: Geological Society of America.

Likens, G.E., Bormann, F.H., Pierce, R.S., Eaton, J.S. and Johnson, N.M> 1977. Biogeochemistry of a forested ecosystem. Springer-Verlag, New York, 148 p.

Little, B.G., Buckley, D.K., Cant, R.V., Jefferiss, A., Stark, J. and Young, R.N. 1975. Land Resources of the Commonwealth of the Bahamas, Volume 5a Grand Bahama. Unpublished Report for the Ministry of Overseas Development, Surbiton, England, 87 p.

Lippmann, F. 1973. Sedimentary Carbonate Minerals. Springer-Verlag, New York, 228 p.

Longman, M.W. 1980. Carbonate diagenetic textures from near-surface diagenetic environments. Bulletin of the American Association of Petroleum Geologists 63: 461-487

Lopez Ramos, E. 1975. Geological summary of the Yucatan peninsula. In: A.E.M. Nairn and F.G. Stehli (Eds.), The Ocean Basins and Margins: The Gulf of Mexico and the Caribbean, pp. 257-282. Plenum Press, New York.

Lovley, D.R. and Philips, E.J.P. 1986. Organic matter mineralization with reduction of ferric iron in anaerobic sediments. Applied and Environmental Microbiology 51: 683-689

MacIntyre, I.G. 1977. Distribution of submarine cements in a modern Caribbean fringing reef, Galeta Point, Panama. Journal of Sedimentary Petrology 47: 503-516

Machel, H.G. and Mountjoy, E.W. 1986. Chemistry and environments of dolomitization – a reappraisal. Earth Science Reviews 23: 175-222

Madigan, M.T., Martinko, J.M. and Parker, J. 2000. Biology of Microorganisms, Ninth Edition. Prentice-Hall International, London. 991 p.

Marcella, L.M. 1994. Potential for Dolomitization Occurring in Sea-Water Salinity Fluids in the Northeastern Yucatan Peninsula. Unpublished MSc thesis, University of New Orleans.

Marin, L.E., Perry, E.C. and Villasuso, M. 1989. Effects of Hurricane Gilbert on the aquifer in northwest Yucatan, Mexico. International Geological Congress Proceedings, Washington D.C. (abstract).

Marin, L.E., Steinich, B., Pacheco, J. and Escolero, O.A. 2000. Hydrogeology of a contaminated sole-source karst aquifer, Merida, Yucatan, Mexico. Geofisica Internacional 39(4): 359-365

Mather, J.D.1975. Development of the groundwater resources of small limestone islands. Quarterly Journal of Engineering Geology 8: 141-150

Matthess, G. and Harvey, J.C. 1982. The Properties of Ground-Water. John Wiley and Sons, New York, 406 p.

Merino, M. and Otero, L. 1991. Atlas Ambiental Costero, Puerto Morelos – Quintana Roo. Ferrandiz SA, Mexico. OF 14640, 80 p.

Morse, J.W. and Mackenzie, F.T. 1990. Geochemistry of sedimentary carbonates. Developments in Sedimentology 48, Elsevier, Amsterdam, 707 p.

Morse, J.W., deKanel, J. and Harris, J. 1979. Dissolution kinetics of calcium carbonate in seawater: VII, The dissolution kinetics of synthetic aragonite and pteropod tests. American Journal of Science 279: 482-502

Mylroie, J.E. and Carew, J.L. 1995. Geology and karst geomorphology of San Salvador Island, Bahamas. Carbonates and Evaporites 10: 193-206

NOAA (National Ocean and Atmospheric Administration) 2002. National Climate data Center Archives. www.ncdc.noaa.gov/oa/ncdc.html (online database).

Nordstrom, D.K., Plummer, L.N., Wigley, T.M.L., Wolery, T.J., Ball, J.W., Jenne, E.A., Bassett, R.L., Crerar, D.A., Florence, T.M., Fritz, B., Hoffman, M., Holdren, G.R., Lafon, G.M., Mattigod, S.V., McDuff, R.E., Morel, F., Reddy, M.M., Sposito, G. and Thraikill, J. 1979. A comparison of computerised chemical models for equilibrium calculations in aqueous systems. In: Jenne, E.A. (Ed) Chemical Modding of Aqueous Systems, Speciation, Sorption, Solubility and Kinetics. American Chemical Society Series 93, p. 857-892

Parkes, R.J., Cragg, B.A.,Bale, S.J., Getliff, J.M., Goodman, K., Rochelle, P.A., Fry, J.C., Weightman, A.J. and Harvey, S.M. 1994. A deep bacterial biosphere in Pacific Ocean Sediments. Nature 371: 410-413

Parkhurst, D.L., 1995. User's guide to PHREEQC: a computer model for speciation, reaction-path, advective-transport, and inverse geochemical calculation. Water-Resources Invest. Report 95-4227, US Geol. Surv. , 143 pp.

Paytan, A., Kastner, M., Campbell, D. and Thiemens, M.H. 1998. Sulfur isotopic composition of Cenozoic seawater sulfate. Science 282: 1459-1462

Perry, E., Swift, J., Gamboa, J., Reeve, A., Sanborn, R., Marin, L. and Villasuso, M. 1989. Geologic and environmental aspects of surface cementation, north coast Yucatan, Mexico. Geology 17: 818-821

Perry, E., Velazquez-Oliman, G. and Marin, L. 2002. The hydrogeochemistry of the karst aquifer system of the Northern Yucatan Peninsula, Mexico. International Geology Review 44: 191-221

Plummer, L.N. 1975. Mixing of seawater with calcium carbonate groundwater. Geological Society of America Memoir 142: 219-236

Plummer, L.N., Busby, J.F., Lee, R.L. and Hanshaw, B.B. 1990. Geochemical modelling of the Madison Aquifer in parts of Montana, Wyoming, and South Dakota. Water Resources Research 26: 1981-2014

Pohlman, J.W., Cifuentes, L.A. and Iliffe, T.M. 2000. Food Web Dynamics and Biogeochemistry of Anchialine Caves: A Stable Isotope Approach. In: Wilkens, H., Culver, D.C. and Humphreys, W.F. (Eds), Ecosystems of the World 30: Subterranean Ecosystems. Elsevier, Amsterdam, Holland, p. 345-358

Prosser, J. and Grey, H.V. (Eds.). NSS Cave Diving Manual – An Overview. The Cave Diving Section of the National Speleological Society, Inc., Florida, USA. 377 p.

QRSS, 2004. http://www.caves.org/project/qrss/qrss.htm

Raistrick, B. 1949. The influence of foreign ions on crystal growth from solution, 1. The stabilization of supersaturation of calcium carbonate solutions by anions possessing O-P-O-P-O chains. Discussions of the Faraday Society 5: 235-237

Reardon, E.J., Allison, G.B. and Fritz, P. 1979. Seasonal chemical and isotopic variations of soil CO_2 at Trout Creek, Ontario. Journal of Hydrology 43(1-4): 355-371

Reddy, M.M. 1977. Crystallization of carbonate carbonate in the presence of trace concentrations of phosphorus-containing anions. I. Inhibition of phosphate and glycerophosphate ions at pH 8.8 and 25°C. Journal of Crystal Growth 41: 287-295

Reddy, M.M. 1978. Distribution, transport, adsorption and precipitation of inorganic phosphorus in natural waters of New York State. Abstract of a Paper of the American Chemistry Society 176: 142-142

Reddy, M.M. and Noncollas, G.H. 1973. The crystallization of calcium carbonate, Part III. Calcite crystal growth inhibition by phosphates. Desalination 12: 61-73

Reeve, A.S. and Perry, E.C. 1994. Carbonate geochemistry and the concentrations of aqueous Mg^{2+}, Sr^{2+} and Ca^{2+}: Western north coast of the Yucatan, Mexico. Chemical Geology 112: 105-117

Rickard, D. and Luther III, G.W. 1997. Kinetics of pyrite formation by the H_2S oxidation of iron(II) monosulphide in aqueous solutions between 25 and 125 degrees C: the rate equation. Geochimica et Cosmochimica Acta 61: 115-134

Robie, R.R., Hemingway, B.S. and Fisher, J.R. 1979. Thermodynamic properties of minerals and related substances at 298.15 K and 1 bar (10^2 Pascals) pressure and at higher temperatures. United States Geological Survey Bulletin 1452: 0-456

Robinson, R.A. and R. H. Stokes. 1970. *Electrolyte Solutions*, 2nd ed. Academic, New York, USA.

Roques, H. 1962. Considerations theoriques sur la chimie des carbonates. Ann. Speleo. 17: 1-41.

Roques, H. 1964. Contribution a l'etude statique et chetique des systems gaz carbonique-eau-carbonate. Ann. Speleo. 19: 255-484.

Rosenfield, J.K. 1979. Interstitial water and sediment chemistry of two cores from Florida Bay. Journal of Sedimentary Petrology 49: 989-994

Ruby, E.G., Wirsen, C.O. and Jannasch, H.W. 1981. Chemolithotrophic sulfur-oxidising bacteria from the Galapagos Rift hydrothermal vents. Applied and Environmental Microbiology 42: 133-143

Rullkotter, J. 2000. Organic Matter: The Driving Force for Early Diagenesis. In: Marine Geochemistry, Schultz, H.D and Zabel, M. (Eds), p. 129-172, Springer-Verlag, Berlin.

Runnels, D.D. 1969. Diagenesis, chemical sediments, and the mixing of natural waters. Journal of Sedimentary Petrology 39: 1188-1201

Sanford, W.E. and Konikow, L.F. 1989. Porosity development in coastal carbonate aquifers. Geology 17: 249-252

Scholle, P.A. 1978. A color illustrated guide to carbonate rock constituents, textures, cements and porosities. Memoirs of the American Association of Petroleum Geologists 27: 241

Schultz, H.D. 2000 Quantification of early diagenesis: dissolved constituents in marine porewater. In: Marine Geochemistry Schultz, H.D. and Zabel, M. (Eds) Springer-Verlag New York pp. 85-128

Schwabe, S.J. 1999. Biogeochemical Investigation of Caves within Bahamian Carbonate Platforms. PhD thesis, Department of Earth Sciences, University of Bristol. 198 p.

Sharpton, V.L., Burke, K., Camargo-Zanoguera, A.,Hall, S.A., Lee, D.S., Marin, L.E., Suarez-Reynoso, G., Quezada-Muneton, J.M., Spudis, P.D. and Urrutia-Fucugauchi, J. 1993. Chixulub multiring impact basin: size and other characteristics derived from gravity analysis. Science 261: 1564-1567

Simkiss, K. 1964a. Variations in the crystalline form of calcium carbonate precipitated from artificial seawater. Nature 201: 492-493

Simkiss, K. 1964b. The inhibitory effects of some metabolites on the precipitation of calcium carbonate from artificial and natural seawater. J. Cons. Int. Explor. Mer. 29: 6-18

Simms, M. 1984. Dolomitization by groundwater –flow systems in carbonate platforms. Transactions of the Gulf Coast Association of Geologists Society 34: 411-420

Slomp, C.P., Van der Gaast, S.J. and Van Raaphorst, W. 1996a. Phosphorus binding by poorly crystalline iron oxides in North Sea sediments. Marine Geochemistry 52: 55-73

Slomp, C.P., Epping, E.H.G., Helder, W. and Van Raaphorst, W, 1996b. A key role for iron-bound phosphorus in authigenic apatite formation in North Atlantic continental platform sediments. Journal of Marine Research 54: 1179-1205

Smart, P.L., Dawans, J.M. and Whitaker, F.F. 1988. Carbonate dissolution in a modern mixing zone, South Andros, Bahamas. Nature 335: 811-813

Smart, P.L., Beddows, P., Doerr, S., Smith, S. and Whitaker, F.F. 2002. Hydrochemical processes and cave development, Caribbean coast, Yucatan peninsula, Mexico. In: J.B. Martin, C.M. Wicks and I.D. Sasowsky (Eds.), Hydrogeology and Biology of Post-Paleozoic Carbonate Aquifers, Special Publication 7. pp. 79-83. Karst Waters Institute.

Socki, R.A. 1984. A Chemical and Isotopic Study of Groundwater From Northwestern Yucatan, Mexico. MSc thesis, Department of Geology, Northern Illinois University. 61 p.

Stern, L., Summers Engel, A., Bennett, P.C. and Porter, M.L. 2002. Subaqueous and subaerial speleogenesis in a sulfidic cave. In: J.B. Martin, C.M. Wicks and I.D. Sasowsky (Eds.), Hydrogeology and Biology of Post-Paleozoic Carbonate Aquifers, Special Publication 7. pp. 89-91. Karst Waters Institute.

Stoessell, R.K.1992. Effects of sulfate reduction on $CaCO_3$ dissolution and precipitation in mixing-zone fluids. Journal of Sedimentary Petrology 62(5): 873-880

Stoessell, R.K. 1995. Dampening of transverse dispersion in the halocline in karst limestone in the northeastern Yucatan Peninsula. Ground Water 33(3): 366-371

Stoessell, R.K., Ward, W.C., Ford, B.H. and Schuffert, J.D. 1989. Water chemistry and $CaCO_3$ dissolution in the saline part of an open-flow mixing zone, coastal Yucatan Peninsula, Mexico. Bulletin of the Geological Society of America 101: 159-169

Stoessell, R.K., Moore, Y.H. and Coke, J.G.1993. The occurrence and effect of sulfate reduction and sulfide oxidation on coastal limestone dissolution in Yucatan cenotes. Groundwater 4(31): 566-575

Sugimura, Y. and Suzuki, Y. 1988. A high temperature catalytic oxidation method for the determination of organic carbon in sea water by direct injection of a liquid sample. Marine Chemistry 24: 105-131

Sundby, B., Gobeil, C., Silcerberg, N., and Mucci, A. 1992. The phosphorus cycle in coastal marine sediments. Limnology and Oceanography 37: 1129-1145

Telling, J. 2002. The Geomicrobiology of Deep-Sea Sediments on the Mid-Atlantic Ridge. PhD thesis, Faculty of Science, University of Bristol.

Teske, A., Brinkhoff, T., Muyzer, G., Moser, D.P., Rethmeier, J. and Jannasch, H.W. 2000. Diversity of thiosulphate-oxidising bacteria from marine sediments and hydrothermal vents. Applied and Environmental Microbiology 66: 3125-3133

Thode, H.G. and Monster, J. 1965. Sulfur-isotope geochemistry of petroleum, evaporites and ancient seas. In: Fluids in Subsurface Environments, Young, A. and Galley, J.E. (Eds.), American Association of Petroleum Geologists, Memoir 4, pp. 367-377

Thomas, C. 1999. Aspects hydrogeologiques du Yucatan (Mexique). Karstologia, 34(2): 9-22.

Thrailkill, J. 1976. Carbonate. Yevjevich, V. (Ed), Karst Hydrology and Water Resources, Water Resources Publication, Fort Collins, p. 745-771

Tuttle, J.H. 1980. Organic carbon utilsation by resting cells of thiosulphate-oxidising marine heterotrophs. Applied and Environmental Microbiology 40: 516-521

Tuttle, J.H., Holmes, P.E. and Jannasch, H.W. 1974. Growth rate stimulation of marine Pseudomonads by thiosulphate. Archives of Microbiology 99: 1-14

Vacher, H.L.1978. Hydrogeology of Bermuda – significance of an across-the-island variation in permeability. Journal of Hydrology 39: 207-226

Vasconcelos, C.V. and McKenzie, J.A. 1997. Microbial mediation of modern dolomite precipitation and diagenesis under anoxic conditions (Lagoa Vermelha, Rio de Janeiro, Brazil). Journal of Sedimentary Research 67(3): 378-390

Vasconcelos, C., McKenzie, J.A., Bernasconi, S., Grujic, D. and Tien, A.J. 1995. Microbial mediation as a possible mechanism for natural dolomite formation at low-temperatures. Nature 377: 220-222

Veni, G. 1990. Maya utilization of karst groundwater resources. Environmental Geology and Water Sciences 16(1): 63-66

Vernon, R.O. 1969. The geology and hydrology associated with a zone of high permeability ('Boulder Zone') in Florida. Society of Mining Engineers, American Institute of Mining Engineers, No. 69-AG-12.

Walter, L.M. and Burton, E.A. 1986. The effect of orthophosphate on carbonate mineral dissolution rates in seawater. Chemical Geology 56: 313-323

Ward, W.C. 1985. Diagenesis. In: W.C. Ward, A.E. Weidie and W. Back (Eds.), Geology and Hydrogeology of the Yucatan and Quaternary Geology of Northeastern Yucatan Peninsula. pp. 74-95. New Orleans Geological Society Publications, New Orleans.

Ward, W.C. 1985b. Recent carbonate sediments of the inner shelf. In: W.C. Ward, A.E. Weidie and W. Back (Eds.), Geology and Hydrogeology of the Yucatan and Quaternary Geology of Northeastern Yucatan Peninsula. pp. 24-61. New Orleans Geological Society Publications, New Orleans.

Ward, W.C. and Brady, M. 1979. Strandline sedimentation of carbonate grainstones, UpperPleistocene, Yucatan Peninsula, Mexico. American Association of Petroleum Geologists Bulletin 63: 362-369

Ward, W.C. and Halley, R.B. 1985. Dolomitisation in a mixing zone of near-seawater composition, late Pleistocene Northeastern Yucatan Peninsula. Journal of Sedimentary Petrology 55: 407-420.

Ward, W.C., Weidie, A.E. and Back, W. 1985. Geology and Hydrology of the Yucatan, New Orleans Geological Society, 160 p.

Ward, W.C., Keller, G., Stinnesbeck, W. and Adatte, T. 1995. Yucatan subsurface stratigraphy: implications and constraints for the Chicxulub impact. Geology 23(10):873-876

Warthmann, R., van Lith, Y., Vasconcelos, C., McKenzie, J.A., Karpoff, A.M. 2000. Geology 28(12): 1091-1094

Weidie, A.E. 1985. Geology of Yucatan Platform. In: W.C. Ward, A.E. Weidie and W. Back (eds.). Geology and Hydrogeology of the Yucatan and Quaternary Geology of Northeastern Yucatan Peninsula pp. 1-12. New Orleans Geological Society Publications, New Orleans.

Wigley, T.M.L. and L.N. Plummer. 1976. Mixing of carbonate waters. Geochimica et Cosmochimica Acta 40: 989-995.

Whitaker, F.F. and Smart, P.L. 1990. Active circulation of saline ground waters in carbonate platforms: Evidence from the Great Bahama Bank, Geology 18: 200-203

Whitaker, F.F., Smart, P.L., Vahrenkamp, V.C., Nicholson, H. and Wogelius, R.A. 1994. Dolomitization by near-normal seawater? Field evidence from the Bahamas. Special Publication of the International Association of Sedimentology 21: 111-132

Whitaker, F.F. 1992. Hydrology, Geochemistry and Diagenesis of Modern Carbonate Platforms in the Bahamas. PhD thesis, Faculty of Science, University of Bristol.

White, W.B. 1984. Rate processes: chemical kinetics and karst landform development. In: La Fleur, R.G. (Ed), Groundwater as a Geomorphic Agent. Oxford University Press, Oxford. p. 277-288.

White, W.B. 1976. Cave minerals and speleothems. In: Ford, T.D. and Cullingford, C.H.D. (Eds), The Science of Speleology, Academic Press, London, p. 267-327

Wicks, C.M., Herman, J.S., Randazzo, A.F. and Jee, J.L. 1995. Water-rock interactions in a modern coastal mixing zone. GSA Bulletin 107(9): 1023-1032

Wright, D.T. 1999. The role of sulphate-reducing bacteria and cyanobacteria in dolomite formation in distal ephemeral lakes of the Coorong region, South Australia. Sedimentary Geology 126(1-4): 147-157

Appendix: List of Media Recipes

A.1. Dilution Media

Dilution Media	Description	Recipe/L distilled water
1	90 % ASW* (aerobic)	1.35 g $MgSO_4$; 22.5 g NaCl; 0.9 g $(NH_4)_3SO_4$; 0.378 g KH_2PO_4; 0.27 g KCl; 0.27 g $CaCl_2$. Mix/heat, allow to cool, then add 0.18 g $NaHCO_3$; 2.48 g $Na_2S_2O_3$; 3 ml vitamins; 2 ml trace elements. Adjust to pH 7.3. Filter sterilize twice through 0.2 μm (Eberhard et al., 1995).
2	90 % ASW (anaerobic)	As (1) above, but without the addition of $Na_2S_2O_3$
3	50 % ASW (aerobic)	0.74 g $MgSO_4$; 12.38 g NaCl; 0.5 g $(NH_4)_3SO_4$; 0.21g KH_2PO_4; 0.15 g KCl; 0.15 g $CaCl_2$. Mix/heat, allow to cool, then add 0.1 g $NaHCO_3$; 2.48 g $Na_2S_2O_3$; 3 ml vitamins; 2 ml trace elements. Adjust to pH 7.3. Filter sterilize twice through 0.2 μm.
4	50 % ASW (anaerobic)	As (3) above, but without the addition of $Na_2S_2O_3$
5	8 % ASW (aerobic)	0.12 g $MgSO_4$; 2.0 g NaCl; 0.08 g $(NH_4)_3SO_4$; 0.03 g KH_2PO_4; 0.024 g KCl; 0.024 g $CaCl_2$. Mix/heat, allow to cool, then add 0.016 g $NaHCO_3$; 2.48 g $Na_2S_2O_3$; 3ml vitamins; 2 ml trace elements. Adjust to pH 7.3. Filter sterilize twice through 0.2 μm.
6	8 % ASW (anaerobic)	As (5) above, but without the addition of $Na_2S_2O_3$

* Artificial Seawater

A.2. Most Probable Number (MPN) Media

MPN Media	Description	Recipe/L distilled water
1	Sulfate Reducing Bacteria	**90 % ASW**: 0.5 g KH_2PO_4; 1 g NH_4Cl; 0.82 g sodium acetate (anhydrous); 0.1 g yeast extract; 0.1 g ascorbic acid; 1.0 g $CaSO_4$; 0.5 g $FeSO_4.7H_2O$; 2 g $MgSO_4.7H_2O$; 2.52 g $NaHCO_3$; 1 ml reazurin (0.1 %); 3.24 g $MgCl_2.H_2O$; 20.7 g NaCl. Make up to 1L in flask with anoxic distilled water, bung with cotton wool, flush with O_2-free N_2 for 10 minutes or until constituents are dissolved. Add 0.1 g thioglycolic acid. Adjust pH to 7.2 to 7.5. Dispense into vials in anaerobic chamber ($N_2/H_2/CO_2$ (90/10/10)), add septa, remove from chamber and autoclave at 121°C for 40 minutes. **50 % ASW:** As above, but with 1.78 g $MgCl_2.H_2O$ and 11.39 g NaCl. **8 % ASW**. As above, but with 0.288 g $MgCl_2.H_2O$ and 1.84 g NaCl.
2	Sulfur Oxidising Bacteria	**90 % ASW**: As dilution media (1) above, but with addition of 2.48 g $Na_2S_2O_3$. **50 % ASW**: As dilution media (3) above, but with addition of 2.48 g $Na_2S_2O_3$. **8 % ASW**: As dilution media (5) above, but with addition of 2.48 g $Na_2S_2O_3$.
3	Anaerobic Heterotrophic Bacteria	**90 % ASW:** 22.23 g NaCl; 11.7 g $MgCl_2$; 8.1 g $NaSO_4$; 1.2 g nutrient broth. Make up to 1000 ml with anoxic distilled water. Autoclave at 121°C for 40 minutes. Dispense under N_2 in laminar flow cabinet. **8 % ASW:** 1.98 g NaCl; 1.04 g $MgCl_2$; 0.72 g $NaSO_4$; 1.2 g nutrient broth. Make up to 1000 ml with oxic distilled water. Autoclave at 121°C for 40 minutes. Dispense in laminar flow cabinet.
4	Aerobic Heterotrophic Bacteria	**90 % ASW:** 22.23 g NaCl; 11.7 g $MgCl_2$; 8.1 g $NaSO_4$; 1.2 g nutrient broth. Autoclave at 121°C for 40 minutes. **8 % ASW:** 1.98 g NaCl; 1.04 g $MgCl_2$; 0.72 g $NaSO_4$; 1.2 g nutrient broth. Autoclave at 121°C for 40 minutes.

MPN Media	Description	Recipe/L distilled water
5	Iron Reducing Bacteria	**90 % ASW**: 0.1 g $CaCl_2.2H_2O$; 0.1 g KCl; 1.5 g NH_4Cl; 0.6 g $NaH_2PO_4.H_2O$; 12.25 g $Fe(III)C_6H_5O_7$; 0.1g $MgSO_4.7H_2O$; 0.005 g $MnCl_2.4H_2O$; 6.8 g sodium acetate (anhydrous); 0.05 g yeast extract; 1 ml reazurin (0.1%); 41.4 g NaCl; 6.48 g $MgCl_2$. Make up to 1000 ml with distilled water. Autoclave at 121oC for 40 minutes, cool overnight under N_2/CO_2 (80:20). Adjust pH to 7-7.2. Add 3 ml vitamins, 2 ml trace elements and 30 ml of sterile HCO_3^- solution in laminar flow cabinet, and dispense under N_2/CO_2 (80:20) flow cabinet (Lovley and Philips, 1986). **8 % ASW**: As above, but with only 0.288 g $MgCl_2.H_2O$ and 1.84 g NaCl.
6	Iron Oxidising Bacteria	**90 % ASW:** 22.23 g NaCl; 11.7 g $MgCl_2$; 8.1 g $NaSO_4$; 0.4 g KH_2PO_4; 0.4 g $MgSO_4.7H_2O$; 0.4 g $(NH_4)_2SO_4$; 33.3 g $FeSO_4$. Make up to 1000 ml with deionised water. Filter sterilize twice through 0.2 μm. Final pH: 2.15 (DSM, German collection of microorganisms and cell cultures, 1993, Medium 70). **8 % ASW**: 1.98 g NaCl; 1.04 g $MgCl_2$; 0.72 g $NaSO_4$; 0.4 g KH_2PO_4; 0.4 g $MgSO_4.7H_2O$; 0.4 g $(NH_4)_2SO_4$; 33.3 g $FeSO_4$. Make up to 1000 ml with deionised water. Filter sterilize twice through 0.2 μm. Final pH: 2.33.

A.3. Sterile additions

	Recipe
Trace elements	1.5 g $FeCl_2.4H_2O$ in 10 ml 25% HCl; 0,19 g $CoCl_2.6H_2O$; 0.1g $MnCl_2.4H_2O$; 0.07 g $ZnCl_2$; 0.062 g H_3BO_3; 0.036 g $Na_2MoO_4.2H_2O$; 0.017 g $CuCl_2.2H_2O$. Make up to 1L and autoclave at 121°C.
Vitamins	4 mg 4-aminobenzoic acid; 1 mg D(+) Biotin; 10 mg Thiamine-HCl; 2 mg Folic acid; 10 mg Pyridoxine-HCl; 5 mg Riboflavin; 5 mg Nicotinic acid; 5 mg DL calcium pantothenate; 5 mg lipoic acid (thioctic acid); 5 mg cyanocobalamine; 300 ml distilled water. Filter-sterilise through 0.2 μm and store refrigerated.
HCO_3^-	Dissolve 84 g $NaHCO_3$ in 1000 ml distilled water, bubble with CO_2 and dispense under CO_2. Leave under positive pressure and autoclave.

Appendix 2
Freshwater Geochemistry Data Set

Site	Cl mM	Na mM	Ca mM	Mg mM	SO_4 mM	pH	HCO_3 mM	IBE	SI-A	SI-C	SI-D	SI-DD	$p\ CO_2$ (%)	Ca_{xs} mM	Mg_{xs} mM	SO_{4xs} mM
Caves																
Abejas	90	78	4.6	9.4	4.5	6.95	7.16	0.48	-0.13	0.01	0.49	-0.08	3.89	2.97	0.81	-0.09
Balam Can Che	52	45	2.4	5.7	2.7	6.96	7.04	-1.48	-0.32	-0.18	0.15	-0.4	3.89	1.48	0.74	0.09
Carwash	16	13	2.3	2.2	0.8	6.91	2.97	4.77	-0.60	-0.46	-0.80	-1.36	2.00	2.03	0.70	0.05
Eden	52	44	3.3	5.9	2.7	6.98	7.07	-1.1	-0.17	-0.03	0.33	-0.22	3.72	2.41	0.87	0.07
Heaven	16	14	2.2	2.2	0.9	6.85	6.95	-3.33	-0.33	-0.19	-0.24	-0.79	5.37	1.93	0.73	0.08
Hilario's Well	35	29	3.6	3.7	1.9	6.92	6.90	-1.18	-0.15	-0.01	0.14	-0.41	4.27	2.99	0.38	0.11
Naranjal	25	20	3.2	3.0	1.4	6.79	7.32	-3.68	-0.25	-0.11	-0.11	-0.67	6.31	2.79	0.63	0.10
Sak Aktun	25	21	2.5	3.2	1.4	6.79	7.59	-3.96	-0.35	-0.2	-0.16	-0.72	6.61	2.07	0.76	0.07
Sak Aktun	25	21	2.0	3.1	1.3	6.80	7.54	-5.48	-0.44	-0.29	-0.25	-0.81	6.46	1.55	0.71	0.07
Taj Mahal	47	40	3.1	5.3	2.5	7.06	6.92	-0.89	-0.12	0.03	0.43	-0.12	3.09	2.24	0.80	0.08
Temple of Doom	34	29	2.8	3.9	1.8	7.03	7.22	-2.65	-0.11	0.03	0.35	-0.21	3.55	2.20	0.61	0.09
Caverns																
Chac Mool	26	21	3.0	3.1	1.4	7.08	6.18	-2.40	-0.07	0.07	0.31	-0.25	2.75	2.53	0.63	0.06
Taj Mahal	60	53	3.3	6.6	3.1	6.73	6.79	0.94	-0.46	-0.31	-0.19	-0.74	6.31	2.27	0.90	0.07
Temple of Doom	35	29	2.4	3.9	1.8	7.26	7.94	-4.19	0.08	0.22	0.79	0.24	2.29	1.80	0.56	0.09
Cenotes																
Angelita	9	7	3.2	1.4	0.4	7.03	7.21	-2.73	0.06	0.21	0.2	-0.36	3.80	3.02	0.54	-0.01
Balam Can Che	26	22	2.4	3.1	1.4	6.98	7.47	-4.12	-0.19	-0.04	0.16	-0.39	4.17	1.95	0.59	0.08
Carwash	15	13	2.0	2.2	0.8	6.82	7.39	-6.21	-0.36	-0.22	-0.27	-0.83	6.17	1.76	0.73	0.04
Chac Mool	16	14	2.1	2.3	0.9	7.05	6.57	-2.94	-0.22	-0.07	0.00	-0.50	3.09	1.81	0.80	0.06
Chac Mool	16	14	2.0	2.3	0.9	7.05	6.56	-3.74	-0.20	-0.06	0.07	-0.48	3.24	1.71	0.74	0.06
Chemuyil	16	14	2.2	2.3	0.9	7.07	6.97	-2.92	-0.13	0.02	0.19	-0.35	3.24	1.89	0.75	0.06
Chemuyil	16	14	2.2	2.3	0.9	6.98	6.97	-4.03	-0.22	-0.08	0.01	-0.54	3.98	1.86	0.73	0.06
Chemuyil	16	14	3.2	2.3	0.9	6.96	6.93	-0.09	-0.09	0.06	0.11	-0.43	4.07	2.86	0.76	0.06
Chemuyil	21	17	2.2	2.7	1.1	6.88	6.97	-4.29	-0.33	-0.19	-0.15	-0.70	5.01	1.86	0.75	0.07
Esmeralda	15	14	1.8	2.1	0.8	7.51	6.87	-3.55	0.22	0.37	0.92	0.39	1.15	1.56	0.68	0.02
Esmeralda	14	11	2.6	2.1	0.7	8.12	6.21	-1.34	0.97	1.11	2.29	1.7	0.26	2.33	0.77	0.04
Naranjal	33	31	2.5	4.2	1.8	7.03	7.41	1.18	-0.16	-0.02	0.34	-0.22	3.63	1.89	1.03	0.11
Naranjal	25	20	2.2	3.1	1.4	6.93	7.32	-6.34	-0.29	-0.14	0.01	-0.54	4.68	1.71	0.68	0.09
Pac Chen	5	4	1.2	1.2	0.3	7.39	3.66	-0.99	-0.24	-0.10	-0.04	-0.59	0.85	1.06	0.74	0.00
Pac Chen	5	4	1.2	1.2	0.2	7.40	3.69	-0.02	-0.22	-0.08	-0.01	-0.56	0.85	1.08	0.76	0.00
Pac Chen	5	5	2.2	1.3	0.3	7.35	4.25	6.87	0.06	0.20	0.34	-0.24	1.10	2.09	0.82	0.03
Ranchero	3	2	1.8	0.4	0.1	7.14	3.67	1.42	-0.27	-0.13	-0.77	-1.32	1.55	1.74	0.15	-0.01
Ranchero	3	2	1.8	0.4	0.1	7.13	3.68	0.78	-0.27	-0.13	-0.77	-1.33	1.62	1.75	0.13	-0.01
Sacbe	16	14	2.3	2.2	0.8	7.04	7.05	-3.16	-0.09	0.05	0.25	-0.34	3.63	2.00	0.72	0.04
Sak Aktun	25	23	2.2	3.2	1.3	6.69	7.61	-1.31	-0.5	-0.36	-0.43	-0.98	8.32	1.75	0.75	0.07
Taj Mahal	62	54	3.3	6.7	3.2	7.03	6.77	0.26	-0.17	-0.03	0.39	-0.15	3.16	2.17	0.87	0.10
The Pit	16	13	3.4	2.2	0.9	6.85	7.36	-0.79	-0.13	0.01	-0.03	-0.58	5.62	3.13	0.72	0.07
The Pit	16	14	2.0	2.3	0.9	6.83	7.09	-4.89	-0.38	-0.24	-0.28	-0.83	5.75	1.74	0.79	0.07
The Pit	17	14	3.3	2.2	0.9	7.07	7.05	-1.03	0.05	0.2	0.37	-0.19	3.24	2.99	0.64	0.10
Tortuga	14	11	2.6	2.1	0.8	6.83	2.87	4.32	-0.63	-0.49	-0.93	-1.49	2.34	2.35	0.74	0.05
Vaca Ha	13	11	3.0	2.0	0.7	6.95	2.69	9.96	-0.48	-0.34	-0.72	-1.28	1.66	2.75	0.68	0.04
Vaca Ha	15	13	2.2	2.2	0.8	7.01	7.57	-6.36	-0.12	0.02	0.2	-0.38	4.17	1.92	0.74	0.04
Zapata	95	82	4.5	10.2	4.9	6.99	2.74	2.63	-0.51	-0.37	-0.23	-0.80	1.35	2.79	1.13	0.15
Wells																
Banana	101	92	3.9	10.5	5.4	7.20	6.82	1.69	0	0.15	0.87	0.31	2.04	2.11	0.86	0.25
Cabanas	87	78	3.7	9.4	4.7	7.13	7.59	0.83	-0.02	0.12	0.8	0.24	2.69	2.19	1.03	0.26
Chan Ha	15	12	2.2	2.1	0.8	6.96	7.27	-5.97	-0.19	-0.04	0.05	-0.53	4.37	1.95	0.73	0.07
Chi Chun Ha	21	17	2.4	2.7	1.1	6.91	7.13	-3.56	-0.26	-0.11	-0.03	-0.58	4.79	2.01	0.74	0.07
Nohoch	16	13	2.5	2.2	0.9	6.72	6.92	-3.09	-0.41	-0.26	-0.44	-1.00	7.24	2.25	0.72	0.08
Pac Chen	5	5	2.3	1.3	0.3	7.49	6.41	-2.50	0.35	0.50	0.90	0.35	1.17	2.19	0.82	0.01
Rancho	3	3	2.1	0.5	0.2	7.33	4.39	2.86	0.04	0.18	-0.17	-0.70	1.17	2.07	0.18	0.08
Taj Mahal	17	16	2.9	2.3	1.1	7.26	5.56	4.40	0.07	0.22	0.46	-0.09	1.66	2.56	0.62	0.26
Tak be Ha	6	5	2.3	0.7	0.3	7.18	5.61	-1.55	0.02	0.16	-0.04	-0.6	2.14	2.23	0.18	0.04
Tankah	43	38	3.2	4.1	2.5	8.02	5.47	0.74	0.75	0.89	2.04	1.48	0.26	2.39	-0.04	0.28
Vida	103	89	4.3	10.6	5.3	7.25	2.75	2.06	-0.29	-0.15	0.24	-0.32	0.72	2.49	0.79	0.16
Xpu Ha - 2	75	68	4.2	8.1	3.9	6.90	10.64	0.22	-0.02	0.13	0.7	0.12	6.61	2.86	0.95	0.13
Xpu Ha -1	49	44	2.7	5.5	2.9	7.32	8.31	-1.18	0.17	0.31	1.08	0.51	2.04	1.82	0.84	0.44

Site	Cl mM	Na mM	Ca mM	Mg mM	SO_4 mM	pH	HCO_3 mM	IBE	SI-A	SI-C	SI-D	SI-DD	p CO_2 (%)	Ca_{xs} mM	Mg_{xs} mM	SO_{4xs} mM
Pumped Wells																
Chac Mool	27	23	2.1	3.3	1.4	6.97	6.44	-3.25	-0.33	-0.18	-0.04	-0.58	3.63	1.63	0.73	0.08
Padus	35	31	1.5	4.4	1.7	7.05	3.85	1.53	-0.59	-0.45	-0.29	-0.88	1.86	0.93	1.03	-0.04
Rancho	9	8	2.6	0.9	0.6	7.02	6.86	-4.88	-0.01	0.14	-0.01	-0.61	3.80	2.49	0.12	0.17
Solimon - 1	184	159	7.6	18.7	8.5	7.09	13.52	0.14	0.42	0.56	1.71	1.09	5.01	4.29	1.18	-0.83
Solimon - 2	73	63	4.4	7.0	3.1	7.40	9.80	-1.01	0.51	0.65	1.68	1.06	2.00	3.07	-0.05	-0.58
Tankah	123	110	4.2	14.8	7.6	7.38	9.11	0.97	0.33	0.47	1.67	1.06	1.78	2.03	3.12	1.40
Tulum	38	32	3.1	5.1	2.1	7.21	7.98	-0.2	0.14	0.29	0.94	0.36	2.57	2.47	1.53	0.17
Xpu-Ha 3	64	57	3.6	6.8	3.5	7.22	11.41	-2.34	0.32	0.46	1.39	0.77	3.63	2.43	0.70	0.25
Y Ha	15	12	2.4	2.3	0.9	7.42	6.38	-2.52	0.26	0.4	0.94	0.36	1.35	2.13	0.86	0.11
Drips																
Heaven	1	1	2.4	0.2	0.1	7.29	4.66	5.59	0.11	0.25	-0.48	-1.04	1.41	2.36	0.12	0.12
Heaven	1	1	2.4	0.3	0.2	7.71	5.10	0.08	0.56	0.71	0.58	0.03	0.58	2.43	0.17	0.15
Heaven	1	1	3.1	0.3	0.2	7.71	5.02	9.93	0.64	0.79	0.69	0.14	0.56	3.08	0.17	0.14
Tak be Ha	2	2	2.1	0.2	0.1	7.81	5.33	-6.82	0.62	0.76	0.57	0.01	0.48	2.04	-0.02	0.00
Tak be Ha	2	2	2.4	0.2	0.1	7.69	5.59	-5.77	0.57	0.72	0.49	-0.06	0.66	2.39	0.01	0.01
Heaven	2	2	2.6	0.2	0.4	8.00	3.80	5.94	0.72	0.86	0.83	0.28	0.21	2.52	0.01	0.25
Tak be Ha	4	2	2.9	0.2	0.2	7.67	5.61	-13.92	0.61	0.75	0.44	-0.11	0.69	2.79	-0.21	0.00
Rainwater																
Rainstorm	0	0	0.0	0.0	0.0	6.80	0.21	20.74	-3.57	-3.42	-6.85	-7.4	0.219	0.02	0.00	0.00
Rainstorm	0	1	0.1	0.0	0.0	8.27	0.21	20.64	-1.7	-1.56	-3.11	-3.66	0.01	0.05	0.02	0.01
Runoff																
Rainstorm	4	4	0.4	0.4	0.3	8.28	0.68	-0.77	-0.49	-0.35	-0.57	-1.12	0.02	0.33	0.01	0.07
Rainstorm	5	5	0.5	0.6	0.5	8.66	1.00	4.33	0.08	0.22	0.67	0.12	0.01	0.40	0.15	0.30
Rainstorm	9	8	0.6	0.9	0.7	8.61	0.76	-1.61	-0.03	0.11	0.52	-0.03	0.01	0.46	0.04	0.26
Rainstorm	13	10	0.8	1.2	1.0	7.62	0.74	-2.69	-0.91	-0.76	-1.22	-1.77	0.10	0.59	0.01	0.40
Surface Pools																
Quarry	18	15	1.8	1.0	0.7	9.50	0.75	1.65	0.98	1.11	2.18	1.48	0.00	1.43	-0.76	-0.25
Nohoch	98	90	2.9	12.0	5.8	8.86	4.77	3.37	1.27	1.4	3.67	2.95	0.02	1.12	2.62	0.84
Mangrove	115	101	6.4	12.6	8.2	7.47	6.61	1.07	0.43	0.57	1.6	1.03	1.02	4.35	1.61	2.44
Mangrove PB	129	118	4.7	13.4	6.7	7.81	5.92	2.68	0.67	0.81	2.3	1.61	0.45	2.41	1.11	0.15
Naval	135	121	5.2	13.1	7.3	8.50	2.74	2.56	1.01	1.14	2.94	2.18	0.03	2.83	0.23	0.53
Mangrove SL	359	316	10.7	35.8	20.0	7.94	6.22	1.39	0.96	1.1	2.96	2.28	0.28	4.30	1.59	1.89
Solimon	661	585	18.0	70.9	38.9	7.91	5.20	2.16	0.99	1.13	3.12	2.42	0.21	6.16	7.77	5.53
Outflows																
Casa Cenote	144	126	5.2	14.7	7.5	6.90	6.79	0.96	-0.23	-0.09	0.42	-0.13	3.89	2.63	0.93	0.20
Casa Cenote	156	138	5.3	15.9	7.8	6.86	6.79	1.55	-0.28	-0.14	0.37	-0.2	4.17	2.47	1.01	-0.05
Casa Cenote	240	211	6.5	24.1	12.0	6.92	5.89	0.63	-0.27	-0.12	0.49	-0.07	2.95	2.17	1.18	-0.10
Casa Cenote	269	234	7.2	26.0	14.0	7.06	5.39	0.3	-0.13	0.01	0.76	0.19	1.95	2.36	0.26	0.42
Ox Bel Ha 1	120	103	5.0	12.3	6.4	6.81	6.74	-0.01	-0.31	-0.16	0.21	-0.35	4.90	2.89	0.83	0.29
Ox Bel Ha 2	130	104	5.0	13.4	6.8	7.03	2.62	-1.14	-0.50	-0.36	-0.13	-0.70	1.12	2.66	1.02	0.21
Ox Bel Ha 3	100	81	4.9	10.5	5.3	6.89	2.70	-0.23	-0.60	-0.46	-0.42	-0.99	1.66	3.06	0.95	0.25
Ox Bel Ha 4	95	84	4.7	10.0	5.0	6.93	2.74	3.29	-0.56	-0.42	-0.36	-0.92	1.55	3.04	0.90	0.16
Xel Ha	159	138	5.2	16.4	8.3	6.81	5.71	0.55	-0.4	-0.26	0.13	-0.43	3.98	2.40	1.22	0.24
Yalku	472	389	8.9	45.3	24.3	7.54	3.47	-1.82	0.18	0.32	1.55	0.95	0.38	0.46	0.28	0.49
Yalku	233	201	6.0	23.1	11.7	7.09	5.28	0.35	-0.15	-0.01	0.75	0.16	1.86	1.79	0.76	-0.13

Appendix 3
Mixing Zone Geochemistry Data Set

Water Type	Cl mM	Na mM	Ca mM	Mg mM	SO_4 mM	HCO_3 mM	pH	IBE	SI-A	SI-C	SI-D	SI-DD	$p\ CO_2$ (%)	Ca_{XS} mM	Mg_{XS} mM	SO_{4XS} mM
FW	41	35	3.8	4	2	7.09	6.95	0.35	-0.10	0.04	0.30	-0.26	4.07	0.0	0.2	0.1
FW	56	47	4.0	6	3	7.64	6.99	-1.77	-0.05	0.09	0.48	-0.08	3.98	0.0	0.0	0.0
UMZ	72	60	4.2	7	4	6.90	6.98	-1.4	-0.12	0.02	0.43	-0.13	3.55	0.0	0.0	0.0
UMZ	98	84	4.6	10	5	7.43	7.01	-0.61	-0.07	0.07	0.63	0.07	3.47	0.1	0.3	-0.1
UMZ	102	87	4.8	11	5	6.70	6.97	0.13	-0.15	0.00	0.49	-0.07	3.39	0.2	0.7	0.0
UMZ	131	106	5.0	13	7	6.40	6.87	-2.23	-0.28	-0.14	0.29	-0.27	3.98	0.1	0.6	0.0
SS	173	156	5.7	17	9	6.26	6.83	1.93	-0.33	-0.19	0.26	-0.30	4.07	0.2	0.9	0.1
SS	200	179	6.3	20	10	6.20	6.80	1.64	-0.35	-0.21	0.25	-0.31	4.27	0.4	1.0	0.1
SS	200	178	6.2	20	10	6.05	6.82	1.34	-0.35	-0.20	0.26	-0.30	3.98	0.3	0.9	0.1
SS	203	187	5.6	20	11	5.99	6.82	2.61	-0.40	-0.25	0.22	-0.35	3.89	-0.3	1.2	0.1
MMZ	225	195	6.3	22	12	6.18	6.85	0.16	-0.32	-0.17	0.36	-0.21	3.72	0.1	0.6	0.1
MMZ	243	199	6.4	22	12	5.98	6.98	-2.62	-0.20	-0.06	0.59	0.03	2.69	0.0	-0.8	-0.4
MMZ	253	223	6.2	24	13	5.22	6.86	0.34	-0.41	-0.26	0.23	-0.33	3.02	-0.3	0.0	0.1
MMZ	294	255	7.1	28	15	5.40	7.00	-0.07	-0.22	-0.07	0.62	0.05	2.24	0.1	0.2	0.0
MMZ	308	248	7.3	28	16	5.28	6.89	-3.25	-0.32	-0.18	0.40	-0.16	2.82	0.1	-0.3	0.0
MMZ	337	289	8.4	34	18	5.01	7.08	0.32	-0.12	0.02	0.83	0.26	1.66	0.8	2.6	0.4
MMZ	337	288	7.8	32	18	4.88	7.12	-0.62	-0.12	0.02	0.83	0.27	1.48	0.2	0.4	0.1
MMZ	341	285	7.5	31	18	5.00	7.07	-2.08	-0.17	-0.03	0.72	0.16	1.70	-0.1	-1.1	0.1
MMZ	366	314	8.1	35	19	4.56	7.05	-0.53	-0.22	-0.07	0.66	0.10	1.62	0.1	0.5	0.1
MMZ	370	320	8.0	35	19	4.61	7.07	-0.18	-0.20	-0.05	0.71	0.14	1.55	0.0	0.4	0.1
MMZ	389	345	8.3	37	20	4.47	7.06	0.89	-0.21	-0.07	0.68	0.12	1.51	0.1	0.3	0.1
LMZ	454	389	9.2	43	24	3.57	7.12	-0.41	-0.23	-0.08	0.68	0.11	1.02	0.2	0.6	0.4
LMZ	526	459	9.9	50	28	2.97	7.02	0.31	-0.40	-0.25	0.38	-0.18	1.05	-0.1	1.3	0.5
LMZ	537	484	10.4	52	28	2.73	7.23	1.81	-0.21	-0.07	0.75	0.19	0.58	0.3	1.9	0.4
BMZ	540	468	10.1	51	28	2.55	7.27	-0.03	-0.21	-0.07	0.75	0.19	0.50	0.0	0.9	0.4
BMZ	541	462	10.2	50	28	2.47	7.28	-0.57	-0.21	-0.06	0.75	0.19	0.47	0.1	0.3	0.2
BMZ	542	464	10.3	51	28	2.39	7.20	-0.45	-0.30	-0.16	0.57	0.01	0.55	0.1	0.7	0.2
SZ	553	482	10.1	53	29	3.86	7.25	0.17	-0.05	0.09	1.08	0.52	0.78	-0.2	1.4	0.2
SZ	559	480	10.9	52	29	2.29	7.36	-0.23	-0.14	0.01	0.88	0.32	0.36	0.6	0.6	0.2
SZ	560	471	10.4	52	29	2.21	7.34	-1.22	-0.19	-0.05	0.79	0.22	0.36	0.0	0.0	0.0
SZ	570	473	10.2	50	30	2.88	7.21	-2.53	-0.22	-0.07	0.73	0.17	0.65	-0.3	-2.7	0.4

Appendix 4
Saline Zone Geochemistry Data Set

Site	Cl mM	Na mM	Ca mM	Mg mM	SO_4 mM	HCO_3 mM	pH	IBE	SI-AN	SI-C	SI-D	SI-DD	$p\ CO_2$ (%)	Ca_{xs} mM	Mg_{xs} mM	SO_{4xs} mM
Shallow Saline Zone (<40 m)																
27 Steps	522	452	10.0	52.3	27.1	2.90	7.19	0.59	-0.86	-0.09	0.72	0.16	0.68	0.52	2.42	0.73
Ak Kimin	545	473	10.1	51.9	28.2	2.50	7.55	0.25	-0.84	0.23	1.39	0.77	0.26	0.67	-0.18	0.68
Ak Kimin	498	484	10.5	53.6	25.8	2.22	7.28	6.32	-0.87	-0.08	0.75	0.16	0.43	1.00	6.05	0.62
Ak Kimin	579	466	9.7	49.2	30.1	2.48	7.31	-4.11	-0.83	-0.04	0.83	0.24	0.46	0.28	-6.16	0.79
Balam Can Che	528	510	9.7	54.3	27.3	2.83	7.12	5.14	-0.89	-0.18	0.59	0.01	0.78	0.20	3.81	0.55
Balam Can Che	556	489	9.9	55.5	28.8	2.44	7.29	1.22	-0.85	-0.06	0.83	0.24	0.46	0.46	2.38	0.72
Casa Cenote	522	500	10.1	49.7	27.0	2.87	7.17	4.29	-0.86	-0.12	0.65	0.09	0.71	0.60	-0.14	0.63
Chac Mool	515	464	9.4	49.2	26.6	2.52	7.15	1.72	-0.89	-0.21	0.48	-0.09	0.66	-0.07	0.06	0.59
Chemuyil	522	460	10.5	50.5	27.2	2.52	7.12	1.11	-0.83	-0.21	0.44	-0.11	0.69	1.08	0.58	0.83
Chemuyil	544	482	10.9	51.5	28.4	2.37	7.18	1.04	-0.81	-0.16	0.53	-0.03	0.56	1.43	-0.54	0.86
Eden	543	456	9.8	53.4	28.1	2.52	7.25	-0.87	-0.86	-0.1	0.73	0.15	0.51	0.33	1.47	0.69
Esmeralda	550	499	10.0	54.0	28.7	2.44	7.08	2.3	-0.85	-0.3	0.32	-0.23	0.72	0.55	1.43	0.89
Hilario's Well	554	479	10.2	52.1	28.8	2.25	7.33	0.03	-0.83	-0.05	0.8	0.22	0.38	0.75	-0.81	0.74
Naranjal	553	482	10.1	52.7	28.8	2.41	7.25	0.17	-0.84	0.09	1.08	0.52	0.78	0.60	-0.18	0.87
Naranjal	512	434	9.6	54.2	27.6	2.78	7.18	-0.05	-0.87	-0.14	0.65	0.09	0.66	0.14	5.23	1.74
Naranjal	542	464	10.3	50.9	28.3	2.39	7.20	-0.45	-0.83	-0.16	0.57	0.01	0.55	0.82	-0.87	0.85
Naranjal	541	462	10.2	50.4	28.2	2.47	7.28	-0.57	-0.83	-0.06	0.75	0.19	0.47	0.76	-1.19	0.87
Naranjal	540	468	10.1	51.0	28.4	2.55	7.27	-0.03	-0.84	-0.07	0.75	0.19	0.50	0.63	-0.65	1.12
Naranjal	559	480	10.9	52.5	29.2	2.29	7.36	-0.23	-0.8	0.01	0.88	0.32	0.36	1.46	-0.97	0.93
Naranjal	560	471	10.4	51.9	29.0	2.21	7.34	-1.22	-0.82	-0.05	0.79	0.22	0.36	0.92	-1.62	0.70
Naranjal	565	486	10.9	52.5	29.4	2.22	7.27	-0.17	-0.8	-0.1	0.68	0.11	0.43	1.43	-1.49	0.88
Taj Mahal	554	471	10.0	54.2	28.6	2.38	7.23	-0.36	-0.85	-0.15	0.62	0.06	0.50	0.53	1.32	0.61
Taj Mahal	548	478	10.0	53.9	28.3	2.31	7.20	0.71	-0.85	-0.19	0.54	-0.02	0.52	0.54	1.52	0.66
Temple of Doom	556	472	10.3	52.9	28.8	2.52	7.31	-0.67	-0.83	-0.01	0.88	0.3	0.45	0.89	-0.28	0.65
Temple of Doom	555	470	9.9	54.5	28.7	2.25	7.30	-0.51	-0.85	-0.09	0.75	0.17	0.41	0.41	1.54	0.65
The Pit	557	486	10.3	51.3	28.8	2.29	7.35	0.21	-0.83	-0.03	0.82	0.26	0.36	0.81	-1.90	0.69
The Pit	555	484	10.4	53.3	27.8	5.84	7.16	0.43	-0.85	0.19	1.27	0.71	1.45	0.91	0.29	-0.23
The Pit	560	517	10.7	50.2	29.1	2.34	7.26	2.28	-0.81	-0.09	0.67	0.11	0.47	1.26	-3.31	0.81
The Pit	558	483	10.7	51.6	28.3	2.31	7.36	-0.01	-0.82	0	0.88	0.31	0.36	1.26	-1.78	0.05
Deep Saline Zone (>40 m)																
Ak Kimin	567	496	10.2	53.1	29.3	2.18	7.33	0.49	-0.83	-0.06	0.8	0.21	0.37	0.75	-1.05	0.70
Ak Kimin	550	475	10.1	51.4	28.8	2.30	7.38	-0.16	-0.84	0.01	0.93	0.34	0.35	0.60	-1.11	1.00
Ak Kimin	558	498	10.6	53.9	29.0	2.57	7.56	1.56	-0.82	0.28	1.49	0.86	0.26	1.19	0.59	0.76
Ak Kimin	547	482	10.0	50.5	28.4	2.49	7.42	0.55	-0.84	0.08	1.07	0.48	0.35	0.56	-1.69	0.73
Angelita	539	466	20.7	47.1	33.5	4.09	6.94	0.1	-0.47	0.11	0.77	0.2	1.70	11.25	-4.43	6.19
Blue Abyss	571	501	15.2	50.5	31.9	2.37	7.24	0.43	-0.63	0.05	0.82	0.24	0.49	5.79	-4.08	3.01
Sabak Ha	658	527	23.4	49.3	35.2	4.24	6.62	-3.67	-0.42	-0.11	0.32	-0.29	3.802	13.98	-13.56	1.93
The Pit	564	493	11.7	51.3	29.6	2.33	7.30	0.29	-0.77	-0.01	0.8	0.23	0.42	2.23	-2.57	1.14
The Pit	574	497	13.4	51.1	31.1	2.43	7.56	-0.24	-0.69	0.32	1.41	0.83	0.23	3.95	-3.72	2.08
The Pit	563	499	13.4	53.0	29.7	2.45	7.17	1.45	-0.71	-0.06	0.67	0.1	0.60	3.94	-0.77	1.26
The Pit	575	506	14.8	51.4	31.8	2.45	7.13	0.64	-0.64	-0.05	0.64	0.05	0.66	5.33	-3.49	2.77
The Pit	577	502	15.9	51.0	32.4	2.48	7.05	0.08	-0.6	-0.09	0.52	-0.07	0.81	6.43	-4.19	3.27
The Pit	583	494	15.5	52.3	32.3	2.45	7.15	-0.85	-0.62	-0.03	0.64	0.09	0.62	6.03	-3.41	2.86